The Effects of Composition and Heat Treatment on the Microstructure and Performance of Cobalt-based Alloys for Molten Zinc Applications

Swansea University
Prifysgol Abertawe

Luis Escott

Thesis submitted to Swansea University in partial fulfilment of requirements for the degree of Engineering Doctorate

Materials and Manufacturing Academy

College of Engineering – Swansea University

2022

Declarations

This work has not previously been accepted in substance for any degree and is not being concurrently submitted in candidature for any degree.

Signed: Luis Escott

Date: 13/07/2022

This thesis is the result of my own investigations, except where otherwise stated. Other sources are acknowledged by footnotes giving explicit references. A bibliography is appended.

Signed: Luis Escott

Date: 13/07/2022

I hereby give consent for my thesis, if accepted, to be available for photocopying and for inter-library loan, and for the title and summary to be made available to outside organisations.

Signed: Luis Escott

Date: 13/07/2022

Abstract

The purpose of this research was to identify and develop cobalt-based superalloys for journal bearing applications by improving the stability and service life of submerged galvanising pot hardware. To achieve this goal the mechanical properties and chemical resistance of four cast cobalt superalloys were investigated. The alloys were subjected to three heat treatments which included a high temperature annealing treatment, a solution treatment and additional age hardening, and a plasma nitriding treatment. The heat-treated alloys were examined and compared to untreated samples to identify any microstructural changes or improvements in material performance.

Four commercially available cobalt-based superalloys were identified for analysis including three cast CoCrW alloys and one cast CoCrMo Tribaloy. It was identified that increasing the carbon and tungsten content, with the CoCrW alloys, increased the area fraction of chromium and tungsten carbide phases in addition to increasing the concentration of alloying elements retained in solid solution. Both factors contributed to increased material hardness. The substitution of tungsten with molybdenum and the absence of carbon, with the CoCrMo Tribaloy, replaced the formation of eutectic carbides with a primary Laves phase that dominated the Tribaloys microstructure. This provided the CoCrMo alloy with enhanced hardness properties compared to the CoCrW alloys.

The untreated alloys were submerged in a molten zinc alloy bath containing 0.35wt.% Al in a series of static immersion tests where the alloys were submerged for times ranging between 1-4 weeks. All the materials reacted with the molten zinc bath resulting in the diffusion of bath species into the alloys microstructure as well as the leaching of alloying elements into the bath. With each alloy, molten metal ingress preferentially occurred in the cobalt rich solid solution phase whereas the carbide and Laves phases were more resistant to bath reactivity. The high area fraction of Laves phase and increased molybdenum concentrations retained in eutectic solid solution with the T-800 Tribaloy, provided the alloy with enhanced chemical resistance to the bath in comparison to the CoCrW alloys. The improved chemical resistance reduced the depth of diffusion and reduced the quantity of cobalt-aluminide formation at the alloys surface.

A plasma nitriding treatment resulted in the formation of a nitrogen rich diffusion layer at the surface of each of the alloys. Increasing the treatment temperature or treatment time produced a thicker diffusion layer with increased concentrations of nitrogen. The formation a nitride layer significantly improved the surface hardness of each of the alloys where increased material hardness correlated with a thicker diffusion layer.

The plasma treated samples were dip tested in a molten zinc bath containing 0.35wt.% Al. The formation of the nitride diffusion layer improved the long-term chemical performance of

the alloys where reduced zinc and aluminium diffusion depths were recorded with the CoCrW alloys after 4-weeks of testing. The nitride treatment generally improved the surface integrity of the alloys where increased levels of alloying elements were retained within the matrix diffusion layer after prolonged bath exposure and each alloy experienced less material loss. There was also a noticeable reduction in the quantity of cobalt-aluminide phases at the alloy's surfaces.

An annealing heat treatment slightly changed the morphology of the alloy's microstructure where phase precipitation within the solid solution phase occurred in addition to low levels of carbide dissolution. Small improvements in material hardness were recorded with the CoCrW alloys whereas the annealing treatment had detrimental effects on the hardness properties of the CoCrMo alloy. Using the nano-properties of the matrix to calculate the mean *H/E* ratio it was predicted that the wear performance of the matrix of the WT-4 and WT-12 alloys were slightly improved by the annealing process.

A solution treatment significantly changed the microstructure morphology of the WT-6 and WT-12 alloys. The solution treatment resulted in extreme coarsening of the chromium and tungsten carbides with the WT-12 alloy and coarsening of the chromium carbides and the precipitation of tungsten rich phases with the WT-6 alloy. Low levels of carbide dissolution were also recorded. A drop in material hardness was recorded with both alloys after the solution treatment. Additional aging treatments did not significantly alter the alloys microstructures further but precipitation within the matrix occurred. This coincided with significant improvements in the hardness properties of both alloys. Calculating the mean *H/E* ratio of the matrix phase in both alloys estimated that no improvements in matrix wear resistance occurred with WT-6 alloy whereas an improvement with the WT-12 matrix was calculated.

Contents

Abstract 2
Contents 4
List of Figures 9
List of Tables 25
Acknowledgments 28
1 Introduction 29
1.1 Background Information 29
1.2 Scope of Research 31
1.3 Thesis Layout 33
2 Literature Review 35
2.1 Corrosion and Corrosion Protection 35
2.2 Overview of the Continuous Hot Dip Galvanising Line 35
2.3 Coating Metallurgy 37
2.3.1 Inhibition Layer Formation in Pure Zinc Baths 38
2.3.2 Influence of Aluminium Additions on Inhibition Layer Formation 39
2.4 Bath Management and Zn-Fe-Al Ternary Phase Stability and Solubility 40
2.4.1 Intermetallic Phase (Dross) Formation on Pot Hardware 42
2.4.2 Cobalt Aluminide Formation 45
2.5 Materials for High Wear and Temperature Resistant Applications 46
2.5.1 Fundamentals of Tribology 47
2.5.1.1 Principles of Wear 48
2.5.1.1.1 Adhesive Wear 48
2.5.1.1.2 Abrasive Wear 48
2.5.1.1.3 Fatigue Wear 49
2.5.1.1.4 Corrosive Wear 50
2.5.1.2 Lubrication 50
2.5.2 Cobalt and Cobalt-based Superalloys 52
2.5.3 Wear and Chemical Reactivity of Cobalt-based Journal Bearings for Molten Zinc Applications 57
2.5.3.1 Chemical Reactivity of Journal Bearings 58
2.5.3.2 Wear Mechanisms Associated with Journal Bearings 60
2.6 Alloy Modification to Improve Wear and Corrosion Resistance 65

2.6.1 Alloy Chemistry 65
2.6.2 Heat Treatments 67
2.6.2.1 Annealing 67
2.6.2.2 Solution Treatment and Age Hardening 68
2.6.3 Surface Engineering 69
2.6.3.1 Diffusion Methods 70
2.6.3.1.1 Nitriding 70
2.6.3.1.2 Carburizing 71
2.6.3.1.3 Carbonitriding and Nitrocarburizing 71
2.6.3.2 S-phase Formation 72
2.6.3.3 Surface Treatment of Cobalt-based alloys 73
2.6.3.4 Coating Methods 74
2.7 Literature Review Findings 76
3 Experimental and Sample Preparation 78
3.1 Experimental Material 78
3.2 Heat Treatments of CoCrW and CoCrMo Alloys 78
3.2.1 High Temperature Annealing 79
3.2.2 Solid Solution and Age Hardening 79
3.2.3 Plasma Nitriding 80
3.3 Static Immersion Testing 80
3.4 Microstructural Analysis 81
3.4.1 Surface Preparation 81
3.4.2 Secondary Electron Microscopy (SEM) and Energy Dispersion X-Ray Spectroscopy (EDS) 81
3.4.3 Phase Area Fraction Analysis 81
3.5 Hardness Measurements 83
3.5.1 Bulk Hardness and Microhardness Analysis 83
3.5.2 Individual Phase Nanoindentation Analysis 84
3.5.2.1 Oliver-Pharr Analysis Method 85
3.5.2.2 Accelerating Property Mapping (XPM) and in-situ Atomic Force Microscopy (AFM) 86
3.5.2.3 Hardness and Elastic Modulus to Characterise Wear Resistance 88
4 Microstructural Characterisation and Mechanical Performance of As-received CoCrW and CoCrMo Alloys 90

4.1 Microstructural Analysis of Untreated Samples....90
4.1.1 As-received WT-4....90
4.1.2 As-received WT-6....93
4.1.3 As-received WT-12....96
4.1.4 As-received T-800....99
4.2 Comparisons of Investigated Alloy Microstructures....102
4.3 Hardness Investigation of the As-received CoCrW and CoCrMo Alloys....106
4.3.1 Macrohardness and Microhardness Analysis of As-received Alloys....106
4.3.1.1 Hardness Analysis of the As-received WT-4 Alloy....106
4.3.1.2 Hardness Analysis of the As-received WT-6 Alloy....107
4.3.1.3 Hardness Analysis of the As-received WT-12 Alloy....108
4.3.1.4 Hardness Analysis of the As-received T-800 Tribaloy....110
4.3.2 Phase Specific Nanoindentation Analysis of the As-received Alloys....111
4.3.2.1 Nanoindentation Analysis of the As-received WT-4 Alloy....111
4.3.2.2 Nanoindentation Analysis of the As-received WT-6 Alloy....115
4.3.2.3 Nanoindentation Analysis of the As-received WT-12 Alloy....118
4.3.2.4 Nanoindentation Analysis of the As-received T-800 Tribaloy....122
4.3.3 Comparisons of Hardness Trends observed in the As-received Alloys....125
4.3.3.1 Bulk Hardness Analysis....125
4.3.3.2 Microhardness Analysis....126
4.3.3.3 Nanoindentation Analysis....127
4.4 Bearing Reactivity with Molten Zinc....131
4.4.1 Static Immersion Testing of the As-received WT-6 Alloy....131
4.4.2 Static Immersion Testing of As-received WT-4....139
4.4.3 Static Immersion Testing of As-received WT-12....146
4.4.4 Static Immersion Testing of As-received T-800....152
4.5 Comparisons of the Chemical Reactivity of the As-received Alloys....158
5 Microstructural and Mechanical Properties of Plasma Nitrided Samples....167
5.1 Surface Modification of the Plasma Nitrided Samples....167
5.2 Compositional Analysis of the Modified Surface Layer....170
5.2.1 Plasma Treated WT-4....170
5.2.2 Plasma Treated WT-6....174
5.2.3 Plasma Treated WT-12....179
5.2.4 Plasma Treated T-800....184

5.3 Thickness of Diffusion Layer 189
5.4 Hardness Investigation of the Modified Surface Layer 192
5.4.1 Surface Hardness of Plasma Treated Samples 192
5.5 Comparisons of Composition and Hardness Trends Observed with the Formation of a Diffusion Layer in the Plasma Treated Alloys 195
5.6 Static Immersion Dip Testing of Plasma Treated CoCrW and CoCrMo Alloys 199
5.6.1 Static Immersion Testing of Plasma Treated WT-6 199
5.6.2 Static Immersion Testing of Plasma Treated WT-4 207
5.6.3 Static Immersion Testing of Plasma Treated WT-12 218
5.6.4 Static Immersion Testing of Plasma Treated T-800 Tribaloy 226
5.7 Comparisons of the Chemical Reactivity of the Plasma Treated Alloys 234
5.8 Comparisons of Untreated and Plasma Treated Alloys 240
5.8.1 Untreated WT-6 samples vs Plasma Nitride WT-6 Samples 240
5.8.2 Untreated WT-4 Samples vs Plasma Nitride WT-4 Samples 243
5.8.3 Untreated WT-12 Samples vs Plasma Nitride WT-12 Samples 245
5.8.4 Untreated T-800 Samples vs Plasma Nitride T-800 Samples 247
6 Effect of High Temperature Thermal (Annealing) Treatments on the Microstructure and Mechanical Performance of Alloy Samples 250
6.1 High Temperature Annealing Heat Treatment 250
6.1.1 Microstructure Analysis of Annealed WT-4 250
6.1.2 Microstructure Analysis of Annealed WT-6 254
6.1.3 Microstructure Analysis of Annealed WT-12 257
6.1.4 Microstructure Analysis of Annealed T-800 261
6.1.5 Hardness Variation with Annealing Heat Treatment 265
6.1.5.1 Macrohardness and Microhardness Analysis of Annealed WT-4 ... 265
6.1.5.1.1 Phase Specific Nanoindentation Analysis of WT-4 267
6.1.5.2 Macrohardness and Microhardness Analysis of Annealed WT-6 ... 272
6.1.5.2.1 Phase Specific Nanoindentation Analysis of WT-6 273
6.1.5.3 Macrohardness and Microhardness Analysis of Annealed WT-12 . 277
6.1.5.3.1 Phase Specific Nanoindentation Analysis of WT-12 279
6.1.5.4 Macrohardness and Microhardness Analysis of Annealed T-800 ... 284
6.1.5.4.1 Phase Specific Nanoindentation Analysis of T-800 286
6.1.6 Comparisons of Changes in Microstructure Morphology and Hardness Trends Observed After a High Temperature Annealing Treatment 290

6.2 Solid Solution and Age Hardening Heat Treatment 293
6.2.1 Microstructure Analysis of Age Hardened WT-4 293
6.2.2 Microstructure Analysis of Age Hardened WT-6 294
6.2.3 Microstructure Analysis of Age Hardened WT-12 297
6.2.4 Hardness Variation of Age Hardened Samples 300
6.2.4.1 Macrohardness and Microhardness Analysis Age Hardened WT-6 300
6.2.4.1.1 Phase Specific Nanoindentation Analysis of WT-6 302
6.2.4.2 Macrohardness and Microhardness Analysis of Age Hardened WT-12 305
6.2.4.2.1 Phase Specific Nanoindentation Analysis of WT-12 306
6.2.5 Comparisons of Changes in Microstructure and Hardness Trends Observed After Solid Solution and Aging Heat Treatment 309
7 Discussion 312
7.1 Untreated Alloys 312
7.2 Plasma Nitride Heat Treatment 313
7.3 Annealing Heat Treatment 315
7.4 Solution and Aging Treatment 317
8 Conclusions and Future Work 319
8.1 Conclusions 319
8.2 Future Work 321
8.2.1 Bearing Wear Testing Rig 322
References 324

List of Figures

Figure 2.1: Typical continuous hot-dip galvanising line. 37

Figure 2.2: a) Image of gas knives and b) schematic of their configuration. 37

Figure 2.3: Zinc-rich corner of the binary Fe-Zn phase diagram 38

Figure 2.4: Zinc-rich corner of the Zn-Al-Fe ternary phase diagram 40

Figure 2.5: a) Image of pot gear and b) schematic of pot gear configuration 44

Figure 2.6 Dross buildup on outer edge of stabilising roll not in contact with strip. 45

Figure 2.7: Example of a sleeve and bush component that forms the journal bearing. 46

Figure 2.8: The Zn-Fe-Co-Al quaternary system at 460℃. 46

Figure 2.9: Example of pressure field generated in journal bearing during operation. 52

Figure 2.10: Stribeck curve demonstrating regimes of lubrication. 52

Figure 2.11: Microstructural analysis of a) Stellite 3 and b) Stellite 6. 56

Figure 2.12: Low stress abrasion data for various cobalt-based alloys demonstrating the importance of carbides and Lave phases. 57

Figure 2.13: Microstructural analysis of a T-800 Tribaloy 57

Figure 2.14: Cobalt aluminide formation on the surface of cobalt-based superalloy after 2-weeks of bath immersion 59

Figure 2.15: a) Weight loss experienced by various alloys after 500h of static dip testing in a molten zinc bath containing 0.15wt.% Al at 465℃ and b) reaction layer thickness as a function of time in a bath containing 0.22wt.% Al. 60

Figure 2.16: Sleeve component before and after a 4-week campaign transitioning between GI and GA bath chemistry: a) Cast sleeve component, b) campaigned sleeve component illustrating material removal and c) campaigned bush component 63

Figure 2.17: Width and depth of surface grooving after testing in bath containing various amounts of aluminium and iron 63

Figure 2.18: Worn surface of various cobalt-based sleeve components after a 4-week campaign 64

Figure 2.19: Fatigue wear resulting in crack formation and material detachment: a) Pickled sample illustrating fatgiue wear and b) Unpickled sample illustrating detached material reacting with the bath…..64

Figure 2.20: CoAl build-up on surface of tested Stellite 6 journal bearing components: a) optical surface view and b) cross section view 64
Figure 2.21: Charpy impact test on un-notched samples. 66
Figure 2.22: comparison of cast and annealed Stellite 6 alloys containing 5wt.% silicon: a) cast sample and b) sample heated to 1000℃ for 30minutes and air cooled. 68
Figure 2.23: Comparison of as-cast alloy and solution treated alloy: a) as-cast alloy and b) alloy after solution treatment at 1280℃ for 4-hours. 69
Figure 2.24: Cross sectional analysis of PSA samples after a 15-hour treatment: a) 460℃ and b) 550℃….74
Figure 3.1: Sectioned sample. 78
Figure 3.2: Example of ImageJ threshold analysis used to calculate the area fraction of specific phases of the alloy's microstructure: a) SEM image of sample, b) area fraction analysis of specific phase and c) Threshold selection. 82
Figure 3.3: Example of ImageJ threshold analysis used to calculate the area fraction of precipitated phases within the cobalt solid solution phase: a) selected area of interest, b) exclusion of everything outside of this area and c) threshold analysis of precipitates within this area. 83
Figure 3.4: Control displacement test to determine appropriate contact force: a) Force vs displacement curves and b) Modulus vs contact depth and c) hardness vs contact depth. 84
Figure 3.5: Typical load-displacement curve produced from nanoindentation 86
Figure 3.6: In-situ SPM topography scan of sample surface after XPM analysis: a) topography scan, b) corresponding mechanical property map, c) selected data points and d) data produced from XPM analysis. 87
Figure 3.7: XPM analysis of cobalt matrix: a) location of XPM analysis and b) load displacement curves for individual indents 88
Figure 4.1: SEM and EDS analysis of the as-received WT-4 alloy illustrating elemental concentration of individual phases. 91
Figure 4.2: Phase composition analysis of as-received WT-4 alloy: Point scan locations and calculated compositions where M = solid solution in the matrix and E = solid solution in the eutectic region. 92
Figure 4.3: Phase area fraction analysis of the as-received WT-4 alloy: ImageJ analysis of SEM image and calculated area fraction of each phase. 92

Figure 4.4: SEM and EDS analysis of the as-received WT-6 alloy illustrating elemental concentration of individual phases. 94
Figure 4.5: Phase composition analysis of as-received WT-6 alloy: Point scan locations and calculated compositions. 95
Figure 4.6. Phase area fraction analysis of the as-received WT-6 alloy: ImageJ analysis of SEM image and Calculated volume fraction of each phase. 95
Figure 4.7 SEM and EDS analysis of the as-received WT-12 alloy illustrating elemental concentration of individual phases. 97
Figure 4.8: Phase composition analysis of as-received WT-12 alloy: Point scan locations and calculated compositions. 98
Figure 4.9: High magnification SEM analysis of the tungsten carbide in the as-received WT-12 alloy. 98
Figure 4.10. Phase area fraction analysis of the as-received WT-12 alloy: ImageJ analysis of SEM image and calculated volume fraction of each phase. 99
Figure 4.11: SEM and EDS analysis of the as-received T-800 Tribaloy illustrating elemental concentration of individual phases. 100
Figure 4.12: Phase composition analysis of as-received T-800 Tribaloy: a) Point scans locations at low magnification, b) Point scan location at high magnification illustrating molybdenum dispersion in the eutectic matrix and calculated compositions. 101
Figure 4.13: Phase area fraction analysis of the as-received T-800 Tribaloy: ImageJ analysis of SEM image and calculated volume fraction of each phase. 102
Figure 4.14: Area fraction analysis of individual phases found in the as received alloys. 104
Figure 4.15: Composition of the cobalt matrix in the as-received CoCrW alloys. 105
Figure 4.16: Composition of the chromium and tungsten carbide phases in the as-received CoCrW alloys. 105
Figure 4.17: Compositional analysis of the phases in the as-received T-800 Tribaloy. 106
Figure 4.18: Surface hardness indentations on the as-received WT-4 alloy: a) Solid solution matrix, b) eutectic region and c) Bulk hardness indentation. 107
Figure 4.19: Surface hardness indentations on the as-received WT-6 alloy: a) Solid solution matrix, b) Chromium carbide network and c) Bulk hardness indentation. 108

Figure 4.20: Surface hardness indentations on the as-received WT-12 alloy: a) Solid solution matrix, b) Tungsten carbide network, c) Chromium carbide and d) Bulk hardness indentation. 109
Figure 4.21: Surface hardness indentations on the as-received T-800 Tribaloy: a) Primary Laves phase, b) Eutectic (Cr-rich), c) Eutectic region (Mo-rich) and d) Bulk hardness of alloy. 110
Figure 4.22: Loading/unloading curve for the cobalt solid solution phase of the as-received WT-4 alloy. 112
Figure 4.23: Nanoindentation analysis of the as-received WT-4 alloy: a) SPM surface image of matrix and eutectic region, b) XPM hardness map, c) XPM hardness histogram, d) XPM modulus map and e) XPM modulus histogram. 113
Figure 4.24: Nanoindentation analysis of the eutectic region of the as-received WT-4 alloy: a) SPM surface image of matrix and eutectic region, b) XPM hardness map, c) XPM hardness histogram, d) XPM modulus map and e) XPM modulus histogram. 114
Figure 4.25: Loading/unloading curves of individual phases of the as-received WT-6 alloy. 116
Figure 4.26: Nanoindentation analysis of the as-received WT-6 alloy: a) SPM surface image of matrix and chromium carbide, b) XPM hardness map, c) XPM hardness histogram, d) XPM modulus map and e) XPM modulus histogram. 117
Figure 4.27: Loading/unloading curves of individual phases of the as-received WT-12 alloy. 119
Figure 4.28: Nanoindentation analysis of the as-received WT-12 alloy: a) SPM surface image of matrix and chromium and tungsten carbides, b) XPM hardness map, c) XPM hardness histogram, d) XPM modulus map and e) XPM modulus histogram. 120
Figure 4.29: Nanoindentation analysis of the as-received WT-12 alloy: a) SPM surface image of the tungsten carbide network, b) XPM hardness map, c) XPM hardness histogram, d) XPM modulus map and e) XPM modulus histogram. 121
Figure 4.30: Loading/unloading curves of individual phases of the as-received T-800 Tribaloy. 123
Figure 4.31: Nanoindentation analysis of the as-received T-800 Tribaloy: a) SPM surface image of the eutectic matrix phases and Laves phase, b) XPM hardness map, c) XPM hardness histogram, d) XPM modulus map and e) XPM modulus histogram. 124
Figure 4.32: Average bulk hardness for the as-received alloys 126

Figure 4.33: Material bulk hardness correlation to the area fraction of carbides or Laves phases present in the microstructure of the as-received alloys. 126
Figure 4.34: Microhardness of the matrix in the As-received alloys. 127
Figure 4.35: Box plot analysis of XPM data for individual phases: a) Matrix hardness, b) Matrix modulus, c) Carbides/Laves hardness and d) Carbides/Laves modulus..... 130
Figure 4.36: Mean H/E ratio of individual phases: a) Matrix phases and b) Carbides/Laves phases. 131
Figure 4.37: Surface condition of the as-received WT-6 alloy after 1-4-week dip testing in a molten zinc bath containing 0.35wt.% Al and saturated with Fe: a) Week 1, b) Week 2, c) Week 3 and d) Week 4. 135
Figure 4.38: Average diffusion depth of the as-received WT-6 alloy after prolonged dip testing in a molten zinc bath containing 0.35wt.% Al and saturated with Fe. 135
Figure 4.39: EDS elemental mapping of the as-received WT-6 alloy after 2-weeks of dip testing in a molten zinc bath containing 0.35wt.% Al and saturated with Fe. 136
Figure 4.40: EDS point scan analysis of the diffusion zone of the as-received WT-6 alloy after 2-weeks of bath immersion: a) Point scan locations and b) Corresponding point scan compositions. 137
Figure 4.41: EDS point scan analysis of the diffusion zone of the as-received WT-6 alloy after 4-weeks of bath immersion: a) Point scan locations, b) EDS map illustrating chromium-rich layer at the surafce, c) High magnification of discrete phase formation and d) Corresponding point scan compositions. 138
Figure 4.42: Surface condition of the as-received WT-4 alloy after 1-4-week dip testing in a molten zinc bath containing 0.35wt.% Al and saturated with Fe: a) Week 1, b) Week 2, c) Week 3 and d) Week 4. 142
Figure 4.43: Average diffusion depth of the as-received WT-4 alloy after prolonged dip testing in a molten zinc bath containing 0.35wt.% Al and saturated with Fe. 142
Figure 4.44: EDS elemental mapping of the as-received WT-4 alloy after 2 weeks of dip testing in a molten zinc bath containing 0.35wt.% Al and saturated with Fe. 144
Figure 4.45: EDS point scan analysis of the diffusion zone of the as-received WT-4 alloy after 2-weeks of bath immersion: a) Point scan locations and b) Corresponding point scan compositions. 144
Figure 4.46: EDS point scan analysis of the diffusion zone of the as-received WT-4 alloy after 4-weeks of bath immersion: a) Point scan locations and b) Corresponding point scan compositions. 145
Figure 4.47: High magnification SEM analysis of the diffusion zone of the as-received WT-4 alloy after 2-weeks of bath immersion illustrating diffusion propagation through the eutectic region. 145

Figure 4.48: Surface condition of the as-received WT-12 alloy after 1-4-week dip testing in a molten zinc bath containing 0.35wt.% Al and saturated with Fe: a) Week 1, b) Week 2, c) Week 3 and d) Week 4. 148
Figure 4.49: Average diffusion depth of the as-received WT-12 alloy after prolonged dip testing in a molten zinc bath containing 0.35wt.% Al and saturated with Fe. 149
Figure 4.50: EDS elemental mapping of the as-received WT-12 alloy after 2 weeks of dip testing in a molten zinc bath containing 0.35wt.% Al and saturated with Fe. 150
Figure 4.51: EDS point scan analysis of the diffusion zone of the as-received WT-12 alloy after 2-weeks of bath immersion: a) Point scan locations and b) Corresponding point scan compositions. 151
Figure 4.52 EDS point scan analysis of the diffusion zone of the as-received WT-12 alloy after 4-weeks of bath immersion: a) Point scan locations and b) Corresponding point scan compositions. 151
Figure 4.53: EDS point scan analysis of the diffusion zone of the as-received WT-12 alloy after 4-weeks of bath immersion: a) High magnification of chromium-rich regions in the diffusion layer and d) Corresponding point scan compositions. 152
Figure 4.54: Surface condition of the as-received T-800 Tribaloy after 1-4-week dip testing in a molten zinc bath containing 0.35wt.% Al and saturated with Fe: a) Week 1, b) Week 2, c) Week 3 and d) Week 4. 155
Figure 4.55: Average diffusion depth of the as-received T-800 Tribaloy after prolonged dip testing in a molten zinc bath containing 0.35wt.% Al and saturated with Fe. 155
Figure 4.56: EDS elemental mapping of the as-received T-800 Tribaloy after 2 weeks of dip testing in a molten zinc bath containing 0.35wt.% Al and saturated with Fe. 157
Figure 4.57: EDS point scan analysis of the diffusion zone of the as-received T-800 Tribaloy after 2-weeks of bath immersion: a) Point scan locations and b) Corresponding point scan compositions. 157
Figure 4.58: EDS point scan analysis of the diffusion zone of the as-received T-800 Tribaly after 4-weeks of bath immersion: a) Point scan locations and b) Corresponding point scan compositions. 158
Figure 4.59: Schematic diagram illustrating the diffusion mechanisms within CoCrW alloys immersed in a molten bath containing 0.35wt.% Al and saturated with Fe. 163
Figure 4.60: Schematic diagram illustrating the diffusion mechanisms within CoCrW alloys immersed in a molten bath containing 0.35wt.% Al and saturated with Fe. 164
Figure 4.61: EDS line scan analysis of the diffusion zone of the as-received WT-6 alloy after 2-weeks of bath immersion illustrating the diffusion process 165

Figure 4.62: High magnification SEM analysis of the diffusion zone of the as-received WT-4 alloy after 3-weeks of bath immersion illustrating how CoAl formation restricts the diffusion process. 165
Figure 4.63: Average diffusion depth of the as-received alloys after prolonged dip testing in a molten zinc bath containing 0.35wt.% Al and saturated with Fe. 166
Figure 5.1: SEM analysis of samples plasma treated for 15 hours at different temperatures: a) WT-4/400°C, b) WT-4/550°C, c) WT-6/400°C, d) WT-6/550°C, e) WT-12/400°C, f) WT-12/550°C, g) T-800/400°C and h) T-800/550°C. 168
Figure 5.2: SEM analysis of samples plasma treated at 475°C for different periods of time: a) WT-4/10h, b) WT-4/20h, c) WT-6/10h, d) WT-6/20h, e) WT-12/10h, f) WT-12/20h, g) T-800/10h and h) T-800/20h. 169
Figure 5.3: SEM and EDS analysis of WT-4 samples treated at 400°C and 550°C for 15-hours illustrating surface diffusion: a) SEM image of sample treated at 400°C, b) Corresponding nitrogen EDS map, c) Corresponding iron EDS map, d) Corresponding oxygen EDS map, e) SEM image of sample treated at 550°C, f) Corresponding nitrogen EDS map, g) Corresponding nitrogen EDS map and h) Corresponding oxygen EDS map..... 172
Figure 5.4: EDS point scan analysis of nitrogen-rich diffusion layer at the surface of a WT-4 sample after nitriding at 550ºC for 15-hours: a) Point scan locations and b) Corresponding point scan compositions. 173
Figure 5.5: Normalised elemental content for treated WT-4 samples after various plasma nitride heat treatments using GDOES analysis: a) 15-hours at 400°C, b) 15-hours at 550°C, c) 475°C for 10-hours and d) 475°C for 20-hours. 173
Figure 5.6: EDS point scan analysis phase formation at the surface of a WT-4 sample after nitriding at 550ºC for 15-hours: a) Point scan locations and b) Corresponding point scan compositions. 174
Figure 5.7: SEM and EDS analysis of WT-6 samples treated at 400°C and 550°C for 15-hours illustrating surface diffusion: a) SEM image of sample treated at 400°C, b) Corresponding nitrogen EDS map, c) Corresponding iron EDS map, d) Corresponding oxygen EDS map, e) SEM image of sample treated at 550°C, f) Corresponding nitrogen EDS map, g) Corresponding iron EDS map and h) Corresponding oxygen EDS map. 177

Figure 5.8: EDS point scan analysis of nitrogen-rich diffusion layer at the surface of a WT-6 sample after nitriding at 550ºC for 15-hours: a) Point scan locations and b) Corresponding point scan compositions. 178
Figure 5.9: Normalised elemental content for treated WT-6 samples after various plasma nitride heat treatments using GDOES analysis: a) 15-hours at 400°C, b) 15-hours at 550°C, c) 475°C for 10-hours and d) 475°C for 20-hours. 178
Figure 5.10: EDS point scan analysis phase formation at the surface of a WT-6 sample after nitriding at 550ºC for 15-hours: a) Point scan locations and b) Corresponding point scan compositions. 179
Figure 5.11: SEM and EDS analysis of WT-12 samples treated at 400°C and 550°C for 15-hours illustrating surface diffusion: a) SEM image of sample treated at 400°C, b) Corresponding nitrogen EDS map, c) Corresponding iron EDS map, d) Corresponding oxygen EDS map, e) SEM image of sample treated at 550°C, f) Corresponding nitrogen EDS map, g) Corresponding nitrogen EDS map and h) Corresponding oxygen EDS map..... 181
Figure 5.12: EDS point scan analysis of nitrogen-rich diffusion layer at the surface of a WT-12 sample after nitriding at 550ºC for 15-hours: a) Point scan locations and b) Corresponding point scan compositions. 182
Figure 5.13: Normalised elemental content for treated WT-12 samples after various plasma nitride heat treatments using GDOES analysis: a) 15-hours at 400°C, b) 15-hours at 550°C, c) 475°C for 10-hours and d) 475°C for 20-hours. 183
Figure 5.14: EDS point scan analysis phase formation at the surface of a WT-12 sample after nitriding at 550ºC for 15-hours: a) Point scan locations and b) Corresponding point scan compositions. 184
Figure 5.15: SEM and EDS analysis of T-800 samples treated at 400°C and 550°C for 15-hours illustrating surface diffusion: a) SEM image of sample treated at 400°C, b) Corresponding nitrogen EDS map, c) Corresponding iron EDS map, d) Corresponding oxygen EDS map, e) SEM image of sample treated at 550°C, f) Corresponding nitrogen EDS map, g) Corresponding nitrogen EDS map and h) Corresponding oxygen EDS map..... 186
Figure 5.16: EDS point scan analysis of nitrogen-rich diffusion layer at the surface of a T-800 sample after nitriding at 550ºC for 15-hours: a) Point scan locations and b) Corresponding point scan compositions. 187

Figure 5.17: Normalised elemental content for treated T-800 samples after various plasma nitride heat treatments using GDOES analysis: a) 15-hours at 400°C, b) 15-hours at 550°C, c) 475°C for 10-hours and d) 475°C for 20-hours. 188
Figure 5.18: Etched T-800 sample illustrating nitrogen diffusion around the circumference of primary Laves phases. 188
Figure 5.19: EDS point scan analysis phase formation at the surface of a T-800 sample after nitriding at 550ºC for 15-hours: a) Point scan locations and b) Corresponding point scan compositions. 189
Figure 5.20: Nitrogen diffusion depths recorded after each plasma nitride treatment for each alloy. 191
Figure 5.21: Nitrogen diffusion depths recorded for each alloy after a 15-hour plasma nitride treatment at various temperatures. 192
Figure 5.22: Nitrogen diffusion depths recorded for each alloy after each plasma treatment: a) Test 1 – changing treatment temperature and b) Test 2 – changing treatment time. 192
Figure 5.23: Changes in bulk hardness and microhardness after each treatment. 194
Figure 5.24: Changes in material hardness experienced for each alloy after each plasma treatment: a) Test 1 – changing treatment temperature and b) test 2 – changing treatment time. 195
Figure 5.25: Correlation between changes in material bulk hardness and microhardness with increased depth of the nitride layer. 198
Figure 5.26: Surface condition of the plasma treated WT-6 alloy after 1-4-week dip testing in a molten zinc bath containing 0.35wt.% Al and saturated with Fe: a) Week 1, b) Week 2, c) Week 3 and d) Week 4. 201
Figure 5.27: Average diffusion depth of the plasma treated WT-6 alloy after prolonged dip testing in a molten zinc bath containing 0.35wt.% Al and saturated with Fe. 202
Figure 5.28: EDS elemental mapping of a plasma treated WT-6 alloy after 2 weeks of dip testing in a molten zinc bath containing 0.35wt.% Al and saturated with Fe. 203
Figure 5.29: EDS point scan analysis of the diffusion zone of the plasma treated WT-6 alloy after 2-weeks of bath immersion: a) Point scan locations and b) Corresponding point scan compositions. 204
Figure 5.30: EDS elemental mapping of a plasma treated WT-6 alloy after 4-weeks of dip testing in a molten zinc bath containing 0.35wt.% Al and saturated with Fe. 206
Figure 5.31: EDS point scan analysis of the diffusion zone of the plasma treated WT-6 alloy after 4-weeks of bath immersion: a) Point scan locations and b) Corresponding point scan compositions. 206

Figure 5.32: Surface condition of the plasma treated WT-4 alloy after 1-4-week dip testing in a molten zinc bath containing 0.35wt.% Al and saturated with Fe: a) Week 1, b) Week 2, c) Week 3 and d) Week 4. 210
Figure 5.33: Average diffusion depth of the plasma treated WT-4 alloy after prolonged dip testing in a molten zinc bath containing 0.35wt.% Al and saturated with Fe. 210
Figure 5.34: EDS elemental mapping of a plasma treated WT-4 alloy after 2-weeks of dip testing in a molten zinc bath containing 0.35wt.% Al and saturated with Fe. 212
Figure 5.35: EDS point scan analysis of the diffusion zone of the plasma treated WT-4 alloy after 2-weeks of bath immersion: a) Point scan locations and b) Corresponding point scan compositions. 212
Figure 5.36: EDS elemental mapping of a plasma treated WT-4 alloy after 4-weeks of dip testing in a molten zinc bath containing 0.35wt.% Al and saturated with Fe illustrating the formation of a CrSi phase. 214
Figure 5.37: EDS point scan analysis of the diffusion zone of the plasma treated WT-4 alloy after 4-weeks of bath immersion: a) Point scan locations and b) Corresponding point scan compositions..... 215
Figure 5.38: EDS elemental mapping of a plasma treated WT-4 alloy after 4-weeks of dip testing in a molten zinc bath containing 0.35wt.% Al and saturated with Fe illustrating an isolated diffusion front (D1) within the diffusion layer. 217
Figure 5.39: EDS point scan analysis of the diffusion zone of the plasma treated WT-4 alloy after 4-weeks of bath immersion: a) Point scan locations and b) Corresponding point scan compositions. 218
Figure 5.40: Surface condition of the plasma treated WT-12 alloy after 1-4-week dip testing in a molten zinc bath containing 0.35wt.% Al and saturated with Fe: a) Week 1, b) Week 2, c) Week 3 and d) Week 4. 221
Figure 5.41: Average diffusion depth of the plasma treated WT-12 alloy after prolonged dip testing in a molten zinc bath containing 0.35wt.% Al and saturated with Fe. 221
Figure 5.42: EDS elemental mapping of a plasma treated WT-12 alloy after 2-weeks of dip testing in a molten zinc bath containing 0.35wt.% Al and saturated with Fe. 223
Figure 5.43: EDS point scan analysis of the diffusion zone of the plasma treated WT-12 alloy after 2-weeks of bath immersion: a) Point scan locations and b) Corresponding point scan compositions..... 223
Figure 5.44: EDS elemental mapping of a plasma treated WT-12 alloy after 4-weeks of dip testing in a molten zinc bath containing 0.35wt.% Al and saturated with Fe. 225

Figure 5.45: EDS point scan analysis of the diffusion zone of the plasma treated WT-12 alloy after 4-weeks of bath immersion: a+b) Point scan locations and c) Corresponding point scan compositions..... 226
Figure 5.46: Surface condition of the plasma treated T-800 Tribaloy after 1-4-week dip testing in a molten zinc bath containing 0.35wt.% Al and saturated with Fe: a) Week 1, b) Week 2, c) Week 3 and d) Week 4. 229
Figure 5.47: Average diffusion depth of the plasma treated T-800 Tribaloy after prolonged dip testing in a molten zinc bath containing 0.35wt.% Al and saturated with Fe. 229
Figure 5.48: EDS elemental mapping of a plasma treated T-800 Tribaloy after 2-weeks of dip testing in a molten zinc bath containing 0.35wt.% Al and saturated with Fe. 231
Figure 5.49: EDS point scan analysis of the diffusion zone of the plasma treated T-800 Tribaloy after 2-weeks of bath immersion: a) Point scan locations and and b) Corresponding point scan compositions. . 231
Figure 5.50: EDS elemental mapping of a plasma treated T-800 Tribaloy after 4-weeks of dip testing in a molten zinc bath containing 0.35wt.% Al and saturated with Fe. 233
Figure 5.51: EDS point scan analysis of the diffusion zone of the plasma treated T-800 Tribaloy after 4-weeks of bath immersion: a+b) Point scan locations and c) Corresponding point scan compositions. 234
Figure 5.52: Schematic diagram illustrating the diffusion mechanisms within plasma treated CoCrW alloys immersed in a molten bath containing 0.35wt.% Al and saturated with Fe. 238
Figure 5.53: Schematic diagram illustrating the diffusion mechanisms within a plasma treated CoCrMo alloy immersed in a molten bath containing 0.35wt.% Al and saturated with Fe. 239
Figure 5.54: Average diffusion depth of the plasma treated alloys after prolonged dip testing in a molten zinc bath containing 0.35wt.% Al and saturated with Fe. 240
Figure 5.55: Surface comparisons of untreated and plasma treated WT-6 samples after different stages of dip testing in a molten zinc bath containing 0.35wt.% Al and saturated with Fe: a) Untreated sample after 2-weeks, b) Plasma treated sample after 2-weeks, c) Untreated sample after 4-weeks and d) Plasma treated sample after 4-weeks. 242
Figure 5.56: Average diffusion depth comparison between untreated and plasma treated WT-6 samples after prolonged dip testing in a molten zinc bath containing 0.35wt.% Al and saturated with Fe. 242
Figure 5.57: Surface comparisons of untreated and plasma treated WT-4 samples after different stages of dip testing in a molten zinc bath containing 0.35wt.% Al and saturated with Fe: a) Untreated sample after

2-weeks, b) Plasma treated sample after 2-weeks, c) Untreated sample after 4-weeks and d) Plasma treated sample after 4-weeks. 244
Figure 5.58: Nitride layer of a treated sample indicating signs of resistance to the diffusion of bath species. 245
Figure 5.59: Average diffusion depth comparison between untreated and plasma treated WT-4 samples after prolonged dip testing in a molten zinc bath containing 0.35wt.% Al and saturated with Fe. 245
Figure 5.60: Surface comparisons of untreated and plasma treated WT-12 samples after different stages of dip testing in a molten zinc bath containing 0.35wt.% Al and saturated with Fe: a) Untreated sample after 2-weeks, b) Plasma treated sample after 2-weeks, c) Untreated sample after 4-weeks and d) Plasma treated sample after 4-weeks. 247
Figure 5.61: Average diffusion depth comparison between untreated and plasma treated WT-12 samples after prolonged dip testing in a molten zinc bath containing 0.35wt.% Al and saturated with Fe. 247
Figure 5.62: Surface comparisons of untreated and plasma treated T-800 samples after different stages of dip testing in a molten zinc bath containing 0.35wt.% Al and saturated with Fe: a) Untreated sample after 2-weeks, b) Plasma treated sample after 2-weeks, c) Untreated sample after 4-weeks and d) Plasma treated sample after 4-weeks. 249
Figure 5.63: Average diffusion depth comparison between untreated and plasma treated T-800 samples after prolonged dip testing in a molten zinc bath containing 0.35wt.% Al and saturated with Fe. 249
Figure 6.1: SEM microstructural analysis of WT-4 samples annealed at 1000°C for different times and different cooling processes with comparisons made to an untreated sample: a) Untreated, b) 1-hour and furnace cooled, c) 2-hours and furnace cooled, d) 4-hours at 1000°C. e) 1-hour and water quenched. ... 252
Figure 6.2: Comparisons of matrix phase precipitation after annealing at 1000°C: a) 1-hour and b) 4-hours. 253
Figure 6.3: EDS point scan analysis of a furnace cooled WT-4 sample after annealing at 1000ºC for 4-hours: a) Point scan locations and b) Corresponding point scan compositions. 253
Figure 6.4: SEM microstructural analysis of WT-4 samples annealed at 1000°C for 2-hours highlighting coarsening of the eutectic phases. 254
Figure 6.5: Crack propagation through microstructure of a water quenched WT-4 sample after annealing at 1000ºC for 1-hour 254

Figure 6.6: SEM microstructural analysis of WT-6 samples annealed at 1000°C for different times and different cooling processes with comparisons made to an untreated sample: a) Untreated, b) 1-hour and furnace cooled, c) 2-hours and furnace cooled, d) 4-hours at 1000°C. e) 1-hour and water quenched. ... 256
Figure 6.7: EDS point scan analysis of a furnace cooled WT-6 sample after annealing at 1000ºC for 4-hours: a) Point scan locations and b) Corresponding point scan compositions. ... 257
Figure 6.8: SEM microstructural analysis of WT-12 samples annealed at 1000°C for different times and different cooling processes with comparisons made to an untreated sample: a) Untreated, b) 1-hour and furnace cooled, c) 2-hours and furnace cooled, d) 4-hours at 1000°C. e) 1-hour and water quenched. ... 259
Figure 6.9: EDS point scan analysis of a furnace cooled WT-12 sample after annealing at 1000ºC for 4-hours: a) Point scan locations and b) Corresponding point scan compositions. ... 260
Figure 6.10: Comparisons of matrix phase precipitation after annealing at 1000°C: a) 1-hour and b) 4-hours. ... 261
Figure 6.11: Crack propagation through microstructure of a water quenched WT-12 sample after annealing at 1000ºC for 1-hour. ... 261
Figure 6.12: SEM microstructural analysis of T-800 samples annealed at 1000°C for different times and different cooling processes with comparisons made to an untreated sample: a) Untreated, b) 1-hour and furnace cooled, c) 2-hours and furnace cooled, d) 4-hours at 1000°C. e) 1-hour and water quenched. ... 263
Figure 6.13: EDS point scan analysis of a furnace cooled T-800 sample after annealing at 1000ºC for 4-hours: a) Point scan locations and b) Corresponding point scan compositions. ... 264
Figure 6.14: Crack propagation through microstructure of a water quenched T-800 sample after annealing at 1000ºC for 1-hour. ... 265
Figure 6.15: Changes in material bulk hardness of the WT-4 alloy after annealing at 1000ºC for various periods of time and after different cooling condition ... 266
Figure 6.16: Changes in microhardness of the matrix and eutectic region of the WT-4 alloy after annealing at 1000ºC for various periods of time and after different cooling conditions: a) Matrix and b) Eutectic region. ... 267
Figure 6.17: Nanoindentation analysis of matrix of the untreated and annealed WT-4 samples: a) SPM grid analysis of untreated sample, b and c) Corresponding XPM hardness and modulus maps, d) SPM grid

analysis of sample annealed at 1000℃ for 4-hours and e and f) Corresponding XPM hardness and modulus map. 270
Figure 6.18: Distribution of hardness and modulus data after each treatment calculated from XMP analysis: a and b) distribution of hardness data and c and d) distribution of modulus data. 271
Figure 6.19: Matrix H/E ratios after various annealing times at 1000°C. 271
Figure 6.20: Changes in material bulk hardness of the WT-6 alloy after annealing at 1000ºC for various periods of time and after different cooling condition. 272
Figure 6.21: Changes in microhardness of the matrix of the WT-6 alloy after annealing at 1000ºC for various periods of time and after different cooling conditions. 273
Figure 6.22: Nanoindentation analysis of matrix of the untreated and annealed WT-6 samples: a) SPM grid analysis of untreated sample, b and c) Corresponding XPM hardness and modulus maps, d) SPM grid analysis of sample annealed at 1000℃ for 4-hours and e and f) Corresponding XPM hardness and modulus map. 276
Figure 6.23: Distribution of hardness and modulus data after each treatment calculated from XMP analysis: a and b) distribution of hardness data and c and d) distribution of modulus data. 277
Figure 6.24: Matrix H/E ratios after various annealing times at 1000°C. 277
Figure 6.25: Changes in material bulk hardness of the WT-12 alloy after annealing at 1000ºC for various periods of time and after different cooling condition. 278
Figure 6.26: Changes in microhardness of the matrix phase of the WT-12 alloy after annealing at 1000ºC for various periods of time and after different cooling conditions. 279
Figure 6.27: Nanoindentation analysis of matrix of the untreated and annealed WT-12 samples: a) SPM grid analysis of untreated sample, b and c) Corresponding XPM hardness and modulus maps, d) SPM grid analysis of sample annealed at 1000℃ for 4-hours and e and f) Corresponding XPM hardness and modulus map. 282
Figure 6.28: Distribution of hardness and modulus data after each treatment calculated from the XMP analysis: a and b) distribution of hardness data and c and d) distribution of modulus data. 283
Figure 6.29: Matrix H/E ratios after various annealing times at 1000°C. 283
Figure 6.30 Changes in material bulk hardness of the WT-12 alloy after annealing at 1000ºC for various periods of time and after different cooling condition. 285

Figure 6.31: Changes in microhardness of the matrix phase and Laves phase of the T-800 Tribaloy after annealing at 1000ºC for various periods of time and after different cooling conditions: a) Matrix and b) Laves phase. 285
Figure 6.32: Nanoindentation analysis of matrix of the untreated and annealed T-800 samples: a) SPM grid analysis of untreated sample, b and c) Corresponding XPM hardness and modulus maps, d) SPM grid analysis of sample annealed at 1000°C for 4-hours and e and f) Corresponding XPM hardness and modulus map. 288
Figure 6.33: Distribution of hardness and modulus data after each treatment calculated from XMP analysis: a and b) distribution of hardness data and c and d) distribution of modulus data. 289
Figure 6.34: Matrix H/E ratios after various annealing times at 1000°C. 290
Figure 6.35: SEM microstructural analysis of WT-4 samples after solution treating at 1275°C for 6-hours and aging at 850°C for different times with comparisons made to an untreated sample: a) Untreated sample, b) Solution treated, c) 2-hour aging, d) 4-hour aging and e) 8-hour aging. 294
Figure 6.36: SEM microstructural analysis of WT-6 samples after solution treating at 1275°C for 6-hours and aging at 850°C for different times with comparisons made to an untreated sample: a) Untreated sample, b) Solution treated, c) 2-hour aging, d) 4-hour aging and e) 8-hour aging. 296
Figure 6.37: EDS point scan analysis of a WT-6 sample aged for 8-hours at 850ºC: a) Point scan locations and b) Corresponding point scan compositions. 297
Figure 6.38: SEM microstructural analysis of WT-12 samples after solution treating at 1275°C for 6-hours and aging at 850°C for different times with comparisons made to an untreated sample: a) Untreated sample, b) Solution treated, c) 2-hour aging, d) 4-hour aging and e) 8-hour aging. 299
Figure 6.39: a and b) High magnification of WT-12 sample after an 8-hour aging treatment at 850°C illustrating precipitation throughout matrix and at grain boundaries. 300
Figure 6.40: Changes in material bulk hardness and matrix microhardness of the WT-6 alloy after solution treating at 1275ºC for 6-hours and additional aging treatments at 850ºC for various periods of time: a) Bulk hardness and b) matrix microhardness 302
Figure 6.41: Distribution of hardness and modulus data after each treatment calculated from the XMP analysis: a and b) distribution of hardness data and c and d) distribution of modulus data. 304

Figure 6.42: Matrix H/E ratios after a solution treatment at 1275℃ and additional aging treatments at 850℃..... 305
Figure 6.43: Changes in material bulk hardness and matrix microhardness of the WT-6 alloy after solution treating at 1275ºC for 8-hours and additional aging treatments at 850ºC various periods of time: a) Bulk hardness and b) matrix microhardness. 306
Figure 6.44: Distribution of hardness and modulus data after each treatment calculated from the XMP analysis: a and b) distribution of hardness data and c and d) distribution of modulus data. 309
Figure 6.45: Matrix H/E ratios after a solution treatment at 1275℃ and additional aging treatments at 850℃..... 309
Figure 8.1: Bearing wear testing rig and tested journal bearing components: a) Bearing rig, b) stabilising roll sleeve and c) half-moon bushing. 323

List of Tables

Table 2.1: Composition (wt%, Co in balance) of various Stellite alloys. 56

Table 2.2: Composition (wt%) of various Tribaloy alloys and estimated volume fraction of Laves phase. 57

Table 2.3: Hardness of phases that can form in the molten zinc bath with reference to a Stellite 6 alloy... 63

Table 3.1: Chemical compositions (wt%) of cobalt-based alloys used in this study. 78

Table 3.2: High temperature annealing treatment parameters and cooling processes (WQ-water quenched, FC- Furnace cooled). 79

Table 3.3: Solid solution and age hardening treatment parameters repeated for each alloy. 79

Table 3.4: Plasma nitriding heat treatment parameters repeated for each alloy. 80

Table 4.1: Average microhardness (Hv) of microstructural phases/regions and bulk hardness (Hv) of the as-received WT-4 alloy. 107

Table 4.2: Average microhardness (Hv) of microstructural phases/regions and bulk hardness (Hv) of the as-received WT-6 alloy. 108

Table 4.3: Average microhardness (Hv) of microstructural phases/regions and bulk hardness (Hv) of the as-received WT-12 alloy. 109

Table 4.4: Average microhardness (Hv) of microstructural phases/regions and bulk hardness (Hv) of the as-received T-800 Tribaloy. 111

Table 4.5: Average mechanical properties for the cobalt solid solution phase of the as-received WT-4 alloy using single nano-indentation analysis. 112

Table 4.6: Average mechanical properties of the cobalt solid solution phase and eutectic region of the as-received WT-4 alloy using XPM analysis. 115

Table 4.7: Average mechanical properties for the individual phases of the as-received WT-6 alloy using single nano-indentation analysis. 116

Table 4.8: Average mechanical properties of the individual phases of the as-received WT-6 alloy using XPM analysis. 118

Table 4.9: Average mechanical properties for the cobalt solid solution phase and chromium carbides of the as-received WT-12 alloy using single nano-indentation analysis. 119

Table 4.10: Average mechanical properties of the cobalt solid solution phase and carbide phases of the as-received WT-12 alloy using XPM analysis. 122
Table 4.11: Average mechanical properties for the individual phases of the as-received T-800 Tribaloy using single nano-indentation analysis. 123
Table 4.12: Average mechanical properties of the cobalt matrix and Laves phase of the as-received T-800 alloy using XPM analysis. 125
Table 5.1 Highest nitrogen concentrations recorded for each alloy. 199
Table 6.1 Area fraction analysis of matrix after each heat treatment with comparison to an untreated WT-4 sample. 252
Table 6.2: Area fraction analysis of individual phases after each heat treatment with comparison to an untreated WT-6 sample. 256
Table 6.3: Volume fraction analysis of individual phases after each heat treatment with comparison to an untreated WT-12 sample. 260
Table 6.4: Volume fraction analysis of individual phases after each heat treatment with comparison to an untreated T-800 sample. 263
Table 6.5: Changes in hardness of the WT-4 samples after each treatment with referecnce to an untreated sample. 267
Table 6.6: Changes in matrix hardness and modulus after each treatment using XPM data. 270
Table 6.7: Changes in hardness of the WT-6 samples after each treatment with referecnce to an untreated sample. 273
Table 6.8: Changes in matrix hardness and modulus after each treatment using XPM data. 276
Table 6.9: Changes in hardness of the WT-12 samples after each treatment with referecnce to an untreated sample. 279
Table 6.10: Changes in matrix hardness and modulus after each treatment using XPM data. 282
Table 6.11: Changes in hardness of the T-800 samples after each treatment with referecnce to an untreated sample. 286
Table 6.12: Changes in matrix hardness and modulus after each treatment using XPM data. 289
Table 6.13: Area fraction analysis of individual phases after each heat treatment with comparison to an untreated WT-6 sample. 296

Table 6.14: Area fraction analysis of individual phases after each heat treatment with comparison to an untreated WT-12 sample. 300
Table 6.15 Variation in matrix composition between an untreated sample and a sample solution treated and aged for 4-hours aging. 300
Table 6.16: Changes in bulk hardness and matrix microhardness calculated as a percentage after solution treating at 1275ºC for 8-hours and additional aging treatments at 850ºC various periods of time with comparisons to an untreated sample. 302
Table 6.17: Changes in matrix hardness and modulus after each treatment using XPM data. 304
Table 6.18: Changes in bulk hardness and matrix microhardness calculated as a percentage after solution treating at 1275ºC for 8-hours and additional aging treatments at 850ºC various periods of time with comparisons to an untreated sample. 306
Table 6.19: Changes in matrix hardness and modulus after each treatment using XPM data. 308

Acknowledgments

Firstly, I would like to thank the Welsh European Funding Office (WEFO), the Engineering and Physical Sciences Research Council (EPSRC), Swansea University and Weartech International for providing me with the opportunity and funding to study on the EngD scheme. My time on the scheme has provided me with crucial industrial experience which helped me transition from academia straight into a working environment.

I would like to express my gratitude to my industrial supervisor, Dean Thomas. Your expertise was vital in giving me a platform to build from with my research and your extensive industrial connections formed the backbone of my thesis. Without your knowledge and leadership, my time on the EngD scheme would have been far more difficult. I would also like to thank the team at Weartech for their support and for generally making Weartech an inviting environment to work in.

I would like to express my appreciation to my academic supervisors, Dr Amit Das and Professor David Penney. My time spent at Swansea University has been a large part of my life which has been an enjoyable experience. As my supervisors and previous lecturers, you have both been a big part of that experience, and your knowledge and guidance throughout that time will not be forgotten.

Finally, I would like to give a special mention to my loving wife, Alex. Thank you for your patience and support during the final stages of the EngD scheme. The writing of the thesis has been a long and arduous task, with many evenings spent apart, but your encouragement has made the journey easier and provided me with the motivation to get the job done.

1 Introduction

1.1 Background Information

Steel is one of the most important construction materials used for automobiles, appliances, and industrial machinery. However, steel is vulnerable to corrosion when exposed to atmospheric conditions. Therefore, protective coatings are often applied to steel components to prevent corrosion from occurring. Zinc or zinc alloy coatings have been extensively used to for the protection of steel where the hot-dip galvanising process is the most frequently used processing technique for the mass production of coated [1]. The coating protects the steel as the zinc is more active and preferentially corrodes instead of the steel by a cathodic reaction that prevents the steel substrate from anodic corrosion. The coating also acts as a physical barrier to the surrounding environment [2].

On a continuous hot-dip galvanising line (CHDG) a steel strip is fed as a continuous ribbon that can be coated in a non-stop process reaching lines speeds of up to 200meters per minute [3]. During the coating process, the steel strip is guided through the molten zinc bath using a series of rolls that are supported by journal bearings. This configuration is referred to as the pot gear or pot hardware. As the steel strip passes through the bath it reacts with the molten zinc to form a metallurgical bond between the zinc coating and steel substrate. Upon exiting the bath, the coated strip passes between regulating air knives that control coating thickness by blowing pressurised gas onto the strip to remove excess zinc. Strip stability is crucial at this stage of the coating process if a thin and uniform coating thickness is to be achieved. This is particularly important for high quality products that are used in industries such as the automotive industry where stringent tolerances, such as weight, thickness and surface finish, must be met during quality control [4].

The degradation of pot hardware contributes to coating surface defects and strip instability which both act to degrade the quality of the coated steel. Consequently, the lines are routinely stopped to replace pot hardware components which has negative effects on productivity. The pot hardware experiences degradation as they are fully submerged in the bath during operation and therefore readily react with the molten zinc. The sink roll, which is made from 316L stainless steel, degrades due to corrosion and results in dross buildup on the surface of the rolls. As the surface of the roll comes into direct contact with the strip, the buildup of dross can result in surface defects on the steel strip or the transfer of dross from the roll into the coating. This reduces the quality of coating as coating defects reduces the mechanical performance of the coating as well as reducing the quality of the surface finish [5]. The journal bearings, which consists of a sleeve component that sits inside a bush component to form the bearing, are generally made from cobalt-based superalloys. The bearings are subjected to an extremely harsh working environment where

a synergy of wear and corrosion mechanisms results in concentrated levels of wear. Therefore, the bearing material needs to possess good corrosion resistance to the molten zinc bath, in addition to good wear resistance as the bearing components come into direct metal-on-metal contact during operation. The microstructure of the cobalt alloys consists of a tough cobalt rich matrix that is strengthened by the dispersion of the extremely hard carbide phases. This provides the alloys with good abrasion and corrosion resistance at elevated temperatures [6]. However, despite their enhanced mechanical properties and corrosion resistance, the bearings are replaced every 2-4 weeks due to the degradation they experience during operation. The high levels of wear experienced by the bearings, which is characterised by deep and wide grooving of the bearing surfaces, has largely been attributed to the formation of cobalt-aluminide particles that form due to reactions that occurs between the bearing material and molten zinc, particularly the aluminium content of the bath. The CoAl particles are extremely hard (1000Hv) and brittle and easily detach from the surface during repeated loading and unloading cycles. The detached material acts as abrasive wear debris when they become entrapped between the bearing contact surfaces. Due to their hardness, which is significantly higher than the hardness of the bearings, the CoAl particles can plough along the surface of the bearings which results in material removal and the formation of additional wear debris.

The relatively short service life of the journal bearings and the negative impacts of degraded pot hardware components on coating quality and line efficiency highlights the importance of identifying better performing materials. Heat treatments and surface engineering of alloys has been extensively used in industry to manipulate the performance of an alloy to improve their mechanical properties and enhance their performance for certain applications. Thermal processes such as annealing and precipitation hardening use specific heating cycles and cooling rates to control grain size, microstructure morphology and phase precipitation which can significantly improve certain mechanical properties of the alloy. Whereas as thermal treatments completely alter the microstructure of the treated component, surface engineering only modifies the surface of the alloy. This has the benefit of the bulk material retaining its toughness whilst the mechanical properties of the surface can be significantly improved. Surface engineering can be used to modify the surface of the alloys or can be implemented with the application of a surface layer. Diffusion methods such as nitriding and carburising rely on the diffusion of nitrogen and/or carbon to improve the mechanical properties of the surface. The diffusion of nitrogen or carbon distorts the lattice by occupying interstitial sites in the matrix which acts to impede dislocation movement [7]. The diffusion of the nitrogen and carbon atoms also results in the formation of compound layers and the formation of carbides and nitrides in the diffusion layer. In the absence of nitride and carbide precipitation, the supersaturated layer is often referred to as expanded austenite or S-

phase and has the benefit of increased hardness and wear resistance without any loss of corrosion resistance. Other surface techniques include laser cladding and thermal sprays. Both methods rely on the application of a coating material that offers better tribological and corrosion properties than the substrate material.

The alloys studied for this research are cobalt-based superalloys that contain various amounts of elements such as cobalt, chromium, tungsten, molybdenum, nickel, iron, silicon and manganese. The main difference between the CoCrW alloys is the level of carbon and tungsten, which ultimately controls the amount and type of carbides that form during solidification. Whereas the CoCrW alloys gain their strength from the dispersion of eutectic chromium and tungsten carbides, the CoCrMo Tribaloy contains significantly high levels of molybdenum and silicon where molybdenum replaces the addition of tungsten. Carbon is also kept to a minimum to prevent carbide formation. This results in the formation of a primary Laves phase which is dispersed in a softer eutectic matrix. The Laves phase is so abundant (30-70 vol%) that it governs the materials mechanical properties. The alloy offers enhanced wear and corrosion resistance compared to the CoCrW alloys, but the alloy is brittle by nature as a consequence.

For the purpose of this thesis, the CoCrW and CoCrMo alloys were exposed to a range of annealing heat treatments, aging treatments, and plasma nitriding heat treatments in an effort to improve their mechanical properties and chemical resistance which could be applied for the use of journal bearing components.

1.2 Scope of Research

The testing and analysis carried out for the purpose of this thesis was performed with the primary aim of improving the performance of cobalt-based journal bearing components that perform a key role in the bath hardware configuration on galvanising lines. The bearings are submerged in molten zinc and are responsible for providing free and stable rotation of the sink roll during the coating process as the steel strip is guided through the molten zinc bath. The bearings experienced concentrated levels of wear which has negative impacts on coating quality and the productivity of the process. Therefore, improving the performance of the bearings can significantly improve the overall efficiency of the continuous hot dip galvanising process. A bearing that experiences less wear, in theory, would generate less vibration if the wear at the bearings surface is smooth. This could potentially minimise coating defects that arise due to strip vibration. An improvement in strip stability would also allow for better control of coating thickness to be achieved, minimising zinc consumption. A more wear resistant bearing would extend the service life of the bearing which would reduce line downtime, increasing productivity, and a bearing that offers better chemical resistance to the molten zinc bath would also reduce the

level of cobalt-aluminide wear debris formation which would decrease the level of degradation experienced by the bearings.

To try and improve the performance of the journal bearing components, three CoCrW alloys and one CoCrMo alloy were analysed to gain an understanding of what materials would be better suited for journal bearing components. Each alloy was subjected to a plasma nitride treatment, an annealing heat treatment, and a solution and aging treatment. The aim of the heat treatments was to improve the mechanical properties and chemical resistance of the alloys. A number of analytical techniques and tests were used to study the relationship between the chemical composition, microstructure and mechanical performance of untreated and treated alloys. In order to identify better performing materials and to enhance the performance of commercially available cobalt-based superalloys, the following objectives were set:

1. Analyse untreated alloys so that comparisons can be made to treated alloys. From this, any changes in microstructure or mechanical properties could be identified.
2. Identify relationship between the untreated alloy's microstructure and the alloy's hardness by carrying out by bulk hardness testing, microhardness testing and phase specific nano-testing.
3. Identify relationship between the untreated alloy's microstructure and the alloy's resistance to molten zinc by carrying out a series of static immersion tests in molten zinc.
4. Investigate the effects of a plasma nitriding treatment where the diffusion layer composition, thickness and hardness are to be analysed.
5. Identify any trends observed with prolonged nitriding treatment or increased nitriding temperature.
6. Identify any improvements in chemical reactivity after alloys were plasma treated by carrying out a series of static immersion tests in molten zinc.
7. Investigate the effects of a high temperature annealing process and a solution and aging process on the microstructure and mechanical properties of the treated alloys, specifically looking at changes in bulk hardness of the alloy and microhardness and nano-hardness of the matrix.
8. Identify any microstructure and hardness trends observed with prolonged annealing times or cooling rates and any trends observed with prolonged aging times after a solution treatment.

1.3 Thesis Layout

The layout of this thesis is divided into eight chapters that covers the introduction and objectives of the current research, literature review detailing research relevant to the current work, a methods and material section, and several results chapters that discuss the mechanical and corrosion properties of untreated and treated alloys. The thesis is concluded with precise summarisation of the most significant observations made during the research where recommendations for future work are also made. A more detailed review of each section is detailed below:

Chapter 1 – Introduction: This section introduces the present research and provides background information on topics relevant to the current research. This includes general information on the continuous hot dip galvanising of strip steel, the application of cobalt-based journal bearings, methods of improving mechanical and corrosion performance of alloys, and a description of the alloys used for this work. The problems associated with the coating process and, more specifically, the journal bearing components are also discussed which highlights the significance of the present research and defines the objectives.

Chapter 2 – Literature Review: The literature review discusses relevant research to the present work. This includes a summary of corrosion and corrosion protection, the continuous hot dip galvanising process, and a detailed explanation of the chemical reactions occurring in the molten zinc bath with journal bearing components. From this information, the problems associated with the galvanising process and their causes are identified. The chapter also provides a detailed description of cobalt-based superalloys with regards to the following aspects: alloy microstructure and composition, mechanical properties, wear performance, and corrosion and erosion resistance. The principles of wear and chemical reactivity with molten zinc that is experienced by the journal bearings during operation are additionally discussed. The literature review is concluded by exploring techniques that are used to improve the performance of cobalt alloys. This includes coating and diffusion techniques that change the microstructure or composition at the surface, or heat treatments that fully alter the microstructure of the alloy.

Chapter 3 – Experimental and Sample Preparation: In this chapter the composition of the selected cobalt-based superalloys for this research is provided. The section also describes the parameters used for certain heat treatments, sample preparation prior to testing or analysis, and the methods used for mechanical testing and material analysis.

Chapter 4 - Microstructural Characterisation and Mechanical Performance of As-received CoCrW and CoCrMo Alloys: This chapter describes the microstructure, hardness, and chemical

reactivity with molten zinc for each of the untreated alloys. The knowledge and data gained from testing and analysis from this area of research provides important information on why the alloys exhibit different mechanical properties and corrosion resistance. This also allowed for any changes in microstructure or alloy performance, after various heat treatments, to be identified.

Chapter 5 - Microstructural and Mechanical Influence of a Plasma Nitriding Heat Treatment: In this chapter the effects of plasma nitriding treatment was investigated where the nitriding temperature and time was varied. The composition, thickness, and hardness of the diffusion layer for each alloy was analysed with comparisons made between the treatment parameters. A series of static dip tests were carried out on each alloy that had been plasma treated at 550℃ for 15-hours to observe any changes in corrosion resistance to the molten zinc bath in comparison to the untreated samples.

Chapter 6 - Microstructural and Mechanical Influence of High Temperature Thermal Treatments: In this area of research, two thermal heat treatments were investigated. This included a high temperature annealing process at 1000℃ where different treatment times and cooling rates were implemented, and a solution and aging treatment. For the aging process the sample was initially solution treated at 1265℃ and quenched after 6-hours. Samples were then aged for different periods of time at 850℃ and furnace cooled. The influence of the different treatment parameters had on the alloys microstructure and hardness was investigated and comparisons made to untreated samples.

Chapter 7 – Discussion: This section discusses the key findings from each area of research and links the results to the alloys performance in industry.

Chapter 8 – Conclusions and Future Work: This section concludes the work carried for the present research where the most significant findings for each area of research is summarised. Future work and suggestions of how to build on the knowledge gained for the current research are also made.

2 Literature Review

2.1 Corrosion and Corrosion Protection

Steel is a widely used material in a number of industries such as construction, energy, packaging and transport due to the materials excellent mechanical properties, versatility and relatively low production costs. However, steel is susceptible to corrosion which can lead to catastrophic material failure if not managed correctly. It was estimated (2017) that the direct cost of corrosion, due to repair, maintenance, and replacement, in order to prevent material failure was between 3-4% of global annual GDP [8].

The galvanic coating of steel as a means of corrosion protection is a widely used method to provide corrosion protection for a range of steel grades. There are several commonly used coating techniques such as thermally sprayed coatings, electroplating or hot-dip galvanising of steel components. However, the continuous hot-dip galvanising (CHDG) of steel remains the most economical process for mass production of coated sheet steel. In this process zinc or zinc alloys are predominantly used as a protective coating and act to protect the steel in two ways. The coating offers barrier protection where the coating acts to separate the steel from the environment, and galvanic protection where the zinc will sacrificially corrode due to it being less noble than steel at ambient temperatures [9–11]. As zinc corrodes it produces an inert oxide layer that reduces the rate of corrosion. This provides zinc with a highly beneficial 'self-healing' characteristic as the reaction will occur on a newly exposed zinc surface that may arise due to non-critical surface damage [12].

2.2 Overview of the Continuous Hot Dip Galvanising Line

The continuous hot dip galvanising (CHDG) process is widely used for the application of a protective zinc coating of sheet steel. The process allows for superior coatings with enhanced corrosion resistance and formability to be produced on an industrial scale. In a conventional CHDG line, outlined in Figure 2.1, the process generally consists of four basic stages: surface preparation, annealing, galvanising and inspection. At the start of the process the steel strip is uncoiled and welded to a previous strip to maintain a continuous supply of strip steel where coating speeds can reach 200m/min. The strip initially passes through adjustable accumulators which allows for the new coil to be welded to the previous coil without stopping the line.

The strip enters a pre-cleaning treatment where it is brushed with an alkaline solution which removes any surface contamination. This enhances coating adherence and prevents contaminants such as iron fines entering the bath. The strip is then rinsed and dried prior to annealing. The sheet

is heated between a range of 500-760°C in a N_2/H_2 reducing atmosphere that removes any surface oxides. During this stage, the heating also allows for recrystallization to occur to give the treated steel the desired mechanical properties.

On exiting the furnace, the sheet passes through a gas jet section that rapidly cools the strip to 460°C prior to bath immersion. The strip enters the bath via a snout that is kept under a vacuum state with an inert atmosphere that prevents any surface oxidation occurring prior to the strip entering the molten zinc/zinc alloy bath. As the steel strip enters the bath a coating is achieved using a configuration of submerged rolls which are often referred to as the pot gear or pot hardware. This will be discussed in greater detail later in the chapter. The pot gear guides the strip through the bath where the bath temperature is specific to the type of coating composition. Galfan has a lower temperature range of 425°C, standard galvanised zinc coatings are kept at around 450°C and a Galvalume bath is kept near 600°C. The line speed determines the immersion time in the bath. Combined, these two factors control the nucleation and growth of the coating which gives the desired mechanical properties and thickness of the coating.

The strip exits the bath vertically and is passed between gas knives that blow air or nitrogen onto the surface of the coated steel to produce a desired coating thickness by removing excess zinc. An example of the air knives and a schematic of their configuration is illustrated Figure 2.2. Gas pressure, distance between the strip and gas knives, strip velocity and gas contact angle are parameters that are used to control coating thickness where strip stability is vital to achieving a uniform coating thickness. Beyond the gas knives the strip passes through a cooling tower which solidifies the coating. For Galvannealed products a second heating furnace is used at this point to allow for further diffusion of iron and zinc where the heating rate, holding temperature, and cooling rate are parameters used to produce an optimised galvanneal coating.

Once the coating has solidified, additional processing steps can be used to give the coating its final mechanical properties. Temper rolls exert a small amount of surface deformation to give the desired surface finish and the strip is also tension levelled to ensure the sheet is flat. Further surface treatments such as chromating or oils can be used to prevent storage stains and oxidation. The strip is then inspected for any surface defects before being cut and recoiled [10,13,14].

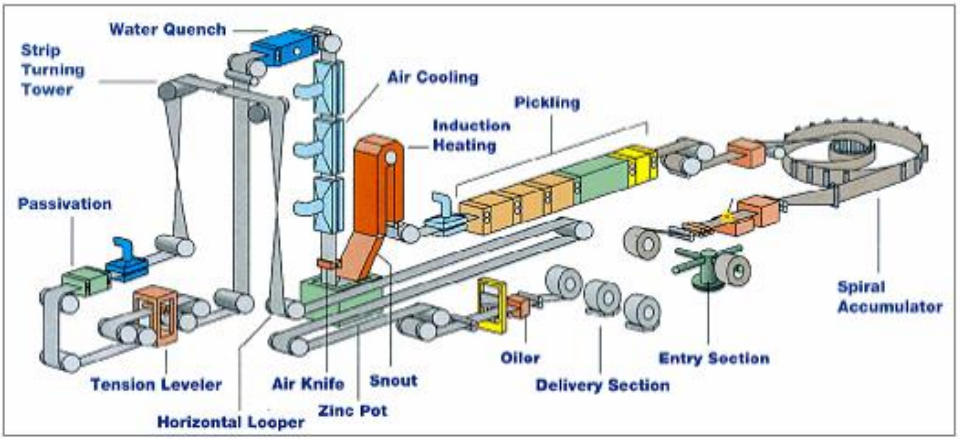

Figure 2.1: Typical continuous hot-dip galvanising line [15].

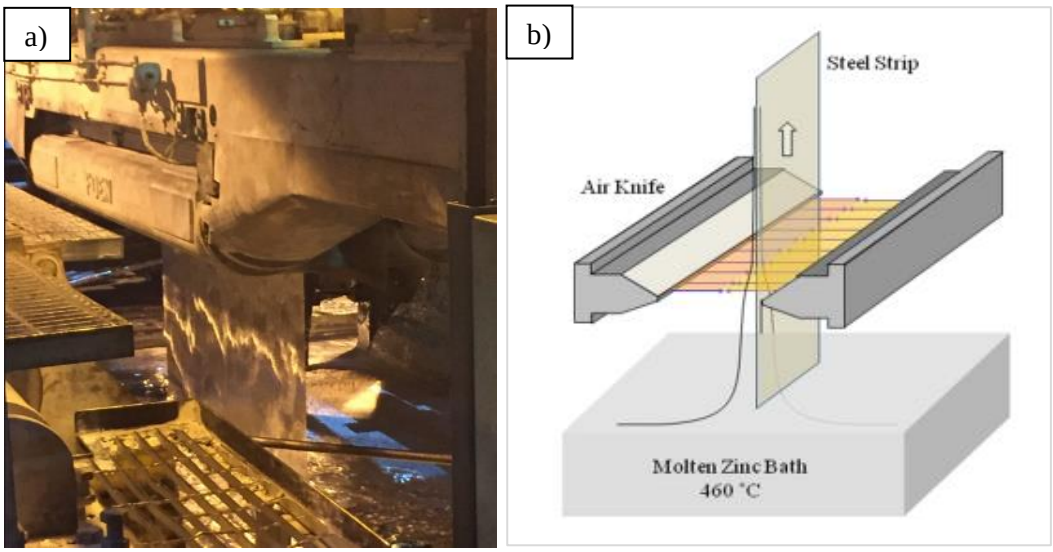

Figure 2.2: a) Image of gas knives [16] *and b) schematic of their configuration* [17].

2.3 Coating Metallurgy

During the hot-dip galvanising process a number of chemical reactions occur as the steel is submerged in the molten zinc bath which results in the formation and growth of intermetallic phases and compounds which form the protective coating on the steel substrate. The characteristics and mechanical properties of the coating can be influenced by the steel composition, bath composition, immersion time, cooling rate and substrate surface roughness [18,19]. Zinc is generally used as a protective metallic coating where the molten zinc is often alloyed with a small amount of aluminium which significantly improves the corrosive and mechanical properties of the coating. However, the addition of aluminium creates a ternary system within the bath and can lead to formation of intermetallic phased in the bath that can have

detrimental effects on coating quality and coating efficiency. In order to gain an understanding of how these potentially harmful phases form, an understanding of the binary Fe-Zn phase diagram is required which will also highlight the importance of aluminium additions if good bath management and enhanced coatings are to be achieved.

2.3.1 Inhibition Layer Formation in Pure Zinc Baths

In the absence of aluminium, when a steel component is immersed in the molten zinc bath, a complex diffusion process occurs which results in a series of intermetallic iron-zinc (Fe-Zn) phases forming on the surface of the steel substrate. The Zn-rich corner of the binary Fe-Zn phase diagram is displayed in Figure 2.3 and demonstrates the main intermetallic phases that can form on the steel substrate during the chemical reaction [10]. It has been identified that the intermetallic compounds consist of delta (σ), zeta (ζ), and gamma (Γ and Γ_1) phases where each phase exhibits different growth kinetics that are dependent on bath temperature and immersion time [20,21]. An outer eta (η) Zn-rich layer which is a solid solution phase of iron in zinc also forms but is not represented in the phase diagram. The gamma phases form closest to the surface and therefore contain the highest weight percentage (wt.%) of iron. Growth of the individual phases makes iron diffusion from the substrate more difficult, therefore the outer layers contain descending wt.% of iron. These phases are extremely brittle and exhibit poor ductility which makes the coating unsuitable for forming as the coating can crack and flake off [22]. To overcome this problem small additions of aluminium are added to bath which acts to suppress the formation of the brittle Fe-Zn phases.

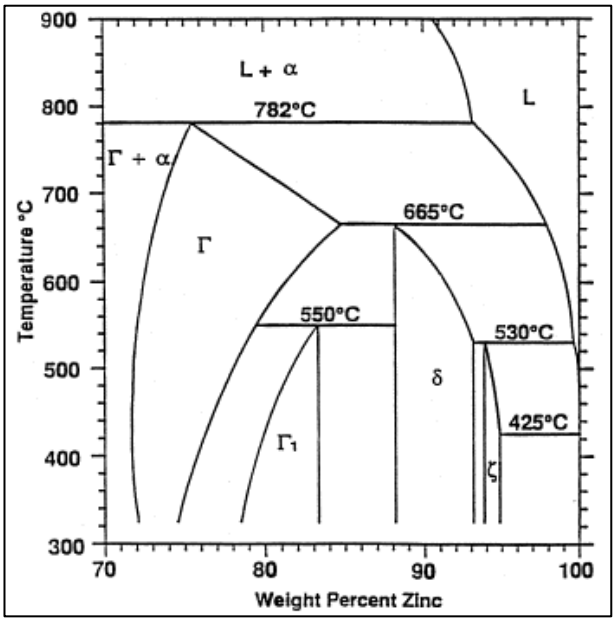

Figure 2.3: Zinc-rich corner of the binary Fe-Zn phase diagram [10].

2.3.2 Influence of Aluminium Additions on Inhibition Layer Formation

In commercial galvanising, small additions of aluminium are added to the bath to improve the surface appearance of the coating, produce thinner and more ductile coatings and to reduce bath oxidation [23]. Additions of between 0.1 and 0.3wt.% Al is usually added to the bath which acts to inhibit the formation of the brittle Fe-Zn intermetallic phases outlined in the previous section. These coatings are often referred to as *Galvanised (GI)* or *Galvanneal (GA)* where galvanneal coatings experience an additional annealing treatment during the process. The inhibition of the Fe-Zn phases is a result of the rapid formation of a thin Fe-Al compound layer which, due to aluminium's greater affinity for iron than zinc, forms on the steel substrate within seconds of entering the bath [24]. The composition of this layer is dependent on the aluminium concentration in the bath. It has been established that when the aluminium content of the bath is maintained above 0.15wt.%, the inhibition layer comprises mainly of Fe_2Al_5, as shown in the Zn-rich corner of the Zn-Al-Fe ternary system in Figure 2.4. The interfacial Fe-Al layer provides good adhesion to the substrate and the absence of the Fe-Zn intermetallic phases, beneath the η layer, improves the formability of the coating [25]. At lower aluminium concentrations, the Fe_2Al_5 layer is thin and discontinuous, and dissolution of the phase occurs. This has been demonstrated by *Min et al* [26] who studied the influence that different aluminium concentration has on inhibition layer formation. Pure iron samples were coated in zinc baths that contained different concentrations of aluminium ranging between 0.00 - 0.8wt.% Al. It was identified that no Fe_2Al_5 layer formed in the 0.00wt.% and 0.1wt.% Al baths whereas a Fe_2Al_5 layer formed in baths containing ≥2wt.% Al where the thickness of the layer increased as the aluminium concentration increased.

In recent years significant research has been carried out with aim of enhancing the corrosion properties of HDG steel, without increasing coating thickness, by altering the bath chemistry [26–29]. Two common Zn-Al based coatings are *Galfan* and *Galvalume* which contain aluminium additions of 5% and 55%, respectively. Both coatings offer superior corrosion resistance compared to standard *Galvanised* or *Galvanneal* coatings which has been attributed to the formation of a passive aluminium-rich phase at the substrate and coating interface [30]. Additional research has found that the addition of small quantities of magnesium further enhances the corrosion resistance of the coating. *Schùrz et al* [31]. found that a Zn-Al-Mg coating provided enhanced corrosion resistance in a salt spray test compared to a conventional zinc coating containing 0.2% aluminium due to the formation of a stable protective layer of zinc aluminium carbonate hydroxide *Prosek et al* [32] found that a 10μm zinc coating containing 1.5% magnesium and aluminium provided similar or better corrosion protection in open and confined configurations compared to a 20μm low aluminium coating and a galfan coating.

Although the addition of aluminium significantly improves the corrosive and mechanical properties of the coating, increased aluminium content in the bath can result in excessive intermetallic phase formation, particularly with Galvalume products that also operate at much higher bath temperature which increases iron dissolution into the bath [33]. A more aggressive working environment has detrimental effects on the performance on the bath hardware and increased formation of intermetallic phases within the bath contributes to coating defects.

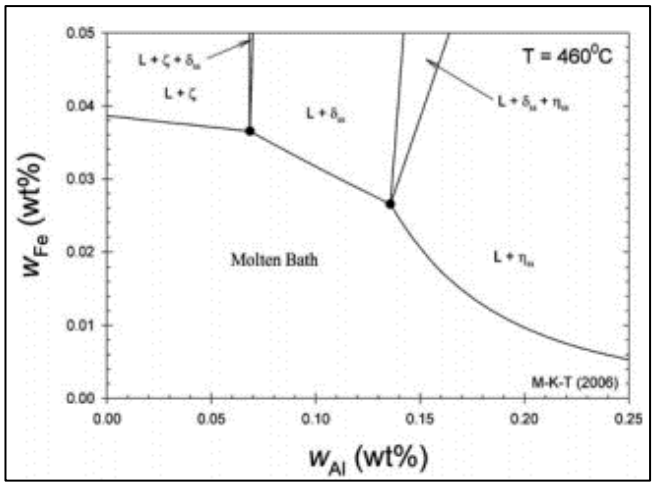

Figure 2.4: Zinc-rich corner of the Zn-Al-Fe ternary phase diagram [34].

2.4 Bath Management and Zn-Fe-Al Ternary Phase Stability and Solubility

Growing demand for higher quality coatings, particularly in industries such as the automotive industry where strict coating thickness tolerances and a high-quality surface finish is needed, the understanding and control of potentially harmful phases within the bath is essential.

During the continuous hot dip galvanising process, the steel strip enters the molten zinc bath at around 460°C. At this temperature, iron atoms have enough mobility to escape the steel strip and enter the bath [35]. Immersed bath hardware also provides a source for iron dissolution into the bath. Iron has limited solubility in molten zinc. At a temperature of 465°C, iron has a solubility limit of around 0.05wt.% in molten zinc. Above this limit iron reacts with the molten zinc to form intermetallic phases which are often referred to as ‘dross’ particles. Dross pickup during the coating process contributes to the formation of surface defects and coating irregularities which can ultimately lead to the rejection of the coated steel during inspection. What makes this process more difficult is that many galvanising lines use a single pot for the application of GI and GA products. During the transition between coatings the chemistry of the pot changes rapidly which results in an increase in dross formation [36]. The quality of the coating during this

transition is often unusable for many high-grade applications. Therefore, good bath management during the transition is important in order to maximise the production of high-quality coatings.

Although aluminium is deliberately added to the bath to reduce dross formation and to produce coatings with enhanced corrosion resistance and mechanical properties, the dissolution of iron results in the establishment of a Zn-Fe-Al ternary system within the bath when solubility limits are exceeded. *Belisle et al* [37] investigated the solubility of iron in a CHDG bath and identified process factors that contributed to the formation of intermetallic phases. This included the dissolution of the steel strip and immersed bath hardware and through iron fines on the surface of the strip due to poor surface preparation. It was found that the solubility of iron in zinc is strongly influenced by aluminium concentration and bath temperature within the range of 0-0.5wt.% Al and 450-480°C, respectively. It was found that increasing the aluminium content above 0.07wt.% significantly decreased the solubility of iron up to a value of 0.3wt.% Al. Above this concentration the changes in iron solubility were less evident. It was also observed that the bath temperature increased the solubility of iron up to 0.3wt.% Al content where increasing the bath temperature above this aluminium concentration had little effect on iron solubility.

The aluminium content and bath temperature are key process parameters that determine the stability of liquid aluminium and iron, and therefore dross formation, in the bath. It also determines the kinetics of nucleation and growth of an inhibition layer that forms at the steel sheet and bath interface. However, even with ideal bath chemistry management, the formation of dross is unavoidable. This is due to the addition of aluminium, iron dissolution and nonuniform bath temperature and chemistry. Although the formation of dross is unavoidable, the level of dross formation can be reduced with close control of the bath chemistry, particularly the aluminium content in the bath. The effective aluminium content (Al_{eff}), which describes the amount of dissolved aluminium in liquid zinc, is the determining factor in forming the desired coating microstructure. The Al_{eff} content also influences the type of dross that forms in the bath which is categorised as top or bottom dross. When the Al_{eff} content is lower than 0.13wt.%, formation of the $FeZn_{10}$ δ phase is favoured. The density of this phase is greater than the density of the molten zinc so the phase sinks to the bottom of the bath to form bottom dross. Al_{eff} content above the knee point, 0.14wt.%, favours the formation of e $Fe_2Al_5Zn_x$ η-phase. This phase has a lower density than the bath and therefore floats on the surface of the bath forming top dross [38]. Although both types of dross particles can have negative effects on coating quality, bottom dross is seen as a more difficult problem for engineers to overcome. Whereas top dross floats on the surface of the bath and can be removed with routine skimming, bottom dross is more difficult to remove due to its location in the bath. Bottom dross is also typically larger in size compared to top dross.

This demonstrates that aluminium is the most influential element included in the zinc bath if good bath management and coating quality is to be achieved. As a result, the Zn-Fe-Al ternary system has extensively been researched and new technologies have been developed to accurately model and measure bath chemistry. Before the development of technology capable of accurately measuring the Al_{eff} content, compositional analysis of the bath chemistry was a difficult task. Bath samples often included aluminium containing dross particles which interfered with the Al_{eff} content analysis. This led to Determining Effective Aluminium (DEAL™) software to be developed by Cominco Ltd. *Tang et al* [39] described how the software was based on detailed analysis of the Zn-Fe-Al ternary system which included studies detailing iron solubility as a function of aluminium content over temperature ranges experienced during galvanising operations. By identifying all the potential phases in the zinc-rich corner of the Zn-Fe-Al ternary system, the optimum compositions for GA and GI coatings were able to be defined.

2.4.1 Intermetallic Phase (Dross) Formation on Pot Hardware

During the coating process the steel strip is guided through the molten zinc bath using a configuration of submerged rolls which is often referred to as the pot gear or pot hardware. An example of the pot gear and a schematic of their arrangement is illustrated in Figure 2.5. The pot gear consists of a sink roll, correcting and stabilising rolls, and journal bearings. The sink roll, which is roughly two meters in length, is supported by the journal bearings and is the largest component in the pot gear assembly. The correction and stabilising rolls are much smaller in size and act to maintain strip stability as the strip exits the bath and passes between the air knives. The pot gear controls the speed and tension of the steel strip as it travels through the molten zinc bath, thus controlling coating metallurgy and coating thickness. All the components are fully submerged and operate in the molten zinc bath where increased temperatures and a corrosive media create an extremely harsh working environment. As a result, the pot gear components readily react with the bath where intermetallic phase formation and dross attachment occurs. The quality of the coating is strongly influenced by the condition of the pot gear components where degradation leads to non-uniform coating thickness and a reduction in surface finish quality. This can contribute to roll skidding, roll lock-up and sheet vibration [40,41]. Therefore, the components have a relatively short service life ranging between 1-6 weeks. The routine stopping of galvanising lines, to carry out maintenance or to replace bath hardware, results in significant energy and production losses. Based on research carried out by the International Lead Zinc Research Organisation (ILZRO), it was estimated that the energy wasted during regular downtime

of a single galvanising line equates to the production losses of 13,000 tons of galvanised steel annually [42].

Generally, two materials are used for pot gear components. The sink roll, correction and stabilising rolls are typically made of a 316L stainless steel (316L SS) whereas the journal bearings, which due to their application require a material with much greater wear resistance, are made of a cobalt superalloy where a commercial grade known as Stellite 6 is often used. The application and performance of the journal bearings will be discussed in greater detail in the following sections. 316L SS is used for the rolls due to its enhanced mechanical properties, resistance to molten Zn-Al and its reasonable manufacturing costs. When the 316L SS rolls are immersed in the molten zinc bath, they react with the bath to form intermetallic phases and experience dross attachment and dross buildup. Phase formation and the extent of dross buildup is linked to conditions such as bath chemistry, bath temperature, bath flow and roll proximity to the strip. *Zhang et* al [43] observed that immersed rolls reacted with the bath to form a $Fe_2Al_5Zn_x$ surface layer but identified that the distribution of dross attachment was not uniform. It was found that samples that were closer to the strip entry experienced increased dross buildup where the particles were smaller in size and that samples located further away from the strip experienced less dross buildup, but the particles were larger in size. This was attributed to flow turbulence and increased availability of iron created by the incoming strip. It was also identified that the $Fe_2Al_5Zn_x$ layer provided a favourable site for the attachment and build-up of dross particles.

The issues associated with the degradation of pot hardware has driven engineers and researchers to identify better performing materials in order to improve coating quality and line efficiency [44,45]. It has been identified that the degradation of the sink roll initiates with the establishment of an Al-rich ($Fe_2Al_5Z_{nx}$) layer at the roll surface. The reaction front then progresses into the substrate resulting in the dissolution of iron and the formation of a Zn-rich layer. This has led to development and application of a number of coatings as a way of reducing roll degradation and dross buildup and therefore increasing service life and productivity. Metallic coatings (Mo and Co) and oxide coatings (Al_2O_3, CaO, ZrO_2) have been used but a high velocity oxygen fuel (HVOF) process is commonly used to apply a WC-Co coating [46,47]. Although the WC-Co coating provides improved durability, deterioration of the coating still occurs with prolonged bath exposure. Failure of the coating can be attributed to dissolution of the cobalt, crack corrosion and weakened adhesion of coating from iron dissolution of the substrate [48]. Recently a novel MoB-CoCr thermal spray coating have been utilised due to their enhanced durability in molten zinc. *Zhang et al* [49] evaluated the performance of a MoB-CoCr and WC-Co coatings in a molten zinc bath. It was determined that MoB-CoCr coating exhibited better resistance to

thermal shock as well as a prolonged lifetime in molten zinc. The improvement in molten zinc durability was attributed to the non-wettability of the coating.

The progressive formation and build-up of dross particles over the course of the campaign continually increases the surface roughness of the rolls. This can lead to an uneven coating or scratch defects as the dross particles are generally harder than the steel strip [46]. It has also been identified that increased levels of dross buildup occur in areas of the roll surface that is not in contact with the steel strip, as shown in Figure 2.6 [50]. This can significantly increase the amount of coating defects when the strip being treated transitions to a wider strip which results in increased dross pickup at the strip edge.

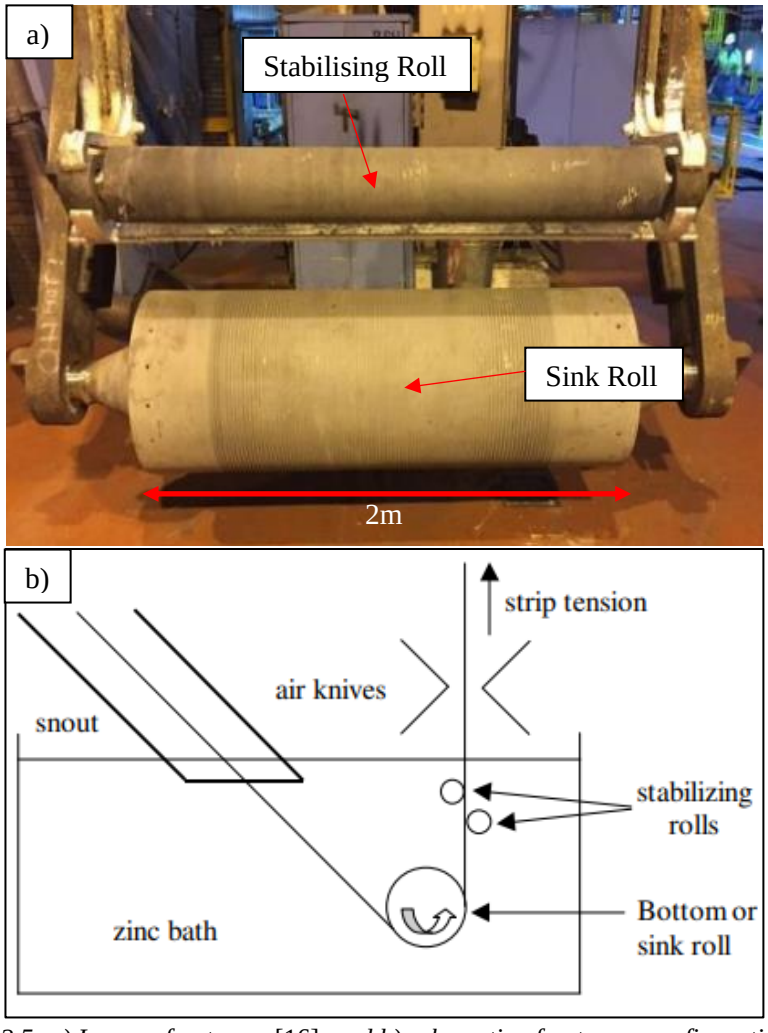

Figure 2.5: a) Image of pot gear [16] *and b) schematic of pot gear configuration* [40].

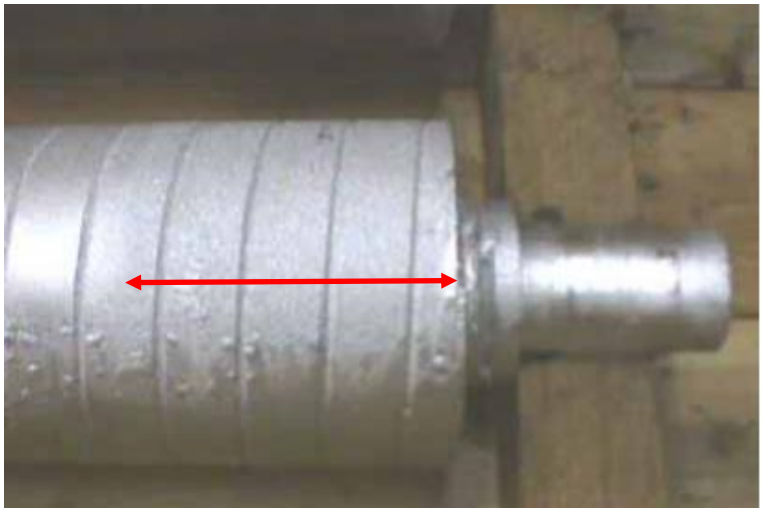

Figure 2.6 Dross buildup on outer edge of stabilising roll not in contact with strip [50].

2.4.2 Cobalt Aluminide Formation

The journal bearings that support the sink roll consist of a sleeve and bush component. The sleeve is attached to the sink roll and sits inside the bush to form the journal bearing, as shown in Figure 2.7. A similar smaller configuration is also used for the stabilising and correcting rolls. The bearing components are often made from Stellite, a commercially available cobalt-based superalloy. These alloys are used because of their enhanced wear and corrosion resistant properties at high temperatures and due to their relatively low cost [51]. The journal bearing configuration frequently involves the pairing of the same or similar Stellite grades for both the sleeve and bush components. The alloys generally consist of a cobalt dendritic matrix which is strengthened by the dispersion of carbide phases throughout the microstructure [52]. Due to the strong infinity of cobalt for aluminium, the cobalt-based alloys have been identified to readily react with the molten zinc alloy bath when aluminium content is as low as 0.015% at 460℃. The liquid region of the Zn-Fe-Co-Al quaternary system is displayed in Figure 2.8. The area of molten zinc in the vicinity of the bearing surface becomes saturated with cobalt which forms a cobalt-aluminide (CoAl) phase instead of the η (Fe2Al5Znx) [53]. This phase forms at the bearing surface as discrete particles and as a continuous CoAl layer. The CoAl phase is extremely hard where a microhardness of over 1000Hv has been recorded [54]. This is significantly harder than Stellite 6, a commonly used alloy for journal bearing applications, which typically has a hardness of 515Hv. The configuration of the journal bearings results in direct metal on metal contact between the bush and sleeve components during operation. Therefore, the formation and entrapment of the CoAl phases between the contact surfaces acts as abrasive wear debris which drastically contributes to excessive wear damage of the bearing surfaces. The degradation of the bearings due to wear and corrosion results in excessive strip vibration during the coating process

which contributes to poor coating quality. The negative effects on coating quality caused by degraded journal bearings forces the lines to be routinely stopped every 2-4 weeks to replace the bearings which reduces line productivity [55].

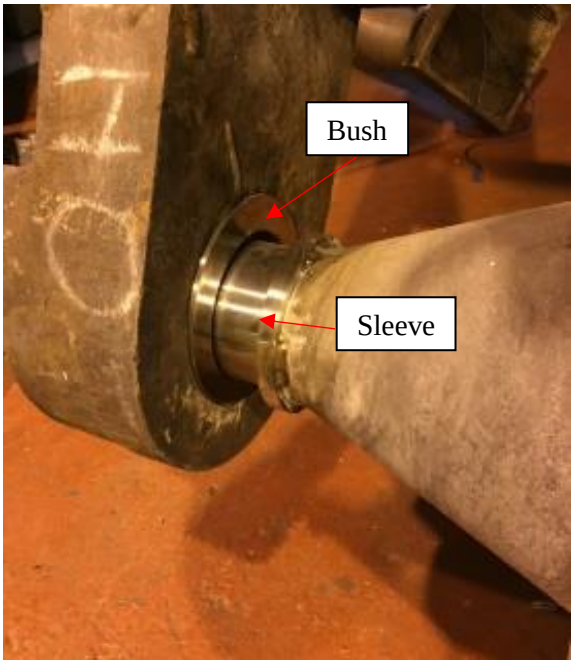

Figure 2.7: Example of a sleeve and bush component that forms the journal bearing [16].

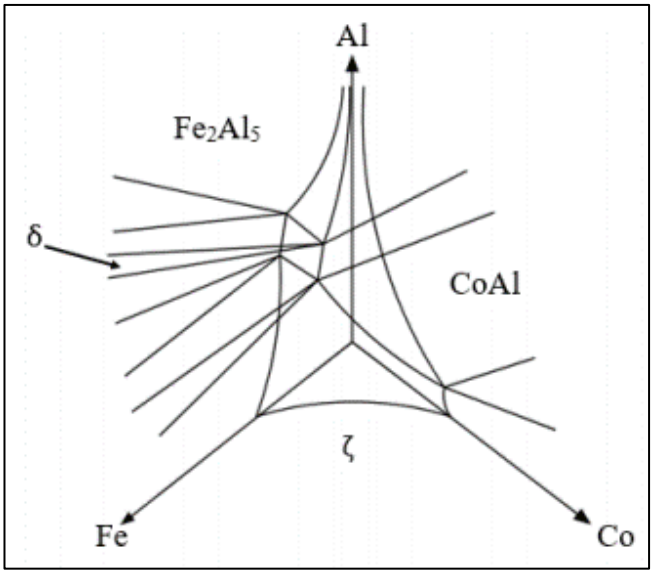

Figure 2.8: The Zn-Fe-Co-Al quaternary system at 460℃ [14].

2.5 Materials for High Wear and Temperature Resistant Applications

Mechanical components that operate in demanding industries such as the aerospace, automotive, nuclear, manufacturing, chemical, mining, and oil industries require superior

mechanical properties to withstand extreme working conditions. The components often operate in environments that combine elevated levels of wear and corrosion as well as high temperatures. Failure of components in such environments can have catastrophic effects on process efficiency, safety of workers, and the environment and can contribute to significant financial loses. To ensure components operate safely and efficiently, a range of materials have been designed with the purpose of improving their wear and corrosion resistance in order to maximise operation efficiency or to prolong their service life. These high-performance alloys are referred to as superalloys and are often categorised into three main classes: iron-based, nickel-based, or cobalt-based alloys. Superior combinations of mechanical, tribological, corrosion and high temperature properties mark these alloys as the best option for high temperature and wear/corrosion resistant applications [56] . Since their discovery they have been developed and modified to enhance their performance for specific industrial applications. Iron, nickel and cobalt are transition metals with consecutive positions in the periodic table. The alloys microstructures consist of an austenitic face-centre cubic (fcc) matrix phase (γ) and a range of carbide phases that precipitate at grain boundaries and interdendritic regions [57]. Thermal treatments and the addition of alloying elements in various amounts can have significant influence on the mechanical properties of the alloy through solid solution strengthening, precipitation hardening or due to the formation of carbides or intermetallic phases [58,59]. For the purpose of this research the application of cobalt-based superalloys will be looked at in detail.

2.5.1 Fundamentals of Tribology

Before discussing the wear and corrosion mechanisms associated with journal bearing components, it is important to understand the individual wear and corrosion mechanisms that commonly occur with wear resistant materials that operate in demanding environments. The word ‘tribology’ is derived from the Greek word ‘Tribos’ meaning rubbing, making the direct translation ‘the science of rubbing’. However, a modern-day definition of the term is ‘the science and technology of interacting surfaces in relative motion and of related subjects and practices’ [60]. The process describes the principles of friction, lubrication, and wear. In the case of journal bearing components, a rotating sleeve that is supported by a static bush which is surround by a small clearance and lubricated by molten zinc. The working environment of journal bearings is extremely harsh and the tribological conditions the bearing experiences during operation directly influences the performance of the bearings, the stability of the steel strip, the quality of the coating, and the service life of the bearings.

2.5.1.1 Principles of Wear

The process of wear is characterised by the loss of material when two surfaces with a relative motion come into contact. Wear is often a consequence of a combination of processes such as mechanical interaction and chemical dissolution in a corrosive medium. The classification of wear is often made difficult as the wear experienced by materials used for demanding applications can result from a combination of wear mechanisms. However, wear is often characterised by the mechanism of material removal where it is generally categorised as adhesive, abrasive, fatigue of corrosive wear. It is worth noting that there are many forms of wear that full under these categories, but they are generally classed as the main mechanisms of wear.

2.5.1.1.1 Adhesive Wear

Adhesive wear, which is also referred to as sliding wear, occurs when two surfaces in relative motion come into contact. Components that are well machined are still rough at a microscopic level where the surface will comprise of localised asperities and valleys. The interaction between the contact surfaces will act to resist sliding motion. This is referred to as the coefficient of friction. When the surfaces come into contact, contact is made at isolated asperities. Even under relatively small loads the local stresses at isolated asperities can become extremely high. Therefore, the asperities will deform elastically or plastically until the contact area can sufficiently support the load. During this contact, a bond between the surfaces may form which may be stronger than the strength of the weaker material/surface. This can result in material failure of the weaker material/surface which can lead to material transfer and retransfer of material from one surface to another or the detachment of material to form a wear debris particle. If adhesion does not occur, then the resistance to motion must be overcome by the deformation or removal of material. This occurs when the yield point is exceeded, and asperities plastically deform or shear.

2.5.1.1.2 Abrasive Wear

Abrasive wear is characterised by the displacement or removal of material and is generally associated with the ploughing of a softer material by a harder one. The process can arise from hard particles that are between or embedded in one or both surfaces that are in relative motion, and due to hard protuberances on one surface that comes into sliding contact with a softer surface. Two-body abrasion describes the wear process caused by hard protuberances or embedded particles and three-body abrasion describes the process when abrasive particles can move freely between the contact surfaces. Two-body abrasive wear results in more severe wear

damage as during three-body abrasive wear, the particles are free to roll between contact surfaces [61]. It has been reported that the hardness, size, and shape of the abrasive wear particles influences the severity of the wear experienced during operation. If wear resistance is taken as the ratio of hardness (*Hm/Ha*), where *Hm* is the hardness of the metal surface and *Ha* is the hardness of the abrasive particle, more severe wear is experienced when the ratio of hardness is below 0.8 [62]. *Stachowiak* described that angular particles were more abrasive than semi-angular or rounded particles, particularly in three-body abrasive wear [63]. It has been proposed that work hardening effects that occur at the surface of the material during contact increases resistance to plastic deformation. Therefore, only larger abrasive particles could deform the work hardened surface [64]. However, this theory can only be applied to ductile materials. *Thakare et al* [65] investigated how particle size influenced abrasive wear of a WC-based sintered coating. It was found that the level of wear experienced a sharp increase when a 180m SiC abrasive was used. The increase in particle size resulted in a fracture-dominant failure of the coating which led to detachment of hard carbide phases which act as abrasive particles.

2.5.1.1.3 Fatigue Wear

Fatigue wear occurs due to cyclic loading and unloading stresses experienced during operation which results in the formation of surface or subsurface cracks. This can occur through rolling contact or through a combination of rolling and sliding contact. Once cracking has initiated, each loading cycle will increase the size of the crack. Once a critical number of cycles has been reached, crack formation can lead to the breakup and detachment of surface material leaving large pits on the surface. The formation of wear debris, from fatigued surface material, can then initiate the onset of adhesive and abrasive wear mechanisms.

It has been discussed that sliding contact between two surfaces results in adhesive and abrasive wear. However, it is possible that asperities can make contact without these mechanisms occurring and still pass each other. This process involves the plastic deformation of at least one of the surfaces. After a certain number of contacts, surface material will fail due to fatigue. Adhesive and abrasive wear rely on direct contact between two sliding surfaces. This interaction can be eliminated with a well-designed and well lubricated bearing. When these mechanisms are eliminated, fatigue wear becomes the dominant failure mechanism [66]. This type of wear is known as rolling contact fatigue (RCF). Although the surfaces do not come into direct contact, opposing surfaces are subjected to high stresses that are transmitted through the lubricant during the motion of rolling. The Hertz equations indicate that the maximum compressive stresses occur at the surface but the maximum shear stress occurs some distance beneath the surface [67]. Hence

the formation of cracks below the surface which result in eventual fragmentation of surface material after a critical number of cycles.

Although subsurface and surface cracking are observed in both rolling and sliding contact fatigue, prior to the critical point of fatigue experienced with rolling contact, the bearing will operate under normal conditions until wear debris is introduced. In contrast, bearings in sliding contact experience gradual deterioration from the start of operation due to the immediate effects of adhesive and abrasive wear.

2.5.1.1.4 Corrosive Wear

Corrosive wear, also referred to as oxidation or chemical wear, is caused due to chemical or electrochemical reactions that occur between the components surface and the surrounding environment or when two surfaces come into contact. The surface interaction can result in the formation of reaction products which can improve the performance of the material if a protective oxide layer forms or the reaction products can act as a source for introduction of wear debris [68,69]. Diffusion can also occur during corrosive wear where the diffusion process can alter the mechanical properties of the parent material and loss of material in the form of material transfer can occur if certain elements are preferentially diffused from the component's microstructure [70]. The synergistic combination of corrosive wear and mechanical wear is known to accelerate the rate of material removal/degradation experienced by components during operation where the combined influence of corrosion and mechanical wear is significantly greater compared to the individual effects of the wear mechanisms [71]. This has been demonstrated in a study carried out by *Chen et al* [72] where the synergistic effects of corrosion and wear of a 316SS alloy submerged in molten zinc was investigated. It was found that tribological effects of corrosion and wear were enhanced by each other. Corrosion resulted in the formation of a brittle scale of the alloys surface which produced abrasive wear debris, accelerating wear, and the effects of wear prohibited the formation of a protective $Fe_2Al_5Zn_x$ layer in molten zinc, which accelerated corrosion. The synergistic effect contributed to 90% of material removal.

2.5.1.2 Lubrication

The primary role of a lubricant is to reduce the coefficient of friction, and therefore reduce the amount of wear, that occurs between surfaces that come into contact, thus increasing the efficient working service life of the bearing. This is achieved as the interposing lubricant carries the load between the two surfaces which prevents asperities from coming into sliding contact.

The lubricant also reduces wear as it acts to reduce vibration, reduces heat generated by the bearing, prevents corrosive wear, and flushes away wear debris.

Fluid film bearings are categorised as hydrostatic or hydrodynamic bearings. Both types of bearings require a pressurised fluid to prevent the surfaces coming into contact. In hydrodynamic bearings, the pressurised fluid is generated due to the rotation of the journal bearing components whereas the pressured fluid of a hydrostatic bearing is generated by an external pump.

The lubricating film required to generate hydrodynamic pressure, with hydrodynamic bearings, is created by a shift in the position of the journal bearings components which occurs as the sleeve rotates during operation creating a lifting pressure. At a standstill, the sleeve component sits on the bottom of the bushing where the components are in full contact. As the sleeve starts to rotate, the eccentricity between the journal bearing centre and the sleeve centre changes which creates an oil convergent between the two surfaces. A visual representation of the pressure distribution of a rotating journal bearing is illustrated in Figure 2.9 where ω and e represent rotation speed and eccentricity, respectively. During rotation, the fluid is drawn into the converging gap and the viscosity of the oil supports the load where the fluid pressure increases as the radial clearance decreases. Hydrodynamic lubrication will only occur when the pressure developed within the fluid is sufficient to fully separate the surfaces [73].

Hydrodynamic bearings are designed to operate in full film lubrication. However, hydrodynamic pressure is dependent on rotation speed, viscosity, load and radial clearance [74]. Therefore, at certain stages of operation, such as start or stop or adverse operation conditions, a hydrodynamic pressure is not established and contact of the journal bearing occurs. During operation there are three lubrication regimes that the bearing can operate in: boundary lubrication, mixed lubrication, and hydrodynamic lubrication. During boundary lubrication, the bearing is in full contact, and the lubricant has negligible influence on minimising friction. Therefore, during this region the coefficient of friction is highest and therefore experience increased levels of wear. This regime occurs under high loads, low rotation speeds and low viscosity. Mixed lubrication occurs when there is a discontinuous lubricant film where some contact of asperities occurs. Although, there is contact between bearing surfaces, the partial establishment of the hydrodynamic film carries some of the load. Therefore, friction, and subsequent wear, is reduced in contrast to boundary lubrication. During hydrodynamic lubrication, no contact of the bearing surfaces occurs. This is the most desirable regime as there is very little wear occurring as the coefficient of friction is significantly reduced [75]. Each of the regimes of lubrication can be represented using a Stribeck curve, as shown in Figure 2.10. The image also gives a visualisation of the tribological interactions between the bearing's surfaces and the fluid film during each regime.

With reference to journal bearings used for bath hardware components during galvanising, the low viscosity of molten zinc, low rotation speeds and high loads means that hydrodynamic lubrication cannot be established and direct metal on metal contact occurs throughout operation [40].

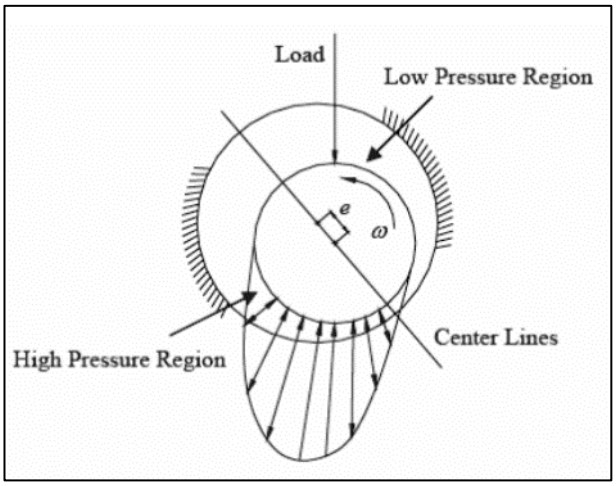

Figure 2.9: Example of pressure field generated in journal bearing during operation [73].

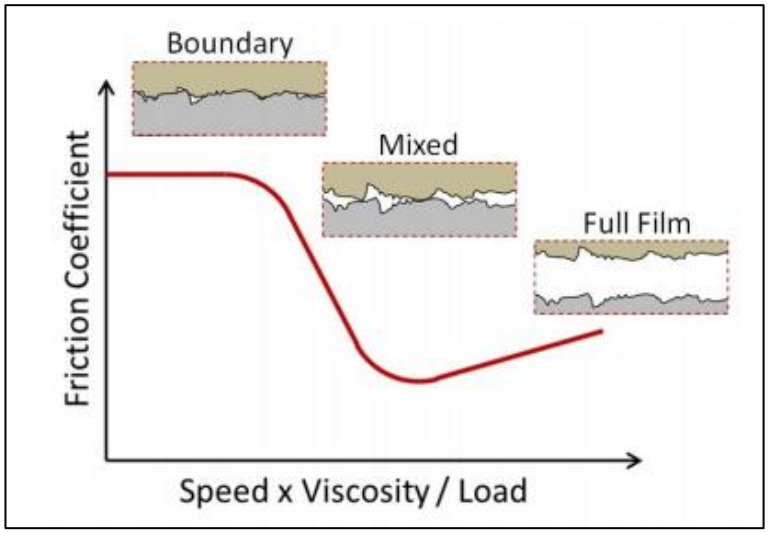

Figure 2.10: Stribeck curve demonstrating regimes of lubrication [76].

2.5.2 Cobalt and Cobalt-based Superalloys

Cobalt has been found to be used as a colouring agent for pottery and glass dating back 2600 years. However, it was not isolated as a metallic until around 1735. The discovery of the metal has been credited to a Swedish chemist, Georg Brandt [77]. The use of cobalt as a metallic alloy can largely be attributed to the CoCrW and CoCrMo ternaries investigated by Elwood Haynes at the start of the 20th century. It was Haynes who first discovered the high strength

properties of binary Co-Cr alloys and later identified the powerful strengthening effects of tungsten and molybdenum additions. These alloys were named Stellite which is now a trademark of the Kennametal Stellite company [78]. Many cobalt-based alloys have been developed that contain various amounts of alloying elements such as chromium (Cr), tungsten (W), molybdenum (Mo), iron (Fe), nickel (Ni), carbon (C), manganese (Mn) and silicon (Si). Altering the alloys chemistry allows for the microstructure and mechanical properties to modified to meet the demands of a particular application. Table 2.1 lists the chemical compositions of typical Stellite CoCrW and CoCrMo alloys.

Table 2.1 demonstrates that the primary difference between the cobalt-based superalloys is the carbon and tungsten content in the alloy's chemistry. Carbon additions determine the type and volume fraction of carbides that form the alloys microstructure during solidification. Therefore, carbon content plays an important role in dictating the structure and mechanical properties of the alloys as the alloys derive their strength from the formation of carbide phases [79]. For example, *Liu et al* [80] analysed the sliding wear and erosion resistance of Stellite 3 and 6 in addition to a novel high tungsten alloy. It was calculated that the microstructure of the Stellite 6 alloy, which contains 1-1.2wt.% carbon, consisted of 20% volume fraction (vol%) of carbide phases. These carbides are predominately chromium-rich eutectic carbides of the M_7C_3 type (where M represents the metal component). The Stellite 3 alloy, which has a carbon content of 2-2.4wt% and a higher tungsten content, the carbides produce approximately 38vol% of the alloy and are of the chromium-rich primary type (M_7C_3) and tungsten-rich eutectic type (M_6C). An example of the microstructure of these alloys is displayed in Figure 2.11. The wear and erosion resistance of the alloys was also tested using a pin on disc wear test and a particle impact test, respectively. The Stellite 3 alloy offered better wear and erosion resistance owing to the microstructure containing a larger amount of carbide phases. The importance of the carbide phases in providing the alloy with good abrasive resistance is summarised in Figure 2.12. Focussing on the Stellite alloys, Stellite 1 has the greatest volume fraction of carbide phases so therefore has the greatest abrasion resistance whilst Stellite 21 has the lowest volume fraction of carbide phases and the lowest abrasion resistance.

Cobalt alloys are generally categorised based on their carbon content which also determines their application. High-carbon (1-3wt%) alloys are designed for high wear resistance, low-carbon (<0.5wt%) alloys are used for high temperature (>500°C) applications, and low-carbon (<0.25wt%) alloys provide corrosion and wear resistance [81]. Alloys with carbon additions below 2wt% possess a hypoeutectic microstructure with primary fcc cobalt dendrites which are surrounded by eutectic M_7C_3 carbides. Co-Cr based alloys that have carbon additions in excess of 2.5wt% show a hypereutectic microstructure which is made up of primary M_7C_3 carbides which

are dispersed in an interdendritic eutectic matrix composing of solid solution and carbides. In the commercial group of Stellite alloys, carbon content tends not to exceed 2.5wt.%. Therefore, these types of alloys are not included in Table 2.1 Alloys with a carbon content, below 0.1wt%, are described as solid solution strengthened alloys [82].

Cobalt is the base element of these alloys, and the element plays a very important role in imparting desirable mechanical properties of the alloy. Cobalt imparts an unstable fcc crystal structure that possesses a very low stacking fault energy. The unstable nature of cobalt arises since pure cobalt, if cooled slowly, transforms from a face centred cubic (fcc) crystal structure to a hexagonal close-packed (hcp) crystal structure at 417°C. However, due to the sluggish nature of this transformation, the fcc structure in cobalt and its alloys is usually retained at room temperature and the hcp formation is triggered by a mechanical stress or the alloy being held at high temperatures for long periods. The low stacking fault energy associated with the unstable fcc structure gives these alloys desirable mechanical properties. It is believed to result in high yield strengths, high work-hardening rates due to interaction between stacking faults, and reduced fatigue damage under cyclic loading. These characteristics help prevent metallic damage during sliding wear. The low stacking fault energy also allows the alloy to absorb stresses through the fcc→hcp transformation which contributes to high resistance to cavitation and erosion-corrosion of cobalt alloys [83].

The chemical composition of Stellite alloys contains large amounts of chromium, typically ranging between 20-30wt.%. Chromium additions within the alloy has a dual function; it is the predominate carbide former where the majority of carbides are chromium rich. Chromium also plays a vital role in strengthening the matrix as a solute atom and it provides the alloy with resistance to corrosion and oxidation. Tungsten and molybdenum are added which improve the alloys wear, corrosion, and oxidation resistance. Elements such as tungsten and molybdenum provide additional strength to the matrix. Due to their relatively large atomic size, they act to impede dislocation movement. When present in high quantities, tungsten and molybdenum also improve the corrosion resistance of the alloy through the formation of carbide and intermetallic phases [81,84].

The addition of certain elements also aids in the formation of a desired crystal structure. Chromium, tungsten, and molybdenum stabilise the hcp structure and decrease the SFE. Whereas, elements such as iron, nickel and copper promote the fcc formation which increases the SFE of the matrix [82,83].

There is another family of cobalt-based superalloys which are known as Tribaloy alloys. The chemical composition of this group of alloys is listed in Table 2.2. Whereas CoCrW alloys are strengthened by the dispersion of carbide phases, the mechanical properties of Tribaloy alloys are

enhanced by the formation of an intermetallic phase, referred to as a Laves phase, which is dispersed in a softer eutectic matrix. Carbon content is kept to an absolute minimum to prevent the formation of carbides [85]. Instead, molybdenum and silicon are added in levels in excess of the solubility limit with the aim of encouraging the precipitation of the C-14 ($MgZn_2$) type phase which has a composition of Co_3Mo_2Si or CoMoSi. An example of a Tribaloy alloy is presented in Figure 2.13. These alloys are generally hypereutectic, and the primary Laves phase is so abundant, making up between 35-70vol% of the microstructure, that it dominates the materials mechanical properties. The role of the matrix in these alloys is far less pronounced than in the CoCrW alloys [86]. The Laves phase is extremely hard which gives the alloy outstanding abrasive resistance but severely limits the alloys ductility and impact strength. The primary Laves phase has a hcp structure and is dispersed in eutectic matrix comprising of smaller secondary intermetallic phases that are surrounded by a cobalt solid solution. The matrix also comprises of cobalt solid solution that is free from the secondary Laves phase. The solid solution phase is strengthened by the addition of chromium which also improves corrosion resistance [87].

The enhanced wear resistance of the Tribaloy alloys, compared to traditional Stellite alloys, is demonstrated in Figure 2.12. The improved wear resistance of the Tribaloy group is attributed to the large volume fraction of hard Laves phases. It is also demonstrated by *Renz et al* [88] who compared the high-temperature sliding wear performance of Stellite 12 and Tribaloy T-400. Results demonstrate that the T-400 has better high temperature hardness and significantly better wear resistance at higher temperatures using a pin on disc test. However, the increased hardness of the Tribaloys makes them brittle by nature.

Table 2.1: Composition (wt%, Co in balance) of various Stellite alloys [89].

Alloy	Process	Cr	W	Mo	C	Fe	Ni	Si	Mn	Others
Stellite 1	Cast	30	13	0.5	2.5	3	1.5	1.3	0.5	
Stellite 3	P/M	30.5	12.5		2.4	5	3.5	2	2	1B
Stellite 6	Cast	29	4.5	1.5	1.2	3	3	1.5	1	
Stellite 6	P/M	28.5	4.5	1.5	1	5	3	2	2	1B
Stellite 21	Cast	27		5.5	0.25	3	2.75	1	1	
Stellite 20	Cast	33	17.5		2.45	2.5	2.5		1	
Stellite 22	Cast	27		11	0.25	3	2.75	1	1	
Stellite 25	Cast	20	15		0.1	3	10	1	1.5	
Stellite 80	Cast	33.5	19		1.9					1B
Stellite 188	Cast	22	14		0.1	3	22	0.35	1.25	0.03La
Stellite 720	Cast	33		18	2.5	3	3	1.5	1.5	0.3B
Stellite 706K	Wrought	29		6	1.4	3	3	1.5	1.5	
Stellite 6B	Wrought	30	4	1.5	1	3	2.5	0.7	1.4	
Stellite 6K	Wrought	30	4.5	1.5	1.6	3	3	2	2	

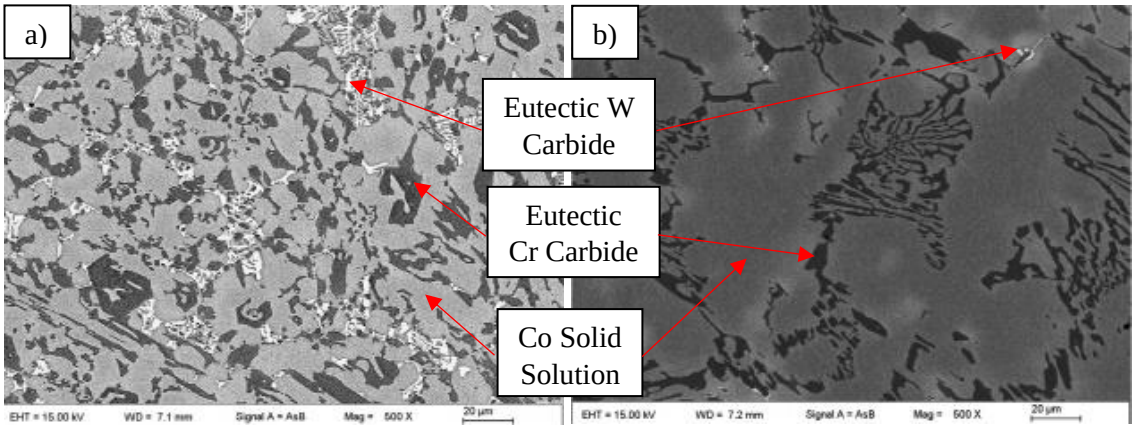

Figure 2.11: Microstructural analysis of a) Stellite 3 and b) Stellite 6 [80].

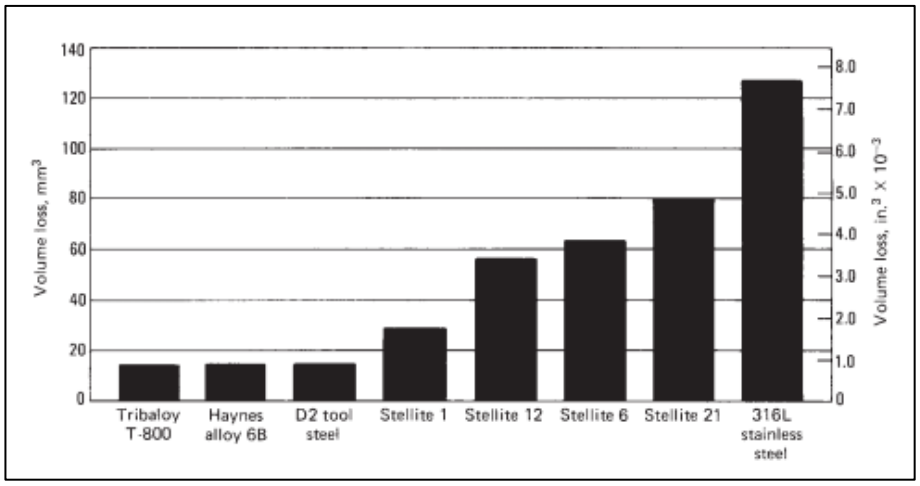

Figure 2.12: Low stress abrasion data for various cobalt-based alloys demonstrating the importance of carbides and Lave phases [83].

Table 2.2: Composition (wt%) of various Tribaloy alloys and estimated volume fraction of Laves phase [89].

Tribaloy alloy	Co	Ni	Cr	Mo	Si	Laves phase content (vol%)
T-100	55			35	10	~65
T-400	62		8.5	28.5	2.6	~45
T-700		50	15	32	3	~60
T-800	52		17	28	3	~55

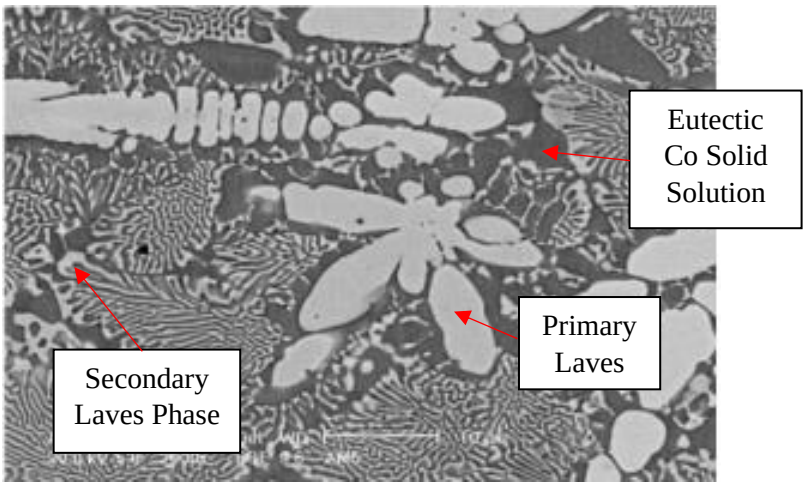

Figure 2.13: Microstructural analysis of a T-800 Tribaloy [90].

2.5.3 Wear and Chemical Reactivity of Cobalt-based Journal Bearings for Molten Zinc Applications

The previous section details how the superior mechanical properties of cobalt-based superalloys make them suitable materials for use in demanding wear applications. In addition to

their wear resistant properties, cobalt-based superalloys offer better chemical resistance to molten zinc compared to standard alloys [70,91]. For this reason, cobalt superalloys are the preferred choice for submerged journal bearing components on galvanising lines. However, due to the extreme nature of the application, the bearings produced from these alloys still experience extreme levels of wear in a relatively short period of time. It has been discussed in sections 2.4.1 and 2.4.2 that the condition of the bath hardware components is critical in producing high quality coated steel as degraded hardware can generate strip vibration which contributes to poor coating quality. As a result, the galvanising lines are routinely stopped every 2-4 weeks to replace worn journal bearing components [55]. The wear mechanisms and chemical reactivity of bearings produces a highly complex wear environment where a number of factors influence each other. The following sections will describe the chemical reactivity of the bearings and the molten zinc bath as well as the wear mechanisms associated with the rolling contact of the bearing components during operation.

2.5.3.1 Chemical Reactivity of Journal Bearings

As discussed in section 2.4.2, cobalt has a strong affinity for aluminium and CoAl particles can readily form when aluminium content in the bath is as low as 0.015wt.% at 460°C. *Zhang et al* [92] studied the reaction of various alloys in molten zinc. An example of CoAl formation at the alloys surface is presented in Figure 2.14a. The image demonstrates the formation of the CoAl phase at the surface of a Stellite 6 alloy in the form of a continuous layer and as discrete particles after 1-hour of bath immersion. Increasing the dip time resulted in an increased depth of diffusion. As aluminium in the reaction layer diffused into the bulk of the alloy, zinc would diffuse into the reaction layer to form zinc-based intermetallic phases behind the diffusion front, as shown in Figure 2.14b. Analysis of the diffusion zone indicated that some cobalt is incorporated in the zinc layer whilst some is leached out into the bath. In this study a T-400 Tribaloy was also tested under the same conditions. Similar to the Stellite 6, Figure 2.14b illustrates that diffusion initiated with the formation and progression of a CoAl layer into the bulk of the alloy and Figure 2.14d shows that this coincided with the formation of a zinc-rich layer behind the diffusion front. In contrast to the Stellite alloy, discrete CoAl particles were not observed at the surface of the T-400 alloys and less zinc was detected in reaction layer comparing similar immersion times. In both alloys, diffusion preferentially occurred in the cobalt-rich phase whereas the carbides and Laves phases were more resistant to the diffusion process. However, after increased exposure to molten zinc, zinc and aluminium was detected in both phases which suggests the phases slowly reacted with the bath. The data indicates that the Tribaloy performed better in molten zinc in terms of a reduced reaction layer thickness in addition to less intermetallic

phase formation at the surface. Enhanced performance of the Tribaloy alloys is further demonstrated in Figure 2.15. Figure 2.15a demonstrates the weight loss experienced by various alloys in a molten zinc bath containing 0.16wt.% Al after 500-hours of static dip testing. The standard 316L SS alloy, which is often used for bath hardware rolls, experienced corrosion rates of 100mg/cm^2 whereas Stellite 6 experienced 60mg/cm^2 in the same period of testing. The T-800 Tribaloy exhibited even greater chemical resistance to molten zinc where a corrosion rate of 0.5mg/cm^2 was calculated [70]. Figure 2.15b displays the thickness of reaction layer that formed on Stellite 6 and three Tribaloy alloys where the Stellite 6 experienced the greatest diffusion depth as a function of time [93]. The enhanced chemical resistance of Tribaloy alloys has been attributed to the large volume fraction of Laves phases and the increased additions of alloying elements retained in the cobalt-rich phase.

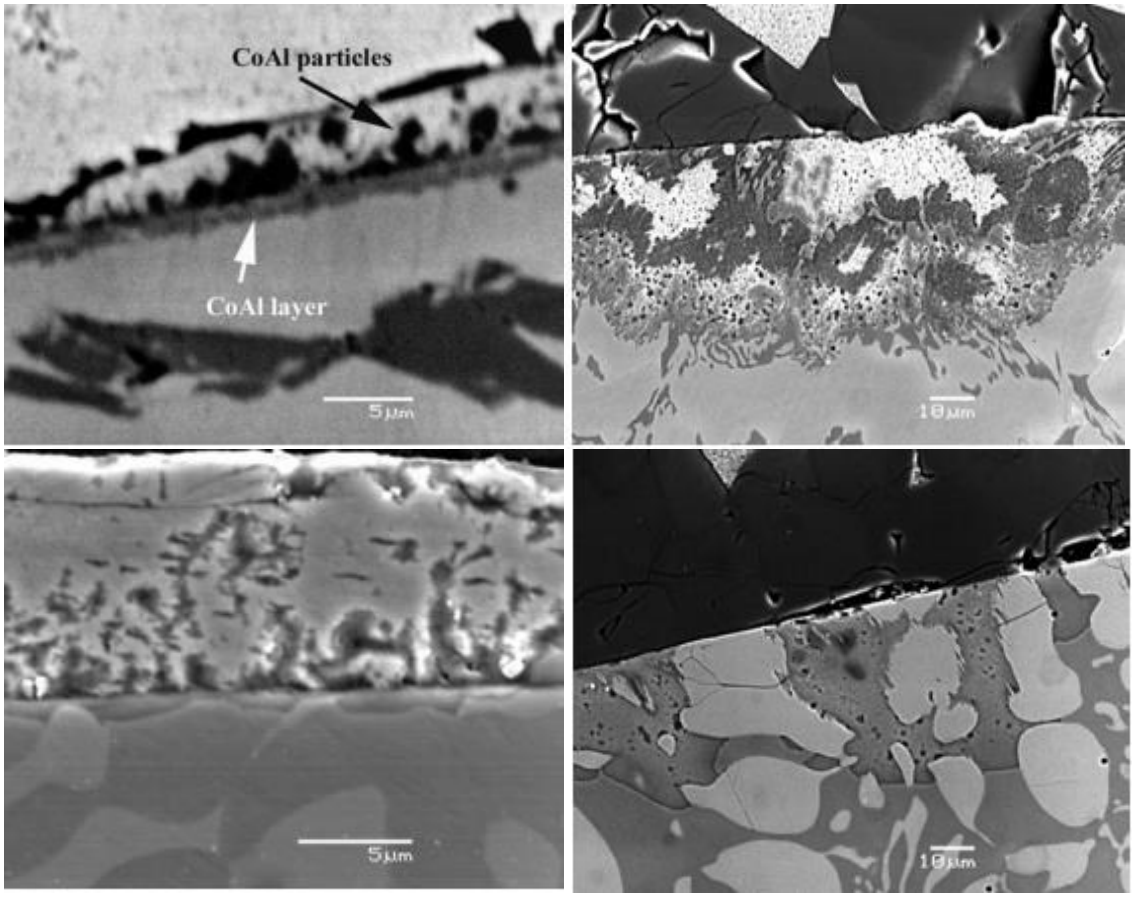

Figure 2.14: Cobalt aluminide formation on the surface of cobalt-based superalloy after 2-weeks of bath immersion [92].

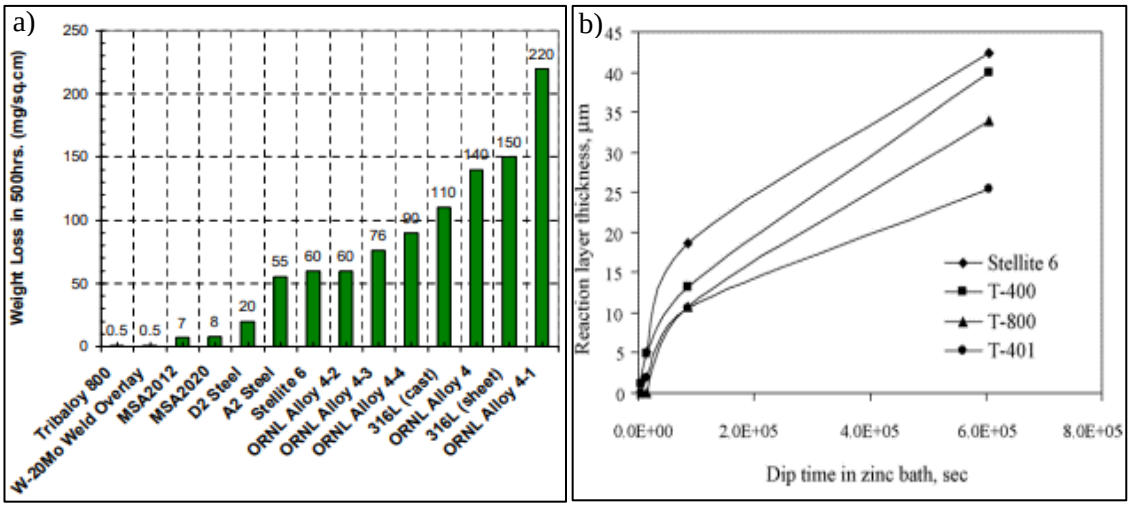

Figure 2.15: a) Weight loss experienced by various alloys after 500h of static dip testing in a molten zinc bath containing 0.15wt.% Al at 465 ℃ [70] *and b) reaction layer thickness as a function of time in a bath containing 0.22wt.% Al* [93].

2.5.3.2 Wear Mechanisms Associated with Journal Bearings

The worn surface of campaigned journal bearing components are often characterised by the existence of deep and wide grooving of the bearings contact surfaces. An example of a sleeve component before and after a 4-week campaign, transitioning between GI and GA bath chemistry, is displayed in Figure 2.16 which demonstrates the degree of wear experienced. The worn component exhibits deep and wide grooving of the surface which creates a series of peaks and troughs that travel parallel to each other around the circumference of the sleeve components surface. The lip at the bottom of sleeve illustrates that significant material removal occurred during operation. A similar wear pattern is observed with the paired bush component where grooving of the surface occurs at the contact area between the components, as shown in Figure 2.16c. Research has shown these grooves can reach millimetres in depth and width where the rotating sleeve generally experience increased levels of wear compared to the stationary bush component [16,53].

Research has determined that there is a strong correlation between the level of wear experienced by journal bearings and the combination of alloys that are used to produce the bearing configuration. The composition of the bath, particularly aluminium content, has also been found to have a strong influence on the level of wear. *Zhang* demonstrated the level of wear experienced by alloys when run against themselves and other materials in an aluminium containing bath. It was found that when self-mated, Stellite 6 experienced increased levels of wear damage, characterised by deep and wide grooving of the surfaces, compared to negligible and shallow grooving when run against a 316L SS sleeve and a laser-clad WC coated sleeve, respectively [94]. A further study by the same author also demonstrated how bath chemistry influenced the wear

behaviour the bearing components. In this study, self-mated Stellite 6 journal bearings were tested in zinc baths containing different levels of aluminium and iron. When tested in a pure zinc bath the surfaces of the components exhibited minor wear characterised by shallow grooving. However, when tested in baths containing aluminium the level of wear significantly increased with increased aluminium and iron content. This is clearly illustrated in Figure 2.17 where deeper and wider grooving of the contact surfaces was recorded with these bath compositions [53].

It has been established that the formation of dross particles in the bath are not directly responsible for the level of wear experienced by the bearings. Table 2.3 presents the hardness of the phases that can form within the bath during galvanising operations. Although the η ($Al_5Fe_2Zn_x$) phase is hard enough to deform the surface of a Stellite 6 alloy, the softer ζ ($FeZn_{13}$) phase would not be hard enough. However, bearings tested in individual baths containing these phases experienced similar levels of wear which suggests other wear mechanisms occur during operation. The concentrated levels of wear experienced in baths containing aluminium has largely been attributed to the formation of cobalt aluminide particles. Table 2.3 shows that the CoAl particles are extremely hard and could act as abrasive wear debris if they became entrapped between the contact surfaces. This has been demonstrated in a study that investigated how changing the bearing design effected the level of wear that was experienced. It was discovered that machining axial grooves on the contact surface of the bush component reduced the severity of wear experienced by the bearing components and reduced the coefficient of friction. The grooved channels were found to act as reservoirs for wear debris thus limiting the amount of abrasive particles between the contact surfaces [95]. This validates the theory that the formation of wear debris plays a significant role in journal bearing degradation.

Figure 2.18 displays a close-up image of a worn cobalt-based sleeve component after a 4-week campaign in molten zinc when paired with a dissimilar cobalt alloy grade. The image demonstrates that the dominant wear mechanism experienced during operation is abrasive wear which is observed in the form of grooving of the bearing surface. However, closer inspection of the surface exhibited other signs of wear. Figure 2.18b identifies evidence of fatigue and/or adhesive wear at the base of the groove tracks and at the asperity peaks. Cross sectional analysis of this sample (Figure 2.19a) demonstrates subsurface crack formation along the width of a groove asperity. The repeated loading and unloading during bearing rotation would likely have led to subsurface cracks forming which would eventually result in material detachment. Although this sample was pickled before analysis, thus removing any surface layers, during operation this detached material would have reacted with the bath to form a large CoAl wear particle. A similar process, taken from a different study, is highlighted in Figure 2.19b which displays a cobalt-based sleeve component where an asperity is in the process of reacting with the bath and detaching from

the parent material. The increased hardness of this particle could potentially result in ploughing of the bearing surfaces if it became entrapped between the contact surfaces. This process would also result in material removal and formation of additional wear debris. Measurement of these detached particles show that they can exceed 1mm in width which is similar to the width and depth of the grooves. Therefore, this is a likely cause of the deformation experienced by the journal bearings.

There is also evidence to suggest that the build-up of CoAl phases on the bearing surfaces is another cause of bearing deformation. Figure 2.20 demonstrates the attachment of a CoAl phase on the surface of journal bearing sleeve after operation. The hardness of this phase would plough the surface of the opposing bearing surface creating grooves on the macro scale. Similar to the interaction of abrasive particles, this process would result in material removal and the formation of additional wear debris.

Detailed analysis of tested bearings has indicated that an extremely complex tribological process occurs during operation. Fatigue and corrosive wear initially act to create abrasive wear debris which results in material removal which, in turn, would chemically react with the bath to form further abrasive wear debris. Therefore, the synergy between the corrosion and wear mechanisms significantly increases the interactions between the mechanisms [96]. This contributes to the extreme levels of wear experienced by the bearings and is the reason for their short service life.

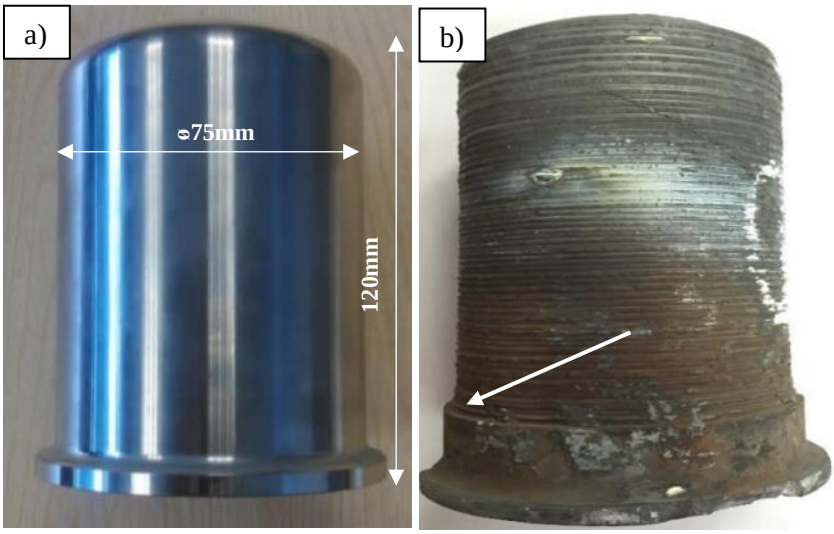

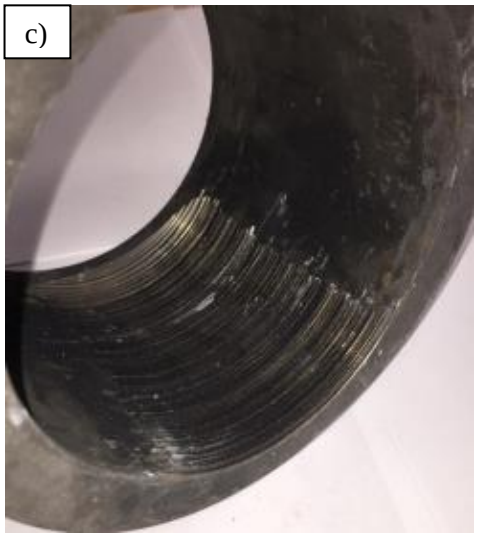

Figure 2.16: Sleeve component before and after a 4-week campaign transitioning between GI and GA bath chemistry: a) Cast sleeve component, b) campaigned sleeve component illustrating material removal and c) campaigned bush component [16].

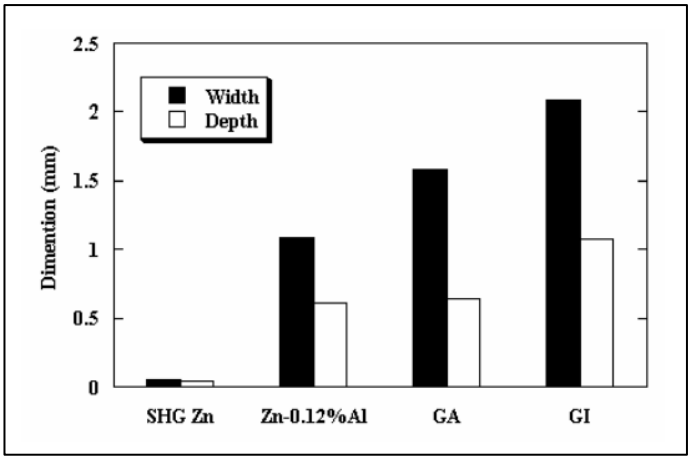

Figure 2.17: Width and depth of surface grooving after testing in bath containing various amounts of aluminium and iron [53].

Table 2.3: Hardness of phases that can form in the molten zinc bath with reference to a Stellite 6 alloy [54].

Material	**Hardness Hv**
ζ ($FeZn_{13}$)	181
δ ($FeZn_7$)	265
Γ (Fe_3Zn_{21})	421
η ($Al_5Fe_2Zn_x$)	693
Stellite 6	515
Al-Fe-Zn-Co-W	760
CoAl	1064

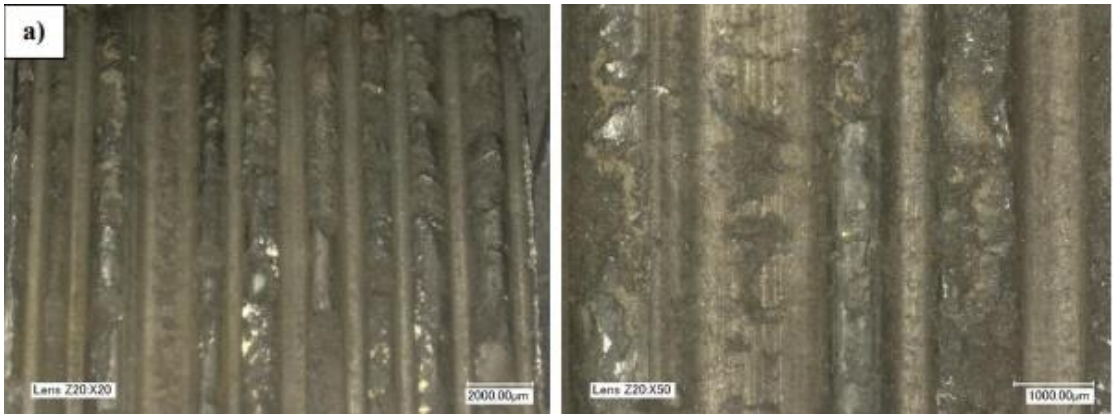

Figure 2.18: Worn surface of various cobalt-based sleeve components after a 4-week campaign [16].

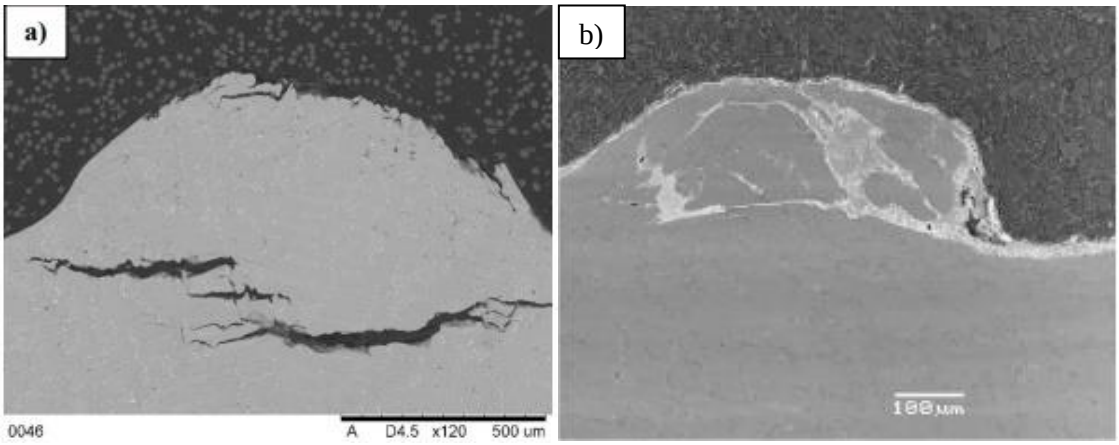

Figure 2.19: Fatigue wear resulting in crack formation and material detachment: a) Pickled sample illustrating fatgiue wear and b) Unpickled sample illustrating detached material reacting with the bath [97].

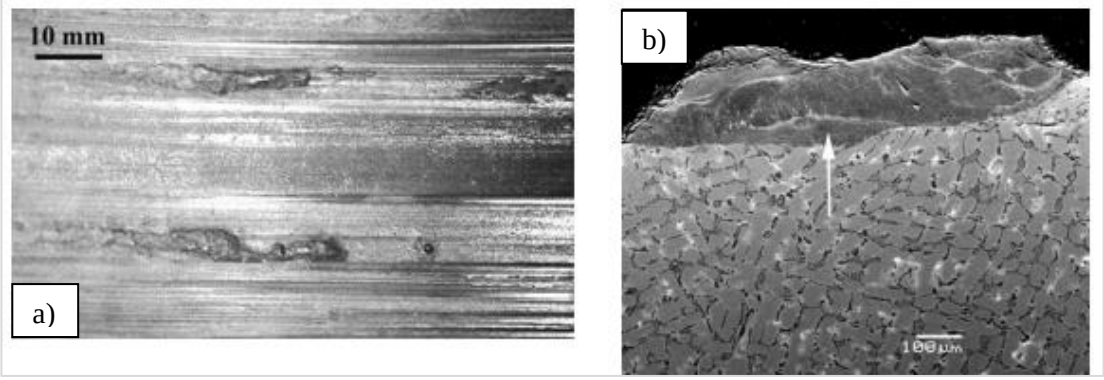

Figure 2.20: CoAl build-up on surface of tested Stellite 6 journal bearing components: a) optical surface view and b) cross section view [98].

2.6 Alloy Modification to Improve Wear and Corrosion Resistance

Due to their versatility and wide application in a number of industries, Stellite and Tribaloy alloys have been significantly researched, particularly their tribological mechanical properties. Two parameters that have been studied to improve the performance of cast components is the modification of the alloys chemistry or by changing the manufacturing processes of the alloy. Another frequently researched method of improving the performance of an alloy is the addition of surface coating. This has led to the development of a number of techniques that involve coating a component with a material that is better suited for wear and corrosion applications.

2.6.1 Alloy Chemistry

Stellite alloys consist of a cobalt rich matrix and the dispersion of a range carbide phases that form at grain boundaries and interdentritic regions where the carbide phases are responsible for strengthening the alloy and providing resistance to abrasion. Changing the chemistry of the alloy can result in phase formation, increased volume fraction of carbide phases, or the strengthening of the matrix through solid solution strengthening. *Shin et al* [99] investigated the effect of molybdenum on the microstructure and mechanical properties of a Stellite 6 coating. Increased molybdenum additions were found to increase the hardness and wear resistance due to the increased volume fraction of carbide phases. *Radu et al* [100] studied the effects of the addition of yttrium (Y) to a Stellite 21 alloy. It was found the addition of yttrium in the range of 0.5-5wt.% coarsened the carbide network and enhanced the high temperature wear performance of the of the alloy, particularly at temperatures above 500°C. This was attributed to the superior mechanical properties of the Y_2O_3 oxide scale at the surface. *Çelik et al* [101] investigated the wear behaviour of Stellite 6 with increased silicon content using a pin on disc test. The addition of silicon increased the hardness and wear resistance of the alloy at low temperatures.

The microstructure of Tribaloy alloys comprise of a large volume fraction of Laves phases which is surrounded by a softer cobalt rich matrix. The Laves phase dominate the microstructure and therefore provide these alloys with excellent wear and corrosion resistance but, consequently, they are extremely brittle and possess low impact strength. This severely limits the potential application of Tribaloys. The brittle nature of the Tribaloy alloys is clearly demonstrated in Figure 2.21 with reference to Stellite 6. The T-800 Tribaloy has the highest volume fraction of Laves phases present in the microstructure (Table 2.2) and is therefore also the hardest alloy with the lowest impact toughness. Attempts have been made to improve the ductility of the alloys by modifying the alloys chemistry to change the microstructure. *Xu et al* [102] developed two new Tribaloy alloys (T-400C and T-401) which contained less molybdenum

and silicon and more cobalt and chromium compared to a typical T-400 grade. The change in composition resulted in the T-400C alloy containing less Lave phases whereas the structure of the T-401 alloy changed to a hypoeutectic structure making the cobalt solid solution the primary phase. Although the ductility of these alloys improved, Figure 2.21 also shows that the T-401 possess better impact resistance than the T-800 and T-400 grades, the change to a hypereutectic structure with the T-401 alloy and the decrease in amount of Laves phases with the T-400C alloy resulted in a decrease in bulk hardness and a reduction in wear resistance under a ball on disc test with the newly developed alloys. It has also been demonstrated that the T-401 Tribaloy is more resistance to molten zinc, in terms of reaction layer thickness, compared to T-800 and T-400. This was attributed to the switch from a hypereutectic microstructure, observed with the T-800 and T-400 grades, to a hypoeutectic microstructure that contained less eutectic constituent [93]. The reduced reaction layer thickness, with comparisons made to T-800, T-400 and Stellite 6, is displayed in Figure 2.15b. The effects of yttrium plus aluminium [103] and rhenium [104] on the oxidation behaviour of T-900 and T-800 Tribaloys, respectively, has also been investigated. The addition of aluminium and yttrium plus aluminium refined the course Laves phase structure typical of T-900 and increased the hardness of the alloys as well as improving the wear resistance of the alloy under dry sliding conditions of a Si_3N_4 ball at room temperature. The addition of aluminium and yttrium also increased the oxidation resistance of the alloy due to selective oxidation, stronger adherence of surface scale, and a finer grain structure which prevented inward diffusion of oxygen and nitrogen. The addition of rhenium increases oxide growth and adherence at higher temperatures which reduces oxidation rate.

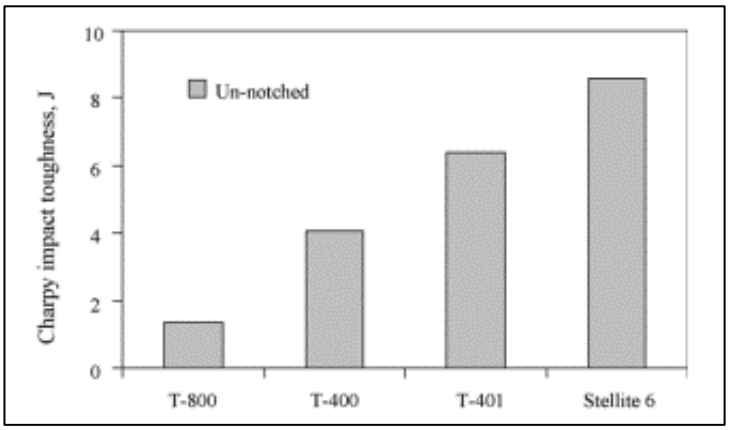

Figure 2.21: Charpy impact test on un-notched samples [93].

2.6.2 Heat Treatments

Various heat treatments are used to alter the microstructure of an alloy, thus changing the mechanical properties, without changing the shape of the component. A series of heating and cooling cycles are often used to control phase formation, precipitation, and grain size to produce an alloy with desired mechanical properties or to relieve changes in mechanical properties experienced during the manufacturing process, such as work hardening.

2.6.2.1 Annealing

During an annealing treatment, a component is heated at a controlled rate, held at certain temperatures for specific times, and then cooled at a controlled rate. During this time, the component is heated above the recrystallisation temperature which reduces the volume of dislocations and controls the level of grain growth. Steels are generally annealed to relieve internal stresses and soften the alloy prior to cold or hot working or to relieve work hardening effects. However, annealing cobalt-based superalloys can have the reverse effect where the annealing treatment can increase the hardness of the alloy. *OSMA et al* [105] found that annealing a Stellite 6 alloy at 1000℃ for 30minutes and subsequent air cooling, promoted the coarsening of interdentritic regions and resulted in diffusion of tungsten from solid solution into interdendritic regions. This contributed to an overall increase in bulk hardness of the alloy. The effects of the annealing treatment on a Stellite 6 alloy containing 5wt.% silicon was also investigated in the same research. The addition of silicon and an annealing treatment resulted in the dispersion of interdentritic phases throughout the dendrites, as shown in Figure 2.22, which contributed to an increase in the bulk hardness of the alloy. *Kuzucu et al* [106] also examined the effects of an annealing treatment on a modified Stellite 6 alloy containing 5wt.% silicon. In this study, samples were annealed at 950℃ for 2-hours and quenched in water as well as nitrogen. The annealing treatment and rapid cooling increased the hardness of the alloys due to the dispersion of interdendritic phases in the dendrites. Another study by *Kuzuca et al* [107] investigated the effects of an annealing heat treatment had on a Stellite 6 alloy containing 6wt.% molybdenum. Annealing the samples at 950℃ for 2-hours and cooling them in water or nitrogen resulted in an fcc→hcp transformation of the matrix, increased the volume fraction of carbide phases and resulted in a more homogenous distribution of the of the carbide phases, compared to a cast sample. This increased the overall hardness of the alloy.

The allotropic nature of cobalt can be fcc or hcp in structure where both structures can be present in metastable form in Tribaloy alloys. *Halstead* [108] identified that both T-800 and T-400 could be softened by annealing at temperatures of over 1000℃ due to a hcp→fcc

transformation of the solid solution phase and the coarsening of the lamellar Laves phases within in the eutectic.

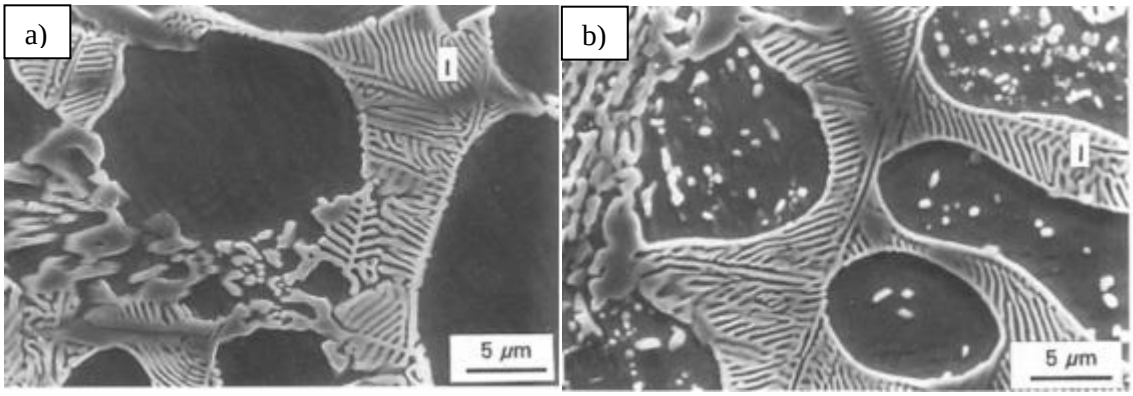

Figure 2.22: comparison of cast and annealed Stellite 6 alloys containing 5wt.% silicon: a) cast sample and b) sample heated to 1000℃ for 30minutes and air cooled.

2.6.2.2 Solution Treatment and Age Hardening

A solution treatment is the initial step in the precipitation or age hardening process. During this stage of heating, the sample is heated to a high temperature (above the solvus temperature) and held for sufficient time to allow for precipitates to diffuse to form homogenous solid solution phase to be produced. The alloy is then rapidly cooled in a quenching process to produce a supersaturated solid solution. This prevents precipitation occurring as atoms do not have time to segregate. Aging is the final stage of the heating process. The alloy is heated to temperature below the solvus which allows atoms to diffuse short distances and segregate at nucleation sites to form precipitates. The objective of precipitation hardening is to produce a microstructure that consists of a solid solution phase that contains a fine dispersion of precipitates that impede dislocation movement which increases the hardness of the alloy.

Ren et al [109] investigated the effects of a solution and aging treatment of a Stellite 12 laser additive manufactured coating. Comparisons were made between samples subjected to three kinds of treatments: solution treatment at 1250℃ for 4-hours and furnace cooled, aging at 950℃ for 12-hours and furnace cooled, and solution treated at 1250℃ for 4-hours plus an aging treatment at 950℃ for 12-hours. The treatments modified the microstructure where the solution treatment dissolved carbides into solid solution, but blocky carbides were formed. The hardness significantly dropped after the solution treatment. The aging treatment resulted in the precipitation of phases throughout the cobalt matrix which increased the hardness of the alloy. A solution and aging treatment formed globular carbides and although the hardness of the alloy increased, the increase in hardness was lower than age hardened sample. A pin on disc wear test indicated that

the sample that was age hardened significantly reduced the wear resistance of the alloy whereas the sample that was solution treated and aged experienced an improvement in wear resistance compared to an untreated sample. Solution treating a CoCrMo Stellite 706K alloy at temperatures ranging between 1235-1250℃ for 30minutes followed by water quenching, resulted in dissolution of some carbides and the coarsening of carbides. Although the hardness of the samples decreased with increased solution treatment temperature, the wear resistance increased at higher treatments. The heat treatment was found to stabilise the fcc structure of the matrix which offered enhanced wear resistance due to a high work hardening effect [110]. *Jaing et al* [52] investigated the microstructure, tensile strength, and stress-rupture properties of a cobalt-based DZ40M alloys in as-cast and solution as well as aged states. A solution treatment at 1280℃ for 4-hours resulted in complete diffusion of carbide phases to produce single-phase supersaturated solid solution. Comparisons of the as-cast and solution treated microstructures are shown in Figure 2.23. Further aging treatments at 950℃ for 12-hours resulted in the dispersion of secondary precipitates at grain boundaries. The solution treated sample increased the room temperature strength of the alloy as well as the tensile elongation. The solution and aged sample increased the strength of the alloy by 50% but severely reduced tensile elongation compared to the as-cast alloy. Stress-rupture tests carried out at 980℃ indicated that stress-rupture life was prolonged three and five times by the solution and aged samples, respectively, but reduced the rupture ductility of both samples.

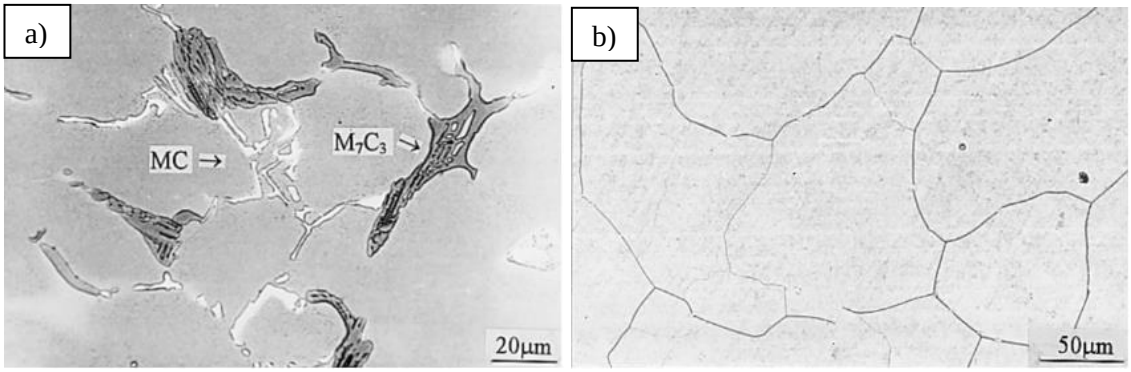

Figure 2.23: Comparison of as-cast alloy and solution treated alloy: a) as-cast alloy and b) alloy after solution treatment at 1280℃ for 4-hours.

2.6.3 Surface Engineering

Wear and corrosion experienced by components used in industry can lead to a significant decrease in performance which can have negative effects on the overall efficiency of the industrial process. In response to this, surface engineering techniques are often implemented to enhance the wear and corrosive performance of the components surface without affecting the mechanical properties of the bulk material. This has the benefit of the treated component retaining its

toughness whilst the surface is modified to better meet the requirements of the application. The types of surface technologies are often divided into two categories: surface modification, where the composition or microstructure of the parent material is altered, and surface coatings, in which a layer that has a different composition and microstructure is added to the surface of the substrate.

2.6.3.1 Diffusion Methods

Surface hardening through diffusion involves the chemical modification of the components surface by the diffusion of certain elements into the substrate. The diffusion of hardening elements such as nitrogen, carbon or boron is a thermochemical process where diffusion depth behaviour generally exhibits a time-temperature dependence. Therefore, increased diffusion depths are usually achieved with longer treatments times and/or higher treatment temperatures.

2.6.3.1.1 Nitriding

Nitriding is a thermochemical treatment that involves the diffusion of nitrogen into the surface of the treated component which acts to improve the mechanical properties at the surface. A major advantage of the nitriding process is that hardening is achieved without the need for quenching. This reduces the risk of distortion of the treated component.

During the nitriding process, precipitation of nitrides occurs when nitrogen solubility in ferrite is exceeded, which is around 6wt.% N. This results in the formation a compound layer (white layer) and a diffusion zone (case) at the surface of the steel component. For pure iron, nitrogen diffuses interstitially in the ferritic lattice of the diffusion zone. For steels with tempered martensite or steels containing nitride forming elements, nitrogen interstitially diffuses with ferrite and nitride precipitates also form in the diffusion zone. This process improves the mechanical properties of the treated components surface. As the nitriding process is a thermochemical process, greater case depths are achieved at higher temperature or longer treatment times which generally increase hardness and wear resistance. The effects of a gas nitriding surface treatment on the mechanical and corrosion properties of a SACM 645 steel were investigated by *Yeh et al* [111]. The investigation found that the nitriding treatment formed a compound layer and diffusion zone that contained nitride precipitates where the thickness of the diffusion layer increased with longer treatments. The nitriding process significantly increased the hardness of the surface and the wear resistance, fatigue limit and corrosion resistance also improved with increased treatment time.

Conventional nitriding techniques involve gas nitriding, salt bath nitriding and plasma nitriding. The gas nitriding process introduces nitrogen into the surface of the treated component by using a gas flow of ammonia (NH_3). Salt bath nitriding is similar to gas nitriding, but the nitrogen activity comes from the liquid salt bath. These techniques have been shown to improve the hardness and wear resistance of the steel component due to the formation of a compound layer and a diffusion zone, previously discussed. However, as these techniques are carried out at higher temperatures to allow sufficient nitrogen diffusion, they generally have negative effects on corrosion resistance. At typical temperatures used for these techniques (>500℃), chromium has enough mobility to form chromium nitrides (CrN) within the diffusion layer. This results in chromium depletion of the matrix and an effective oxide film cannot be formed which reduces the corrosion resistance as a consequence [111]. Therefore, a plasma nitriding technique was developed to improve the mechanical performance without reducing corrosion resistance. In this process, plasma is formed by high-voltage electrical energy in a vacuum. Nitrogen ions are accelerated and impinge on the surface of the treated component which is connected as a cathode. The bombardment of ions removes the surface oxide film which allows for uniform case depths and better uptake of nitrogen.

2.6.3.1.2 Carburizing

The carburizing process involves the diffusion of carbon into the surface of the substrate and is often applied using gas, salt bath and plasma techniques. The diffusion process provides gradual change in carbon concentration and carbide volume, in contrast to the bulk material, which increases the mechanical properties and corrosion resistance of the surface. When carburizing steels, the temperatures usually range between 850-950℃. At this temperature austenite, which has a high carbon solubility limit, is the stable crystal structure. The surface is hardened when the carbon rich layer is quenched to form martensite. Carbon content is maintained between 0.8-1wt.% to prevent embrittlement or increased carbide formation at the surface. *Vikas et al* [112] demonstrated that the hardness, wear resistance and tensile strength of a low carbon steel increased with increased carburizing temperature and time.

2.6.3.1.3 Carbonitriding and Nitrocarburizing

Carbonitriding and nitrocarburizing are hybrid techniques that involve the diffusion of both carbon and nitrogen into the surface of the component. The nitrocarburizing technique involves more nitrogen diffusion than carbon, and the carbonitriding technique involves more carbon diffusion than nitrogen. Carbonitriding alters the austenitic composition at the surface and

increased hardness is achieved via quenching to form martensite. Nitrogen is added which allows for low-carbon alloys to achieve a similar surface hardness to high alloy carburized steels without the need for extreme quenching processes which can result in component distortion. Compared to carburizing the case depth is generally shallower due to the lower treatment temperatures. However, the diffusion of nitrogen increases the hardening effect.

Nitrocarburizing differs from traditional nitriding as the carbon and nitrogen gradient experienced during diffusion, allows for a similar surface structure to be achieved at much shorter process times when performed at slightly higher treatment temperatures. Nitrocarburizing treatments can be classified as ferritic and austenitic categories. Ferritic nitrocarburizing is carried at relatively lower temperatures and therefore does not involve phase transformation at the surface which minimises distortion [113]. Austenitic nitrocarburizing is performed at a higher temperature than ferritic nitrocarburizing which allows for a thicker compound layer to form. The formation of iron-carbon-nitrogen layer also forms between the compound layer and diffusion zone. After quenching, the austenite layer is transformed into martensite which has a high hardness and acts to support the compound layer. This gives the layer improved load bearing capacity [114].

2.6.3.2 S-phase Formation

As discussed in the previous sections, thermochemical treatments involving the diffusion of nitrogen and/or carbon can significantly improve the surface hardness and wear resistance of a treated component. However, this generally results in a decrease in corrosion resistance. This occurs due to the temperature at which traditional nitriding techniques are performed which can allow for CrN formation within the diffusion layer. Although the formation of these phases improves surface hardness and wear resistance, the depletion of chromium leaves the surface vulnerable to corrosion. *Zhang and Bell* discovered that a low temperature nitriding treatment could improve the surface hardness and wear resistance of the material but the diffusion zone retained the same corrosion resistance equivalent to the substrate material [115]. The low temperature treatment results in a diffusion layer that consists of a metastable phase that is supersaturated with nitrogen. The phase is known as expanded austenite γ_N, S-phase, or *m* phase. The formation of this phase is responsible for the increased mechanical and tribological properties at the surface with no detrimental effects on the materials corrosion resistance [116]. The formation of the S-phase can also be achieved using carburising [117], nitrocarburisng [118] and carbonitriding techniques. [119]. The formation of the S-phase has also been identified in CoCr alloys by low temperature plasma carburising [120], plasma nitriding and plasma carbonitridng [121].

2.6.3.3 Surface Treatment of Cobalt-based alloys

Improving the surface hardness and wear resistance of steel alloys via surface diffusion techniques has been extensively researched whereas the treatment of CoCr alloys has received less attention. However, the use and treatment of CoCr alloys for biomaterials has received significant research [122]. Owing to their wear and corrosion resistant properties, CoCrMo alloys are widely used for orthopaedic implants as the alloy provides good wear resistance during metal-on-metal contact and the formation of a Cr_2O_3 film provides corrosion protection [123]. However, the formation of wear debris and release of metal irons can occur due to wear and/or fretting corrosion of the implant. Over time this can lead to implant failure, osteolysis or allergic reactions. Plasma immersion ion implantation (PIII) is an advanced surface technique that has been used to improve the performance of medical implants. The PIII process differs from conventional ion implantation in that the treated components are surrounded by a high density plasma and a series of negative, high voltage pulses are to applied which implants ions into the target [124]. The PIII process results in the formation of a hard and wear resistant surface layer which significantly reduces the formation of wear debris material. However, even at low temperatures (350°C) where no CrN precipitates form, the complete formation of a protective Cr_2O_3 layer cannot form which lowers the materials corrosion resistance. It is believed that the affinity of chromium for nitrogen reduces the mobility of chromium [125].

Although there is limited literature available regarding the diffusion treatment of Stellite alloys, attempts have been made to improve the mechanical properties of various Stellite grades using plasma surface alloying (PSA) techniques. *Oliveira et al* [126] investigated the effects of a low temperature plasma carbonitriding on the cavitation erosion resistance of a Stellite 250 alloy. Samples were treated at 380°C for times ranging between 3-15 hours. The treatment resulted in the formation of dual layer of S-phase which comprised of a top layer of nitrogen S-phase and a carbon S-phase layer beneath it. The thickness of the layer ranged between 4-14.7μm where a maximum hardness of 1000Hv was measured. Increased S-phase layer thickness and hardness occurred after a longer treatment. A 9-hour plasma treatment resulted in the greatest improvement in cavitation erosion resistance, despite a thicker and harder layer forming after a 15-hour treatment.

The effects on the wear properties of a Stellite 12 alloy after a plasma treatment was examined by *Chen et al* [127]. In this study a series of plasma treatments were carried out at temperatures between 400-550°C using both nitrogen and carbon. Results indicated that the thickness of the diffusion layer increased after longer treatment times and after higher treatment

temperatures. The formation of a dual S-phase layer of Nitrogen and carbon was observed after a treatment at 460℃ whereas a treatment at a higher temperature of 550℃ resulted in the precipitation of a top layer. An example of the cross sections is displayed in Figure 2.24. The surface hardness increased 2-3 times following a PSA treatment with nitrogen and carbon and the sliding wear of the alloy in air and 3.5% NaCl solution increased by 99% and 96%, respectively.

Kim et al [128] explored the effects of plasma nitriding and plasma nitrocarburizing treatments at different temperatures on Stellite 6. A maximum increase of 1300HK was achieved with a plasma nitriding treatment where the thickness of the compound layer reached around 8μm. The increase in hardness was due to the precipitation of CrN. The plasma nitrocarburizing resulted in a much thicker compound and diffusion layer (30μm) but a lower hardness of 1200HK was recorded.

The corrosive wear performance of a single and double layer Stellite 6 weld cladding after a nitriding treatment was studied by *Brownlie et al* [129]. Samples were gas nitride at 520℃ for 72-hours and then the erosion-corrosion resistance was tested using an impinging slurry jet at different angles. The nitriding process increased the hardness of the cladding from 400Hv to 680Hv where the hardness gradually decreased moving into the bulk of the cladding. The treatment was found to reduce the corrosion resistance of the cladding, but the nitride cladding demonstrated smaller total mass loss, compared to an untreated sample, at a 20° impingement. The reduction in material loss was attributed to an increase in hardness which improved sliding abrasion resistance, although no benefits were observed under direct impingement conditions.

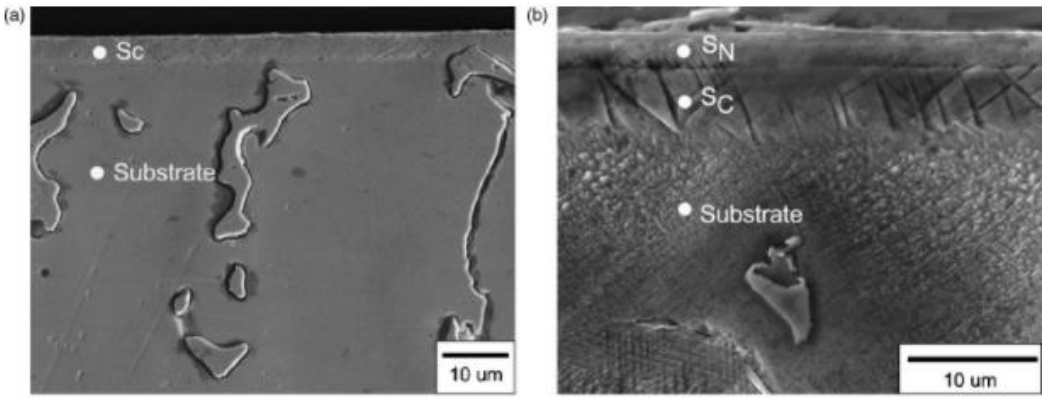

Figure 2.24: Cross sectional analysis of PSA samples after a 15-hour treatment: a) 460℃ and b) 550℃ [127].

2.6.3.4 Coating Methods

Another method of improving the performance of a material is by the application of a protective surface layer with a material that possesses enhanced wear and corrosion resistant

properties. Examples of coating techniques are laser cladding, spray coatings and plasma coatings. With each technique, the bulk material generally has a different composition and microstructure compared to the coating material. Therefore, the application of a surface coating has the benefit of the bulk material retaining its ductility and toughness whilst the coating provides increased wear and corrosion resistance.

The enhanced performance of Stellite and Tribaloy alloys in high wear and corrosive environments is well documented. Therefore, the application of these alloys has been utilised as surface coatings for components that operate in demanding applications. Laser cladding is a frequently used process that involves a high-powered laser beam that melts the coating material in a continuous manner that forms a metallurgical bond with the substrate. This results in a coating that compact and pore free, with a fine microstructure that has a strong bond with the substrate. This produces a coating that possesses high hardness and enhance wear and corrosion resistance. The application of Stellite and Tribaloys via laser cladding has been extensively researched where research has focussed on microstructure and mechanical property evolution [130–132] and process refinement [133–135].

The versatility of cobalt-based alloys has led to the development of several other techniques that involve their application. High-velocity oxygen fuel (HVOF) is a common spray technique used to apply cermet coatings such as WC/Co and MoB/CoCr coatings. With this technique feedstock material is heated to near or above the melting point by a high-velocity combustible gas stream and is deposited on the substrate material. When the spay contacts the surface, the fine droplets solidify rapidly to form the coating. In this process the substrate is kept relatively cool compared to the coating. This avoids substrate distortion and microstructural changes of the coating and substrate material. Activated combustion high-velocity air fuel (AC-HVAF) is a similar spray technique to HVOF but better coating density and lower oxide content can be achieved with AC-HVAF [136]. Plasma coating are applied in a similar way to the HVOF and AC-HVAF coatings where the coating material is in the form of a powder is injected into a high temperature flame where it is heated and accelerated to a high velocity. The heated powder then rapidly cools as it comes into contact with the substrate to form the coating.

Comparative studies of various coating techniques have shown that laser cladding generally forms a better wear and corrosion resistant coating. Laser cladding offers a strong bonding strength of a thick, compact and pore free coating where there is little heat affected zone and therefore small amounts of dilution. Thermal spray techniques tend to produce coatings that contain higher levels of porosity and microcracks within the coating [137,138]. This is illustrated by *Kusmoko et al* [139] who investigated the performance of Stellite 6 produced using laser cladding, HVOF and plasma spraying techniques. It was found the laser clad coating produced

the best surface finish where the plasma and HVOF coatings had higher roughness. The laser clad coating contained no porosity or cracks. This provided the material with a higher microhardness and better corrosion resistance under a pin-on-plate wear test compared to the other coating techniques.

The degradation experienced by bath hardware on galvanising lines has been outlined in previous sections. Molten metal diffusion of the 316L SS sink roll occurs due to the breakdown of the protective chrome oxide layer and journal bearing components are exposed to a combination of concentrated wear and corrosion as reactions with the bath and consequences of direct metal-on-metal contact occurs. Therefore, surface coatings have been used to combat the effects of wear and/or corrosion. Due to the large size of the sink roll spay coatings have been used to enhance their performance in molten zinc where WC/Co or MoB/CoCr coatings are often used. These coatings offer good resistance to molten metal diffusion but porosity and the microcracks within the coatings allows zinc to penetrate the coating. This results in large sections of material detachment if cracks join or delamination of the coating if the zinc is able to reach the substrate [48,96]. Laser clad WC coatings are commonly used to coat 316L SS sleeves. The coating provides good wear and corrosion resistance to increase their service life. Laser clad coating consist of WC carbides that are embedded in a softer solid solution phase. It has been shown that molten zinc preferentially diffuses into the solid solution phase of the coating and that prolonged bath exposure results in the detachment of carbide phases [92].

2.7 Literature Review Findings

Wear experienced when two surfaces come into contact is an extremely complex interaction which is amplified significantly when the components are also exposed to a corrosive environment. In the case of the current research, this interaction involves journal bearings that are submerged in molten zinc during operation on a galvanising line. The areas explored in this chapter investigated the microstructure and mechanical/corrosive properties of various grades of cobalt-based superalloys in addition to several heat treatments that are often used to improve the performance of these alloys. This research provided a better understanding of the alloys and their performance in industry as well as highlighting potential heat treatments that could improve the performance of the journal bearing components.

Research and initial testing indicated that improving the performance of journal bearing components would require an improvement in wear resistance or chemical resistance of the alloys, ideally a combination of the two properties. From the literature it was established that, although many efforts have been made in researching various properties of cobalt-based alloys, the

available data is still very limited and becomes even more restricted when looking at specific alloy grades.

From the literature, the investigation of a limited number of modified Stellite 6 alloys was identified for a high temperature annealing process. It was also found that solution treating cobalt alloys was generally restricted to grades with low carbon content, although limited data on Stellite alloys was found. However, the data available did indicate improvements in alloy performance could be achieved via both heat treatments. Therefore, changes in microstructure and material hardness were investigated after each of the heat treatments mentioned. With each heat treatment process, treatment parameters such as time and temperature were also varied to observe how the treatments influenced the alloys microstructure and mechanical properties.

It was discovered that diffusion treatments of medical cobalt grades have received significant levels of research. But the heat treatment of Stellite grades via diffusion processes was restricted to several research papers where it was found that a nitriding treatment successfully improved the hardness and wear resistance of the treated alloys. Therefore, the current research looked to expand upon the limited available data by investigating the effects of a nitriding treatment of a range of cobalt alloys as well as studying how the nitriding heat treatment temperature and time influenced the microstructure and mechanical properties of the alloys. The performance of Stellite grades in molten zinc has generally been restricted to untreated cast components. Therefore, the performance of several cobalt alloys in molten zinc was also investigated after a nitriding treatment to identify any changes in resistance to bath reactivity.

The four alloys used in this study are common grades of cobalt-based alloys which have also been frequently used to produce journal bearing components. Therefore, the focus of this research was to improve the hardness and chemical resistance of these alloys which would, in theory, improve their performance during operation.

3 Experimental and Sample Preparation

3.1 Experimental Material

The alloys investigated for this research were cast and machined to size at Weartech International Ltd. The chemical composition of the alloys is presented in Table 3.1. It is worth noting that these alloys are similar in composition to trademarked Stellite alloys produced by Kenematal Stellite Company. The samples were cast into a bar form and machined to a 2.5cm diameter and then sectioned to be 2.5cm in length. A hole was also drilled through the sample at one end to allow the samples to be suspended in the molten zinc bath and suspended during the plasma nitriding heat treatment ensure that the circumference of the sample was exposed to the plasma treatment. An example of sectioned sample is displayed in Figure 3.1.

Table 3.1: Chemical compositions (wt%) of cobalt-based alloys used in this study.

Alloy	C	Cr	Co	W	Ni	Fe	Si	Mo	Mn	Hardness (Hv)
WT-4	0.8	30	Bal.	14	<3	<3	1.5	<1	<1	440-520
WT-6	1.1	28	Bal.	4	<3	<3	1.1	<1	<1	370-490
WT-12	1.4	29	Bal.	8	<3	<3	1.5	<1	<1	440-550
T-800	0.08	17	Bal.	0	0	0	3. 5	29	0	580-740

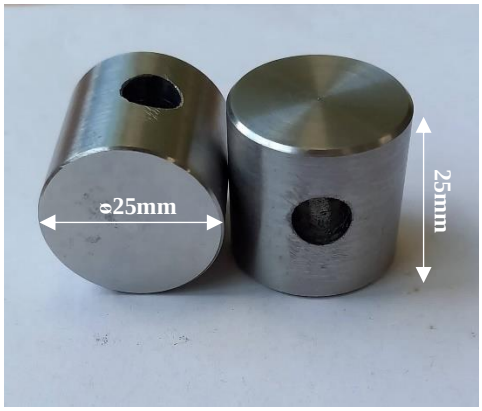

Figure 3.1: Sectioned sample.

3.2 Heat Treatments of CoCrW and CoCrMo Alloys

Various heat treatments were performed on each of the alloys received from Weartech with the aim of altering their microstructures to improve their mechanical properties and corrosion resistance. Each alloy was exposed to various high temperature annealing heat treatments, precipitation hardening heat treatments and plasma nitriding heat treatments. The parameters for each heat treatment are outline in the following sections.

3.2.1 High Temperature Annealing

A high temperature annealing heat treatment was carried out using a Carbolite furnace. Sectioned samples of each alloy were heated slowly to ensure that the entire sample was at a uniform temperature and then held at 1000°C for 1, 2- and 4-hour periods. The samples were then furnaced cooled to room temperature. One set of samples was cooled via a water quenching process after a 1-hour heat treatment to observe how the cooling process influenced the materials microstructure and mechanical properties. The heat treatment parameters for the annealing process are outlined in Table 3.2.

Table 3.2: High temperature annealing treatment parameters and cooling processes (WQ-water quenched, FC- Furnace cooled).

	Annealing Time (Hours at 1000°C) and Cooling Process			
WT-4	1-Hour - WQ	1 Hour - FC	2 Hour - FC	4 Hour - FC
WT-6	1-Hour - WQ	1 Hour - FC	2 Hour - FC	4 Hour - FC
WT-12	1-Hour - WQ	1 Hour - FC	2 Hour - FC	4 Hour - FC
T-800	1-Hour - WQ	1 Hour - FC	2 Hour - FC	4 Hour - FC

3.2.2 Solid Solution and Age Hardening

A solid solution and age hardening process was also carried out using the same Carbolite furnaces. Sectioned samples were initially subjected to a solid solution heat treatment which involved slowly heating the samples to 1275°C for 6-hours. The aim of this treatment is to promote diffusion of carbide phases to produce a supersaturated solid solution phase. Therefore, following a 6-hour solution treatment the samples were water quenched to prevent precipitation occurring during cooling. After the solution treatment and quenching process, samples were heated at 850°C for 2, 4 and 8-hours and then furnace cooled to room temperature. The solid solution and age hardening treatment parameters that were performed on each alloy are displayed in Table 3.3.

Table 3.3: Solid solution and age hardening treatment parameters repeated for each alloy.

Solid Solution Treatment Time (hours at 1275°C)	**Ageing Temperature (°C)**	**Ageing Time (hours)**
6	No age hardening	No age hardening
6	850	2
6	850	4
6	850	8

3.2.3 Plasma Nitriding

A plasma nitriding diffusion treatment was performed on sectioned samples of each alloy. The work was carried out at JJ Castings LTD. Two separate tests were carried out to investigate how changing the treatment temperature and treatment time influenced any changes in microstructure, mechanical properties, and corrosion resistance. The treatment temperatures and times varied between 400-550°C and 10-20 hours, respectively. The nitriding treatment parameters are detailed in Table 3.4 and were repeated for each alloy.

Table 3.4: Plasma nitriding heat treatment parameters repeated for each alloy.

Test 1		**Test 2**	
Treatment time (h)	**Treatment temperature (°C)**	**Treatment time (h)**	**Treatment temperature (°C)**
15	400	10	475
15	450	15	475
15	500	20	475
15	550		

3.3 Static Immersion Testing

Sectioned samples of the CoCrW and CoCrMo alloys provided by Weartech were subjected to static immersion dip testing under laboratory conditions using furnaces at Swansea University. All samples were secured using pure tungsten wire and suspended in a molten zinc alloy bath, ensuring the samples were fully submerged, and held at a temperature of 465°C. The bath was a molten zinc alloy containing 0.35wt.% Al and saturated with Fe. The molten zinc used for the tests was taken directly from a zinc bath at a Tata steel site in Shotton, North Wales. Taking the zinc directly from the bath would provide more relatable data concerning the chemical reactions occurring in the zinc bath at that site. Before immersing the samples, the zinc bath was heated and held at 465°C to ensure the bath was fully molten and at a uniform temperature. The samples were also held at a temperature of 465°C for a sufficient period prior to bath immersion to avoid any potential effects of thermal shock which may have resulted in cracking of the material. Each alloy was immersed for 1-4-week periods where one sample was periodically removed from the bath to observe molten zinc dissolution characteristics and related chemical reaction mechanisms that occur at the alloys surface. Analysis of the samples at these intervals would also give an indication of the rate at which diffusion occurs with each alloy. The data would provide an understanding of how the cobalt-based alloys react with the molten bath as well as demonstrating which alloys provide the best chemical resistance. A four-week test was chosen as this is a typical campaign length of a journal bearing at Shotton's Tata Steel.

3.4 Microstructural Analysis

3.4.1 Surface Preparation

After the samples were heat treated or dip tested, they were mounted in a conducting resin (Bakelite) leaving a cross section of the samples surface exposed. A Buehler automated polisher was used to grind and polish the samples where several grinding and polishing stages were used to prepare the surface for analysis. The samples were ground from a 320 grit SiC paper to a 1200 grit SiC paper and then polished to a 0.05micron finish leaving a mirror finish and scratch free surface. In between each step the grinding stage and the samples were rinsed with water to avoid any contamination from the previous grinding stage. After the final polishing stage, the sample was rinsed with ethanol and dried using hot air.

3.4.2 Secondary Electron Microscopy (SEM) and Energy Dispersion X-Ray Spectroscopy (EDS)

As-received, heat treated, and dip tested samples were analysed using a ZEISS EVO scanning electron microscope (SEM), fitted with an Energy Dispersion X-Ray (EDS) detector. Samples were cross sectioned to allow for specific phases, surface reaction layers and diffusion layers to be investigated using SEM and EDX techniques. Qualitative analysis provided data on the presence of specific elements and quantitative analysis provided information on the amount of those elements. The EDS instrument used for this research has a limitation in accurately measuring carbon content to produce reliable wt.% measurement. Therefore, the elemental compositions produced using EDS analysis only display the metallic elements detected in the alloy's microstructure.

3.4.3 Phase Area Fraction Analysis

ImageJ software is a Java-based open-source image analysis package developed by the National Institute of Health (NIH) [140]. In this study, an image thresholding technique was used to calculate the area fraction of individual phases within the microstructure of untreated and treated alloys. The technique was carried out on SEM images where the software divided the image into two classes, typically referred to as foreground and background. To calculate the area fraction of specific phases, a pixel cut-off value was used such that every pixel lower than that value was considered one class, while every pixel greater than that value was considered the other class. The values were then converted into an area fraction of the image to measure individual phases. Analysis of untreated and treated samples would provide data on how the heat treatments

effected the morphology of the alloy's microstructure. An example of the thresholding technique is displayed in

Figure 3.2 which illustrates the area fraction analysis of the carbide phases of a WT-12 alloy. Area fraction analysis of precipitated phases within the cobalt solid solution phase of the alloys required an additional step prior to the threshold calculation, as shown in Figure 3.3. This involved selecting a certain area of the image and excluding everything outside of the selected area.

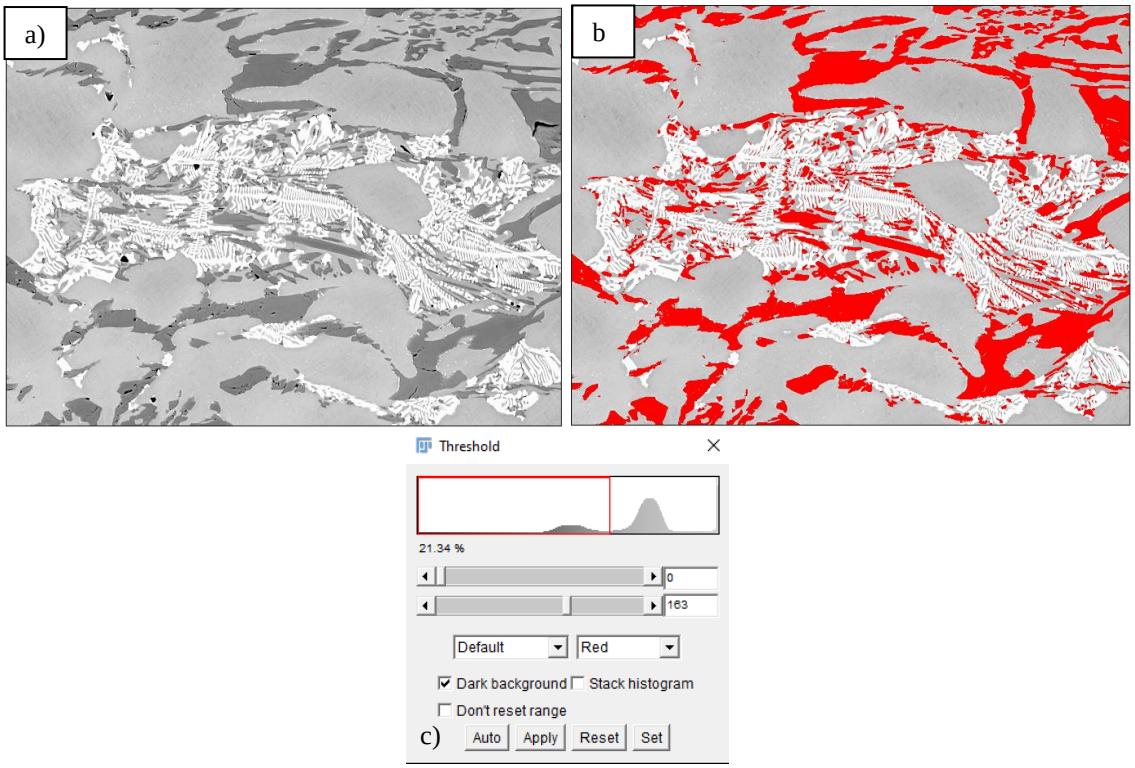

Figure 3.2: Example of ImageJ threshold analysis used to calculate the area fraction of specific phases of the alloy's microstructure: a) SEM image of sample, b) area fraction analysis of specific phase and c) Threshold selection.

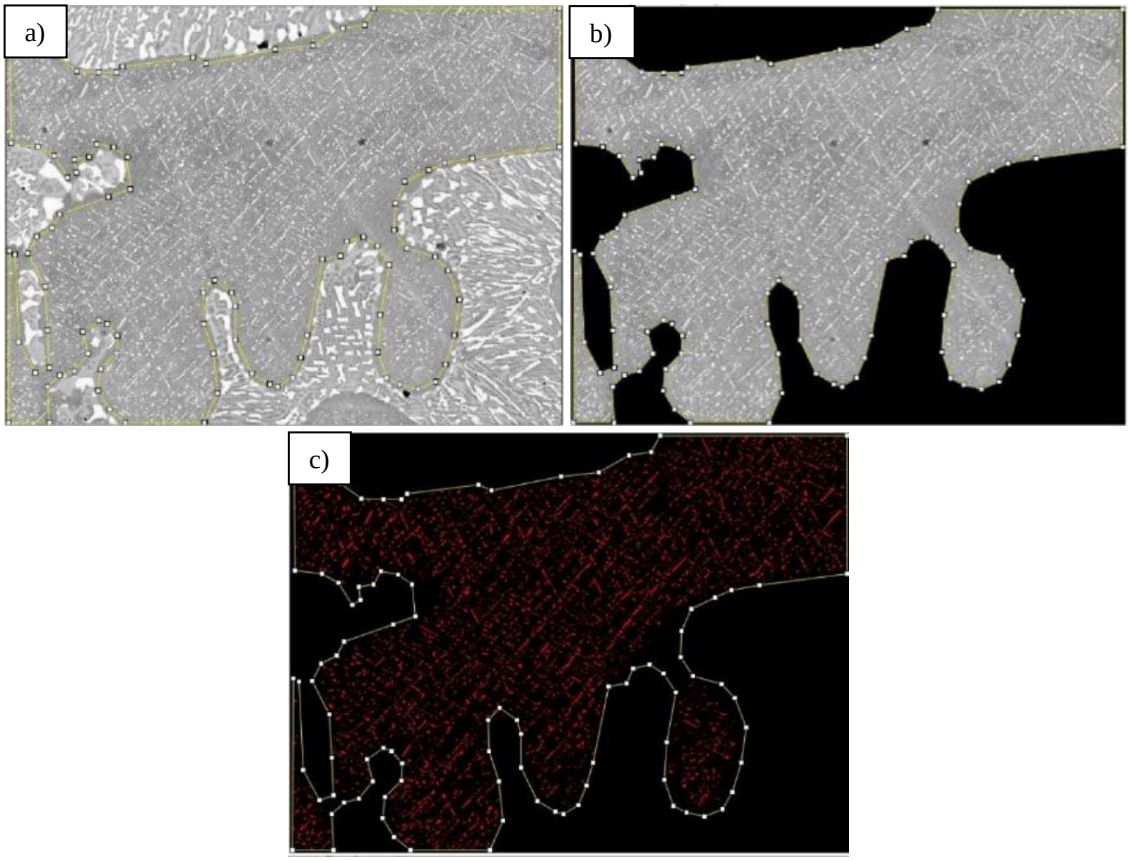

Figure 3.3: Example of ImageJ threshold analysis used to calculate the area fraction of precipitated phases within the cobalt solid solution phase: a) selected area of interest, b) exclusion of everything outside of this area and c) threshold analysis of precipitates within this area.

3.5 Hardness Measurements

3.5.1 Bulk Hardness and Microhardness Analysis

Macro and microhardness surface measurements were taken using an Innovtest hardness tester with a Vickers pyramid indenter. A calibration block was tested prior to carrying out hardness measurements to ensure accurate readings were being produced. Room temperature readings were taken using a 10kg load for bulk hardness readings and a 50g load was used for microhardness analysis of individual phases. A ten second dwell time was used in both tests to create an indent on the samples surface. From these indents the hardness of the material was calculated. At least five measurements were taken to produce an average hardness value. A minimum distance greater than three times the diagonal width of an indent was left between indents to ensure the effects of work hardening were avoided.

3.5.2 Individual Phase Nanoindentation Analysis

Hardness *(H)* and elastic modulus *(E)* for specific phases was measured using nano-indentation analysis. Indentations were carried out at room temperature using a Bruker Hysitron TI980 Nanoindenter fitted with a Berkovich tip. Material hardness *H* and elastic modulus *E* was calculated using the Oliver & Pharr method [141]. The method is described in more detail in the following section.

To ensure that an appropriate force was being used to produce an efficient displacement depth that would generate accurate and reliable readings, a control displacement test was carried out prior to testing. To do this, several indentations were made to produce specific displacement depths. The results would then indicate an appropriate force required to produce a certain contact depth that would produce consistent data. An example of the results produced from the displacement test is given in Figure 3.4. As would be expected, a smaller force was required to produce a shallower displacement depth whereas a much greater force was required to produce a larger displacement depth. The modulus and hardness vs contact depth results (Figure 3.4b and c) show that at shallow contact depths (~30nm) the hardness and modulus values produced were slightly higher than values produced at greater displacement depths. This suggests that these readings may have been influenced by indentation size effects (ISE) and therefore the readings do not give an accurate representation of mechanical properties of the phase being tested [142]. Comparing the results indicated that after a certain displacement depth, which occurred at a depth of around 100nm, the hardness and modulus results became more consistent whereby increasing the applied force, thus increasing the displacement depth, produced similar results generated at a lower force and displacement depths. Therefore, to obtain consistent and reliable hardness and modulus readings, a contact depth of around 100nm was needed. The displacement curve graph (Figure 3.4a) indicates that to achieve this displacement depth, an applied force of 2000μN was required.

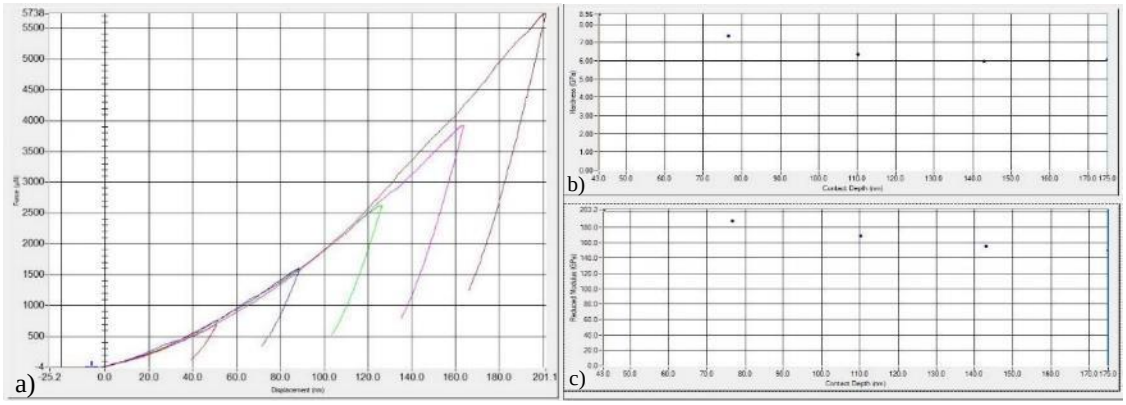

Figure 3.4: Control displacement test to determine appropriate contact force: a) Force vs displacement curves and b) Modulus vs contact depth and c) hardness vs contact depth.

3.5.2.1 Oliver-Pharr Analysis Method

A materials hardness can be described as its resistance to plastic deformation and has been traditionally calculated by dividing the maximum indentation load (*Pmax*) by the projected contact area (*A*), as shown in Equation 1.

$$H = \frac{Pmax}{A} \qquad \textit{Equation 1}$$

Traditional hardness testing measures the indentation produced on the material surface to calculate the contact area (*A*) which would then be used to calculate material hardness (*H*). This approach would be difficult for nanoindentation techniques as the indentation produced on the materials surface would be nanometres in length and would require advanced microscopy to measure. Therefore, Oliver and Pharr developed a method that calculates the contact area under load (*Aop*) as a technique to measure material hardness and Youngs modulus. In this technique, a load-displacement plot is generated where the contact area under load is calculated by measuring the slope of the unloading section of the load-displacement plot produced by the indentation. A typical load-displacement plot is displayed in Figure 3.5.

The load-displacement plot can then be analysed using Equation 2 where *S=dP/dh* is the experimental measured stiffness of the upper section of the unloading-displacement plot, and *Er* is the reduced modulus.

$$S = \frac{dP}{dh} = \frac{2}{\sqrt{\pi}} Er\sqrt{Aop} \qquad \textit{Equation 2}$$

The effects of using a non-rigid indenter tip on the load-displacement behaviour can be effectively accounted for by defining the reduced modulus (*Er*) using equation 3, where *E* and *V* are the Youngs modulus and Poisson's ratio for the material being tested and *Ei* and *Vi* correspond to Youngs modulus and Poisson's ratio of the indenter [141].

$$\frac{1}{Er} = \frac{(1-v^2)}{E} + \frac{(1-vi^2)}{Ei} \qquad \textit{Equation 3}$$

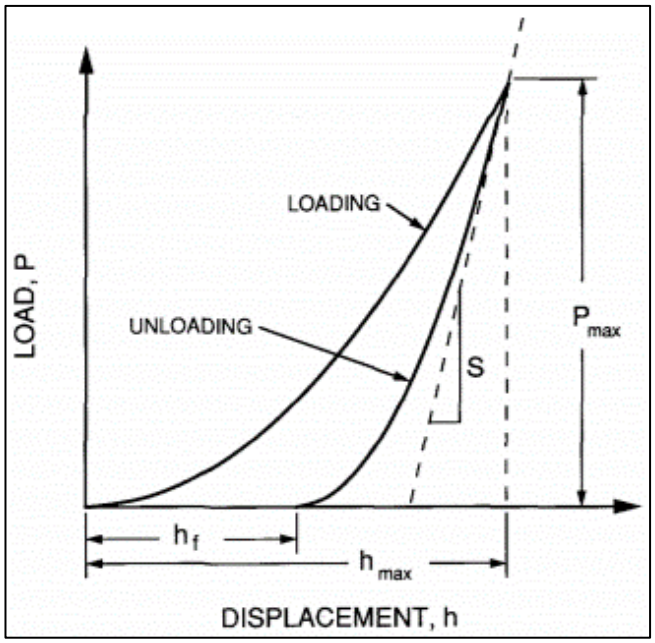

Figure 3.5: Typical load-displacement curve produced from nanoindentation [141].

3.5.2.2 Accelerating Property Mapping (XPM) and in-situ Atomic Force Microscopy (AFM)

High speed nanoindentation was implemented to produce mechanical property maps of the alloys surface using Accelerating Property Mapping (XPM). The technique produced a matrix of 225 indents that covered a 45µm x 45µm area of the samples surface. The grid provides sufficient coverage of the alloys surface to highlight contrasts in mechanical properties of different phases to produce a property map. An example of a hardness property map created from XPM analysis is displayed in Figure 3.6. The technique was also used to produce large sets of hardness and modulus data for specific phases as a large number of indents could be carried on a single phase, as shown in Figure 3.7. XPM analysis was carried out at several locations of the alloys microstructure to produce average hardness and modulus values for individual phases.

After indentation, in-situ atomic force microscopy (AFM) was performed on the test area to generate a topography image of the samples surface which displayed the locations of individual indents. This allowed for the mechanical properties of specific indents made on certain phases to be identified as well as presenting a clear correlation between the XPM maps and the tested area of the alloy's microstructure. From this analysis, data relating to a certain phase could be examined. This is illustrated in Figure 3.6 where the AFM scan was used to identify indents made only on the matrix phase to produce data specific to that phase.

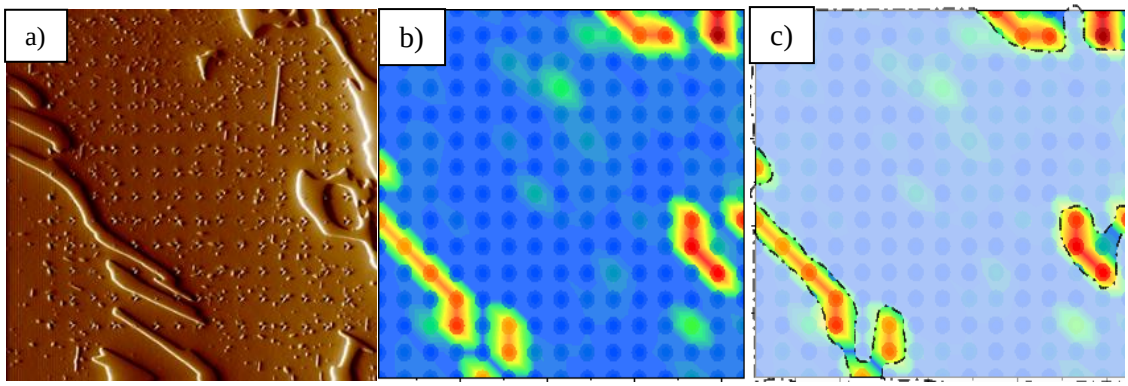

d)

Statistic	Modulus (GPa)	Hardness (GPa)
Number of Points	207	207
Missing Points	18	18
Mean	197.49	6.7307
Standard Deviation	29.046	1.049

Figure 3.6: In-situ SPM topography scan of sample surface after XPM analysis: a) topography scan, b) corresponding mechanical property map, c) selected data points and d) data produced from XPM analysis.

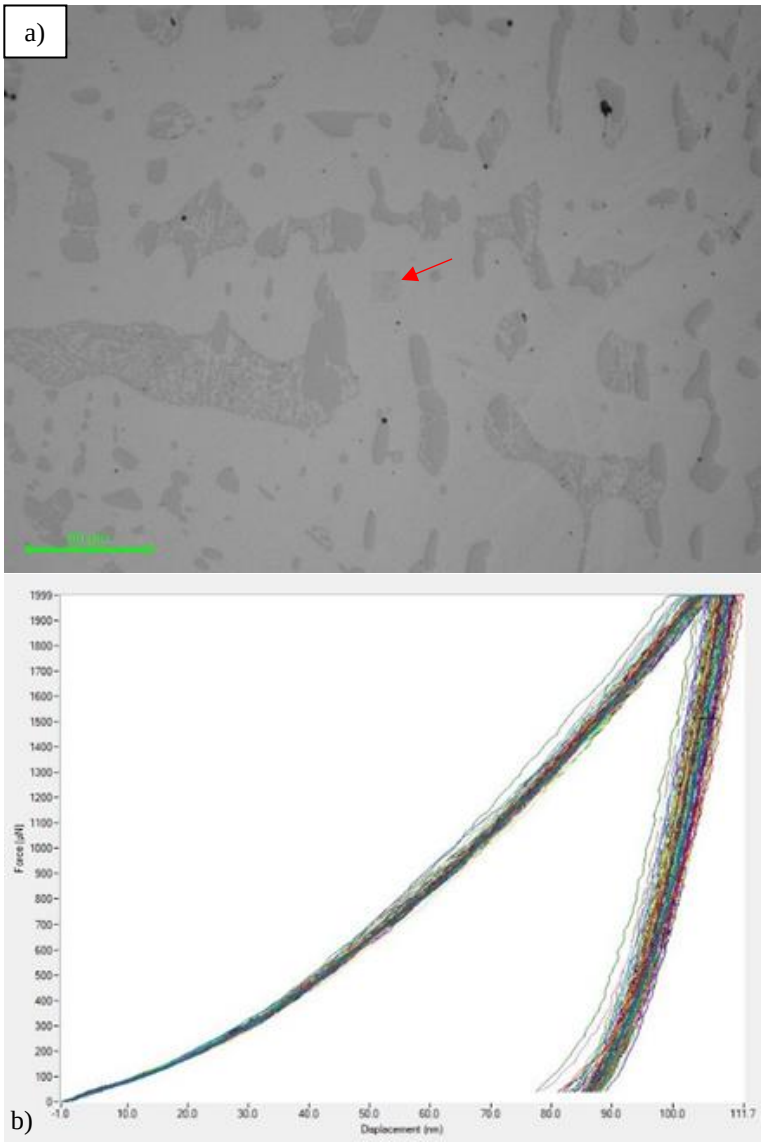

Figure 3.7: XPM analysis of cobalt matrix: a) location of XPM analysis and b) load displacement curves for individual indents.

3.5.2.3 Hardness and Elastic Modulus to Characterise Wear Resistance

Wear studies have shown that a materials elastic modulus (*E*) strongly influences the materials wear resistance. This indicates that material hardness is not a defining factor in determining the tribological performance of a material. It has been recognised that using a materials *H* and *E* to produce a *H/E* ratio can provide an indication of a materials wear resistance [143,144]. The *H/E* ratio measures the amount of elastic strain an alloy can be subjected to prior to the onset of yielding. Materials with higher elastic strains prior to failure normally possess greater wear resistant properties therefore a high *H/E* ratio is desirable for materials used for wear applications [145].

The *H* and *E* values produced for each alloy were used to produce a mean *H/E* ratio for individual phases of untreated and treated alloys to provide an indication of any changes in wear performance.

4 Microstructural Characterisation and Mechanical Performance of As-received CoCrW and CoCrMo Alloys

4.1 Microstructural Analysis of Untreated Samples

4.1.1 As-received WT-4

Figure 4.1 displays the microstructure of the as-received hypereutectic WT-4 alloy using SEM and EDS analysis. Analysis revealed two distinct regions present in the alloy's microstructure: a primary solid solution dendritic matrix with interdendritic eutectic region. EDS point scan analysis indicated that the microstructure consists of Co-rich dendrites (dark grey regions) containing levels of chromium and tungsten, and chromium-rich (light grey regions) and tungsten-rich (white regions) eutectic phases. The composition of these phases is presented in Figure 4.2. Literature reports that α-cobalt is the primary solid solution phase in cobalt solid solution which is strengthened by chromium-rich $Cr_{23}C_6$ carbides and tungsten-rich $(Co,W)_6C$ carbides [146]. Area fraction analysis of the individual phases confirms primary α-cobalt solid solution phase contributing to 50% area fraction of the alloy's microstructure. The area fraction for individual phases is shown in Figure 4.3. The eutectic region makes up for the remaining 50% of the microstructure. However, a combined area fraction of 50% carbide phases seemed unlikely due to the carbon content (~0.8wt.%) of the alloy not being sufficient to result in such a high-volume fraction of carbide phases. Closer inspection of the eutectic region (Figure 4.2) revealed that the eutectic region consisted of three phases. Point scans identified the tungsten-rich carbides (white regions) and the chromium-rich carbides (light grey regions), but it also revealed a cobalt-rich eutectic phase (dark grey regions) with slightly lower cobalt and slightly higher chromium content compared to the primary cobalt-rich matrix. This suggests that the eutectic regions of the microstructure consist of a mixture of tungsten carbides, chromium carbides and CoCrW solid solution.

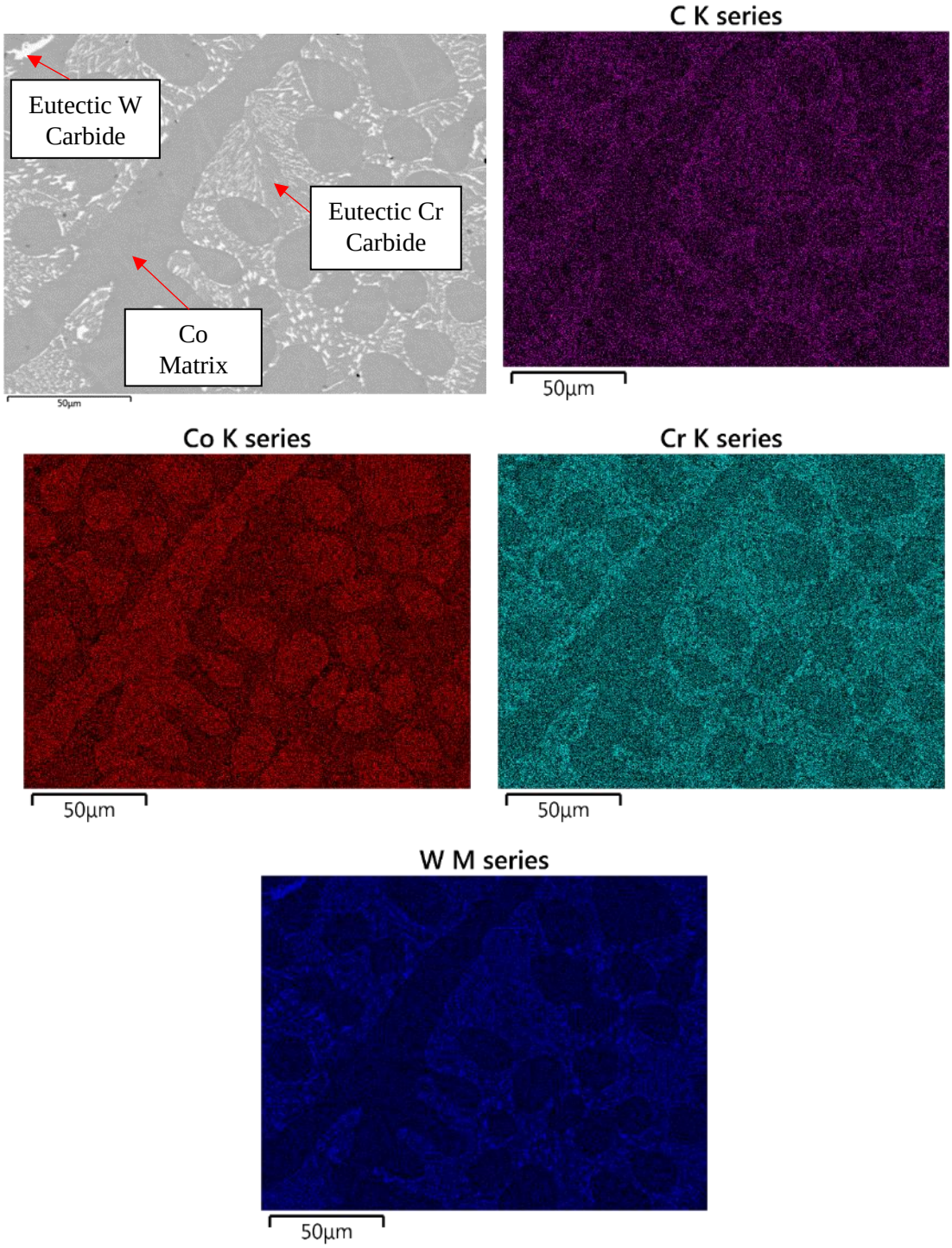

Figure 4.1: SEM and EDS analysis of the as-received WT-4 alloy illustrating elemental concentration of individual phases.

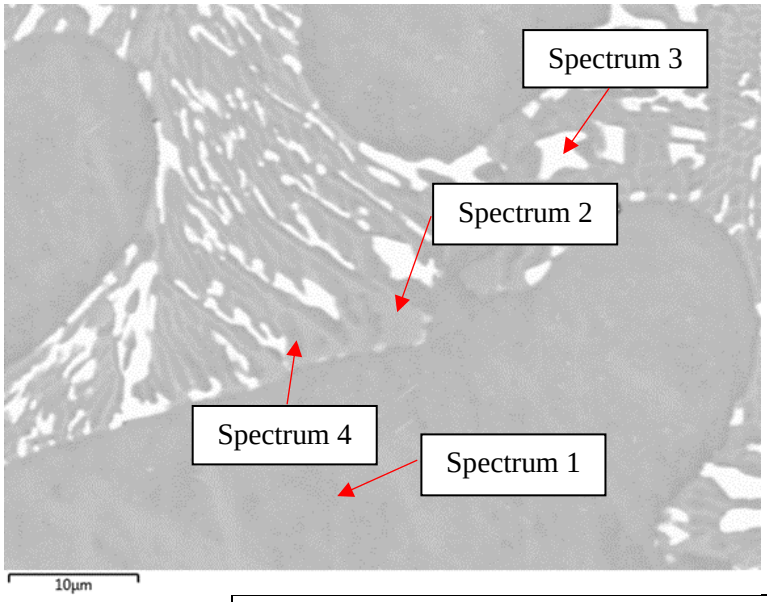

		Element wt.%						
Spectrum	Description	Co	Cr	W	Ni	Fe	Si	Mn
1	Co Solid Solution (M)	55.5	26.33	10.6	3	2.93	1.1	0.63
2	Cr Carbide	31.17	47.76	17.15	1.29	2.03	-	0.59
3	W Carbide	26.03	22.83	46.86	0.85	0.8	2.57	-
4	Co Solid Solution (E)	47.47	33.7	12.53	2.17	2.63	0.77	0.53

Figure 4.2: Phase composition analysis of as-received WT-4 alloy: Point scan locations and calculated compositions where M = solid solution in the matrix and E = solid solution in the eutectic region.

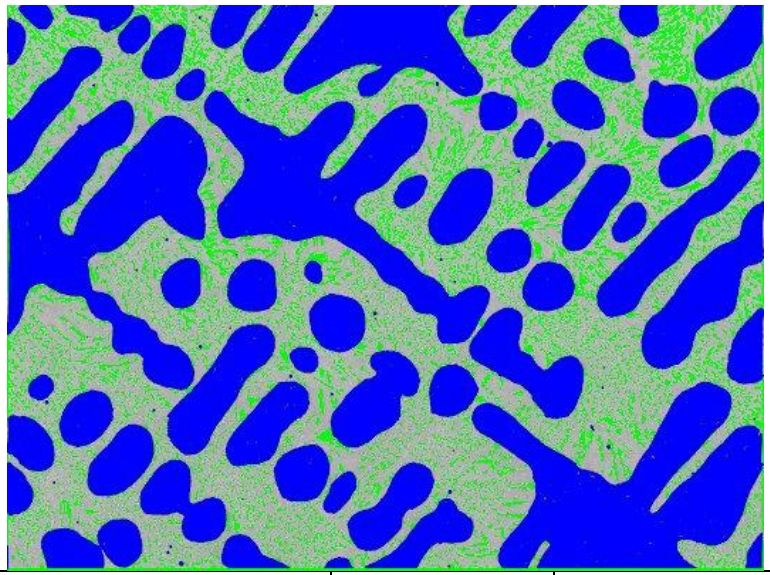

As-received WT-4 phases	**Colour**	**Area fraction %**
Co Solid Solution (matrix)	Blue	49.6% (±1.7)
Eutectic Region	Grey + Green	48.8% (±2.8)
W Eutectic	Green	11.1% (±1.9)
Cr Eutectic	-	18.2% (± 2.2)
Co Solid Solution (eutectic)	-	19.2% (± 1.8)

Figure 4.3: Phase area fraction analysis of the as-received WT-4 alloy: ImageJ analysis of SEM image and calculated area fraction of each phase.

4.1.2 As-received WT-6

Due to excellent wear and corrosion resistant properties at elevated temperatures, WT-6 is a cobalt-based alloy commonly used to produce journal bearing components for galvanising bath hardware. The microstructure of the hypoeutectic alloy is illustrated in the SEM and EDS images in Figure 4.4. The images indicate that the alloy consists of three distinct phases: a solid solution dendritic matrix (grey regions) and two eutectic phases (dark grey and white regions). EDS point scan analysis was performed to calculate the composition of these phases. Figure 4.5 illustrates the alloys microstructure at higher magnification and displays the locations of the point scans and the corresponding phase compositions. Analysis revealed that the dark grey and white phases are chromium-rich and tungsten-rich, respectively, and the matrix is cobalt-rich. Previous research has identified these phases as chromium-rich Cr_7C_3 carbides and tungsten-rich $(CoW)_6C$ carbides, while α-cobalt is the solid solution phase [51,147]. The α-cobalt phase (light grey regions), which contains chromium and tungsten in solid solution, dominates the alloys microstructure making up 83% area fraction of the microstructure. The matrix is predominately strengthened by the dispersion of chromium-rich carbides (dark grey regions), which constitute 17% area fraction. In addition to the chromium-rich carbides, a small amount (<1% area fraction) of a tungsten-rich carbide (white regions) were also observed. The calculated area fraction for each phase is displayed in Figure 4.6.

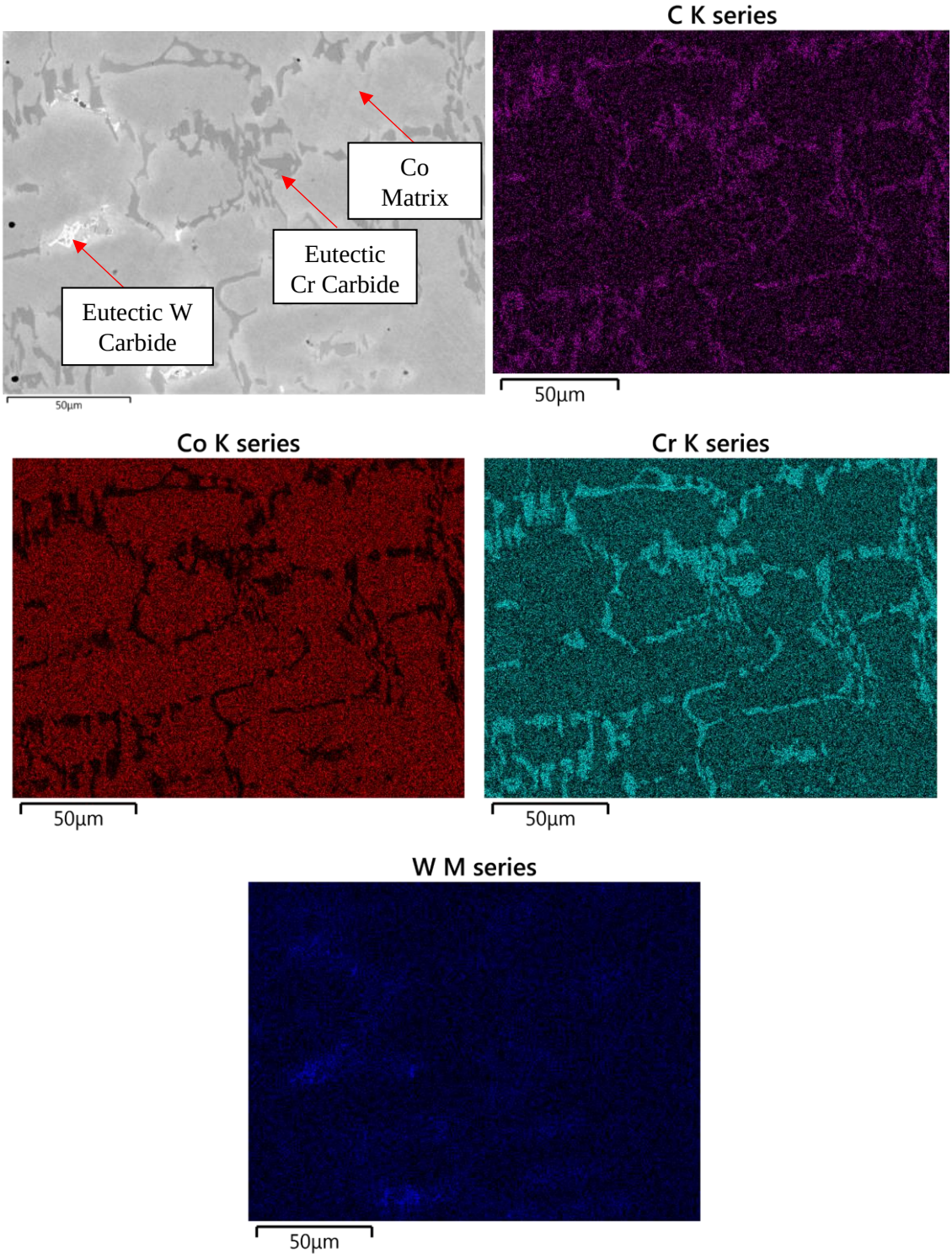

Figure 4.4: SEM and EDS analysis of the as-received WT-6 alloy illustrating elemental concentration of individual phases.

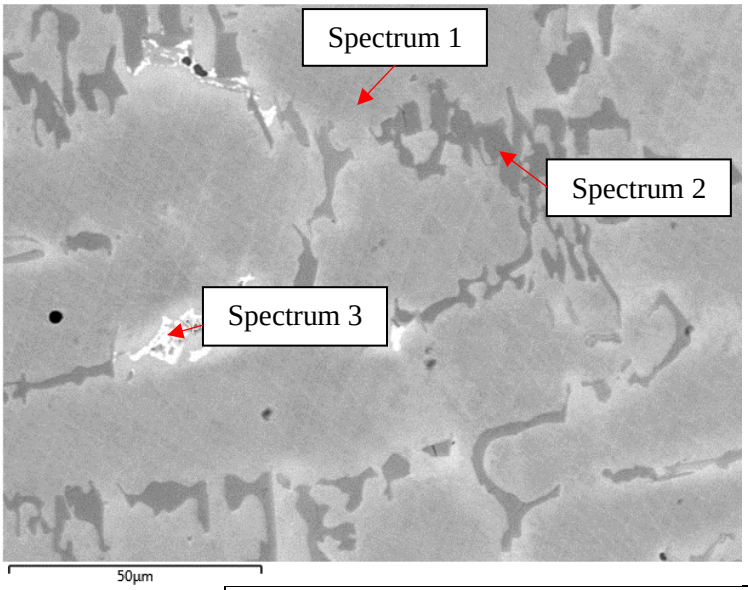

		Element wt.%						
Spectrum	Description	Co	Cr	W	Ni	Fe	Si	Mn
1	Co solid solution	63.21	24.63	4.07	3.13	3.07	1.43	0.47
2	Cr Carbide	13.33	80.27	4.9	-	1.07	-	-
3	W Carbide	28.67	22.93	43.41	1.3	0.95	2.73	0.45

Figure 4.5: Phase composition analysis of as-received WT-6 alloy: Point scan locations and calculated compositions.

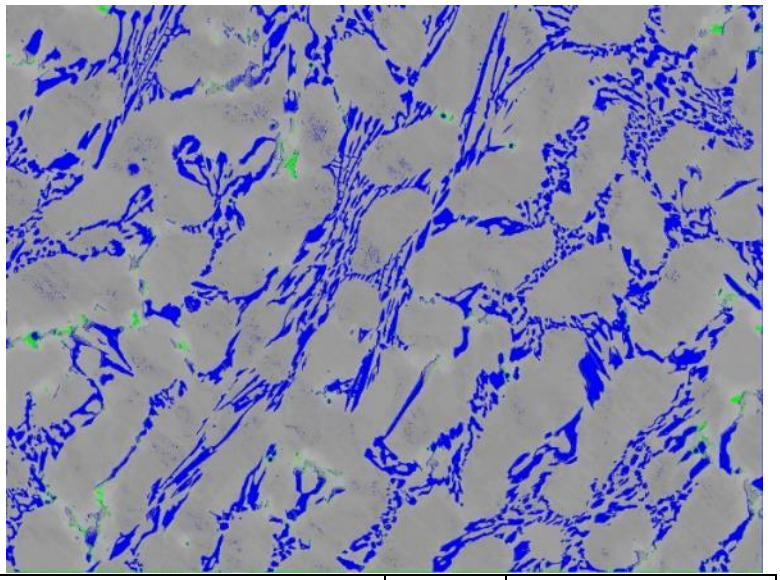

As-received WT-6 phases	**Colour**	**Area fraction %**
Solid solution	Grey	83.8% (±0.9)
Cr eutectic	Blue	17% (±0.2)
W eutectic	Green	0.2% (±0.1)

Figure 4.6. Phase area fraction analysis of the as-received WT-6 alloy: ImageJ analysis of SEM image and Calculated volume fraction of each phase.

4.1.3 As-received WT-12

Figure 4.7 illustrates the microstructure of the as-received hypoeutectic WT-12 alloy investigated using SEM and EDS analysis. Similar to the WT-6 alloy, analysis suggests the formation of three distinct phases. EDS point scans of these phases indicate a cobalt-rich matrix (light grey regions) and chromium-rich (dark grey regions) and tungsten-rich phases (white regions). The location of the point scans and the composition of the phases are summarised in Figure 4.8. It has been identified that α-cobalt is the primary solid solution phase with chromium-rich Cr_7C_3 carbides and tungsten-rich $(CoW)_6C$ carbides embedded within the matrix that act to strengthen the alloy [148]. The microstructure of the WT-12 alloy is dominated by the formation of the α-cobalt solid solution phase (light grey regions) which makes up 74% of the alloy's microstructure. It is apparent from the SEM images that the increase in carbon and tungsten content for this alloy, compared to the WT-6 alloy, results in a significant increase in the amount of tungsten carbide to 19% area fraction of the microstructure. The structure of the tungsten-rich $(CoW)_6C$ carbide is displayed at high magnification in Figure 4.9, which has been referenced as a 'skeleton like' structure [149,150]. The SEM image demonstrates that tungsten carbide consists of a fine structure surrounded by α-cobalt solid solution and has chromium carbides embedded within the structure. The remainder of the microstructure consists of 19% area fraction of the chromium carbide phase. The calculated area fraction for each phase is summarised in Figure 4.10.

In addition to the formation of the chromium and tungsten carbides, EDS analysis of the matrix revealed that significant amounts of chromium and tungsten are also retained in solid solution.

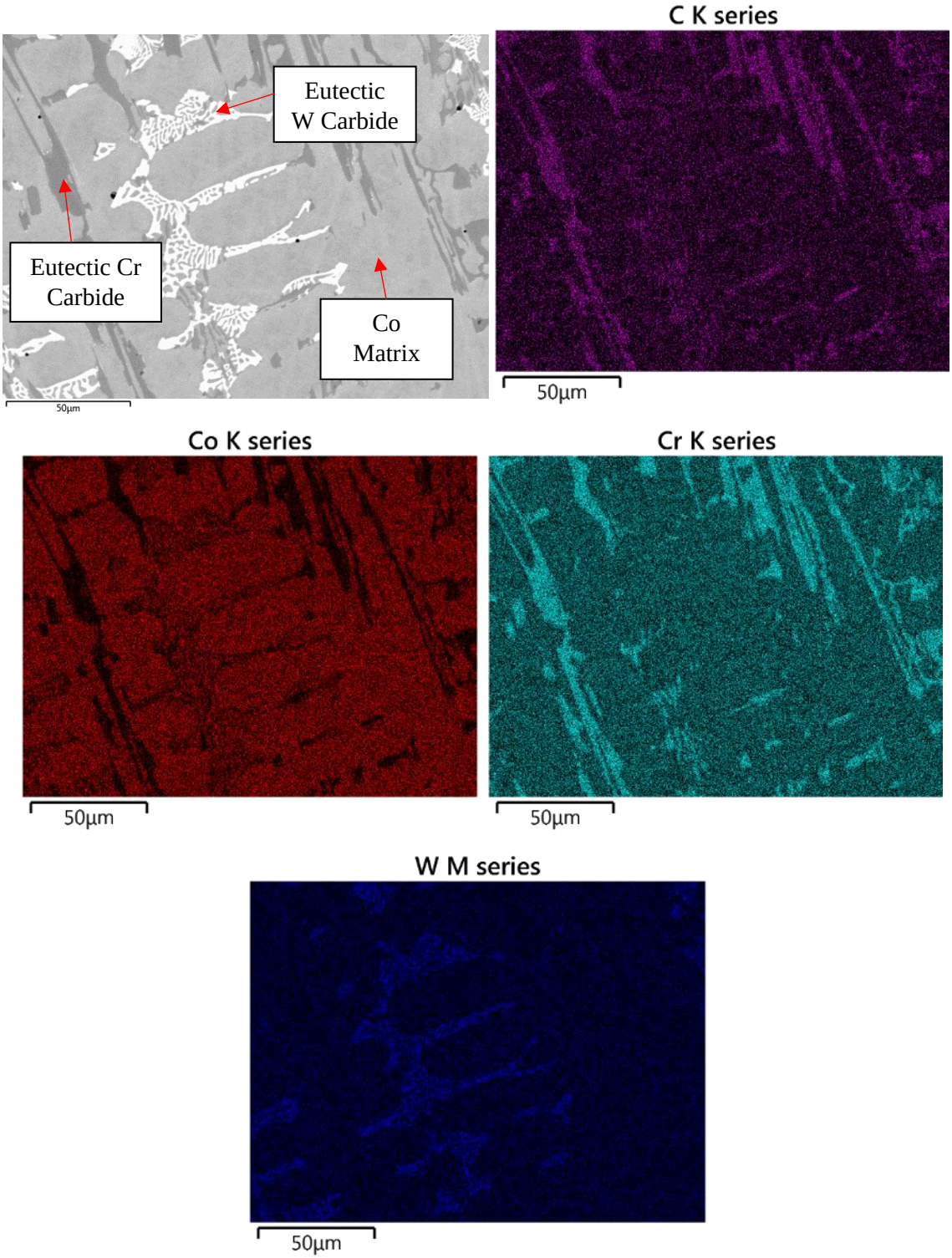

Figure 4.7 SEM and EDS analysis of the as-received WT-12 alloy illustrating elemental concentration of individual phases.

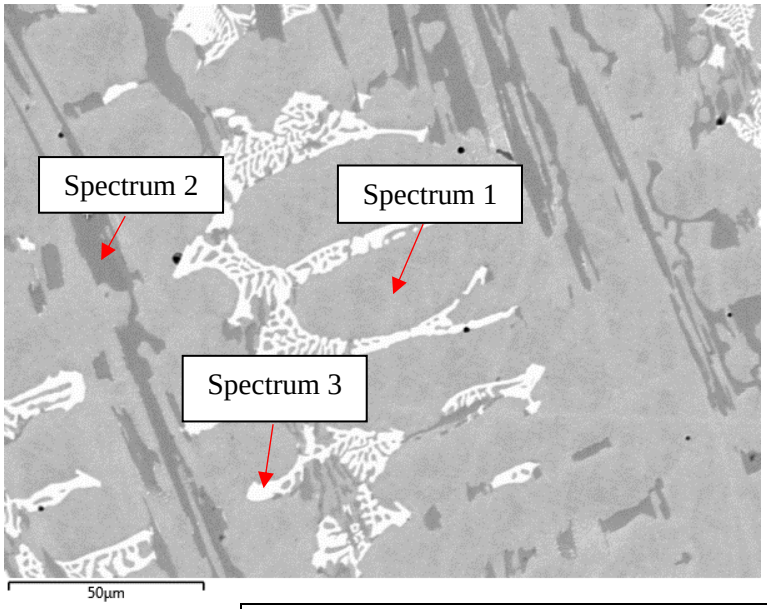

		Element wt.%						
Spectrum	Description	Co	Cr	W	Ni	Fe	Si	Mn
1	Co solid solution	59.3	25.83	6.97	2.87	2.77	1.8	0.47
2	Cr Carbide	10.47	81.17	7.37	-	1	-	-
3	W Carbide	25.73	22.83	46.5	1.3	0.73	2.73	-

Figure 4.8: Phase composition analysis of as-received WT-12 alloy: Point scan locations and calculated compositions.

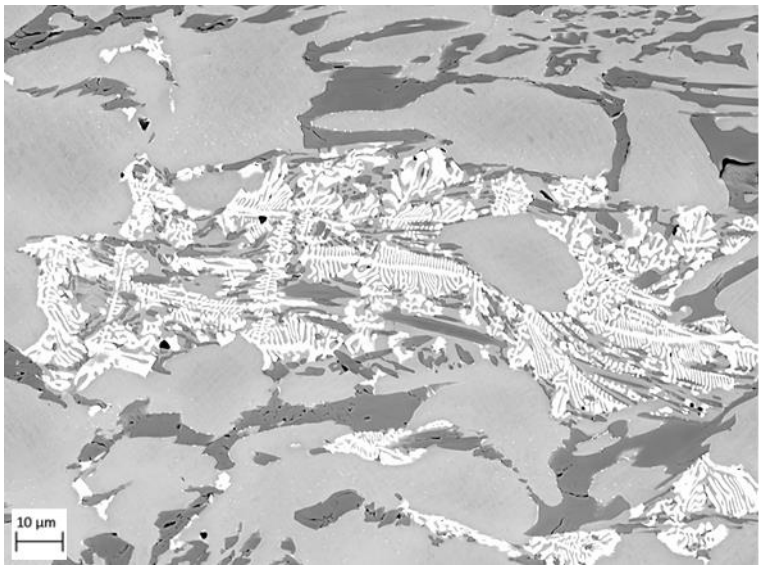

Figure 4.9: High magnification SEM analysis of the tungsten carbide in the as-received WT-12 alloy.

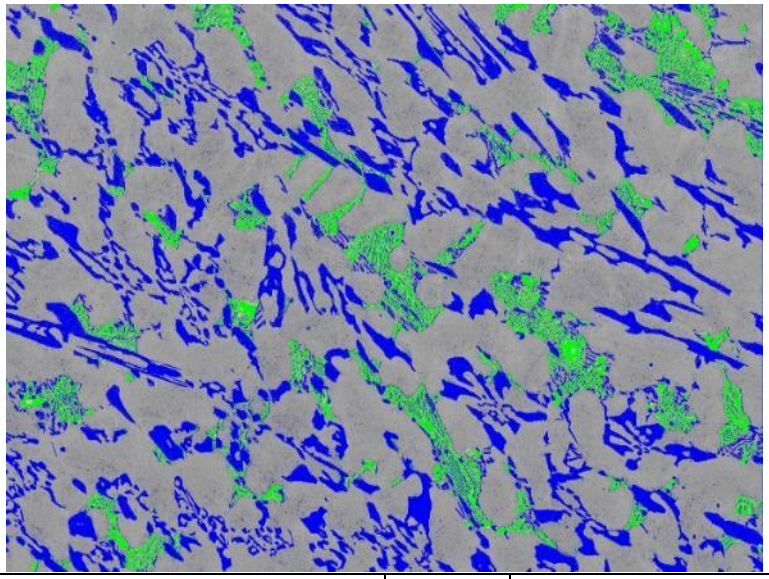

As-received WT-12 phases	Colour	Area fraction %
Solid solution	Grey	74.4% (±3.5)
Cr eutectic	Blue	19.3% (±3.8)
W eutectic	Green	7.6% (±0.6)

Figure 4.10. Phase area fraction analysis of the as-received WT-12 alloy: ImageJ analysis of SEM image and calculated volume fraction of each phase.

4.1.4 As-received T-800

The CoCrMo T-800 Tribaloy has a different microstructure compared to the CoCrW alloys as it replaces tungsten with high levels of molybdenum. The T-800 Tribaloy also contains as low carbon as possible to prevent carbide formation. The microstructure and elemental maps of T-800 Tribaloy is displayed in Figure 4.11. The SEM and EDS images illustrate predominance of a large volume fraction of a primary dendritic Laves phase in the microstructure and a eutectic mixture of cobalt-rich solid solution and secondary Laves phases. Point scans analysis of the composition of the phases (Figure 4.12) revealed that the primary and secondary Laves phases (Light grey) are of similar composition and that the eutectic region consists of two cobalt-rich phases, one rich in molybdenum (Light grey eutectic) and the other rich in chromium (dark grey eutectic). The relatively high addition of silicon exists mainly in the Laves intermetallic phase although small amounts are retained in the solid solution phase. The ternary Laves phase is of the C-14 ($MgZn_2$) type, which has a CoMoSi composition. The Laves phase has a hexagonal close packed (hcp) structure whereas the eutectic cobalt solid solution matrix is a mixture of fcc and hcp phases [87,151]. High additions of molybdenum (~30wt%) results in a large area fraction (~60%) of the intermetallic primary and secondary Laves phase forming within the microstructure. Increased molybdenum additions also result in a high level of molybdenum being retained in solid solution. This is highlighted in Figure 4.12b where high levels of molybdenum

can be seen to be retained in solid solution as well as the precipitation of a high cobalt-molybdenum phase, which is dispersed within the eutectic solid solution region. The area fraction of each phase is reported in Figure 4.13.

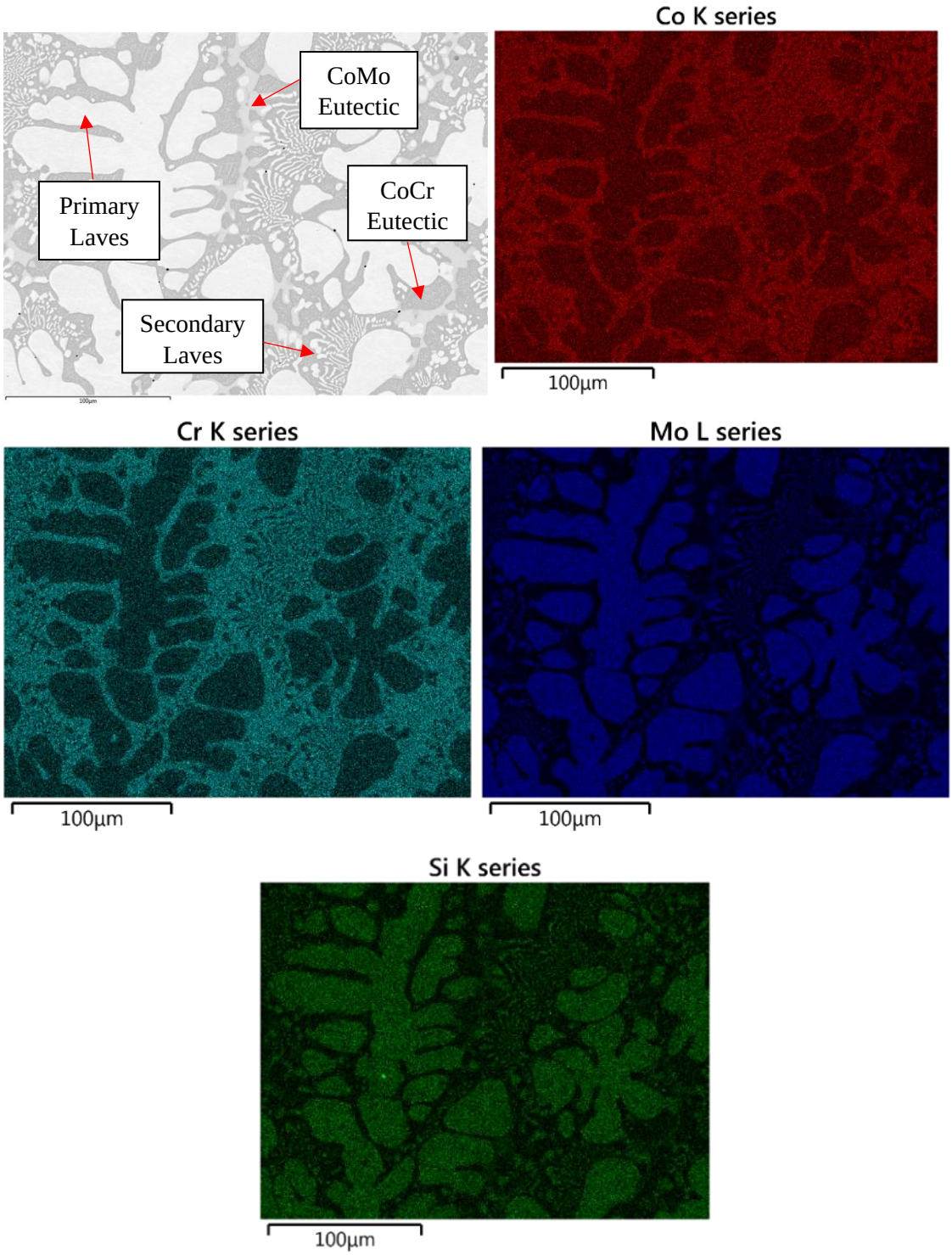

Figure 4.11: SEM and EDS analysis of the as-received T-800 Tribaloy illustrating elemental concentration of individual phases.

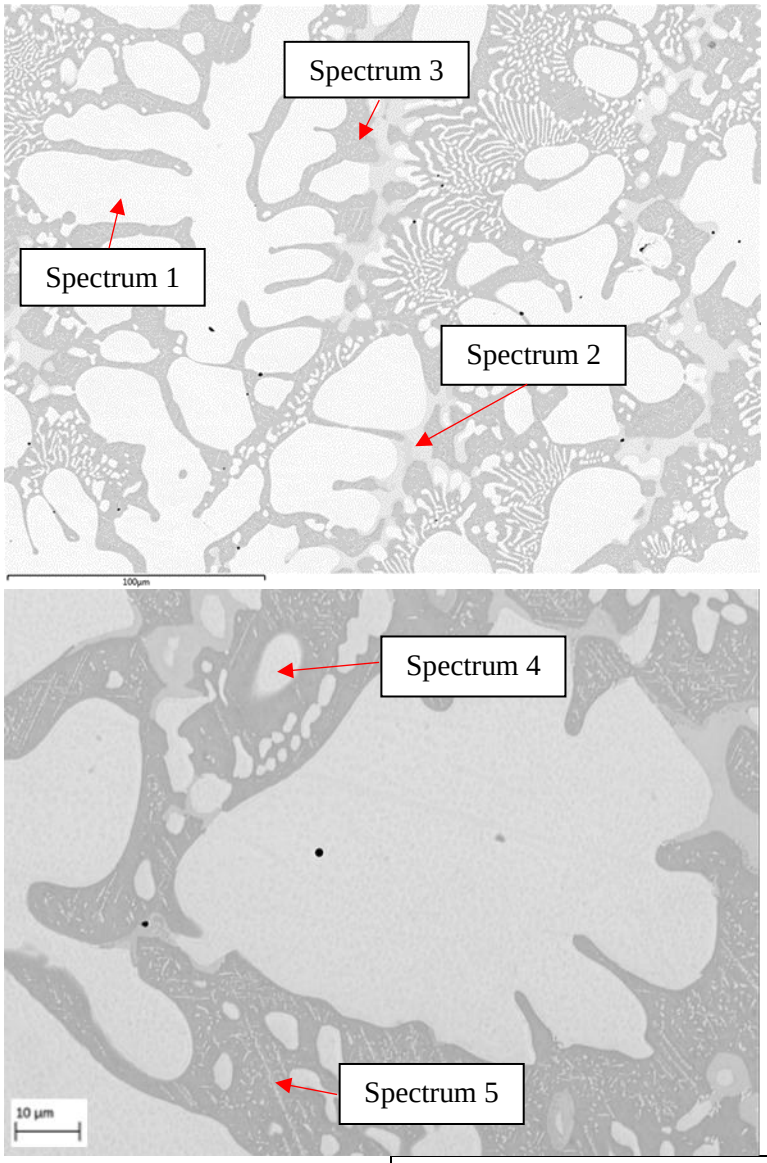

		Element wt.%					
Spectrum	Description	Mo	Co	Cr	Si	Ni	Fe
1	Laves Phase (Primary)	46.13	36.87	10.83	4.56	0.81	0.7
2	Eutectic Solid Solution (CoMo)	26.9	44.9	23.1	2.5	1.3	1.36
3	Eutectic Solid Solution (CoCr)	8.2	61.8	24.65	1.85	1.5	2
4	Laves Phase (Secondary)	44.07	37.13	12.83	4.37	0.73	0.87
5	Precipitate	21.9	52.83	19.6	2.76	1.35	1.56

Figure 4.12: Phase composition analysis of as-received T-800 Tribaloy: a) Point scans locations at low magnification, b) Point scan location at high magnification illustrating molybdenum dispersion in the eutectic matrix and calculated compositions.

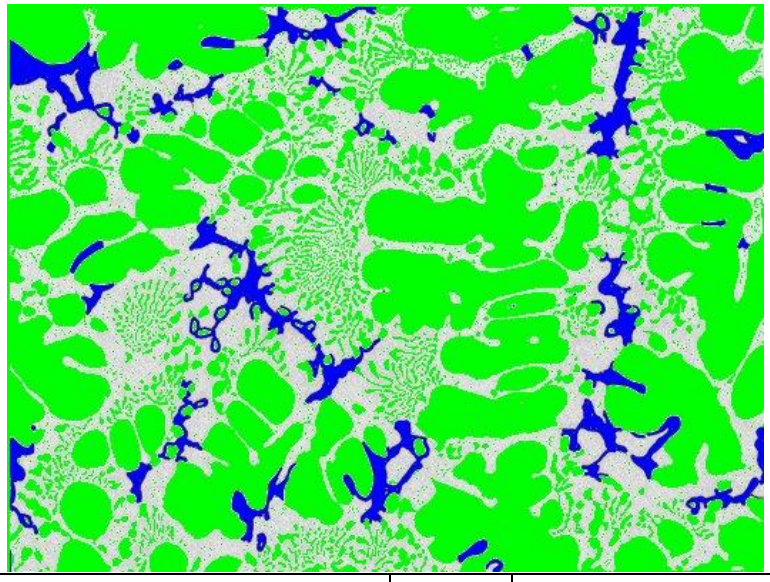

As-received T800 phases	Colour	Area fraction %
Laves Phase (Primary + Secondary)	Green	54.3% (±1.4)
CoCr Eutectic Solid Solution	Grey	36.5% (±1)
CoMo Eutectic Solid Solution	Blue	9.7% (±1.9)

Figure 4.13: Phase area fraction analysis of the as-received T-800 Tribaloy: ImageJ analysis of SEM image and calculated volume fraction of each phase.

4.2 Comparisons of Investigated Alloy Microstructures

As the carbon content with the WT-4, WT-6 and WT-12 alloys is less than 2wt%, the alloys have hypoeutectic microstructures. As a result, the cobalt matrix forms first followed by carbide formation in a eutectic reaction. Analysis of the CoCrW alloys revealed that their microstructures consist of varying amounts of α-cobalt solid solution strengthened by chromium and tungsten carbides. In addition to carbide formation, high levels of chromium and tungsten were also retained in the solid solution. This was also the case for the T-800 Tribaloy where, in addition to primary Laves phase formation, levels of molybdenum were retained in solid solution.

Figure 4.14 compares the area fraction of the α-cobalt phase and the chromium and tungsten carbides for the CoCrW alloys where the data for the WT-4 alloy includes the volume fraction of the primary α-cobalt solid solution phase and the CoCrW solid solution phase that exists in the eutectic regions of the microstructure. The graph also displays the volume fraction of Laves phases and eutectic solid solution phases for the T-800 Tribaloy. Comparing the CoCrW alloys demonstrates how carbide formation is strongly influenced by carbon and tungsten additions. Comparing the WT-6 and WT-12 alloys, which have similar microstructures, shows how increased carbon and tungsten additions in the WT-12 alloy results in a significant increase in the volume fraction of carbide phases, particularly tungsten carbides. However, although the

WT-4 alloy has the lowest carbon content, compared with the WT-6 and WT-12 alloys, it has the largest volume fraction of carbides. This is due to the significantly high levels of tungsten in the alloy (~14wt%) resulting in increased tungsten carbide formation. Addition of chromium also plays an important role in carbide formation but as the chromium content is kept at around 30wt.% for each alloy, the graphs do not show effects of varying chromium content on the carbide formation. However, due to the high level of chromium, carbide formation is dominated by chromium carbides.

As would be expected, increasing the weight percentage of carbide forming elements to the alloy's composition leads to a smaller fraction of the α-cobalt solid solution phase in the microstructure. This is demonstrated with the WT-6 alloy. The alloy has lowest additions of carbide forming elements and therefore has the highest balancing additions of cobalt, resulting in a higher volume fraction of the α-cobalt phase.

Although similar phases formed in the CoCrW alloys, the changes in alloying additions resulted in the phases having slightly different compositions where the phase composition correlates to the amount of alloying additions of certain elements. Figure 4.15 and Figure 4.16 compare the compositions of similar phases in the as-received CoCrW alloys. Figure 4.15 indicates that the cobalt matrix of the WT-6 has a higher cobalt concentration compared to the WT-4 and WT-12 alloys due to the alloy having the highest cobalt content. The graph also indicates that greater levels of tungsten is retained in solid solution as the alloying addition of tungsten increases. The WT-4 alloy, which has the highest additions of tungsten, has the greatest level of tungsten retained in the α-cobalt solid solution and the WT-6 alloy, which has the lowest alloying addition of tungsten, has the lowest amount of tungsten in solid solution. Tungsten levels retained in solid solution for the WT-12 alloy falls between the other two alloys. The level of chromium retained in solid solution remained similar for the CoCrW alloys as the alloying addition of chromium is around 30wt.% for each alloy. Figure 4.16 compares the composition of the eutectic carbide phases in the CoCrW alloys. The results demonstrate that the composition of the tungsten carbides is comparable for each alloy and that chromium carbides in the WT-6 and WT-12 alloys are also of similar composition. This suggests increased carbon and tungsten content in the WT-12 alloy, compared to WT-6, does not change the composition of the phases that form but increases the volume of carbides formed. EDS analysis detected that the chromium carbides in the WT-4 alloy contained lower levels of chromium and higher levels of tungsten. It has been identified in the literature that chromium carbides in the WT-4 alloy are of the $Cr_{23}C_6$ type while the WT-6 and WT-12 alloys have Cr_7C_3 carbides. The difference in chromium content could be due to the carbides being of different nature or due to tungsten replacing chromium. The accuracy of the point scan could also influence the calculated composition of the chromium

carbide phase. It was identified that the eutectic region consists of a fine structure, therefore the location of the point scan might not have been completely withing the chromium carbide phase.

The T-800 Tribaloy has a completely different microstructure compared to the CoCrW alloys. Due to high additions of molybdenum and silicon, the intermetallic Laves phase is the primary phase and the alloy has a hypereutectic microstructure. The microstructure consists of primary CoMoSi intermetallic dendrites and a lamellar eutectic mixture which has secondary Laves phases embedded in it. Figure 4.14 illustrates how the microstructure is dominated by the primary and secondary intermetallic Laves phases that make up 60% of the alloy's microstructure. Figure 4.17 displays how the primary and secondary Laves phase have similar compositions. It was identified that the eutectic region in the alloys microstructure predominately consists of cobalt solid solution with high levels of chromium retained in solid solution but also contains an intermetallic phase high in molybdenum.

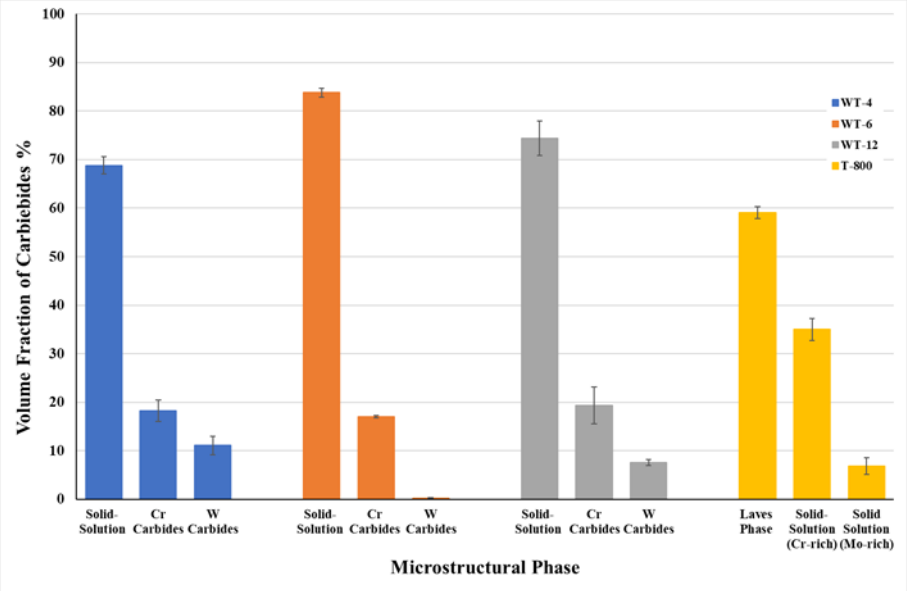

Figure 4.14: Area fraction analysis of individual phases found in the as received alloys.

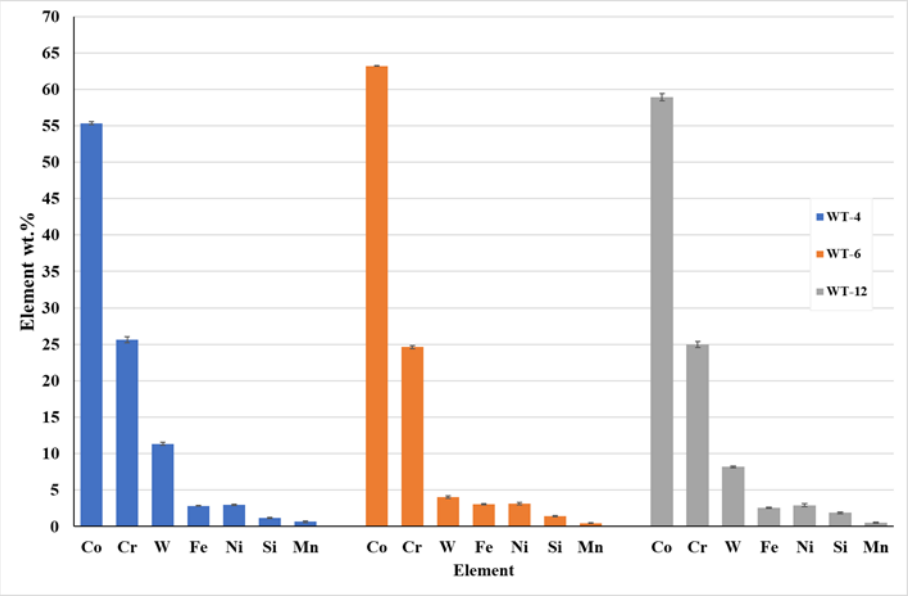

Figure 4.15: Composition of the cobalt matrix in the as-received CoCrW alloys.

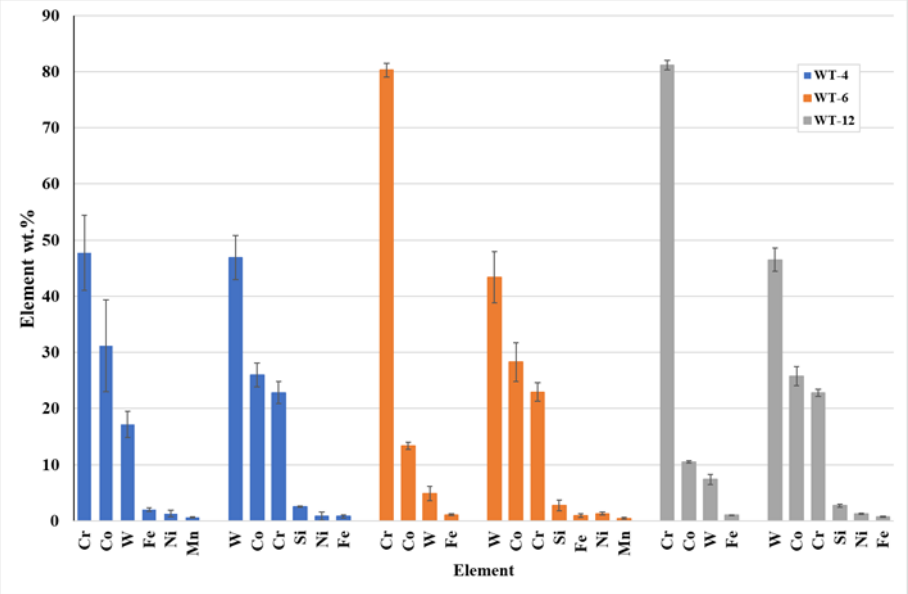

Figure 4.16: Composition of the chromium and tungsten carbide phases in the as-received CoCrW alloys.

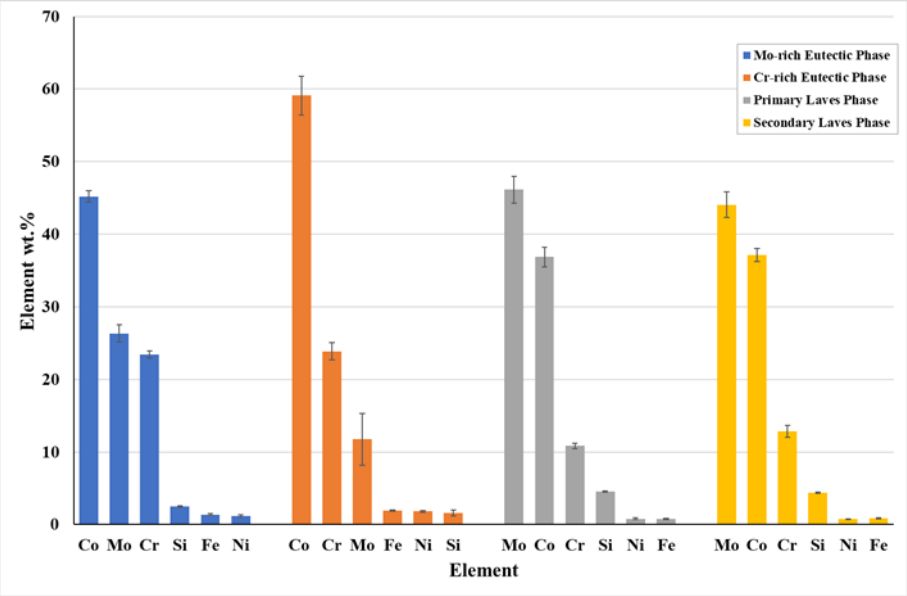

Figure 4.17: Compositional analysis of the phases in the as-received T-800 Tribaloy.

4.3 Hardness Investigation of the As-received CoCrW and CoCrMo Alloys

4.3.1 Macrohardness and Microhardness Analysis of As-received Alloys

4.3.1.1 Hardness Analysis of the As-received WT-4 Alloy

The as-received WT-4 alloy has a microstructure that comprises of a primary cobalt-rich solid solution matrix and a eutectic region consisting of a mixture of chromium carbides, tungsten carbides and solid solution. Single indentation of the solid solution phase was possible, however, the phases in the eutectic regions were too small to enable hardness measurement on individual phases. Therefore, the indentation carried out on the eutectic regions provides hardness data on a combination of the phases that the indenter tip covered. The eutectic region has a significantly higher hardness than matrix due to the presence of the carbide phases, which indicates that the cobalt matrix provides the alloy with toughness and the eutectic carbide phases strengthen the alloy. Examples of indentations made on each phase is shown in Figure 4.18. The average hardness for the cobalt solid solution phase, the eutectic region and the bulk hardness of the alloy is summarised in Table 4.1. The low standard deviation for the matrix and bulk hardness readings suggests that these values are reliable and are comparable to results found in literature [146]. However, the hardness of the eutectic region is strongly influenced by the phases included in the indention as the region consists of a mixture of carbide phases and solid solution. This is reflected in the relatively large standard deviation.

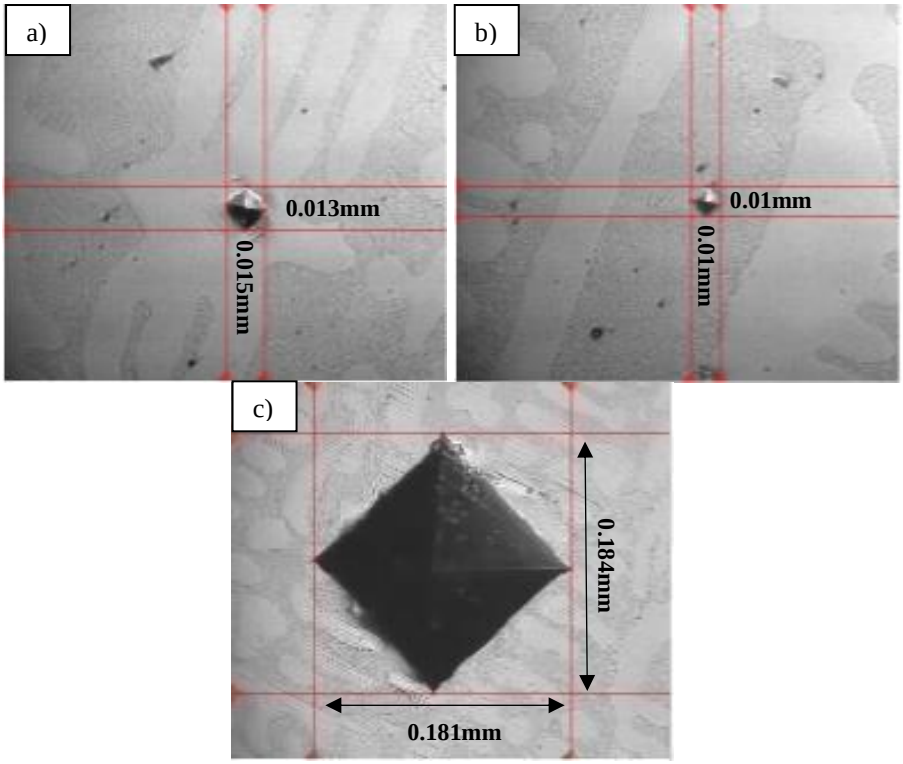

Figure 4.18: Surface hardness indentations on the as-received WT-4 alloy: a) Solid solution matrix, b) eutectic region and c) Bulk hardness indentation.

Table 4.1: Average microhardness (Hv) of microstructural phases/regions and bulk hardness (Hv) of the as-received WT-4 alloy.

Phase	Co Matrix	Eutectic Region	Bulk
Hardness (Hv)	480.53 (±10.36)	839.06 (±133.86)	564.31 (±8.22)

4.3.1.2 Hardness Analysis of the As-received WT-6 Alloy

The WT-6 alloy is predominantly a two-phase alloy that consists of a cobalt matrix that is strengthened by chromium carbides. A small amount (<1% volume fraction) of a tungsten carbide phase was also observed to form. Figure 4.19 illustrates how the indentation could be confined within the cobalt solid solution matrix enabling appropriate hardness readings while the chromium carbides were often too small to measure their hardness. Therefore, the hardness readings are influenced by the surrounding softer matrix and the actual hardness of the carbide phase would be significantly higher. However, indentations that included the chromium carbides give an indication of the contribution of carbides to matrix strengthening as these readings were significantly higher than the solid solution phase. The average hardness for the cobalt solid solution phase and areas strengthened by chromium carbides are summarised in Table 4.2 in addition to the average bulk hardness of the alloy. The consistency of the values for the solid solution phase and the overall bulk hardness of the alloy indicates that these values are reliable

and representative of their hardness. The bulk hardness is comparable to results found in the literature whereas the microhardness of the cobalt-rich matrix is slightly higher [152].

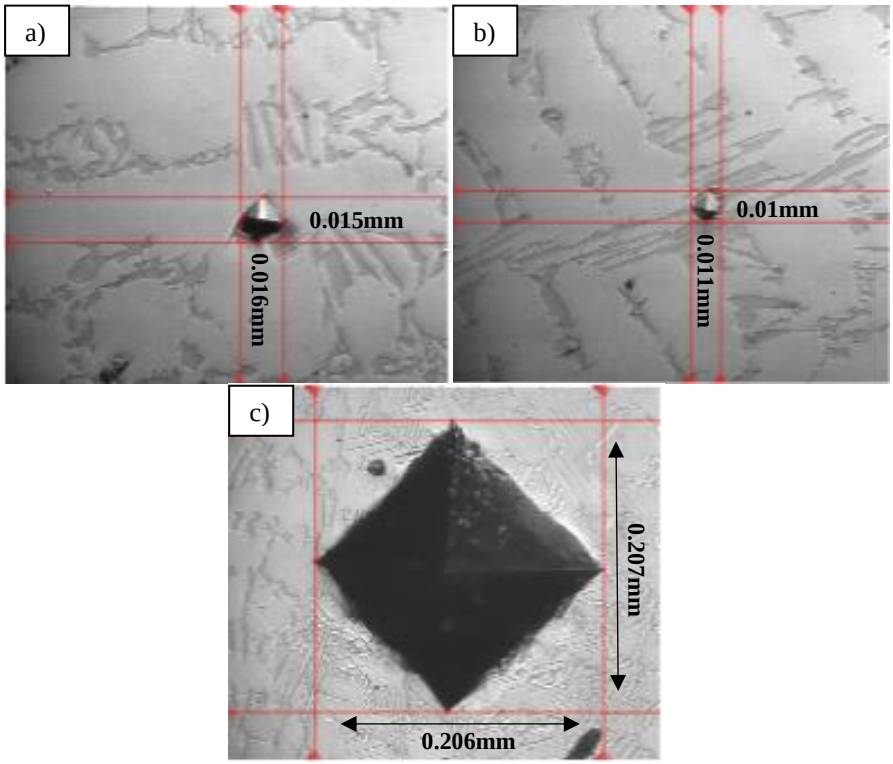

Figure 4.19: Surface hardness indentations on the as-received WT-6 alloy: a) Solid solution matrix, b) Chromium carbide network and c) Bulk hardness indentation.

Table 4.2: Average microhardness (Hv) of microstructural phases/regions and bulk hardness (Hv) of the as-received WT-6 alloy.

Phase	Co Matrix	Cr Carbide	Bulk
Hardness (Hv)	399.67(±14.5)	782 (±89.5)	429.33 (±13.8)

4.3.1.3 Hardness Analysis of the As-received WT-12 Alloy

The WT-12 alloy consists of a cobalt matrix that is strengthened by a large volume fraction of eutectic chromium and tungsten carbides. Microhardness assessment was carried out on these phases as well as bulk hardness measurement of the overall microstructure. Figure 4.20 provides images of the hardness indentations and the measured hardness values are summarised in Table 4.3. The images show that indentation of the solid solution matrix was possible, but indentation could not be confined to a single tungsten carbide particle. Increased carbon and chromium content, compared to WT-6, resulted in larger chromium carbides forming, which allowed for indentation to be made on a single particle. The low standard deviation for the solid

solution phase and bulk hardness readings indicates a consistent value for these phases was measured. Although the standard deviation is low for the tungsten carbide network, these readings would have been influenced by the solid solution and chromium carbides. Therefore, these values give a good indication of how the tungsten carbides strengthen the matrix, but they do not give an accurate hardness value of the phase itself. Despite the chromium carbides being large enough to produce an indentation on an individual phase, the large standard deviation suggests that the average hardness value produced is not an accurate hardness of the phase. Although indentation was successfully produced on an individual phase, the hardness value may have been influenced by the solid solution phase as the indentation was often in close proximity to the softer cobalt matrix.

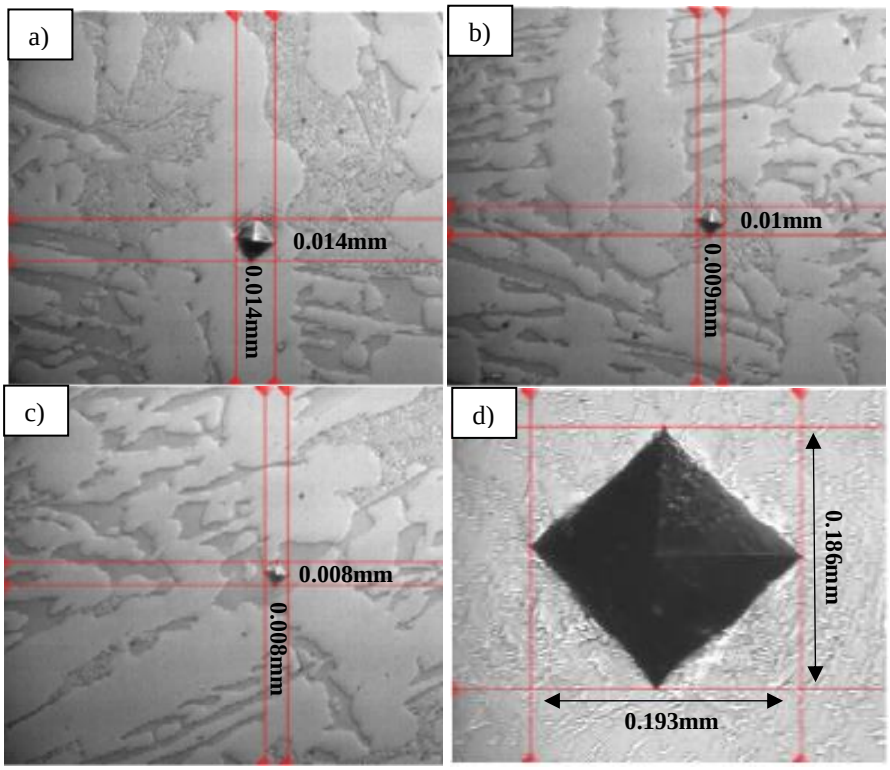

Figure 4.20: Surface hardness indentations on the as-received WT-12 alloy: a) Solid solution matrix, b) Tungsten carbide network, c) Chromium carbide and d) Bulk hardness indentation.

Table 4.3: Average microhardness (Hv) of microstructural phases/regions and bulk hardness (Hv) of the as-received WT-12 alloy.

Phase	Co Matrix	Cr Carbides	W Carbide Network	Bulk
Hardness (Hv)	462.37(±15.73)	1474.13(±110.32)	1031.9(±23.58)	510.56 (±11.41)

4.3.1.4 Hardness Analysis of the As-received T-800 Tribaloy

The T-800 Tribaloy consists of a primary Laves phase and a eutectic mixture of cobalt-rich solid solution (CoCr-rich and CoMo-rich phases) and secondary Laves phases. Microhardness measurements were taken from the primary Laves phase, the CoCr-rich eutectic solid solution and the bulk hardness of the alloy was measured. However, microhardness evaluation of the secondary Laves phase was not possible and readings from the CoMo-rich solid solution phase were difficult to obtain due to the small size of these phases. Figure 4.21 illustrates the indentations made on these phases and the average hardness values are summarised in Table 4.4. The values obtained for the primary Laves phase, cobalt solid solution and the overall bulk hardness of the alloy are consistent with the values reported in the literature [151]. Although indentation was successfully produced on a single CoMo-rich eutectic solid solution phase, due to the close proximity of surrounding phases, the average value calculated is unlikely to represent the actual hardness of the phase. However, the results show that this phase is significantly harder than the CoCr-rich solid solution phase. The brittle nature of this alloy is highlighted in Figure 4.21d as cracking was observed around the indents in the microstructure.

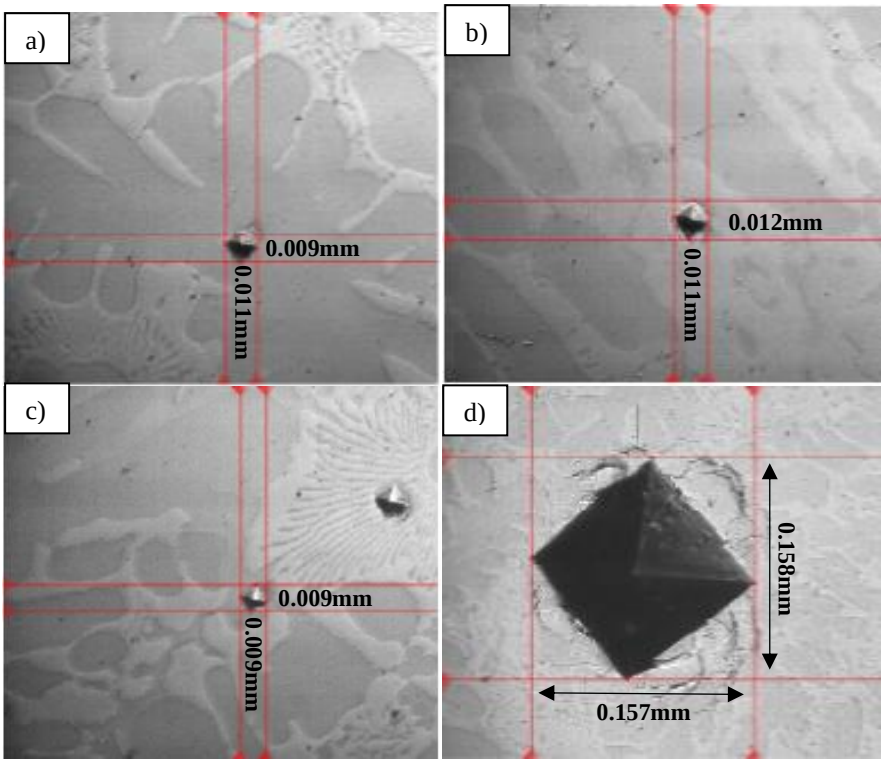

Figure 4.21: Surface hardness indentations on the as-received T-800 Tribaloy: a) Primary Laves phase, b) Eutectic (Cr-rich), c) Eutectic region (Mo-rich) and d) Bulk hardness of alloy.

Table 4.4: Average microhardness (Hv) of microstructural phases/regions and bulk hardness (Hv) of the as-received T-800 Tribaloy.

Phase	Primary Laves Phase	CoCr Eutectic	CoMo Eutectic	Bulk
Hardness (Hv)	1219.8 (±63.7)	720.7 (±45.1)	1073.4 (±75.7)	747.72(±30.6)

4.3.2 Phase Specific Nanoindentation Analysis of the As-received Alloys

4.3.2.1 Nanoindentation Analysis of the As-received WT-4 Alloy

The WT-4 alloy has a microstructure that consists of a cobalt solid solution matrix and a eutectic region that comprises of a mixture of chromium carbides, tungsten carbides as well as solid solution. The loading/unloading curves created from single indentation analysis of the cobalt matrix is displayed in Figure 4.22. On average the matrix had a hardness and modulus of 8GPa and 230.3GPa, respectively. The average results are summarised in Table 4.5, which also includes the mean H/E ratio. The morphology of the eutectic region made it very difficult to perform single indents on the individual phases due to the fine structure. Even when utilising SPM analysis of the samples surface, the different phases could not be distinguished from each other for single phase analysis. However, XPM analysis did highlight differences in mechanical properties of the phases in the alloy's microstructure. In-situ SPM analysis of the tested area of the samples surface identifies the location of individual indents and the corresponding mechanical property maps created using XPM analysis are presented in Figure 4.23. The maps highlight a clear difference in mechanical properties between the cobalt matrix and the eutectic region with the eutectic region having a higher hardness and modulus. When the data is plotted as a histogram the hardness values for the cobalt matrix falls within a narrow band while the indentations made in the eutectic region produce a wide range of hardness values with a flatter peak. The modulus histogram (Figure 4.23e) does not clearly identify peaks for the individual phases as the peaks merge together. Using XPM data from different locations found that the matrix had a hardness of 7.87GPa and a Youngs modulus of 230.74GPa. Comparing Table 4.5 and Table 4.6 demonstrates that similar results for the matrix were obtained from single indentation and XPM analysis.

XPM analysis was also performed on the eutectic region to provide data on the overall mechanical properties of the phase. Figure 4.24a presents the in-situ SPM image of the eutectic area where 225 indentations were performed and the resulting mechanical property maps. A wide range of results were produced for both hardness and modulus, which can be attributed to the indentations falling on individual phases as well as at phase boundaries. Overall, the eutectic region had an average hardness and modulus, as calculated from several locations, of 14.34GPa and 271.49GPa, respectively. The results for both phases of the alloys microstructure are

presented in Table 4.6. The data indicates that the eutectic region has a higher hardness and modulus than the matrix, which results in the eutectic phase having a higher H/E ratio. This suggests that the eutectic region also offers more wear resistance compared to the matrix.

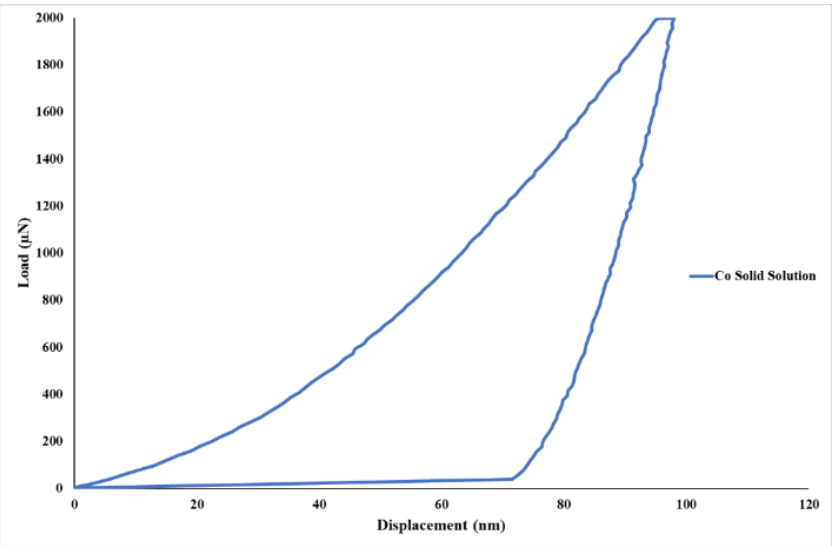

Figure 4.22: Loading/unloading curve for the cobalt solid solution phase of the as-received WT-4 alloy.

Table 4.5: Average mechanical properties for the cobalt solid solution phase of the as-received WT-4 alloy using single nano-indentation analysis.

Mechanical Property / Phase	Hardness (GPa)	Youngs Modulus (GPa)	Mean *H/E* Ratio
Co Matrix	8 (±0.34)	230.3 (±7.53)	0.0347

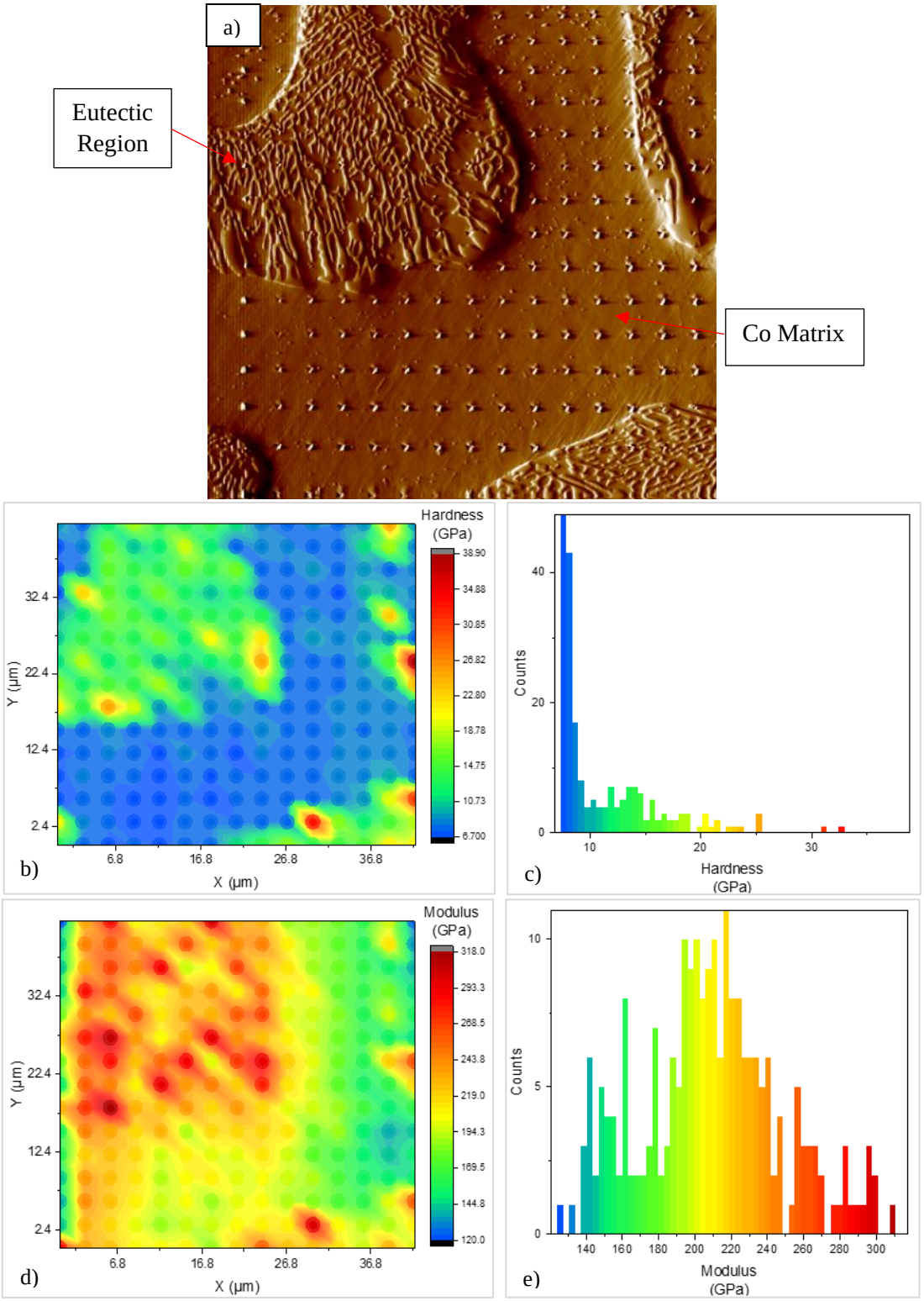

Figure 4.23: Nanoindentation analysis of the as-received WT-4 alloy: a) SPM surface image of matrix and eutectic region, b) XPM hardness map, c) XPM hardness histogram, d) XPM modulus map and e) XPM modulus histogram.

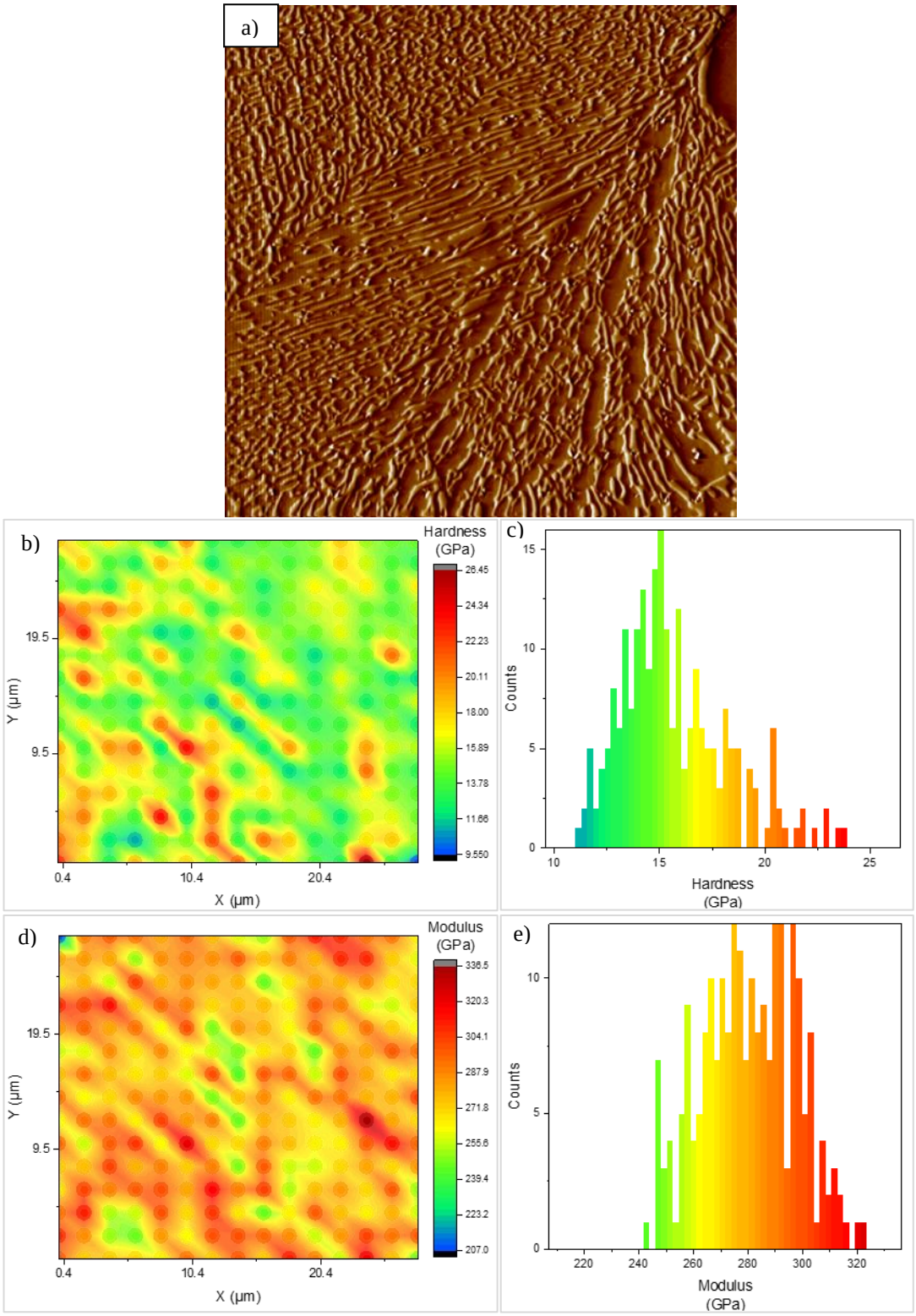

Figure 4.24: Nanoindentation analysis of the eutectic region of the as-received WT-4 alloy: a) SPM surface image of matrix and eutectic region, b) XPM hardness map, c) XPM hardness histogram, d) XPM modulus map and e) XPM modulus histogram.

Table 4.6: Average mechanical properties of the cobalt solid solution phase and eutectic region of the as-received WT-4 alloy using XPM analysis.

Phase	No. of Data Points	Hardness (GPa)	Modulus (GPa)	Mean H/E Ratio
Co Solid Solution	300	7.87 (±0.64)	230.74 (±7.27)	0.0341
Eutectic Region	300	14.34 (±2.53)	271.49 (±17.27)	0.0529

4.3.2.2 Nanoindentation Analysis of the As-received WT-6 Alloy

The microstructure of the as-received WT-6 alloy is dominated by a cobalt solid solution matrix along with eutectic chromium carbides and very small volume fraction of tungsten carbides. Single indentation was performed on the cobalt matrix and eutectic chromium carbide phases. However, due to the small volume fraction of the tungsten carbide (<1%), it was difficult to identify this phase using the optical microscopy capabilities of the nanoindentor. Therefore, it could not be tested. The loading/unloading curves for the matrix and chromium carbides are presented in Figure 4.25. The results show that the carbide phase is significantly harder, having a hardness of 29.25GPa compared to the cobalt matrix with a hardness of 7.65GPa. The chromium carbide phase also has a high modulus of 301.11GPa compared to 231.75GPa of the matrix. The average values for each phase are reported in Table 4.7 in addition to the calculated H/E ratio.

XPM analysis of the surface is illustrated in Figure 4.26, which maps the hardness and modulus of the different phases in the microstructure of the as-received WT-6 alloy. Following indentation, in-situ SPM analysis was performed on the test area, which generated an image of the samples surface and displays the locations of individual indents. Correlating the SPM image to the XPM maps demonstrate that the chromium carbides have a significantly higher hardness and modulus compared to the cobalt solid solution phase. When the data is plotted as a histogram, two distinct peaks are produced in each graph corresponding to the two phases where the first and second peaks represent the cobalt matrix and the chromium carbides, respectively, as shown in Figure 4.26c and e. XPM analysis was performed at several locations to produce the hardness and modulus for each phase. The hardness and modulus of the matrix and chromium carbides are 7.47GPa and 215.82GPa and 27.61GPa and 284.56GPa, respectively. From these results, a mean *H/E* ratio is produced for each phase. The ratios clearly indicate that chromium carbides offer more wear resistance compared to the matrix. The calculated mechanical properties for each phase are summarised in Table 4.8. These values are in accordance with the single indentation data (Table 4.7).

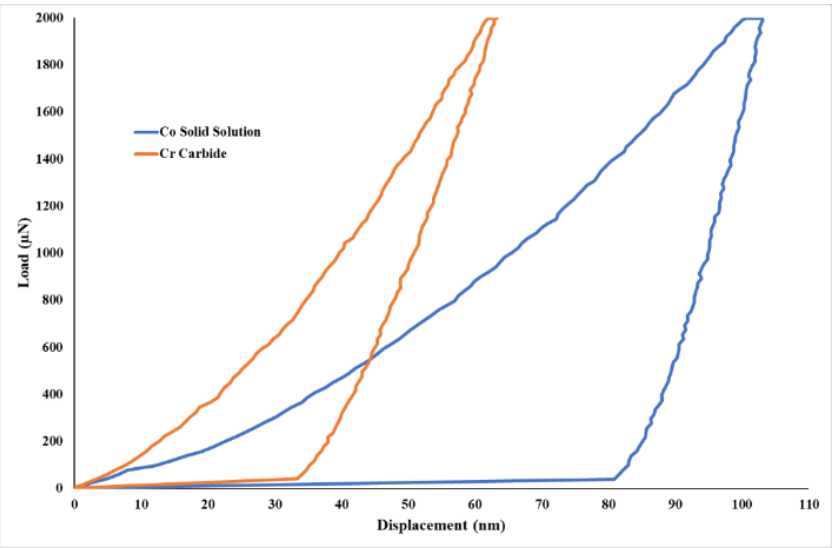

Figure 4.25: Loading/unloading curves of individual phases of the as-received WT-6 alloy.

Table 4.7: Average mechanical properties for the individual phases of the as-received WT-6 alloy using single nano-indentation analysis.

Mechanical Property / Phase	Hardness (GPa)	Youngs Modulus (GPa)	Mean H/E Ratio
Co Matrix	7.65 (±0.24)	231.75 (±6.09)	0.0330
Cr Carbide	29.25 (±1.81)	301.11 (±23.68)	0.0971

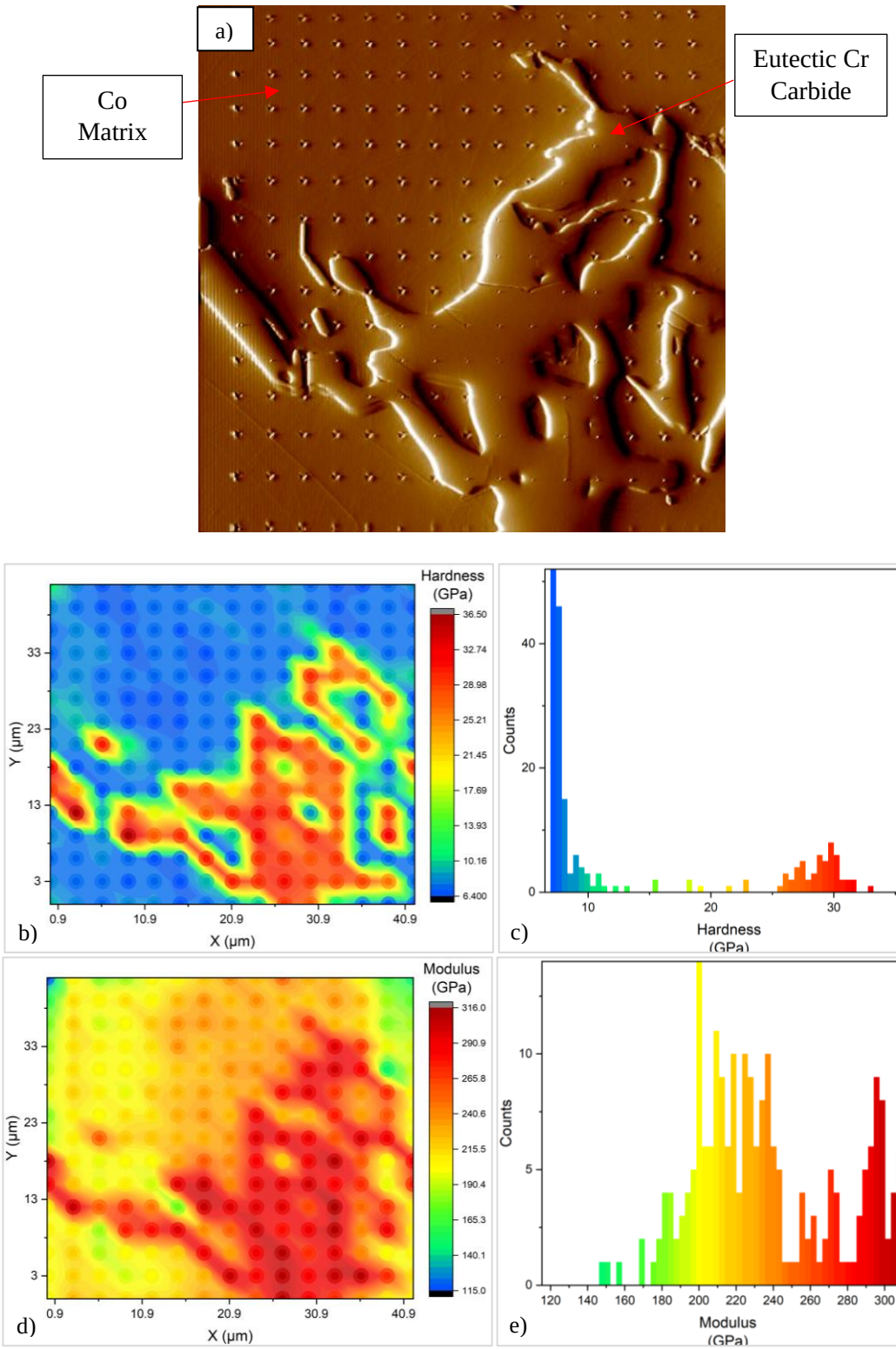

Figure 4.26: Nanoindentation analysis of the as-received WT-6 alloy: a) SPM surface image of matrix and chromium carbide, b) XPM hardness map, c) XPM hardness histogram, d) XPM modulus map and e) XPM modulus histogram.

Table 4.8: Average mechanical properties of the individual phases of the as-received WT-6 alloy using XPM analysis.

Phase	No. of Data Points	Hardness (GPa)	Modulus (GPa)	Mean H/E Ratio
Co Matrix	300	7.5 (±0.49)	220.36 (±6.32)	0.0340
Cr Carbide	80	27.61 (±1.1)	284.56 (±8.48)	0.0970

4.3.2.3 Nanoindentation Analysis of the As-received WT-12 Alloy

Single indentation analysis was performed on the cobalt matrix and chromium carbides phases that exist in the as-received WT-12 alloy. Individual loading/unloading curves for each phase is displayed in Figure 4.27. Despite the tungsten carbide being easy to identity, due to the fine 'skeleton like' structure of the carbide network, it was very difficult to get a reliable reading from the phase. Therefore, it was not included in the single indentation analysis. The results show that the matrix is strengthened by the chromium carbides as they are significantly harder than the cobalt matrix and have a higher modulus. The average hardness, modulus and the calculated *H/E* ratio for the matrix and the chromium carbide phases are summarised in Table 4.9.

XPM analysis was carried out on the overall microstructure of the alloy as well as analysis of individual phases. Figure 4.28a illustrates grid indentation that includes all phases present in the microstructure of the as-received WT-12 and displays the correlating mechanical property maps. The maps (Figure 4.28b+d) demonstrate a clear contrast between the matrix and carbide phases where the carbides have a higher hardness and modulus. When plotted as a histogram the peaks that represent the matrix and chromium carbides are easily identified but the data that represents the tungsten carbide tended to merge with or fall between the matrix and chromium carbide peaks. This is due to the fine structure of the tungsten carbide phase often resulting in indentations being performed at the phase boundary rather than in the interior of the phase.

To give a better indication of the mechanical properties of the tungsten carbide, XPM analysis was performed specifically on a tungsten carbide phase that was large enough to include a large array (15x15) of indent measurements. Figure 4.29 displays an SPM image of a tungsten carbide phase after grid indentation and demonstrates that all 225 indents were performed on the carbide network. It was identified in Figure 4.9 that the morphology of the tungsten carbide often formed as a fine structure that had cobalt solid solution within the structure as well as small chromium carbides embedded in the network. Therefore, the SPM image was closely inspected to identify indentations made on a single tungsten phase and the mechanical properties for those specific readings were analysed. Results indicated that the hardness and modulus of this phase reached a maximum of 24GPa and 300GPa, respectively. However, producing an average value for this phase produces lower values of 18GPa and 251GPa. The relatively large standard deviation of the results is most likely due to the fine structure of the carbide phase resulting in the surrounding

softer matrix influencing the results. These results suggest that although the tungsten carbide is significantly harder than the matrix, it is not as hard as the chromium carbides. In addition to analysis of indents made on a single phase, XPM data was used to investigate the mechanical properties of the tungsten carbide network. Arrays produced in these areas would include readings that were produced on solid solution and chromium carbide phases as well as indents made at phase boundaries. This data does not provide information on the mechanical properties of the tungsten carbides but provides an indication of how these regions of the microstructure influence the performance of the alloy. The average hardness and modulus for each phase is summarised in Table 4.10. The calculated *H/E* ratios demonstrate how the carbides provide the alloy with improved wear resistance as both values are higher than the matrix. Comparing the results for the matrix and the chromium carbide from single indentation and XPM analysis (Table 4.9 and Table 4.10) demonstrates that similar values were produced in each test.

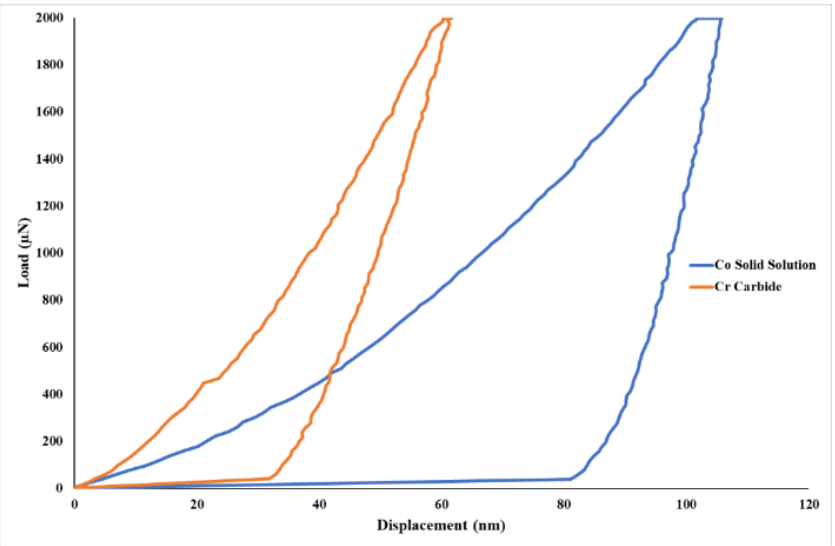

Figure 4.27: Loading/unloading curves of individual phases of the as-received WT-12 alloy.

Table 4.9: Average mechanical properties for the cobalt solid solution phase and chromium carbides of the as-received WT-12 alloy using single nano-indentation analysis.

Mechanical Property / Phase	Hardness (GPa)	Youngs Modulus (GPa)	Mean H/E Ratio
Cobalt Solid Solution	7.35 (±0.36)	226.46 (±4.24)	0.0325
Chromium Carbide	29.25 (±1.32)	313.76 (±8.8)	0.0932

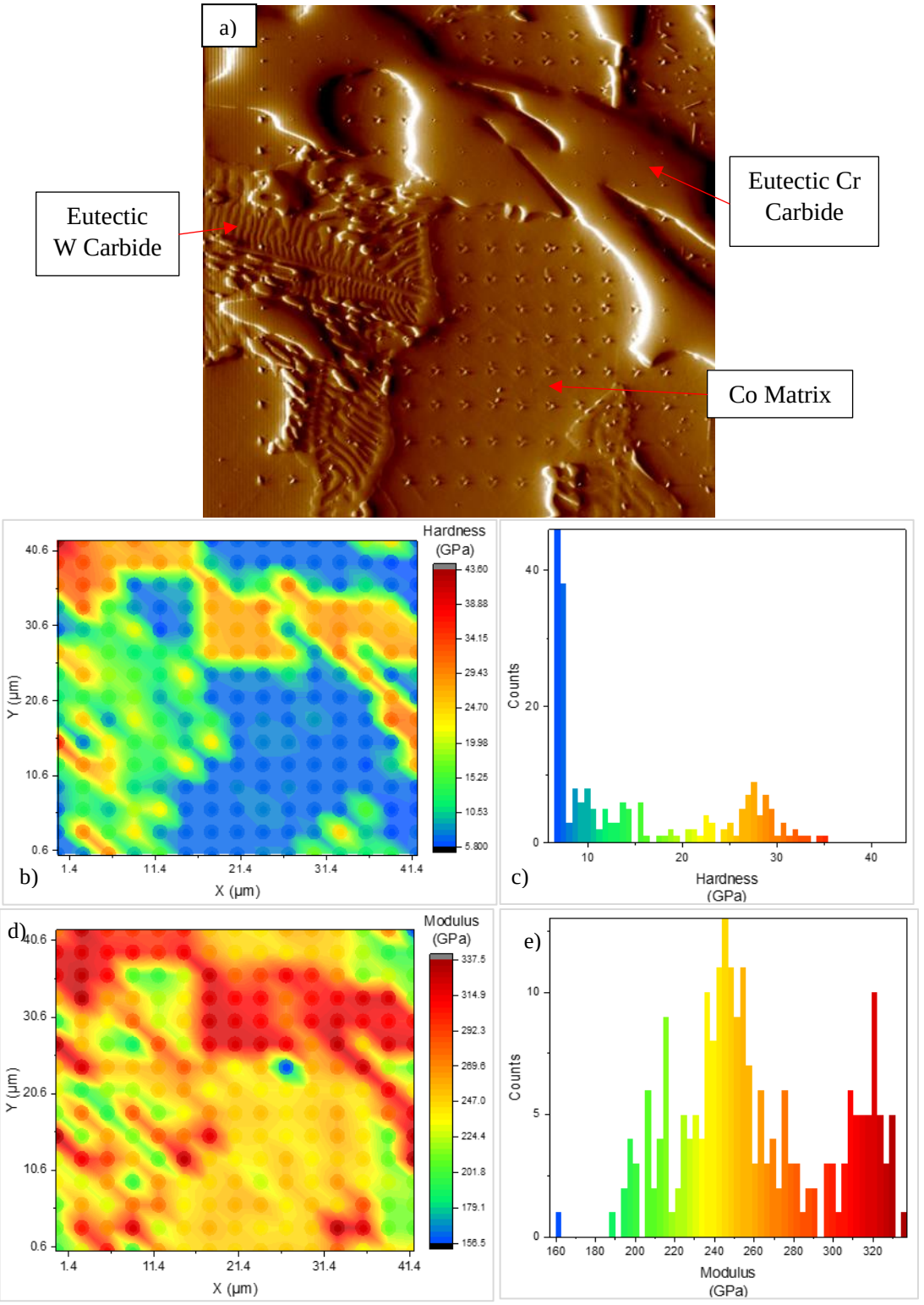

Figure 4.28: Nanoindentation analysis of the as-received WT-12 alloy: a) SPM surface image of matrix and chromium and tungsten carbides, b) XPM hardness map, c) XPM hardness histogram, d) XPM modulus map and e) XPM modulus histogram.

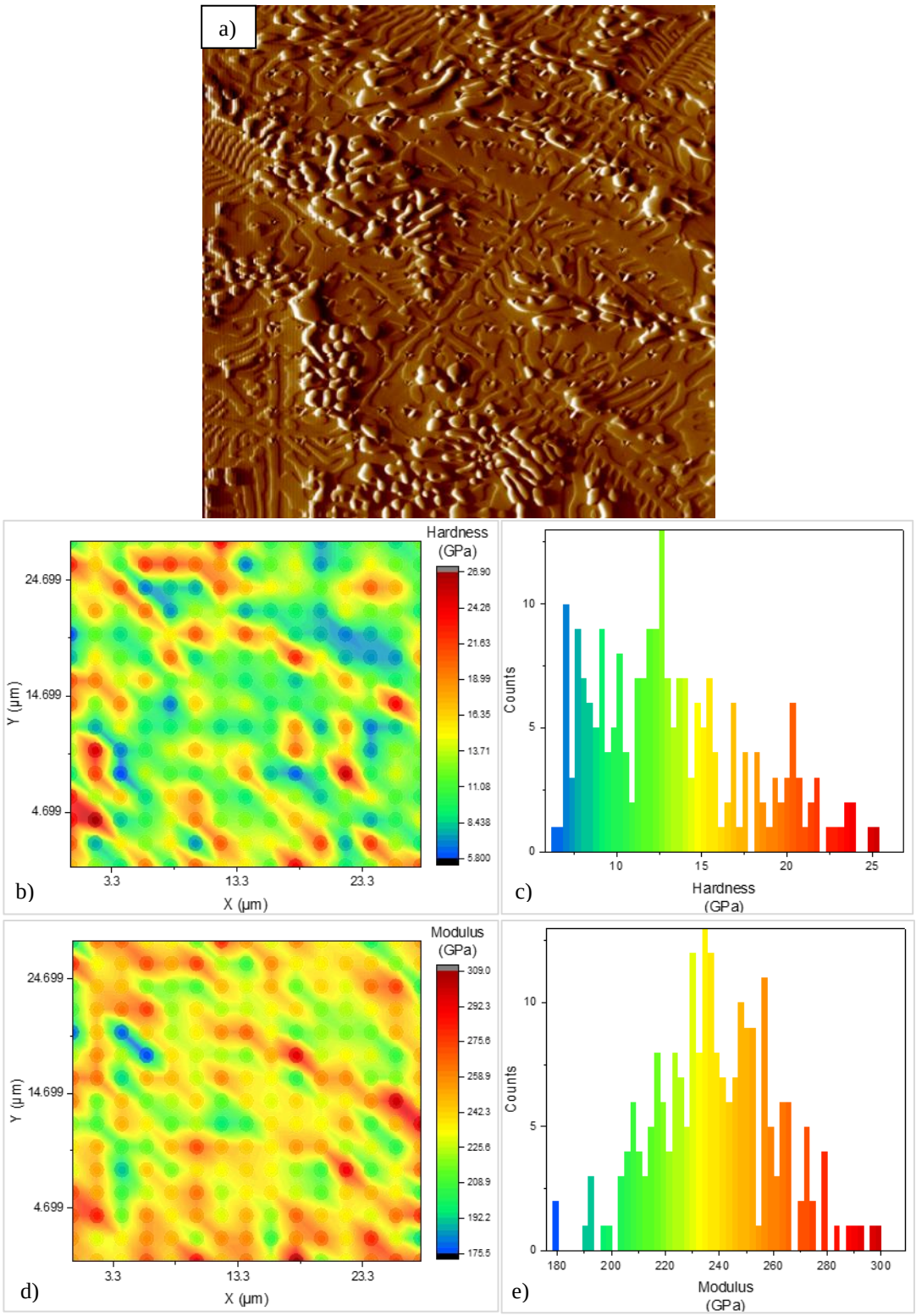

Figure 4.29: Nanoindentation analysis of the as-received WT-12 alloy: a) SPM surface image of the tungsten carbide network, b) XPM hardness map, c) XPM hardness histogram, d) XPM modulus map and e) XPM modulus histogram.

Table 4.10: Average mechanical properties of the cobalt solid solution phase and carbide phases of the as-received WT-12 alloy using XPM analysis.

Phase	No. of Data Points	Hardness (GPa)	Modulus (GPa)	Mean H/E Ratio
Co Matrix	300	7.58 (±0.4)	235.58 (±7.42)	0.0322
Cr Carbide	130	27.47(±2.08)	302.81(±2.08)	0.0907
W Carbide – Single Phase	15	18.2 (±4.02)	251.5 (±23)	0.0724
W Carbide – Network	300	14.97 (±5.82)	266.47 (±24.58)	0.0562

4.3.2.4 Nanoindentation Analysis of the As-received T-800 Tribaloy

The microstructure of the as-received T-800 Tribaloy consists of a primary intermetallic Laves phase that is dispersed in a eutectic mixture consisting of cobalt solid solution with an embedded secondary Laves phase and a molybdenum-rich cobalt solid solution phase free from secondary Laves phase. Single indentation analysis of each phase revealed that the primary and secondary Laves phases have a similar hardness and modulus of 25GPa and 328GPa, respectively. This is significantly higher than the cobalt solid solution, which has a hardness and modulus of 10GPa and 240GPa, respectively. The CoMo-rich intermetallic phase found in solid solution has a hardness of 22GPa, significantly harder than the CoCr-rich solid solution phase but lower than the Laves phase. Despite this phase being more than twice as hard as the cobalt matrix, both solid solution phases have a similar modulus. Loading/unloading curves for the individual phases are displayed in Figure 4.30 and the average results for each phase are summarised in Table 4.11, which also display the calculated *H/E* ratios for each phase.

In-situ SPM imaging following grid indentation is displayed in Figure 4.31a. The image indicates indentations made were performed across the primary Laves phase and both solid solution phases found in the eutectic. Analysing the hardness map (Figure 4.31b) clearly displays a significant difference in hardness between the Laves phase and the cobalt matrix. However, due to the similar hardness of the Laves phase and the molybdenum-rich solid solution phase there is no clear contrast between the two phases on the hardness map. This is also highlighted in the hardness histogram in Figure 4.31c. Despite the indentation grid covering three different phases, the histogram only displays two distinct peaks. This is due to the peaks of the Laves phase and molybdenum-rich eutectic phase merging together as they have similar hardness. The Young's modulus mechanical property map (Figure 4.31d) produces a clearer contrast between the phases. When plotted as a histogram (Figure 4.31e), the data produces three clear peaks corresponding to the individual phases.

XPM analysis was performed on each phase at different locations to produce average hardness and modulus values. The calculated hardness and modulus for the Laves phase, cobalt

matrix and the molybdenum-rich solid solution phases were 22.46GPa and 308.6GPa, 10.84GPa and 239.76GPa, and 20.18GPa and 251.5GPa, respectively. From the results a mean H/E ratio was calculated to give an indication of the wear resistance of each phase. The results suggest that the Laves phase provides increased levels of wear resistance compared to the cobalt matrix. The results also suggest that the molybdenum-rich eutectic phase has a high wear resistance, which would act to strengthen the matrix. Comparing data from the single indentation and XPM analysis (Table 4.11 and Table 4.12) indicates that slightly lower values were obtained for the Laves phase whereas similar results were obtained for the eutectic phases found in the matrix. The small difference in values for the Laves phase may be due to the brittle nature of the phase which often produced a wider range of results. As the data created from XPM analysis was produced using a much bigger data set, 300 indents compared to 5 with single indentation, it can be assumed the XPM data provides a better representation of the overall mechanical properties of the phase. This is also reflected in the smaller standard deviation produced from the XPM data.

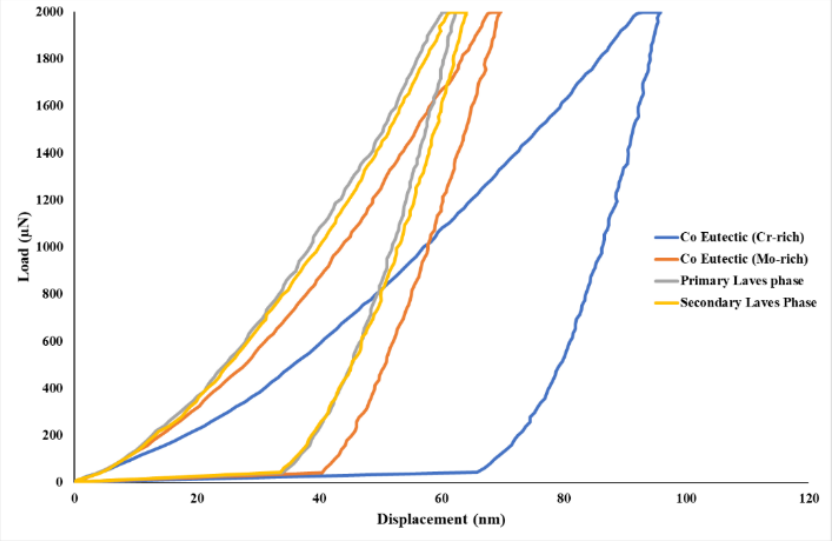

Figure 4.30: Loading/unloading curves of individual phases of the as-received T-800 Tribaloy.

Table 4.11: Average mechanical properties for the individual phases of the as-received T-800 Tribaloy using single nano-indentation analysis.

Mechanical Property / Phase	Hardness (GPa)	Youngs Modulus (GPa)	Mean H/E Ratio
Primary Laves	25.09 (±1.45)	328.6 (±14.18)	0.0764
Co Matrix (Cr-rich)	10.49 (±1.37)	240 (±7.65)	0.0437
Co Matrix (Mo-rich)	21.48 (±1.3)	262.4 (±7.28)	0.0819

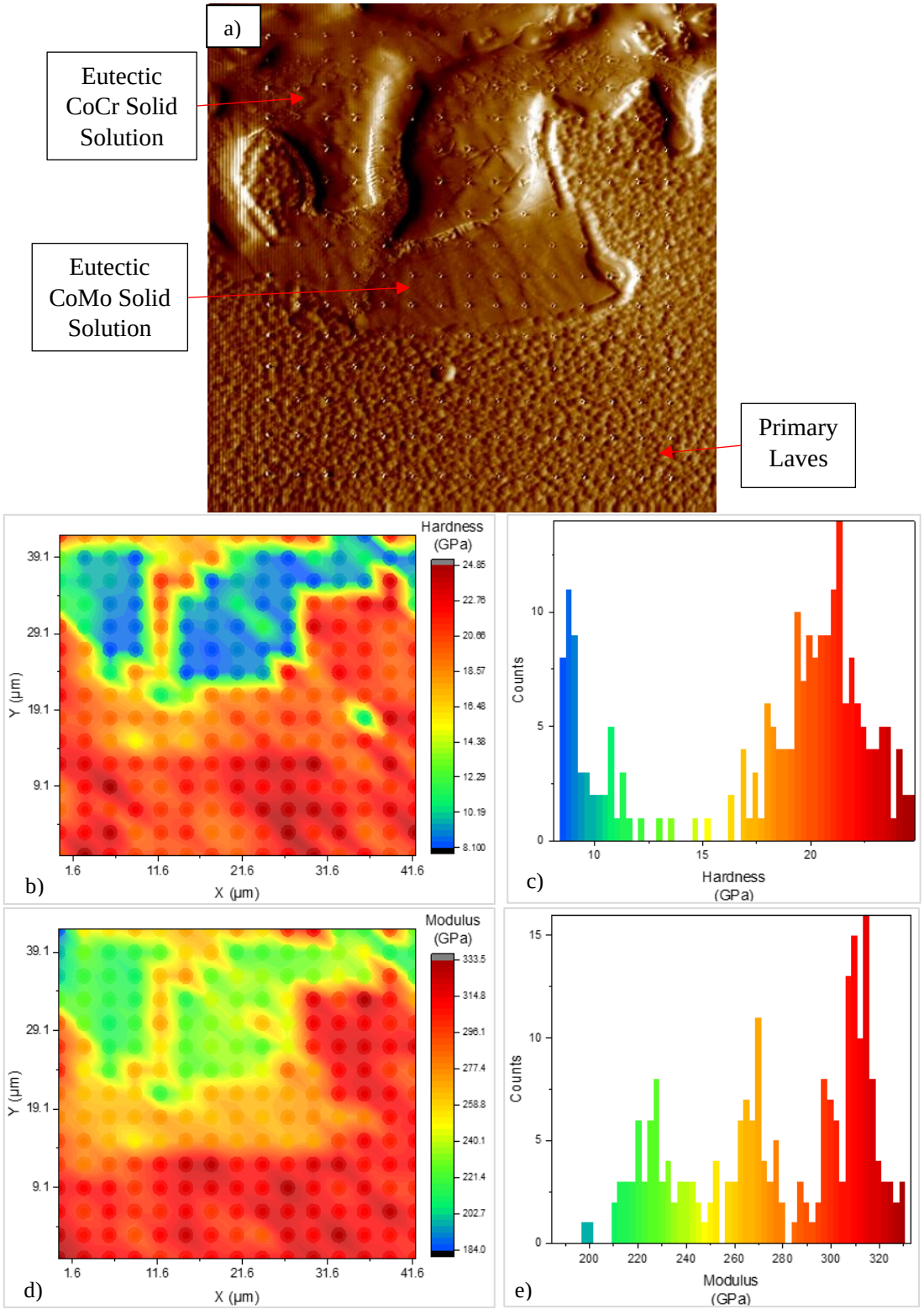

Figure 4.31: Nanoindentation analysis of the as-received T-800 Tribaloy: a) SPM surface image of the eutectic matrix phases and Laves phase, b) XPM hardness map, c) XPM hardness histogram, d) XPM modulus map and e) XPM modulus histogram.

Table 4.12: Average mechanical properties of the cobalt matrix and Laves phase of the as-received T-800 alloy using XPM analysis.

Phase	No. of Data Points	Hardness (GPa)	Modulus (GPa)	Mean H/E Ratio
Primary Laves	300	22.46 (±0.4)	308.6 (±7.94)	0.0728
Co Matrix (Cr-rich)	100	10.84 (±1.2)	239.76 (±8.73)	0.0452
Co Matrix (Mo-rich)	70	20.18 (±0.84)	261.9 (±5)	0.0771

4.3.3 Comparisons of Hardness Trends observed in the As-received Alloys

4.3.3.1 Bulk Hardness Analysis

Comparing the average bulk hardness values for these samples indicates that the WT-6, WT-12 and T-800 alloys comply with the hardness standards stated by Weartech (Table 2.1), whereas the hardness of the WT-4 alloy is slightly higher.

Figure 4.32 shows the average bulk hardness for each alloy. The results confirm that the WT-6 alloy has the lowest hardness, the WT-4 and WT-12 alloys have a higher and similar hardness where the WT-4 is slightly harder, and the T-800 Tribaloy alloy has the greatest hardness value. The hardness of each alloy can be attributed to the volume fraction of carbides/Laves phases present in the microstructure which is determined by the alloy's chemical composition. Figure 4.33 demonstrates a clear correlation between overall material bulk hardness and the volume fraction of carbides/Laves phase present in the microstructure where increasing the volume fraction of these phases increases the hardness of the alloy. This is demonstrated with WT-6 having the lowest hardness (~430Hv) and lowest volume fraction of carbides (~18%) and the T-800 Tribaloy having the highest hardness (~750Hv) and the highest volume fraction of Laves phase (~60%). This trend is also shown by comparing the CoCrW alloys. The WT-12 and WT-4 alloys both have a higher volume fraction of carbide phases present in the microstructure, with 27% and 30% respectively, and are therefore harder than the WT-6 alloy. The WT-4 alloy consists of a slightly higher volume fraction of carbide phases compared to the WT-12 alloy and consequently has a slightly higher hardness.

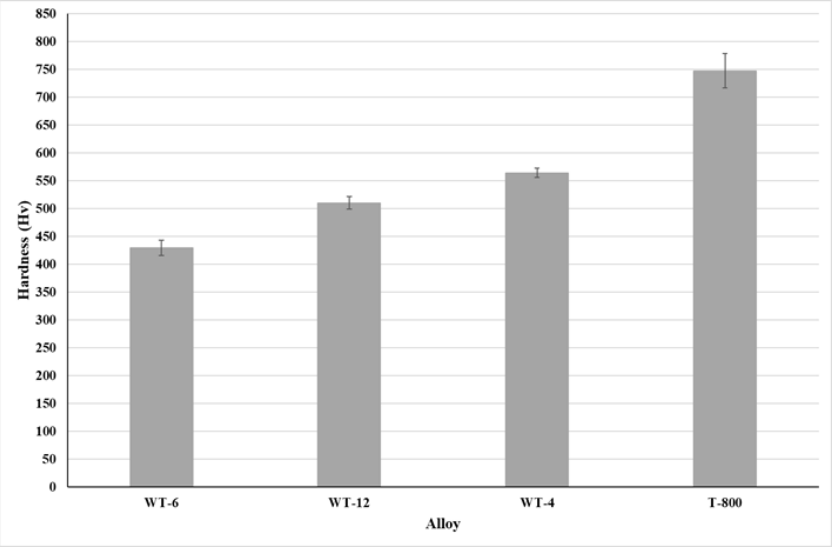

Figure 4.32: Average bulk hardness for the as-received alloys

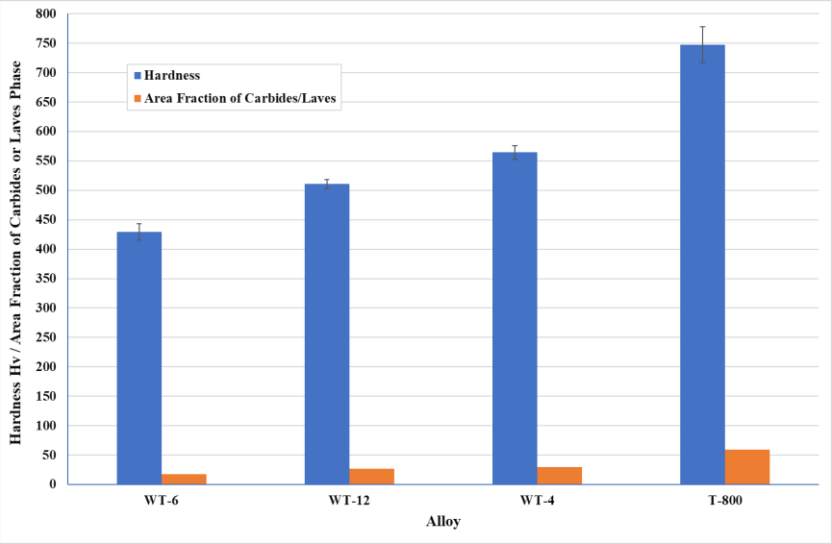

Figure 4.33: Material bulk hardness correlation to the area fraction of carbides or Laves phases present in the microstructure of the as-received alloys.

4.3.3.2 Microhardness Analysis

Microhardness analysis of the individual phases in each alloy demonstrate that the alloys consist of a relatively softer cobalt solid solution matrix and harder carbides or Laves phases that act to strengthen the alloys. Comparing the differences in microhardness for similar phases in each alloy highlights how alloy composition plays an important role in determining the hardness of individual phases and therefore the overall mechanical properties of the alloy. It was not possible to get accurate hardness data for the carbide phases in the CoCrW alloys as the indentation produced was often larger than the phase being tested. Therefore, hardness comparisons for these phases could not be made. However, consistent readings were achieved for

the solid solution phase in each alloy. The average microhardness values obtained for this phase in each alloy is displayed in Figure 4.34. Comparing the CoCrW alloys, the results show that the matrix of the WT-6 alloy has the lowest hardness of 400Hv whereas the matrix of the WT-12 and WT-4 alloys have a higher hardness of 460Hv and 480Hv, respectively. Comparing Figure 4.15 and Figure 4.34 reveals how certain elements influence the mechanical properties of this phase. It was found that the cobalt-rich matrix had similar chromium content in each alloy (~25wt.%) but contained varying levels of tungsten retained in solid solution. Therefore, it can be said that tungsten additions act as the predominant matrix strengthening element in these CoCrW alloys where increased tungsten retained in solid solution increases the hardness of the phase. This is due to the larger atomic size of tungsten atoms which produce stronger solid solution strengthening. Comments cannot be made on the microhardness effects of chromium additions as chromium additions remained consistent for each alloy. The hardness of the CoCr-rich solid solution phase in the T-800 Tribaloy is significantly higher than the comparable CoCr-rich phases in the CoCrW alloys. The phase contains a similar level of chromium (~25wt.%) but molybdenum acts as the strengthening element, replacing tungsten. Both molybdenum and tungsten act as substitutional strengthening elements but the T-800 Tribaloy contains significantly more molybdenum, compared to tungsten additions in the CoCrW alloys, which results in more molybdenum being retained in solid solution significantly increasing the hardness of the phase.

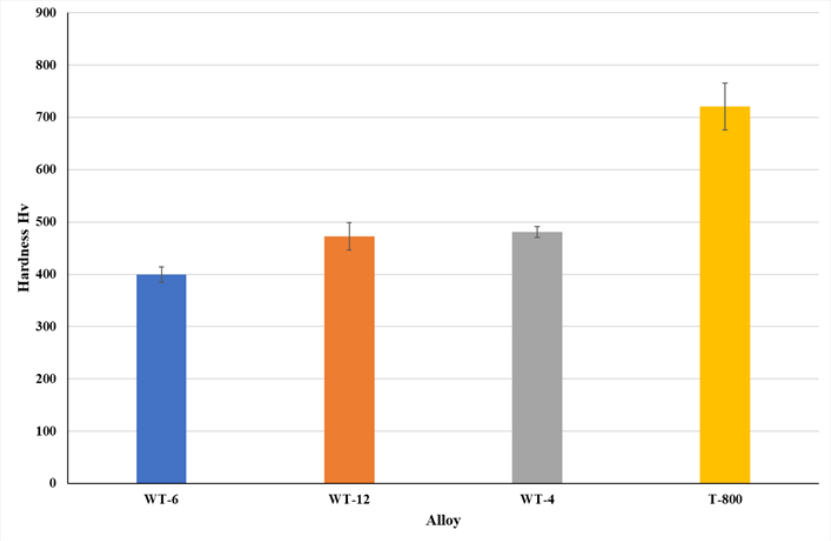

Figure 4.34: Microhardness of the matrix in the As-received alloys.

4.3.3.3 Nanoindentation Analysis

It was identified with each sample that the data produced using XMP analysis was comparable to the data produced from single indentation analysis where similar hardness and

modulus results were produced for each phase. This indicates that XPM analysis is reliable method for rapidly producing large sets of data that give and accurate representation of the phase being tested.

Hardness and modulus data for the matrix and carbides/Laves phases in each alloy is shown in Figure 4.35. The graphs also include data on both Co-rich solid solution constituent of the eutectic in the T-800 alloy as well as providing data on the eutectic region of the WT-4 alloy. The XPM data is statistically plotted as a box plot which presents the distribution of data and provides a better understanding of the overall mechanical performance of the individual phases. The results demonstrate that the carbides and Laves phases have a significantly higher hardness and modulus than the matrix as they act to strengthen and provide wear resistance to the alloys.

Comparing the hardness of the matrix phases of the CoCrW alloys (Figure 4.35a) indicates a similar distribution of hardness readings for each alloy where the WT-4 alloy recorded higher hardness readings. The box plot reveals that 50% of the hardness readings with the WT-4 alloy were higher than 75% of the hardness readings for the WT-6 and WT-12 alloys. This can be attributed to the higher levels of tungsten retained in solid solution of the WT-4 alloy. The microhardness results (Figure 4.34) indicated a significant difference in hardness between the CoCrW alloys where the matrix of WT-6 alloy had a lower microhardness. The microhardness reading would provide data on a combination of phases included within the matrix whereas the scale of the nanoindenter would produce data specific to the matrix phase. Comparing the data would suggest that although the specific hardness of the matrix phase is similar for each CoCrW alloy, the overall hardness of the matrix of the WT-4 and WT-12 alloys may increase due to the formation of fine precipitates or carbides within the matrix that may form due to the higher tungsten content of the alloys. The nanoindentation data indicates that the matrix of the T-800 Tribaloy is significantly harder than the matrix of the CoCrW alloys where 75% of readings were higher than the hardest reading recorded with the WT-4 alloy. Comparing the solid solution phases indicates that the CoMo-rich is harder than the CoCr-rich phase. This can be attributed to the high levels of molybdenum found in each phase.

The data indicates that the modulus of the matrix varied slightly in each alloy. The WT-6 had the lowest readings in addition to the lowest maximum modulus reading. Overall, the modulus of the WT-12 alloy was higher than the WT-4 alloy. The CoCr solid solution phase of the T-800 in the matrix produced the biggest data range and median value was higher than over 50% of the highest readings with the WT-12 alloy, 75% of the readings with the WT-4 alloy and higher than the maximum modulus recorded with the WT-6 sample. CoMo-rich solid solution phase had the highest modulus where all values were higher than 75% of the readings recorded with the CoCr-rich phase.

Due to the small size of the carbides in the WT-6 and WT-12 alloys, reliable data could not be produced using microhardness analysis. However, nanoindentation indicates that the hardness of the chromium carbides in the two alloys produced similar hardness values. Although the hardness results were very similar, the carbides in the WT-6 had a lower modulus. This may be due to the finer structure of the carbides in this alloy compared the larger carbides in the WT-12 alloy. The chromium carbides were found to be harder than the Laves phase in the T-800 Tribaloy but the Laves phase had a slightly higher modulus.

The hardness data for the tungsten carbide phase of the WT-12 alloy produced a wide range of results which suggests that an accurate value was not determined using XPM analysis. It was identified that indents made on the fine structure may have been influenced by the surrounding softer matrix. Although the data for the WT-4 alloy does not give data on the individual carbide phases, the results do give an indication of how the eutectic region influences the alloys mechanical properties. The wider distribution of results can be attributed to the individual phases identified in the eutectic region where the higher readings would represent the chromium and tungsten carbides and the lower readings would represent the CoCrW phase.

The hardness and modulus data gathered from XPM analysis was used to calculate mean *H/E* ratios to give an indication of the wear performance of individual phases/regions in the alloy's microstructure. The mean *H/E* ratio is a measure of the elastic strain an alloy can withstand prior to the onset of yielding. Materials that have higher elastic strains prior to yielding generally have increased wear resistant properties. Therefore, a high *H/E* ratio is important for components used for wear resistant applications. The results for each phase are shown in Figure 4.36. The matrix of the CoCrW alloys exhibit similar *H/E* ratios but is lower than the matrix of the T-800 Tribaloy. The results suggest that the matrix of the T-800 Tribaloy, which contains increased levels of molybdenum, would provide better wear resistance than the matrix of the CoCrW alloys. The molybdenum-rich solid solution phase had a much higher ratio than the rest of the CoCr-rich solid solution phase which suggests that this phase would provide the matrix with elevated levels of wear resistance at localised sites. As the carbide and Laves phases act to strengthen the alloys, they had significantly higher ratios than the matrix phases. Although the eutectic region of the WT-4 alloy contained a combination of phases, including solid solution, the *H/E* ratio was higher than the matrix which shows indicates that the eutectic region provides the alloy with improved wear resistant properties.

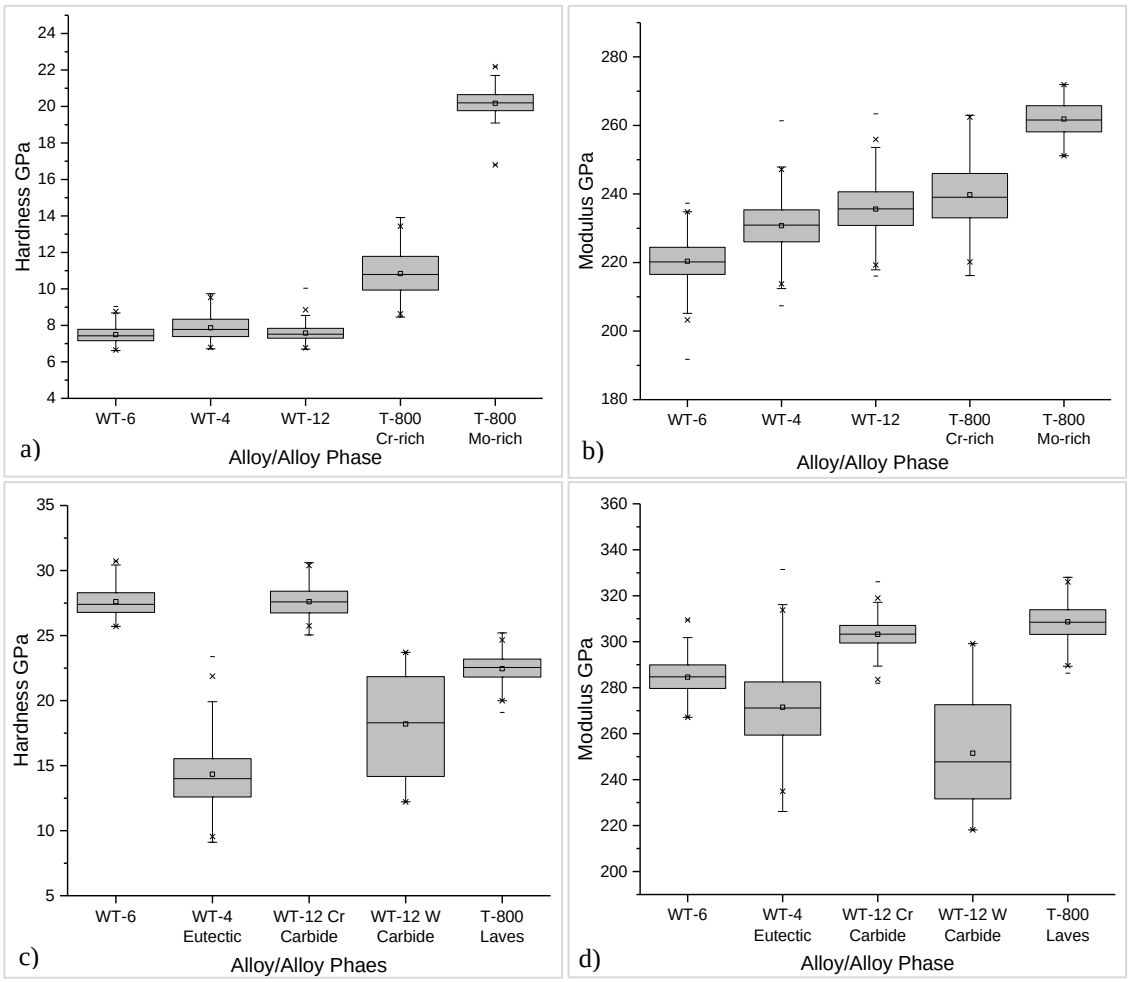

Figure 4.35: Box plot analysis of XPM data for individual phases: a) Matrix hardness, b) Matrix modulus, c) Carbides/Laves hardness and d) Carbides/Laves modulus.

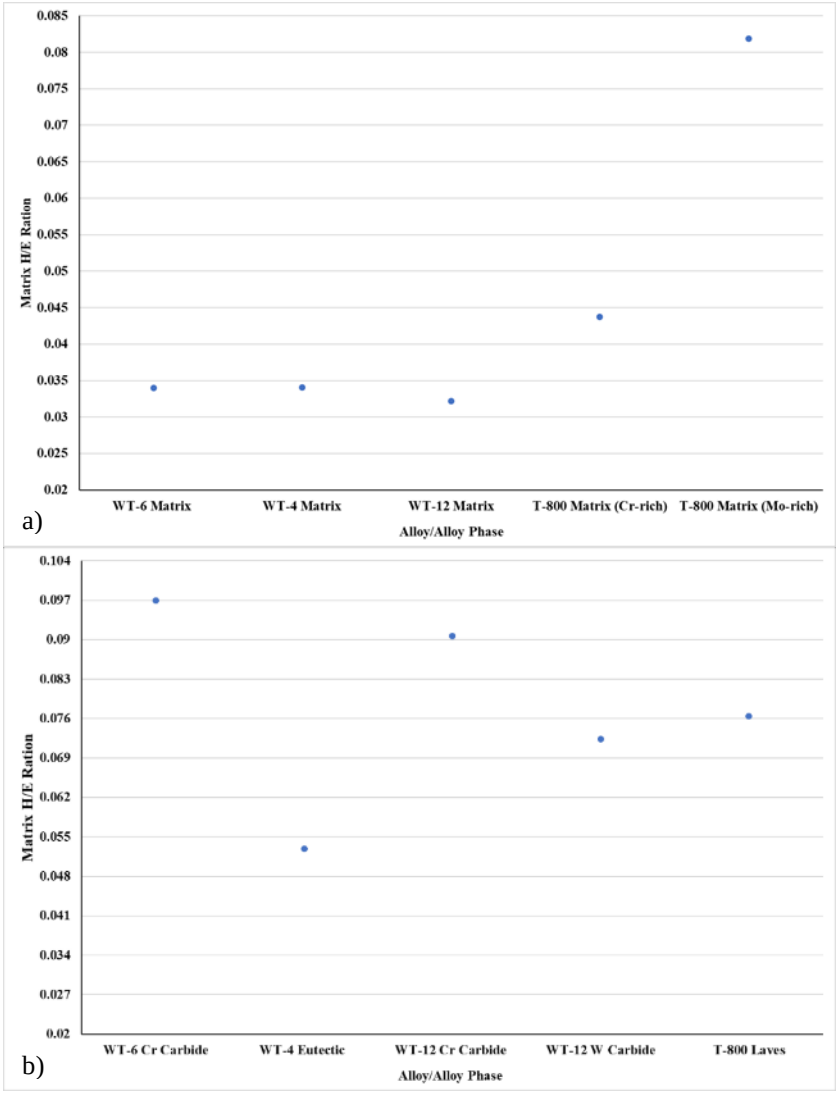

Figure 4.36: Mean H/E ratio of individual phases: a) Matrix phases and b) Carbides/Laves phases.

4.4 Bearing Reactivity with Molten Zinc

4.4.1 Static Immersion Testing of the As-received WT-6 Alloy

Figure 4.37 displays the as-received WT-6 alloy after static dip testing for 1-4-weeks. Figure 4.37a indicates that the immersed sample reacted with the bath after 1-week of testing. Even at this early stage of bath immersion there are clear signs of diffusion occurring beneath the alloys surface in addition to reaction layers forming above it. SEM analysis highlights that diffusion occurred predominately in the cobalt matrix of the alloy where diffusion continued to penetrate through the matrix and deeper beneath the alloys surface as dipping time progressed. Figure 4.38 demonstrates the average diffusion depth reached after each stage of dip testing. An average of 50μm was reached after dip testing for 1-week which then progressively increased to an average of 94μm after 4-weeks. It is worth noting at this point of testing it was often

problematic to define the original surface of the sample for diffusion measurement as it was difficult to judge if the reaction layer was forming at or beneath the apparent surface of the sample. As labelled in Figure 4.37d carbide phases were often observed in areas above the reaction layer. It is unclear whether these carbides were located in their original position or if they had fragmented and detached from the surface. Assuming the latter would suggest that the sample experienced significant levels of material removal during the diffusion process. If that is the case, the average diffusion depth would be underestimated as measurements would have been made from a point beneath the original surface location of the sample. Examination of the samples highlighted that the diffusion process occurring beneath the circumference of the surface was not uniform, particularly after longer bath exposure. After all stages of dip testing some areas of the surface suffered increased levels of diffusion whereas other areas experienced lower levels of reactivity. This is observed in the analysis of the samples surface after each stage of testing and is also indicted on the graph by the relatively large standard deviation of the diffusion measurements.

As the diffusion process progressed, the formation of an intermetallic phase was observed to form behind the diffusion front. Formation of this phase was observed to occur after the first week of testing and similar to diffusion depth, the quantity of the intermetallic phase progressively became more apparent after each stage of testing to the point where, by week 4, the diffusion layer mainly consists of the intermetallic phase. The surface of the WT-6 alloy after 2-weeks of dip testing using EDS mapping is shown in Figure 4.39. Elemental concentration maps demonstrate that the diffusion layer becomes enriched in aluminium and zinc where the process has a high aluminium diffusion front which progresses through the cobalt matrix leaving a zinc-rich phase behind it. The maps also highlight how the area becomes depleted in cobalt and chromium and enriched with iron.

EDS point scan analysis performed on the cobalt matrix identifies how the composition of the diffusion layer changes with increased exposure to the molten zinc alloy bath. Comparisons between samples immersed for 2 and 4 weeks are displayed in Figure 4.40 and Figure 4.41, respectively. EDS point scan analysis after 2 weeks of testing (Figure 4.40) revealed that the diffusion layer contains high levels of zinc where the area just below the surface (Spectrum 1) predominately consisted of zinc (80wt.%). Only small amounts of cobalt (2.5wt.%), aluminium (1.5wt.%) and iron (2.2wt.%) were detected in this area. The significant decrease in cobalt, compared to the original composition of the matrix, indicates that high levels of cobalt are diffusing out from the samples surface. The concentration of zinc decreased to 50wt% by the mid-point of the diffusion layer (Spectrum 2) and then decreased further to 17wt% at the diffusion front (Spectrum 3). The level of cobalt, aluminium and iron gradually increased moving into the

bulk of the alloy where levels increased to 38wt.%, 20wt.% and 9wt.%, respectively, at the diffusion front. This signifies that aluminium and iron diffuses into the alloy's microstructure faster than zinc.

In addition to diffusion and the subsequent formation of a zinc-rich intermetallic phase beneath the alloys surface, SEM analysis revealed the formation of a layer at the bearings surface and the attachment of large particles. The morphology of these phases appeared to change as dip time progressed. EDS analysis of this phase revealed that the layer at the surface was a CoAl phase and the larger particles seen attached were a dross phase. The CoAl phase (Spectrum 4) typically consists of 43wt.% cobalt, 30wt.% aluminium and 19wt.% iron with small amounts zinc and the dross phase typically has a composition of 40wt.% aluminium, 28wt.% iron and 22wt.% zinc. After 1-2-weeks of dip testing the CoAl layer on the surface, where formed, was largely continuous and uniform and was often observed to survive beneath the dross phase where a bonding between the phases was a frequent occurrence, as shown in Figure 4.37a-b. As dip time increased to 3-weeks the CoAl layer became more irregular in shape and any evidence of the dross phase was reduced in size. By week 4 there was little evidence of both phases suggesting that they either detached from the bearing surface, dissolved into the bath or they took part in the diffusion process within the alloy.

By the fourth week of testing (Figure 4.41) the sample shows elevated levels of corrosion where the sample experienced significant material removal which coincided with the removal of the CoAl intermetallic layer. The diffusion layer noticeably takes on a different appearance where diffusion depth and intermetallic phase formation significantly increases. The formation of a continuous layer is also observed at the surface of the sample. Closer inspection of this area reveals that the layer has two distinct regions; an outer region (Spectrum 1) that is zinc (63wt.%) and chromium-rich (25wt.%) and a slightly darker region (Spectrum 2) which is chromium (51wt.%) and zinc-rich (25wt.%) with high levels of tungsten (11wt.%) and silicon (9.4wt.%). The difference in chromium levels in this region is clearly illustrated in the EDS map in Figure 4.41b. At this stage, the diffusion layer is dominated by the formation of the zinc-rich intermetallic phase. The area beneath the chromium rich layer (Spectrum 3) was zinc-rich (80wt.%) with additions of chromium and tungsten. Only traces of cobalt and aluminium were detected throughout this phase. As the diffusion front was approached (Spectrum 5) zinc levels decreased to 17wt.% and cobalt, aluminium and iron levels increased to 34wt.%, 19wt.% and 11wt.%, respectively. Analysis of the diffusion front at higher magnification (Figure 4.41c) revealed the presence of discrete particles than can be observed as small white phases. EDS analysis of these particles (Spectrum 6) revealed they were a tungsten-rich phase that typically had a composition of 40wt.% tungsten, 25wt.% zinc, 15wt.% cobalt and 10wt.% aluminium.

Despite progressive diffusion and intermetallic phase formation the surface of the alloy remained largely intact after two weeks of immersion however, by the third week of testing the alloy experienced increased levels of material breakup and detachment. The level of detachment became more severe by the fourth week of testing where larger areas of material detachment was often observed resulting in a rough surface, as demonstrated in Figure 4.37d.

Whereas the cobalt matrix phase was susceptible to diffusion, the chromium carbide phases in the microstructure of the WT-6 alloy were more resistant and appeared to impede the diffusion process. This is illustrated in Figure 4.37b where the carbide phases are observed obstructing the path of diffusion and restricts penetration to the narrow channels between the carbide phases. However, despite their initial resistance to diffusion the carbide phases did eventually show signs of diffusion with prolonged testing. This was observed by blurred boundaries of the carbide phases. This mainly occurred in areas predominantly consisting of the zinc-rich intermetallic phase that would have been exposed to the diffusion process for longer periods of time. Spectrum 5 (Figure 4.41a) indicates that the chromium carbide phases contained reduced chromium content and levels of zinc and aluminium around the outer edges of the carbide phases. Although the chromium carbides were more resistant to diffusion, they were prone to cracking. Cracking of the carbides was observed after all stages of dip testing near the surface of the samples. This may be explained by stresses caused by volume changes in the matrix and the formation of the intermetallic phase which cause stresses on the carbide phases which leads to fracture.

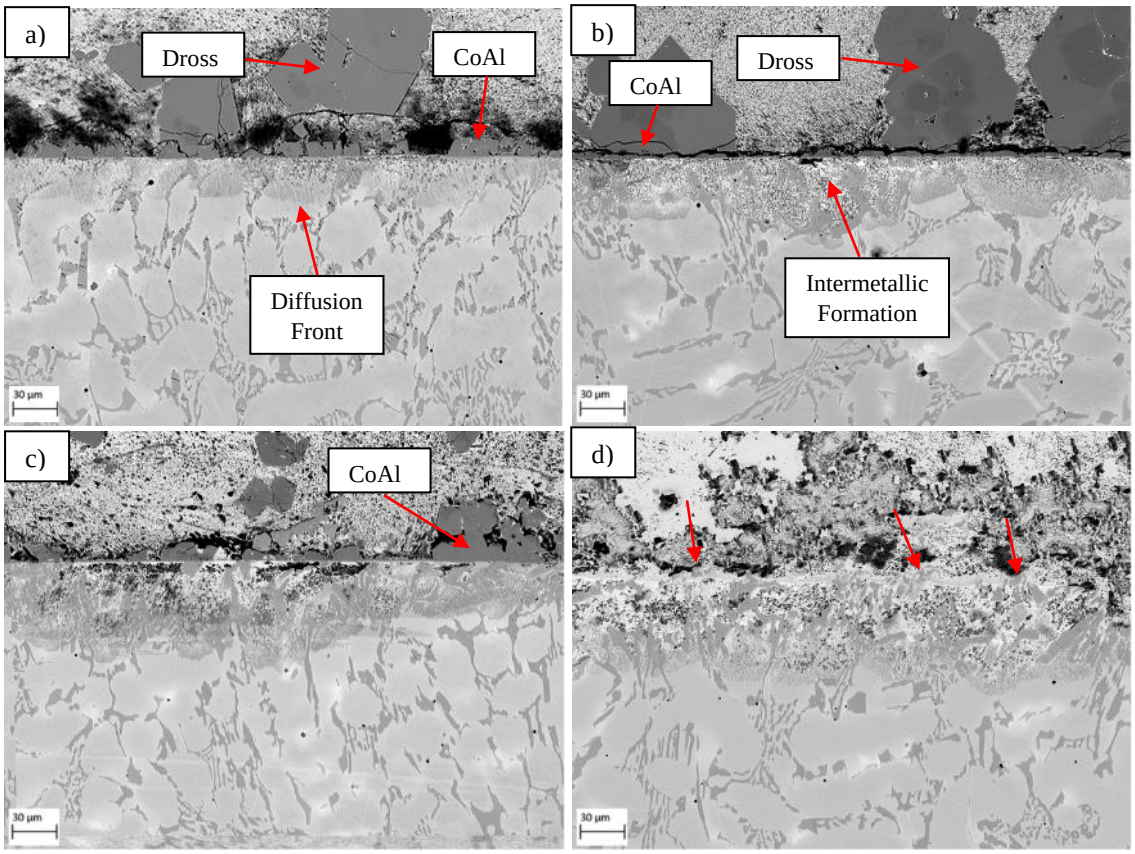

Figure 4.37: Surface condition of the as-received WT-6 alloy after 1-4-week dip testing in a molten zinc bath containing 0.35wt.% Al and saturated with Fe: a) Week 1, b) Week 2, c) Week 3 and d) Week 4.

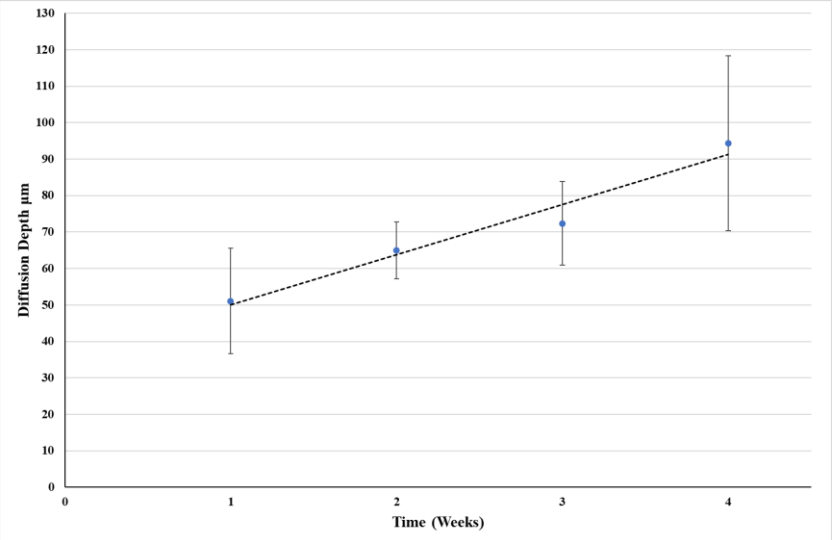

Figure 4.38: Average diffusion depth of the as-received WT-6 alloy after prolonged dip testing in a molten zinc bath containing 0.35wt.% Al and saturated with Fe.

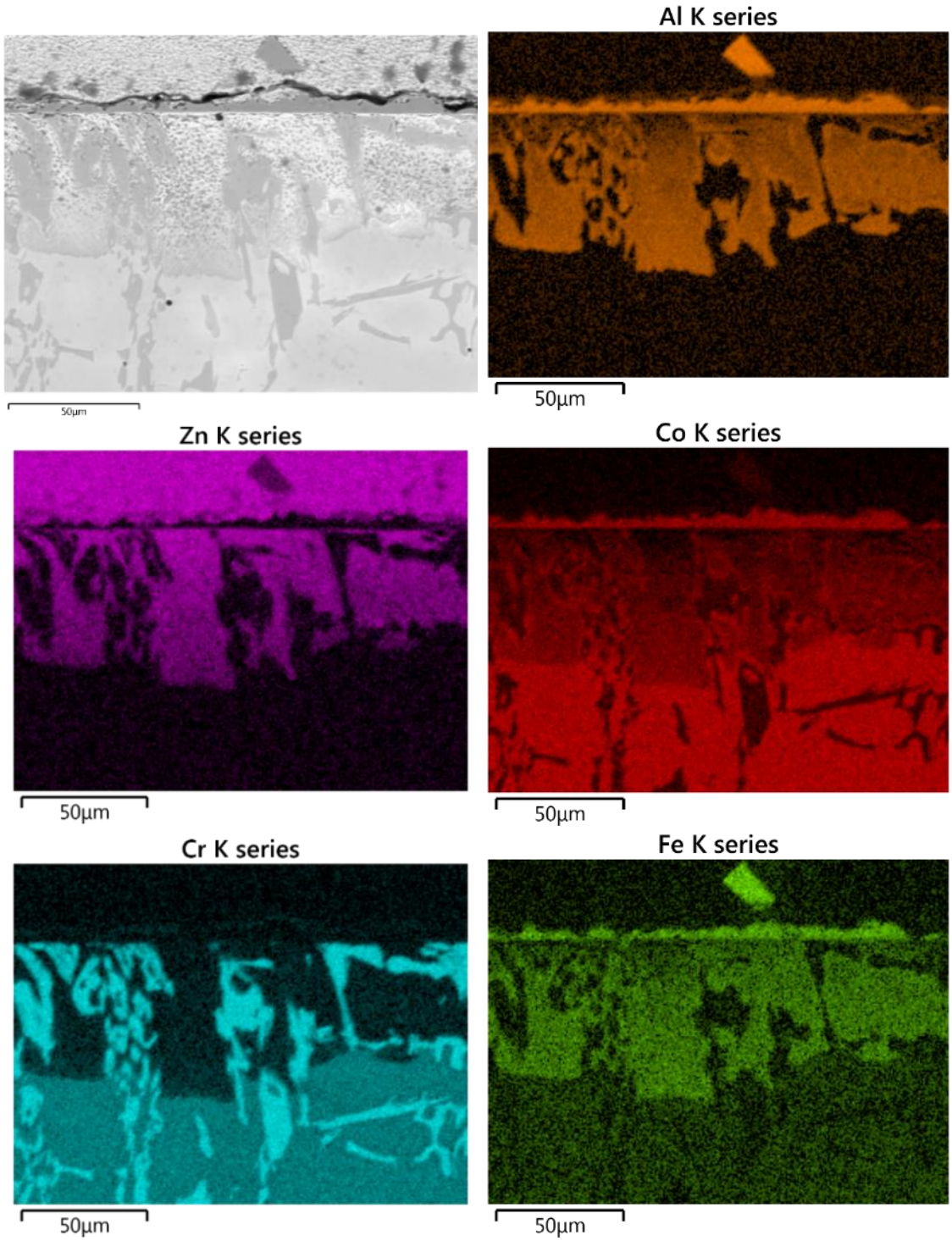

Figure 4.39: EDS elemental mapping of the as-received WT-6 alloy after 2-weeks of dip testing in a molten zinc bath containing 0.35wt.% Al and saturated with Fe.

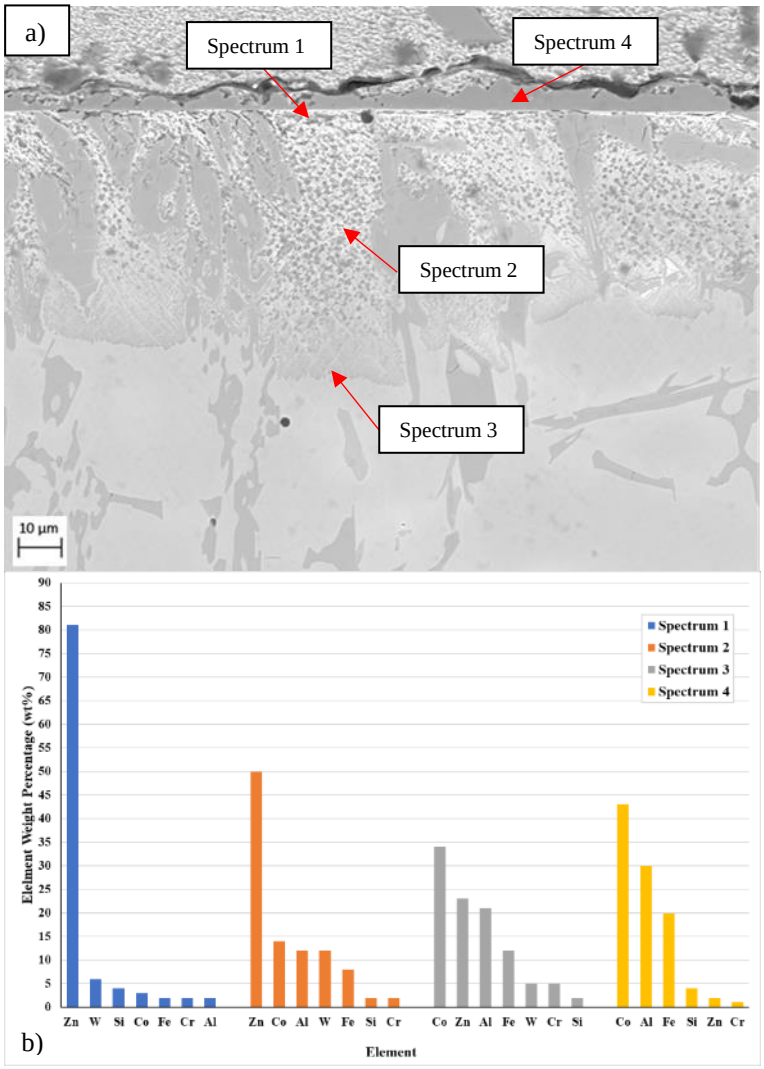

Figure 4.40: EDS point scan analysis of the diffusion zone of the as-received WT-6 alloy after 2-weeks of bath immersion: a) Point scan locations and b) Corresponding point scan compositions.

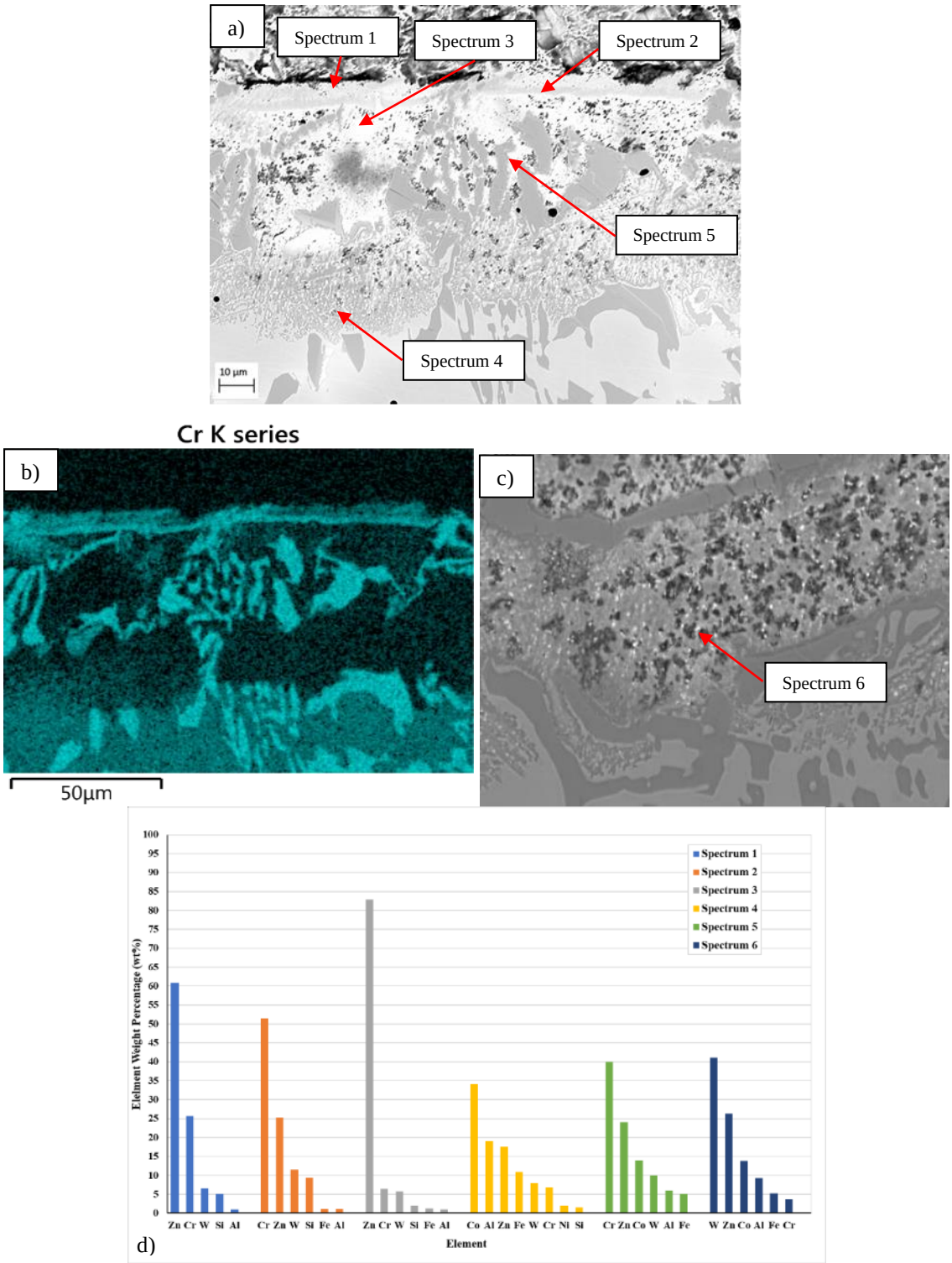

Figure 4.41: EDS point scan analysis of the diffusion zone of the as-received WT-6 alloy after 4-weeks of bath immersion: a) Point scan locations, b) EDS map illustrating chromium-rich layer at the surafce, c) High magnification of discrete phase formation and d) Corresponding point scan compositions.

4.4.2 Static Immersion Testing of As-received WT-4

SEM analysis of the WT-4 alloy after progressive dip testing for 1-4 weeks periods are presented in Figure 4.42. The alloy is observed to react with the molten zinc bath after dip testing for 1-week where the diffusion of atomic species from the bath into the alloys surface occurred simultaneously to phase formation at the surface. Diffusion was observed to mainly occur in the cobalt matrix whereas the eutectic regions, although not totally immune to diffusion, offered more resistance to the diffusion process. Diffusion was observed to take preferential routes through the dendritic matrix where the surrounding eutectic regions were often less effected by diffusion, as shown in Figure 4.42a.

Due to the irregular size and orientation of the dendritic matrix phases some areas experienced greater levels of diffusion. i.e., diffusion reached greater depths when the dendrites were longer and perpendicular to the alloys surface. On average, diffusion reached depths of 55μm after 1-week testing. This gradually increased after 2 and 3-weeks of bath immersion where diffusion reached depths of 80μm by the 3rd week. A more significant increase in diffusion depth was recorded by week 4 where diffusion reached 140μm. The average diffusion depths after each week of dip testing are summarised in Figure 4.43. SEM analysis demonstrated how some areas of the surface experienced increased levels of diffusion which was often related to the orientation and size of the dendritic matrix. This trend was observed after each stage of testing but was more evident by the fourth week of testing. This is further demonstrated by the large standard deviation of the diffusion measurements after this period of testing.

EDS mapping of a sample that had been tested for two-weeks is displayed in Figure 4.44. The elemental concentration maps give an indication of the chemical reactions taking place in the diffusion layer beneath the alloys surface. The analysis confirms that diffusion mainly occurs in the cobalt matrix where the process has a high aluminium diffusion front which penetrates the alloys surface leaving a zinc-rich phase behind it. This process was observed after the first week of testing and progressively increased with prolonged exposure to molten zinc. The EDS maps highlight how the diffusion layer becomes severely depleted in cobalt and chromium and that the diffusion front is enriched with aluminium and iron with the zinc-rich intermetallic phase subsequently forming behind it. It was also noticed that areas of the diffusion layer became concentrated in tungsten which suggests that whereas elements such as chromium and cobalt are leached out from the bulk of the material, tungsten is retained in the diffusion layer. This is due to its large atomic size which makes it less mobile than the other elements involved in the diffusion process.

EDS analysis was performed on the diffusion layer after each stage of dip testing to observe how the process changed with prolonged immersion in the molten zinc bath. Figure 4.45

and Figure 4.46 compares the composition of the diffusion layer between a sample dipped for 2-weeks and 4-weeks, respectively. The locations of the scans are identified in the figures and the compositions are summarised in the corresponding graphs. After 2-weeks of testing (Figure 4.45) it was identified that the area just below the samples surface (Spectrum 1) has a composition of 33wt.% zinc, 32wt.% tungsten, 18wt.% cobalt, 10wt.% aluminium and 3wt.% chromium and iron. Moving into the bulk of the material indicates that zinc levels decrease, and cobalt, aluminium and iron levels increase where the composition at the diffusion front (Spectrum 3) was 36wt.% cobalt, 20wt.% aluminium, 16wt.% zinc, 14wt.% tungsten, 10wt.% iron and 4wt.% chromium. The low levels of the cobalt and chromium and high levels of tungsten indicates that chromium and cobalt is more susceptible to bath reactivity and appears to be leached out of the alloy whilst the tungsten is retained in the diffusion layer of the matrix due to reduced mobility. SEM analysis also highlighted how the outer edge of the of the dendrites (Spectrum 4) contained higher levels of cobalt compared to the centre of the phase which indicates that cobalt diffuses out from the centre of the dendrites during the diffusion process.

In addition to the diffusion layer forming beneath the surface of the sample, a CoAl reaction layer was also observed to form at the alloys surface. The CoAl phase (Spectrum 5) typically has a composition of 52wt.% cobalt, 30wt.% aluminium, 13wt.% iron and 3wt% zinc. Although the formation of this layer was continuous along the surface of the samples, it was irregular in shape and size. The formation of the CoAl phase was often viewed in regions beneath the surface of the sample which was observed to occur as early as the first week of testing, as shown in Figure 4.42a. The image indicates areas of the matrix that were occupied by the CoAl intermetallic phase. This may be a result of the transformation of the matrix into the CoAl phase or the detachment of matrix material and subsequent CoAl formation at the newly exposed surface. The CoAl phase was less frequently observed with prolonged dip testing, particularly after four-weeks, which suggests it detached from the surface or experienced levels of diffusion.

By the third and fourth week of testing there are clear signs of an intermetallic phase forming. The phase is clearly visible in Figure 4.42d as the white region within the matrix. This phase became more apparent with prolonged bath exposure which suggests it forms as a result of increased levels of diffusion. EDS analysis was performed on this phase and at different locations of the diffusion layer to determine the composition at specific locations. The locations of the individual readings and corresponding compositions are summarised in Figure 4.46. Spectrum 1 reveals that the phase is zinc and tungsten-rich and typically has a composition of 58wt.% zinc, 34wt.% tungsten, 4wt.% chromium and 2wt.% aluminium. The regions surrounding these tungsten-rich phases (Spectrum 2), which was often the outer circumference of the dendrites, was predominantly zinc-rich (90wt.%) with small amounts of tungsten and traces of cobalt, chromium

and silicon. This demonstrates that the matrix becomes completely depleted in cobalt with prolonged testing. Comparing Spectrums 3 and 4 indicates that the zinc levels decrease moving towards the diffusion front and cobalt, aluminium and iron levels increased.

The formation of another phase was also observed at the surface of the sample after dip testing, as shown in Figure 4.44a. Elemental mapping of the sample indicates that the phase is chromium and silicon rich. Point scan analysis (Spectrum 5, Figure 4.46) confirmed that the phase was predominately chromium-rich and typically has a composition of 75wt.% chromium, 14wt.% silicon with additions of tungsten and zinc. In the early stages of dip testing the formation of this CrSi phase was not regularly witnessed. However, in the isolated locations where it was recorded, the formation coincided with increased levels of diffusion occurring beneath the surface of the phase, as shown in Figure 4.44. The CrSi is believed to form as a result of the diffusion of the carbide phases and/or diffusion of chromium that is retained in solid solution. Therefore, the formation of the phase became more frequent with prolonged dip testing when the samples had experienced elevated levels of diffusion.

Investigation of the samples after dip testing show how the eutectic region of the microstructure impedes and slows down the diffusion process. However, despite improved resistance to diffusion, the EDS maps demonstrate that the eutectic regions of the microstructure still experienced levels of diffusion where cobalt levels were depleted, and levels of aluminium and zinc increased. Figure 4.47 displays the eutectic region reacting with the molten zinc bath at high magnification (x1500). Closer inspection of the eutectic region revealed that although diffusion was impeded by the fine lamellar structure of the chromium and tungsten carbides, diffusion of aluminium and zinc was able to propagate through the CoCrW solid solution phase that was identified in Figure 4.2.

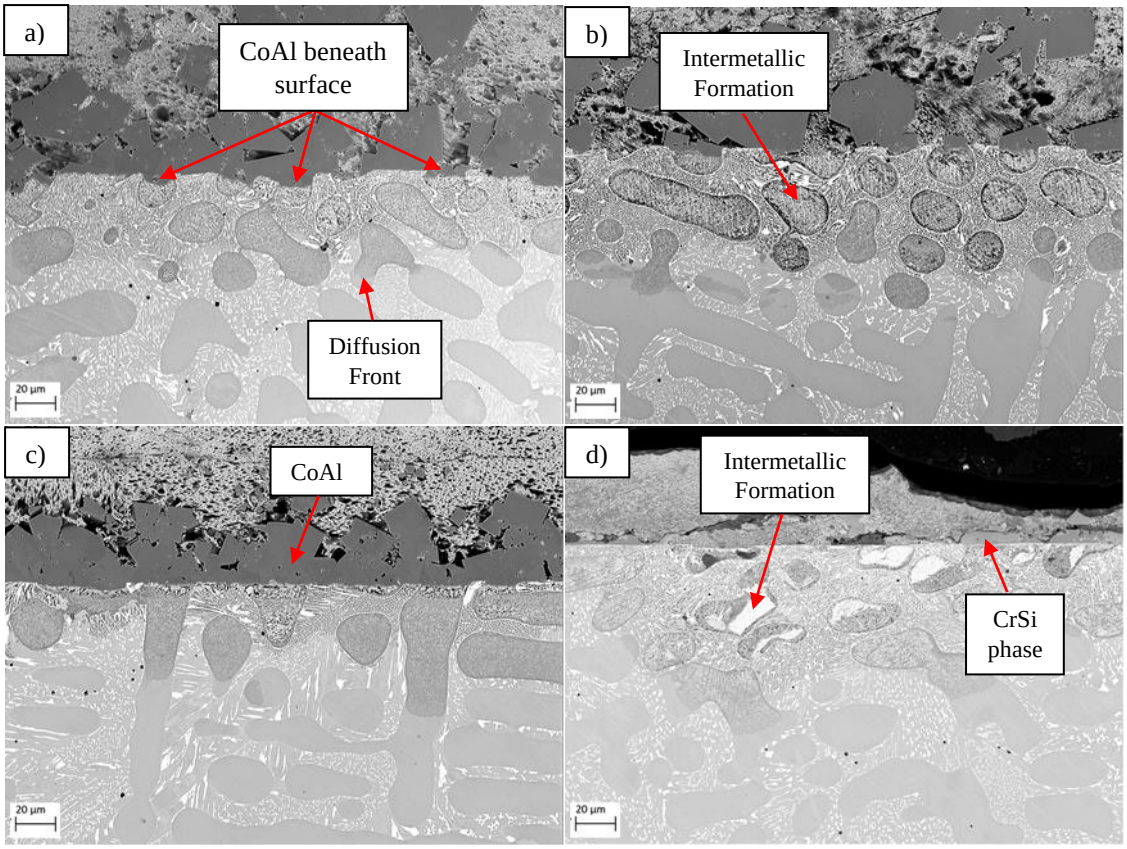

Figure 4.42: Surface condition of the as-received WT-4 alloy after 1-4-week dip testing in a molten zinc bath containing 0.35wt.% Al and saturated with Fe: a) Week 1, b) Week 2, c) Week 3 and d) Week 4.

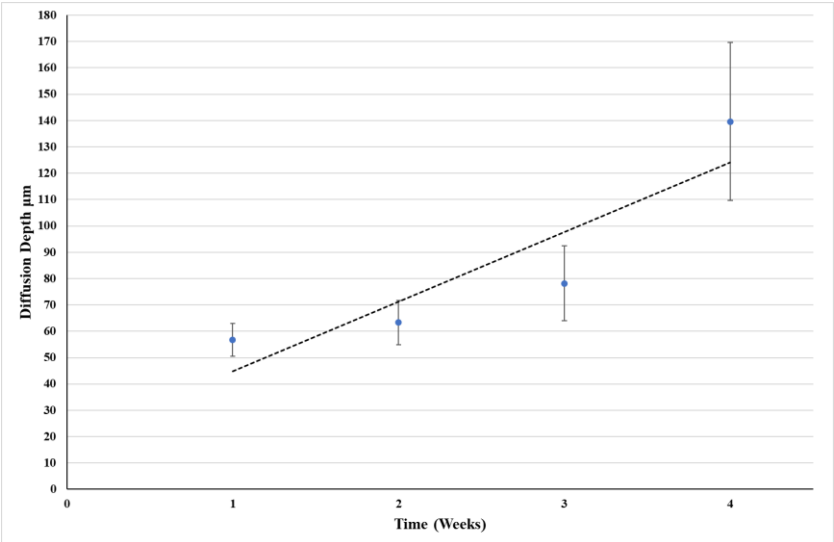

Figure 4.43: Average diffusion depth of the as-received WT-4 alloy after prolonged dip testing in a molten zinc bath containing 0.35wt.% Al and saturated with Fe.

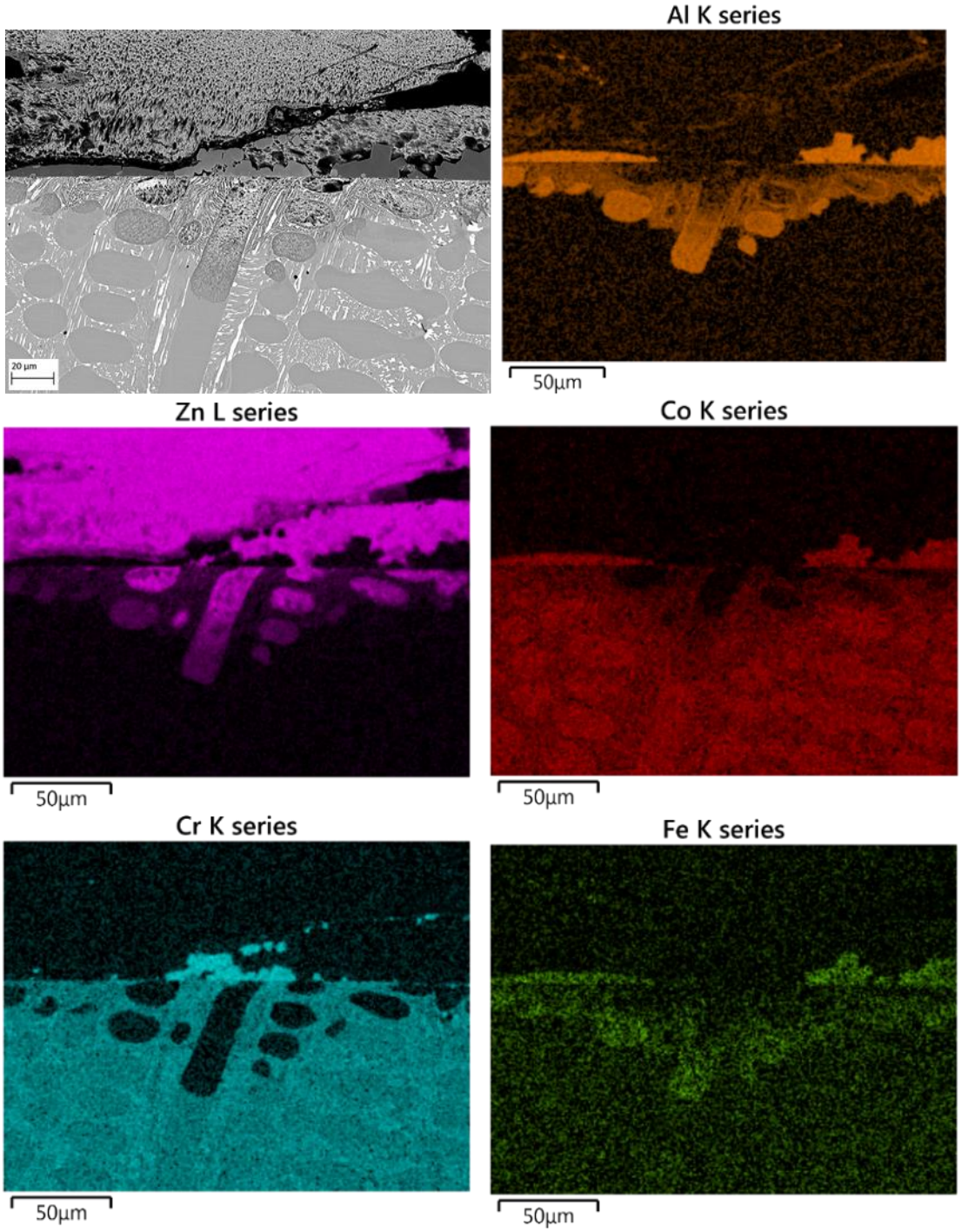
Al K series
20 µm
50µm
Zn L series
50µm
Co K series
50µm
Cr K series
50µm
Fe K series
50µm

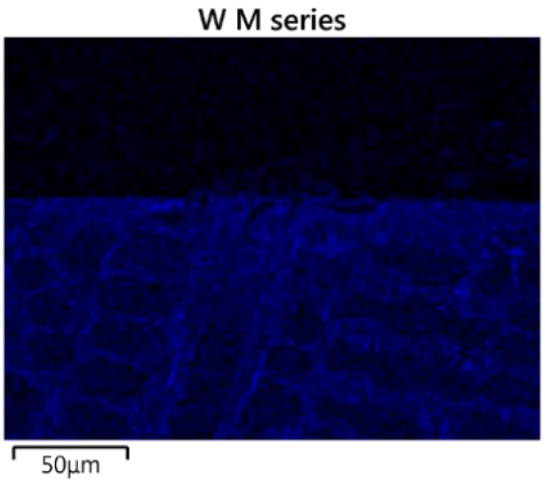

Figure 4.44: EDS elemental mapping of the as-received WT-4 alloy after 2 weeks of dip testing in a molten zinc bath containing 0.35wt.% Al and saturated with Fe.

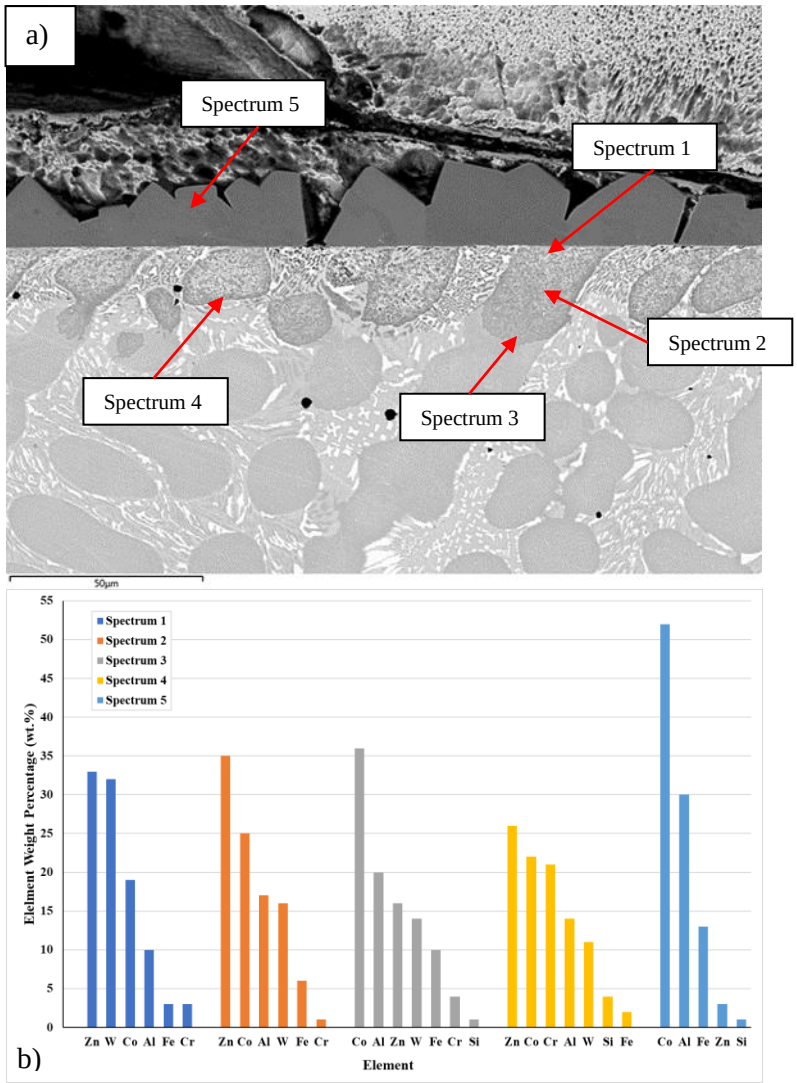

Figure 4.45: EDS point scan analysis of the diffusion zone of the as-received WT-4 alloy after 2-weeks of bath immersion: a) Point scan locations and b) Corresponding point scan compositions.

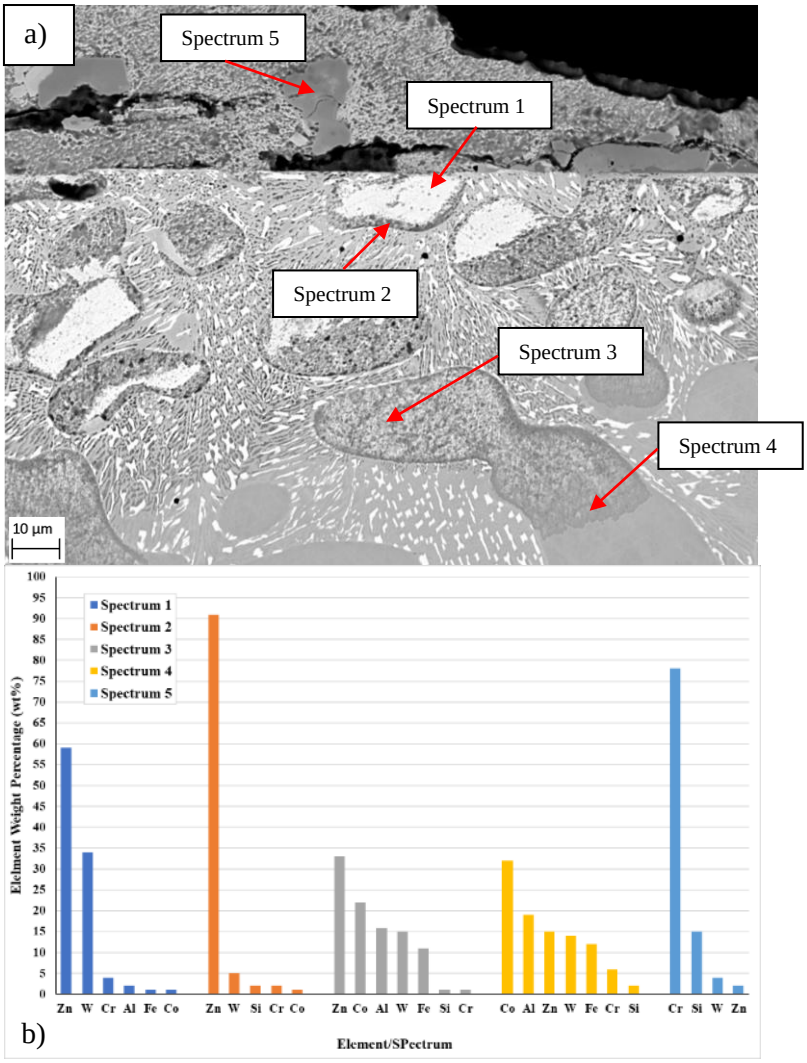

Figure 4.46: EDS point scan analysis of the diffusion zone of the as-received WT-4 alloy after 4-weeks of bath immersion: a) Point scan locations and b) Corresponding point scan compositions.

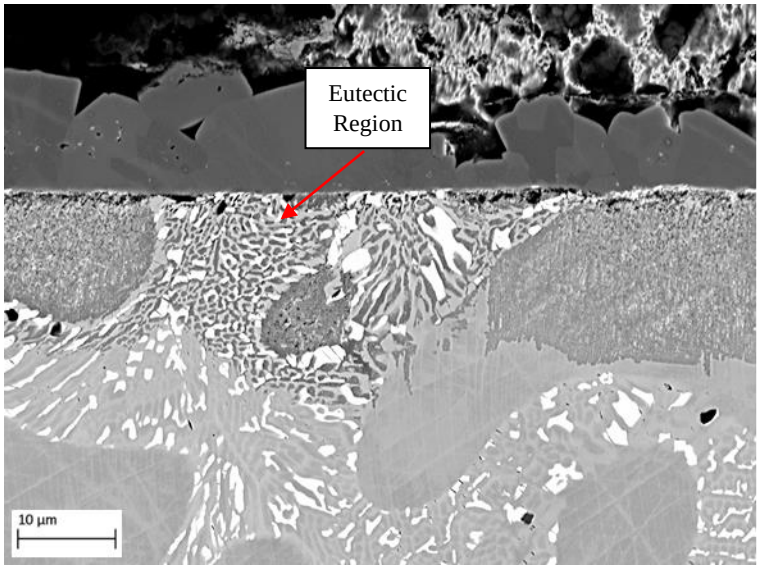

Figure 4.47: High magnification SEM analysis of the diffusion zone of the as-received WT-4 alloy after 2-weeks of bath immersion illustrating diffusion propagation through the eutectic region.

4.4.3 Static Immersion Testing of As-received WT-12

The surface condition of the WT-12 samples after different periods of dip testing are represented in Figure 4.48. After 1-week immersion the alloy is observed to react with the bath resulting a clear diffusion layer forming beneath the surface in addition to a reaction layer forming at the surface. This suggests a simultaneous diffusion process of elements in the bath diffusing into the surface of the alloy and elements diffusing out from the alloy to form the layer at the surface.

The images highlight how the cobalt matrix is vulnerable to diffusion whereas the chromium and tungsten carbides offer more resistance and appear to impede the diffusion process. This is clearly demonstrated in Figure 4.48a where a much shallower diffusion depth is observed due to the presence of the carbide phases where they restrict diffusion. Despite their resistance to diffusion, the carbides near the surface of the samples were prone to cracking. Cracking of the carbides was observed after each stage of dip testing and is likely caused due to stresses introduced from the change in matrix and intermetallic formation.

Average diffusion depths measured after each stage of dip testing are displayed in Figure 4.49. After the first week of testing the diffusion reached 40μm which gradually increased to 50μm by the second week. More significant increases were experienced by the third and fourth week of bath immersion where depths of 80μm and 120μm were reached, respectively. It was observed that some areas of the alloy experienced greater levels of diffusion. This is observed in the SEM images and is highlighted by the relatively large standard deviation of the diffusion measurements.

Elemental mapping of the surface provides an indication of the diffusion process. Figure 4.50 displays a sample after 2-weeks of dip testing. The maps indicate how molten metal diffusion mainly occurs in the cobalt matrix whereas the carbide phases are observed to resist aluminium and zinc diffusion. The diffusion layer has a high aluminium concentration front which results in the depletion of cobalt and chromium and an increase in zinc and iron. This process was observed after the first week of testing and continued to become more apparent as bath immersion time increased.

EDS point scan analysis was performed at certain locations of the diffusion layer to identify the composition of the phases that form due during the diffusion process. The locations of the point scans and their compositions are displayed in Figure 4.52 and Figure 4.54 which make comparisons between samples that were dip tested for two- and four-week periods, respectively. Analysis of the sample that was immersed in the bath for 2-weeks reveals that the region below the surface (Spectrum 2) is typically zinc-rich (42wt.%) with high levels of chromium (32wt.%) and tungsten (15wt.%) in addition to small amounts of cobalt (7wt.%) and aluminium (2wt.%).

Moving away from the surface of the sample towards the diffusion front results in a decrease in zinc and chromium and an increase in cobalt, tungsten, aluminium, and iron. Spectrum 4 indicates that the composition at the diffusion front was 39wt.% cobalt, 22wt.% aluminium, 16wt.% zinc, 10wt.% tungsten, 7wt.% iron and 5wt.% chromium. The high levels of chromium at the surface, which decreased moving into the bulk of the alloy, suggests that chromium diffuses towards the surface of the sample. In addition to the diffusion layer beneath the surface, CoAl phases formed at the surface. The phase (Spectrum 1) typically had a composition of 56wt.% Co, 26wt.% Al and 11wt.% Fe in addition to small amounts of zinc.

Prolonged exposure to the molten bath resulted in increased levels of diffusion occurring beneath the surface of the sample and resulted in the formation of a CrSi phase at the surface which became more frequent with longer periods of testing. Figure 4.52 displays a sample after four-weeks of bath immersion and details the composition of the diffusion layer in certain areas in addition to the reaction layers at the surface. Analysis identified that the CrSi phase (Spectrum 1) consisted of 76wt.% chromium, 15wt.% silicon and 7wt.% tungsten with small amounts of zinc and iron. Although the CoAl layer at the surface was observed after each stage of testing, the morphology of the layer was observed to change. In the earlier stages of testing (weeks 1 and 2) the shape and size of the CoAl phases were irregular, but the layer was continuous along the surface. In the latter stages of testing (weeks 3 and 4) the phase became smaller in size and was observed breaking up and detaching from the surface. The area just below the surface (Spectrum 3) is predominantly zinc-rich (87wt.%) with additions of tungsten (7wt.%), chromium (3wt.%) and cobalt (3wt.%). Comparing the composition of this area after 4 weeks of testing to a similar position after 2 weeks indicates a significant increase in zinc levels and a decrease in chromium. It can be assumed that the depletion in chromium concentration beneath the samples surface is a result of the formation of the CrSi phase at the surface in addition to chromium diffusing into the bath. Moving towards the diffusion front indicates that zinc levels decrease, and tungsten, chromium, cobalt and aluminium levels increase. At the diffusion front (Spectrum 5) the region contains high levels of cobalt (34wt.%), aluminium (19wt.%), zinc (16wt.%) and iron (15wt.%). Examination of the diffusion layer also revealed chromium-rich regions which appeared to consist of several phases. This area is presented at higher magnification in Figure 4.52 which also displays point scan locations and the corresponding compositions. The SEM image demonstrates a darker grey phase, a lighter grey phase and a white phase. It was established that all the phases were chromium-rich but contained varying amounts of tungsten and silicon. The lighter grey phase (Spectrum 1) was chromium-rich with higher levels of tungsten (17wt.%) than silicon (13wt.%), the darker grey phase (Spectrum 2) was chromium-rich with higher levels of silicon (14wt.%) than tungsten (9wt.%) and the white phase (Spectrum 3) was chromium-rich (47wt.%) with

significantly higher levels of tungsten (28wt.%) in addition to cobalt (14wt.%) and silicon (9wt.%).

Although the carbide phases were more resistant to the diffusion process, they did experience levels of dissolution in the latter stages of dip testing. This is demonstrated in Figure 4.48c-d where the carbide interface of both the chromium and tungsten carbides became blurred and appeared to be reacting with the bath. This is observed as a lighter region around the circumference of the chromium carbide phase. EDS analysis performed on the circumference of the carbide phases detected reduced chromium content and levels of aluminium and zinc. The dissolution of the chromium carbide phases could potentially be a reason for the increased levels of chromium that were recorded in the diffusion layer in addition to the formation of the CrSi phase at the surface. Aluminium and zinc were also detected within the tungsten carbide phase indicating the phase experienced dissolution.

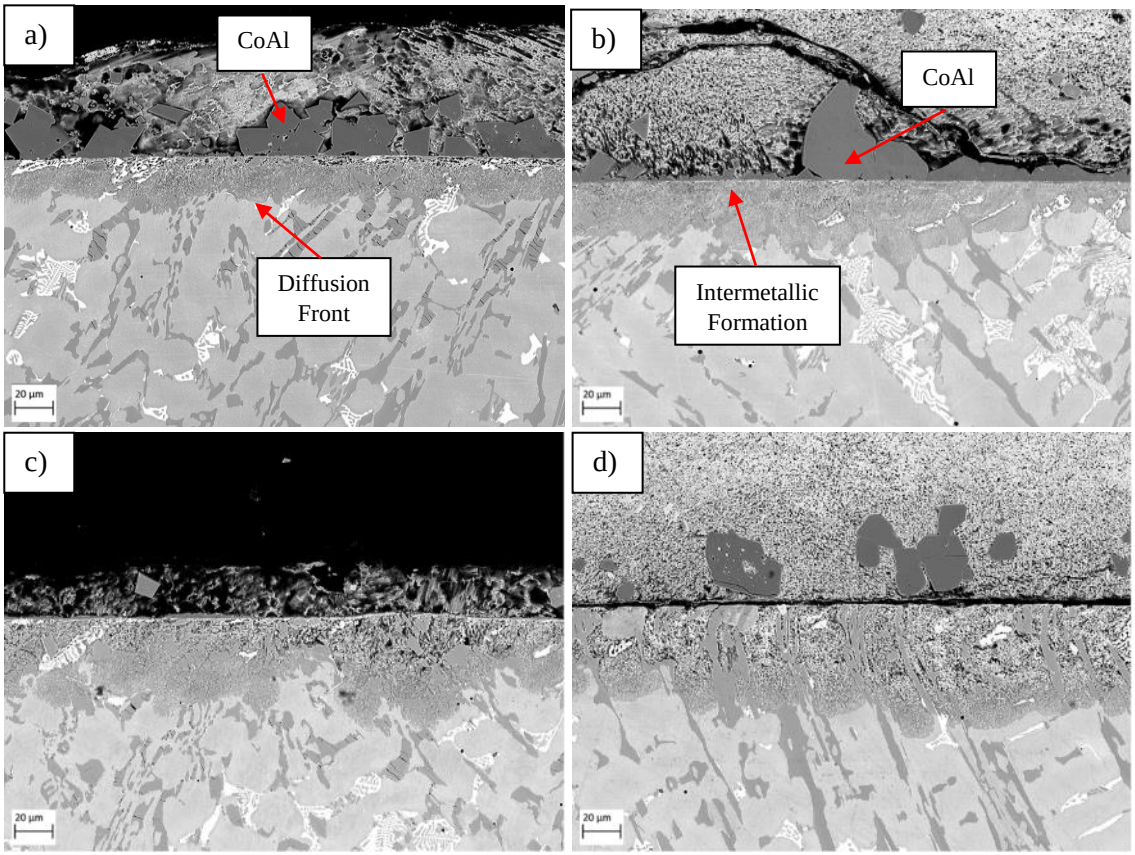

Figure 4.48: Surface condition of the as-received WT-12 alloy after 1-4-week dip testing in a molten zinc bath containing 0.35wt.% Al and saturated with Fe: a) Week 1, b) Week 2, c) Week 3 and d) Week 4.

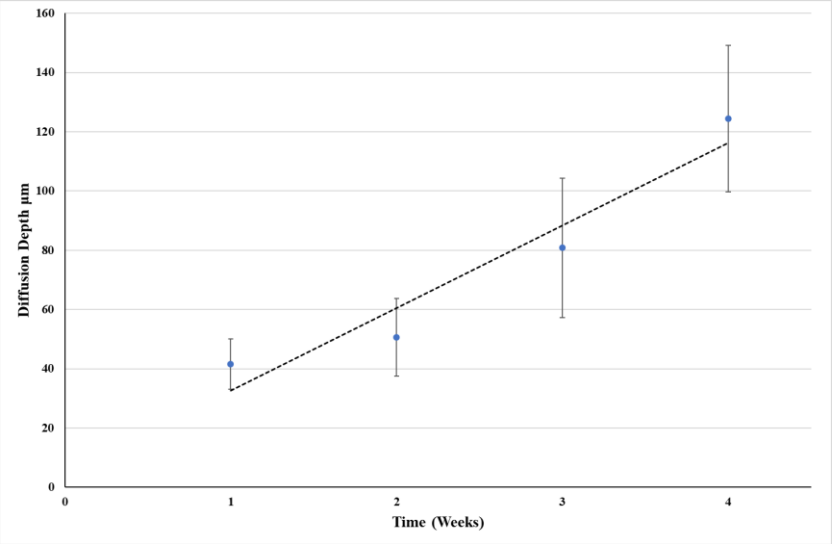

Figure 4.49: Average diffusion depth of the as-received WT-12 alloy after prolonged dip testing in a molten zinc bath containing 0.35wt.% Al and saturated with Fe.

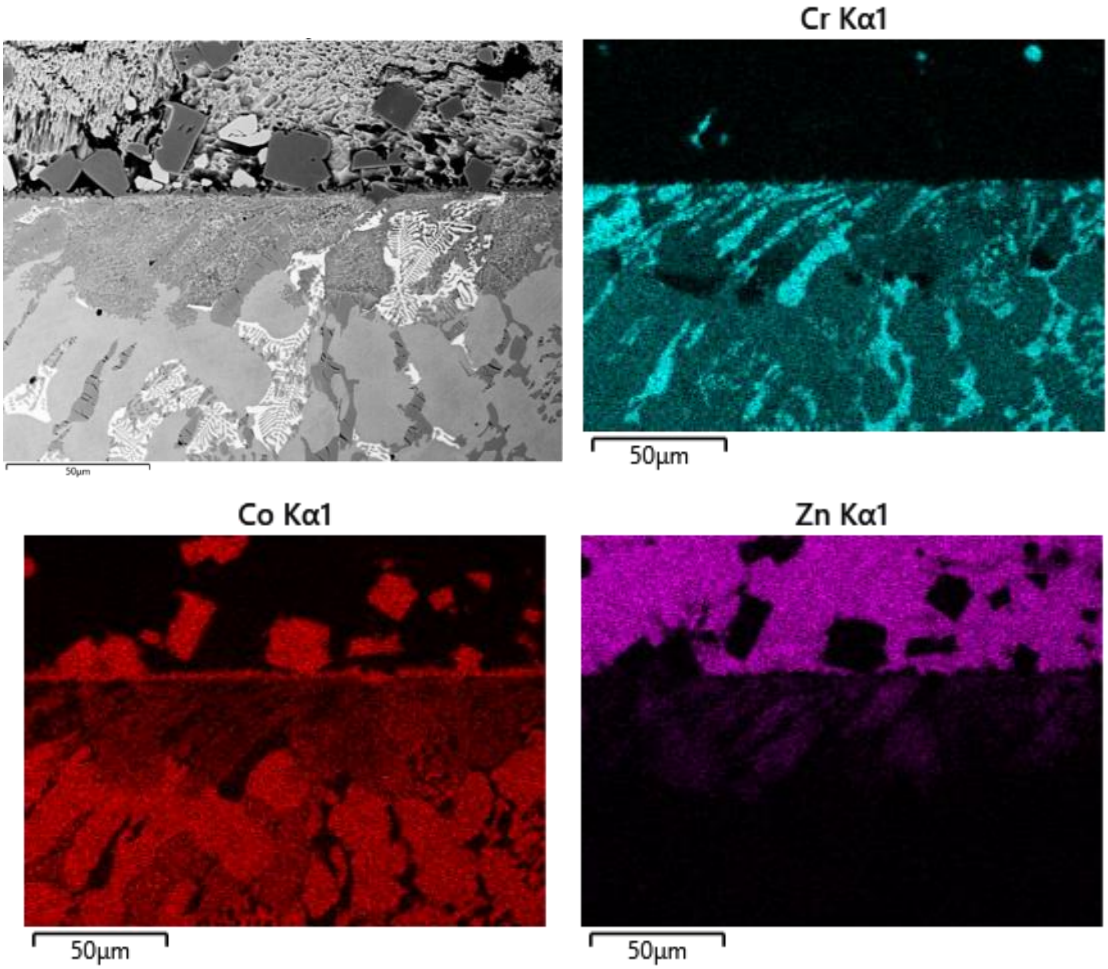

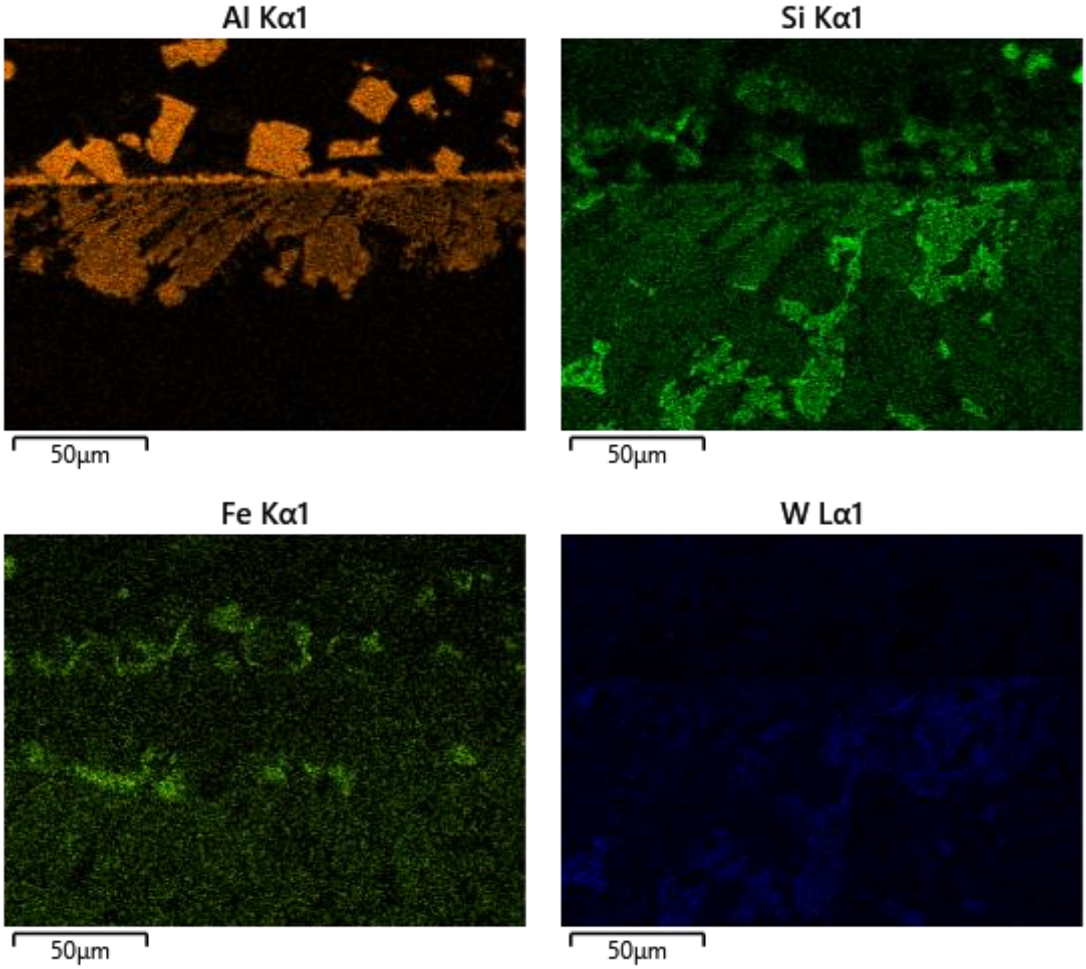

Figure 4.50: EDS elemental mapping of the as-received WT-12 alloy after 2 weeks of dip testing in a molten zinc bath containing 0.35wt.% Al and saturated with Fe.

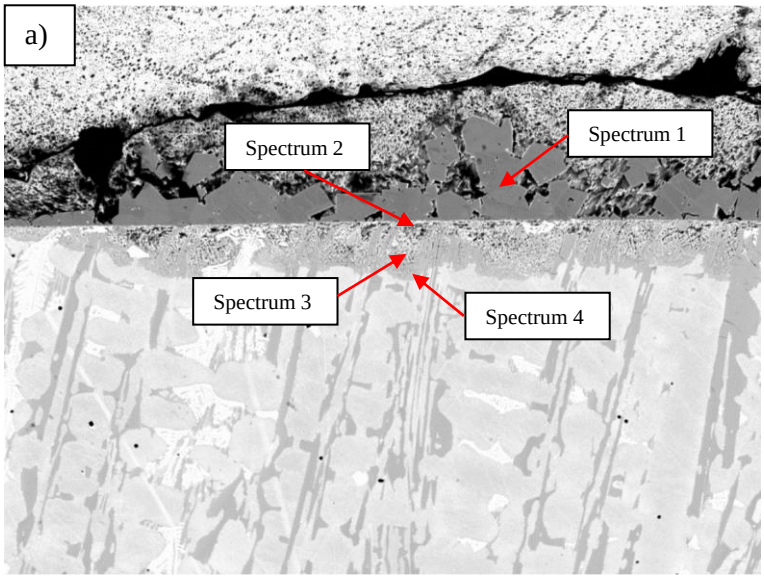

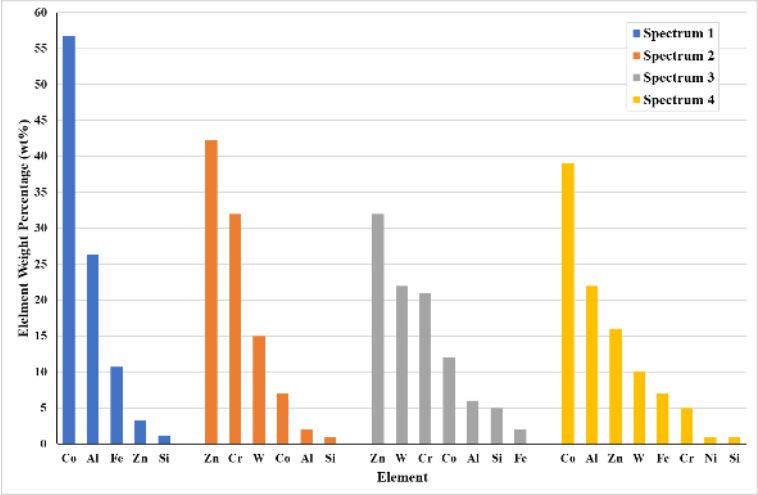

Figure 4.51: EDS point scan analysis of the diffusion zone of the as-received WT-12 alloy after 2-weeks of bath immersion: a) Point scan locations and b) Corresponding point scan compositions.

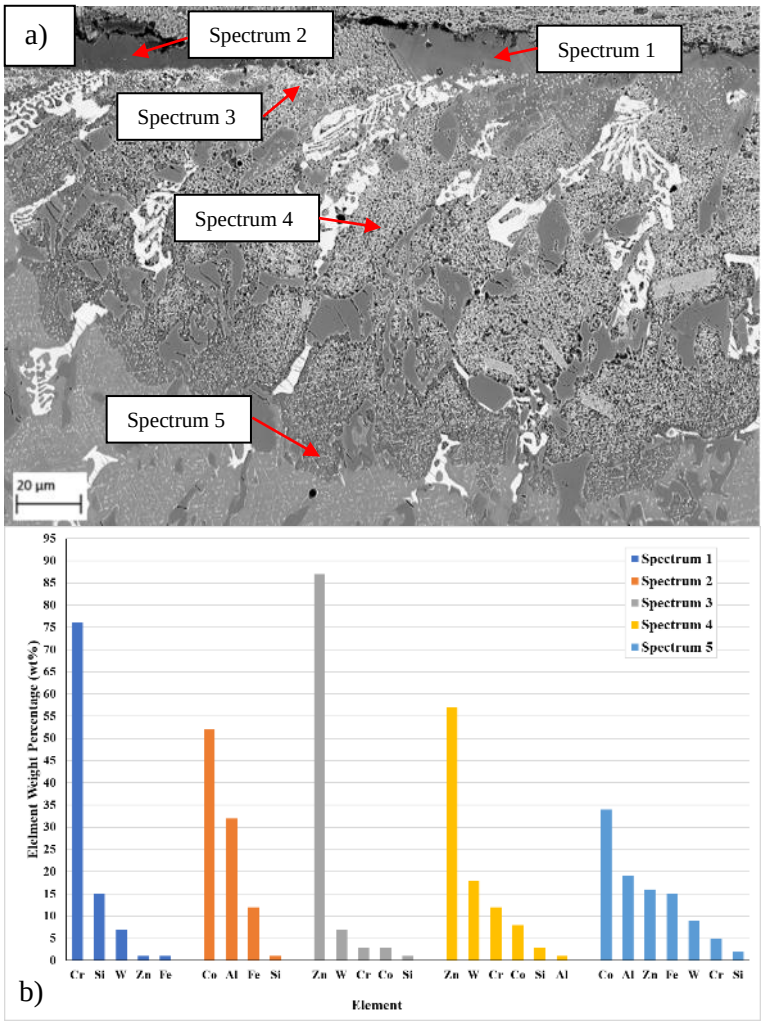

Figure 4.52 EDS point scan analysis of the diffusion zone of the as-received WT-12 alloy after 4-weeks of bath immersion: a) Point scan locations and b) Corresponding point scan compositions.

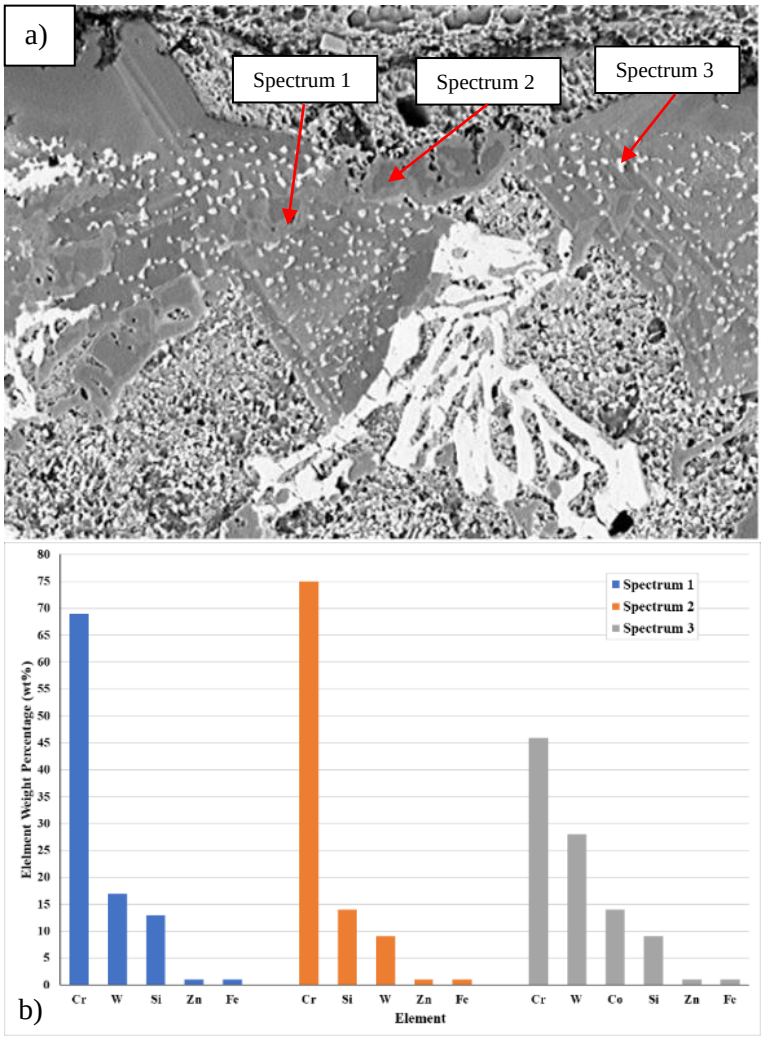

Figure 4.53: EDS point scan analysis of the diffusion zone of the as-received WT-12 alloy after 4-weeks of bath immersion: a) High magnification of chromium-rich regions in the diffusion layer and d) Corresponding point scan compositions.

4.4.4 Static Immersion Testing of As-received T-800

Figure 4.54 presents the T-800 Tribaloy after dip testing for 1-4-week periods. The alloy was observed to react with the molten zinc bath after the first week and the level of diffusion continued to increase with increased immersion time. Diffusion occurred beneath the surface of the samples in addition to isolated phases forming at the surface. Diffusion occurred mainly in the cobalt matrix whereas the primary Laves phase was more resistant to the diffusion process. The secondary Laves phases embedded in the eutectic regions of the microstructure were also more resistant to diffusion. Although the Laves phases were more resistant to the diffusion process, they were susceptible to cracking which often produced a path for molten metal ingress. Diffusion experienced in the eutectic regions of the microstructure often led to material detachment which was observed as early as the first week of testing and became more severe with

longer bath exposure. Figure 4.55 illustrates the average diffusion depths reached after each stage of testing. Diffusion was recorded to reach 20μm after the first week of testing which gradually increased to 35μm after the second week in the bath. Larger increases were observed after 3-4-weeks of testing where diffusion reached 60μm and 85μm, respectively.

The diffusion process is illustrated in Figure 4.56 using EDS elemental mapping of a sample that had been immersed in the molten bath for 2-weeks. The concentration maps highlight how the cobalt phase is vulnerable to diffusion where the process consequently results in the depletion of cobalt, molybdenum and chromium in these areas and the enrichment of zinc, iron and aluminium. In the early stages of dip testing (weeks 1 and 2) clear signs of diffusion are observed in the eutectic regions of the microstructure. By weeks 3 and 4, large areas of the diffusion layer, which had not detached from the surface, appeared to have transformed into an intermetallic phase. Point scan analysis was performed on samples dipped for 2 and 4-week periods to identify and make comparisons of the composition of the diffusion layer at specific locations and after different periods of time. Figure 4.57 and Figure 4.58 demonstrates the locations of individual point scans after each stage of dip testing and summarises the corresponding compositions. Analysis of an as-received T-800 sample identified that the eutectic region consists of two solid solution phases; a CoCr-rich phase that produced the majority of the matrix and a less frequent phase that is CoMo-rich. Figure 4.57 examines how the individual phases react to the diffusion process in the early stages of bath immersion. Spectrums 3 and 4 were performed on the eutectic CoCr solid solution phase. Spectrum 3 reveals that the region just below the surface has high levels of zinc (37wt.%), molybdenum (36wt.%) and aluminium (24wt.%) with low level of cobalt (2wt.%) and iron (1wt.%). At the diffusion front (Spectrum 4) the level of cobalt (24wt.%) and iron (11wt.%) increases and zinc (21wt.%) and molybdenum (11wt.%) concentrations decrease whereas the aluminium (22wt.%) content remains fairly consistent. This demonstrates that as aluminium and iron diffusion progresses into the bulk of the alloy, subsequent zinc diffusion occurs behind it. The low levels of cobalt at the surface suggests that cobalt diffuses out from the surface of the alloy. This corresponds to the identification of a CoAl phase (spectrum 1) at the surface which typically had a composition of 62wt.% cobalt, 34wt.% aluminium, 4wt.% zinc and 2wt.% iron. Spectrum 3 identified high levels of molybdenum at the surface of the alloy which suggests that molybdenum largely remains in the bulk of the alloy. However, discrete particles were observed at the surface (Spectrum 2) that were predominantly zinc (81wt.%) phases contained levels of molybdenum (4wt.%) and cobalt (3wt.%). This indicates that despite the elements increased resistance to the diffusion process, small levels of molybdenum diffuse out from the alloy to form phases at the surface. Spectrum 5 was performed on a eutectic CoMo solid solution phase that had experienced levels of diffusion.

Analysis detected high levels of molybdenum (41wt.%), zinc (30wt.%) and aluminium (26wt.%) with low levels of cobalt (2wt.%) and iron (1wt.%). The depletion of cobalt and chromium in this phase suggest that they have diffused out whereas the high level of molybdenum further demonstrate the element is more resistant to diffusion. Like tungsten in the CoCrW alloys, this may be due to the large atomic size of molybdenum atoms which impede its movement. At this stage of dip testing the primary Laves phase also exhibits signs of dissolution, primarily at the surface where the phase would have been exposed to the bath for the longest periods of time. Spectrum 6 indicates that the region is molybdenum-rich (37wt.%) but also contains high levels of zinc (22wt.%) and aluminium (18wt.%).

Examination of the diffusion layer after prolonged dip testing demonstrates the formation of several intermetallic phases. SEM analysis highlights these phases as lighter and darker regions within the diffusion layer. Spectrum 1 (Figure 4.58) demonstrates how the darker region is chromium-rich (52wt.%) with high levels of zinc (15wt.%), molybdenum (14wt.%), silicon (10wt.%) and aluminium (9wt.%) whereas the lighter region, Spectrum 2, is zinc-rich (41wt.%) with high levels of molybdenum (35wt.%) and aluminium (23wt.%). The diffusion front (Spectrum 3) becomes depleted in cobalt (29wt.%) and chromium (5wt.%) and enriched in aluminium (22wt.%), zinc (21w.t%) and iron (9wt.%). Analysis of the primary Laves phases indicates that the dissolution in this phase increases with prolonged bath exposure. Spectrum 4 indicates high levels of zinc (37wt.%) and aluminium (23wt.%) in a Laves phase. Only traces of cobalt and chromium were detected at this point of testing. The depletion in chromium content in both the solid solution phase and primary Laves would explain the formation of the chromium-rich phase observed to form in the diffusion layer.

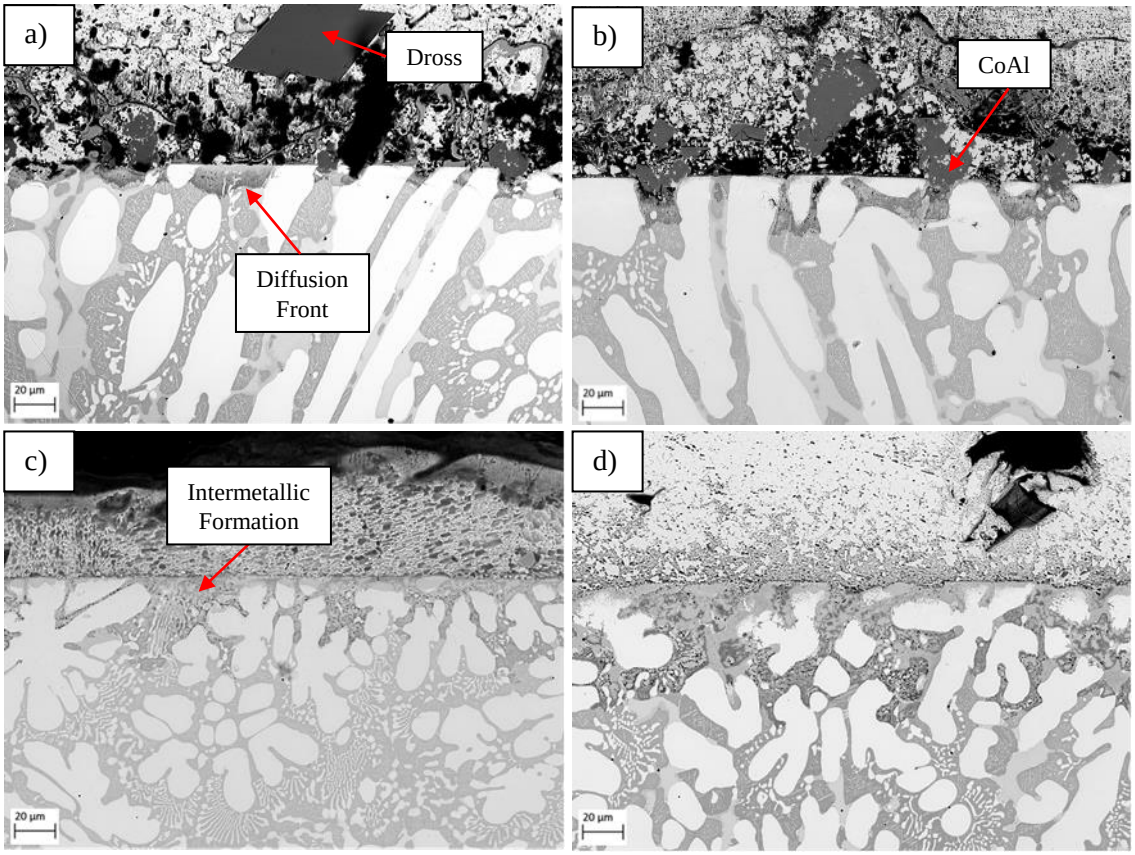

Figure 4.54: Surface condition of the as-received T-800 Tribaloy after 1-4-week dip testing in a molten zinc bath containing 0.35wt.% Al and saturated with Fe: a) Week 1, b) Week 2, c) Week 3 and d) Week 4.

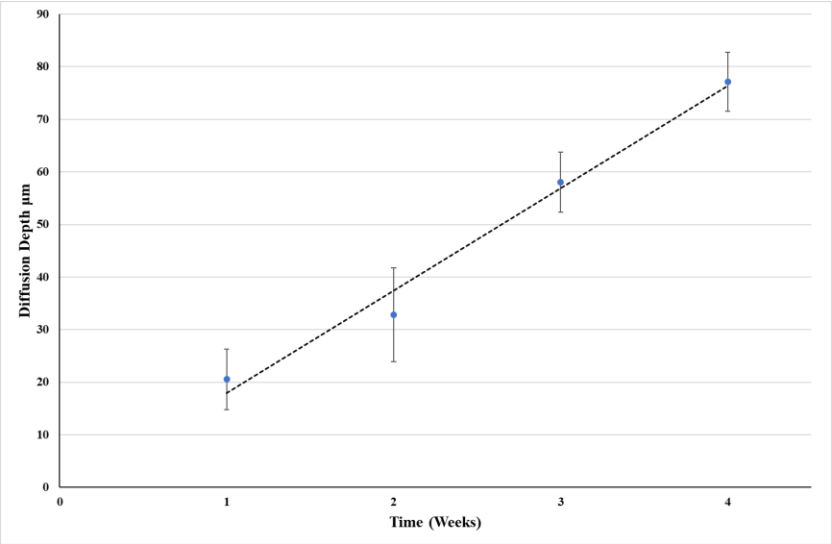

Figure 4.55: Average diffusion depth of the as-received T-800 Tribaloy after prolonged dip testing in a molten zinc bath containing 0.35wt.% Al and saturated with Fe.

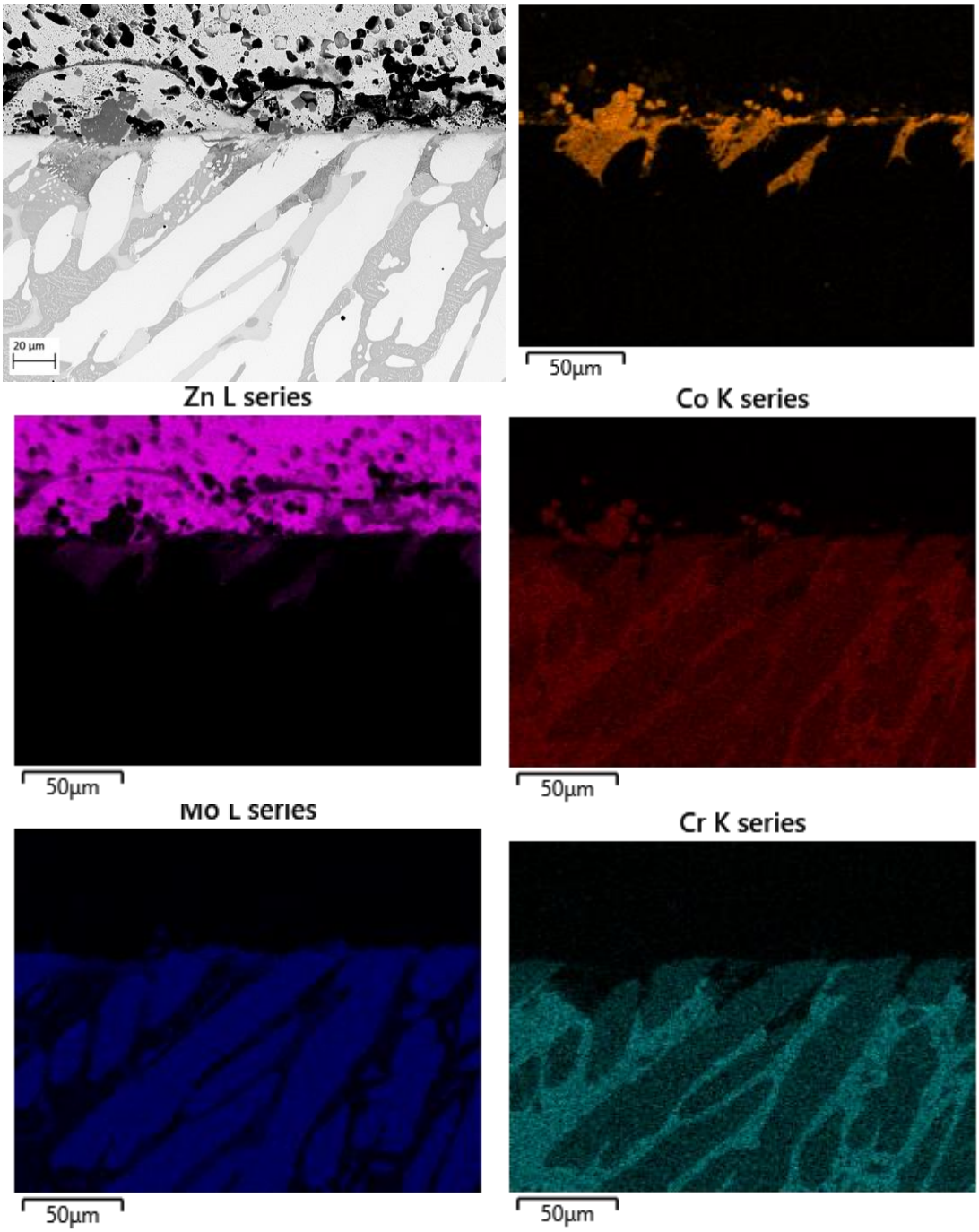
Al K series
20 µm
50µm
Zn L series
50µm
Co K series
50µm
Mo L series
50µm
Cr K series
50µm

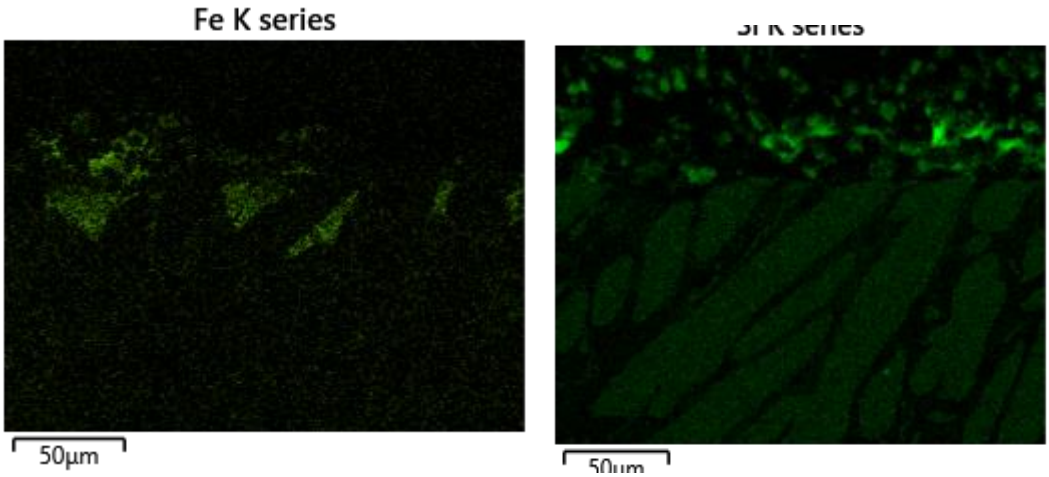

Figure 4.56: EDS elemental mapping of the as-received T-800 Tribaloy after 2 weeks of dip testing in a molten zinc bath containing 0.35wt.% Al and saturated with Fe.

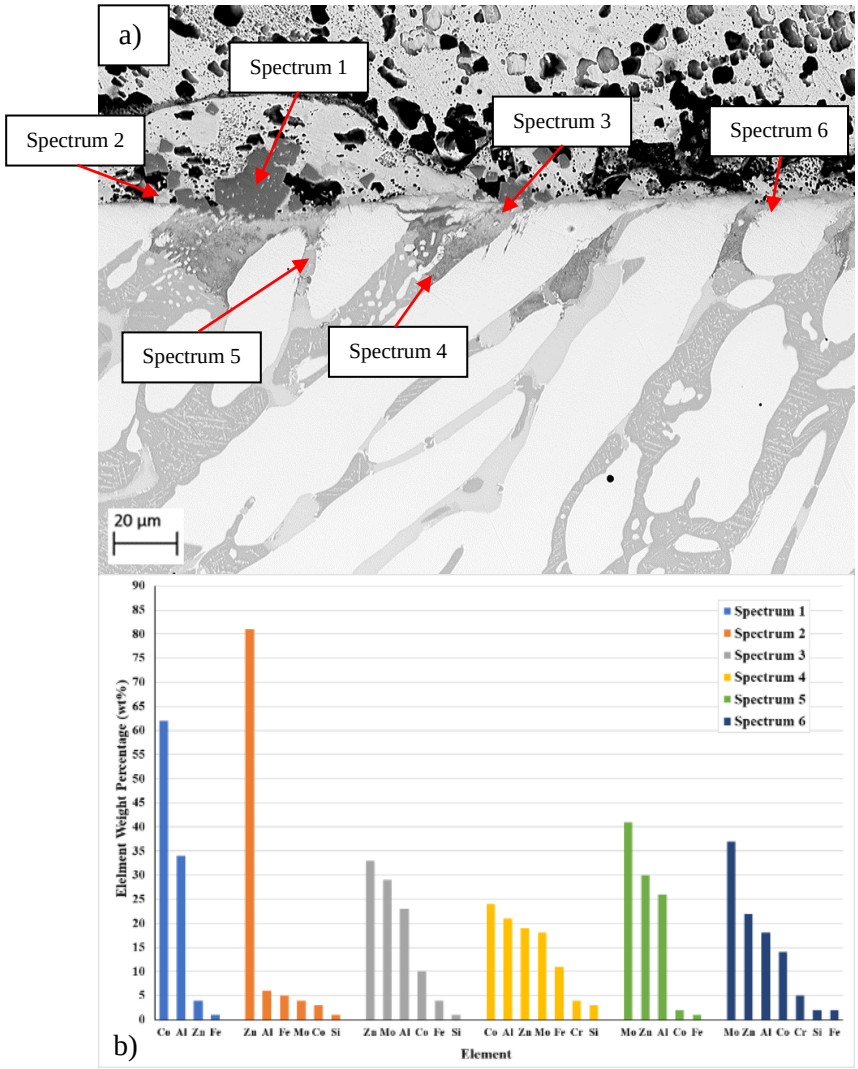

Figure 4.57: EDS point scan analysis of the diffusion zone of the as-received T-800 Tribaloy after 2-weeks of bath immersion: a) Point scan locations and b) Corresponding point scan compositions.

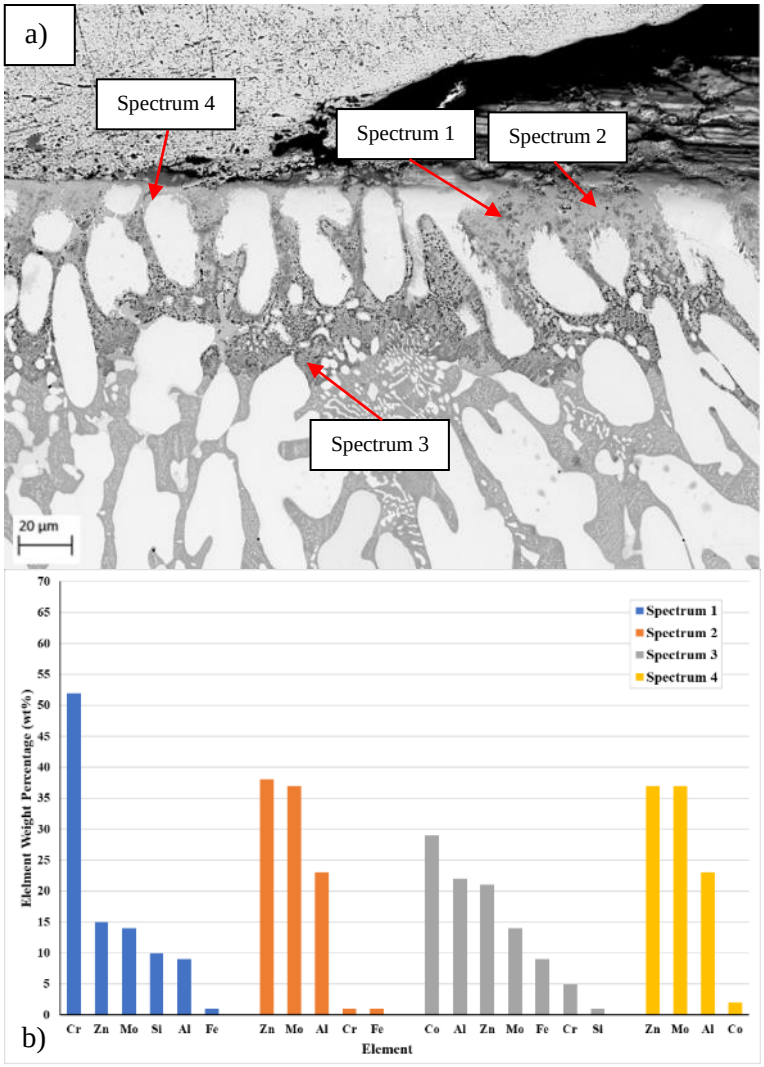

Figure 4.58: EDS point scan analysis of the diffusion zone of the as-received T-800 Tribaly after 4-weeks of bath immersion: a) Point scan locations and b) Corresponding point scan compositions.

4.5 Comparisons of the Chemical Reactivity of the As-received Alloys

The CoCrW and CoCrMo alloys were all observed to react with the aluminium containing molten zinc bath where diffusion layers beneath the surface occurred in addition to intermetallic phase formation at the surface. With each alloy the depth of the diffusion layer increased with prolonged dipping time. The diffusion process frequently resulted in the detachment of material at the surface, leaving a rough surface, where the level of detached material increased with prolonged dipping time. Detailed EDS analysis of the diffusion layer demonstrated that reactivity between the immersed material and the molten bath is an extremely complicated process where increased exposure to the bath resulted in a continuous phase evolution process as diffusion was also a continuous process. Although the composition of the diffusion layer after prolonged dip testing varied between each alloy, the initial stages of the diffusion process was very similar. For

each alloy, the cobalt matrix was susceptible to diffusion and was the preferred route for molten metal ingress. This is due to cobalt's strong affinity for aluminium. The formation of CoAl phases has been recorded in molten zinc baths containing as little as 0.015wt% aluminium. Therefore, it can be assumed that the diffusion process begins with the reaction of the cobalt matrix and the formation of CoAl phases and the subsequent diffusion of aluminium into the bulk of the alloy. As immersion time increased the diffusion process continued to progress into the bulk of the alloys creating a concentration gradient where the diffusion front contained higher levels of aluminium than at the surface. This process also indicates that the reaction with aluminium is the initial stages of the diffusion process. Iron also has a high affinity for aluminium, therefore the diffusion front contained high levels of iron. As aluminium diffusion progressed into the bulk of the alloy, zinc would then diffuse in behind the diffusion front to form various zinc-based intermetallic phases. This process is illustrated in

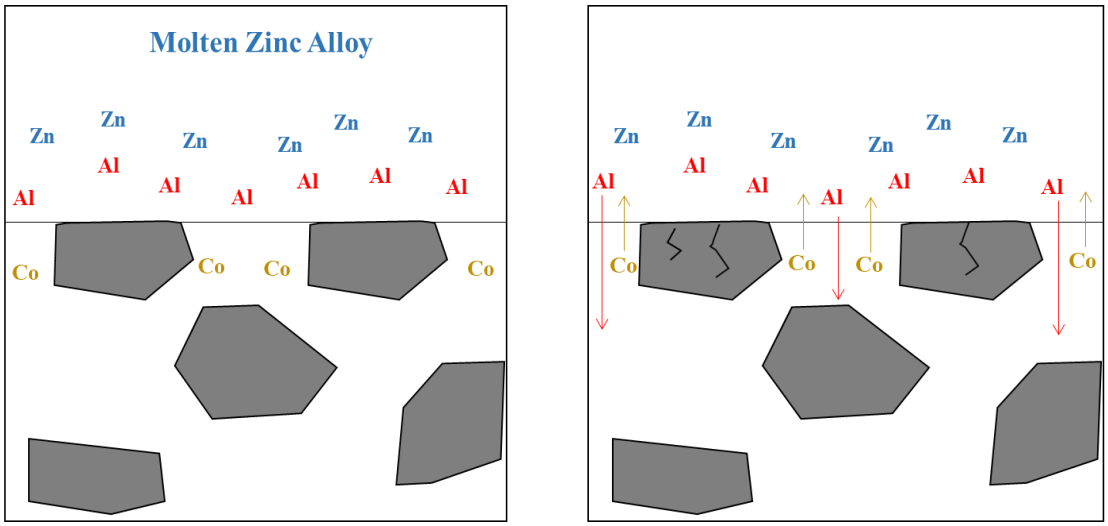

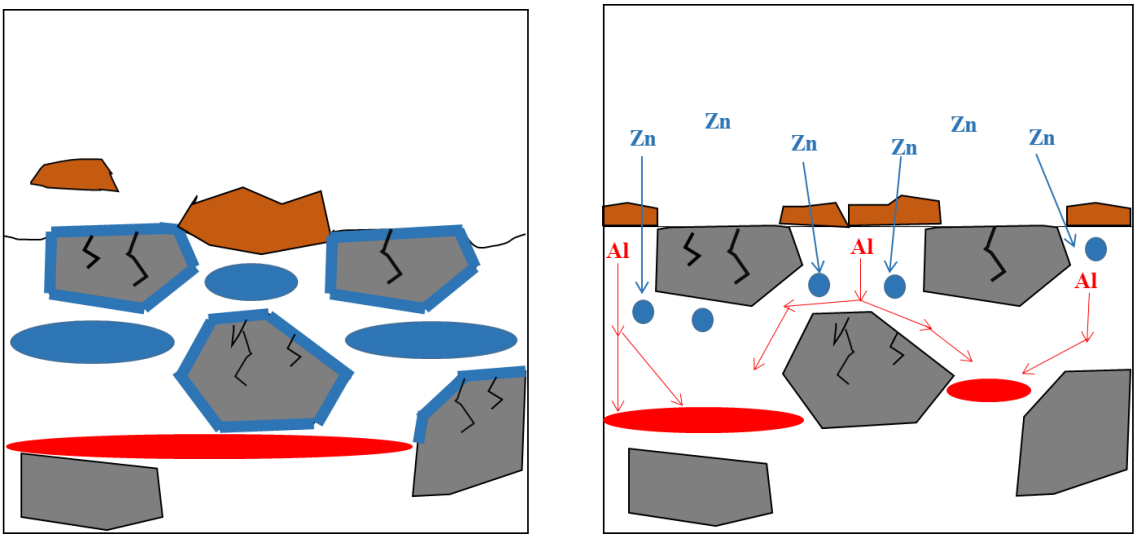

Figure 4.59 and Figure 4.60 which demonstrates the diffusion process experienced by the CoCrW and CoCrMo alloys, respectively. The dramatic depletion of cobalt in the reaction layer suggests that significant levels of the element are leached out from the alloy to form the CoAl phase or diffuse out into the bath. The diffusion process, experienced in the early stages of testing, is clearly illustrated in Figure 4.61 using an EDS line scan tool. The line scan includes the CoAl layer at the surface and the diffusion layer formed in the cobalt matrix. The individual element graphs demonstrate that; the CoAl layer at the surface contains high levels of cobalt, aluminium and iron, the diffusion front is aluminium and iron and rich, and that the diffusion layer (moving towards the surface) becomes gradually depleted in cobalt and enriched in zinc. At this stage of dip testing this trend was generally observed with each alloy, although diffusion depths and the concentration of certain elements varied between alloys depending on their chemistry.

The reactions became more complex and alloy specific after longer periods of bath immersion which can be related to their standard alloy compositions. The formation of a zinc-rich intermetallic phase with relatively high levels of chromium and tungsten was observed with the WT-6 alloy which dominated large areas of the diffusion layer. Within the diffusion layer, discrete tungsten-rich phases were observed to form. Chromium was observed to diffuse towards the surface of the alloy which resulted in a chromium and zinc-rich layer forming at the surface. Increased tungsten content of the WT-4 alloy resulted in the formation of a zinc and tungsten-rich intermetallic phase which formed as a result of the diffusion of cobalt and chromium from the matrix. A CrSi phase was also observed to form at the surface which became more frequent with prolonged testing which confirms that chromium was leached from the alloy. The reaction layer of the WT-12 was dominated by a zinc-rich intermetallic phase that contained high levels of tungsten and chromium. Chromium-rich regions were observed forming beneath the surface of the alloy which consisted of three distinct chromium-rich phases with varying amounts of

tungsten and silicon. Similar to the WT-4 alloy, a CrSi phase formed at the surface which increased in quantity with longer dip times. Prolonged exposure to the molten bath results in two distinct phases forming in the diffusion layer of the T-800 Tribaloy. One phase is chromium-rich with high levels of zinc, molybdenum, silicon and aluminium and the other phase is zinc-rich with high levels of molybdenum and aluminium. Discrete particles were seen to form on the surface which were predominately zinc phases but contained levels of molybdenum and cobalt indicating diffusion of molybdenum from the bulk of the alloy. Higher levels of tungsten in the CoCrW alloys and molybdenum in the CoCrMo alloy were retained in the diffusion layer suggesting they were more resistant to the diffusion process. This is most likely due to their large atomic radius which would have hindered diffusion.

The formation of a CoAl phase formed with each alloy after the initial stages of testing. With the CoCrW alloys the formation of this phase was continuous at the surface although the morphology of the phase varied. The formation of the CoAl phase was more isolated with the CoCrMo T-800 Tribaloy, forming single particles rather than a continuous layer. It was also often observed, particularly in the early stages of dip testing, that large dross particles would attach to the surface of the alloys. This dross particle has been identified as a Fe_2Al_5 phase [92,153]. The dross and the CoAl phases would frequently form a bond where the CoAl phase was observed to survive beneath the dross particle at the surface. The attachment of the CoAl and dross phases became less frequent with longer periods of bath immersion where the CoAl phase became smaller in size and appeared to detach from the surface. It was also recorded in the later stages of testing that the composition of the CoAl phase changed with the depletion of cobalt and aluminium. This suggest that the phase may form in the earlier stages of dip testing but then is subjected to diffusion with prolonged bath exposure. The detachment of phases from the surface may also be due to the surface of the samples transforming into a zinc-rich intermetallic phase. EDS analysis confirmed that the surface of the samples becomes predominantly zinc-based which would prevent the formation and attachment of the CoAl phases at the surface. It was also observed, with the CoCrW alloys, that the formation of the CoAl phase or attachment of the dross phase at the surface influenced the level of diffusion occurring beneath them. This is clearly demonstrated in Figure 4.62 which indicates how the formation of the CoAl phase at the surface reduced the diffusion depth beneath it. The regions below the surface either side of the CoAl phase appear to be in more advanced stages of diffusion. This suggests that the formation of the CoAl may delay the rate at which diffusion occurs. This theory coincides with the more significant increases in diffusion depths experienced after the third and fourth week of testing compared to the first and second week. It was observed that the attachment of the CoAl phase at the samples surface became less frequent after prolonged bath exposure. If the attachment of the CoAl phases

does slow down the diffusion process, then the detachment of these phases would result in increased levels of diffusion, as experienced in the diffusion measurements for these stages of testing.

The carbide phases of the WT-6 and WT-12 alloys and the Laves phases of the T-800 Tribaloy offered increased resistance to the diffusion process. However, in the later stages of testing all phases exhibited signs of dissolution. This was confirmed using EDS which detected less chromium, tungsten, and molybdenum, in the relevant carbide and Laves phases, in addition to the presence of zinc and aluminium. The eutectic region of the WT-4 alloy consists of a fine structure of chromium and tungsten carbides and CoCrW phase. Although the eutectic regions offered increased resistance to diffusion, diffusion of aluminium and zinc was observed to propagate through the CoCrW phase.

It was quickly established that the T-800 Tribaloy offered the best chemical resistance to the molten zinc bath. The microstructure of the alloy is dominated by a primary Laves phase which offered increased resistance to diffusion. As the Laves phase dominates the microstructure, the volume fraction of the cobalt matrix, which is more susceptible to diffusion, is reduced which subsequently reduced the amount of reaction phases forming at the surface. Comparing and ranking the performance of the CoCrW alloys in terms of their chemical resistance to molten zinc and aluminium diffusion presented a difficult task as the diffusion process was extremely complicated. The level of diffusion varied at different locations of the samples surface and diffusion varied significantly between the alloys, so direct comparisons could not easily be made. The average depth of the diffusion layer after each stage of testing was one method used to compare the chemical performance of each alloy. Figure 4.63 compares the average diffusion depths experienced by each alloy after each stage of dip testing. In addition to the T-800 Tribaloy experiencing decreased levels of phase formation at the surface of the samples via diffusion, the graph also indicates the T-800 samples experienced the lowest average diffusion depths after each stage of testing. Comparing the average diffusion depths for the CoCrW alloys indicates the WT-12 alloy experienced the lowest levels of diffusion in the early stages of testing (weeks 1 and 2) whereas the WT-6 and WT-4 alloys experienced similar and higher diffusion depths. More significant increases in diffusion depths were experienced after 3 and 4 weeks of testing with the WT-4 and WT-12 alloys which resulted in higher average diffusion depths compared to the WT-6 alloy. Increased diffusion depths experienced with the WT-4 and WT-12 alloys may have been influenced by the reduced area fraction of the cobalt matrix exposed to the bath which may have allowed for a stronger inward diffusion of bath species. This may explain why the WT-4 alloy experienced the greatest depths of diffusion despite the matrix containing higher levels of tungsten than the WT-6 and WT-12 alloys.

The results suggest the WT-6 alloy possesses better long-term chemical resistance to the molten zinc bath compared to the WT-4 and WT-12 alloys. However, the results become less straightforward when the alloys microstructures and the individual diffusion processes experienced by each alloy are looked at in more detail. It was highlighted that it was often difficult to establish the original surface of the WT-6 samples after longer bath exposure times. Measurements taken from a location beneath the original surface would not give a true reflection of the diffusion depth which would coincide with a shallower diffusion measurement. The microstructure of the WT-4 and WT-12 alloys consist of a higher area fraction of carbide phases, compared to the WT-6 alloy, which offer increased chemical resistance to the bath. Despite the WT-6 alloy experiencing shallower diffusion depths, the increased area fraction of the cobalt matrix resulted in larger areas of the alloys surface experiencing increased levels of diffusion and subsequent transformation of the matrix into zinc intermetallic phases. EDS analysis also recorded higher levels of zinc beneath the surface of the WT-6 alloy, compared to the WT-4 and WT-12 alloys which retained higher levels of alloying elements in the diffusion layer. This demonstrates that the WT-4 and WT-12 alloys experienced less inward diffusion of bath species. This is likely due higher levels of alloying elements retained in solid solution of the cast WT-4 and WT-12 alloys which would slow down the rate of diffusion.

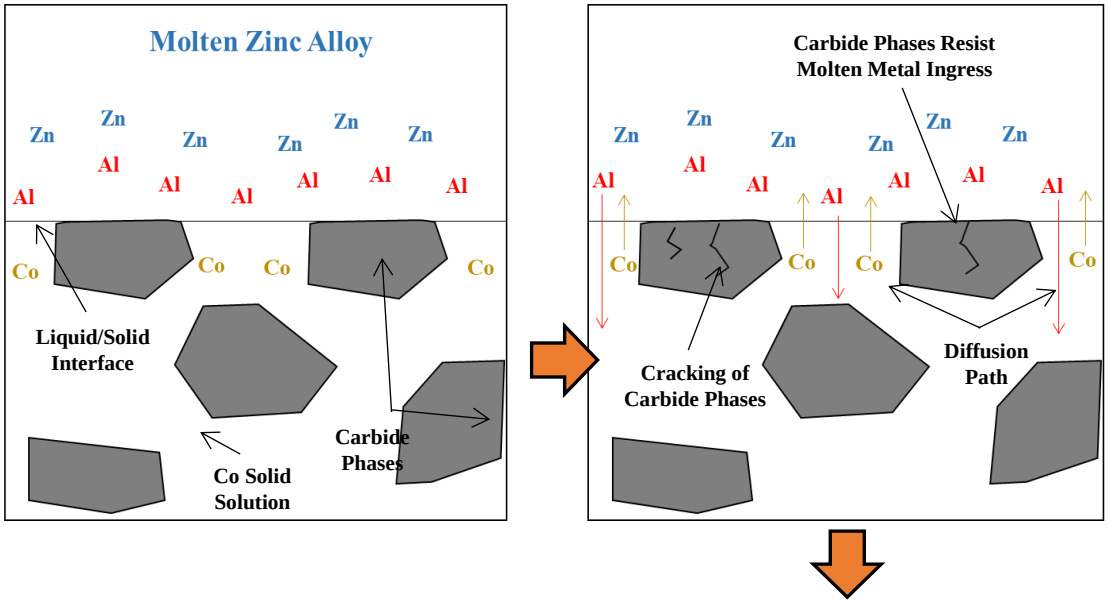

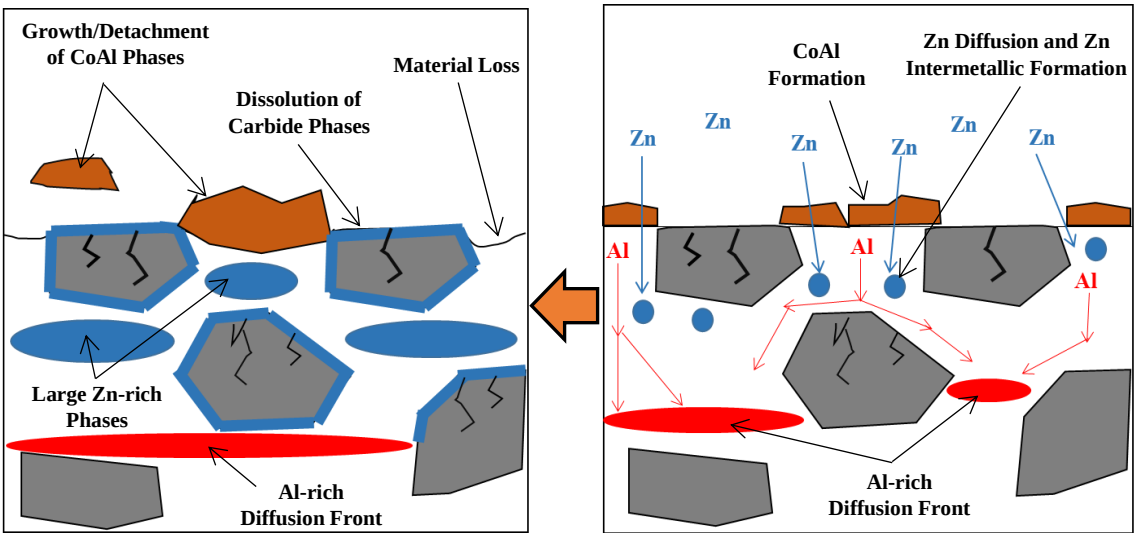

Figure 4.59: Schematic diagram illustrating the diffusion mechanisms within CoCrW alloys immersed in a molten bath containing 0.35wt.% Al and saturated with Fe.

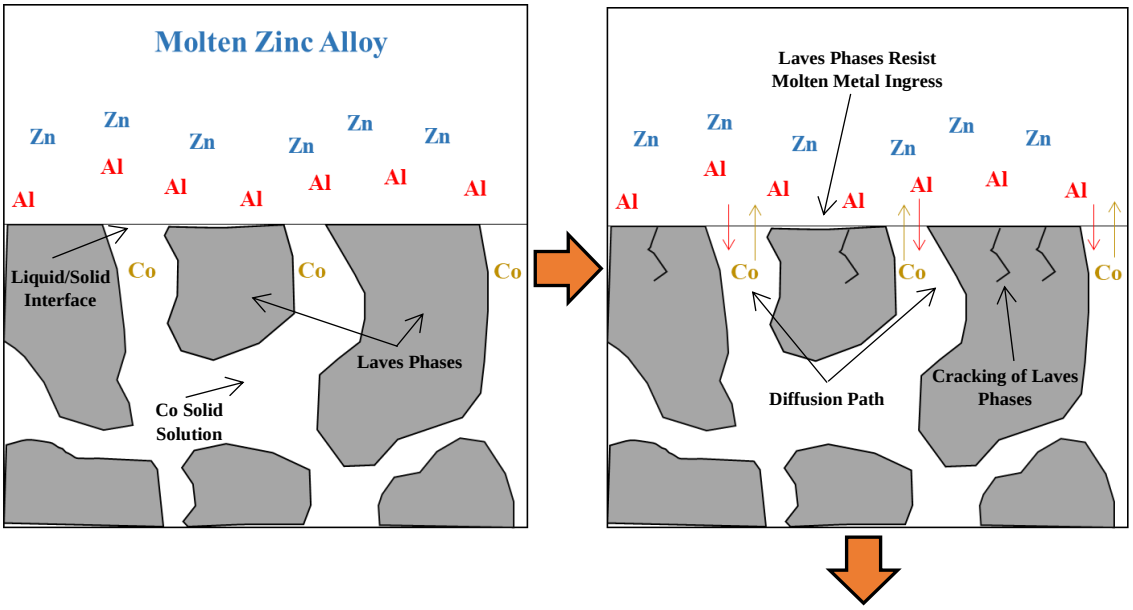

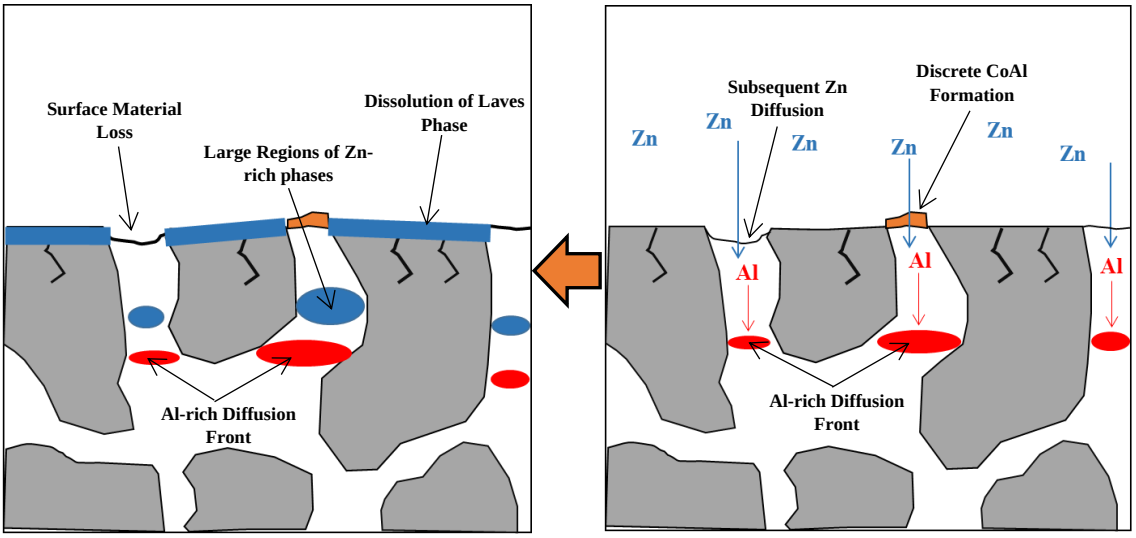

Figure 4.60: Schematic diagram illustrating the diffusion mechanisms within CoCrMo alloys immersed in a molten bath containing 0.35wt.% Al and saturated with Fe.

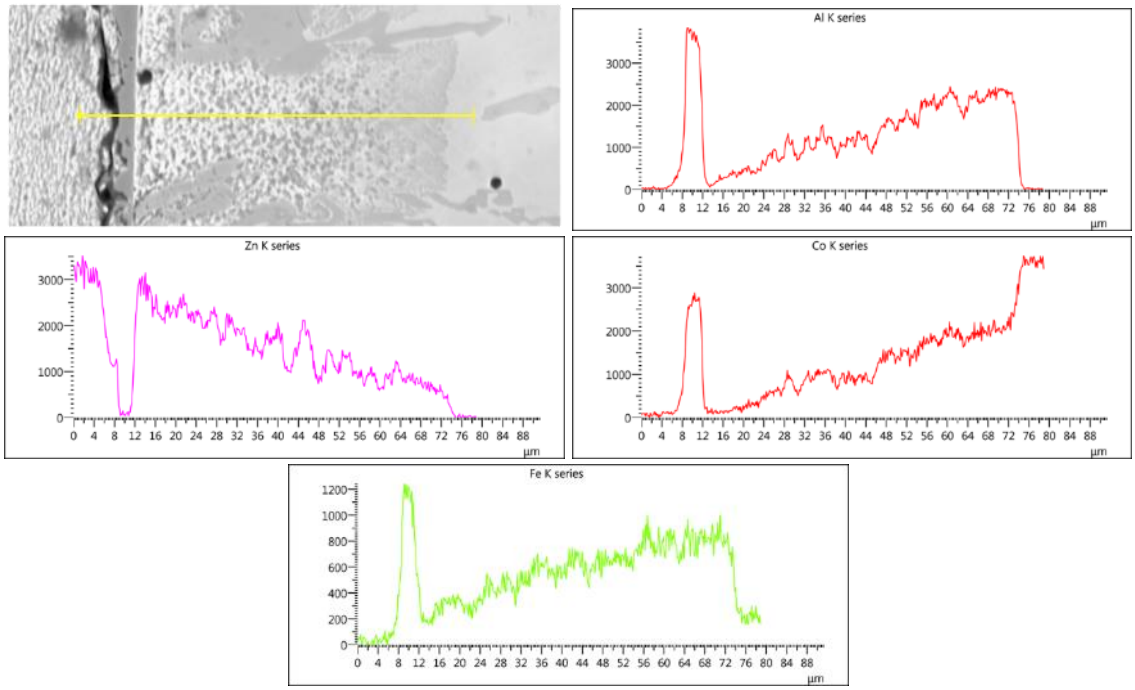

Figure 4.61: EDS line scan analysis of the diffusion zone of the as-received WT-6 alloy after 2-weeks of bath immersion illustrating the diffusion process.

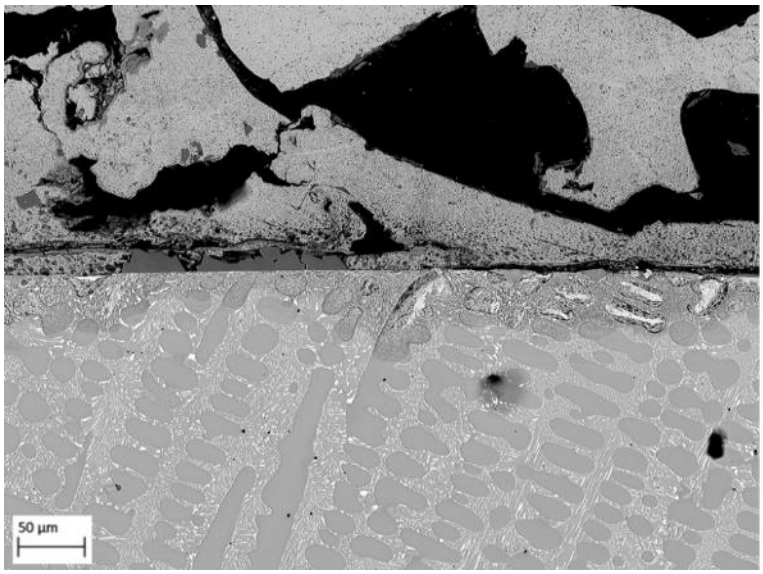

Figure 4.62: High magnification SEM analysis of the diffusion zone of the as-received WT-4 alloy after 3-weeks of bath immersion illustrating how CoAl formation restricts the diffusion process.

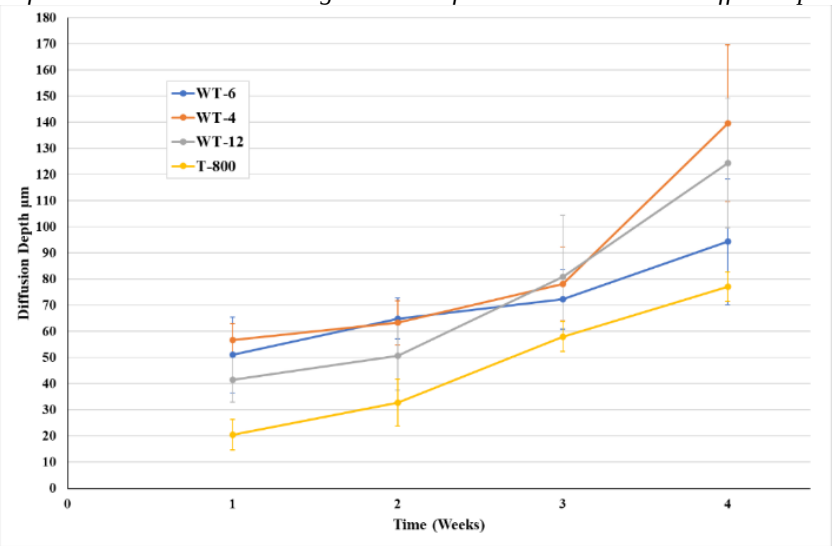

Figure 4.63: Average diffusion depth of the as-received alloys after prolonged dip testing in a molten zinc bath containing 0.35wt.% Al and saturated with Fe.

5 Microstructural and Mechanical Properties of Plasma Nitrided Samples

5.1 Surface Modification of the Plasma Nitrided Samples

Figure 5.1 and Figure 5.2 display the cross-sections of the microstructures of the treated alloys after plasma nitriding at different temperatures and for different periods of time, respectively. The images illustrate the formation of a relatively uniform diffusion layer beneath the surface of the treated samples that formed in the cobalt matrix of the microstructure. This was observed with each alloy and after each treatment. From the SEM analysis, a clear boundary can be observed between the formed surface layer and the substrate of the samples. However, the formation of the layer was less distinctive at lower treatment temperatures and shorter treatments times. Figure 5.1 demonstrates that treating the alloys at higher temperatures resulted in a thicker modified layer at the surface of the sample when compared to samples treated at lower temperatures. Differences in layer thickness were less distinctive with samples treated at the same temperature for different periods of time, as shown in Figure 5.2.

Analysis revealed how diffusion occurred in the cobalt matrix of each alloy whereas the carbide phases appear to resist and impede the diffusion process. This is identified in Figure 5.1c and Figure 5.2e where the depth of the diffusion layer is reduced due to the presence of the carbide phases at the surface. With the WT-4 samples (Figure 5.1a and b and Figure 5.2a and b) diffusion was observed within the eutectic regions of the microstructure but the depth of diffusion were shallower compared to diffusion experienced in the matrix. This is due to the carbide phases within the eutectic regions restricting the diffusion process. However, some diffusion was experienced in the cobalt-rich phase within the structure, as highlighted in Figure 5.1b and Figure 5.2b.

The diffusion process often resulted in the cracking of carbide and Laves phases near the surface of the samples, which was observed after each heat treatment. The increase in material hardness experienced after the plasma nitriding process is due to the diffusion of nitrogen atoms that occupy interstitial sites within the crystal lattice of the parent metal/alloy, which results in lattice expansion and an increase in resistance to dislocation movement. Therefore, cracking of the carbide and Laves phases, which are brittle by nature, is likely due to the introduction of internal stresses caused by nitrogen diffusion into the crystal structure of the treated alloys.

In addition to the formation of a diffusion layer beneath the surface of the alloys, the heat treatment often resulted in the formation of a very thin surface layer and increased surface roughness, which was more noticeable after higher treatment temperatures and longer treatment times.

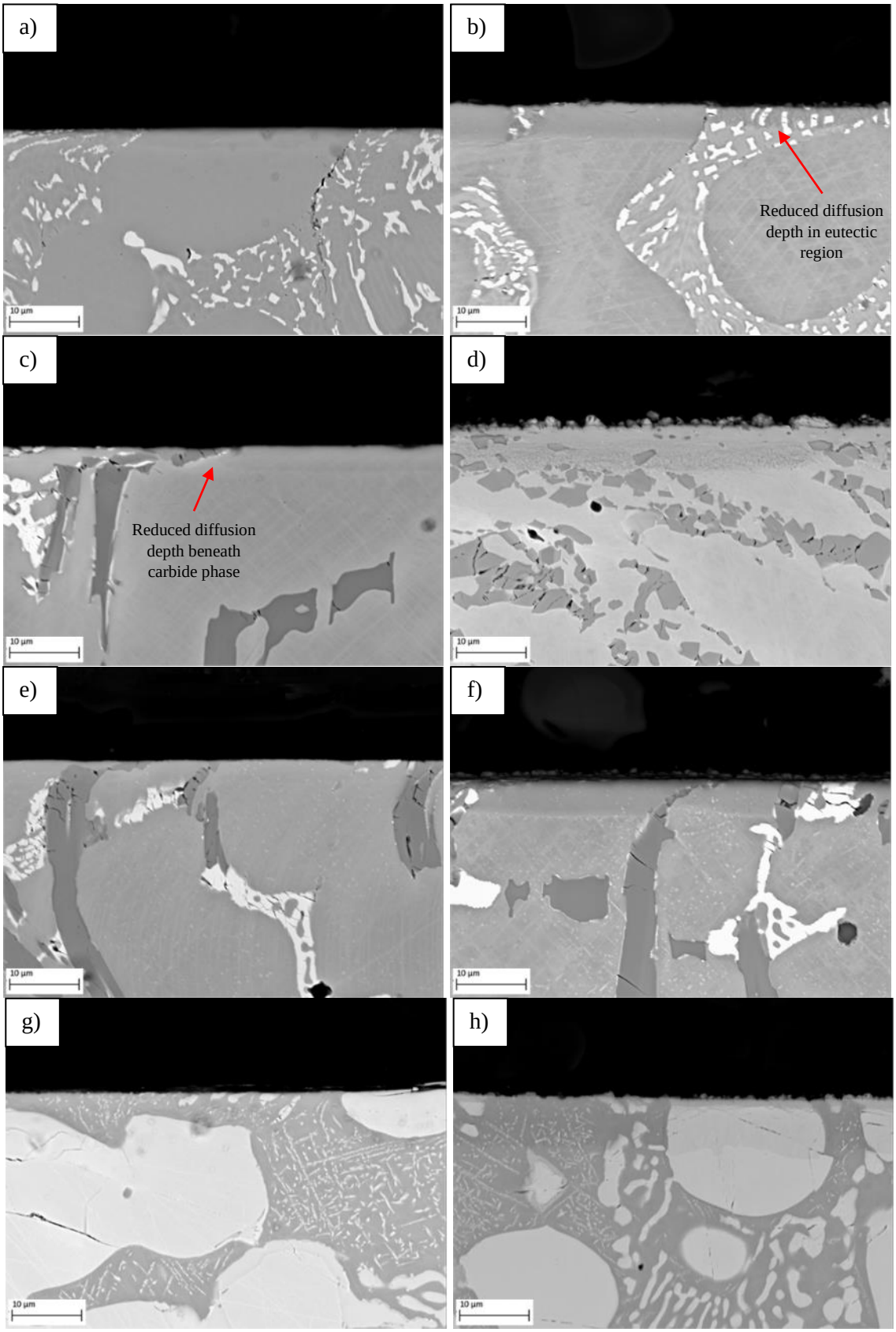

Figure 5.1: SEM analysis of samples plasma treated for 15 hours at different temperatures: a) WT-4/400℃, b) WT-4/550℃, c) WT-6/400℃, d) WT-6/550℃, e) WT-12/400℃, f) WT-12/550℃, g) T-800/400℃ and h) T-800/550℃.

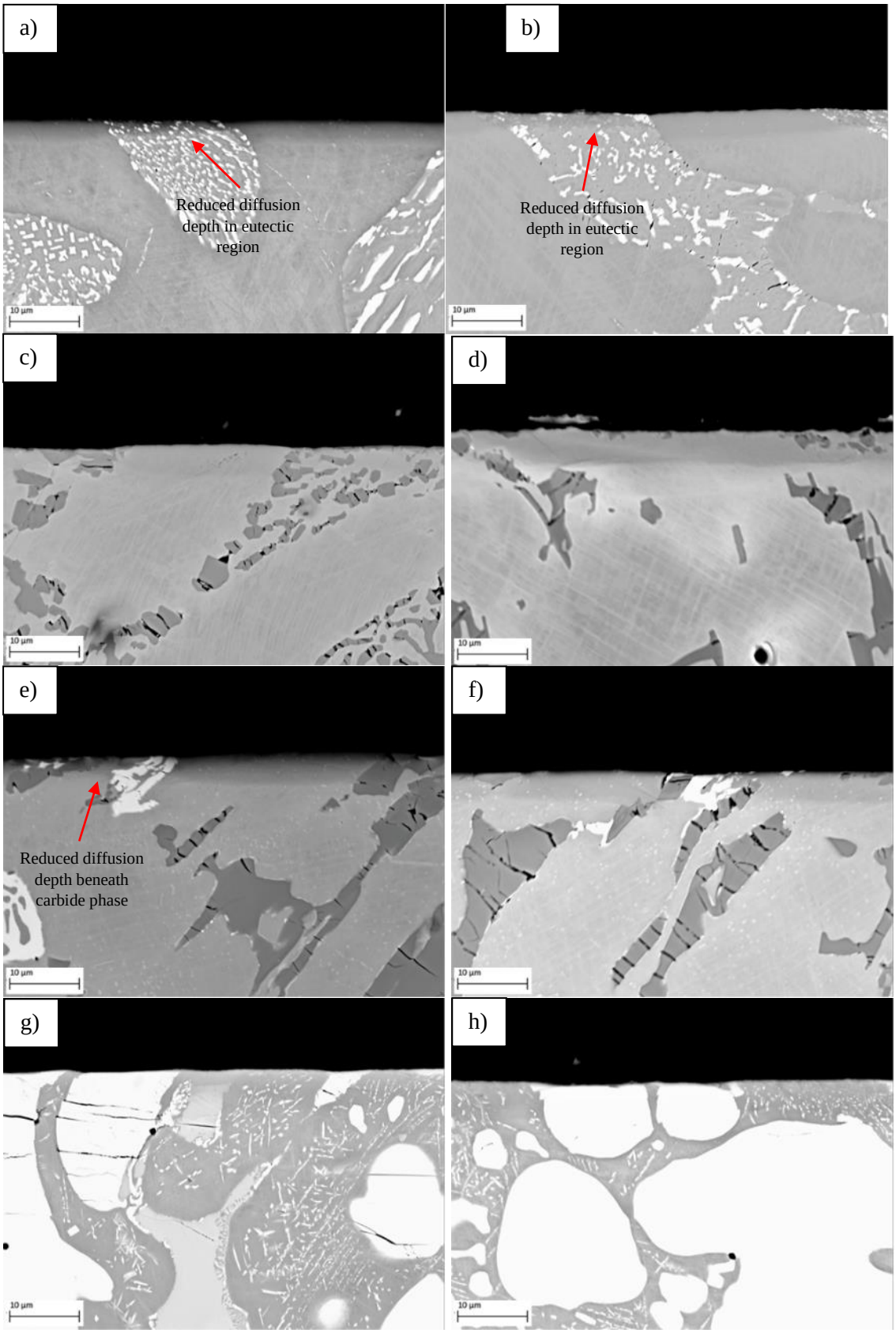

Figure 5.2: SEM analysis of samples plasma treated at 475°C for different periods of time: a) WT-4/10h, b) WT-4/20h, c) WT-6/10h, d) WT-6/20h, e) WT-12/10h, f) WT-12/20h, g) T-800/10h and h) T-800/20h.

5.2 Compositional Analysis of the Modified Surface Layer

5.2.1 Plasma Treated WT-4

EDS analysis of the treated samples confirmed the diffusion of nitrogen into the surface of the WT-4 alloys after each heat treatment. EDS maps are shown in Figure 5.3, which display samples after a 15-hour plasma nitride treatment at 400°C and 550°C, respectively. Comparing the maps illustrates a clear contrast in the nitrogen diffusion layer where greater depths were reached with samples treated at higher temperatures. In addition to increased diffusion depth, nitrogen concentration also appeared to increase. This trend was also observed with samples treated for longer periods of time. EDS point scan analysis of the modified surface layer confirmed this. Highs of around 12wt.% nitrogen content were detected at the surface of the samples treated at 550°C for 15-hours and for 20-hours at 475°C. It was found that nitrogen concentration was greatest at the surface for these samples which then, moving into the bulk of the alloy, gradually decreased for a short distance before rapidly decreasing as the substrate was approached. This is demonstrated in Figure 5.4 which displays the composition of the diffusion layer at different regions from the alloys surface. By contrast, below 3wt.% nitrogen was detected in the surface of the sample treated at 400°C for 15-hours and around 6wt.% nitrogen content was detected in the sample treated for 10-hours at 475°C. The sample treated at 400°C for 15-hours experienced a rapid decrease in nitrogen concentration moving into the bulk of the alloy whereas the decrease in concentration with the sample treated for 10-hours at 475°C was more gradual. A similar correlation was recorded implementing normalised data using GDOES analysis. Levels of nitrogen were detected for longer periods of time with the samples treated at a higher temperature and for longer periods of time, as shown in Figure 5.5b and Figure 5.5d, respectively. This represents a thicker diffusion layer at the samples surface. Nitrogen was detected for shorter periods of time with the samples treated at lower temperatures and for shorter times (Figure 5.5a and Figure 5.5c) which correlates to a thinner diffusion layer.

In addition to the diffusion of nitrogen, EDS and GDOES analysis identified an increase in iron concentration at the surface of the treated samples where increased iron content was detected with samples treated at higher temperatures and after longer treatment times. Iron concentration was greatest at the surface of the samples which then quickly decreased moving into the bulk of the alloy. This is demonstrated comparing Figure 5.3c and Figure 5.3g where greater concentrations of iron were detected with the sample treated at a higher temperature. Iron detection displayed in Figure 5.5 correlates to the depth of iron diffusion where iron detected for longer GDOES analysis times corresponds to a greater diffusion depth.

In addition to the formation of the nitride diffusion layer, SEM analysis identified the formation of thin layer at the surface of the samples where the composition was found to vary at different locations. Figure 5.6 illustrates point scan locations and the correlating compositions. Spectrum 1 illustrates the general composition of the layer which consisted mainly of cobalt with high levels of chromium, nitrogen, iron, and levels of oxygen. Point scan analysis also identified particles that contained high levels of iron and oxygen (Spectrum 2) and particles that were contained high levels of chromium and oxygen (Spectrum 3). This would suggest that the samples experienced oxidation during treatment. Comparing the EDS maps (Figure 5.3d and Figure 5.3h) suggests increased oxidation was experienced with the sample treated at a higher temperature.

The eutectic region of the alloy's microstructure was observed to impede the diffusion of nitrogen where diffusion depth was shallower in comparison to the matrix. It was observed that the chromium and tungsten carbide phases resisted the diffusion process, but nitrogen was able to diffuse into the cobalt-rich solid solution phase found in the eutectic region. Although nitrogen diffusion depth was limited in these areas, elevated levels of nitrogen concentration was often recorded.

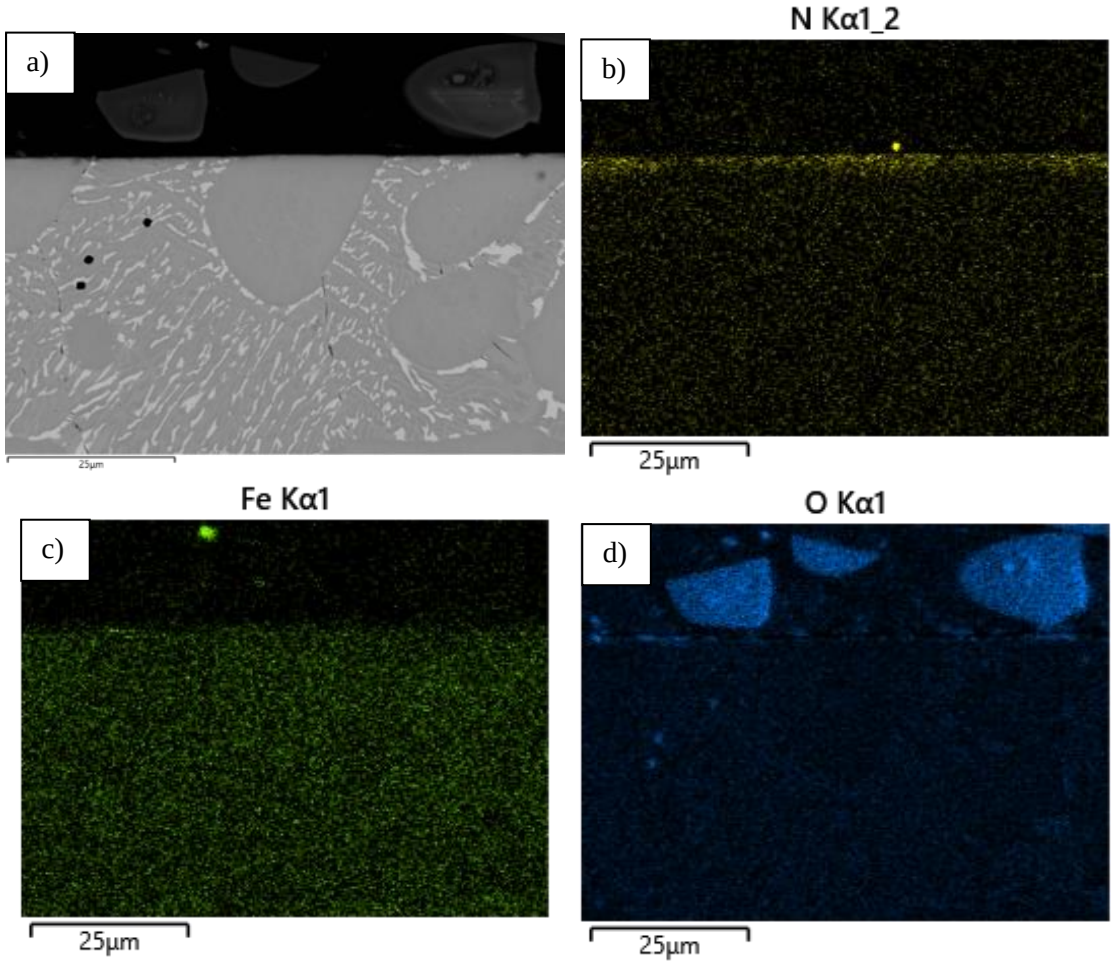

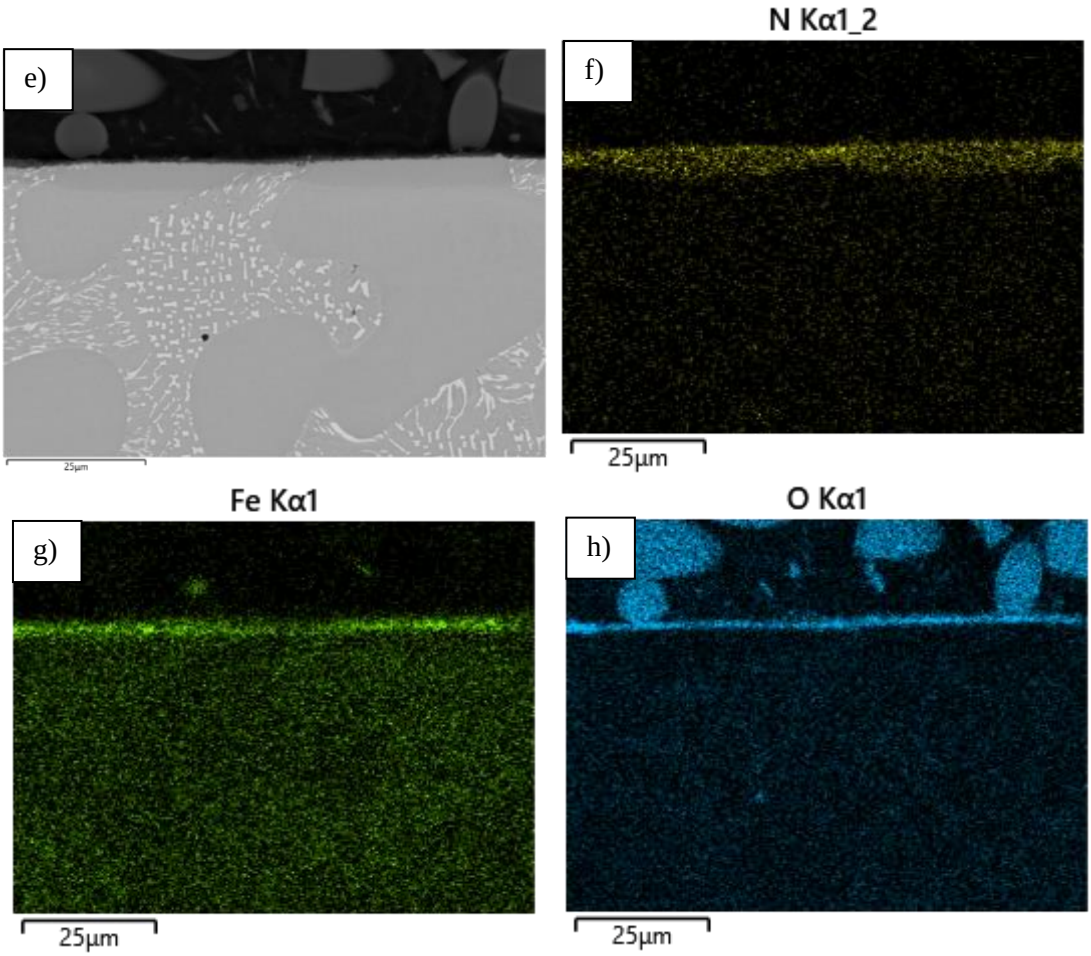

Figure 5.3: SEM and EDS analysis of WT-4 samples treated at 400°C and 550°C for 15-hours illustrating surface diffusion: a) SEM image of sample treated at 400°C, b) Corresponding nitrogen EDS map, c) Corresponding iron EDS map, d) Corresponding oxygen EDS map, e) SEM image of sample treated at 550°C, f) Corresponding nitrogen EDS map, g) Corresponding nitrogen EDS map and h) Corresponding oxygen EDS map.

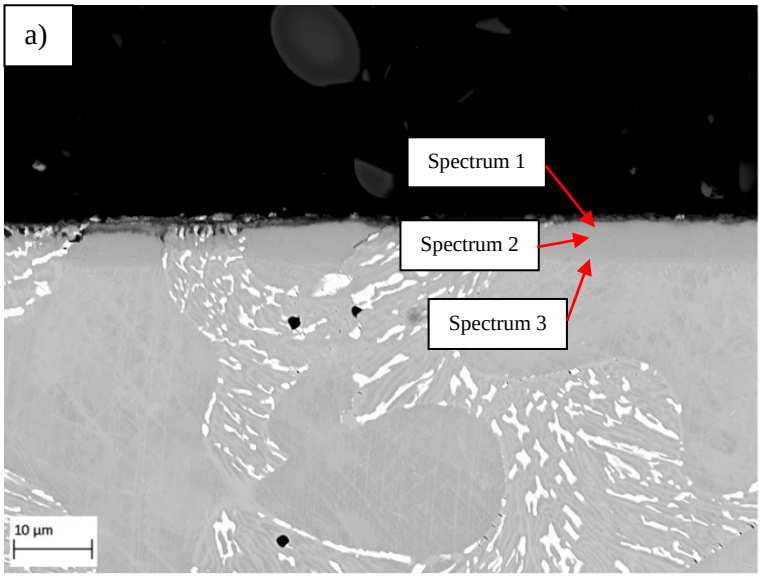

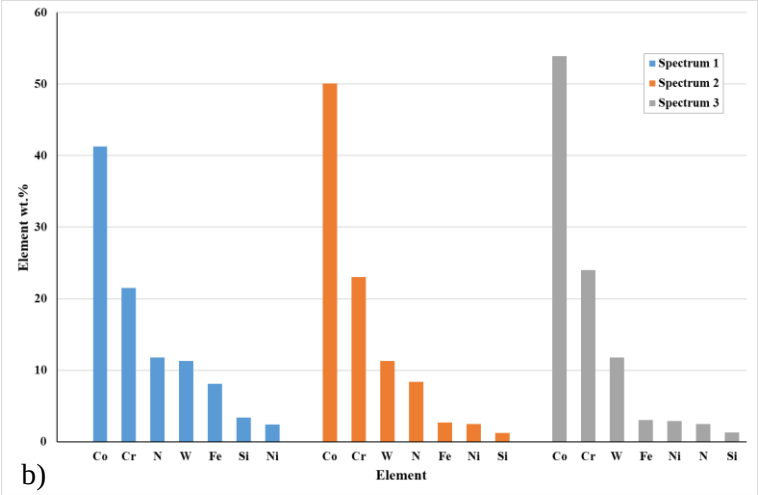

Figure 5.4: EDS point scan analysis of nitrogen-rich diffusion layer at the surface of a WT-4 sample after nitriding at 550ºC for 15-hours: a) Point scan locations and b) Corresponding point scan compositions.

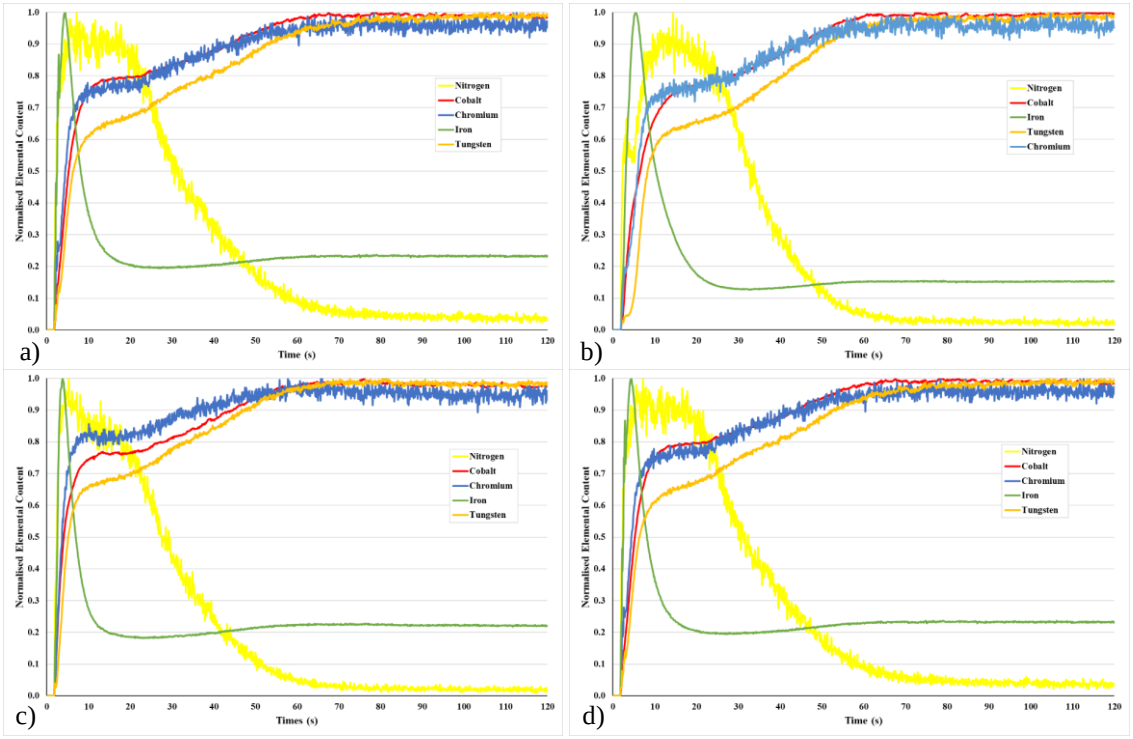

Figure 5.5: Normalised elemental content for treated WT-4 samples after various plasma nitride heat treatments using GDOES analysis: a) 15-hours at 400°C, b) 15-hours at 550°C, c) 475°C for 10-hours and d) 475°C for 20-hours.

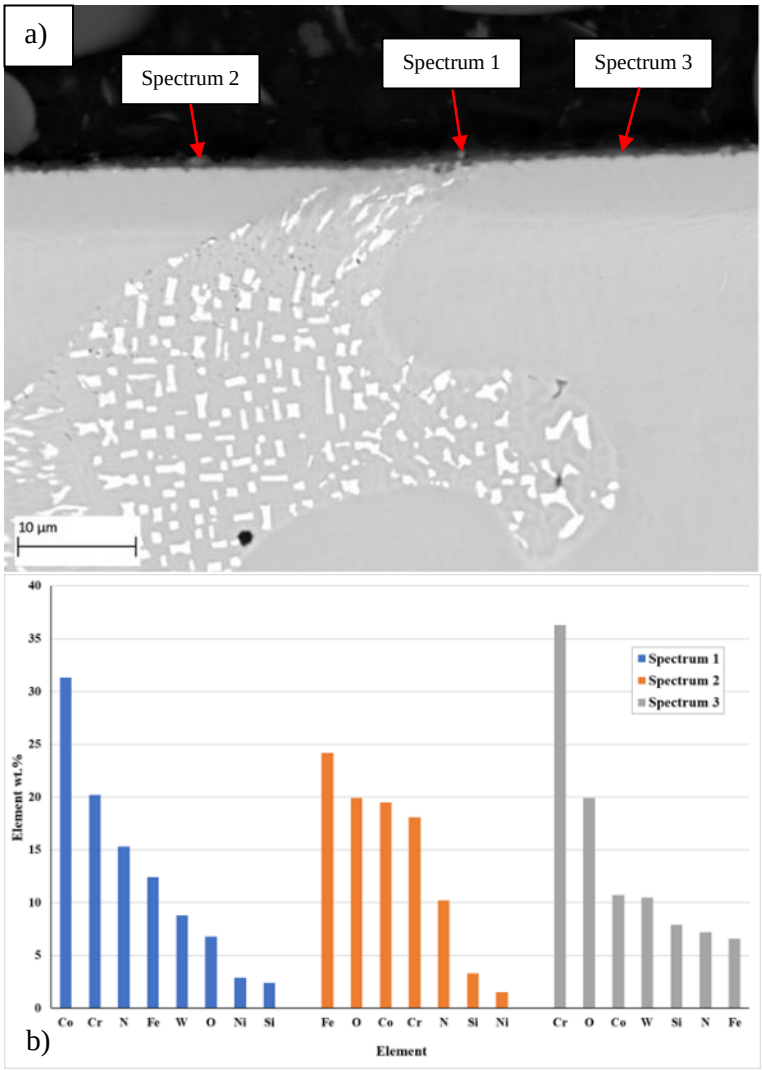

Figure 5.6: EDS point scan analysis phase formation at the surface of a WT-4 sample after nitriding at 550ºC for 15-hours: a) Point scan locations and b) Corresponding point scan compositions.

5.2.2 Plasma Treated WT-6

SEM analysis of the treated WT-6 samples identified the diffusion of nitrogen into the bulk of the alloy after each heat treatment where increased diffusion depths and nitrogen concentrations were experienced with samples treated at higher temperatures and for longer treatment times. This is demonstrated in Figure 5.7 which compares EDS data of samples treated at 400°C and 550°C for 15-hours. In addition to increased levels of nitrogen diffusion, the elemental maps also highlight increased levels of iron diffusion at the surface of the samples after increased treatment temperature and time. The carbide phases within the microstructure were observed to resist the diffusion of nitrogen and acted to impede the depth of diffusion. The maps also reveal clears signs of oxidation along the surface of the samples.

EDS point scan analysis performed on the diffusion layer beneath the surface of the treated samples identified differences in nitrogen concentrations between samples treated for different times and at different temperatures. Figure 5.8 displays the sample treated at 550°C for 15-hours and illustrates the change in composition of the diffusion layer moving into the bulk of the alloy. It was found that around 8wt.% nitrogen has diffused into the surface of the sample treated at 550°C for 15-hours. Nitrogen concentration remained at a similar concentration for several microns before gradually decreasing until the substrate boundary was reached. Lower levels of nitrogen diffusion were experienced as the treatment temperature was reduced. The sample treated at 400°C experienced below 4wt.% nitrogen diffusion at the surface where nitrogen levels quickly decreased moving into the bulk of the alloy. High levels of nitrogen were identified with the sample treated for 20-hours at 475°C where 10wt.% nitrogen content was measured in the regions near the surface. The concentration quickly decreased to around 8wt.% where it remained consistent for several microns before gradually decreasing moving into the bulk of the alloy. Decreasing the treatment time resulted in reduction in the level of nitrogen diffusion. The sample treated for 10-hours at 475°C experienced below 5wt.% nitrogen diffusion at the surface before gradually decreasing to the standard composition of the matrix phase moving into the bulk of the material. Correlating data was observed using normalised GDOES data (Figure 5.9) where nitrogen was detected for longer periods of time, representing a thicker diffusion layer, with the samples treated at higher temperatures and for longer times.

A thin layer was observed at the surface of the samples after the plasma treatments. A sample treated at 550°C for 15-hours is displayed in Figure 5.10 which demonstrates the composition of the surface layer at different locations. Analysis identified the layer was mainly cobalt based which contained varying levels of chromium, iron, nitrogen, and oxygen. Isolated particles that contained significantly higher levels of cobalt and iron were also identified. The detection of oxygen suggests that the samples experienced levels of oxidation during treatment.

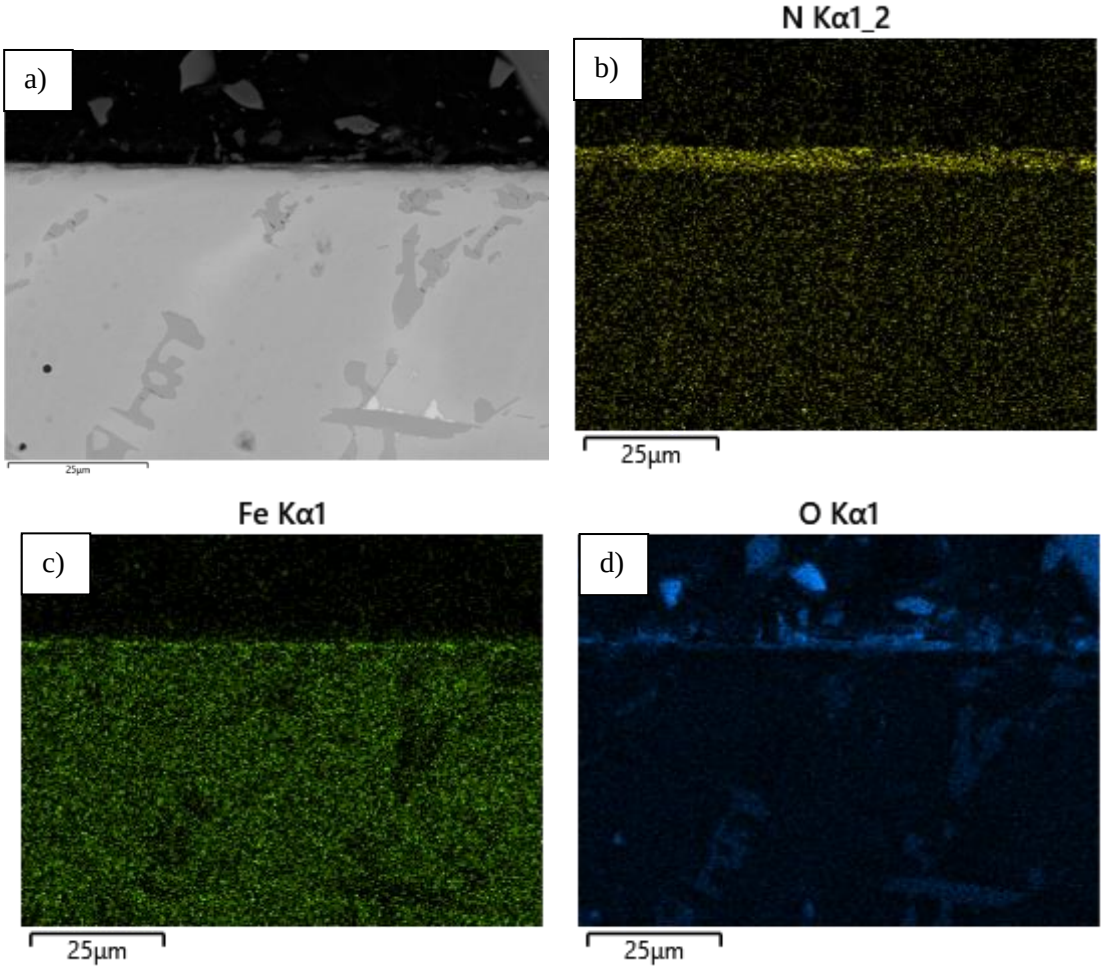
a)
b)
N Kα1_2
25µm
c)
Fe Kα1
25µm
d)
O Kα1
25µm

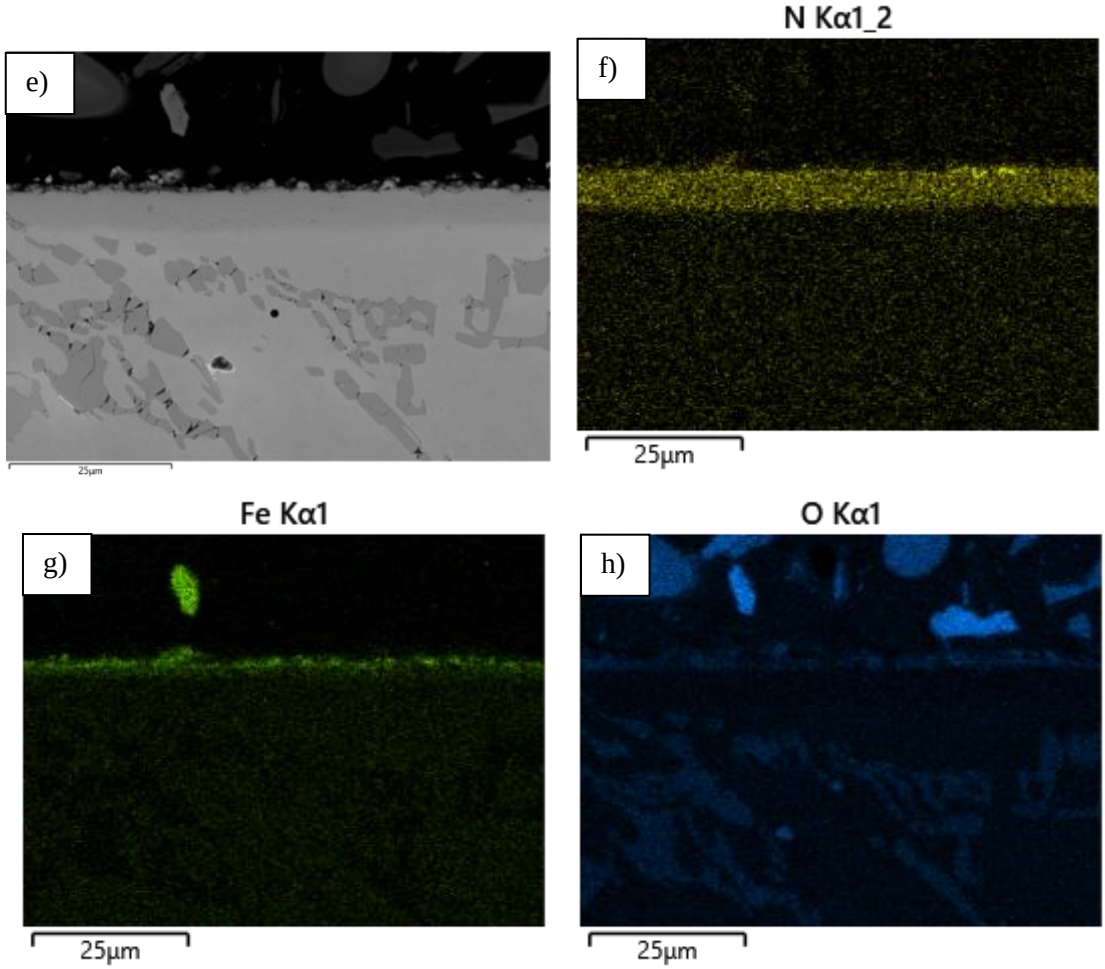

Figure 5.7: SEM and EDS analysis of WT-6 samples treated at 400°C and 550°C for 15-hours illustrating surface diffusion: a) SEM image of sample treated at 400°C, b) Corresponding nitrogen EDS map, c) Corresponding iron EDS map, d) Corresponding oxygen EDS map, e) SEM image of sample treated at 550°C, f) Corresponding nitrogen EDS map, g) Corresponding iron EDS map and h) Corresponding oxygen EDS map.

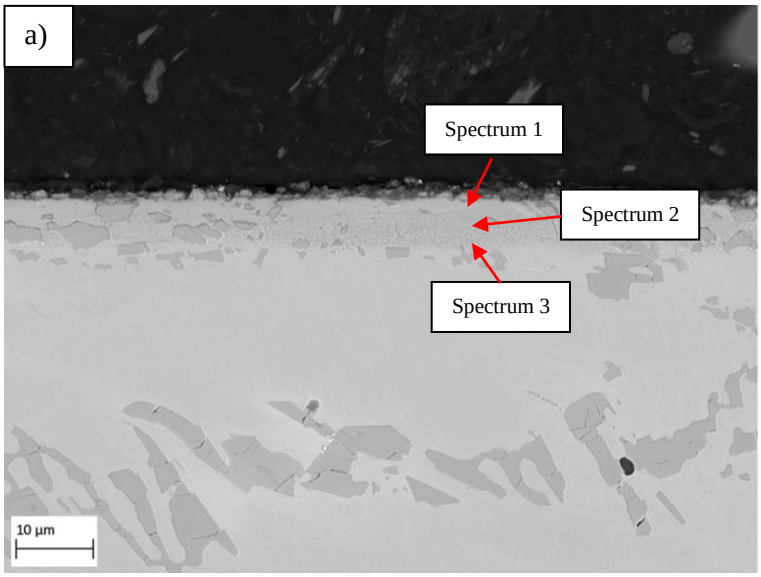

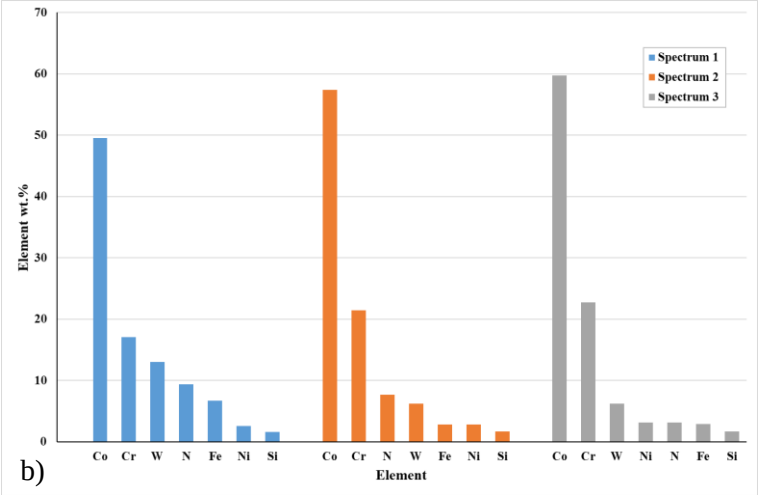

Figure 5.8: EDS point scan analysis of nitrogen-rich diffusion layer at the surface of a WT-6 sample after nitriding at 550ºC for 15-hours: a) Point scan locations and b) Corresponding point scan compositions.

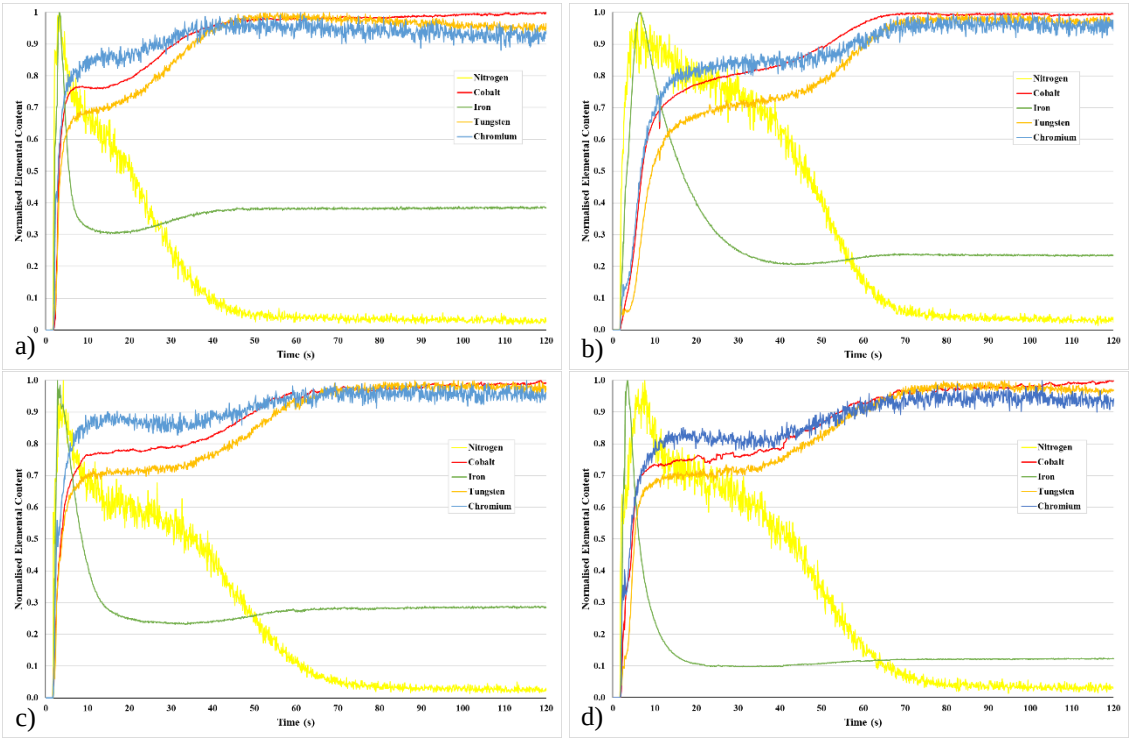

Figure 5.9: Normalised elemental content for treated WT-6 samples after various plasma nitride heat treatments using GDOES analysis: a) 15-hours at 400°C, b) 15-hours at 550°C, c) 475°C for 10-hours and d) 475°C for 20-hours.

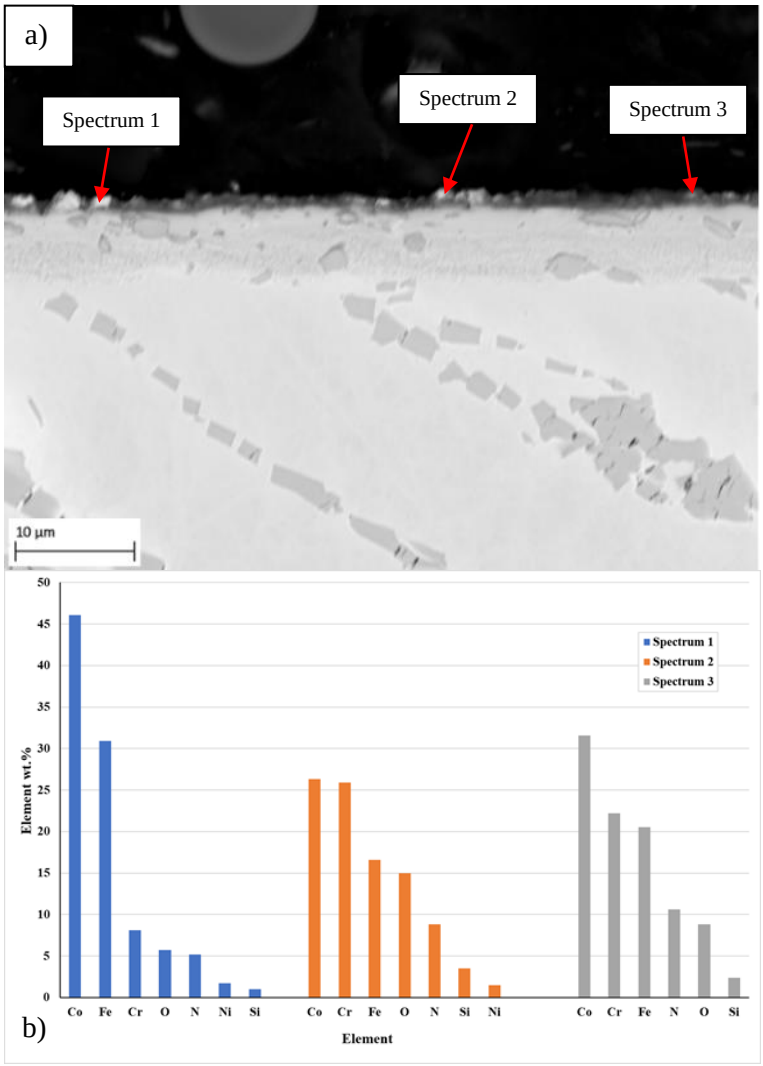

Figure 5.10: EDS point scan analysis phase formation at the surface of a WT-6 sample after nitriding at 550ºC for 15-hours: a) Point scan locations and b) Corresponding point scan compositions.

5.2.3 Plasma Treated WT-12

WT-12 samples after a plasma treatment at 400°C and 550°C for 15-hours are shown in Figure 5.11. Diffusion of nitrogen was observed to occur in the cobalt matrix whereas the carbide phases in the microstructure were observed to resist and impede the diffusion process.

It was discovered that diffusion of nitrogen occurred after each heat treatment, but the concentration of nitrogen and diffusion depth varied between treatments. Increased nitrogen concentration and a thicker diffusion layer occurred with the samples treated at higher temperatures and longer treatments. This is demonstrated in Figure 5.11 which compares samples treated at 400°C and 550°C, respectively, where increased nitrogen concentration and diffusion depth was identified with the sample treated at a higher temperature. The maps also highlight increased iron diffusion in the samples treated at higher temperatures. Similar trends were

observed comparing the samples treated at 475°C for various treatment times where increased nitrogen and iron concentrations and diffusion depths were experienced with longer treatment times. This is further demonstrated in Figure 5.13 which displays normalised GDOES analysis data. The figure compares samples treated at 400°C and 550°C for 15-hours (Figure 5.11a-b) and samples treated for 10-hours and 20-hours at 475°C (Figure 5.13c-d). The graphs indicate that nitrogen levels were detected for longer periods of time with the samples treated at higher temperatures and for longer periods of time. The extended detection of nitrogen correlates to a thicker diffusion layer. This was also the case for iron detection.

Using EDS point scan analysis, it was found that below 5wt.% nitrogen diffused into the surface of the sample treated at 400°C. Nitrogen concentration was greatest at the surface which quickly decreased moving into the bulk of the material. Nitrogen concentration increased with increased treatment temperature where the sample treated at 550°C experienced nitrogen levels of around 7wt.% near the surface. Compared to the sample treated at 400°C, the decrease in nitrogen concentration was more gradual. EDS point scan analysis of the sample treated at 550°C is displayed in Figure 5.12 and details the composition of the diffusion layer at various locations from the surface. Nitrogen content for the sample treated for 20-hours at 475°C was recorded at around 7wt.% near the surface of the sample. The concentration was observed to quickly decrease to around 5wt.% nitrogen where it remained consistent for a few microns before gradually decreasing as the substrate material was approached. A similar process occurred with the sample treated for 10-hours at 475°C but highs of around 5wt.% nitrogen content were recorded at the surface.

A thin layer formed on the surface of the samples after each treatment. Figure 5.14 revealed that the composition varied in different locations, but it was mainly cobalt with varying level of iron, chromium, nitrogen, and oxygen.

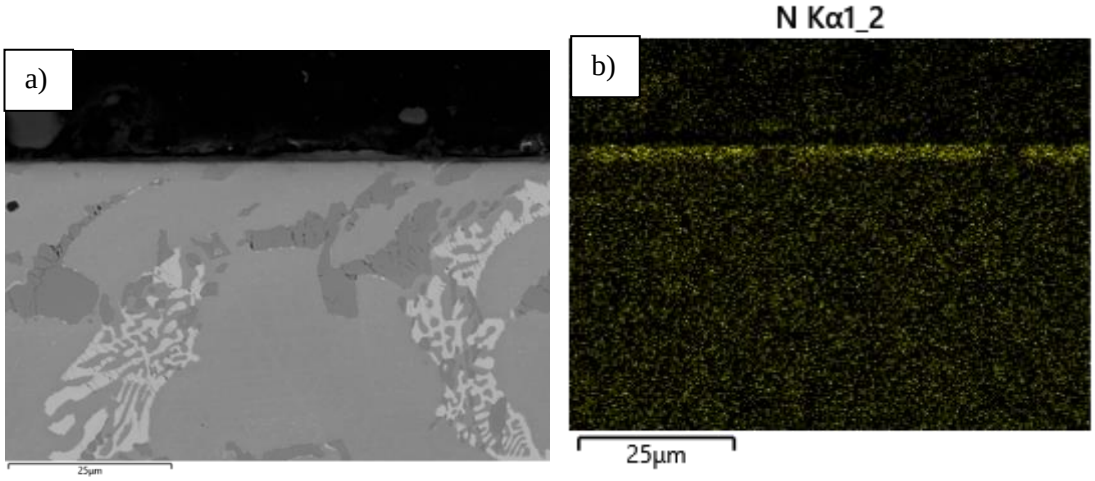

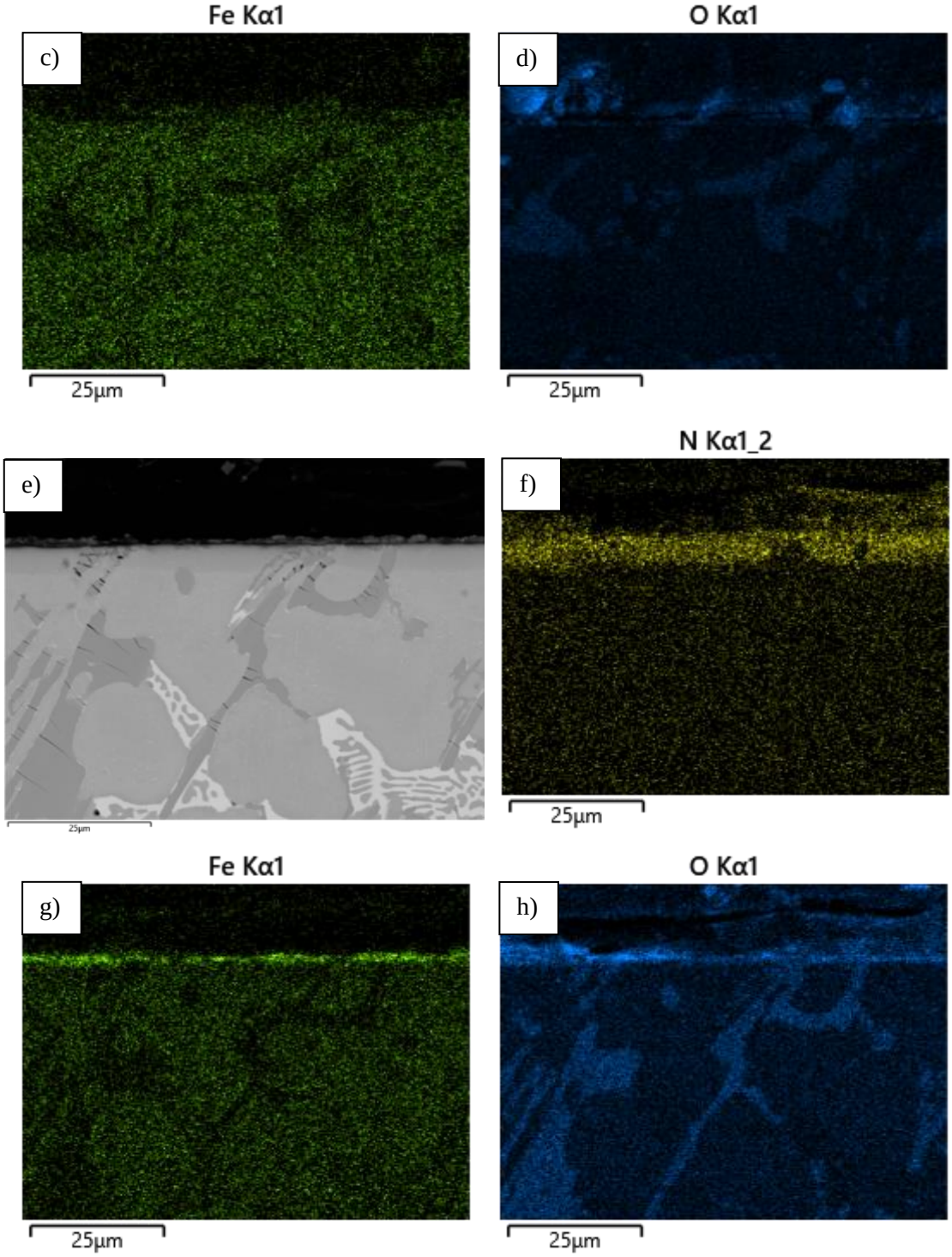

Figure 5.11: SEM and EDS analysis of WT-12 samples treated at 400°C and 550°C for 15-hours illustrating surface diffusion: a) SEM image of sample treated at 400°C, b) Corresponding nitrogen EDS map, c) Corresponding iron EDS map, d) Corresponding oxygen EDS map, e) SEM image of sample treated at 550°C, f) Corresponding nitrogen EDS map, g) Corresponding nitrogen EDS map and h) Corresponding oxygen EDS map.

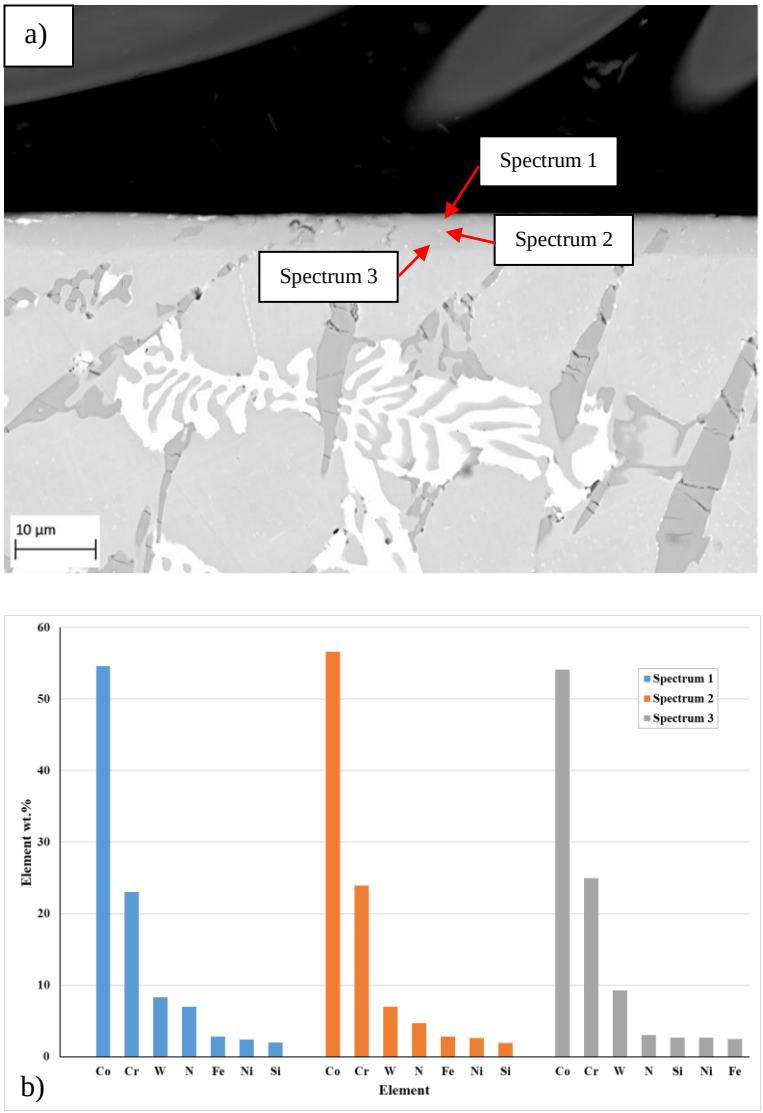

Figure 5.12: EDS point scan analysis of nitrogen-rich diffusion layer at the surface of a WT-12 sample after nitriding at 550ºC for 15-hours: a) Point scan locations and b) Corresponding point scan compositions.

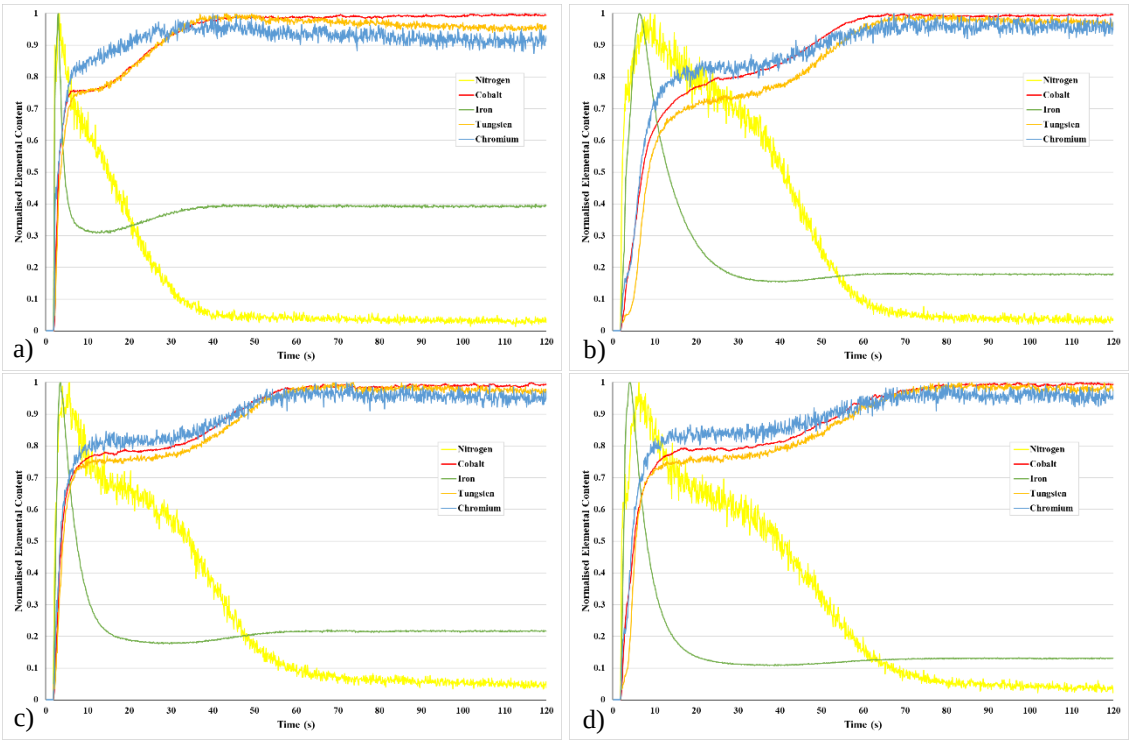

Figure 5.13: Normalised elemental content for treated WT-12 samples after various plasma nitride heat treatments using GDOES analysis: a) 15-hours at 400°C, b) 15-hours at 550°C, c) 475°C for 10-hours and d) 475°C for 20-hours.

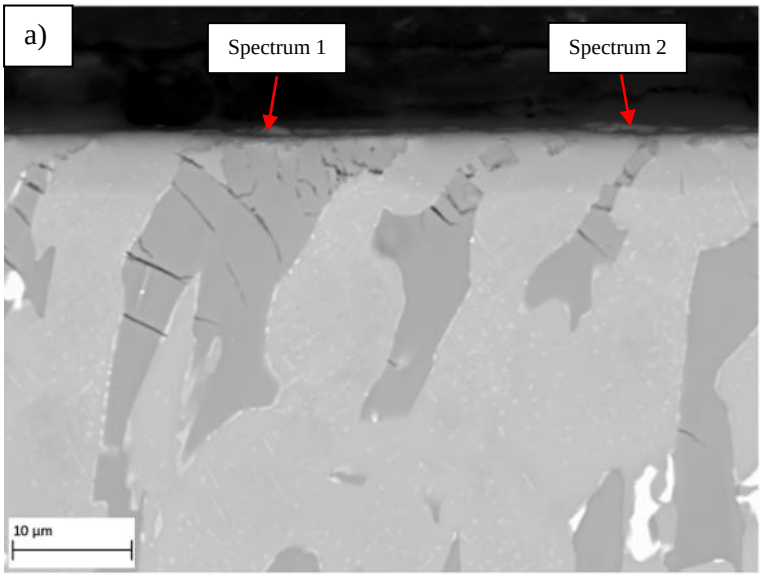

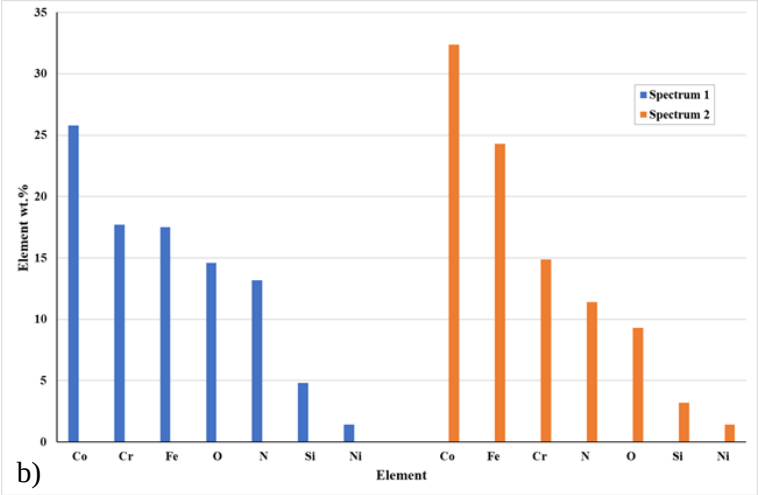

Figure 5.14: EDS point scan analysis phase formation at the surface of a WT-12 sample after nitriding at 550ºC for 15-hours: a) Point scan locations and b) Corresponding point scan compositions.

5.2.4 Plasma Treated T-800

The plasma nitride treatment resulted in the diffusion of nitrogen into the surface of the T-800 samples after each heat treatment where nitrogen concentration and nitrogen diffusion depth were observed to increase with increased treatment temperature and time. This is demonstrated in Figure 5.15 which displays EDS analysis of samples treated at 400°C and 550°C. Comparing the samples illustrates a clear contrast in nitrogen concentration and diffusion depth between the samples. A similar process occurred comparing samples treated for longer periods of time where increased nitrogen concentration and diffusion depth was recorded with the sample treated for longer treatment times. The elemental maps highlight that the diffusion of nitrogen occurred in the cobalt matrix whereas the Laves phases resisted the diffusion process, as shown in Figure 5.15b and Figure 5.15f. In addition to nitrogen diffusion, a similar diffusion process occurred with iron where increased iron concentrations and diffusion depths were recorded after increased treatment times and temperatures.

Qualitative analysis of the samples surface to investigate element concentration was carried out using normalised data produced using GDOES analysis. The graphs (Figure 5.17) illustrate prolonged detection of nitrogen and iron which correlates to greater diffusion depths. The diffusion layer was also quantitatively analysed using EDS point scan analysis to determine the nitrogen concentrations after each treatment. Analysis identified higher levels of nitrogen concentrations were recorded with the samples treated at higher treatment temperatures and longer treatment times. Above 6wt.% nitrogen content was detected with the samples treated at 475°C for 20-hours. This decreased to around 5wt.% where it remained consistent for several microns before gradually decreasing moving into the bulk of the alloy. With the sample treated at

550°C for 15-hours, around 5wt.% nitrogen was detected at the surface of the sample. The nitrogen concentration then gradually decreased as the substrate was approached, as shown in Figure 5.16 using EDS point scan analysis of the diffusion layer. Reducing the treatment temperature and time resulted in less nitrogen diffusion where lower levels of nitrogen were detected in the diffusion layer. Above 4wt.% and 5wt.% nitrogen content was detected with the samples treated at 400°C for 15-hours and 10-hours at 475°C, respectively. In both samples nitrogen content rapidly decreased moving away from the surface of the sample.

A uniform diffusion layer generally formed at the surface of the sample; however, it was identified that increased nitrogen diffusion depth occurred at the matrix and Laves phase interface. This is demonstrated in Figure 5.18 where an etched sample reveals the diffusion of nitrogen around the circumference of a Laves phase. This process is also highlighted in the nitrogen elemental map in Figure 5.15b.

In addition to the formation of a diffusion layer beneath the surface of each sample, analysis identified the formation of a thin layer on the surface which contained isolated particles. Point scan analysis was performed to determine the composition of the layer at various locations. The results are displayed in Figure 5.19. The composition varied at different locations of the surface, but the layer was found to be mainly cobalt where some regions contained high levels of cobalt and iron (Spectrum 1) and other areas contained higher levels of chromium (Spectrum 3). Both phases contained various amounts of nitrogen, oxygen, and molybdenum. A molybdenum-rich particle containing high levels of nitrogen, oxygen, chromium and cobalt was also detected (Spectrum 2).

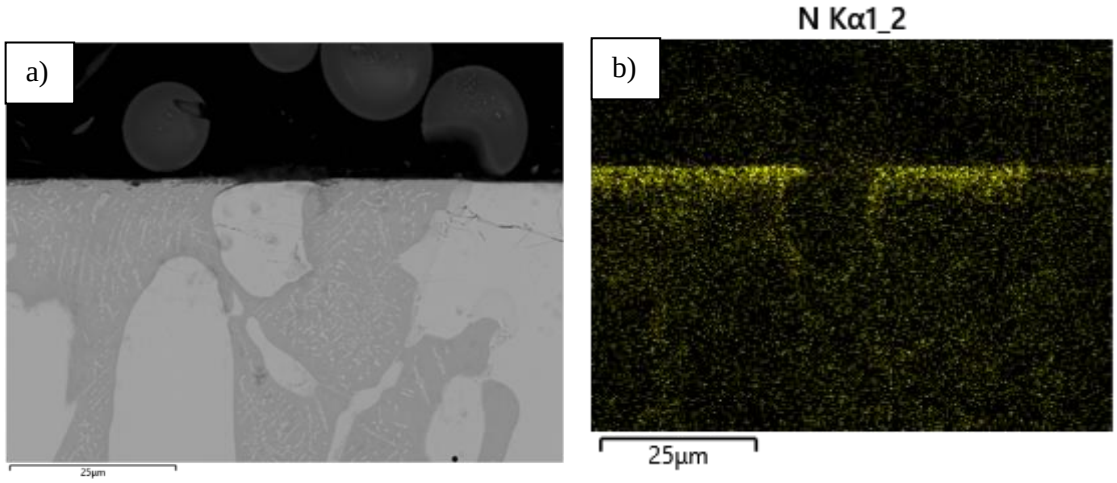

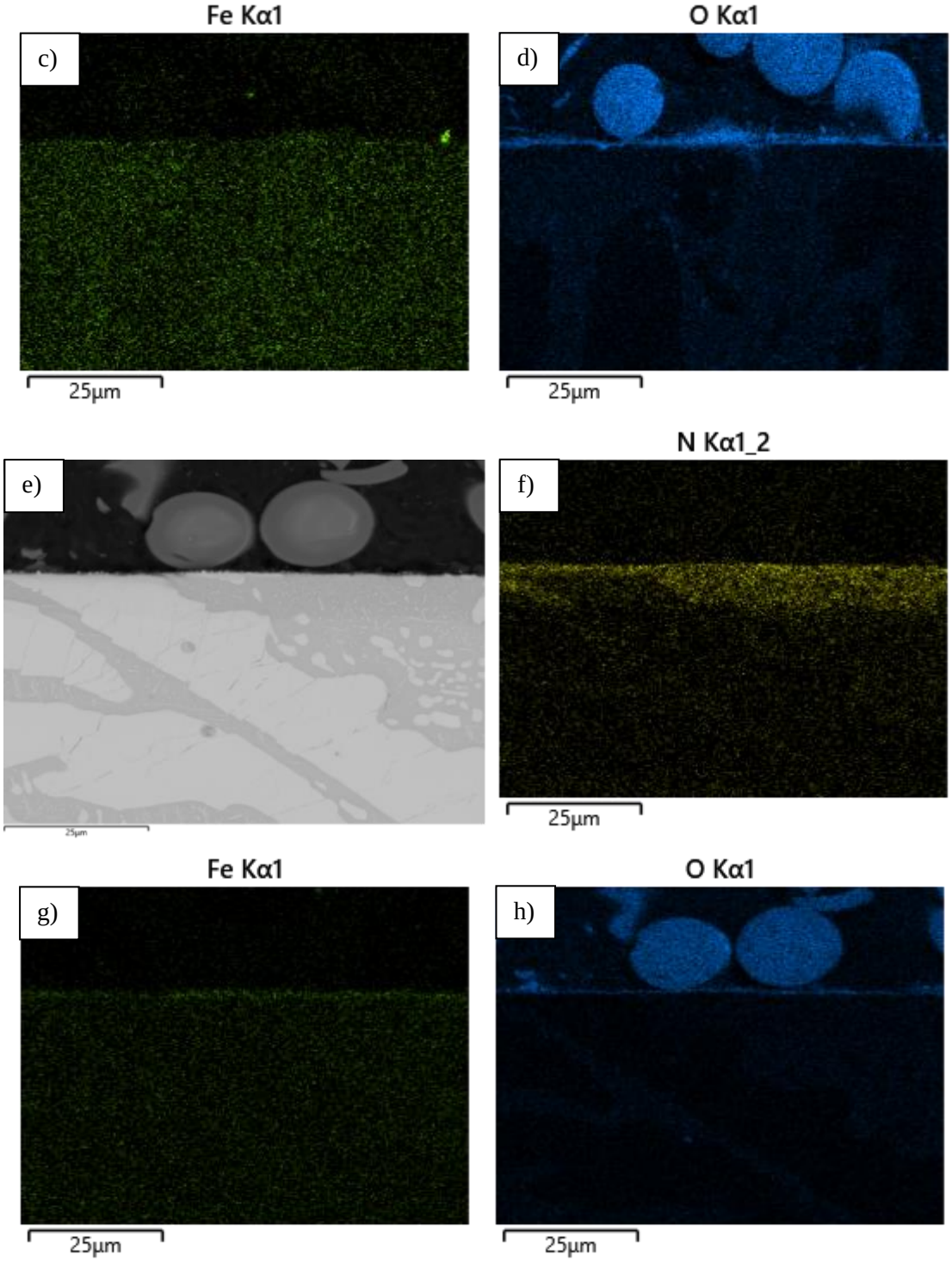

Figure 5.15: SEM and EDS analysis of T-800 samples treated at 400°C and 550°C for 15-hours illustrating surface diffusion: a) SEM image of sample treated at 400°C, b) Corresponding nitrogen EDS map, c) Corresponding iron EDS map, d) Corresponding oxygen EDS map, e) SEM image of sample treated at 550°C, f) Corresponding nitrogen EDS map, g) Corresponding nitrogen EDS map and h) Corresponding oxygen EDS map.

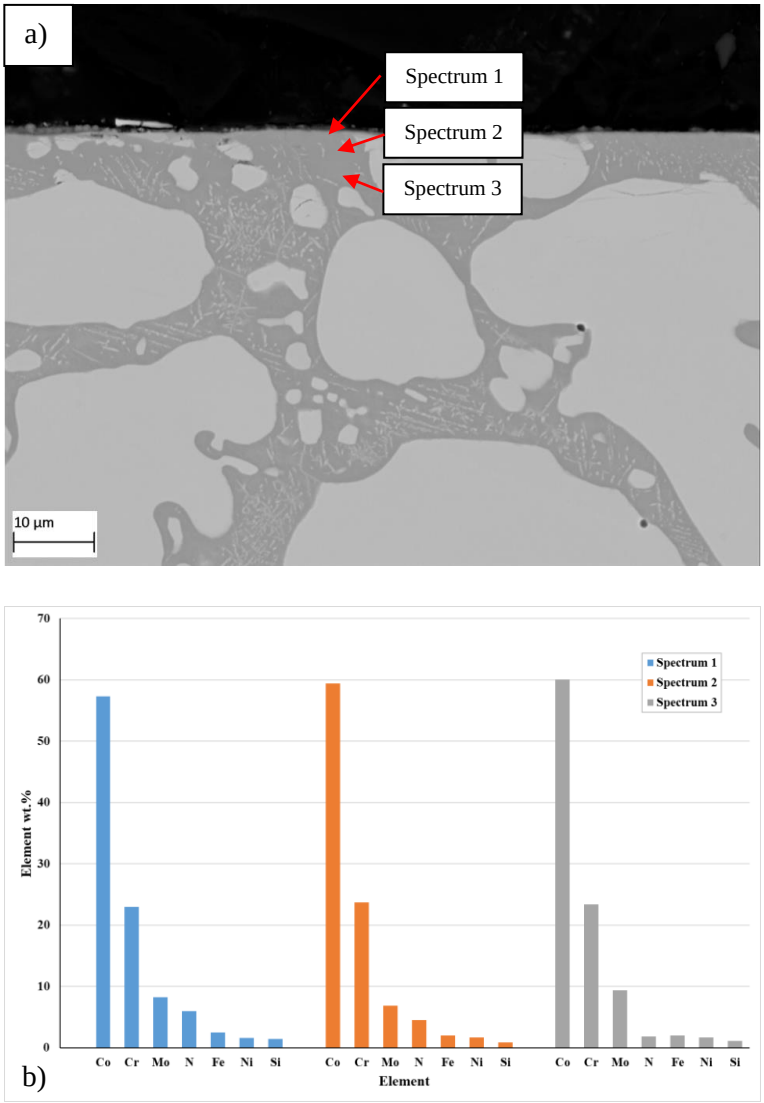

Figure 5.16: EDS point scan analysis of nitrogen-rich diffusion layer at the surface of a T-800 sample after nitriding at 550ºC for 15-hours: a) Point scan locations and b) Corresponding point scan compositions.

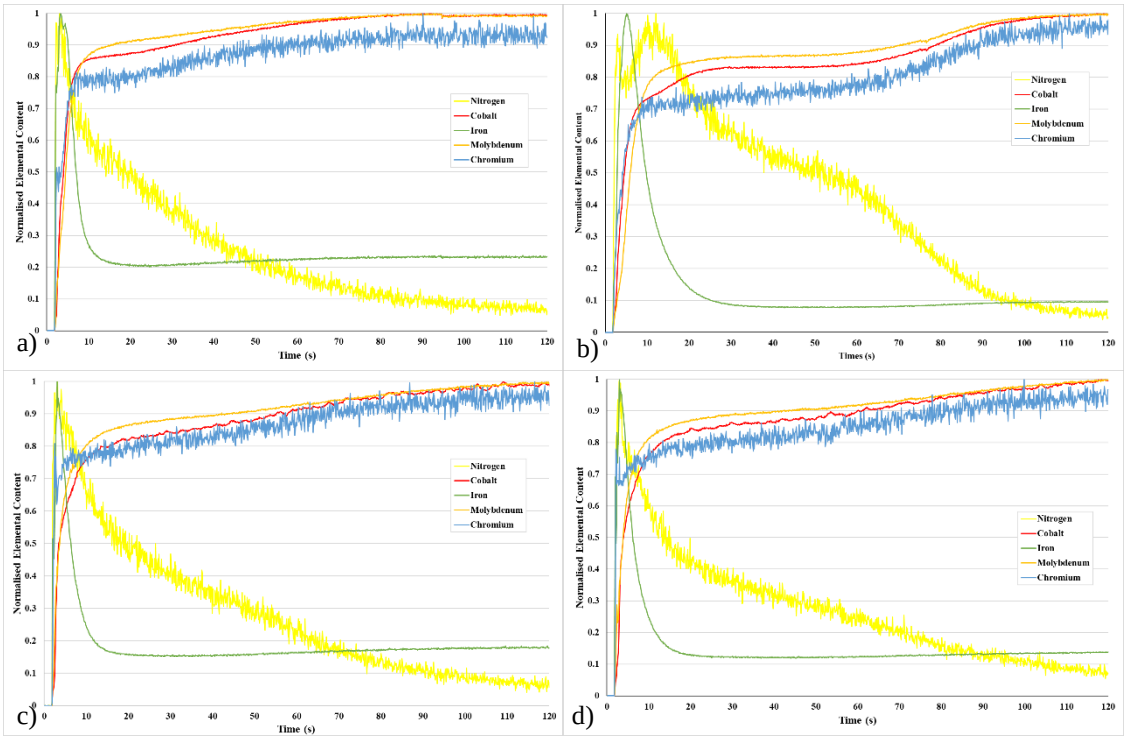

Figure 5.17: Normalised elemental content for treated T-800 samples after various plasma nitride heat treatments using GDOES analysis: a) 15-hours at 400°C, b) 15-hours at 550°C, c) 475°C for 10-hours and d) 475°C for 20-hours.

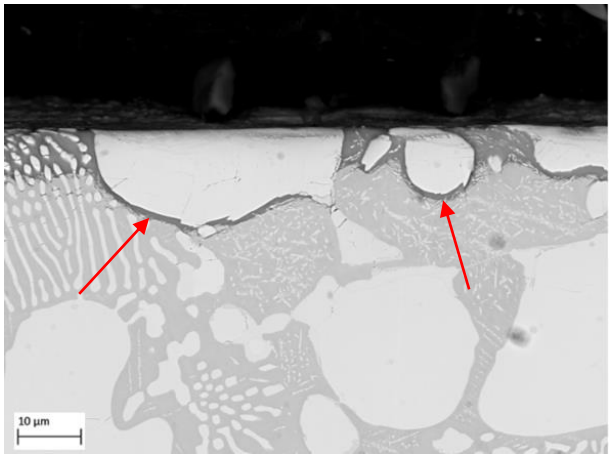

Figure 5.18: Etched T-800 sample illustrating nitrogen diffusion around the circumference of primary Laves phases.

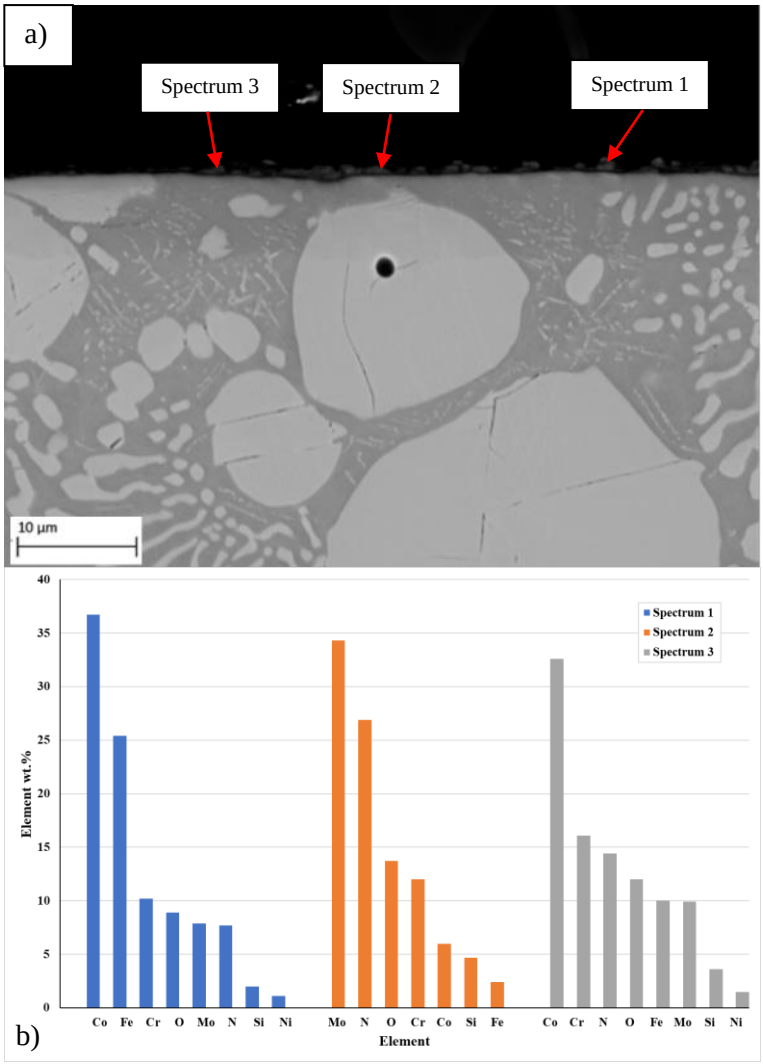

Figure 5.19: EDS point scan analysis phase formation at the surface of a T-800 sample after nitriding at 550ºC for 15-hours: a) Point scan locations and b) Corresponding point scan compositions.

5.3 Thickness of Diffusion Layer

The depth of nitrogen diffusion was measured using an EDS line scan tool. The diffusion measurements for each alloy after each plasma treatment are presented in Figure 5.20. The results show that for each alloy, periodically increasing the treatment temperature or time resulted in a gradual increase in the thickness of the nitrogen diffusion layer. The rate at which the diffusion depth increased was greater in Test 1 and more gradual in Test 2. This suggests that changing the treatment temperature has a greater influence on the diffusion process. With each alloy the greatest depth of nitrogen diffusion occurred in Test 1 after a treatment at 550ºC for 15-hours. This indicates that greater diffusion depths were achieved in Test 1 despite longer treatment times at 475ºC being carried out in Test 2. Similarly, greater diffusion depths were recorded in Test 2 after a 10-hour treatment at 475ºC compared to samples in Test 1 that were treated for a longer

treatment time of 15-hours but at a lower treatment temperature of 400ºC. This process is further demonstrated comparing the diffusion data for the 15-hour treatment from Test 2 and the 450ºC and 500ºC treatments from Test 1. Each sample was treated for 15-hours but at various temperatures. The results for these tests are presented in Figure 5.21. The greatest diffusion depth occurred with the samples treated at the highest temperature (500ºC) and the lowest diffusion depth occurred after the lowest treatment temperature (450ºC). The diffusion measurements for the samples treated at a temperature between this range (475ºC), fell between the higher and lower treatment temperature measurements.

Figure 5.22 compares the depth of nitrogen diffusion measure in the matrix phase of each alloy after each treatment. The results indicate that the T-800 Tribaloy experienced the greatest diffusion depths in the eutectic solid solution phase in both tests where a maximum depth of 11.4μm and 10.5μm was recorded in Test 1 and Test 2, respectively. The CoCrW alloys experienced more comparable diffusion depths after each heat treatment, particularly in Test 1. For each alloy, the greatest diffusion depths were recorded after nitriding at 550°C for 15-hours. Diffusion depths after this treatment ranged between 6.4-7.4μm where the WT-4 and WT-12 alloys experienced the largest and smallest diffusion depths, respectively. Although there are only minor differences in diffusion depths between the samples after each heat treatment, in both Test 1 and Test 2, the WT-4 alloy experienced the greatest diffusion depth, and the WT-12 alloy experienced the shallowest depth of diffusion at higher temperatures and longer treatment times. The WT-12 samples also experienced the lowest levels of diffusion in Test 1 and Test 2 at a low treatment temperature and shorter treatment time.

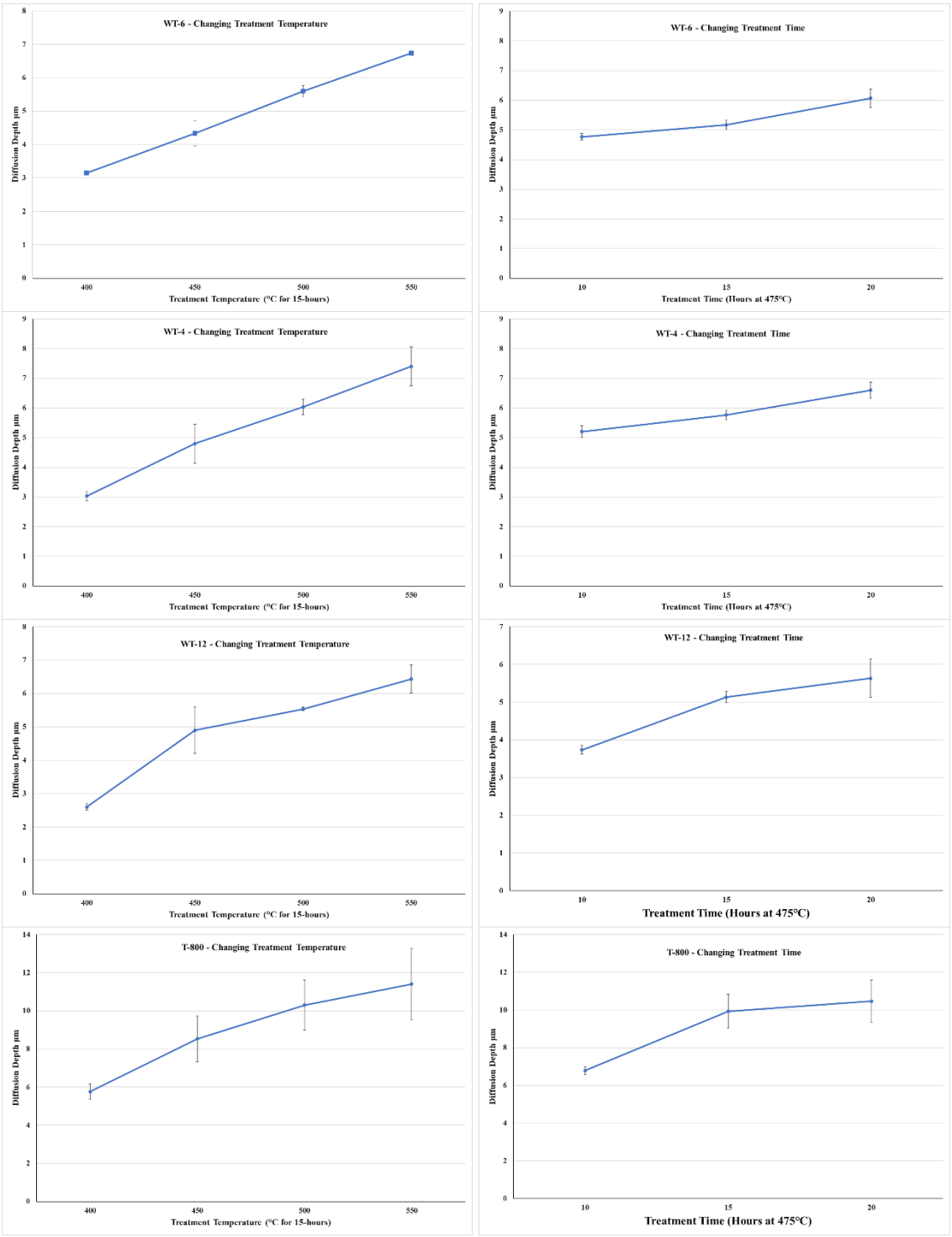

Figure 5.20: Nitrogen diffusion depths recorded after each plasma nitride treatment for each alloy.

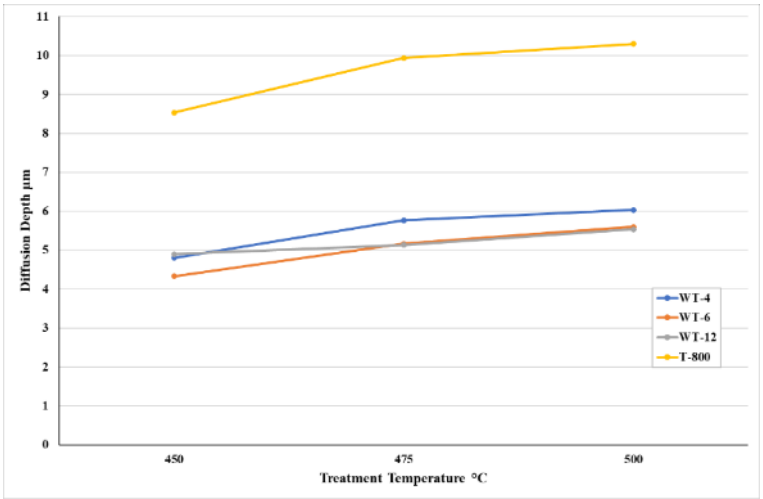

Figure 5.21: Nitrogen diffusion depths recorded for each alloy after a 15-hour plasma nitride treatment at various temperatures.

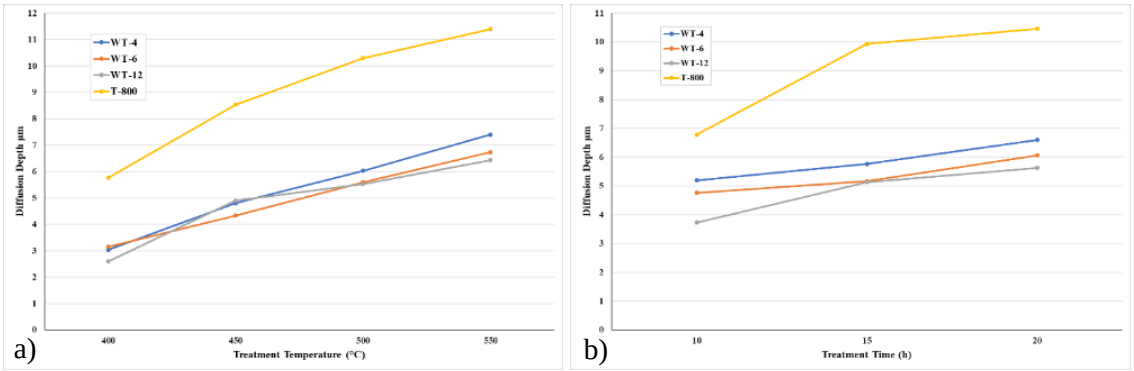

Figure 5.22: Nitrogen diffusion depths recorded for each alloy after each plasma treatment: a) Test 1 – changing treatment temperature and b) Test 2 – changing treatment time.

5.4 Hardness Investigation of the Modified Surface Layer

5.4.1 Surface Hardness of Plasma Treated Samples

Changes in material hardness for each alloy after various plasma treatment times and temperatures are summarised in Figure 5.23. Using an increased load (10kg), the graphs demonstrate the influence that the diffusion layer has on the bulk hardness of the material. A smaller load (1kg) was used to analyse the microhardness of the diffusion layer to give a better representation of its hardness with reduced influence from the substrate material.

With reference to the untreated samples, the hardness data illustrates that the plasma nitriding process significantly increased the hardness of each alloy where the hardness gradually increased with higher treatment temperatures and longer treatment times. Comparing the hardness data from Test 1 (changing treatment temperature for a 15-hour treatment) and Test 2 (changing treatment time at 475ºC) shows that increasing the treatment temperature and treatment time resulted in a gradual increase in material hardness. Analysis of the hardness data suggests that

changing the temperature of the nitriding treatment has a greater influence on changes in material bulk hardness. This is demonstrated by comparing the hardness data for the 15-hour treatment at 475ºC from Test 2 and the 450ºC and 500ºC treatments from Test 1. Each test was treated for a 15-hour duration but at different temperatures. Each of the alloys experienced greater increases in hardness when treated at the higher temperature of 500ºC and each alloy experienced lower increases in material hardness when treated at the lower temperature of 450ºC. The hardness values for the samples treated at a temperature between this range (475ºC) fell in between the tests. This is further demonstrated where greater increases in hardness were achieved for each alloy in Test 2 after a 10-hour treatment at 475ºC compared to samples in Test 1 which were treated for a longer treatment time of 15-hours but at a lower treatment temperature of 400ºC. On the contrary, all alloys achieved the greatest increase in material hardness when treated at 550 ºC for 15-hours despite samples being treated for a longer period at 475ºC in Test 2.

Despite there being a clear trend that treatment temperature had a greater influence on the change in material hardness, comparing hardness data for the samples treated at 500ºC for 15-hours (Test 1) and the samples treated at 475ºC for 20-hours (Test 2) recorded similar hardness values. This suggests that lower treatment temperatures can be compensated for by longer treatment times if increased changes in material hardness are to be achieved.

The microhardness data recorded significantly higher hardness readings compared to the bulk hardness analysis due to the lower load producing a more representative hardness value for the diffusion layer. Despite the significant difference in recorded hardness values after each heat treatment, the microhardness data displays similar trends to the bulk hardness data where the hardness of the diffusion layer gradually increased with increased treatment time and treatment temperature. However, comparing individual trends between Test 1 and Test 2 did not correlate to the trends observed with the bulk hardness readings. This suggests that either the hardness behaviour of the diffusion layers is influenced by the treatment time and temperature in a different way or due to the location of the microhardness readings. It is unknown where the microhardness indents were being produced so they could have been significantly influenced by indents produced on the softer cobalt matrix or the harder carbide/Laves phases.

Comparisons in hardness between each alloy after each treatment are displayed Figure 5.24. The highest and lowest hardness readings were recorded with T-800 Tribaloy and the WT-6 alloy, respectively. These results are to be expected due to the standard hardness of the untreated alloys. However, the hardness of the untreated WT-4 and WT-12 alloys were more comparable where the WT-4 was slightly harder. Comparisons between the WT-4 and WT-12 samples indicates similar increases in hardness were experienced with the lower treatment temperatures

and shorter treatment times but longer treatment temperatures and times resulted in higher increases in hardness with the WT-12 alloy.

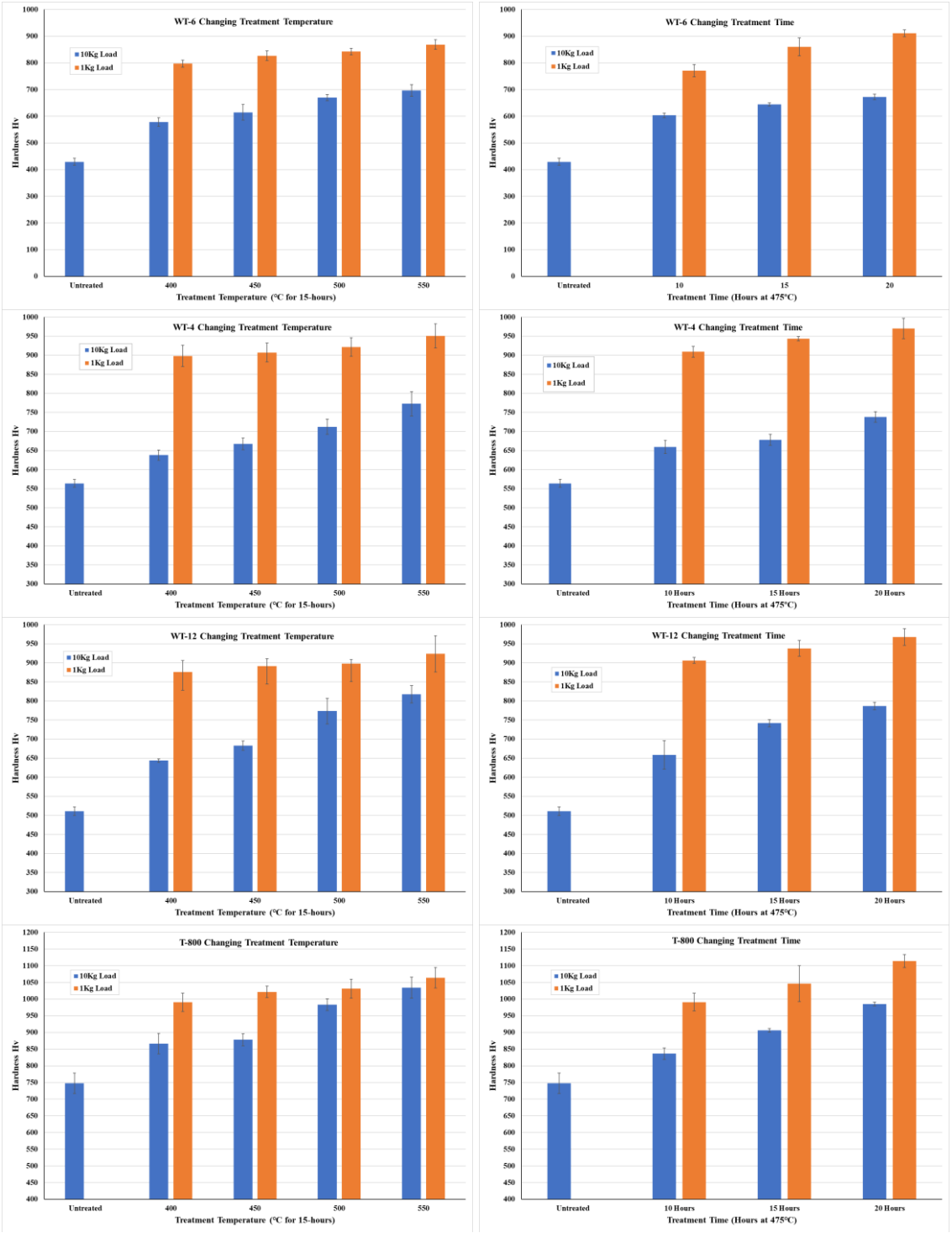

Figure 5.23: Changes in bulk hardness and microhardness after each treatment.

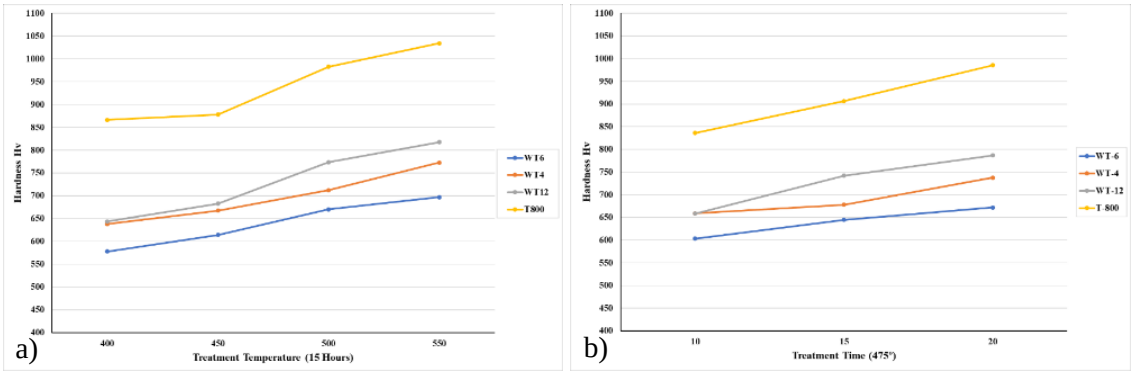

Figure 5.24: Changes in material hardness experienced for each alloy after each plasma treatment: a) Test 1 – changing treatment temperature and b) test 2 – changing treatment time.

5.5 Comparisons of Composition and Hardness Trends Observed with the Formation of a Diffusion Layer in the Plasma Treated Alloys

Cross-sectional SEM and EDS analysis of the plasma treated samples revealed the formation of nitrogen diffusion layer at the samples surface where a clear diffusion boundary was observed between the nitride layer and the substrate material. This occurred with each alloy and after each heat treatment. The diffusion of nitrogen occurred in the cobalt matrix phase whereas the carbide/Laves phases resisted the diffusion process. Although the carbide and Laves phases were more resistant to nitrogen diffusion, the phases near the surface were often observed to include cracks after the sample was treated. This is due to the brittle nature of the phases and the compressive stresses produced by the expansion of the lattice which is caused by nitrogen atoms diffusing into alloys microstructure.

Although the GDOES analysis was not calibrated correctly to accurately measure nitrogen diffusion depth or concentration, the data did provide an insight on how the individual treatments influenced the depth of diffusion. The results suggested that longer element detection times correlated to a deeper diffusion layer and shorter times represented a shallower diffusion layer. From this theory the data suggested that higher treatment temperatures and longer treatment times resulted in a larger diffusion layer as nitrogen was detected for longer periods of time. This was confirmed using EDS analysis where measurement of the diffusion layer using a line scan tool verified that increasing the temperature or length of the treatment resulted in nitrogen diffusing deeper into the alloys surface to produce a larger diffusion layer. Analysis of the diffusion depth data highlighted that the diffusion depth was more sensitive to the treatment temperature whereby higher treatment temperatures resulted in greater diffusion depths. This was clarified comparing samples treated at slightly different temperatures for 15-hours which indicated that small changes in treatment temperature resulted in differences in diffusion depth where the higher temperature

resulted in the greatest diffusion depth and the lower temperature experienced the least diffusion depth. This was the case for each alloy.

Compositional analysis of the diffusion layer revealed that after each treatment nitrogen concentration was always greatest at the surface of the sample, although the T-800 sample treated for 15-hours at 550℃ did experience a slight increase in nitrogen concentration in the region below the surface. Generally, moving away from the surface of the sample into the bulk of the alloy resulted in nitrogen levels gradually decreasing until the diffusion boundary was reached, and the composition of the matrix returned to the standard chemistry of the solid solution phase. It was observed that the rate at which nitrogen concentration decreased related to the treatment conditions where shorter treatment times and lower temperatures resulted in a more rapid decrease in nitrogen concentration whilst higher treatment temperatures and longer treatment times experienced more gradual declines in nitrogen content. Table 5.1 lists the highest nitrogen concentrations detected in the diffusion layer for each alloy after the highest and lowest treatment temperatures in Test 1 and the longest and shortest treatment times in Test 2. Analysis of the EDS data highlighted that the treatment parameters influenced nitrogen concentrations of the diffusion layer whereby increased temperature and longer treatments increased the nitrogen content. The data indicates that with each alloy the highest nitrogen concentrations recorded after a 15-hour treatment at 550℃ in Test 1 or after a treatment at 475℃ for 20-hours in Test 2. Decreasing the temperature or duration of the plasma treatment resulted in a gradual reduction in the concentration of nitrogen. After the 550℃ treatment (Test 1) and the 20-hour treatment (Test 2), similar maximum concentrations of nitrogen in the diffusion layer were detected with the WT-12 and WT-4 alloys whereas slightly higher nitrogen concentrations were detected in Test 2 with the WT-6 and T-800 alloys. This suggests that despite the lower treatment temperatures in Test 2, higher levels of nitrogen diffusion can be achieved with longer treatment times. In all cases, higher nitrogen concentrations were detected with the samples treated for 10-hours at 475℃ (Test 2) compared with the samples treated at 400℃ for 15-hours (Test 1). This indicates that despite shorter treatment times, increased nitrogen diffusion occurred at higher treatment temperatures.

In addition to the treatment conditions influencing the level of nitrogen diffusion, Table 5.1 shows that the individual alloys experienced various levels of diffusion. The WT-4 alloy recorded the greatest nitrogen concentrations (12wt.%) whilst the T-800 Tribaloy experienced the lowest levels of nitrogen diffusion (6wt.%). The WT-6 and WT-12 experienced maximum concentrations of 10wt.% and 7wt.%, respectively.

The hardness data revealed similar trends that were observed with the diffusion depth measurements where the hardness of the treated samples progressively increased after higher treatment temperatures and longer treatment times. There was also a clear correlation between the

change in hardness and the temperature where increased treatment temperature resulted in greater changes in hardness. This was also clarified looking at the samples treated for 15-hours at differences temperature where he higher and lower temperatures resulted in the greatest and lowest changes in hardness, respectively.

It has been established that increasing the treatment time or temperature resulted in greater increases in material hardness and the formation of a thicker diffusion layer at the samples surface. Figure 5.25 presents the relationship between changes in hardness and the thickness of the diffusion layer for each alloy after each heat treatment. The graph clearly demonstrates that an increase in hardness correlates to an increase in the thickness of the diffusion layer. It was identified that larger diffusion layers were formed at higher treatment temperatures in Test 1. This resulted in greater increases in hardness despite equal or greater nitrogen concentrations being detected in the samples from Test 2. For example, with the WT-4 samples, highs of 12wt.% nitrogen content were detected in the test carried out at 550℃ in Test 1 and the 20-hour test in Test 2. However, the thickness of the diffusion was greater in Test 1 which resulted in this sample experiencing a greater increase in hardness. This also occurred with the WT-6 and T-800 samples where greater concentrations of nitrogen were detected in the diffusion layer in Test 2. However, greater increases in hardness were recorded in Test 1 due to the formation of a larger diffusion layer. This is likely due to how quickly the nitrogen concentration decreased moving into the bulk of the alloy. Increased nitrogen content at the surface would have a reduced effect on the hardness of the sample compared to a deeper diffusion layer, particularly at high loads where the indenter tip would have produced an indent which was greater than the thickness of the diffusion layer. Examining the microhardness data reinforces this theory. Higher concentrations of nitrogen were detected after a 20-hour treatment in Test 2 with the WT-6 and T-800 alloys which resulted in greater microhardness when compared to tests carried out at 550℃ in Test 1, despite a thicker diffusion layer former in Test 1. A smaller load would have produced a shallower indentation therefore higher nitrogen content at the surface would have a greater effect on the hardness reading.

Despite the similarities in hardness of the untreated WT-4 and WT-12 alloys, the results indicate that although the WT-12 alloy experienced lower levels of nitrogen diffusion and a smaller diffusion layer, the alloy experienced greater increases in material hardness. This suggests that the strengthening mechanisms experienced with this alloy has a greater influence on material hardness with this alloy.

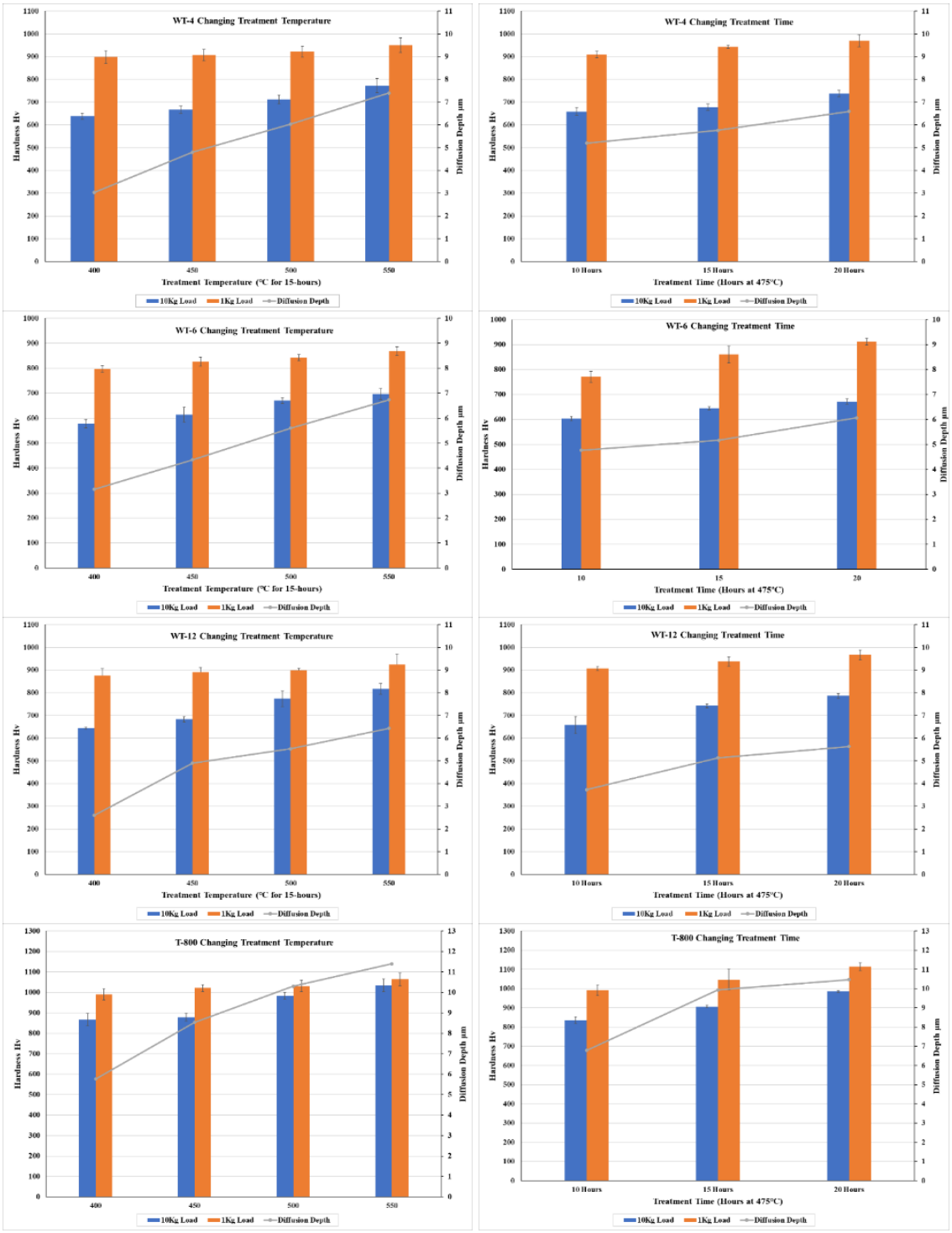

Figure 5.25: Correlation between changes in material bulk hardness and microhardness with increased depth of the nitride layer.

Table 5.1: Highest nitrogen concentrations recorded for each alloy.

		N wt.%			
		WT-4	WT-6	WT-12	T-800
Test 1	550°C for 15-Hours	12	8	7	5
	400°C for 15-Hours	3	4	4	4
Test 2	20 Hours at 475°C	12	10	7	6
	10 Hours at 475°C	6	5	5	5

5.6 Static Immersion Dip Testing of Plasma Treated CoCrW and CoCrMo Alloys

5.6.1 Static Immersion Testing of Plasma Treated WT-6

SEM analysis of the plasma treated WT-6 samples after various immersion times in a molten zinc bath are displayed in Figure 5.26. Despite the successful diffusion of nitrogen into the surface of the WT-6 samples, they were still observed to react with the bath after each stage of testing. After the first week of immersion the sample displays signs of diffusion occurring beneath the surface of the sample as well as reaction phases forming at the surface. Surface analysis revealed that the cobalt matrix was susceptible to the diffusion process where diffusion penetrated deeper into the bulk of the alloy through this phase after prolonged testing. The chromium carbides in the microstructure were more resistance to diffusion and impeded the diffusion process. Cracking of the carbide phases was a frequent occurrence after each stage of testing. However, the nitriding process resulted carbide crack formation, so this is not a direct consequence of molten metal ingress.

The average diffusion depths recorded after each stage of testing are summarised in Figure 5.27 which also indicates the standard deviation of measurements. Diffusion was recorded to reach 55μm after the first week which gradually increased by an average of 10μm after each progressive stage of dip testing where diffusion reached 85μm by the fourth week of testing.

The images highlight how different areas of the samples surface experienced various levels of diffusion where some areas were more affected than others. After the earlier stages of dip testing the initial diffusion depth was uniform. However, after prolonged bath exposure some areas of the sample experienced increased diffusion penetration depth. This is demonstrated by the gradual increase in standard deviation measurements after each stage of testing, as shown in Figure 5.27.

The diffusion process resulted in the formation of an intermetallic phase within the matrix of sample which formed behind the diffusion front. This was observed to occur after the first week of testing and became more apparent as the dip time progressed. After the first week of testing the diffusion depth was shallow and the formation of the intermetallic phase occupied small areas

of the diffusion layer. By the fourth week of testing the diffusion depth was much greater and large areas of the diffusion layer were dominated by the presence of an intermetallic phase. A thin layer beneath the surface of the samples was observed after each stage of testing which became more distinctive after longer tests. Point scan analysis was performed after each stage of testing to determine the composition of the diffusion layer and reaction phases at specific locations. Figure 5.29 and Figure 5.31 display differences in composition of the diffusion layer at different locations after two and four weeks of bath immersion, respectively. Analysis of the sample after 2-weeks of bath immersion (Figure 5.29) confirmed that the thin layer at the surface (Spectrum 1) contained high levels of zinc (47wt.%) and additions of aluminium (17wt.%), chromium (18wt.%) and nitrogen (10wt.%). The presence of nitrogen at this location identifies the nitrogen layer that formed after the plasma nitriding treatment. The survival of this layer after 2-weeks of testing is clearly visible in the EDS mapping of this sample in Figure 5.28. Analysis of the region just below the nitride region (Spectrum 2) indicates that the area is predominately zinc (89wt.%) with small amounts of tungsten (5wt.%), chromium (3wt.%), nitrogen (2wt.%), and cobalt (1wt.%). Moving into the bulk of the alloy (Spectrum 3) experienced a decrease in the zinc (20wt.%) concentration whereas cobalt (30wt.%), chromium (19wt.%) and tungsten (9wt.%) levels increased. High levels of aluminium (14wt.%) were also detected in this region. Increased levels of cobalt were detected at the diffusion front (Spectrum 4) in addition to high levels of aluminium (21wt.%) and iron (9wt.%). The formation/attachment of particles on the surface of the dipped samples were also identified. The EDS maps illustrate the surface phases contained high levels of cobalt, aluminium, and iron and identifies formation/attachment of CoAl and dross particles. The phases were often attached to the surface in isolated locations where the size and morphology was irregular.

EDS mapping of a sample after dip testing for 4-weeks is displayed in Figure 5.30. The elemental maps highlight that the nitrogen layer at the surface of the sample is still present after this stage of testing. Point scan analysis identified that the region (Spectrum 5, Figure 5.31) contained 13wt.% nitrogen, high levels of zinc (53wt.%) and aluminium (24wt.%) and low levels of chromium (5wt.%), cobalt (1.5wt.%), silicon (1.4wt.%) and iron (1wt.%). Although the depth of diffusion and intermetallic phase formation significantly increased after 4-weeks of testing, the diffusion process remained similar. The diffusion front was observed to be rich in aluminium and iron where the region behind it becomes depleted in cobalt and chromium. The depletion of cobalt and chromium subsequently results in the formation of a zinc-rich intermetallic phase. Spectrum 1 indicates that the region beneath the nitrogen layer is zinc-rich (40wt.%) but contained high levels of chromium (31wt.%). Levels of aluminium (10wt.%), tungsten (6.3wt.%) and silicon (5.2wt.%) were also recorded in this area but there were only traces of cobalt detected. Slightly

below this region (Spectrum 2) a significant increase in zinc content was detected where the area mainly consists of zinc (82.3wt.%) with low levels of tungsten (6.5wt.%), aluminium (3.6wt.%), cobalt (3.4wt.%), iron (2.1wt%) and chromium (1.4wt.%). The depletion of chromium content in this area of the microstructure and high levels detected at the surface indicates that chromium diffuses towards the surface of the sample. Zinc levels decreased moving into the bulk of the alloy where the diffusion front contains higher levels of aluminium and iron.

It was observed that the attachment of CoAl and dross phases decreased after longer bath exposure where the volume and size of the phases decreased. This could indicate that the phases detached from the surface after longer dip times or that they diffused into the bath or into the alloy. In addition to CoAl formation, the EDS maps display a CrSi phase. Spectrum 6 identified that the phase was predominantly chromium (78.5wt.%) with high levels of silicon (15.1wt.%) and low levels of zinc (3.4wt.%). It was discovered the surface of the sample contained high levels of chromium and relatively high levels of silicon, so it is most likely that this process resulted in the formation and detachment of the CrSi phase.

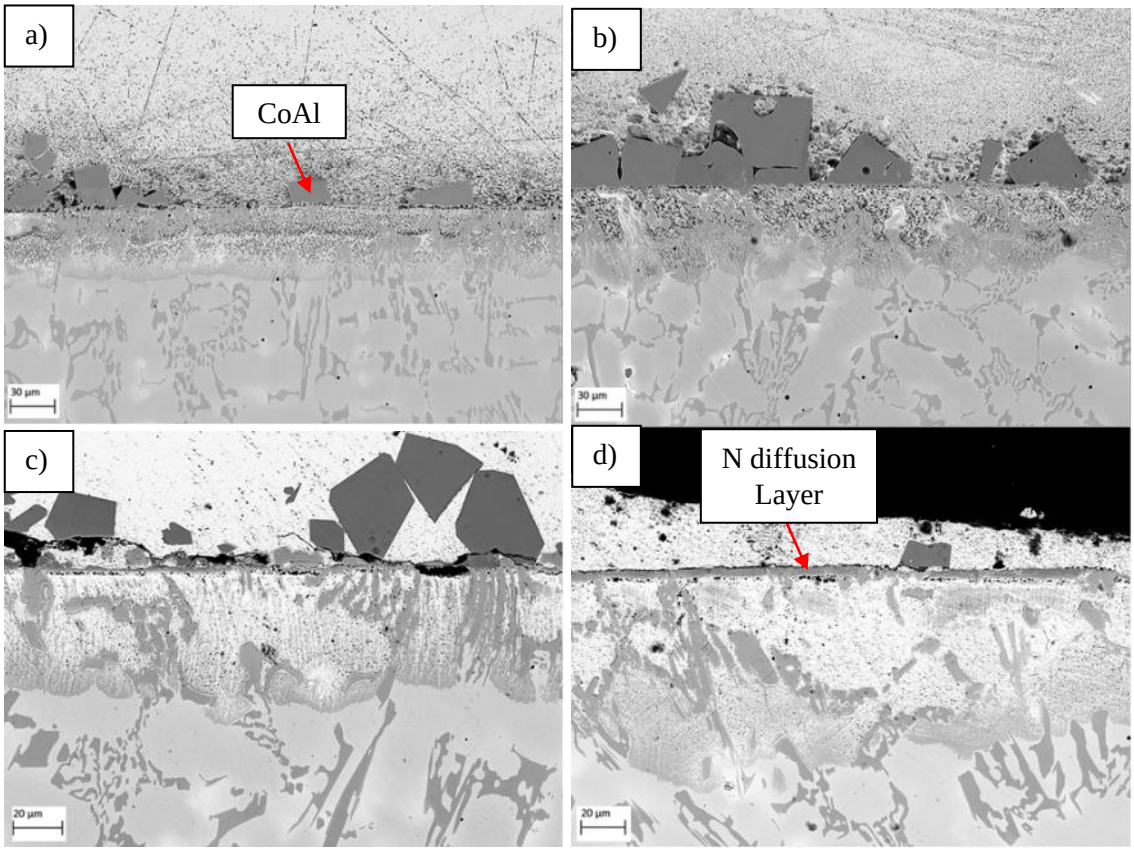

Figure 5.26: Surface condition of the plasma treated WT-6 alloy after 1-4-week dip testing in a molten zinc bath containing 0.35wt.% Al and saturated with Fe: a) Week 1, b) Week 2, c) Week 3 and d) Week 4.

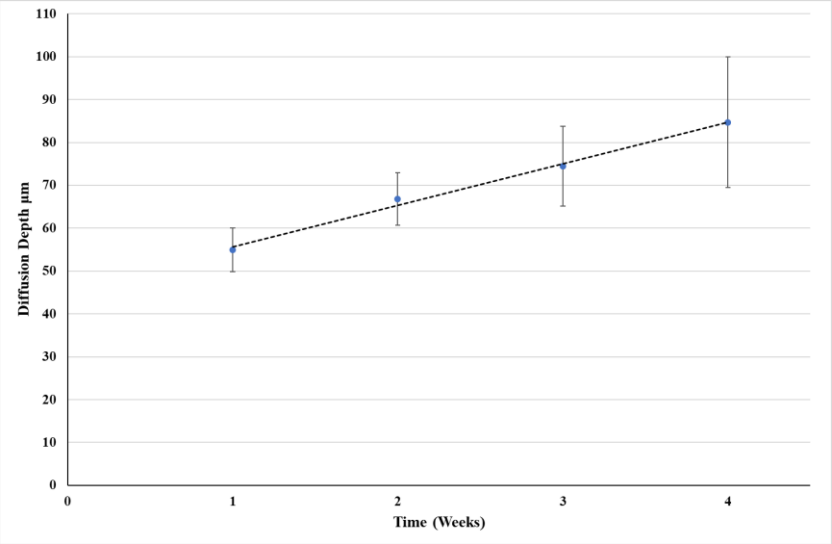

Figure 5.27: Average diffusion depth of the plasma treated WT-6 alloy after prolonged dip testing in a molten zinc bath containing 0.35wt.% Al and saturated with Fe.

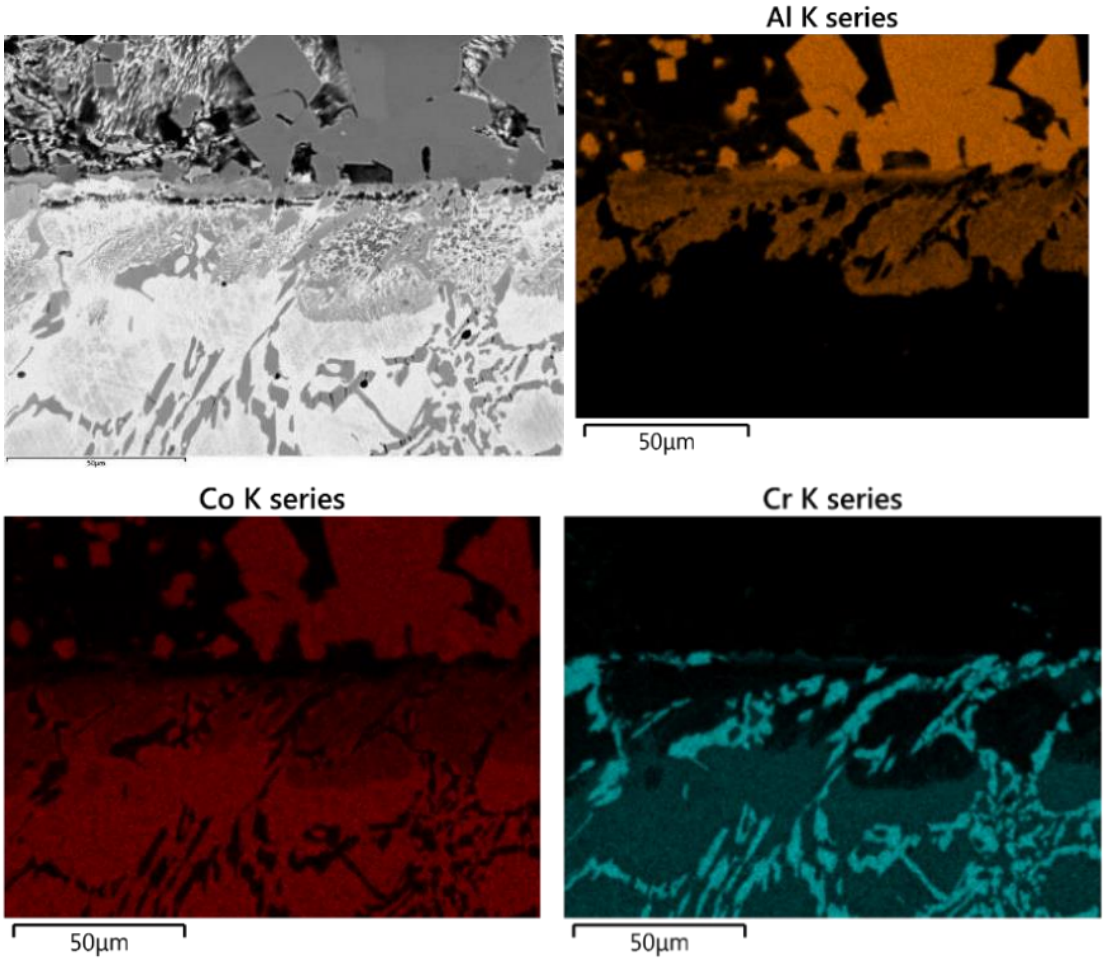

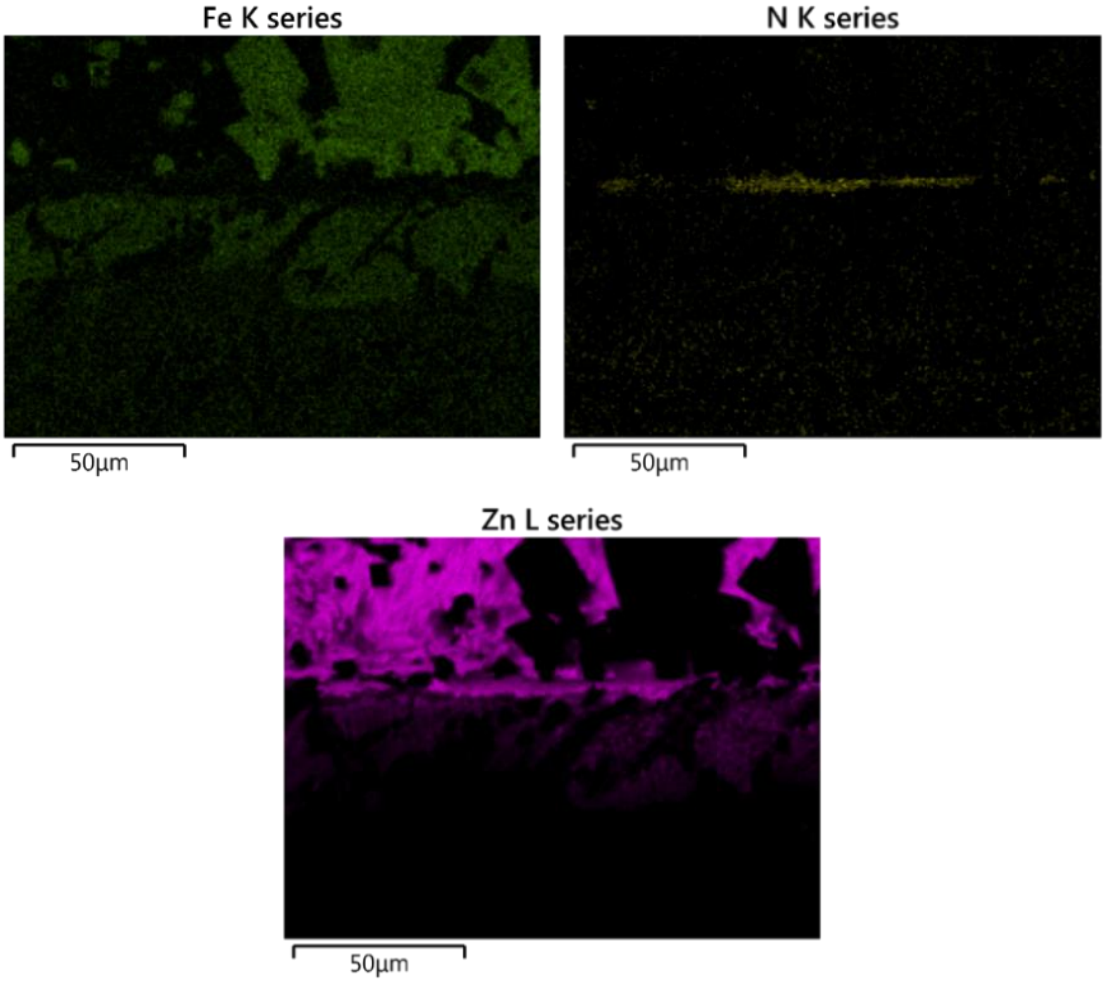

Figure 5.28: EDS elemental mapping of a plasma treated WT-6 alloy after 2 weeks of dip testing in a molten zinc bath containing 0.35wt.% Al and saturated with Fe.

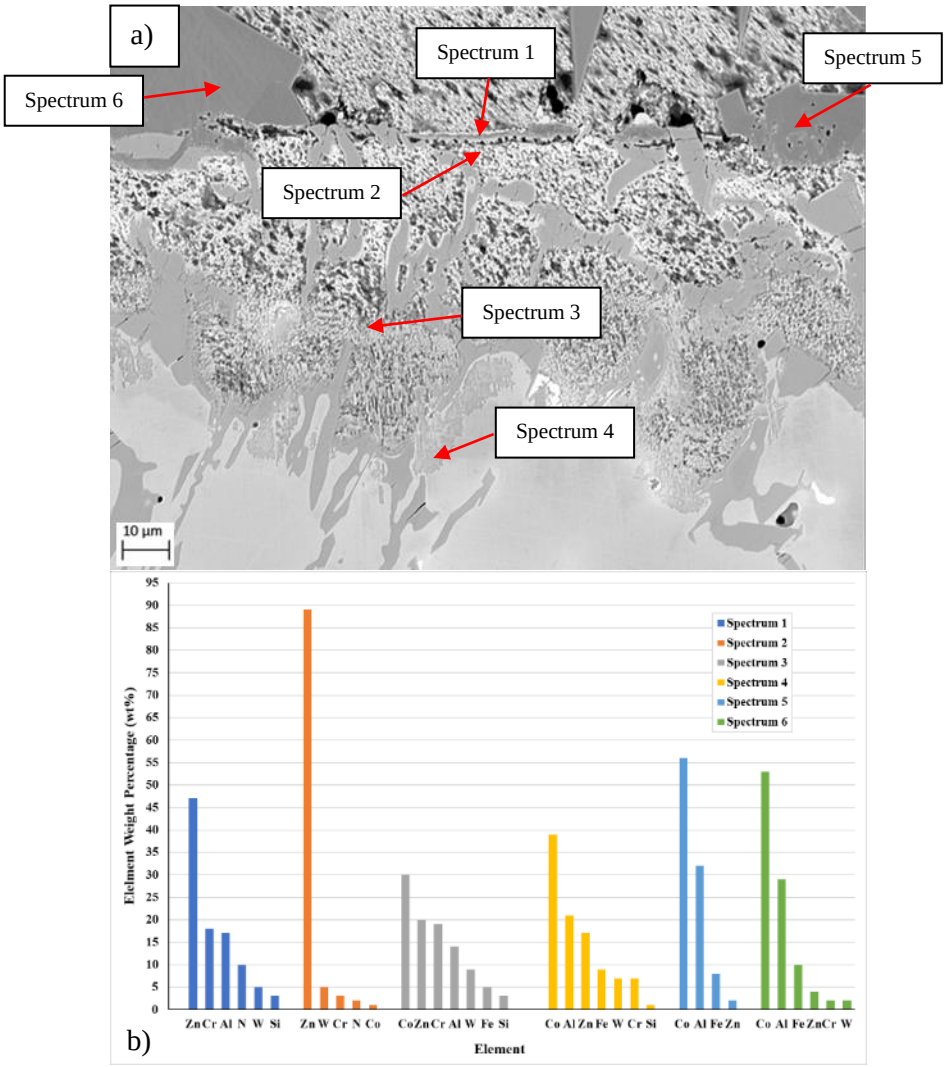

Figure 5.29: EDS point scan analysis of the diffusion zone of the plasma treated WT-6 alloy after 2-weeks of bath immersion: a) Point scan locations and b) Corresponding point scan compositions.

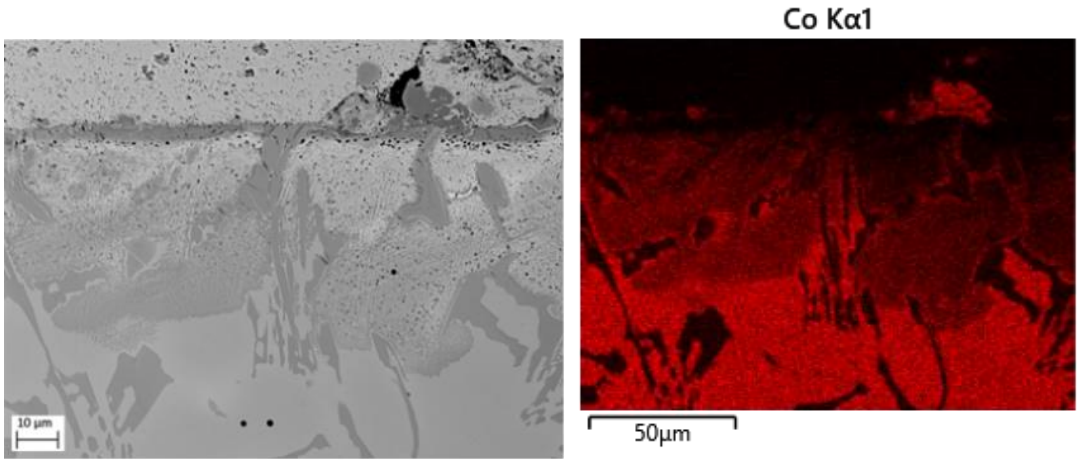

Cr Kα1

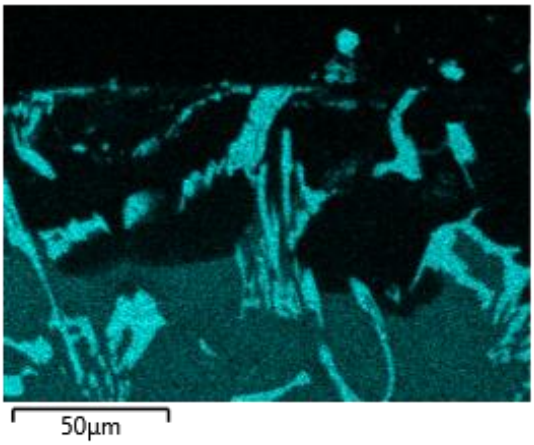

Al Kα1

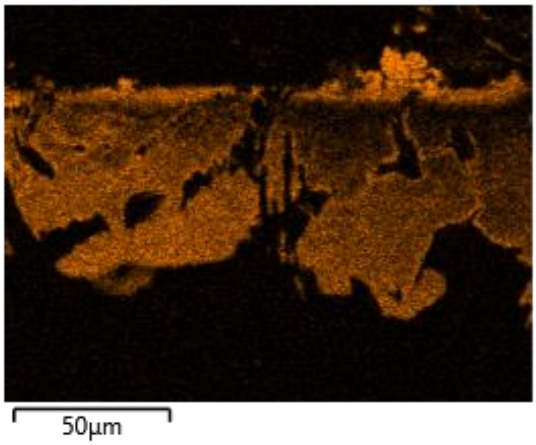

Zn Kα1

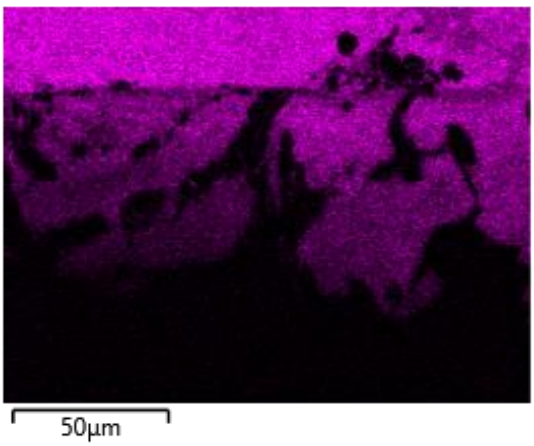

N Kα1_2

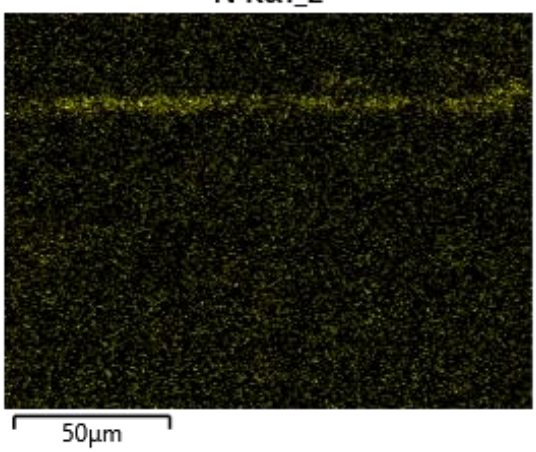

Fe Kα1

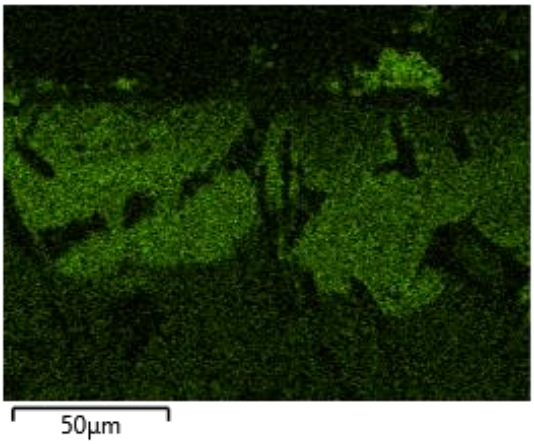

Si Kα1

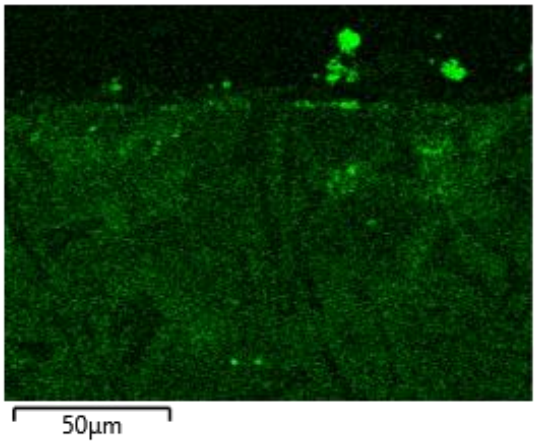

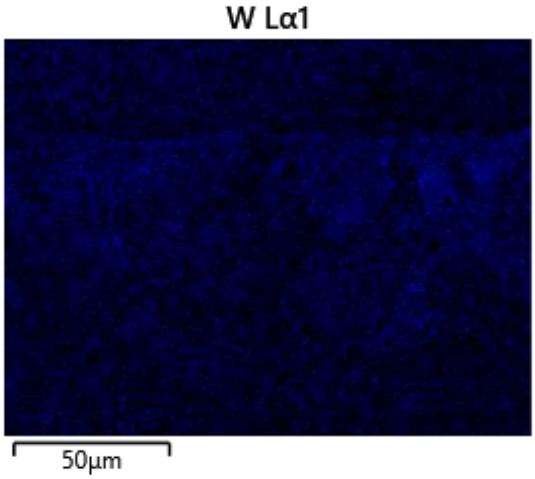

Figure 5.30: EDS elemental mapping of a plasma treated WT-6 alloy after 4-weeks of dip testing in a molten zinc bath containing 0.35wt.% Al and saturated with Fe.

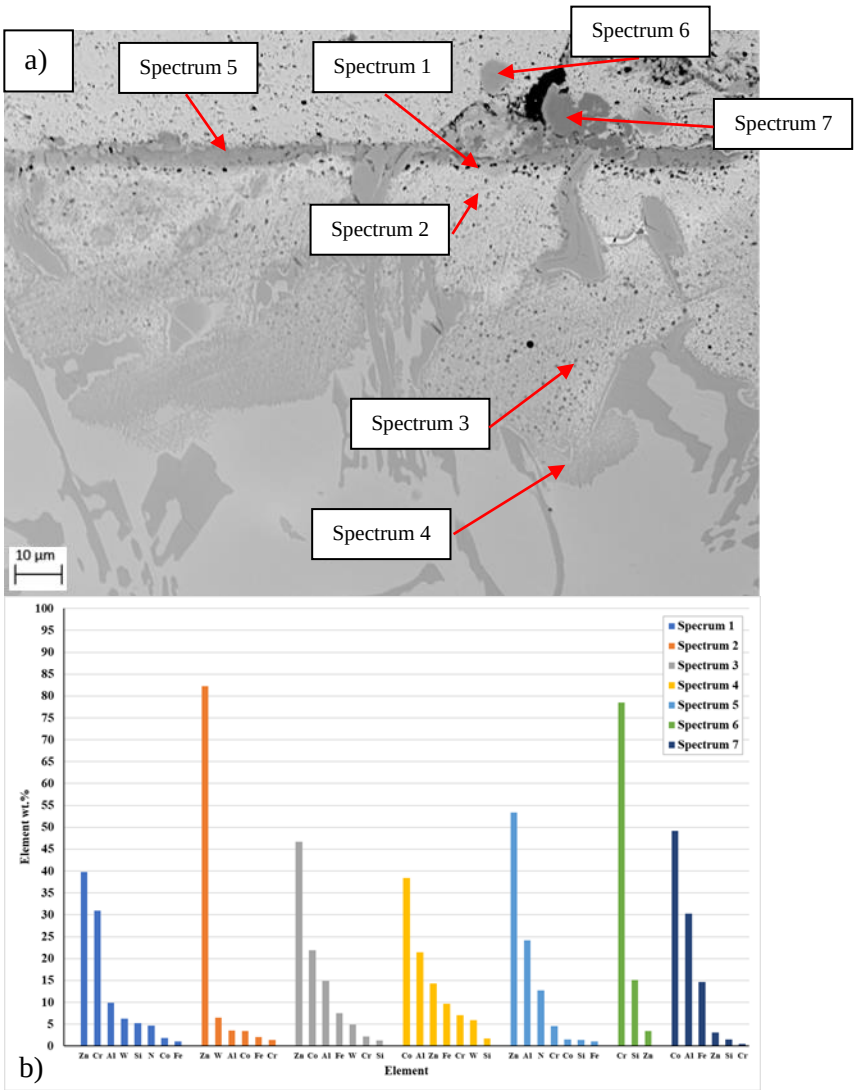

Figure 5.31: EDS point scan analysis of the diffusion zone of the plasma treated WT-6 alloy after 4-weeks of bath immersion: a) Point scan locations and b) Corresponding point scan compositions.

5.6.2 Static Immersion Testing of Plasma Treated WT-4

Figure 5.32 displays the plasma treated WT-4 samples after progressive dip testing in molten zinc. The samples are seen to react with the molten zinc bath after each stage of dip testing where diffusion is observed to progress into the bulk of the alloy. Phase formation and particle attachment was also observed at the surface. The eutectic regions of the microstructure offered more resistance to the diffusion process whereas the cobalt matrix phase experienced increased levels of diffusion. The diffusion front progressed into the bulk of the alloy through the matrix and subsequent intermetallic phase formation occurred behind it. The depth of diffusion and quantity of the intermetallic phase increased with longer bath immersion times. Figure 5.33 displays the average diffusion depth after each stage of dip testing. The graph indicates that diffusion depth gradually increased after each stage of testing. The average diffusion depth reached 40μm after the first week of testing which increased by around 20μm after each stage of testing to a maximum depth of 95μm. Diffusion depth was fairly uniform after the first week of testing but became more irregular with prolonged testing. This is illustrated in the SEM images and is represented by the larger standard deviation of the diffusion measurements after longer bath exposure.

EDS analysis of a sample after a 2-week dip test is displayed in Figure 5.35. The image highlights a layer beneath the surface of the sample that forms in the matrix which appears to be in different stages of the diffusion process. Spectrum 1 indicates a cobalt-rich (48.1wt.%) area which contains high levels of chromium (21.9wt.%), nitrogen (10.5wt.%) and tungsten (9.5wt.%), and lower levels of zinc (4wt.%). The presence of nitrogen confirms this region is the diffusion layer that formed after the plasma treatment. The survival of the nitrogen layer is also highlighted in the EDS elemental maps after two weeks of testing, as shown in Figure 5.34. Spectrum 2 determines the composition of a phase observed in the similar location of a neighbouring cobalt dendrite to Spectrum 1. However, analysis of this region found it was zinc-rich (41wt.%) with high levels of aluminium (23.1 wt.%), nitrogen (14.9 wt.%), chromium (8.4 wt.%) and tungsten (9.1 wt.%) where only traces of cobalt were detected. This suggests that Spectrum 2 was performed in area that was in a more advanced stage of diffusion and had experienced elevated levels of cobalt depletion whereas Spectrum 1 shows signs of diffusion resistance. Analysis of the area beneath the surface nitride layer (Spectrum 3) shows mainly zinc (73.9 wt.%) with high levels of tungsten (13.3 wt.%) and lower amounts of iron (4.6 wt.%), aluminium (3 wt.%), chromium (2.3 wt.%), silicon (1.5 wt.%) and cobalt (1.4wt.%). Zinc levels decreased moving into the bulk of the alloy which coincided with cobalt levels increasing. Aluminium and iron concentration increased as the diffusion front (Spectrum 6) was approached.

After 4-weeks of testing the diffusion process varied at different locations of the samples surface. Figure 5.36 and Figure 5.38 display elemental mapping of the surface after 4-weeks of bath immersion. Figure 5.36 represents the dominant diffusion process that was observed over the majority of the samples surface and Figure 5.38 displays the diffusion process that was observed in isolated areas. Comparing the images indicates the survival of the nitride layer and that the diffusion occurring at the diffusion front is comparable where it contains increased levels of aluminium and iron. The regions behind the diffusion front becomes depleted in cobalt and chromium which allows for a zinc intermetallic phase to form. However, the images illustrate a clear contrast in diffusion experienced beneath the nitride layer. Inspection of the diffusion layer in the region beneath the nitride layer in Figure 5.38 illustrates a complex diffusion process where there appears to be separate diffusion front within the diffusion layer which has been labelled as D1 in the image. Comparing the elemental maps at this location indicates that the second diffusion front contains high levels of chromium and silicon where a chromium and silicon-rich area is also observed beneath the nitride layer.

Point scan analysis was performed throughout the diffusion layer to produce a clearer indication of the diffusion process experience in both separate diffusion processes which were portrayed in the EDS maps. Figure 5.37 illustrates the diffusion process that dominated the samples surface. Spectrum 1 and Spectrum 2 identify the surface nitride layer where 13.2wt.% and 9.7wt.% nitrogen content was identified, respectively. Spectrum1 detected higher levels of zinc of aluminium and traces of cobalt whereas higher chromium and tungsten levels were detected in Spectrum 2 in additions to low levels of cobalt. The area beneath the nitride layer (Spectrum 3) mainly composed of zinc (75wt.%) with high levels of aluminium (11.3wt.%). Only small amounts of chromium and cobalt were detected in this region. The difference in composition between Spectrums 2 and 3 suggest that the nitride layer is less reactive to the diffusion process and hinders the loss of alloying elements. Moving into the bulk of the alloy results in zinc levels dropping which coincides with an increase in cobalt. Aluminium and iron levels were also observed to increase as the diffusion front (Spectrum 5) was approached. Throughout the diffusion layer there were areas that appeared to have experienced increased levels of diffusion which were observed as the bright regions. Spectrum 6 identifies a region that contains high levels of zinc (53.9wt.%) and tungsten (41.5wt.%) where only small amounts of chromium, aluminium and iron were detected.

Compositional analysis of areas of the diffusion layer that contained a separate diffusion front is presented in Figure 5.39. Spectrum 1 identifies the nitride layer at the surface which contained zinc (49.9wt.%), aluminium (27wt.%), nitrogen (13.6wt.%) and low levels of chromium, tungsten cobalt and iron. The area beneath the nitride layer (Spectrum 2) mainly

consisted of zinc (61.4wt.%) and tungsten (32.1wt.%) with low levels of chromium, cobalt, and aluminium. EDS mapping identified a diffusion front (D1) and a region beneath the nitride layer that contained high levels of chromium and silicon. Point scan analysis confirmed that the secondary diffusion front (Spectrum 3) contained high levels of chromium (66wt.%), tungsten (14.7wt.%) and silicon (12.3wt.%) with low levels of zinc and aluminium. The area between this front and the nitride layer (Spectrum 4) contained high levels of chromium (60.2wt.%), tungsten (18.2wt.%) and silicon (10.3wt.%) with additions of cobalt, zinc, aluminium, and iron. The results demonstrate that the majority of cobalt had been depleted in these locations but due to the high levels of alloying elements, such as chromium and tungsten, there was little bath species detected in these regions. Moving beyond this secondary diffusion front (Spectrum 5) results in a significant increase in zinc (73wt.%) concentrations. Small levels of cobalt, zinc, aluminium, and iron levels were detected whilst tungsten (18.9wt.5) levels remained high. This is due to their atomic size which would reduce their mobility during diffusion. The diffusion front (Spectrum 6) contained increased levels of aluminium (18wt.%) and iron (10wt.%).

After all stages of dip testing the formation and attachment of surface phases and particles was observed. These phases were identified to be CoAl phases (Spectrum 7 in Figure 5.37 and Figure 5.39) or dross particles. The volume and size of the CoAl phases and dross particles appeared to significantly decrease with prolonged testing which suggests diffusion or detachment of the phases. The formation of a CrSi phase was also identified which became more frequent after longer bath exposure times. This phase is clearly visible in the EDS maps presented in Figure 5.36 and is also identified in Figure 5.37. The EDS maps illustrates how formation of the phase at the surface leaves the region beneath significantly depleted in chromium and cobalt.

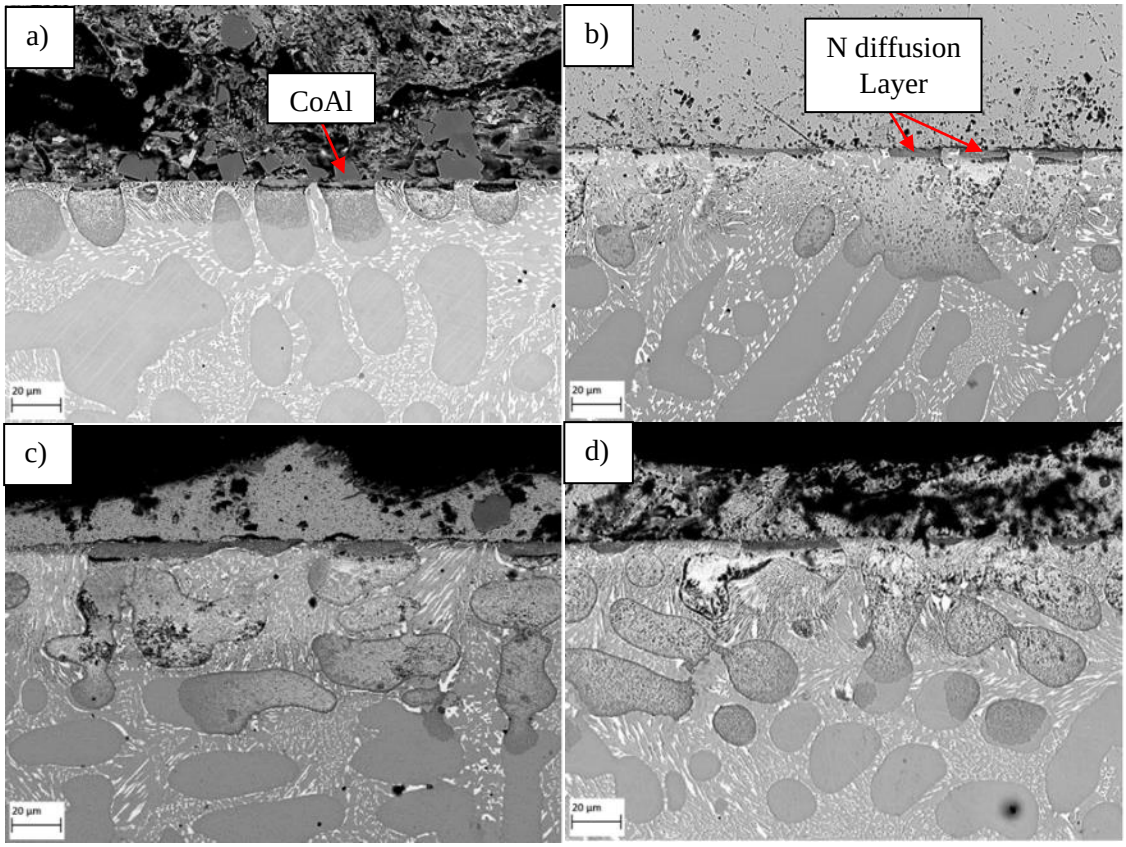

Figure 5.32: Surface condition of the plasma treated WT-4 alloy after 1-4-week dip testing in a molten zinc bath containing 0.35wt.% Al and saturated with Fe: a) Week 1, b) Week 2, c) Week 3 and d) Week 4.

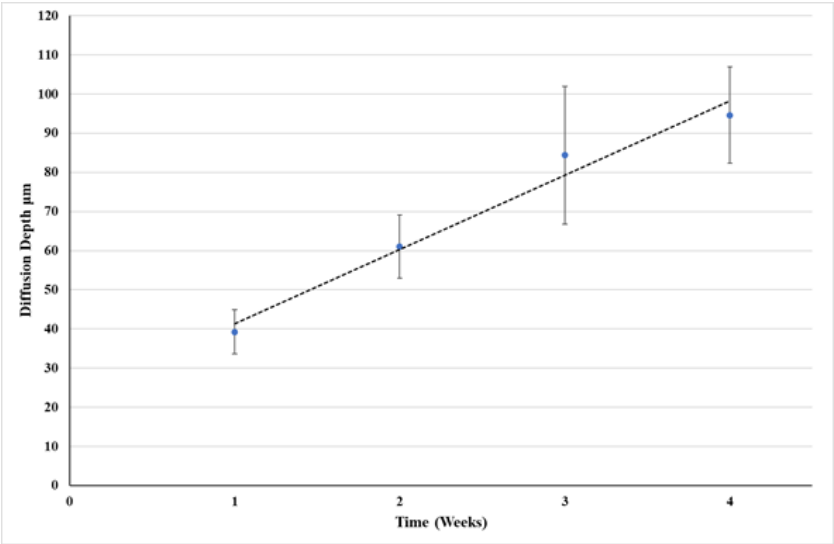

Figure 5.33: Average diffusion depth of the plasma treated WT-4 alloy after prolonged dip testing in a molten zinc bath containing 0.35wt.% Al and saturated with Fe.

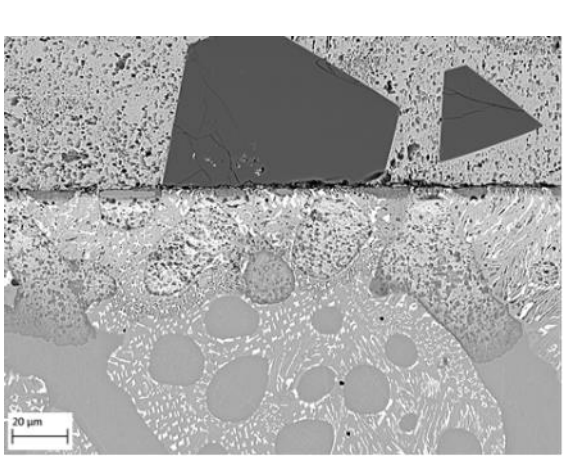

Al K series

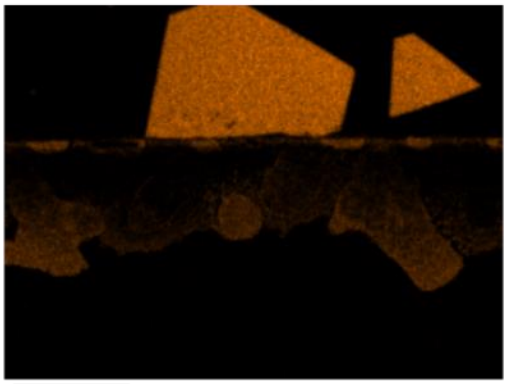

Co K series

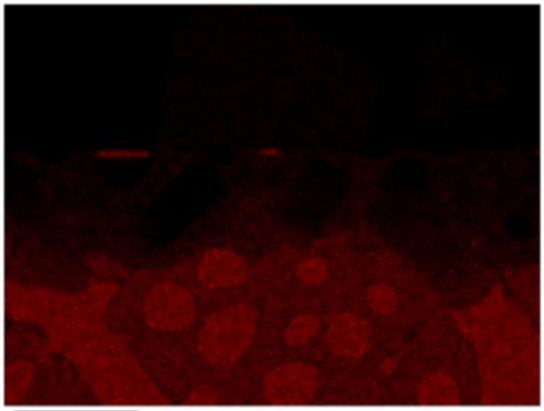

Cr K series

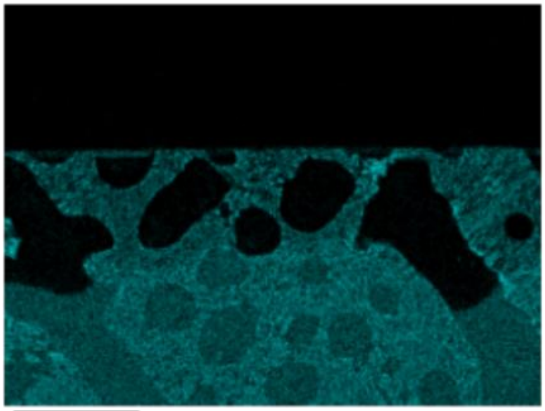

Fe K series

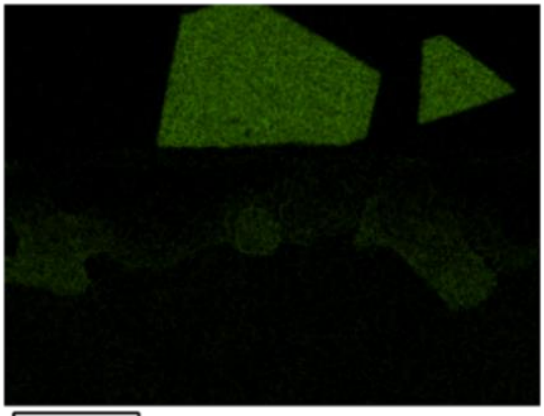

N K series

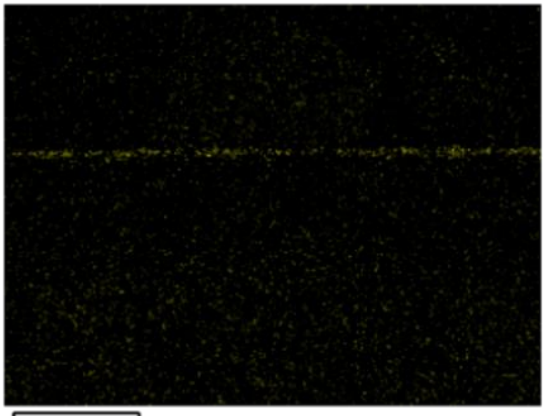

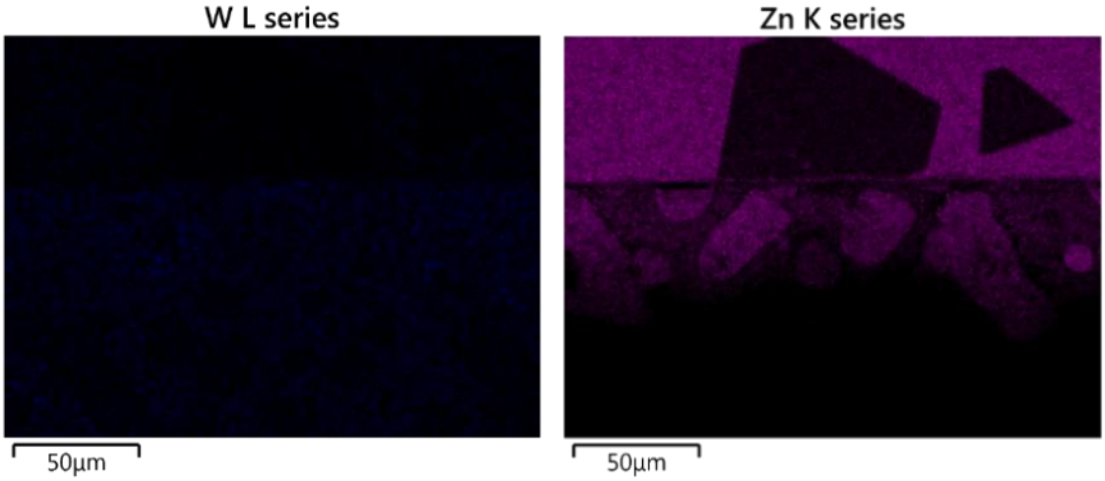

Figure 5.34: EDS elemental mapping of a plasma treated WT-4 alloy after 2-weeks of dip testing in a molten zinc bath containing 0.35wt.% Al and saturated with Fe.

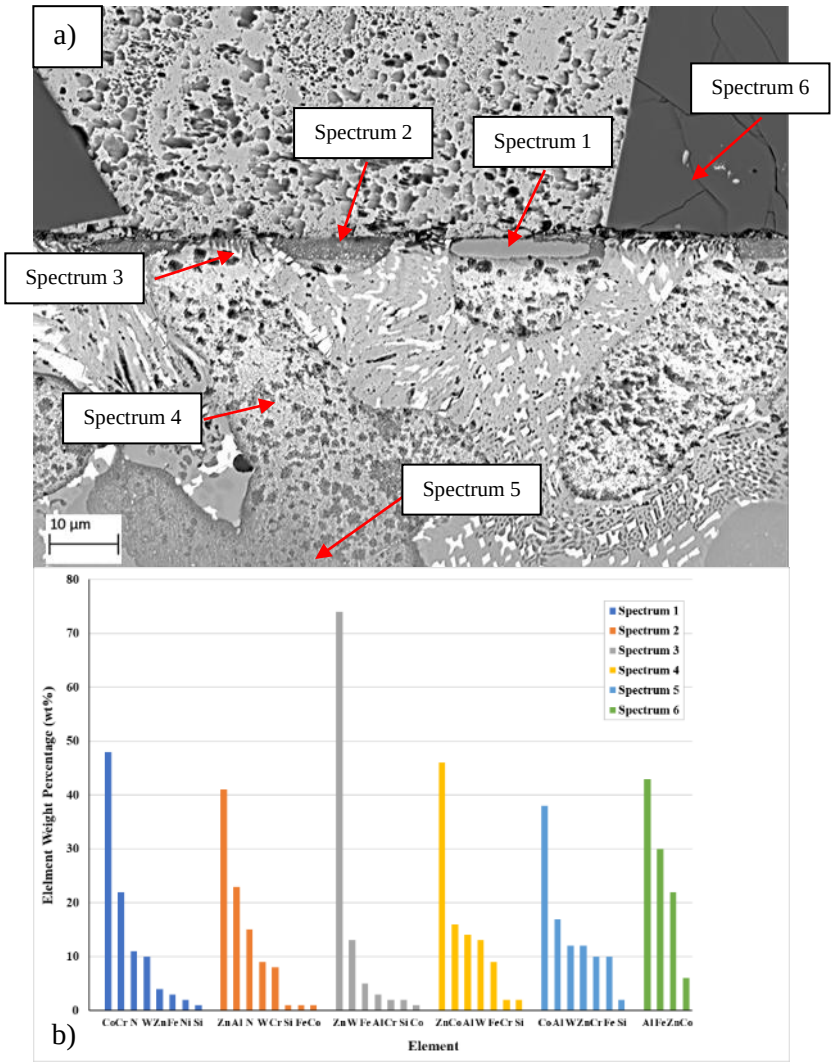

Figure 5.35: EDS point scan analysis of the diffusion zone of the plasma treated WT-4 alloy after 2-weeks of bath immersion: a) Point scan locations and b) Corresponding point scan compositions.

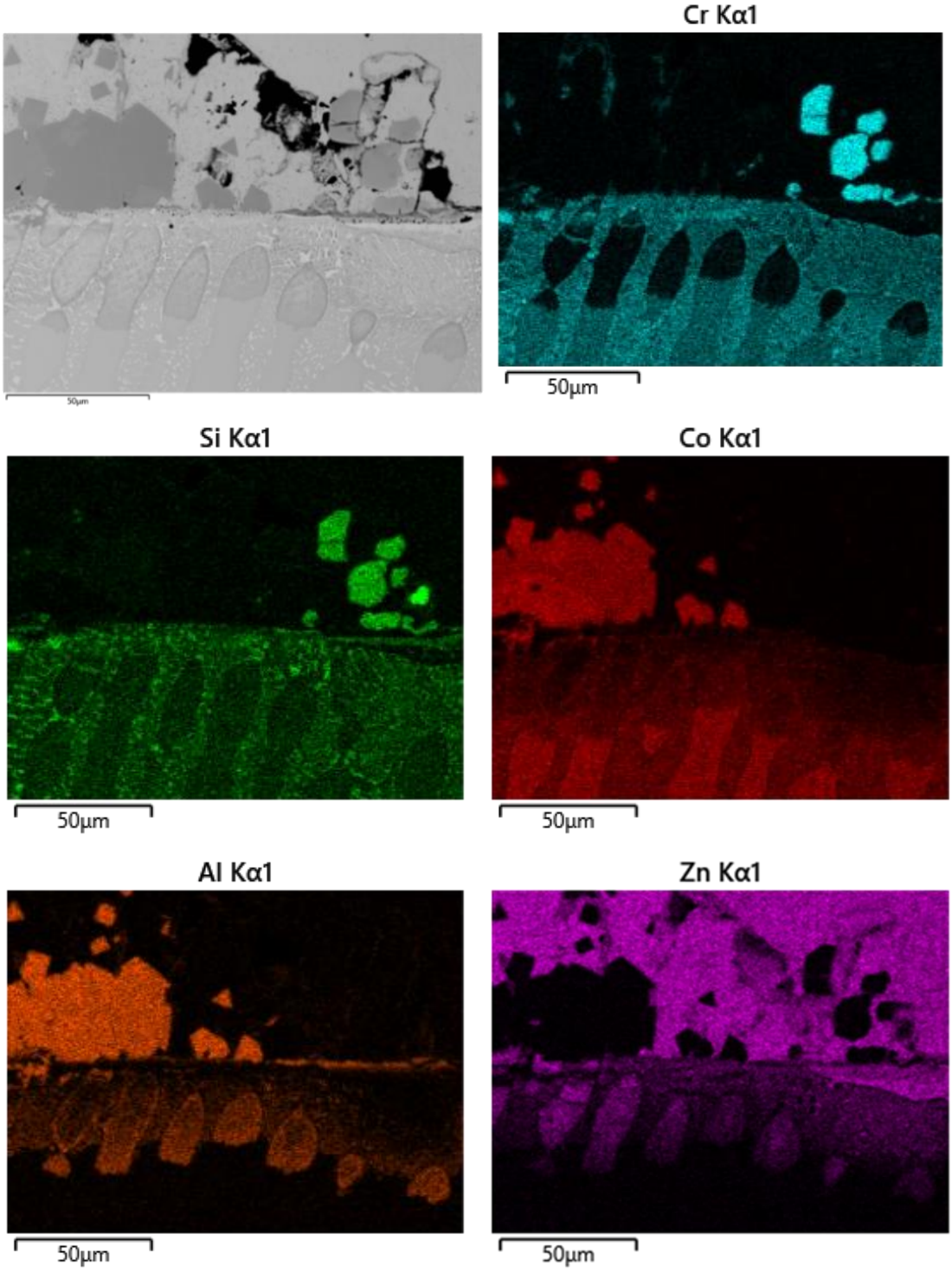
Cr Kα1
50µm
Si Kα1
50µm
Co Kα1
50µm
Al Kα1
50µm
Zn Kα1
50µm

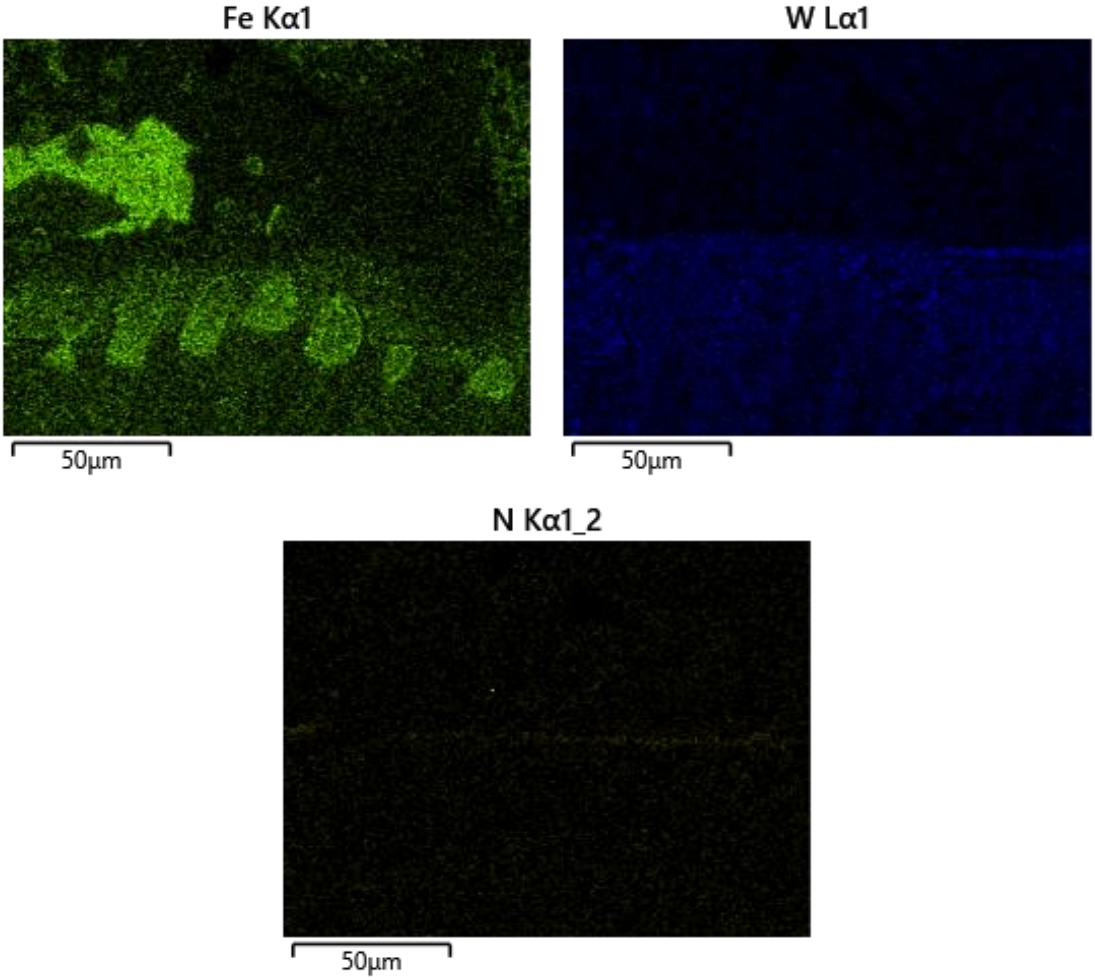

Figure 5.36: EDS elemental mapping of a plasma treated WT-4 alloy after 4-weeks of dip testing in a molten zinc bath containing 0.35wt.% Al and saturated with Fe illustrating the formation of a CrSi phase.

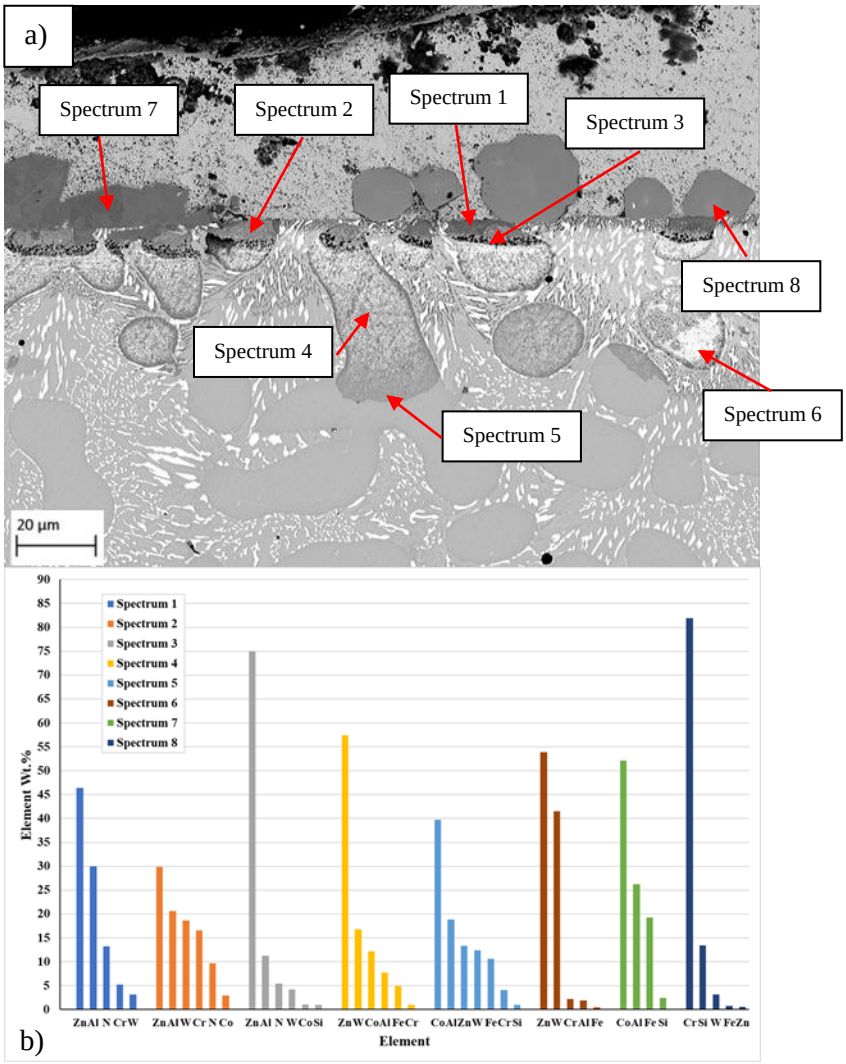

Figure 5.37: EDS point scan analysis of the diffusion zone of the plasma treated WT-4 alloy after 4-weeks of bath immersion: a) Point scan locations and b) Corresponding point scan compositions.

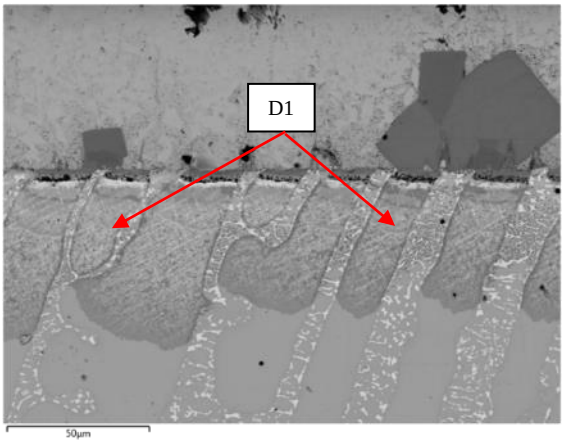
D1
50µm

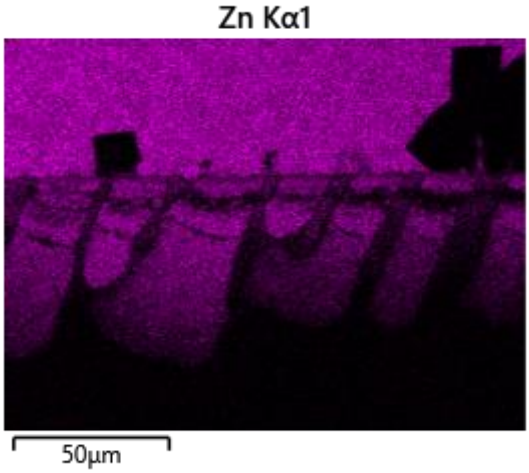
Zn Kα1
50µm

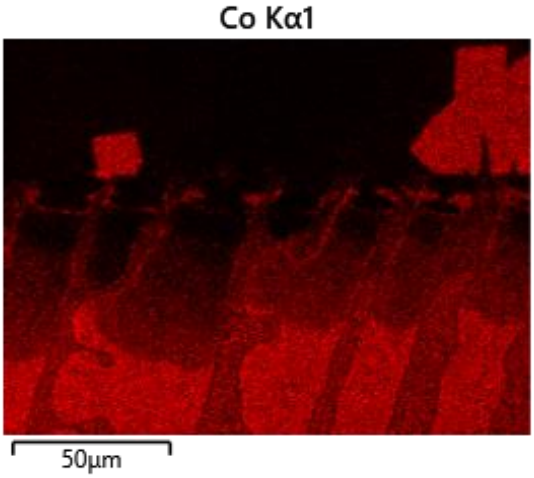
Co Kα1
50µm

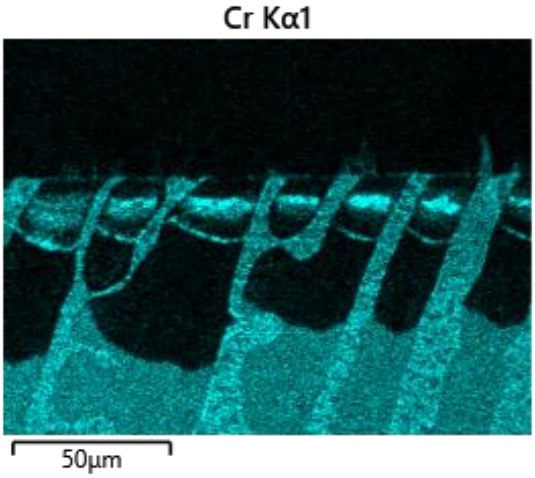
Cr Kα1
50µm

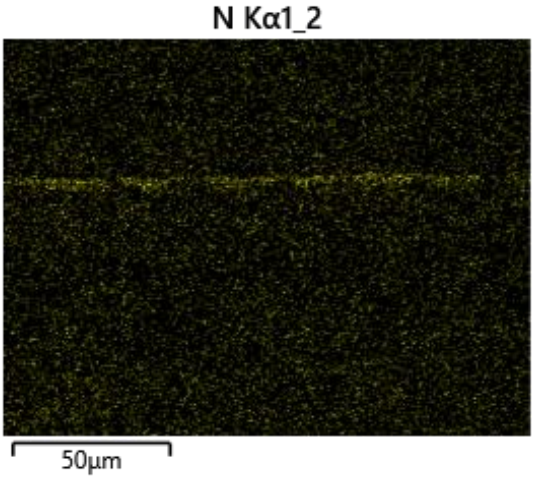
N Kα1_2
50µm

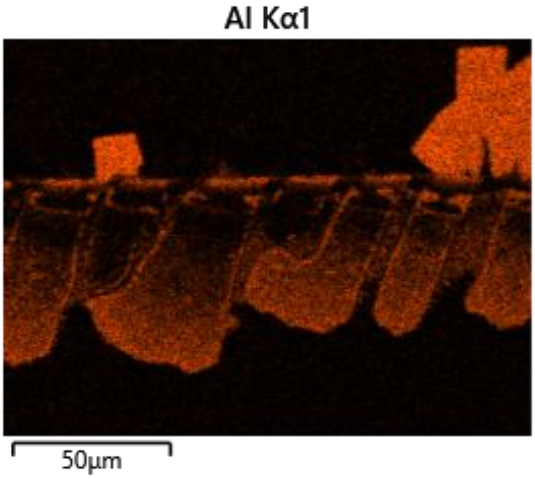
Al Kα1
50µm

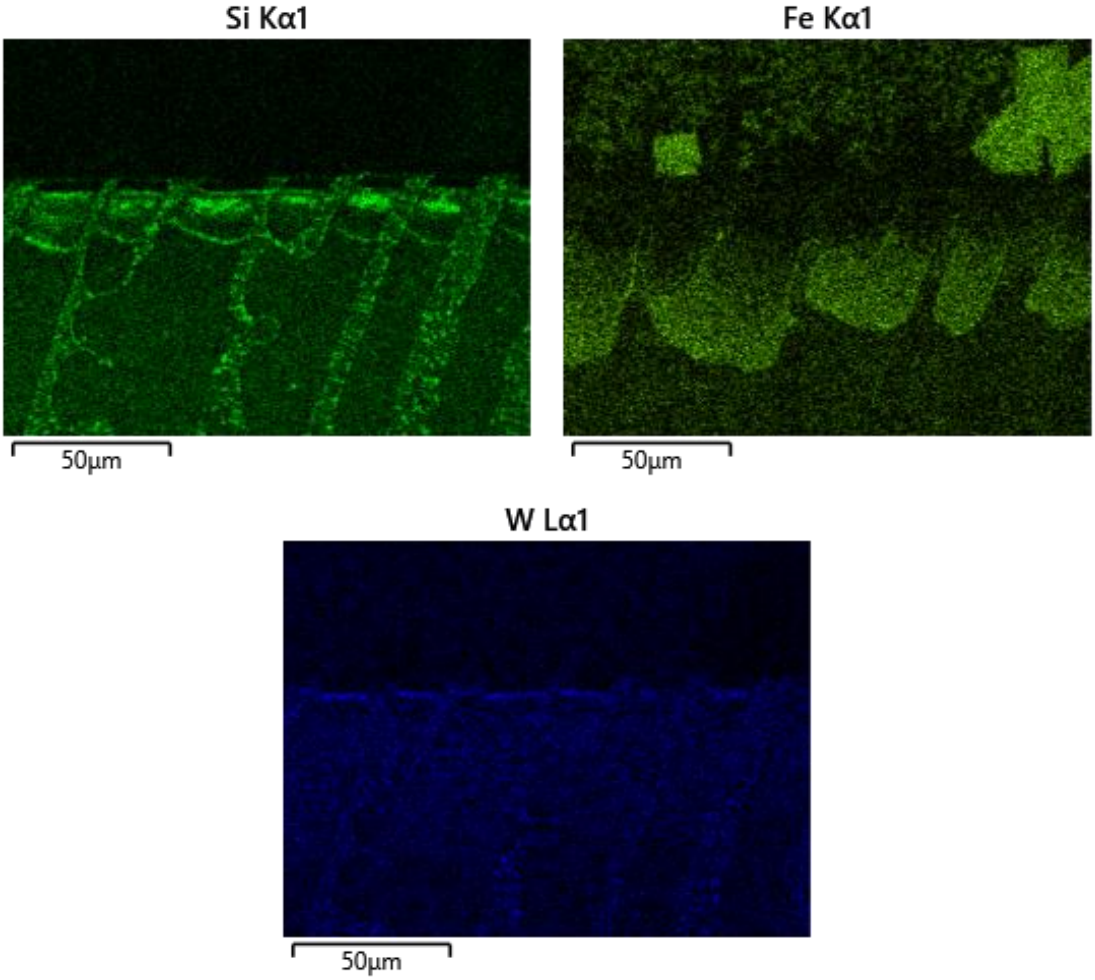

Figure 5.38: EDS elemental mapping of a plasma treated WT-4 alloy after 4-weeks of dip testing in a molten zinc bath containing 0.35wt.% Al and saturated with Fe illustrating an isolated diffusion front (D1) within the diffusion layer.

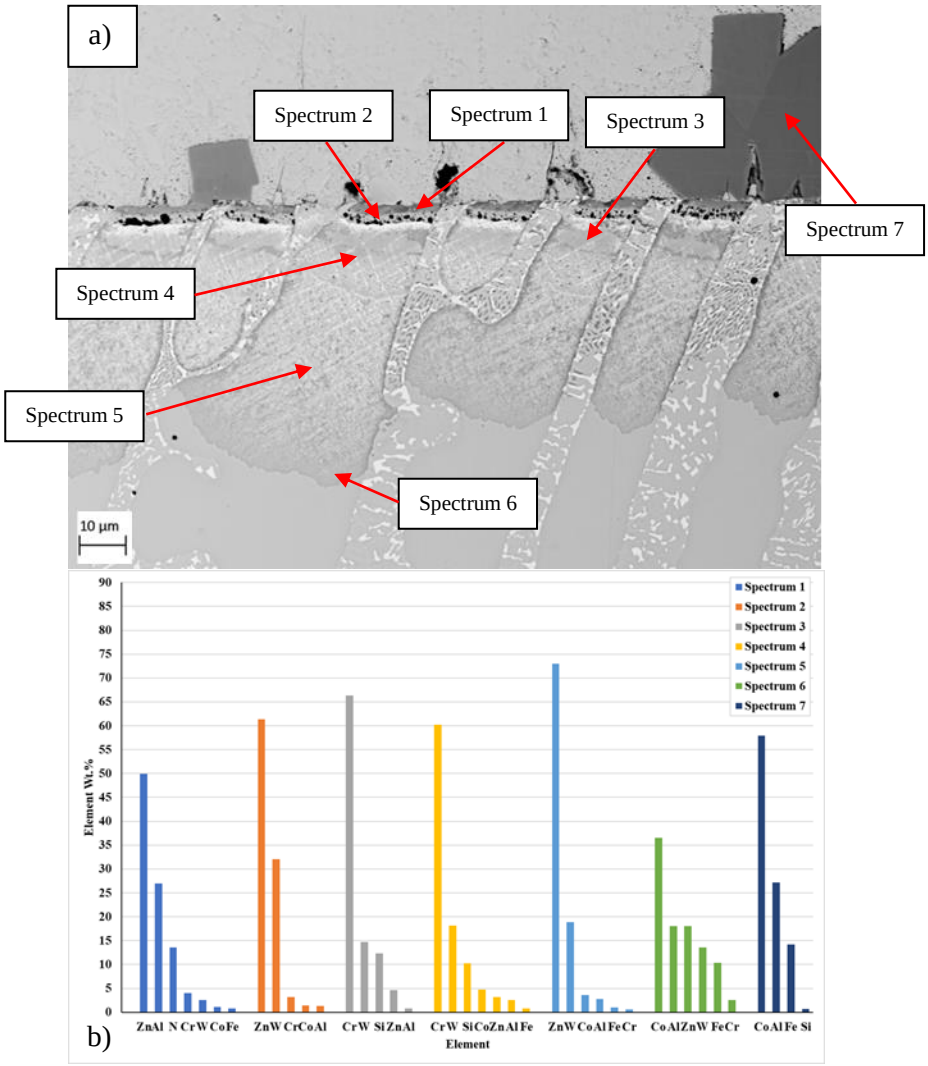

Figure 5.39: EDS point scan analysis of the diffusion zone of the plasma treated WT-4 alloy after 4-weeks of bath immersion: a) Point scan locations and b) Corresponding point scan compositions.

5.6.3 Static Immersion Testing of Plasma Treated WT-12

The surface condition of the treated WT-12 samples after prolonged bath exposure are shown in Figure 5.40. SEM analysis indicates that samples reacted with the molten zinc bath after the first week of dip testing and chemical reactivity continued after each stage of tester. Diffusion was observed to gradually progress through the cobalt matrix where the diffusion depth penetrated deeper into the alloy's microstructure with increased dip time. Initially the diffusion depth was uniform where an average depth of 42µm was reached after the first week of testing. However, increased bath exposure led to increased diffusion depths where average depths of 56µm, 75µm and 92µm were recorded after the second, third and fourth week of testing, respectively. The average diffusion depths reached after each stage of testing is displayed in Figure 5.41. The graph also shows the standard deviation for the diffusion measurements, which demonstrates the

irregular diffusion depths observed from SEM analysis where some areas of the microstructure experienced greater levels of diffusion.

Analysis of the samples revealed that the initial stages of the diffusion process consist of a diffusion front which is followed by the subsequent formation of an intermetallic phase behind it as cobalt and chromium are depleted from the alloy. The onset of the diffusion front is visible in Figure 5.40a and the formation of the intermetallic phase can is observed in Figure 5.40b. The quantity of this phase becomes more evident with longer dip times as the zinc intermetallic phase occupies larger areas of the diffusion layer, as shown in Figure 5.40c+d. The images also highlight the nitride layer beneath the surface of the sample. In addition to diffusion occurring beneath the surface of the samples after each stage of testing, formation and the attachment of phases and particles also occurred at the surface.

EDS mapping of a sample after 2-weeks of bath exposure is displayed in Figure 5.42. The image highlights how the diffusion front contains high levels of aluminium and iron and that the matrix region behind it becomes depleted in cobalt and chromium and enriched in zinc. The maps also highlight the nitride layer at the surface which appears to contain concentrated levels of aluminium, zinc, and chromium. Point scan analysis of this area is displayed in Figure 5.43. It was confirmed that the nitride layer at the surface had reacted with the bath. Spectrum 1 indicates that the nitride layer remained at the surface but reacted with the elements in the bath. 13.3wt.% nitrogen content was detected in addition to high levels of zinc (49.8wt.%) and aluminium (21wt.%). The nitride layer also contained levels of chromium (8.3wt%) and tungsten (3.9wt.%) but only traces of cobalt were detected. The region beneath the nitride layer consisted mainly of zinc (77.9wt.%) with high levels of tungsten (11.9wt.%) and small amounts of iron, aluminium, silicon, and chromium. No cobalt was detected in this region which indicates its diffusion into the bath or formation of CoAl phases at the surface. Further point scans of the diffusion layer confirmed that moving into the bulk of the alloy results in zinc level decreasing and an increase in aluminium and iron levels as the diffusion front was approached.

Elemental mapping highlighted the survival of the nitrogen layer after 4-weeks of testing, as shown in Figure 5.44. A similar diffusion process experienced with shorter dip times is observed after prolonged testing, but the depth of diffusion is much greater, and the level of intermetallic phase formation is more extreme where most of the diffusion layer has transformed into the zinc-rich phase. Analysis of the nitride layer, which remained present at the surface, revealed that the composition was similar to the composition recorded after 2-weeks of testing. This is illustrated by comparing Spectrum 1 in Figure 5.43 (2-week test) and Spectrum 1 in Figure 5.45 (4-week test). It was identified that the region is zinc-rich (52.6wt.%) with high levels of aluminium (23.3wt.%) and nitrogen (10.3wt.%) in addition to small quantities of chromium,

tungsten, silicon, and cobalt. After this stage of bath exposure, large areas of the diffusion layer has transformed into a zinc-rich intermetallic phase, as shown in Figure 5.40d and Figure 5.45a. Inspection of the intermetallic phase highlights isolated regions that persist within the phase. These regions are highlighted in Figure 5.45b which display the calculated composition of the areas. Spectrum 3 identifies a region that is consists mainly of zinc (67wt.%) and tungsten (27.5wt.%) and has low levels of aluminium, chromium, and iron. Analysis of the light grey regions (Spectrum 4) identified areas of the diffusion layer which are almost entirely zinc based (96wt.%) where only traces of other elements were detected. This indicates how tungsten experiences lower levels of diffusion, which is most likely due to its large atomic size, and that by this stage of bath exposure the exhaustion of alloying elements is almost completely replaced by zinc. Dark grey areas (Spectrum 5) were also observed and were found to contain high levels of cobalt (30.2wt.%), zinc (29.9wt.%) and aluminium (18.9wt.%) and often persisted in close proximity to carbide phases. Zinc levels decreased moving towards to the diffusion front which coincided with aluminium and iron levels increasing as aluminium continued to diffuse into the alloy.

After all stages of dip testing CoAl phases and dross particles were seen to form and attach to the surface of the samples. However, the frequency of these phases decreased with prolonged testing. The formation of a CrSi phase was also recorded which became more frequent with increased testing. The formation of this phase is illustrated in Figure 5.44 and the composition is calculated in Figure 5.45 (Spectrum 6).

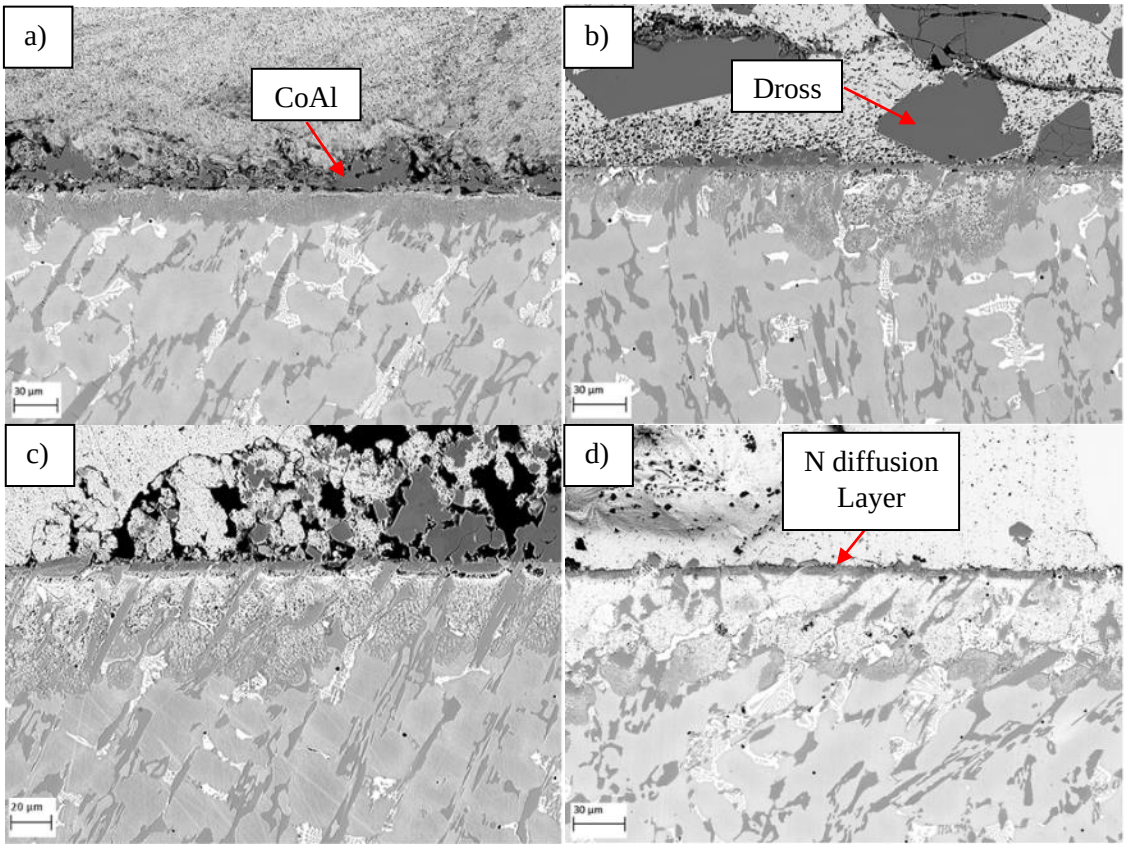

Figure 5.40: Surface condition of the plasma treated WT-12 alloy after 1-4-week dip testing in a molten zinc bath containing 0.35wt.% Al and saturated with Fe: a) Week 1, b) Week 2, c) Week 3 and d) Week 4.

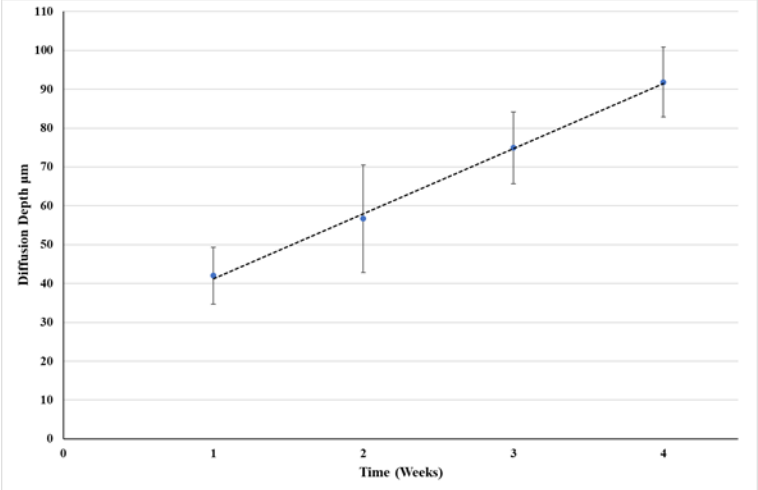

Figure 5.41: Average diffusion depth of the plasma treated WT-12 alloy after prolonged dip testing in a molten zinc bath containing 0.35wt.% Al and saturated with Fe.

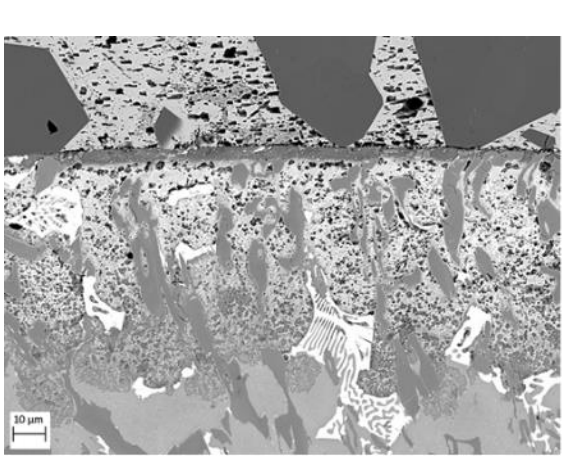

Al K series

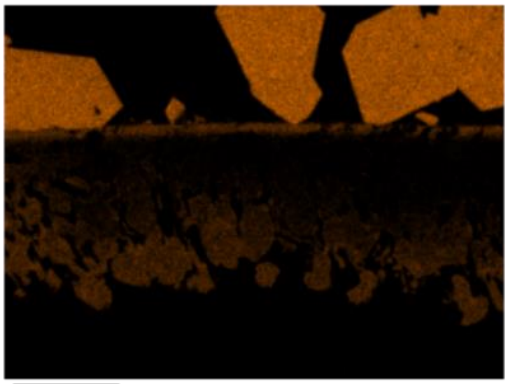

Co K series

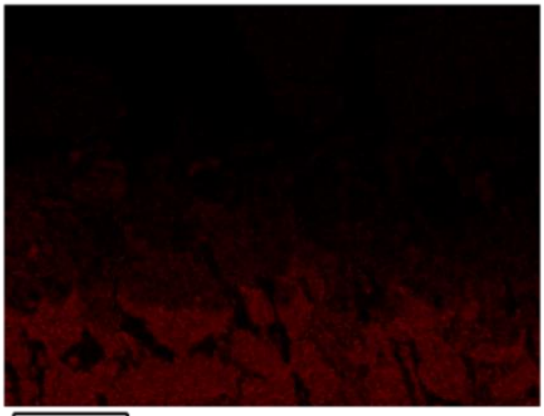

Cr K series

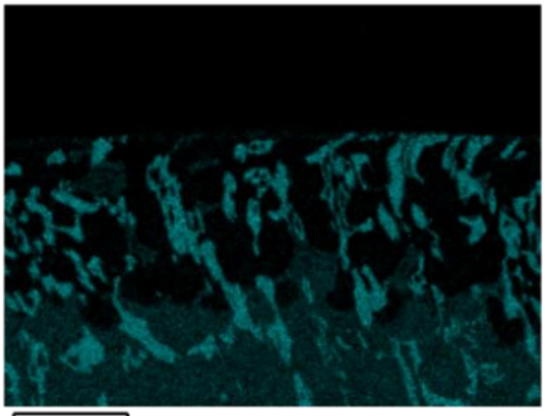

Fe K series

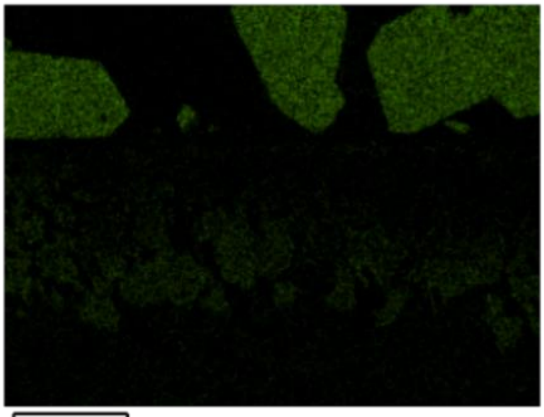

N K series

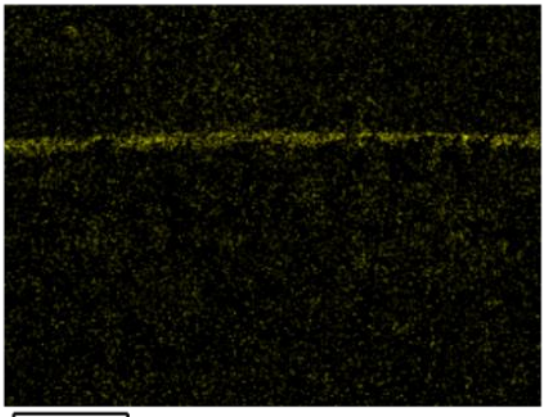

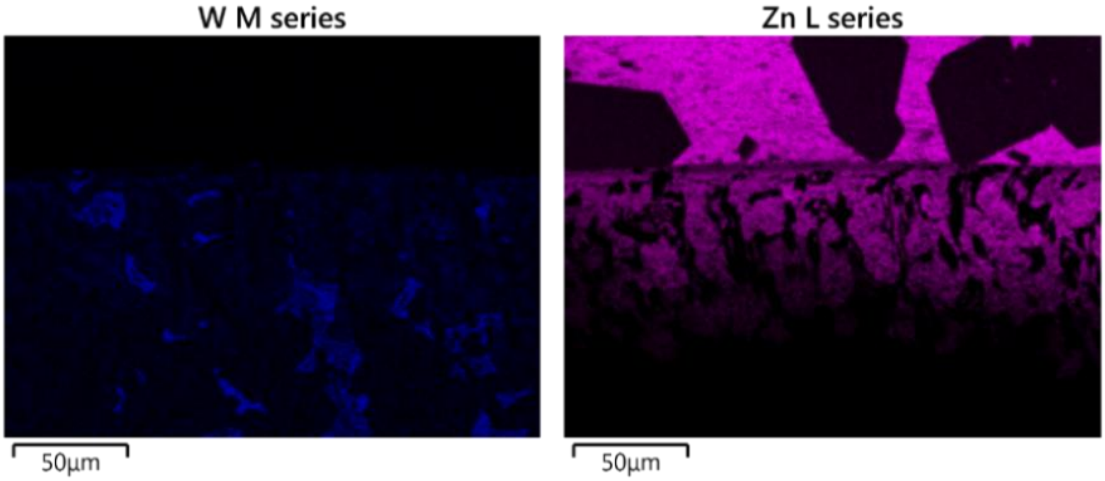

Figure 5.42: EDS elemental mapping of a plasma treated WT-12 alloy after 2-weeks of dip testing in a molten zinc bath containing 0.35wt.% Al and saturated with Fe.

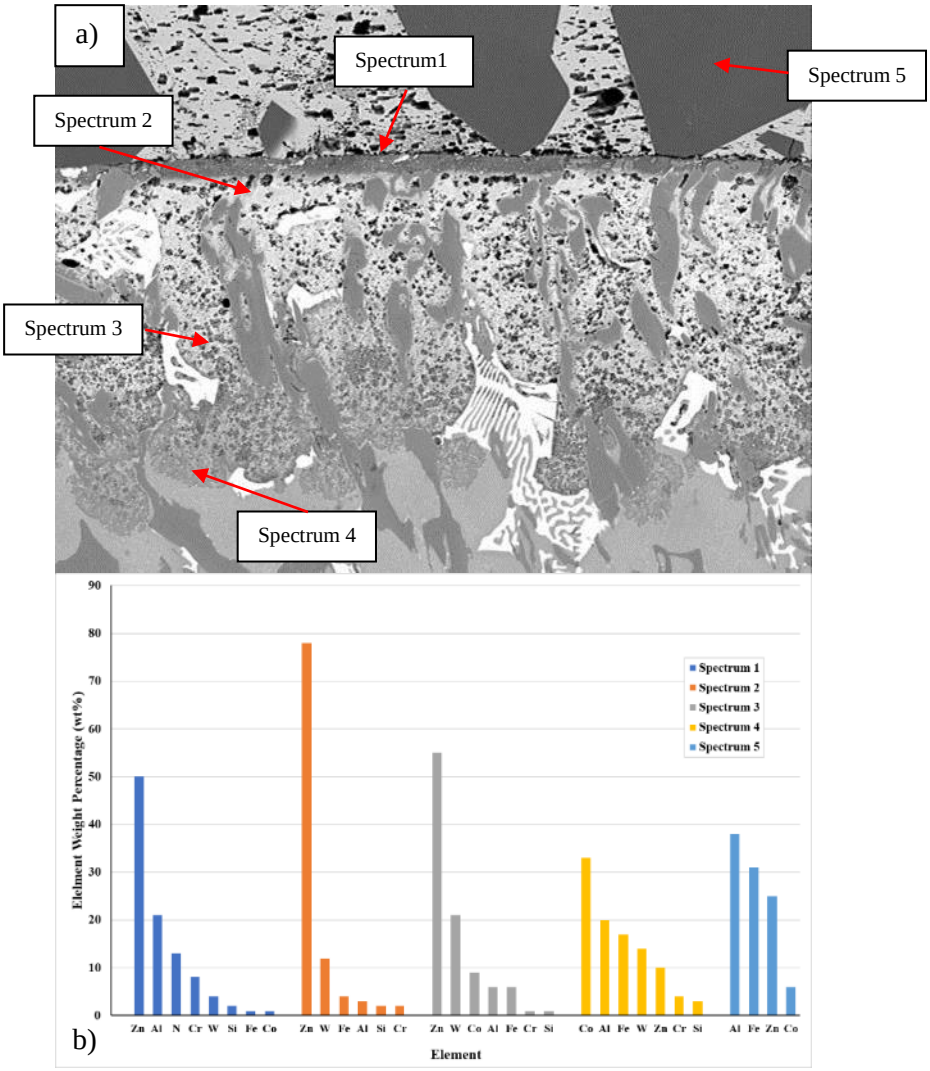

Figure 5.43: EDS point scan analysis of the diffusion zone of the plasma treated WT-12 alloy after 2-weeks of bath immersion: a) Point scan locations and b) Corresponding point scan compositions.

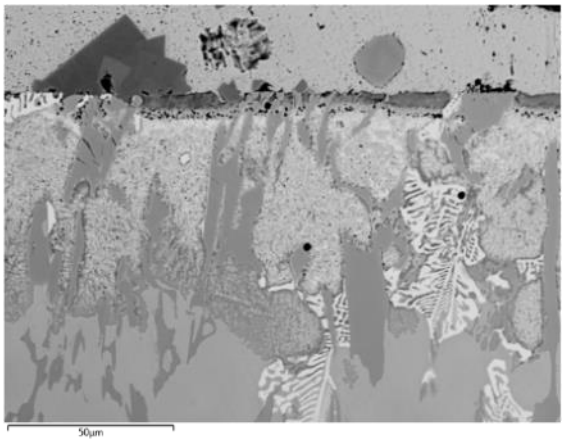

Co Kα1

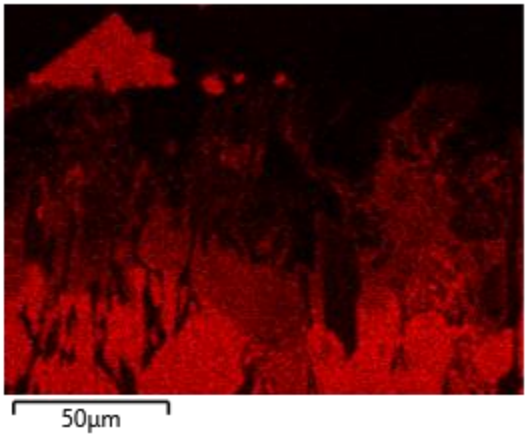

Cr Kα1

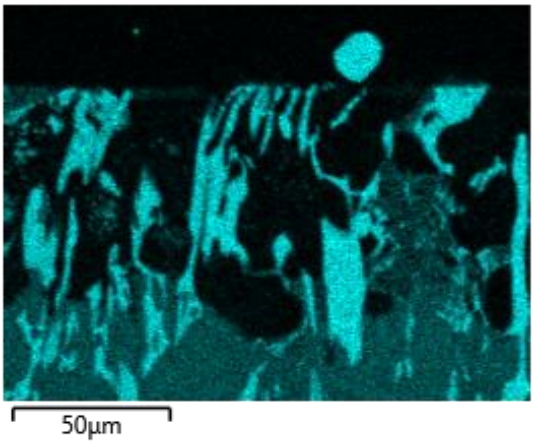

Zn Kα1

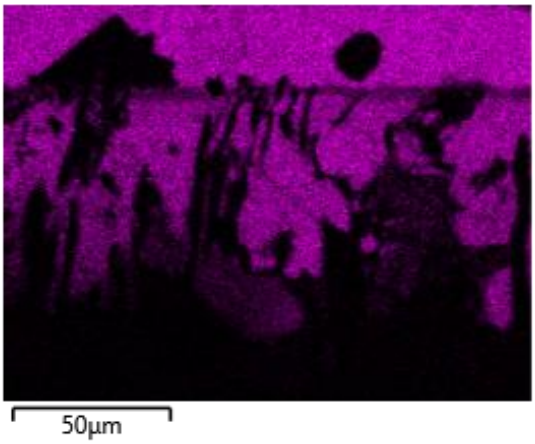

Al Kα1

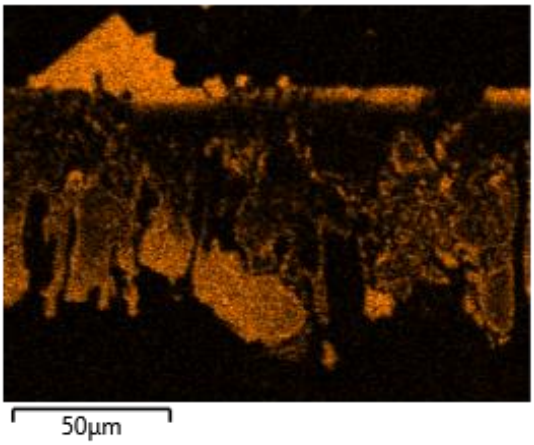

Si Kα1

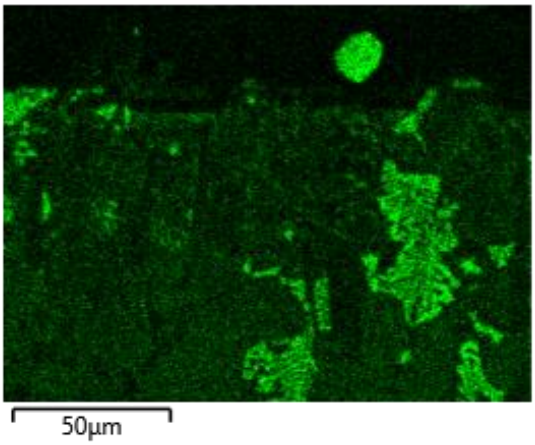

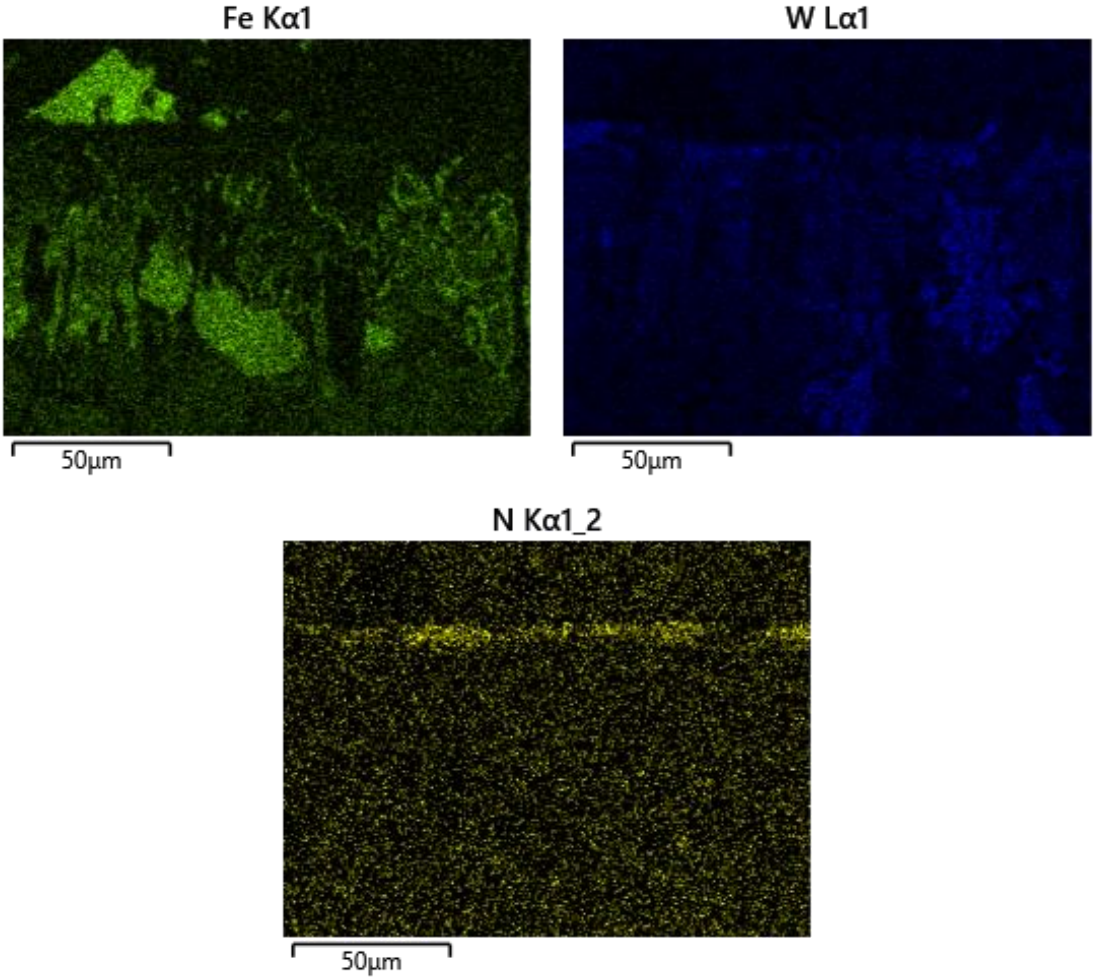

Figure 5.44: EDS elemental mapping of a plasma treated WT-12 alloy after 4-weeks of dip testing in a molten zinc bath containing 0.35wt.% Al and saturated with Fe.

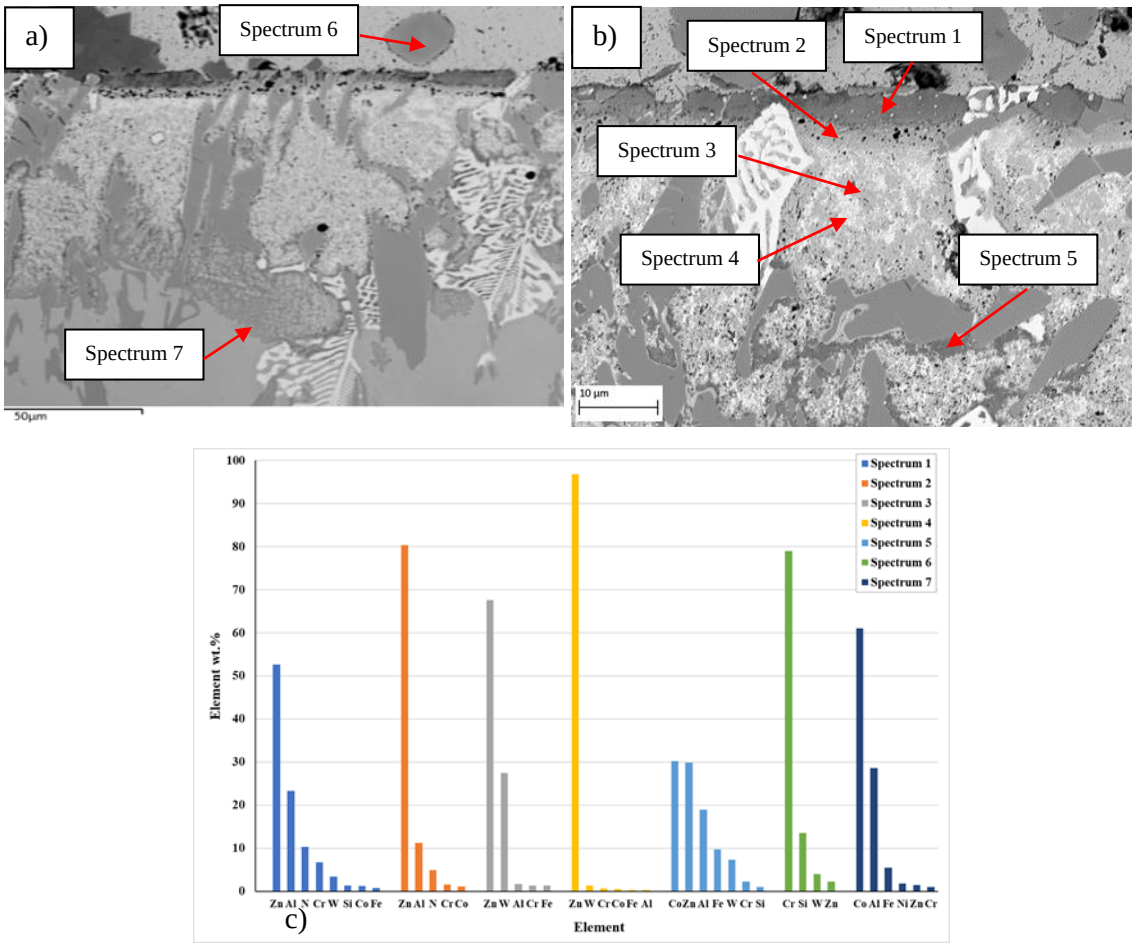

Figure 5.45: EDS point scan analysis of the diffusion zone of the plasma treated WT-12 alloy after 4-weeks of bath immersion: a+b) Point scan locations and c) Corresponding point scan compositions.

5.6.4 Static Immersion Testing of Plasma Treated T-800 Tribaloy

Cross sections of dip tested treated T-800 samples are displayed in Figure 5.46 which illustrate how the samples reacted with the molten zinc bath after each stage of testing. Despite the formation of a nitride layer after plasma treating the sample, the alloy readily reacted with the bath after the first week of testing. Analysis demonstrated that the Laves phase resisted the diffusion process whereas the eutectic solid solution was more susceptible to diffusion and was the preferred route for molten metal ingress. A shallower diffusion layer was observed in the earlier stages of dip testing but by the third and fourth week of testing large areas of the cobalt matrix had experienced levels of diffusion which consequently resulted in the formation of intermetallic phases behind the diffusion front.

The average diffusion depths after each stage of testing are shown in Figure 5.47. Diffusion reached an average depth of 23µm after the first week of testing which gradually

increased after each stage of testing where a maximum average of 75μm was measured after the fourth week of testing. It is worth noting that the maximum diffusion depth was measured from the greatest point of diffusion reached in the microstructure. After each test it was observed that diffusion often occurred at the eutectic matrix and Laves phase interface where deeper penetration occurred in these regions, as shown in Figure 5.46a+b. Therefore, large diffusion depths were often recorded in isolated regions of the microstructure whereas large sections of the matrix closer to the surface were less affected by the diffusion process. This resulted in larger average diffusion depths being produced which could potentially exaggerate the severity of diffusion if the figures were looked at independently.

Elemental concentration maps of a sample tested for 2-weeks (Figure 5.48) highlights the nitride layer beneath the surface of the sample which correlates to the SEM images where the layer can be observed as a darker grey region beneath the surface. The maps demonstrate how the matrix becomes depleted in cobalt and chromium as aluminium, zinc and iron diffuses into the alloy's microstructure. The composition of the diffusion layer at various locations is displayed in Figure 5.49. Analysis confirmed the survival of the nitride layer (Spectrum 1) where 12wt.% nitrogen content was detected. This region contained high levels of zinc (45wt.%) and aluminium (23.9wt.%) and relatively high levels of chromium (10.3wt.%). Only small amounts of cobalt were detected in this region which suggests it had been leached out of the alloy. Spectrum 2 recorded a slight decrease in zinc concentration (36wt.%) whereas aluminium (25wt.%) levels remained at a similar concentration recorded at the surface. This area of the diffusion layer was almost completely depleted in cobalt (2wt.%) whereas molybdenum (29.8wt.%) levels increased significantly which coincided with a significant drop in chromium content (1.2wt.%). The depletion of cobalt illustrates that large region of the eutectic matrix experienced high levels of cobalt diffusion which would have been lost into the bath as there was little evidence of CoAl formation at the surface of the sample. The drop in chromium concentration suggests that chromium diffuses towards the surface of the sample whereas molybdenum is less mobile and is therefore more resistant to the diffusion process. Compared to the standard composition of the matrix, the diffusion front (Spectrum 3) contained significantly less cobalt and chromium which confirms they are more susceptible to diffusion. Zinc (22.6wt.%) levels decreased at the diffusion front whilst aluminium (20wt.%) and iron (9wt.%) content remained high.

Elemental mapping of the diffusion layer after a 4-week dip test is presented in Figure 5.50. Analysis of the sample indicates a similar diffusion process that was experienced after shorter periods of bath exposure. However, the depth of diffusion and the volume of intermetallic phase formation is greater. Two distinct regions within the diffusion layer were observed after longer testing which are observed as lighter and darker grey areas. Correlating these regions to

the EDS maps highlight isolated areas of diffusion layer that contain high concentrations of chromium. The EDS maps indicate that the nitride layer at the surface of the sample which indicates there was minimal signs of material loss. Large areas of the diffusion layer are observed to become depleted in cobalt and chromium which is replaced with zinc, aluminium, and iron where iron concentrations appear to be greatest at the diffusion front. The composition of the diffusion layer at various locations after 4-weeks of testing is displayed in Figure 5.51. Spectrum 1 indicates the region at the surface still contained relatively high levels of nitrogen (8.8wt.%) High levels of zinc (59.7wt.%) and aluminium (19.9wt.%) and low levels of molybdenum (7.2wt.%), chromium (2.5wt.%) and cobalt (1.3wt.%) were also detected in the nitride layer. Spectrums 2 and 3 were performed in similar regions of the diffusion layer and determined the composition of the lighter and darker regions that were observed. Spectrum 2 indicates the region beneath the nitride layer contains significantly less zinc (31.4wt.%) whilst only a slight drop in aluminium (16.9wt.%) was recorded. High concentrations of chromium (20.6wt.%) and molybdenum (20.2wt.%) were also detected. Spectrum 3 illustrates that the darker regions are chromium-rich (28.5wt.%) and contain relatively high levels of silicon (6.2wt.%). It was revealed that both areas contained low levels cobalt which indicates the loss of the element into the bath. At the diffusion front (Spectrum 4) high levels of aluminium (22.1wt.%) and iron (7.4wt.%) and low levels of zinc (10.3wt.%) was identified. This confirms that the initial diffusion of aluminium and iron into the alloy is subsequently followed by zinc diffusion. Due to its atomic size and reduced mobility, relatively high levels of molybdenum were detected throughout the diffusion layer.

Only small quantities of CoAl phase formation at the surface were witnessed after all stages of testing. Zinc-rich phases were also discovered after all stages of testing that contained low quantities of molybdenum, cobalt and chromium which can be attributed to the elements diffusing out from the alloy. The detection of molybdenum demonstrates that although the element was generally more resistant to diffusion, small quantities were leached from the alloy into the bath.

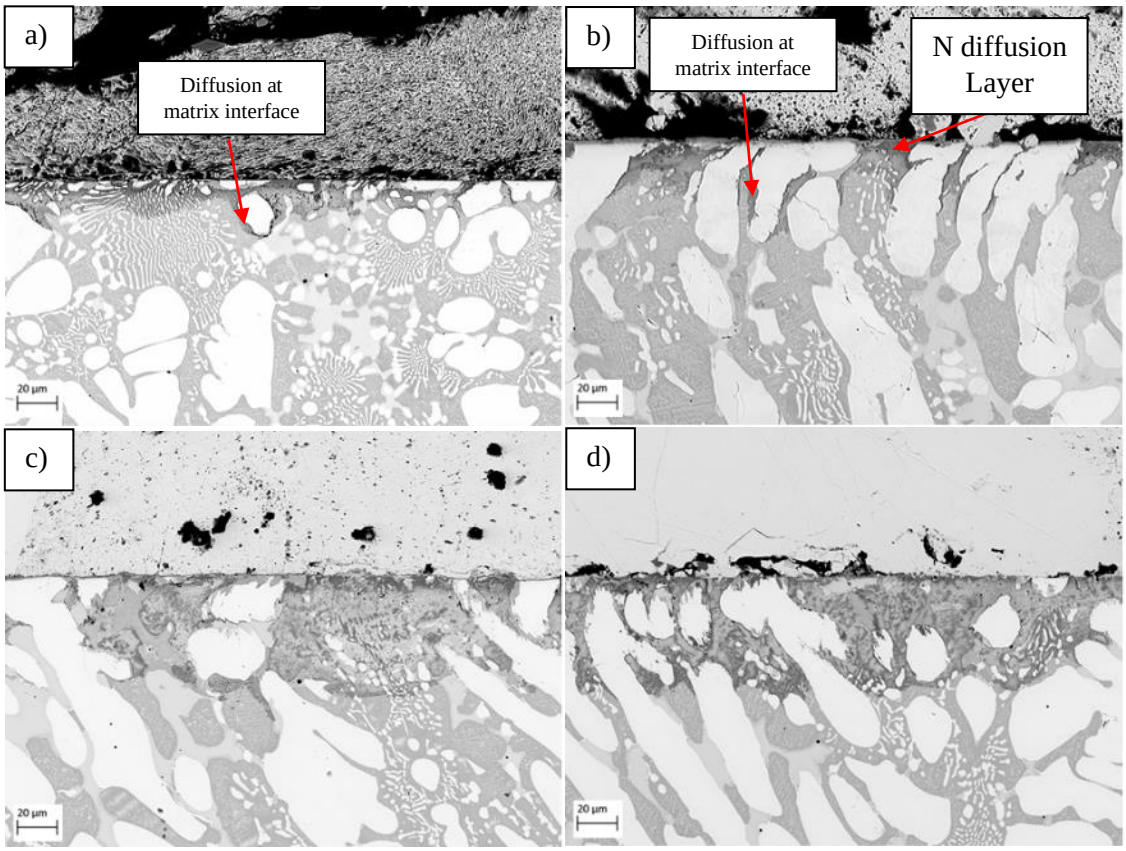

Figure 5.46: Surface condition of the plasma treated T-800 Tribaloy after 1-4-week dip testing in a molten zinc bath containing 0.35wt.% Al and saturated with Fe: a) Week 1, b) Week 2, c) Week 3 and d) Week 4.

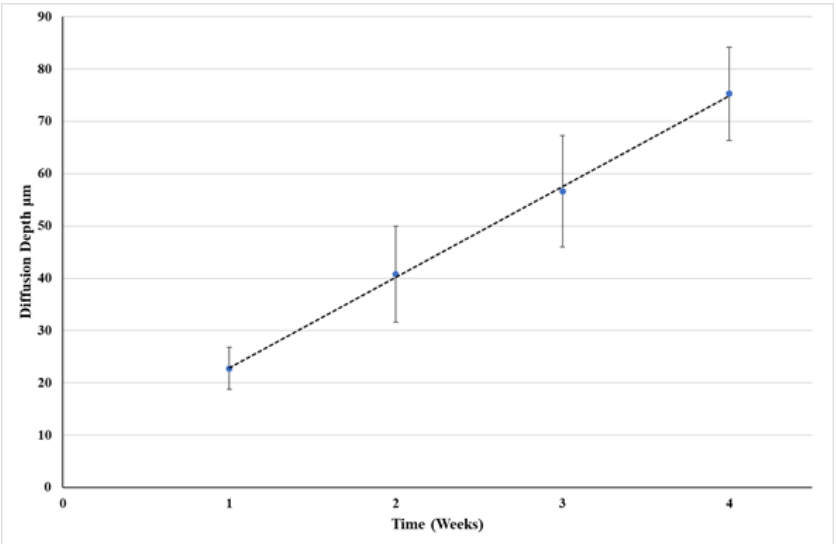

Figure 5.47: Average diffusion depth of the plasma treated T-800 Tribaloy after prolonged dip testing in a molten zinc bath containing 0.35wt.% Al and saturated with Fe.

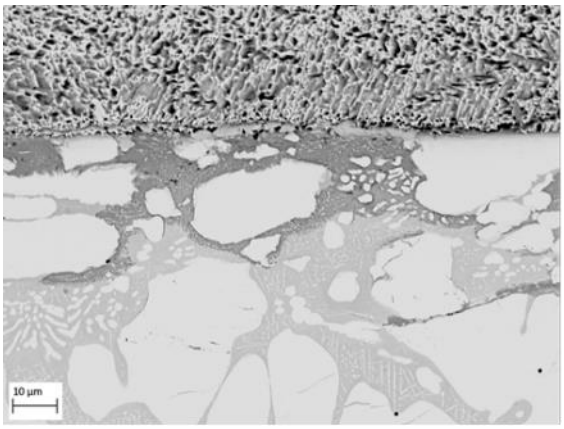

Co K series

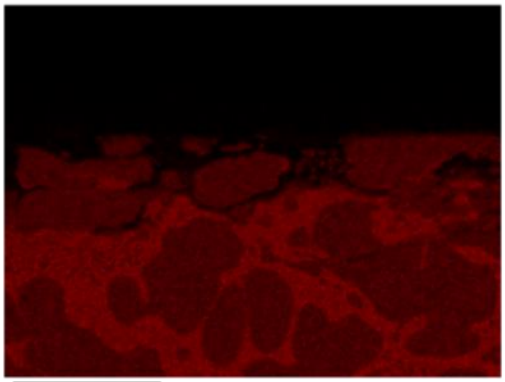

Cr K series

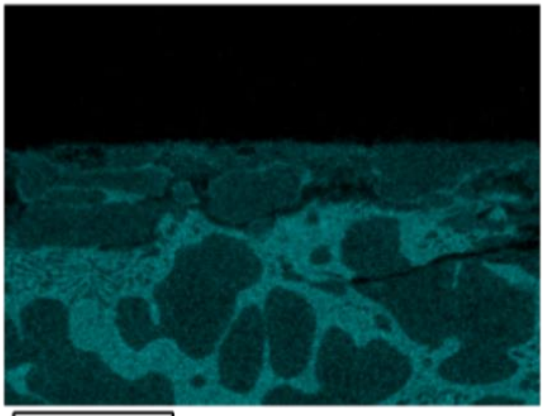

Mo L series

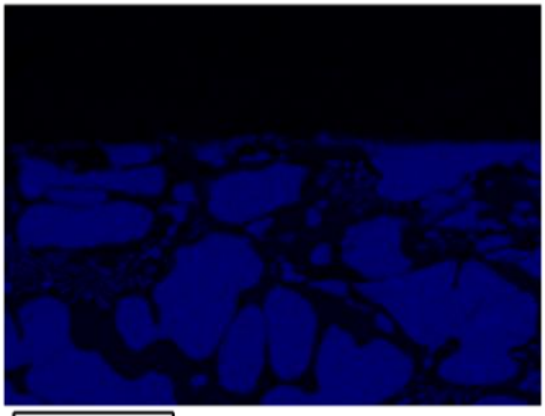

Al K series

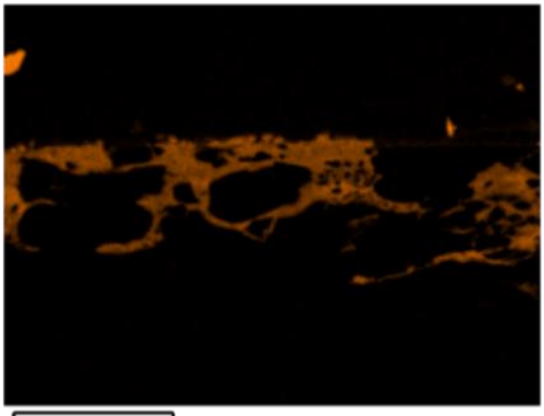

N K series

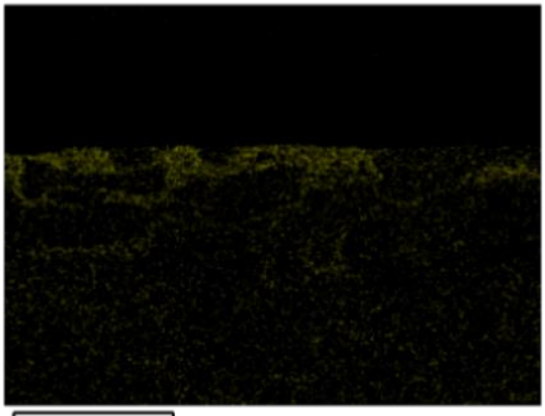

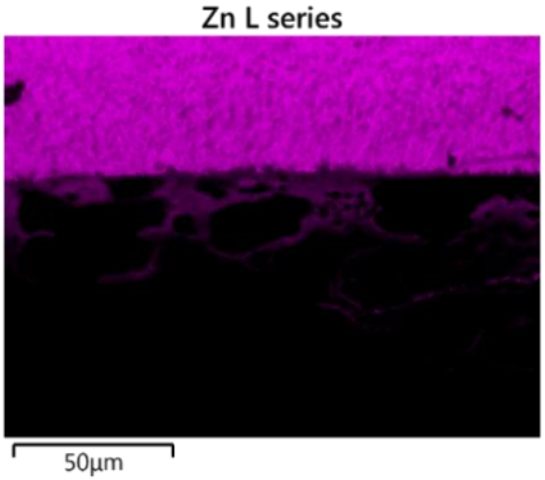

Figure 5.48: EDS elemental mapping of a plasma treated T-800 Tribaloy after 2-weeks of dip testing in a molten zinc bath containing 0.35wt.% Al and saturated with Fe.

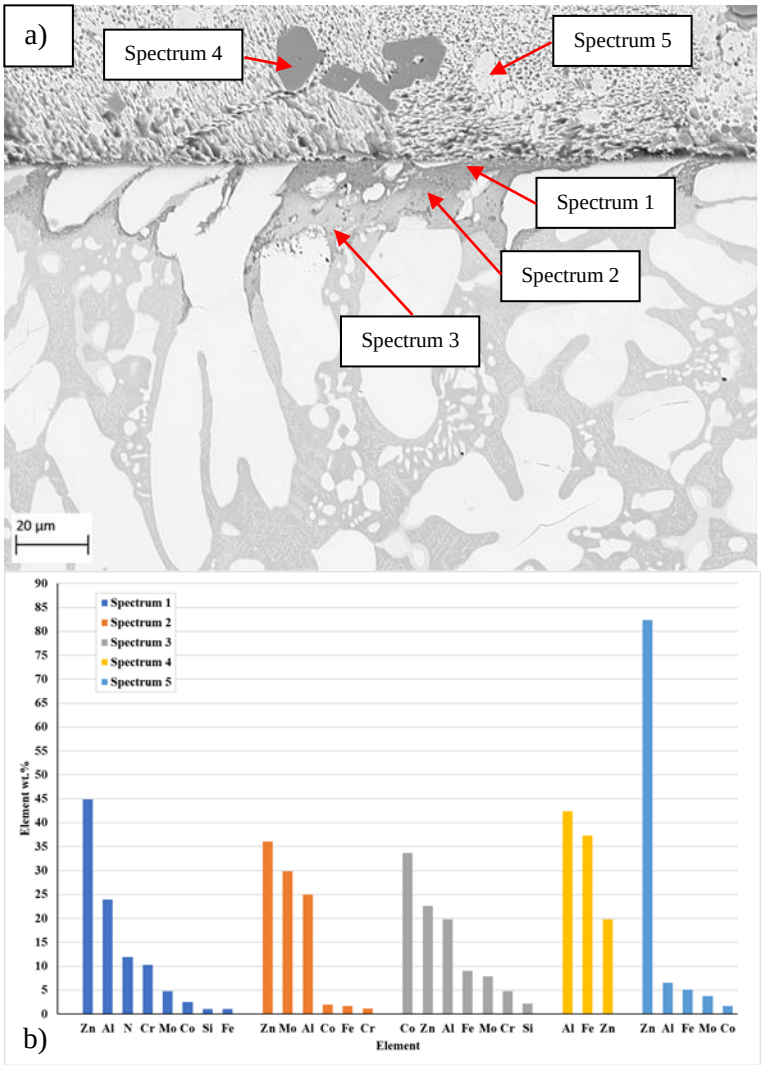

Figure 5.49: EDS point scan analysis of the diffusion zone of the plasma treated T-800 Tribaloy after 2-weeks of bath immersion: a) Point scan locations and and b) Corresponding point scan compositions.

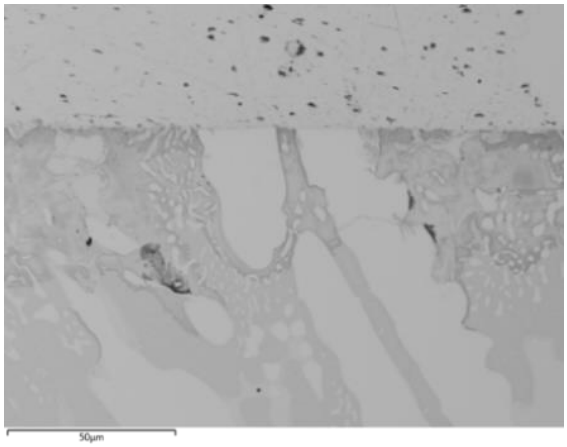

Co Kα1

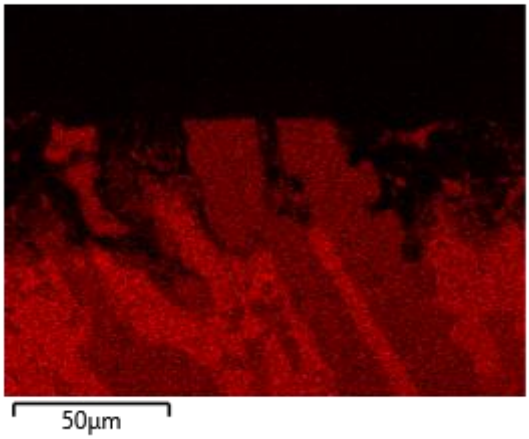

Mo Lα1

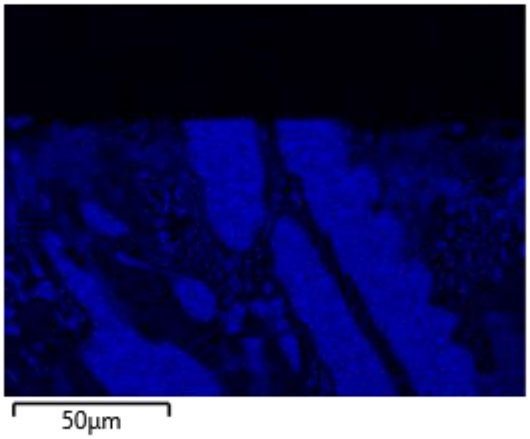

Zn Kα1

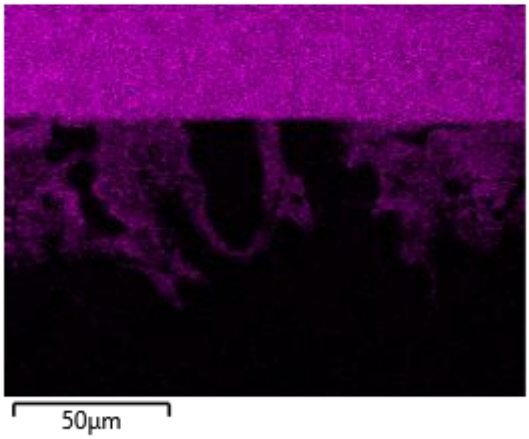

Cr Kα1

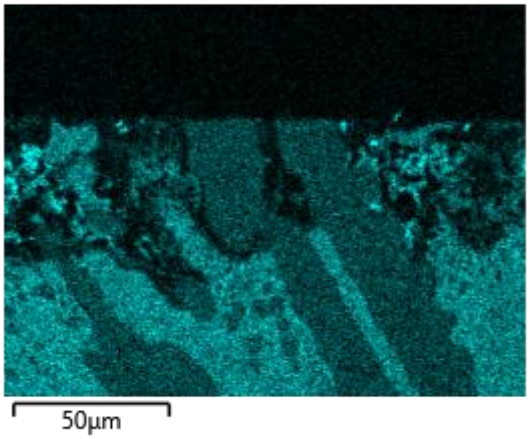

Al Kα1

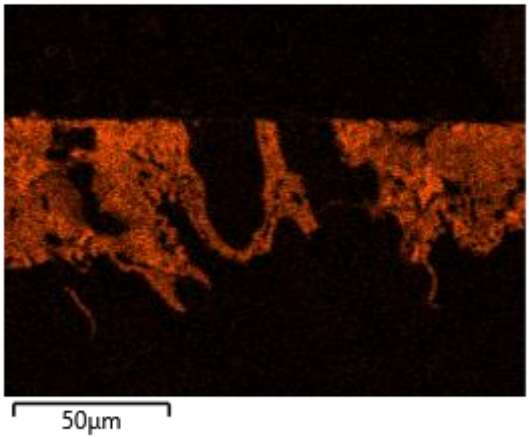

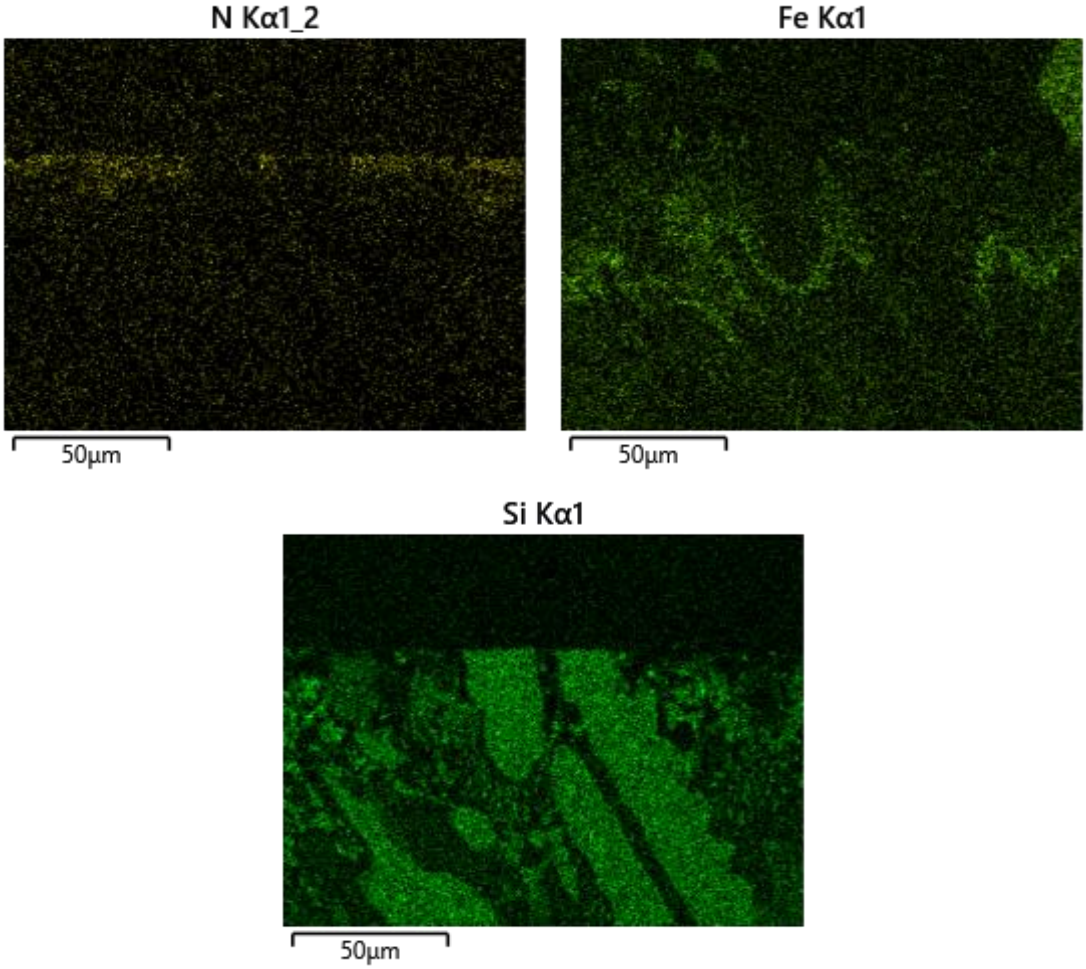

Figure 5.50: EDS elemental mapping of a plasma treated T-800 Tribaloy after 4-weeks of dip testing in a molten zinc bath containing 0.35wt.% Al and saturated with Fe.

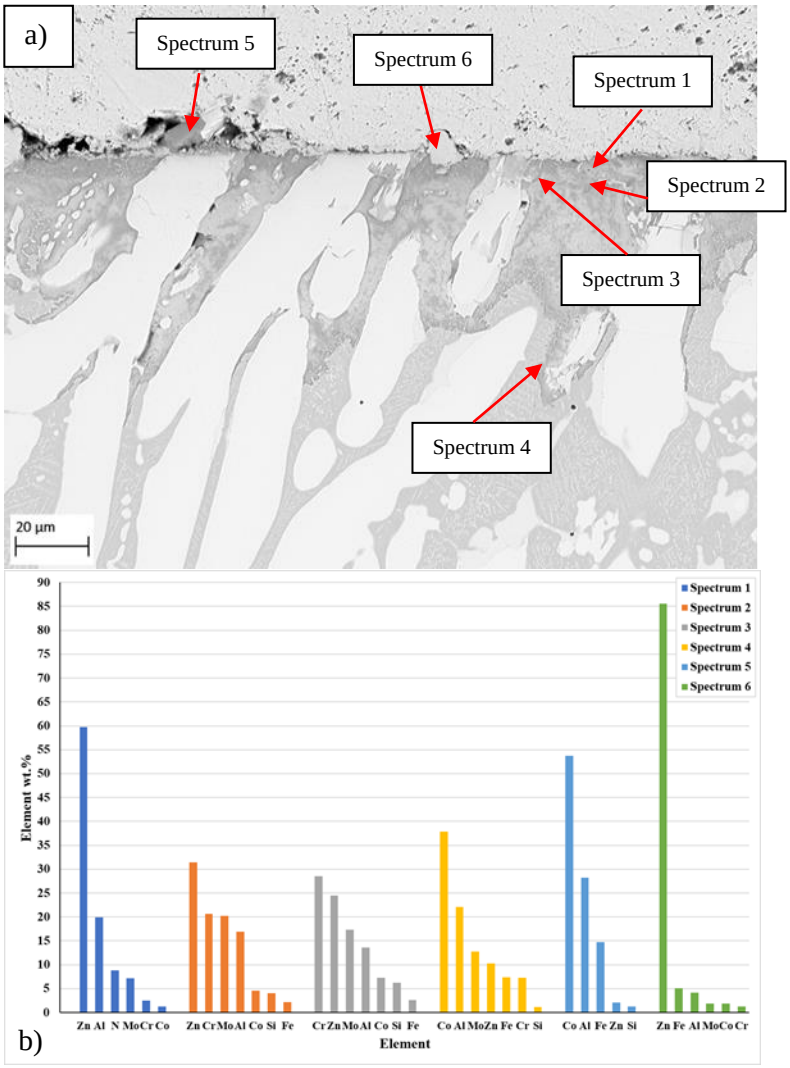

Figure 5.51: EDS point scan analysis of the diffusion zone of the plasma treated T-800 Tribaloy after 4-weeks of bath immersion: a+b) Point scan locations and c) Corresponding point scan compositions.

5.7 Comparisons of the Chemical Reactivity of the Plasma Treated Alloys

It was identified that the plasma nitride treatment resulted in the diffusion of nitrogen atoms into the surface of the alloys which resulted in the formation a thin modified surface layer that typically contained between 5-12wt.% nitrogen content after plasma nitriding at higher temperatures and longer treatment times. The survival of the nitride layer was detected with each alloy where relatively high levels of nitrogen was detected after each stage of dip testing. Although the nitride layer was seen to react with the bath, the endurance of the layer, even after prolonged bath exposure, demonstrates that it experiences low levels of diffusion and that nitrogen atoms are not readily leached out into the bath. The survival of the nitride layer also indicates the samples experienced very little material loss during testing. Despite the endurance of the nitride layer the diffusion of bath species into the alloy's microstructure still occurred with

each alloy. Diffusion of zinc, aluminium and iron occurred after the first week of testing and diffusion progressively continued with increased testing. Detailed analysis of the diffusion layer revealed an extremely complex diffusion process occurred with each alloy where the continuous ingress of bath species into the bulk of the alloy resulted in complex phase formation within the alloys matrix. In the early stages of testing the diffusion process, experienced with the plasma treated samples, demonstrated similar chemical behaviour to the performance of the untreated alloys when exposed to the molten bath. However, phase formation and diffusion rate differed slightly after longer bath exposure. The initial stages of the diffusion process resulted in the establishment of a diffusion front which preferentially advanced through the matrix of the alloys microstructure. It was identified that the diffusion front experienced with the CoCrW contained high concentrations of aluminium and iron. This can be attributed to high affinity of cobalt and iron for aluminium. With the CoCrMo alloy the diffusion front contained high levels of iron but aluminium content remained consistent throughout the diffusion layer. With both alloy groups the diffusion of aluminium and iron was subsequently followed by the diffusion of zinc which resulted in the formation of zinc-rich intermetallic regions forming behind the diffusion front. This diffusion process left the matrix extremely depleted in cobalt and chromium. The loss of cobalt resulted in the formation of CoAl phases at the surface of each alloy which confirmed that the nitride layer did not prevent the loss of cobalt from the alloy. The diffusion process experienced by the plasma treated CoCrW and CoCrMo alloys is schematically drawn in Figure 5.52 and Figure 5.53, respectively.

Minimal material loss was observed with any of the treated samples. Even after prolonged bath exposure the surface of the samples remained smooth, and the nitride layer persisted at the surface. Significant cracking of the carbide and Laves phases was recorded after dip testing. It was identified that the expansion of the crystal structure caused due to nitrogen diffusion resulted in the cracking of the carbide/Laves phases, prior to static immersion. Therefore, failure of these phases is due to a combination of initial cracking introduced by plasma nitride treatment and due stresses caused from the diffusion of bath species into the alloy's microstructure.

Prolonged testing resulted increased diffusion depths and larger quantities of intermetallic phase formation within the diffusion layer where chemical reactions were more specific to each alloy. The diffusion layer that formed with the WT-6 alloy, after a 4-week test, remained consistent with the diffusion experienced in early stages of testing. However, diffusion depth was greater and intermetallic phases occupied larger volumes of the cobalt matrix. Isolated regions that contained increased levels of chromium were identified within the diffusion layer which formed beneath the nitride layer. Two diffusion processes were observed with the WT-4 alloy. Generally, the diffusion layer was zinc-rich with high levels of tungsten. However, isolated areas

demonstrated regions where a chromium-rich diffusion front that contained high levels of silicon formed behind the leading diffusion front which contained high levels of aluminium and iron. A chromium and silicon-rich region was also observed beneath the nitride layer. Several areas of the diffusion layer that formed with the WT-12 alloy were found to have contrasting elemental compositions. Some areas consisted almost purely of zinc whereas other areas contained high levels of tungsten. Regions that were cobalt-rich were also identified which were often located around the outer edges of the carbide phases. Increased levels of diffusion experienced with the T-800 Tribaloy resulted in a diffusion layer that contained areas comprising of high levels of zinc and chromium and areas that were chromium-rich that contained high levels of silicon. Tungsten and molybdenum concentrations detected in the diffusion layer remained relatively high after each of stage of testing. This is due to their large atomic size which would reduce their mobility during the diffusion process.

Analysis of the nitride layer for each alloy found that it contained relatively high levels of aluminium and chromium after each stage of testing. Although it has not been verified this could suggest that the nitride layer could potentially reduce the quantity of aluminium diffusing into the alloy in addition to limiting chromium loss into the bath. It was observed that each alloy exhibited regions containing high levels of chromium at the nitride layer and substrate interface which could also suggest the impedance of chromium diffusion into the bath.

With the CoCrW alloys, the quantity and size of the CoAl particles decreased with increased testing. Although CoAl formation was a frequent occurrence with the CoCrW alloys, particularly in the early stages of testing, the CoCrMo Tribaloy displayed little evidence of CoAl formation at the surface. However, cobalt depletion of the diffusion layer was recorded after each stage of testing. This could suggest that the nitride layer encourages the detachment of the CoAl phases. The formation of a CrSi phase was also observed to form with the CoCrW alloys. This phase was observed in the earlier stages of testing but became more frequent after longer dip times when the alloys had experienced increased levels of chromium loss. Although it was identified that tungsten and molybdenum was relatively resistant to the diffusion process, isolated phases containing additions of the elements were identified. This indicates that small quantities of the elements were leached out into the bath and reacted to form intermetallic phases.

Comparing the performance of the plasma treated alloys demonstrated that the T-800 Tribaloy offered the best chemical resistance to the molten zinc bath which can be attributed to the microstructure mainly consisting of a primary Laves phase, which was more resistant to diffusion, and due to high additions of molybdenum that is retained in solid solution. Figure 5.54 displays the average diffusion depth measured after each stage of testing for each alloy. The results indicate that the T-800 Tribaloy experienced the lowest average diffusion depths as well

as the lowest range of measurements after each stage of testing compared to the CoCrW alloys. In addition to shallower diffusion depths, there was little evidence of CoAl phase formation at the surface whereas the formation of this phase was a frequent occurrence with the CoCrW alloys, particularly in the early stages of testing.

Due to the complex nature of the diffusion process, which varied significantly between the CoCrW alloys, ranking of the performance of individual alloys was difficult. Figure 5.54 indicates that the WT-4 and WT-12 alloys experienced similar levels of diffusion during the first and second week of testing whereas the WT-6 alloy experienced greater diffusion depths after the first week. However, by the second week of test the diffusion measurements between the three alloys was more comparable. After the third week of testing the range of diffusion measurements increased significantly with each alloy as areas of the microstructures experienced contrasting levels of diffusion. By this stage of testing the WT-4 alloy had experienced the greatest depth of diffusion penetration in addition to the large range of measurements, whereas the WT-6 and WT-12 alloys experienced similar levels of diffusion. After 4-weeks of bath immersion lower diffusion depths were recorded with the WT-6 alloy and increased diffusion depths were recorded with the WT-4. The results indicate that WT-6 displays the lowest diffusion gradient indicating the slowest diffusion kinetics of the alloys. However, taking into consideration the microstructure and the behaviour of the individual alloys when exposed to molten zinc, the results become less straight forward. During testing, the WT-6 alloy has a larger surface area of the matrix phase which is exposed to the bath. Therefore, diffusion of bath species would spread laterally through the phase while short circuit diffusion to greater depths may have occurred with the WT-4 and WT-12 alloys. The WT-6 alloy also experienced higher saturations of zinc and aluminium at the surface which may have slowed down the rate of diffusion. The diffusion layer that formed with the WT-4 and WT-12 alloys also retained higher levels of alloying additions such as tungsten and chromium which could potential maintain better mechanical properties at the surface.

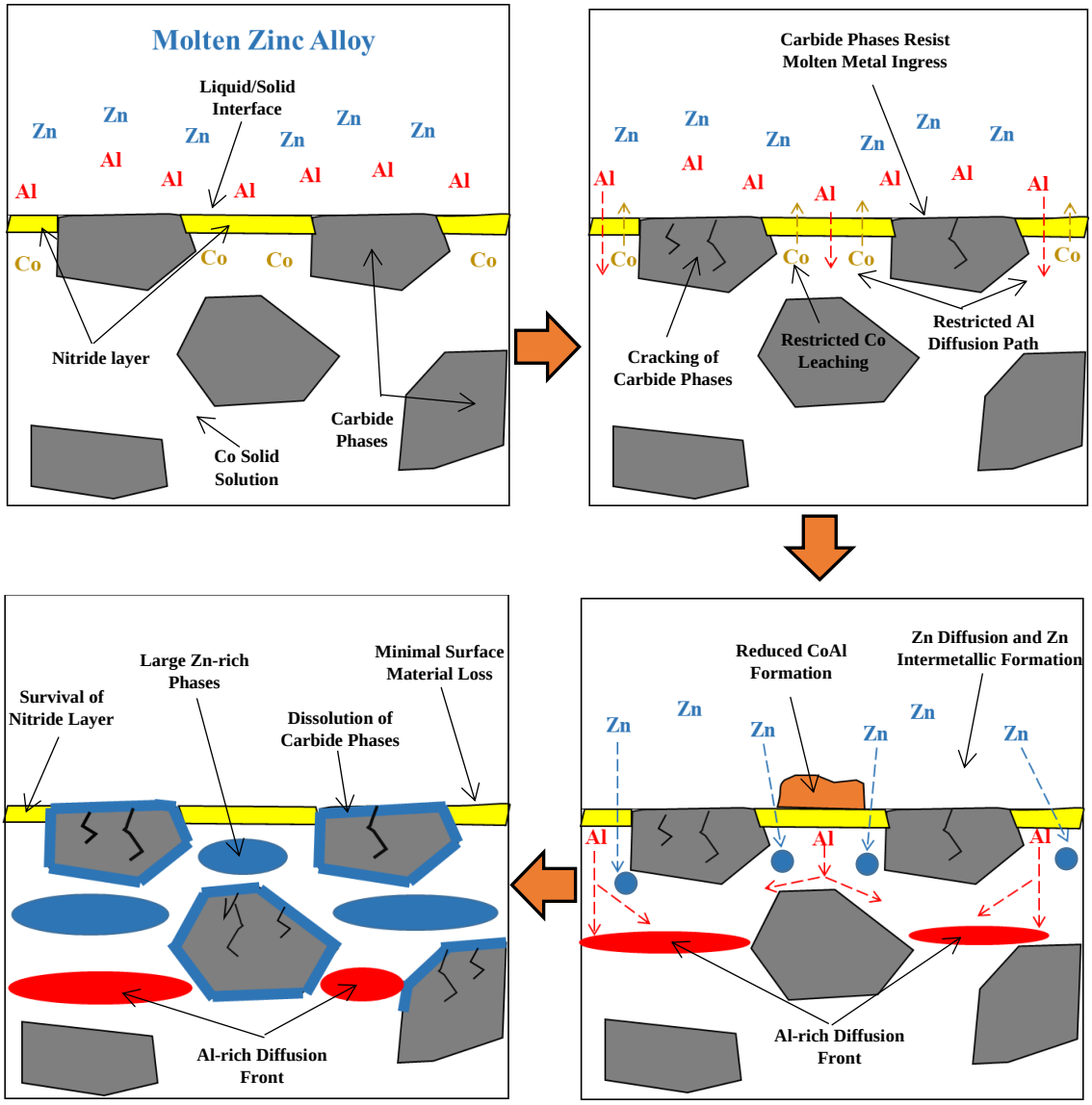

Figure 5.52: Schematic diagram illustrating the diffusion mechanisms within plasma treated CoCrW alloys immersed in a molten bath containing 0.35wt.% Al and saturated with Fe.

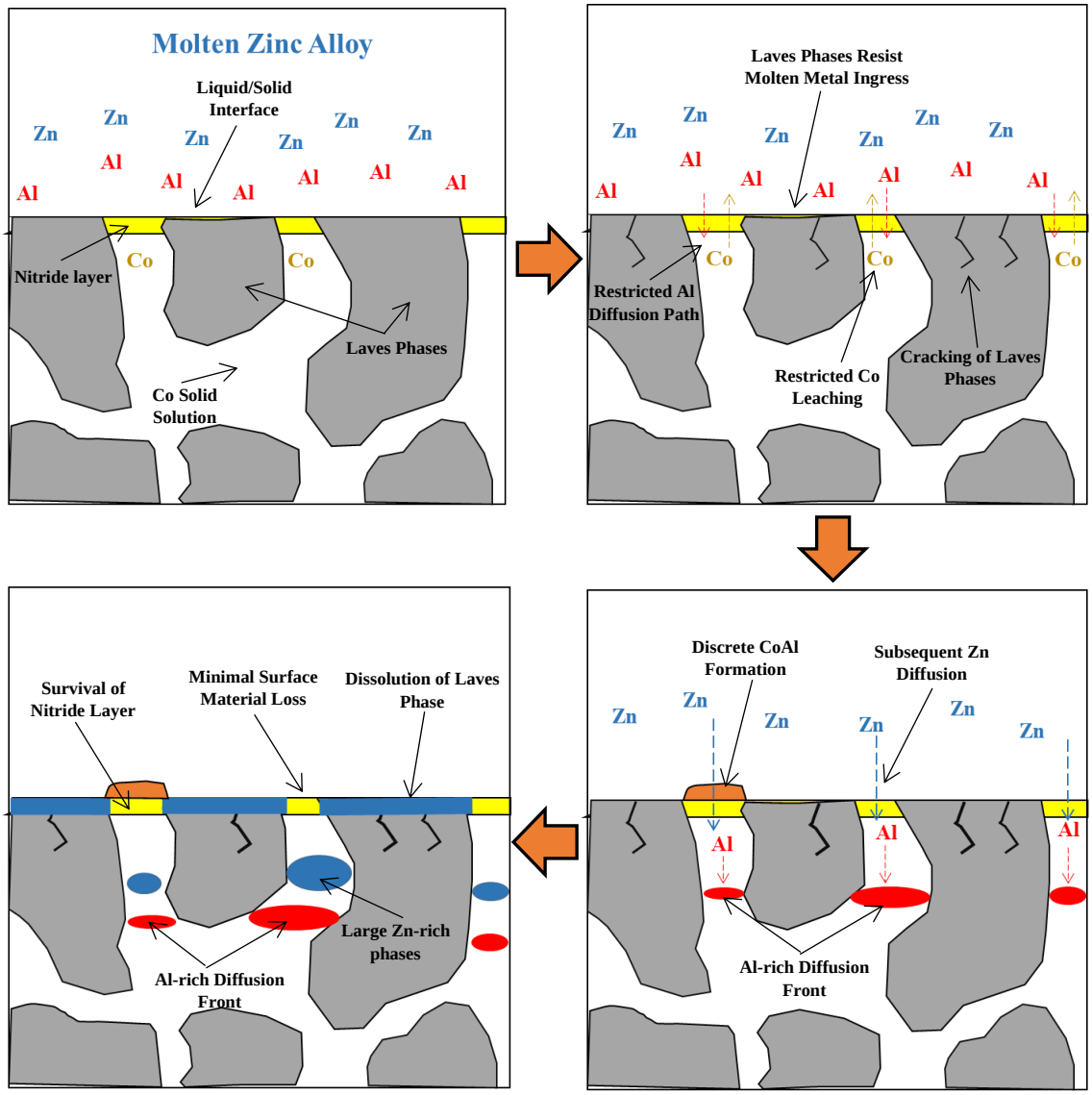

Figure 5.53: Schematic diagram illustrating the diffusion mechanisms within a plasma treated CoCrMo alloy immersed in a molten bath containing 0.35wt.% Al and saturated with Fe.

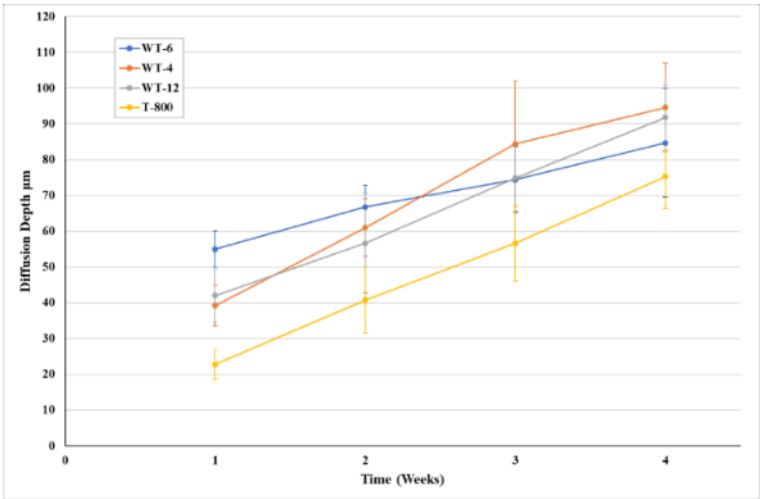

Figure 5.54: Average diffusion depth of the plasma treated alloys after prolonged dip testing in a molten zinc bath containing 0.35wt.% Al and saturated with Fe.

5.8 Comparisons of Untreated and Plasma Treated Alloys

The previous sections have investigated the chemical performance of the untreated and plasma treated alloys when submerged in molten zinc. The following section will make direct comparisons between the samples to identify any changes in chemical performance of the alloys when exposed to molten zinc.

5.8.1 Untreated WT-6 samples vs Plasma Nitride WT-6 Samples

Figure 5.55 compares the untreated and plasma treated WT-6 samples after 2 and 4-week static immersion tests and Figure 5.56 compares the average diffusion depth after each stage of testing. Comparing the samples after 2-weeks of testing (Figure 5.55a and b) portrays a similar diffusion process where CoAl formation is observed at the surface of both samples which indicates the diffusion of cobalt into the bath. Diffusion of bath species into the alloys microstructure resulted in the large areas of the matrix transforming into a zinc-rich intermetallic phase. The average diffusions depths and data ranges for the untreated and treated samples were also similar in the early stages of testing. This suggest that nitride layer has limited effects on the alloy's chemical resistance in the early stages of molten zinc exposure.

Analysis of the samples dipped for longer times (Figure 5.55c+d) illustrates a clear change in alloy performance where the treated sample appears to be in a significantly better condition after testing compared to the untreated sample which was dipped for the same time. This is also represented in the diffusion measurements comparing the treated and untreated sample. After 3-weeks of testing the average diffusion depth and data range is similar. However, by the fourth week of testing the average diffusion depth for the untreated sample is slightly higher than the treated due to the larger range is of diffusion measurements. This correlates to the SEM

analysis which indicates that elevated levels of diffusion were experienced with the untreated sample. The rough surface of this sample indicates that the alloy experienced significant material loss during testing where the regions that experienced increased levels of diffusion and material loss consisted almost purely of zinc. In comparison, the surface of the treated alloy is much smoother, and a uniform nitride layer is observed at the surface which indicates the sample experienced minimal material loss after 4-weeks of bath immersion. However, the diffusion layer still became depleted in cobalt.

It was identified that the diffusion layer of the untreated sample, after 4-weeks of testing, became almost completely depleted in chromium which resulted a chromium-rich layer forming at the alloys surface. Relatively high levels of chromium were observed beneath the nitride layer of the treated sample in addition chromium-rich areas throughout the diffusion layer, as shown in Figure 5.55d. It was identified that the nitride layer contained high levels of zinc, aluminium, and nitrogen in addition to levels of chromium, cobalt ad iron. Therefore, the survival of the nitride layer may hinder the diffusion and loss of chromium into the bath. However, in both tests CrSi phases were recorded at the surface of the samples, particularly after longer tests, which indicates that chromium was still able to diffuse into bath during testing.

Comparing both sets of data would suggest that the formation of the nitride layer, which is visible in Figure 5.55b and d, does not improve the chemical resistance of the alloy in the initial stages of bath exposure as cobalt was still leached from the alloy resulting in CoAl formation and the diffusion of bath species resulted in transformation of the alloys matrix. However, the persistence of the nitride layer after prolonged bath exposure may hinder the leaching of alloying elements, particularly chromium, into the bath. The survival of the nitride layer also significantly reduced the level of material loss experienced in the later stages of testing.

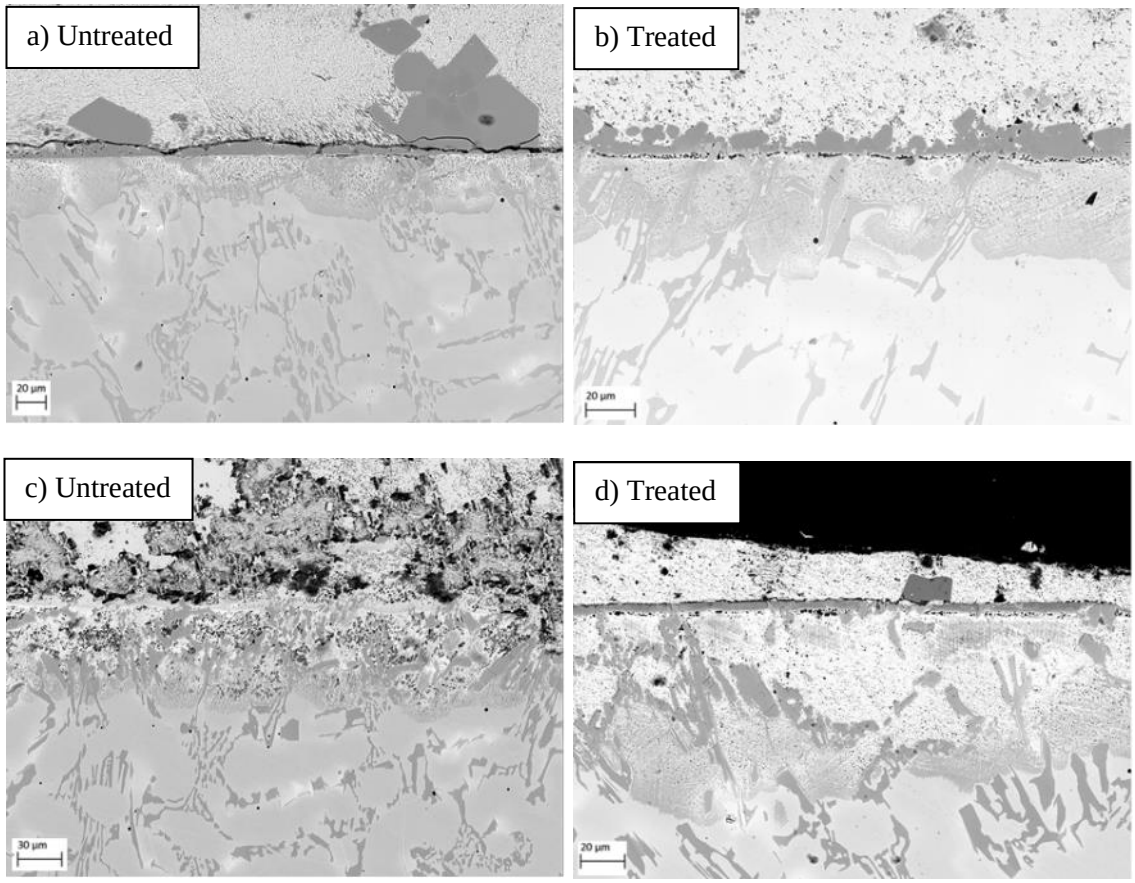

Figure 5.55: Surface comparisons of untreated and plasma treated WT-6 samples after different stages of dip testing in a molten zinc bath containing 0.35wt.% Al and saturated with Fe: a) Untreated sample after 2-weeks, b) Plasma treated sample after 2-weeks, c) Untreated sample after 4-weeks and d) Plasma treated sample after 4-weeks.

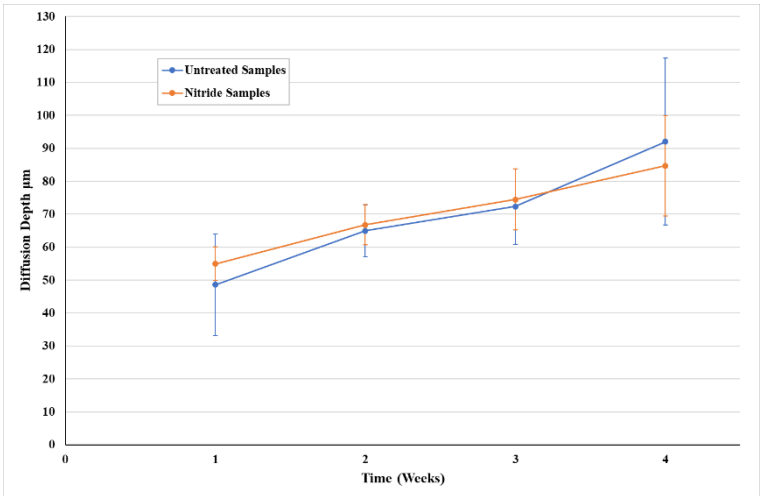

Figure 5.56: Average diffusion depth comparison between untreated and plasma treated WT-6 samples after prolonged dip testing in a molten zinc bath containing 0.35wt.% Al and saturated with Fe.

5.8.2 Untreated WT-4 Samples vs Plasma Nitride WT-4 Samples

Comparisons between untreated and plasma treated WT-4 samples after 2 and 4-week dip tests are displayed in Figure 4.50. The images demonstrate that after 2-weeks of testing both samples exhibit signs of diffusion where surface phase formation and diffusion into the alloy's matrix occurred. This involved the depletion of cobalt and chromium from the alloys matrix which was replaced by aluminium, iron, and zinc. This consequently resulted in the formation of a zinc-rich intermetallic phase behind the diffusion front. This confirms that, even in the early stages of testing, the nitride layer did not prevent the loss of cobalt from the alloy or bath species diffusing into the alloy. The images indicate that, in the early stages of testing, the untreated sample experienced material removal where the existence of the CoAl phase can be seen below the surface of the sample. This would have occurred due to removal of surface material and the formation of the CoAl phase at the newly exposed surface. This was not experienced with the treated samples where the existence of the nitride layer remained uniform at the samples surface. The nitride layer was observed to react with the molten zinc bath where it became depleted in cobalt. However, there were some areas that appeared to have resisted the diffusion process where areas of the nitride layer still contained relatively high levels of cobalt, as shown in Figure 4.50d. This suggests that the nitride layer may provide some resistance to the diffusion process during the early stages of bath exposure. This is highlighted in Figure 5.58 which displays a plasma treated sample after dip testing for 1-week. The image highlights an area of the nitride layer that had resisted the diffusion process which consequently resulted in a shallower diffusion depth beneath it. This theory is demonstrated further in Figure 5.59 which displays the measured diffusion depths after each stage of testing. After the first week of testing the plasma treated sample experienced lower diffusion depths. However, similar diffusion depths were recorded after the 2 and 3 weeks of dip tests. This suggests that the nitride layer provides limited diffusion resistance in the early stages of exposure to the molten bath.

Figure 5.57c and d display samples after 4-weeks of bath immersion. After this stage of testing, it is apparent that the untreated sample has experienced increased levels of diffusion where the diffusion layer is dominated by the zinc-rich intermetallic phase. It was identified that the diffusion layer of the untreated sample becomes depleted in cobalt and chromium whereas high levels of tungsten were retained throughout the diffusion layer. The areas containing high levels of tungsten are observed as the bright white areas throughout the diffusion layer. A similar diffusion process was observed with the plasma treated sample where areas became enriched in tungsten as chromium and cobalt diffused out of the alloy. However, comparing the images demonstrates that the untreated sample experienced greater levels of diffusion. Figure 5.59 also

indicates that the untreated sample experienced a significantly larger average diffusion depth in addition to a larger data range.

The existence of the nitride layer appeared to impede the diffusion of chromium as high concentrations were detected in the areas beneath the surface layer. However, CrSi phases were identified in both tests which indicates that some chromium was still leached out into the bath despite the presence of the surface nitride layer.

Comparing the data suggest that the nitride layer provided limited resistance to the diffusion process in the early stages of bath exposure where shallower diffusion depths were recorded in addition to minimal material loss. Although both sets of samples experienced elevated levels of cobalt depletion throughout the diffusion layer, the treated sample did retain higher levels of chromium where it believed that the nitride layer hindered chromium diffusion. This may be the reason why diffusion was able to penetrate deeper into the untreated alloys microstructure.

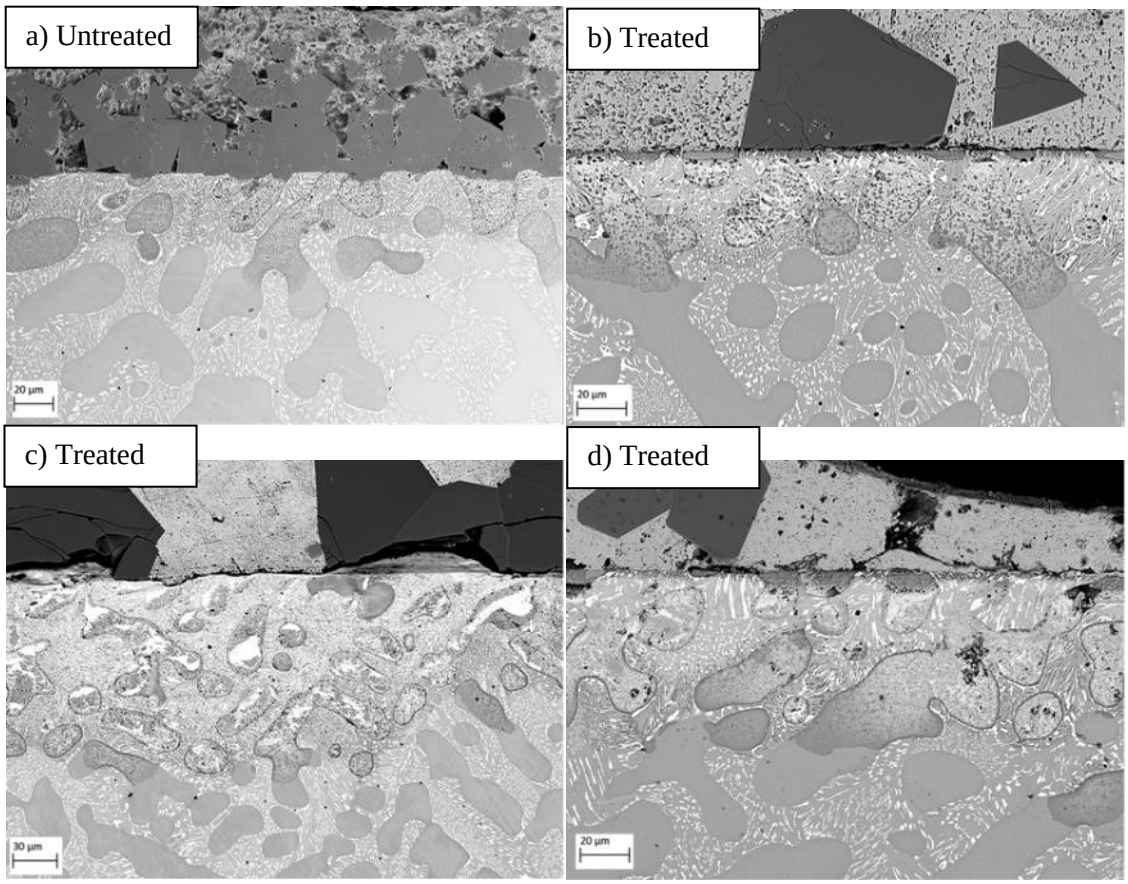

Figure 5.57: Surface comparisons of untreated and plasma treated WT-4 samples after different stages of dip testing in a molten zinc bath containing 0.35wt.% Al and saturated with Fe: a) Untreated sample after 2-weeks, b) Plasma treated sample after 2-weeks, c) Untreated sample after 4-weeks and d) Plasma treated sample after 4-weeks.

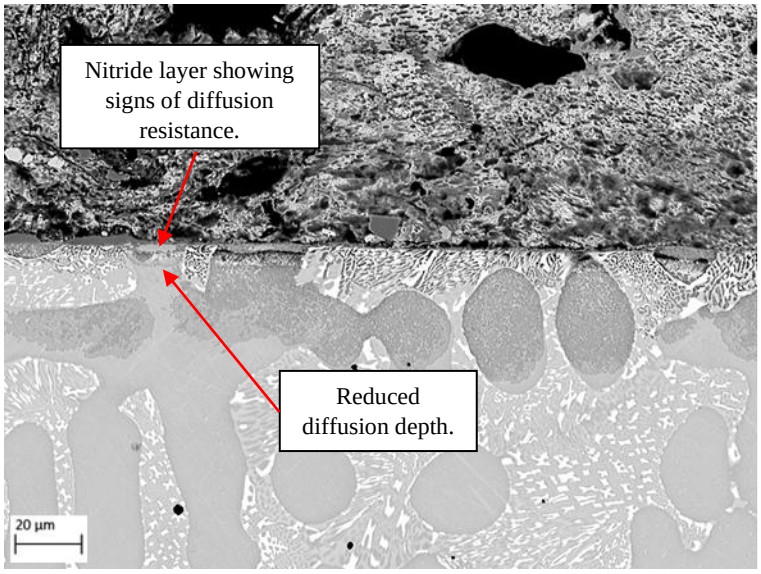

Figure 5.58: Nitride layer of a treated sample indicating signs of resistance to the diffusion of bath species.

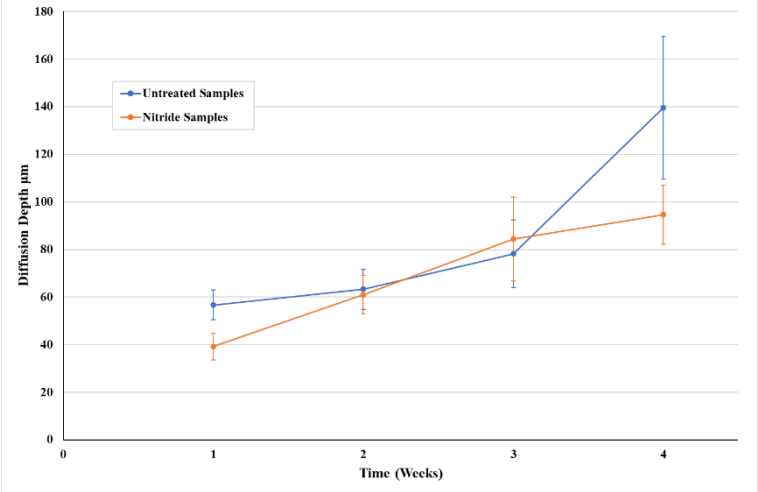

Figure 5.59: Average diffusion depth comparison between untreated and plasma treated WT-4 samples after prolonged dip testing in a molten zinc bath containing 0.35wt.% Al and saturated with Fe.

5.8.3 Untreated WT-12 Samples vs Plasma Nitride WT-12 Samples

SEM analysis of untreated and plasma treated WT-12 samples are displayed in Figure 5.60 which illustrate the chemical performance of the alloys after 2 and 4-weeks of bath immersion. Comparing the samples that were dipped for 2-weeks (Figure 5.60a+b) indicate that, despite the survival of the nitride layer with the treated sample, a similar diffusion process was observed with both tests. The diffusion of aluminium, iron, and zinc into the matrix of the alloy resulted in the matrix becoming depleted in cobalt and chromium. This process subsequently

resulted in the matrix transforming into a zinc-rich intermetallic phase. The diffusion of cobalt into the bath also resulted in for the formation of a CoAl phase at the surface of the samples. This shows that the survival of the nitride layer was not sufficient in preventing the loss of cobalt into the bath. The diffusion measurements after each stage of testing are displayed in Figure 5.61. The results indicate that similar diffusion measurements were recorded after the first and second week of testing. However, by the third week of testing the range of diffusion measurements with the untreated sample increased significantly which resulted in a slightly higher average diffusion depth. This trend continued after 4-weeks of testing where the average diffusion depth for the untreated sample was considerably greater than the diffusion depth experienced with the plasma treated sample. This would suggest that the nitride layer improves the long-term performance of the alloy when exposed to molten zinc. Comparing the samples after 4-weeks of testing demonstrates how the zinc-rich intermetallic phase occupies large areas of the diffusion layer. Chromium-rich areas that contained varying amounts of tungsten and silicon were observed to form beneath the surface of the untreated sample, but the diffusion became severely depleted in alloying elements and consisted mainly of zinc. The diffusion layer of the treated alloy generally contained higher levels of alloying elements, particularly chromium, in addition to areas that contained high levels of chromium. Therefore, it is assumed that the nitride layer hinders chromium diffusion into the bath. However, formation of a CrSi phase was observed in both tests which became more frequent after longer testing times. This indicates that the nitride layer did not completely prevent chromium diffusing into the bath.

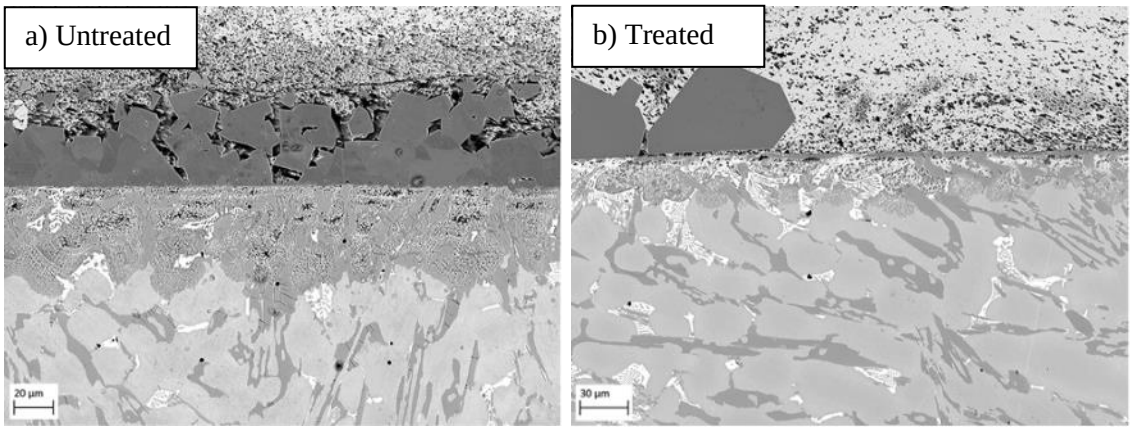

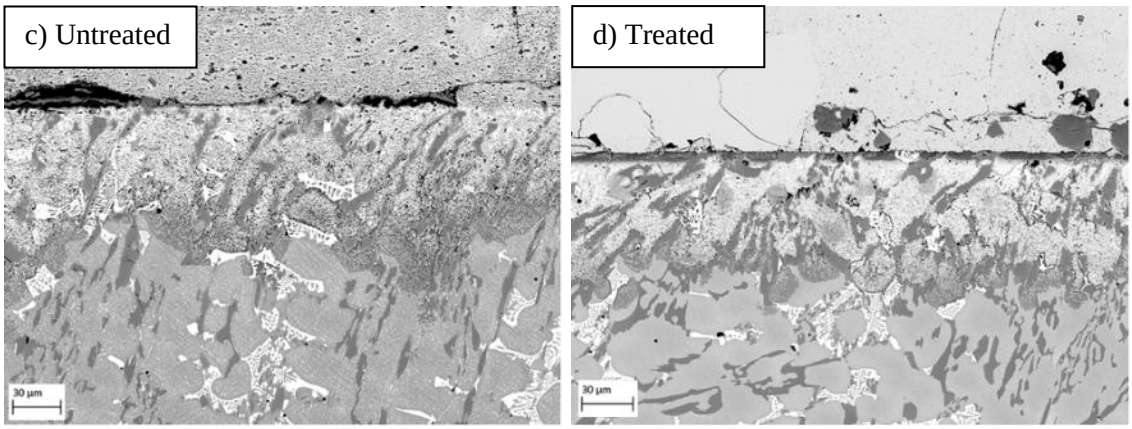

Figure 5.60: Surface comparisons of untreated and plasma treated WT-12 samples after different stages of dip testing in a molten zinc bath containing 0.35wt.% Al and saturated with Fe: a) Untreated sample after 2-weeks, b) Plasma treated sample after 2-weeks, c) Untreated sample after 4-weeks and d) Plasma treated sample after 4-weeks.

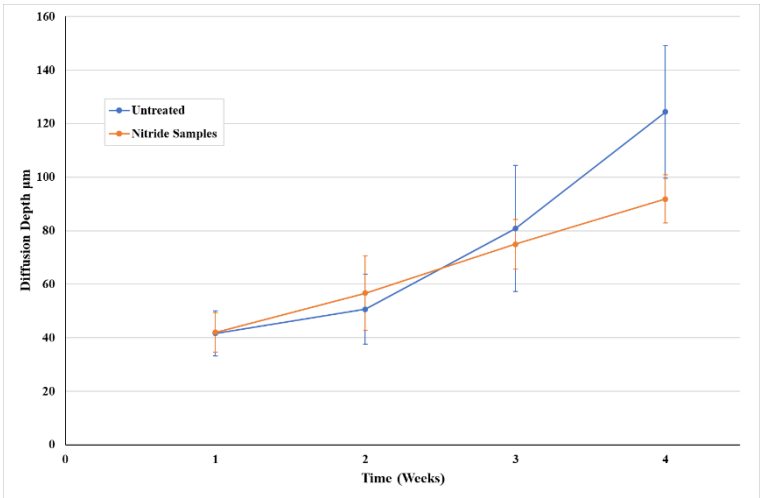

Figure 5.61: Average diffusion depth comparison between untreated and plasma treated WT-12 samples after prolonged dip testing in a molten zinc bath containing 0.35wt.% Al and saturated with Fe.

5.8.4 Untreated T-800 Samples vs Plasma Nitride T-800 Samples

The microstructures of untreated and plasma treated T-800 samples after static dip testing for 2 and 4-weeks are displayed in Figure 5.62. The images illustrate that both samples reacted with the molten bath which led to the depletion of cobalt and chromium from the matrix. Areas of the matrix were observed to detach in the early stages of testing with the untreated samples which often resulted in CoAl formation in these areas, as shown in Figure 5.62a. The surface of the plasma treated sample experienced minimal signs of material removal, after 2 weeks of testing, and the survival of a uniform nitride layer can be seen at the surface. SEM imaging of the surface of the plasma treated sample highlighted a significant reduction in the quantity of CoAl

formation. This could be due to the nitride layer reducing the amount of cobalt diffusing from the alloy or could be due to the nitride layer promoting the detachment of the phase.

Comparing the diffusion depth measurements (Figure 5.63) indicates that similar depths were recorded after each stage of testing, although slightly larger measurements were recorded after the second week of testing with the treated sample. Analysis of the treated T-800 samples identified that increased nitrogen diffusion depth often occurred at the matrix interface. It was also identified that molten metal ingress often penetrated deeper into the alloys microstructure by travelling along the matrix and Laves phase interface. This process often produced larger diffusion measurements that could potentially produce a false representation of the extent of diffusion if looked at independently. This is highlighted in Figure 5.63. The image demonstrates how diffusion was able to penetrate to greater depths along the matrix interface whereas the majority of diffusion occurred closer to the surface and the general diffusion depth was lower.

Comparing the samples treated for longer periods (Figure 5.63c and d) reveals a similar diffusion process in both tests. The depletion of cobalt and chromium experienced in the matrix was replaced with aluminium, zinc, and iron content. This resulted in the formation of a zinc-rich intermetallic phase forming in the matrix in all samples. Both tests identified areas containing high levels of chromium which appeared as darker regions within the diffusion layer. The recorded diffusion measurements were also similar after third and fourth week of testing in both sets of tests. However, comparisons of the diffusion layers showed that the surface of the treated samples were generally in better condition. The untreated sample experienced increased levels of material loss and larger areas of the diffusion layer had transformed into a zinc-rich intermetallic phase. The diffusion layer of the plasma treated samples contained increased levels of alloying elements.

These results indicate that the nitride layer reduced material loss in the early stages of testing in addition to reducing the quantity of CoAl formation. Although similar diffusion depths were experienced with the untreated and treated samples, it does appear the long-term survival of the nitride layer does reduce the extremity of zinc intermetallic phase formation after increased bath exposure. This is likely due to the higher alloying elements being retained in the diffusion layer at the alloys surface.

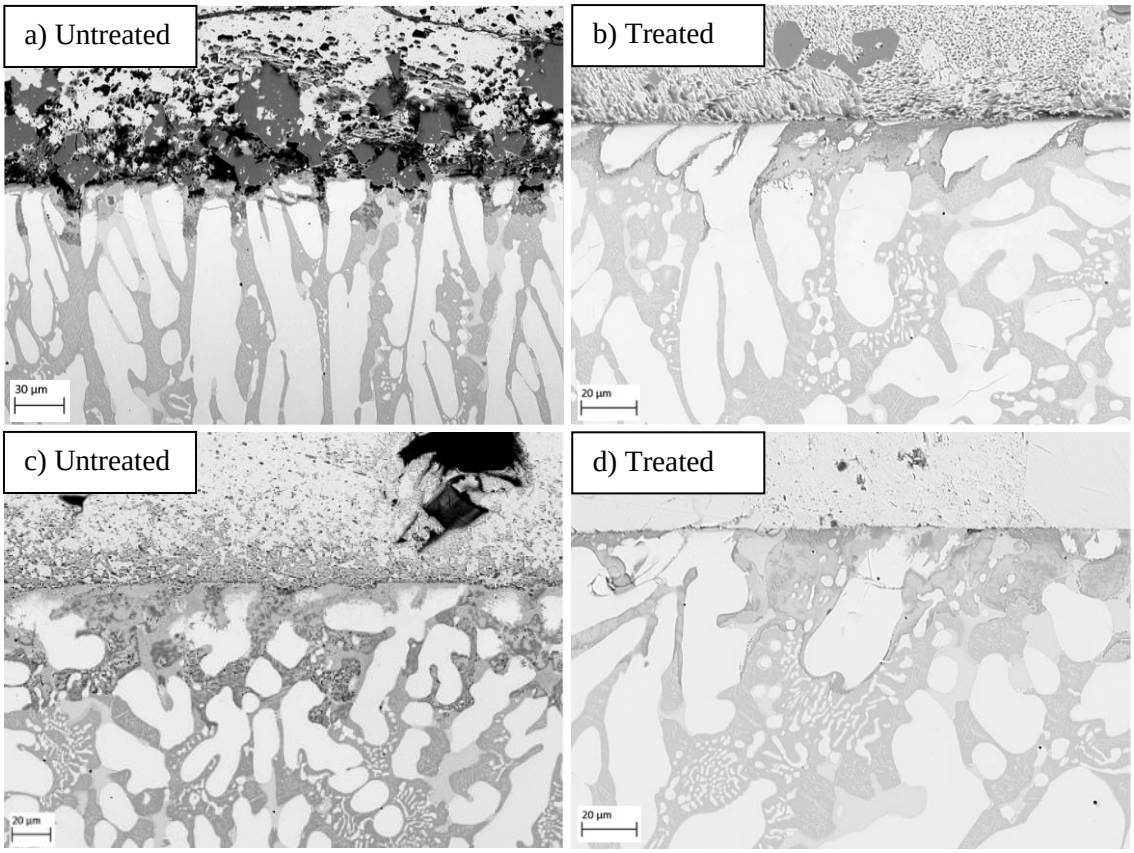

Figure 5.62: Surface comparisons of untreated and plasma treated T-800 samples after different stages of dip testing in a molten zinc bath containing 0.35wt.% Al and saturated with Fe: a) Untreated sample after 2-weeks, b) Plasma treated sample after 2-weeks, c) Untreated sample after 4-weeks and d) Plasma treated sample after 4-weeks.

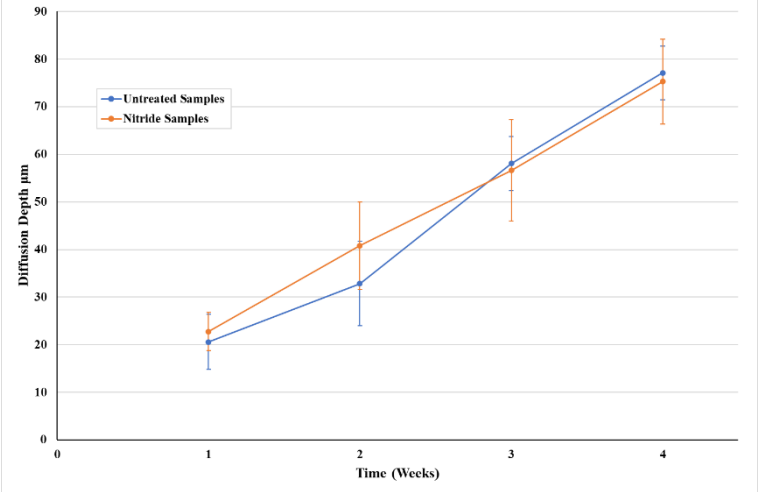

Figure 5.63: Average diffusion depth comparison between untreated and plasma treated T-800 samples after prolonged dip testing in a molten zinc bath containing 0.35wt.% Al and saturated with Fe.

6 Effect of High Temperature Thermal (Annealing) Treatments on the Microstructure and Mechanical Performance of Alloy Samples

6.1 High Temperature Annealing Heat Treatment

The alloys were annealed at 1000℃ for times ranging between 1-4-hours. The samples were furnace cooled to room temperature, although one group of samples were water quenched after a 1-hour annealing treatment. From literature, it has been recorded that heat treating at this temperature results in coarsening of carbide phases and precipitation of fine carbides within the alloys matrix. The overall effect can result in improved alloy hardness.

6.1.1 Microstructure Analysis of Annealed WT-4

Figure 6.1 illustrates the microstructures of the WT-4 samples annealed at 1000°C for various periods of time with comparisons made to an untreated sample. After each heat treatment the morphology of the microstructure remains similar to the untreated sample where it comprises of dendritic primary cobalt solid solution matrix and a eutectic region that consists of a mixture of chromium carbides, tungsten carbides and a cobalt-rich phase. The area fraction of the matrix was calculated after each treatment to identify any signs of microstructural changes. The results are summarised in Figure 6.1 and indicate that there were only minor changes in the area fraction of the matrix compared to an untreated sample. This would suggest that there was minimal dissolution of the eutectic carbide phases into solid solution after a treatment at 1000°C. Although there was no increase in the solid solution phase after heat-treating the alloy at 1000°C for 1-hour, precipitation occurred within the matrix which became more apparent as the treatment time increased. Comparisons between samples annealed for 1-hour and 4-hours, respectively, are shown in Figure 6.2. The images highlight how the precipitates are finer in appearance in the sample that was annealed for 1-hour where it was calculated that the precipitates occupied an area fraction of around 7% of the matrix. In contrast, the precipitates are more spherical and coarser with the sample annealed for a longer 4-hour treatment and the precipitates had an estimated area fraction of around 10%. This demonstrates that a prolonged annealing treatment results in increased precipitation as well as coarsening of the precipitated phases.

EDS analysis of the matrix of a furnaced cooled sample after a 4-hour treatment is displayed in Figure 6.3. Point scan analysis of the precipitated phase (Spectrum 1) revealed that it is predominantly tungsten based with high cobalt and chromium content. It was observed that the precipitation of this phase did not occur in the outer circumference of the cobalt dendrites. Comparing the EDS data to the untreated sample revealed that the outer area of the dendrites

(Spectrum 2) contained higher levels of cobalt and lower levels of chromium and tungsten. A similar composition was also detected in the centre of the dendrite. The reduction of chromium and tungsten retained in solid solution suggests that these elements precipitate from solid solution to form the precipitate phase after the annealing treatment. In addition to the changes experienced in the matrix of the sample, small changes were recorded in the eutectic region of the alloy microstructure. Figure 6.4 demonstrates areas of the eutectic region where the phases appear to have coarsened as a result of the thermal treatment.

One sample was also water quenched after annealing at 1000°C for a 1-hour (Figure 6.1e). Despite the sample displaying similar diffusion behaviour to the furnace cooled samples, the quenching process resulted in significant crack formation due to thermal shock, as shown in Figure 6.5. Examination of the sample highlights that crack propagation generally occurred due to failure at the matrix and eutectic interface.

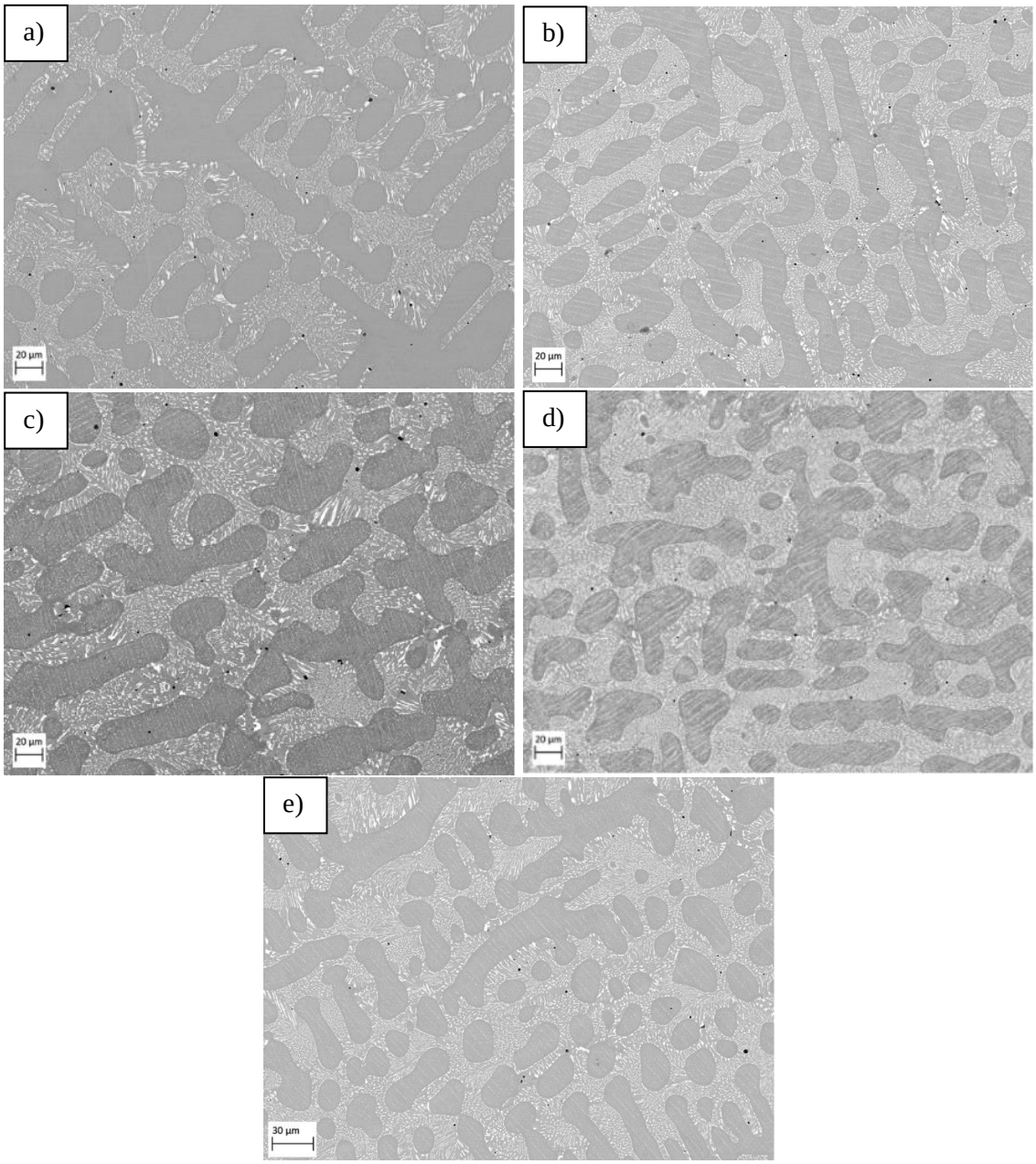

Figure 6.1: SEM microstructural analysis of WT-4 samples annealed at 1000°C for different times and different cooling processes with comparisons made to an untreated sample: a) Untreated, b) 1-hour and furnace cooled, c) 2-hours and furnace cooled, d) 4-hours at 1000°C. e) 1-hour and water quenched.

Table 6.1: Area fraction analysis of matrix after each heat treatment with comparison to an untreated WT-4 sample.

Treatment	**Matrix Area fraction %**
Untreated	49.6% (±1.7)
1-Hour	48.7% (±0.2)
2-Hour	48.5% (±1.6)
4-Hour	48.2% (± 0.4)
Quenched	47.8% (± 0.3)

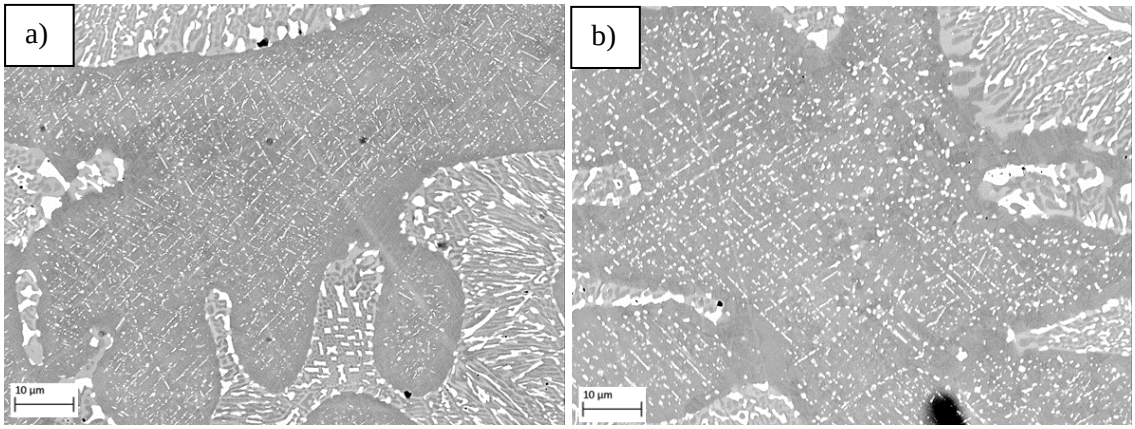

Figure 6.2: Comparisons of matrix phase precipitation after annealing at 1000°C: a) 1-hour and b) 4-hours.

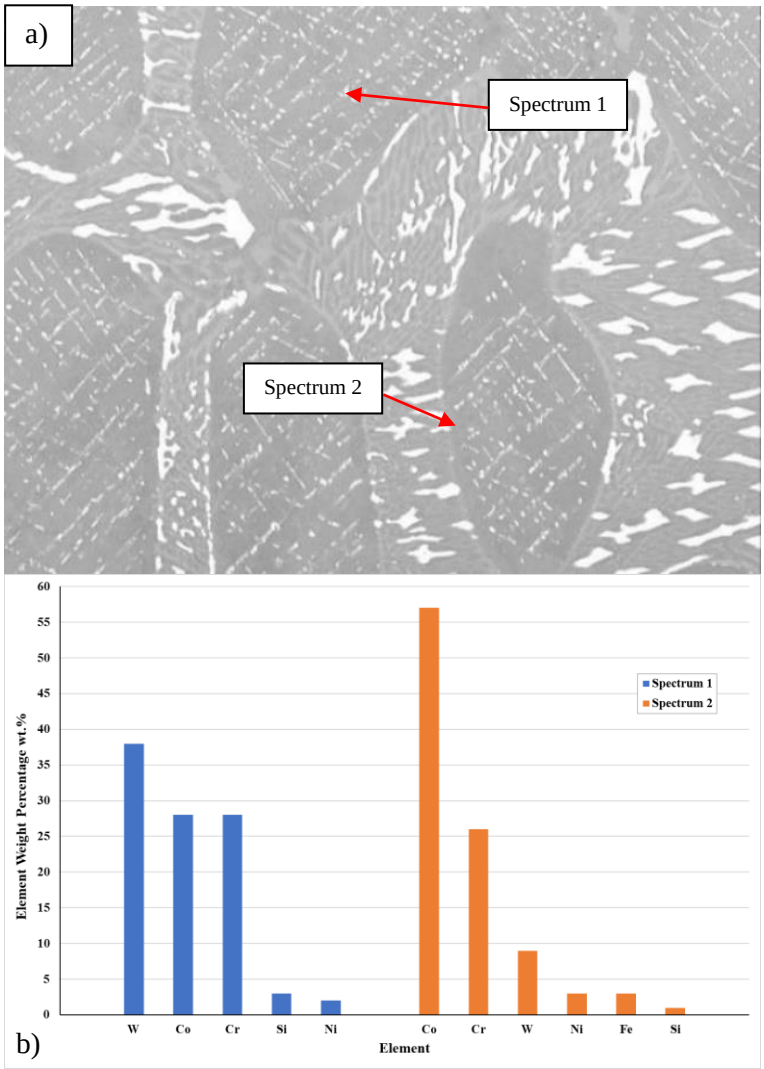

Figure 6.3: EDS point scan analysis of a furnace cooled WT-4 sample after annealing at 1000ºC for 4-hours: a) Point scan locations and b) Corresponding point scan compositions.

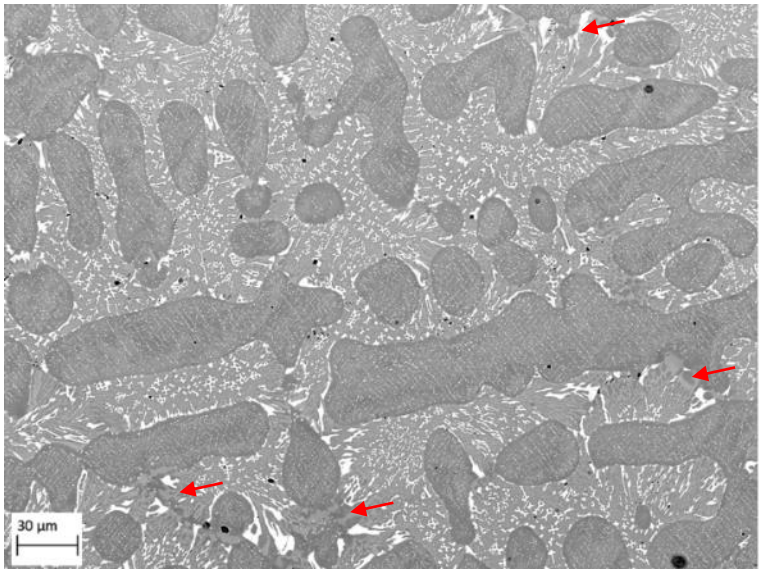

Figure 6.4: SEM microstructural analysis of WT-4 samples annealed at 1000°C for 2-hours highlighting coarsening of the eutectic phases.

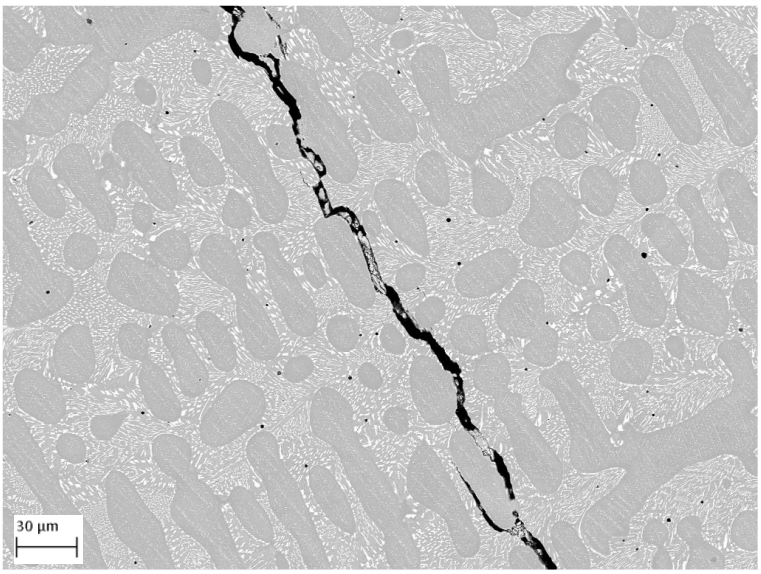

Figure 6.5: Crack propagation through microstructure of a water quenched WT-4 sample after annealing at 1000ºC for 1-hour.

6.1.2 Microstructure Analysis of Annealed WT-6

SEM analysis of the microstructures of the as-received and heat-treated WT-6 samples are presented in Figure 6.6. Analysis demonstrates that the microstructure remains largely unchanged after the annealing heat treatments where it consists of a cobalt solid solution matrix, chromium carbides and a small amount of tungsten carbides. However, area fraction analysis of the phases observed a small increase in the level of tungsten-rich phases after the annealing process. Area fraction analysis performed after each heat treatment is summarised in Table 6.2. The results indicate that the area fraction of the tungsten containing phase increased from around

0.2% in the untreated sample, to a range between 2-3% in the annealed samples. Precipitation of the tungsten phases, observed as white phases in the SEM images, generally formed large clusters of small precipitates, as illustrated in Figure 6.6. Analysis of the matrix also revealed the precipitation of another phase which is visible as a dark grey phase within the solid solution matrix, as shown in Figure 6.7. Precipitation of these phases were observed with each of the furnace cooled samples and the sample that was water quenched. EDS was performed on both phases to determine their composition. The composition of the phases is summarised in Figure 6.7. The darker precipitate (Spectrum 1) was identified to be chromium rich, and the composition of the white phase varied depending on their size, which may have been influenced due to the accuracy of the analysis, but Spectrum 2 demonstrates that they contained high levels of tungsten. Chemical analysis of the matrix of the treated samples identified that the areas of solid solution surrounding the precipitated phases experienced a decrease in chromium and tungsten concentration due to precipitation. Although the formation of the tungsten rich precipitates was frequently observed throughout the microstructure of the treated samples, the formation of the chromium rich precipitates only occurred in isolated areas of the matrix. Therefore, it was difficult to quantify how increasing the annealing time influenced the level of precipitation of this phase.

The area fraction of the chromium carbide phase remained similar after each heat treatment which was comparable to the untreated sample, suggesting the heat treatment had minimal effect on this phase. The composition of this phase also remained consistent after the heat treatments which confirms that the phase was largely unaffected by the heat treatment. Small decreases in the area fraction of the cobalt matrix were observed which correlated with an increase in the tungsten-rich phases. The results also indicate that the area fraction of individual phases remains consistent after each heat treatment which suggests that the microstructure experienced minor changes in morphology after the initial 1-hour heat treatment.

There appeared to be no difference in microstructure morphology and phase composition comparing the sample that was water quenched following annealing for a 1-hour treatment and the samples that were furnace cooled. There were also no signs of crack propagation that may have been caused due to thermal shock during quenching.

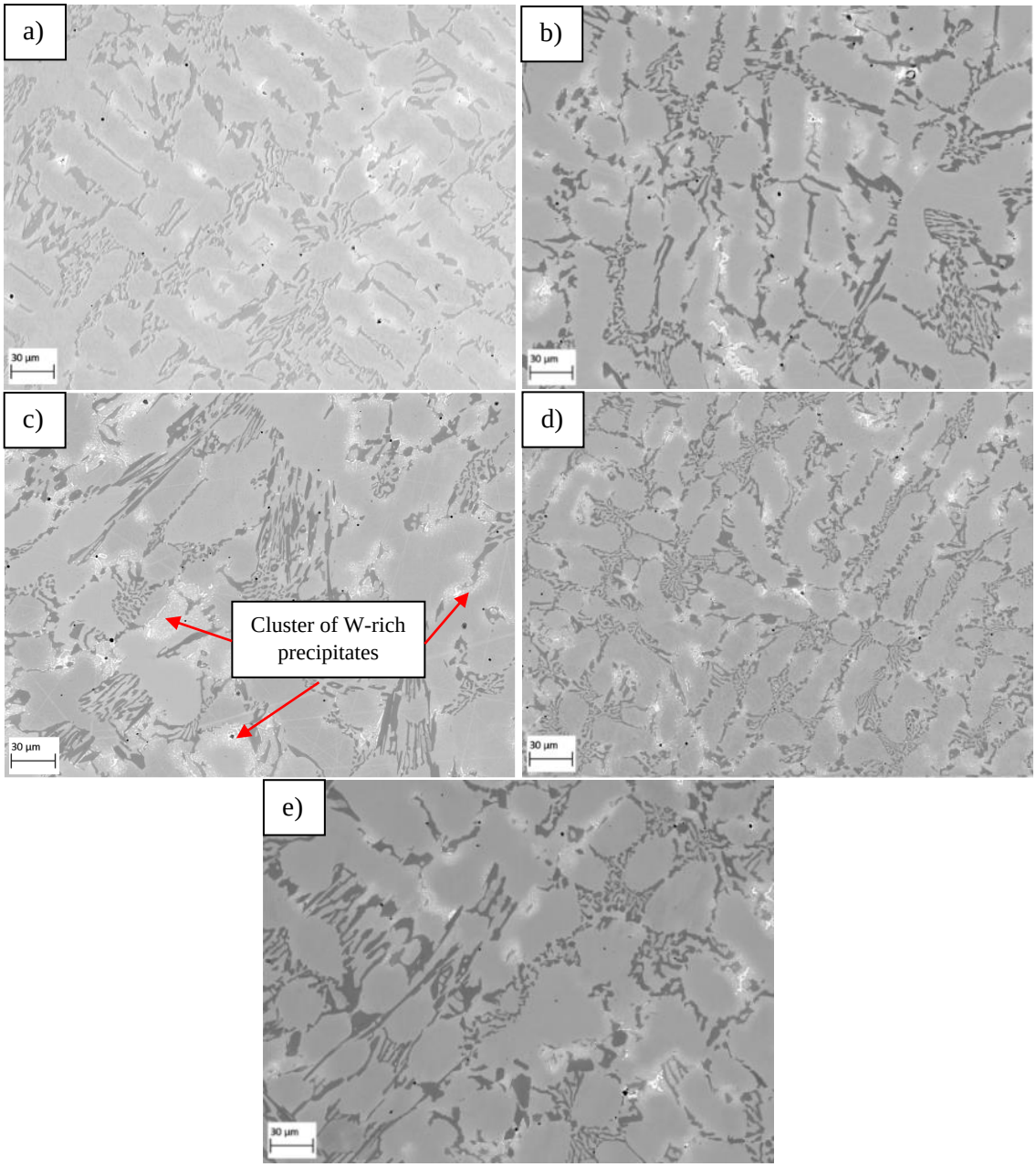

Figure 6.6: SEM microstructural analysis of WT-6 samples annealed at 1000°C for different times and different cooling processes with comparisons made to an untreated sample: a) Untreated, b) 1-hour and furnace cooled, c) 2-hours and furnace cooled, d) 4-hours at 1000°C. e) 1-hour and water quenched.

Table 6.2: Area fraction analysis of individual phases after each heat treatment with comparison to an untreated WT-6 sample.

Treatment / Phase	As received	1 Hour	2 Hour	4 Hour	Quenched
Co Matrix	83.8% (±0.9%)	80.12% (±0.78)	81.05% (±0.75)	80.82% (±0.55)	80.48% (±0.91)
Cr Carbide	17% (±0.2%)	17.34% (±0.67)	16.46% (±0.82)	16.96% (±1.07)	17.65% (±0.96)
W Carbide + Precipitate	0.2% (±0.1%)	2.9% (±0.75)	2.66% (±0.4)	3.12% (±0.37)	2.3% (±0.27)

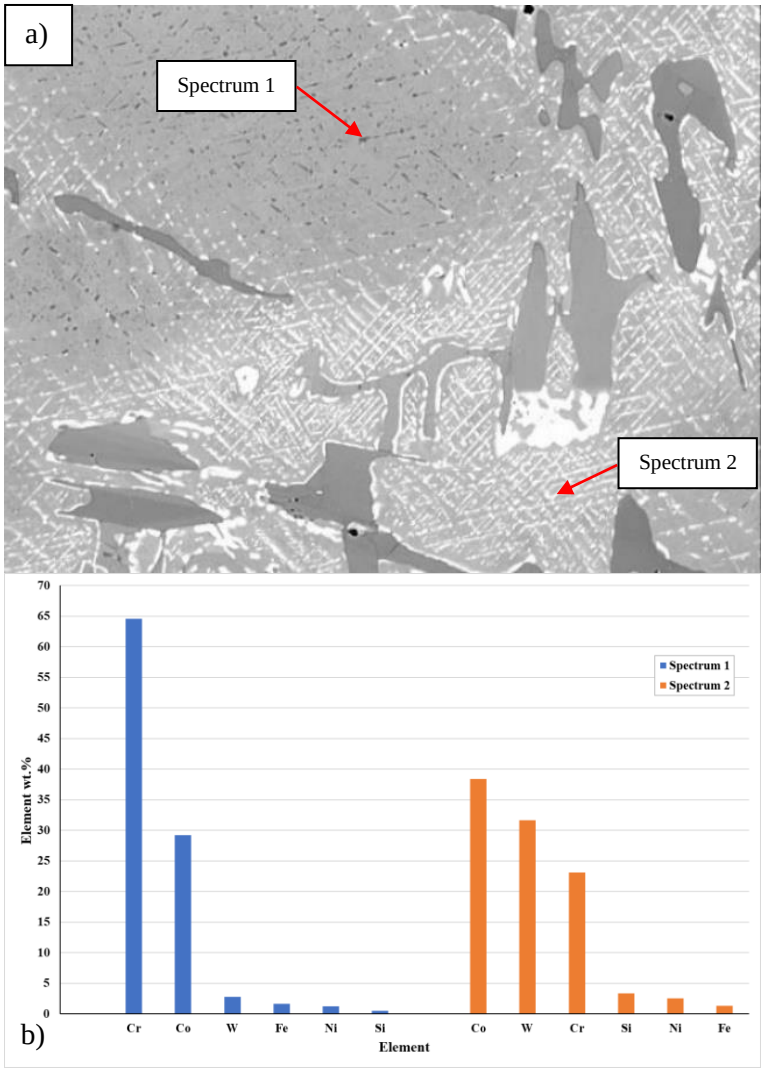

Figure 6.7: EDS point scan analysis of a furnace cooled WT-6 sample after annealing at 1000ºC for 4-hours: a) Point scan locations and b) Corresponding point scan compositions.

6.1.3 Microstructure Analysis of Annealed WT-12

Figure 6.8 displays the microstructure of the heat-treated WT-12 samples with comparisons made to an untreated sample. The microstructure of the treated samples consisted of chromium and tungsten carbides that are dispersed within a dendritic matrix. This is comparable to the microstructure of the untreated alloy. However, SEM analysis demonstrated that the heat treatment resulted in precipitation throughout the cobalt matrix, as shown in Figure 6.9. Precipitation of this phase occurred after each annealing treatment and appeared to become more evident with a longer treatment.

It appears, from the SEM analysis, that the chromium carbide phases (dark grey) decrease in size and volume after a prolonged annealing treatment of 4-hours. The change in chromium carbide morphology is demonstrated in Figure 6.8d. This suggests that the chromium phases

experience levels of diffusion during the annealing process. Area fraction analysis of the individual phases confirmed that the chromium-rich phases experienced levels of diffusion. Calculating the area fraction of each phase (Table 6.3) indicates a decrease in the chromium phase which gradually decreased with increased treatment time. The area fraction was recorded to decrease from around 19% with the untreated sample to around 11% after a 4-hour treatment. The dissolution of this phase resulted in the area fraction of the cobalt matrix and tungsten rich phases changing with prolonged heat treatments. Due to their similar colour, the calculated area fraction of the tungsten-rich phases includes the larger tungsten rich phases and the smaller precipitated tungsten phases. The initial 1-hour treatment resulted in a significant decrease in the volume fraction of the cobalt matrix and an increase in the tungsten-rich phases. The small decrease in the chromium-rich phase suggests that this initial increase in the tungsten-rich phase is mainly due to precipitation within the matrix. The gradual decrease in the chromium-rich phase, after 2 and 4-hour treatments, coincided with an increase of the cobalt matrix. Due to the small changes in the area fraction of the tungsten-rich phases, this suggests that chromium diffused into solid solution rather than resulting in further increases in tungsten rich phase formation.

EDS analysis of the sample treated for 4-hours is displayed in Figure 6.9. Analysis revealed that the composition of the precipitated phase (Spectrum 1) varied but was generally tungsten-rich with high levels of cobalt and chromium. After a 1-hour treatment, the formation of this phase resulted in areas of the matrix becoming depleted in chromium and tungsten. However, after each treatment the level of chromium and tungsten in isolated areas of the matrix increased in concentration. It was identified that the areas of the matrix that contained higher levels of alloying elements often occurred in close proximity to carbide phases, demonstrated by Spectrum 2. The increase in chromium and tungsten content would suggest the chromium rich phases experienced levels of diffusion into solid solution. This was confirmed by analysing the composition of the chromium phase (Spectrum 3) which neighboured the location of Spectrum 2 in Figure 6.9. Analysis revealed a significant decrease the level of chromium when compared to the general composition of these phases in an untreated sample. This theory is in line with the calculated reduction in the area fraction of the chromium phase. Calculating the area fraction of precipitated phases within the matrix revealed that a longer annealing time increased the level of precipitation. An area fraction of 11% was calculated after a 1-hour treatment which increased to 15% with the sample treated for 4-hours. A comparison of the microstructures is presented in Figure 6.10. The images highlight that prolonged annealing also resulted in the coarsening of the precipitates.

The microstructure of the water quenched sample is shown in Figure 6.8e. The image demonstrates similar changes in microstructure that were observed with the samples that were

furnace cooled where the precipitation of a tungsten-rich ternary phase formed within the matrix. This process resulted in a reduction in the area fraction of the cobalt matrix. The rapid cooling of the sample resulted in significant material failure, as shown in Figure 6.11. The image displays severe failure of the materials microstructure where crack propagation occurred through the fracturing of the chromium-carbide.

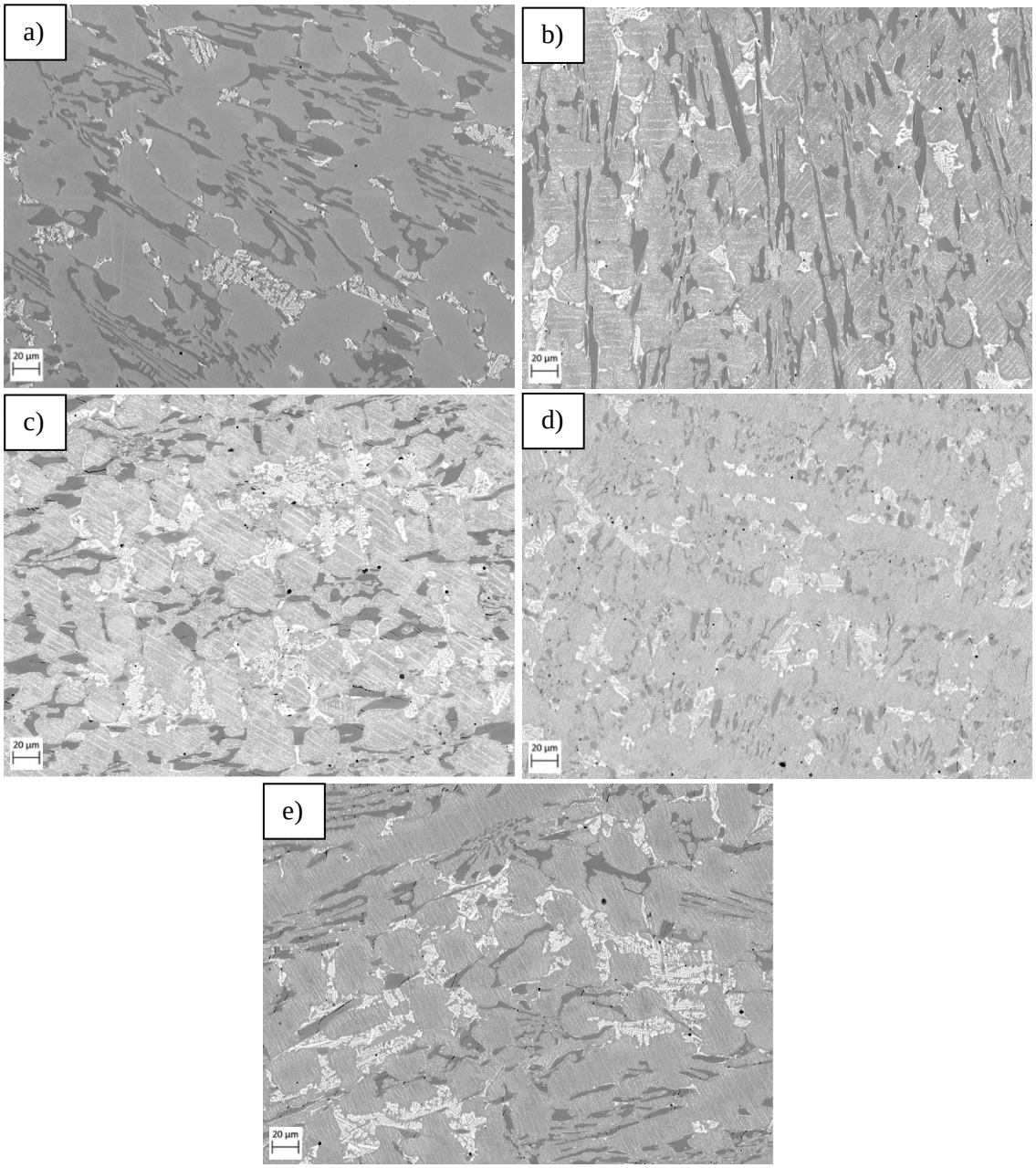

Figure 6.8: SEM microstructural analysis of WT-12 samples annealed at 1000°C for different times and different cooling processes with comparisons made to an untreated sample: a) Untreated, b) 1-hour and furnace cooled, c) 2-hours and furnace cooled, d) 4-hours at 1000°C. e) 1-hour and water quenched.

Table 6.3: Volume fraction analysis of individual phases after each heat treatment with comparison to an untreated WT-12 sample.

Treatment / Phase	As received	1 Hour	2 Hour	4 Hour	Quenched
Co Matrix	74.4% (±3.5%)	67.22% (±1.33)	70.48% (±2.5)	75.94% (±1.57)	75.14% (±3.37)
Cr Carbide	19.3% (±3.8%)	18.52% (±1.24)	14.09% (±1.65)	11.32% (±0.8)	15.91% (±2.08)
W Carbide + Precipitate	7.6% (±0.6%)	17.64% (±1.18)	16.56% (±1.02)	15.02% (±1.68)	14.4% (±2.6)

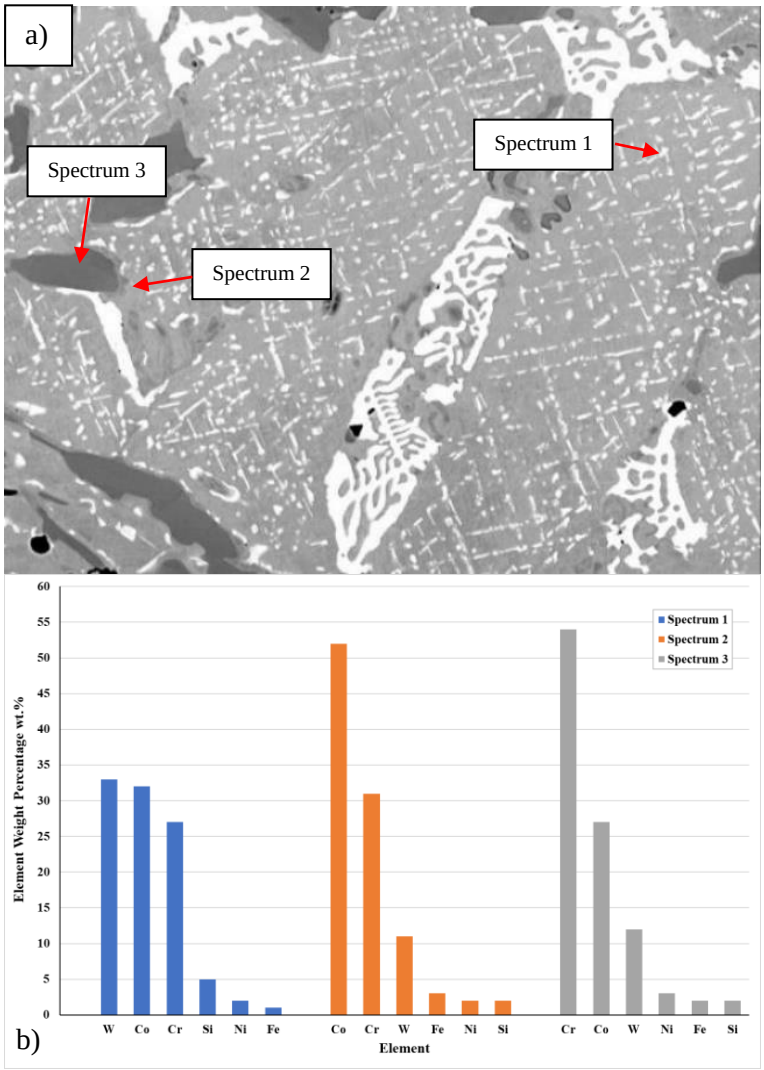

Figure 6.9: EDS point scan analysis of a furnace cooled WT-12 sample after annealing at 1000ºC for 4-hours: a) Point scan locations and b) Corresponding point scan compositions.

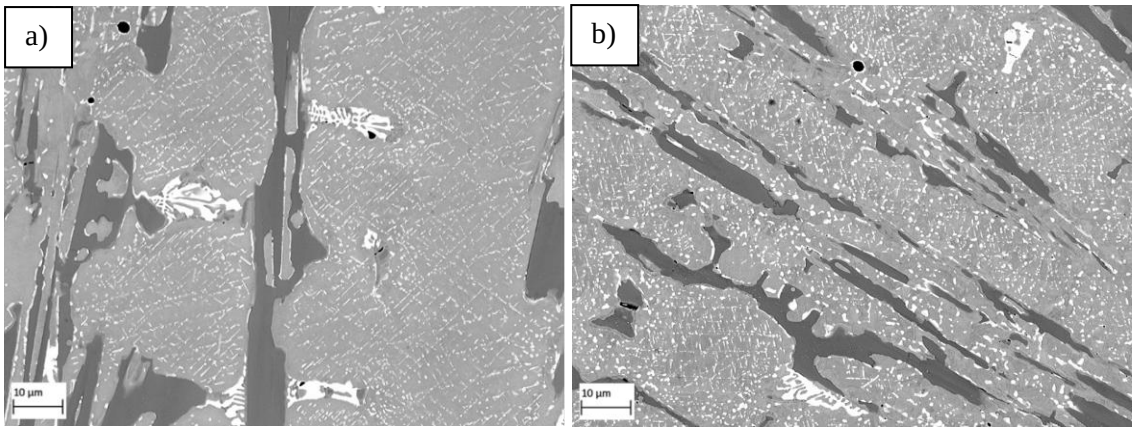

Figure 6.10: Comparisons of matrix phase precipitation after annealing at 1000°C: a) 1-hour and b) 4-hours.

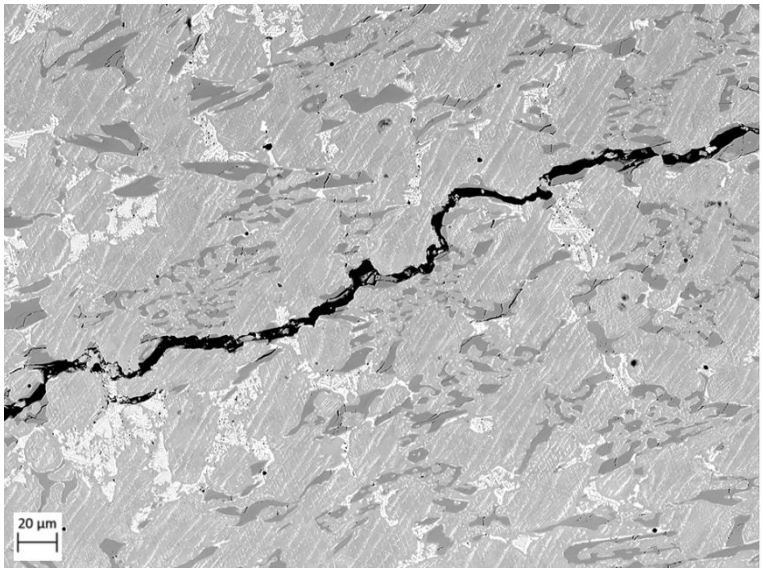

Figure 6.11: Crack propagation through microstructure of a water quenched WT-12 sample after annealing at 1000ºC for 1-hour.

6.1.4 Microstructure Analysis of Annealed T-800

The microstructures of the T-800 samples after heat-treating for various times at 1000ºC are presented in Figure 6.12 where comparisons are made to an untreated sample. The microstructure of the untreated T-800 Tribaloy consisted of a primary Laves phase and eutectic mixture of solid solution and secondary Laves phases. After heat-treating the samples, minor changes to the microstructure were observed. The primary Laves phase was largely unaffected by the heat treatments and the composition of this phase remained comparable to the as-received sample. However, it was identified that the phase boundaries were occasionally seen to be become slightly blurred, particularly at longer treatment times, suggesting that the phase experienced some levels of diffusion. It was also observed that the secondary Laves phases in the eutectic

matrix became more spherical in shape after heat treating, as opposed to a finer laminar structure seen in the untreated T-800 Tribaloy. More significant changes were observed in the alloy's eutectic solid solution phase. Due to the high alloying additions of molybdenum with this alloy's chemistry, small precipitates containing high levels of molybdenum were observed in the matrix of the untreated sample. However, there was a clear increase in the quantity of precipitated phases in the matrix after annealing the samples. Area fraction analysis of the individual phases after each treatment is presented in Table 6.4. Due to their colour, the primary/secondary Laves phases, and the precipitates would have been included in the same calculation. The results show that after a 1-hour treatment the area fraction of the Laves phases and precipitates increases whilst the area fraction of the eutectic CoMo solid solution phase decreases. This trend continued with increased annealing time. The area fraction of the matrix remained consistent after each treatment. It was calculated that the precipitates occupied around 14% of the matrix area in an untreated sample. This increased to around 18% with the sample annealed for 1-hour which increased further to 20% with the sample annealed for 4-hours. The results indicate that the annealing treatment results in increased precipitation within in the matrix which also coincides with the dissolution of the eutectic CoMo solid solution phase. The results also suggest that there was little evidence of the Laves phases dissolving into solid solution.

EDS analysis of a sample annealed at 1000°C for a 4-hour treatment is displayed in Figure 6.13. The precipitate (Spectrum 1) was found to contain higher levels of molybdenum, chromium and silicon compared to the precipitated phase in the untreated sample. It was identified that the formation of the precipitate depleted the surrounding matrix of alloying elements, particularly molybdenum. Figure 6.13 also highlights the dissolution of the eutectic CoMo solid solution phase where it appeared to break up into smaller phases which were located around its circumference. Spectrum 2 identified a molybdenum-rich phase that was a similar composition to the Laves Phase and the second phase (Spectrum 3) was found to have a similar composition to the larger CoMo solid solution phase. This process is reflected in the area fraction analysis of the individual phases where it was calculated that the quantity of precipitates increased whilst the quantity of the CoMo phase decreased. From this data it can be proposed that the formation of the precipitates within in the matrix arises due to precipitation of alloying elements from solid solution and the diffusion and breakup of the CoMo solid solution phase.

Similar changes in microstructure morphology were experienced with the quenched sample as were observed with the samples that were furnace cooled. However, due to the brittle nature of the T-800 Tribaloy and its poor resistance to thermal shock, the quenching process resulted in multiple large cracks throughout the microstructure. Cracks were seen to propagate through the extremely hard primary Laves, as shown in Figure 6.14.

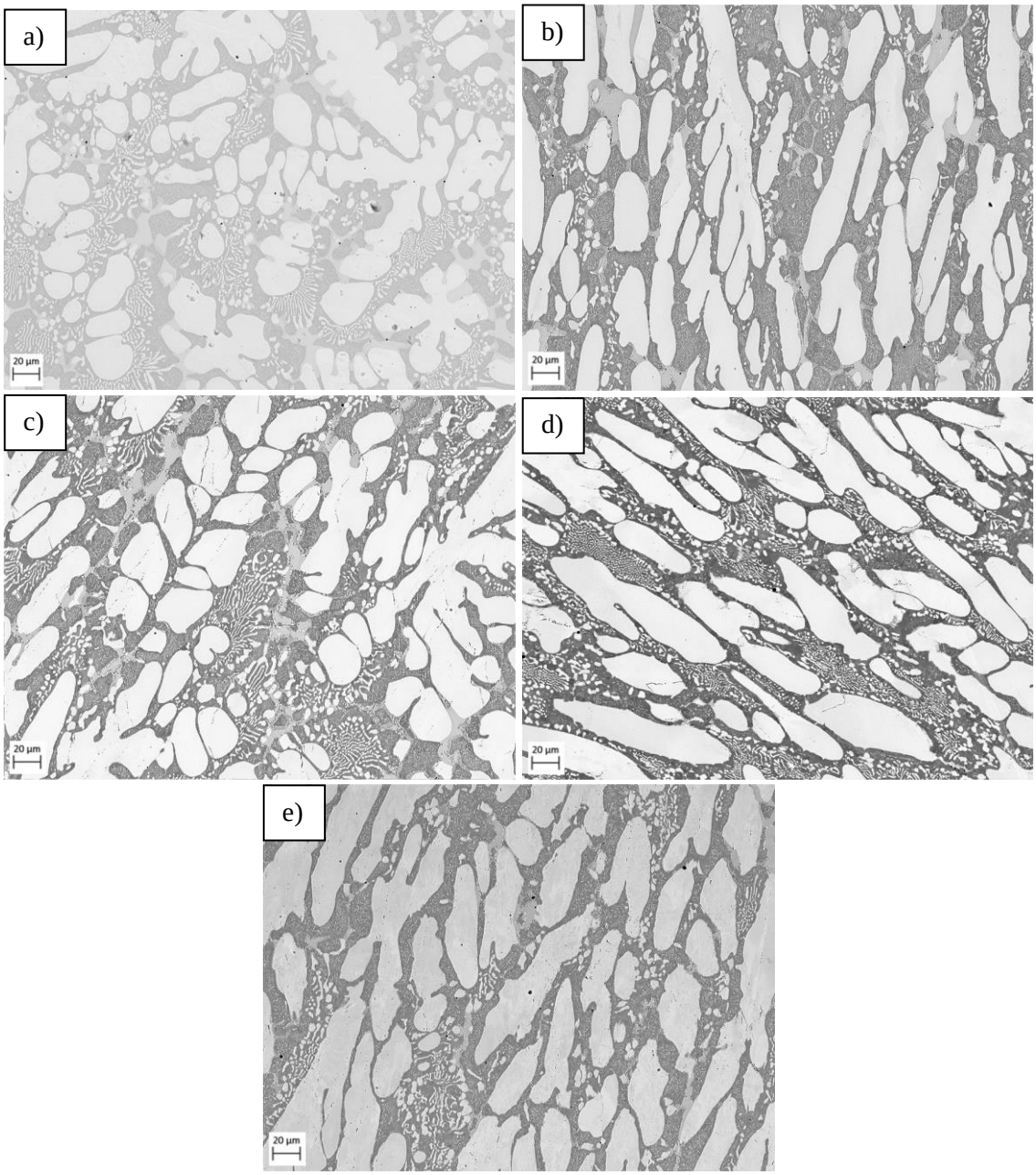

Figure 6.12: SEM microstructural analysis of T-800 samples annealed at 1000°C for different times and different cooling processes with comparisons made to an untreated sample: a) Untreated, b) 1-hour and furnace cooled, c) 2-hours and furnace cooled, d) 4-hours at 1000°C. e) 1-hour and water quenched.

Table 6.4: Volume fraction analysis of individual phases after each heat treatment with comparison to an untreated T-800 sample.

Treatment / Phase	As received	1 Hour	2 Hour	4 Hour	Quenched
Laves Phase + Precipitates	54.3% (±1.4)	56.89% (±0.8)	56.4% (±0.5)	57.7% (±0.7)	59.5% (±2.7)
Eutectic (CoCr)	36.5% (±1)	34% (±0.8)	36.5% (±0.9)	36.7% (±0.3)	36.4% (±2.8)
Eutectic (CoMo)	9.7% (±1.9)	7.8% (±0.7)	6.6% (±0.7)	7% (±0.7)	5.6% (±1.1)

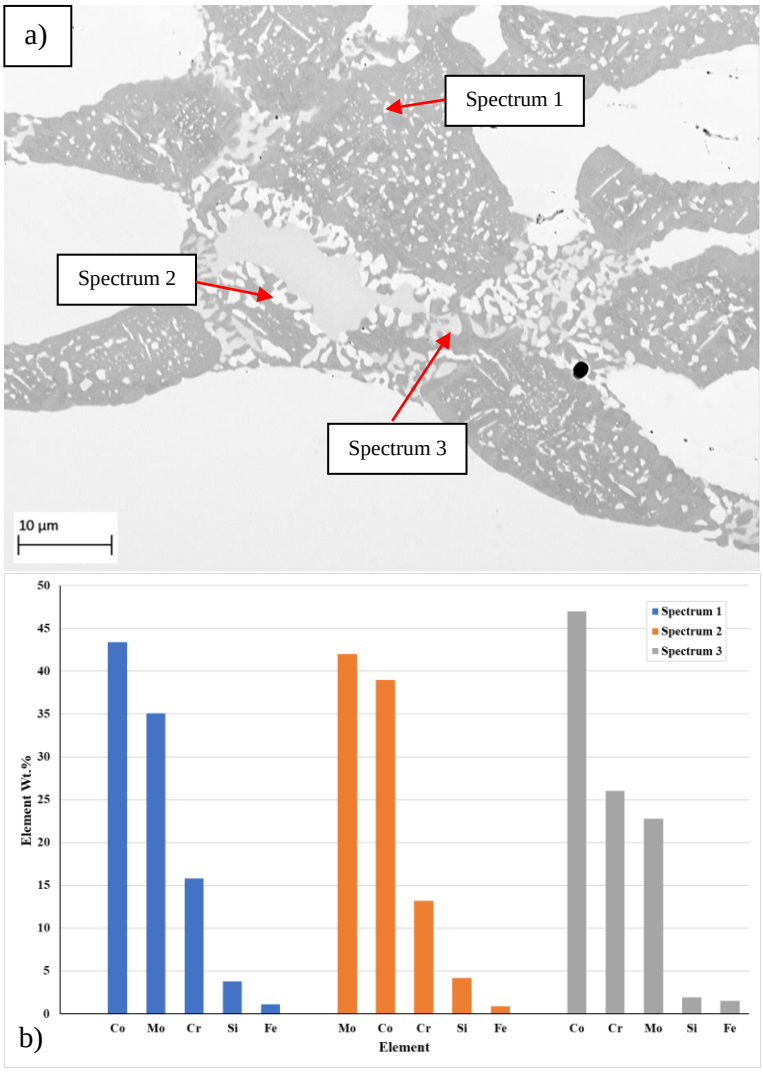

Figure 6.13: EDS point scan analysis of a furnace cooled T-800 sample after annealing at 1000ºC for 4-hours: a) Point scan locations and b) Corresponding point scan compositions.

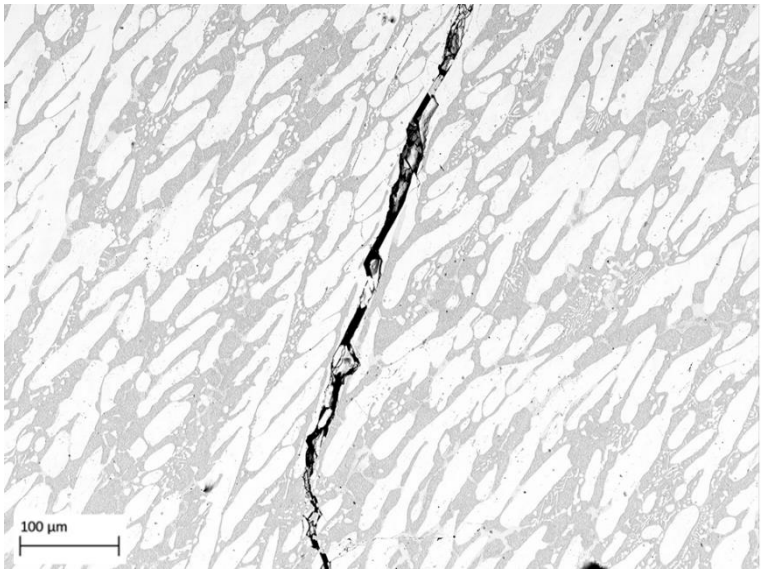

Figure 6.14: Crack propagation through microstructure of a water quenched T-800 sample after annealing at 1000ºC for 1-hour.

6.1.5 Hardness Variation with Annealing Heat Treatment

6.1.5.1 Macrohardness and Microhardness Analysis of Annealed WT-4

Figure 6.15 displays the changes in material bulk hardness of the WT-4 samples after various annealing heat treatments were carried out. Table 6.5 summarises the changes in hardness and calculates the change as a percentage with comparison to an untreated sample. Hardness values taken at a higher load indicate that the heat treatments had little effect on the overall material hardness as only minor changes in material bulk hardness were experienced. This indicates that the heat treatment has little effect on the alloys bulk hardness even at longer treatment times. The sample that was quenched following a 1-hour heat treatment experienced the greatest increase in material hardness where a 7% increase was recorded, compared to an untreated sample. However, it was identified that the alloy experienced significant cracking caused by thermal shock and is therefore unsuitable for a quenching process.

Microhardness analysis of the cobalt matrix and the eutectic region are presented in Figure 6.16. The results indicate a small increase in hardness of the matrix after the alloy was heat treated. As with the bulk hardness readings, the biggest increase in hardness was recorded after a 1-hour treatment where the hardness of the matrix increased from 480Hv to 541Hv, an increase of 12%. The matrix hardness did not increase further with increased treatment time but gradually decreased after a 2 and 4-hour treatment. This indicates that after the initial 1-hour treatment, further annealing has a detrimental effect on the microhardness of the matrix. Although the hardness was observed to decrease after longer treatments, the hardness was still slightly higher

compared to an untreated sample. The largest increase in matrix hardness was recorded after the sample was quenched following a 1-hour treatment. However, it has already been identified that the WT-4 alloy is unsuitable for quenching due to crack propagation. Microhardness analysis of the eutectic region produced a wide range of hardness readings. This is due to the region comprising of multiple phases which consists of carbide phases and a cobalt-rich phase. Therefore, the hardness results would have been strongly influenced by what phases were included in the analysis. However, the results do suggest that the annealing heat treatment increased the hardness of the eutectic region. This is likely due to the coarsening of carbide phases after the annealing treatment that was identified in section 6.1.1. Similar to the changes in hardness experienced in the matrix, greater increases were recorded after shorter treatment times where longer treatments resulted in a decrease in hardness compared to the initial increase in hardness.

From the results, the small changes in bulk hardness can be attributed to a combination of the heat treatment improving the hardness of the matrix and eutectic region of the alloys microstructure.

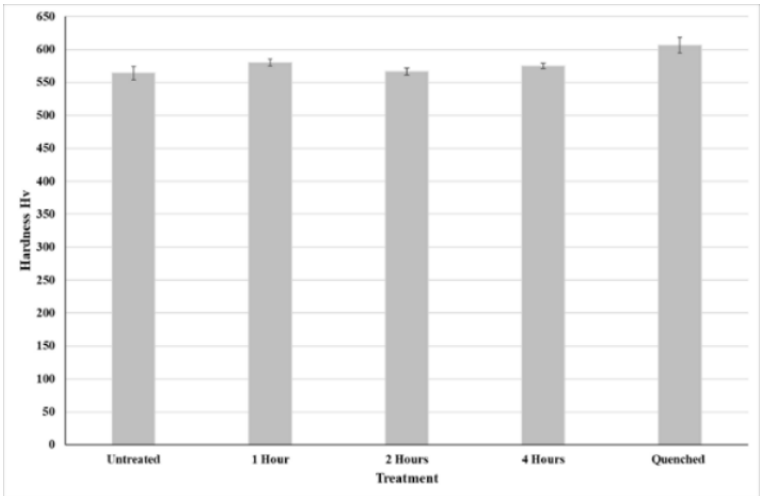

Figure 6.15: Changes in material bulk hardness of the WT-4 alloy after annealing at 1000ºC for various periods of time and after different cooling condition

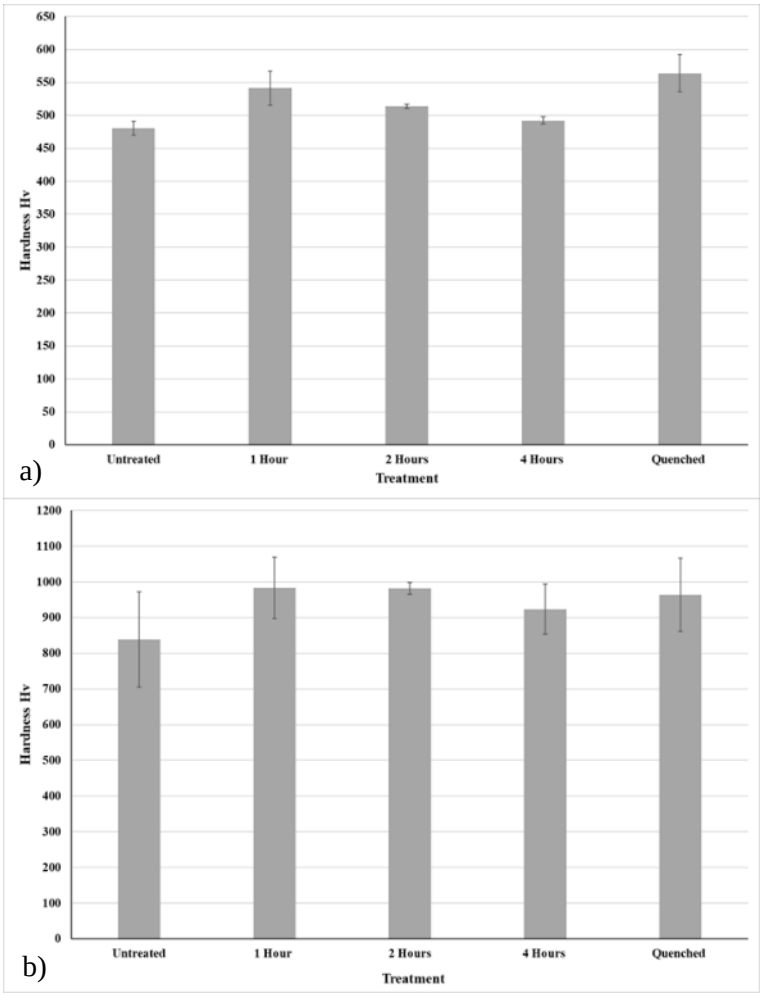

Figure 6.16: Changes in microhardness of the matrix and eutectic region of the WT-4 alloy after annealing at 1000ºC for various periods of time and after different cooling conditions: a) Matrix and b) Eutectic region.

Table 6.5: Changes in hardness of the WT-4 samples after each treatment with referecnce to an untreated sample.

	Bulk		Matrix		Eutectic	
Treatment	Hardness Hv	% Change	Hardness Hv	% Change	Hardness Hv	% Change
Untreated	564.31 (±8.22)	-	480.53 (±10.36)	-	839.06 (±133.86)	-
1 Hour	579.91(±5.2)	2.76	541.53 (±26.08)	12.70	983.37 (±85.97)	17.20
2 Hour	566.61(±5.3)	0.41	513.69 (±2.77)	6.90	981.75 (±16.56)	17.01
4 Hour	575.1(±4.36)	1.9	492.3 (±5.86)	2.45	924.1 (±70.13)	10.14
Quenched	606.33(±11.89)	7.45	563.67 (±28.36)	17.30	963.4 (±102.97)	14.82

6.1.5.1.1 Phase Specific Nanoindentation Analysis of WT-4

SEM analysis of the microstructure of the treated WT-4 samples identified phase precipitation within the alloy's matrix. Formation of this phase was also identified using SPM topography scans of the sample's surfaces. Figure 6.17a and d compare the surfaces an untreated sample and a sample annealed at 1000ºC for 4-hours. The analysis highlights the presence of the

precipitated ternary phase throughout the matrix of the treated sample. XPM mapping performed within the matrix highlight how the precipitates influence the mechanical properties of the matrix after the annealing process. Comparing the mechanical property maps for the samples indicates that the precipitate is harder than the surrounding cobalt matrix. Whereas the hardness of the solid solution in the untreated sample remains uniform throughout the phase, localised regions of increased hardness can be observed within the matrix of the annealed sample. These regions can be attributed to the formation of the ternary phase. The maps also indicate that the precipitated phases have an increased modulus.

Table 6.6 displays the average changes in mechanical properties after each heat treatment using the XPM data. An average increase in hardness and modulus of the matrix was experienced after the initial 1-hour treatment. The average hardness increased further after a 2-hour treatment although the modulus remained similar. A longer 4-hour treatment did not continue this trend and a decrease in hardness and modulus was recorded. However, compared to an untreated sample, the average modulus remained at a similar value but a slight increase in hardness was experienced. Figure 6.18 displays the distribution of hardness and modulus data of the treated samples with comparisons made to an untreated sample. The hardness data (Figure 6.18a+b) illustrates an increase in the range of hardness values after a 1-hour treatment. A higher minimum value also demonstrates the matrix did not experience any reduction in hardness. Further improvements in hardness were recorded after a 2-hour treatment. The lowest value recorded with this sample is higher than the upper quartile range of the untreated sample. Therefore, all hardness readings were higher than 75% of the values recorded with the untreated sample. The increase in hardness correlates to a shift in hardness data to the right of the histograms, as shown in Figure 6.18b. The longer 4-hour treatment resulted in a drop in hardness compared to the sample treated for 2-hours. Compared to the untreated sample, a slightly lower minimum and maximum value was recorded. This indicates that a longer treatment time has detrimental effects on the hardness of the matrix. It was identified that prolonged annealing resulted in increased precipitation and coarsening of the precipitated phases within the matrix. This is reflected in the number outliers that were recorded after longer treatment times which represent hardness readings that were performed on/near the precipitates.

Figure 6.18c-d displays the distribution of the XPM modulus data for the treated samples. The sample treated for 1-hour produced a wide data range compared to the untreated sample where the minimum value was higher than the minimum value recorded with the untreated sample. This demonstrates that the treatment improved the modulus of the matrix. The median line for this sample is at a similar value to the maximum value of the untreated sample which indicates that 50% of the modulus readings for the 1-hour treated sample were higher than the

maximum value recorded with the untreated sample. Comparing the samples treated for 1 and 2-hours shows that the sample annealed for 2-hours had a lower range of modulus readings where a lower maximum modulus reading was recorded. Compared to the untreated sample, the sample annealed for 2-hours had a similar minimum modulus value to the lower quartile for the untreated sample. This demonstrates that all the readings for the treated sample were higher than lowest 25% of readings recorded with the untreated sample. A drop in modulus was recorded with the sample treated for 4-hours. Although a higher maximum value was recorded, compared to untreated sample, the lowest value recorded was significantly lower. The median line for the 4-hour treated sample was similar to the upper quartile range of the untreated sample which shows that only 50% of the readings were higher than the lowest 25% of readings with the untreated sample. This demonstrates that a longer annealing treatment has detrimental effects on the modulus of the matrix.

The results indicate that shorter treatment times had positive effects on the mechanical properties of the matrix whereas longer treatment times had detrimental effects on the hardness and modulus of the matrix. This is likely to be due to increased precipitation of the ternary phase, experienced after prolonged annealing, which resulted in chromium and tungsten depletion from solid solution.

Figure 6.19 demonstrates that the annealing treatment increased the H/E ratio of the matrix. A minor increase occurred after a 1-hour treatment but increasing the treatment time to 2-hours resulted in a more significant increase. A longer 4-hour treatment caused the H/E ratio to decrease to a similar value recorded after a 1-hour treatment. This demonstrates that the wear resistance of the matrix can be improved with a 2-hour annealing treatment.

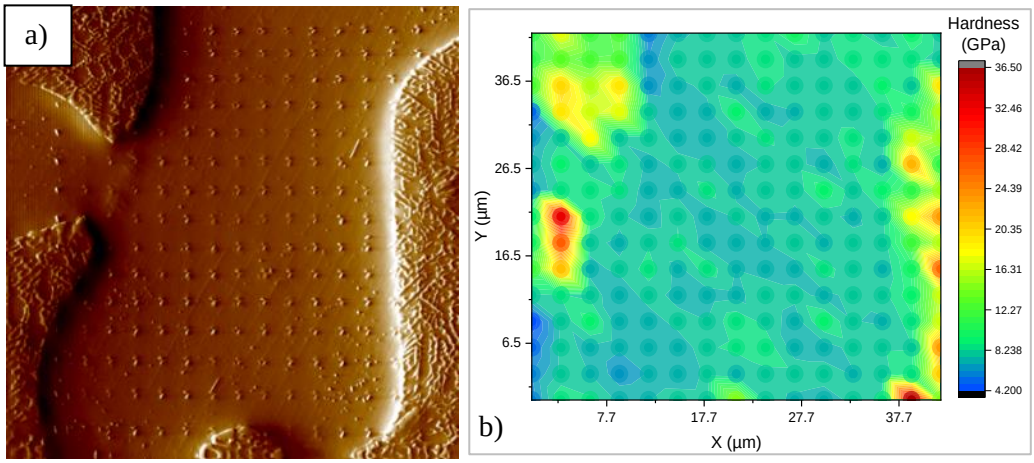

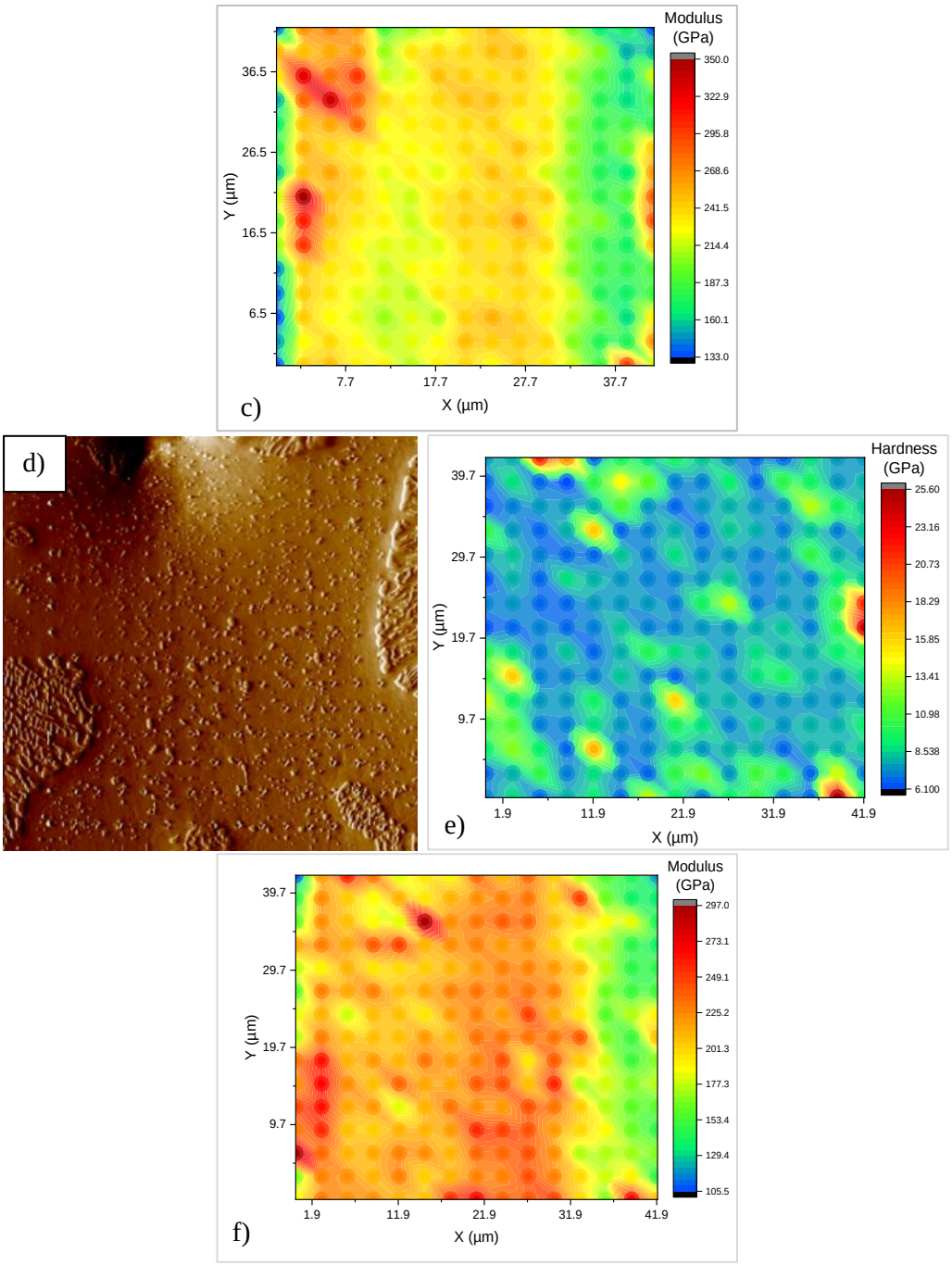

Figure 6.17: Nanoindentation analysis of matrix of the untreated and annealed WT-4 samples: a) SPM grid analysis of untreated sample, b and c) Corresponding XPM hardness and modulus maps, d) SPM grid analysis of sample annealed at 1000°C for 4-hours and e and f) Corresponding XPM hardness and modulus map.

Table 6.6: Changes in matrix hardness and modulus after each treatment using XPM data.

Phase/Annealing Treatment	Hardness (GPa)	Reduced Modulus (GPa)
Co Solid Solution - Untreated	7.87 (±0.64)	230.74 (±7.26)
Co Solid Solution - 1 Hour	9.09 (±1.03)	252.15 (±16.48)
Co Solid Solution - 2-Hours	11.3 (±1.29)	249.31 (±9.03)
Co Solid Solution - 4-Hours	8.39 (±2.37)	227.34 (±14.32)

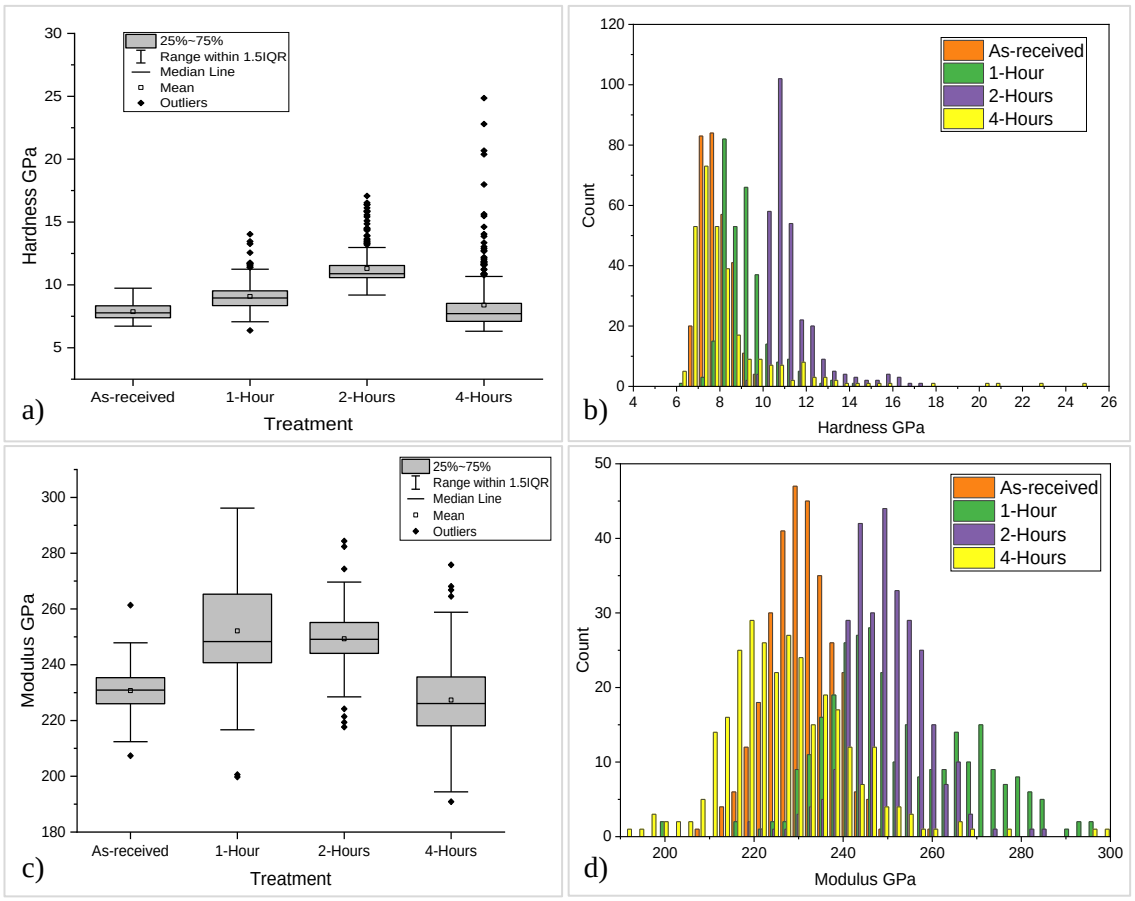

Figure 6.18: Distribution of hardness and modulus data after each treatment calculated from XMP analysis: a and b) distribution of hardness data and c and d) distribution of modulus data.

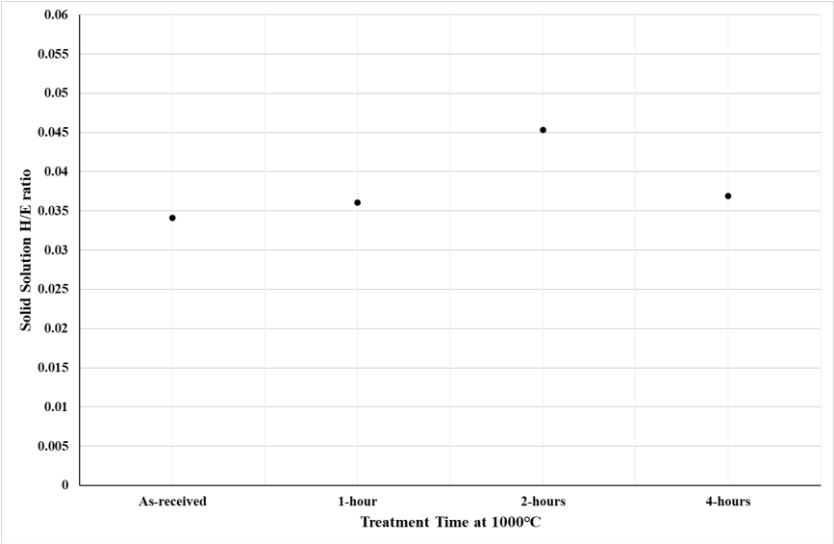

Figure 6.19: Matrix H/E ratios after various annealing times at 1000°C.

6.1.5.2 Macrohardness and Microhardness Analysis of Annealed WT-6

Changes in material bulk hardness and matrix microhardness experienced with the WT-6 samples after annealing for different times is displayed in Figure 6.20 and Figure 6.21, respectively, with references made to an untreated sample. The results are summarised in Table 6.7. The results indicate that the annealed furnace cooled samples experienced minor increases in hardness ranging between 3-6%, compared to an untreated sample. Although there was little variation in the bulk hardness between the treated samples, the highest average hardness and highest maximum value was recorded with the sample that was annealed for 1-hour. Compared to the furnace cooled samples, the sample that was water quenched after a 1-hour annealing treatment experienced a much greater increase in hardness where the hardness increased from 429Hv to 532Hv, an overall increase in material hardness of 24%.

Microhardness analysis performed on the alloy's matrix indicates a small change in hardness with the samples that were furnace cooled. The changes in hardness ranged between 2-7% where the greatest increase in hardness was experienced with the sample treated for 2-hours. With this sample the hardness increased from 400Hv, with the untreated sample, to 429Hv. As experienced with the bulk hardness measurements, the greatest increase in microhardness was recorded with the sample that was water quenched after a 1-hour treatment where an increase of 25% was recorded where hardness increased by 100Hv, compared to an untreated sample.

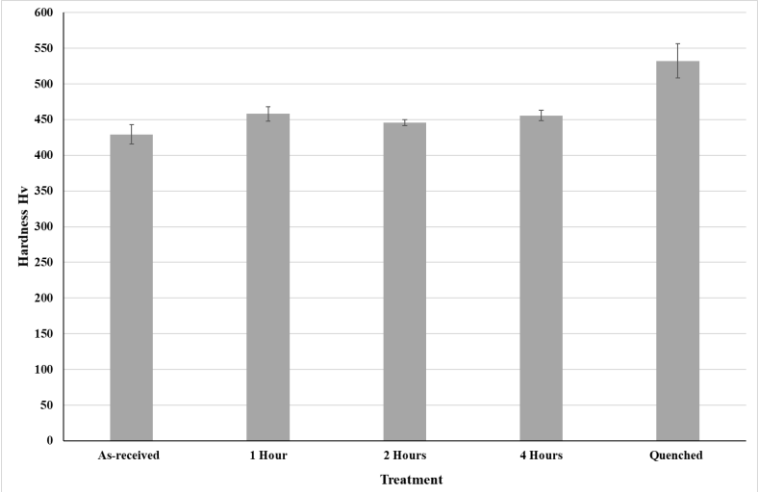

Figure 6.20: Changes in material bulk hardness of the WT-6 alloy after annealing at 1000ºC for various periods of time and after different cooling condition.

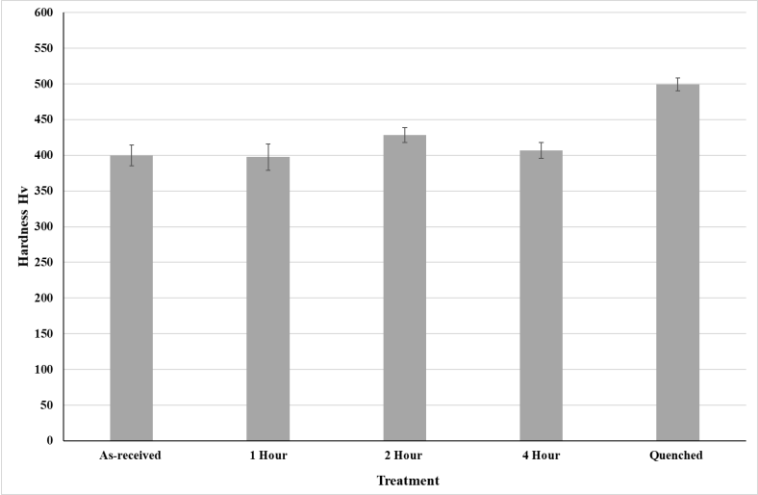

Figure 6.21: Changes in microhardness of the matrix of the WT-6 alloy after annealing at 1000ºC for various periods of time and after different cooling conditions.

Table 6.7: Changes in hardness of the WT-6 samples after each treatment with referecnce to an untreated sample.

	Bulk		Matrix	
Treatment	Hardness Hv	% Change	Hardness Hv	% Change
Untreated	430.31 (±10)	-	399.67 (±14.5)	-
1 Hour	457.99 (±10.29)	6.38	407.03 (±18.08)	1.84
2 Hour	446.05 (±4.13)	3.61	428.54 (±10.32)	7.22
4 Hour	455.81 (±7.19)	5.88	414.43 (±5.19)	3.69
Quenched	532.1 (±23.92)	23.60	499.18 (±9.16)	24.90

6.1.5.2.1 Phase Specific Nanoindentation Analysis of WT-6

Analysis of the microstructures of the WT-6 samples after the annealing process revealed the precipitation of a ternary phase throughout the matrix that was found to contain high levels of chromium and tungsten. Topography scans of the samples surface also highlights the formation of these phases, as shown in Figure 6.22d, which displays a sample after a 4-hour treatment. Figure 6.22 compares the mechanical property maps, created using XPM analysis, of the matrix for an untreated sample and a sample treated for 4-hours. Differences in hardness within the matrix indicates that the precipitated phase is harder than the surrounding matrix. Table 6.8 displays the average hardness and modulus calculated from XPM analysis of the matrix. The results indicate that the furnace cooled samples and the quenched sample experienced small reductions in average hardness after the annealing treatment. The distribution of XPM data is shown in Figure 6.23. In addition to the decrease in average hardness, Figure 6.23a displays that the treated samples experienced lower hardness values in the data range compared to the untreated sample. The upper quartile for the untreated sample is greater than the maximum value for the

treated samples which shows that 25% of the values recorded with the untreated sample were greater than the highest values recorded with the treated samples. The results also show that the lower quartile for the untreated sample is greater than the upper quartile values for the treated samples which indicates that 75% of the hardness data for the untreated is greater than 75% of the highest values recorded with treated samples. The drop in hardness is demonstrated in Figure 6.23b where the hardness peak for the treated samples shifts to the left of the graph.

The increase in outlier values, which correlate to the precipitated phases, suggests that the volume of precipitated phases increased with longer treatments. This is in line with the calculated increase in area fraction of the precipitates after a longer annealing described in section 6.1.2. The lowest hardness values and most outliers were recorded with the sample treated for 4-hours. This proposes that the increased formation of precipitates results in a decrease in hardness of the matrix as alloying elements precipitate out from solid solution to form the ternary phase.

The 1-hour annealing treatment resulted in an increase in modulus. However, longer treatments resulted in a gradual decrease in modulus compared to an untreated sample. The modulus of the quenched sample remained similar to the untreated sample. The distribution of modulus data is presented in Figure 6.23c-d. The data demonstrates that the median line and maximum value for the untreated sample were a similar to the minimum value and lower quartile of the sample treated for 1-hour. This shows that all the modulus readings with the treated sample are greater than 50% of readings of the untreated sample and that 75% of readings with the treated sample are higher than the highest value recorded with the untreated sample. Longer treatment times were observed to have negative effects on the matrix modulus. The maximum modulus value for the sample treated for 2-hours is a similar value to the upper quartile range of the untreated sample. This indicates that the greatest 25% of modulus readings with the untreated sample were higher than the highest reading recorded with the annealed sample. Further reductions in modulus were experienced with the sample treated for 4-hours where the majority of values were below the lowest values recorded with the untreated sample, signifying a clear drop in modulus. The changes in modulus are demonstrated in Figure 6.23d where increases and decreases in modulus experienced with the 1-hour and 4-hour treated samples, respectively, correlate to data peaks shifting to right with the 1-hour treatment and a peak shift to the left with the sample treated for 4-hours. Comparing the untreated sample and the quenched sample exhibits small improvements in modulus. The minimum modulus values are similar, but the quenched sample has a higher upper and lower quartile range and a greater maximum value.

Calculating the matrix H/E ratios after each treatment (Figure 6.24) reveals that a quenched sample and a furnace cooled sample after a 1-hour annealing treatment resulted in the H/E ratio decreasing. A longer 2 and 4-hour treatment resulted in the ratio increasing again but

no significant improvements were recorded when compared to an untreated sample. This would suggest that the annealing treatment does not improve the wear resistance of the matrix.

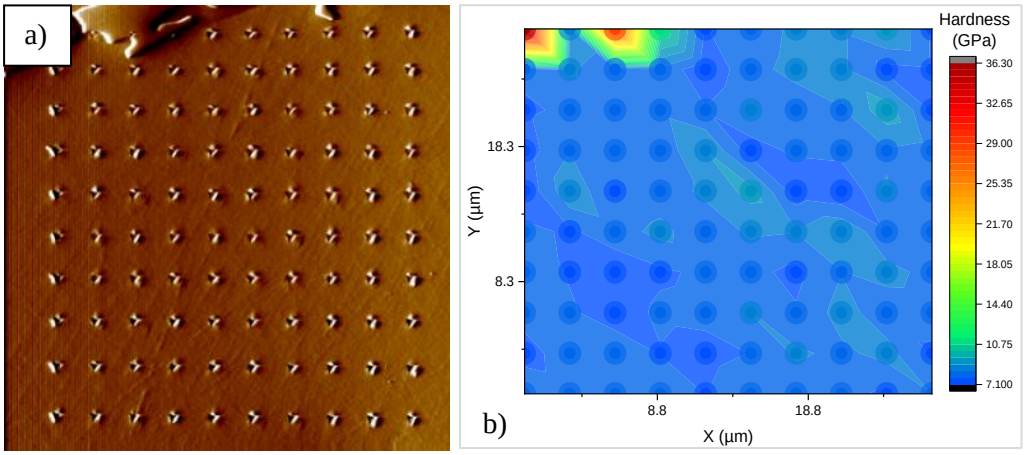

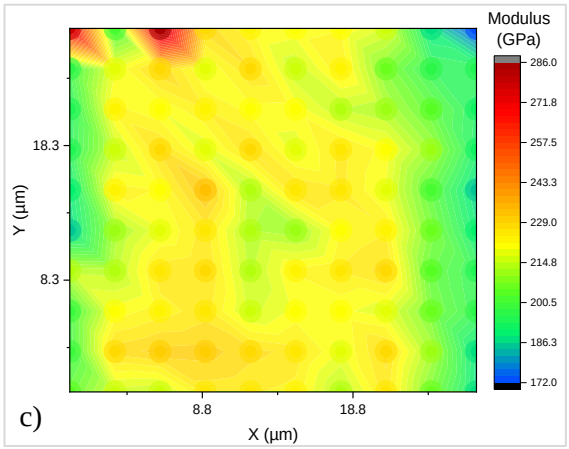

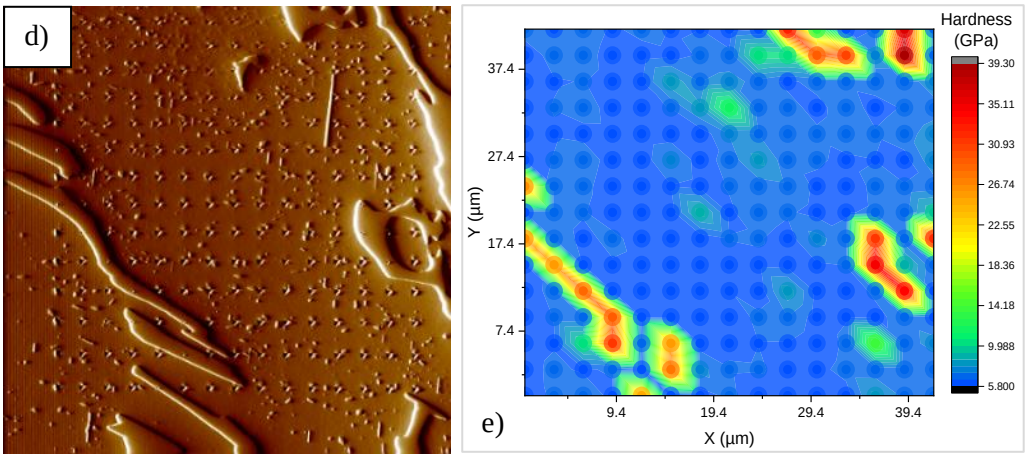

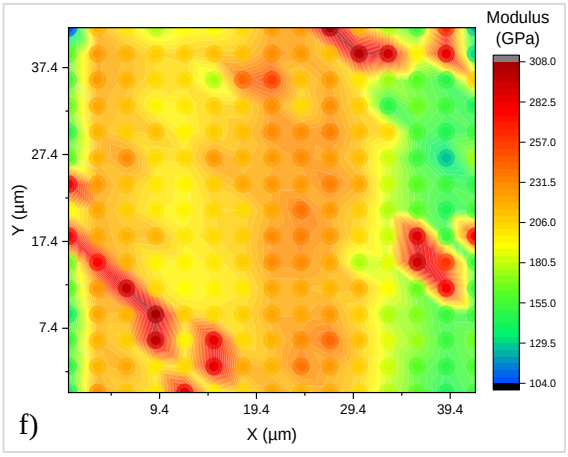

Figure 6.22: Nanoindentation analysis of matrix of the untreated and annealed WT-6 samples: a) SPM grid analysis of untreated sample, b and c) Corresponding XPM hardness and modulus maps, d) SPM grid analysis of sample annealed at 1000℃ for 4-hours and e and f) Corresponding XPM hardness and modulus map.

Table 6.8: Changes in matrix hardness and modulus after each treatment using XPM data.

Phase/Treatment	Hardness (GPa)	Modulus (GPa)
Co Solid Solution - Untreated	7.5 (±0.49)	220.36 (±6.32)
Co Solid Solution - 1 Hour	6.68 (±0.25)	245.23 (±9.36)
Co Solid Solution - 2 Hours	6.99 (±0.33)	208.77 (±6.14)
Co Solid Solution - 4 Hours	6.77 (±0.82)	192.23 (±6.14)
Co Solid Solution - Quenched	6.81 (±0.36)	223.61 (±7.82)

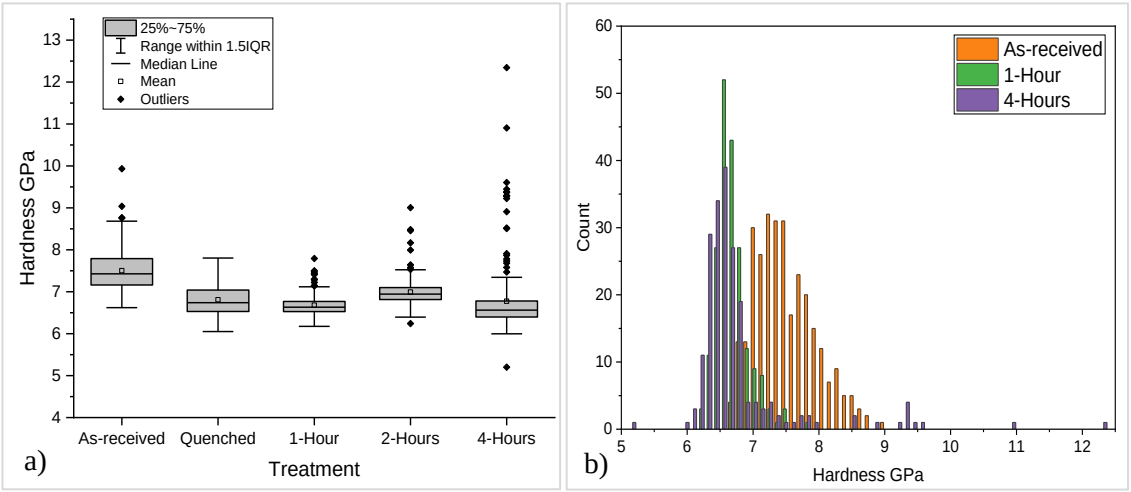

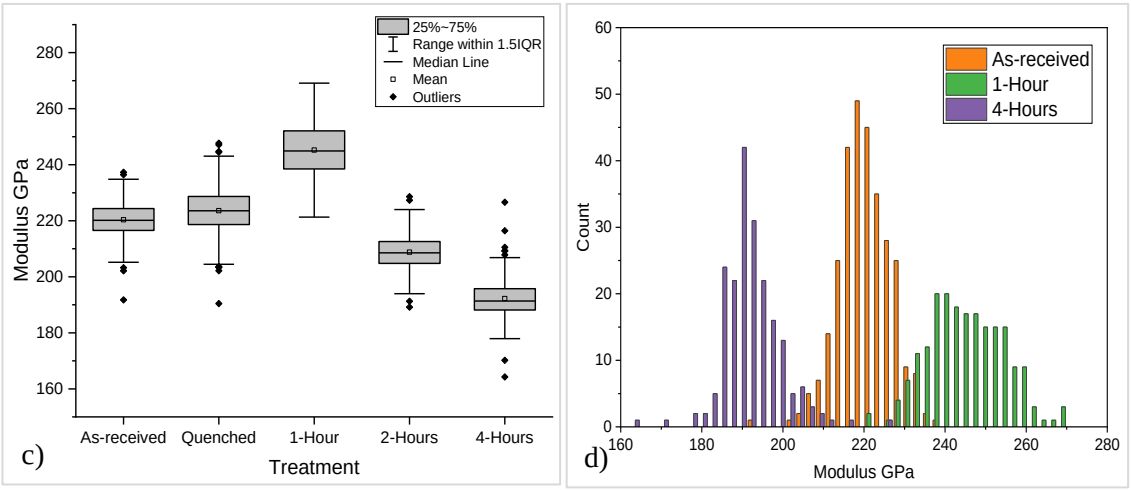

Figure 6.23: Distribution of hardness and modulus data after each treatment calculated from XMP analysis: a and b) distribution of hardness data and c and d) distribution of modulus data.

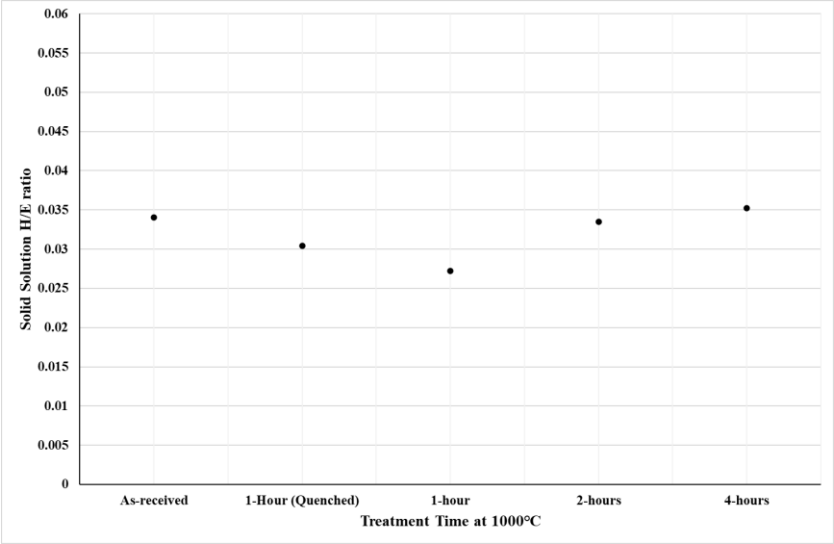

Figure 6.24: Matrix H/E ratios after various annealing times at 1000°C.

6.1.5.3 Macrohardness and Microhardness Analysis of Annealed WT-12

Bulk hardness and microhardness analysis of the treated WT-12 samples with reference to an untreated sample are displayed in Figure 6.25 and Figure 6.26, respectively. The average results and changes in hardness as a percentage are summarised in Table 6.9. The bulk hardness results demonstrate that the heat treatments increased the overall hardness of the samples after each treatment. The furnaced cooled samples experienced a small change in hardness where increases in material hardness ranged between 8-10%. Comparing the furnaced cooled samples shows that only minor differences in hardness were recorded between the treated samples where maximum average bulk hardness of 559Hv was recorded with the sampled annealed for 4-hours. The sample water quenched after a 1-hour treatment experienced an increase in hardness of 19%.

However, it was concluded that the alloy is unsuitable for quenching as the rapid cooling process resulted in severe crack propagation caused by thermal shock.

Microhardness analysis of the matrix (Figure 6.26) indicates that each annealing treatment resulted in an increase in hardness. Changes in microhardness for the furnace cooled samples ranged between 10-16% where the samples treated for 1 and 4-hours experienced the greatest increase in hardness. Compared to an untreated sample, the hardness of the treated samples increased from 472Hv to around 547Hv on average. The results show that the initial increase in hardness after a 1-hour treatment was followed by a decrease in hardness of the matrix with the sample treated for 2-hours, although the hardness was still higher compared to the matrix of an untreated sample. A 4-hour treatment resulted in a recovery in hardness of the matrix where a similar hardness to the sample treated for 1-hour was recorded. Compared to the furnace cooled samples, the water quenched sample experienced slightly higher increases in material hardness where an average increase of 17% was measured.

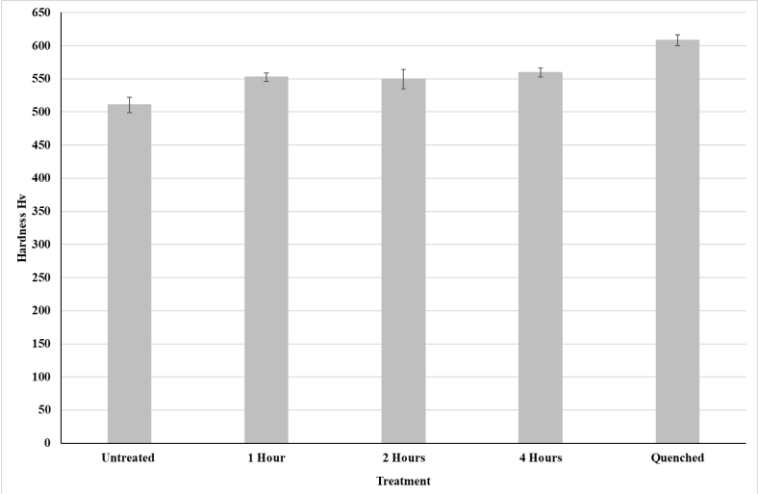

Figure 6.25: Changes in material bulk hardness of the WT-12 alloy after annealing at 1000ºC for various periods of time and after different cooling condition.

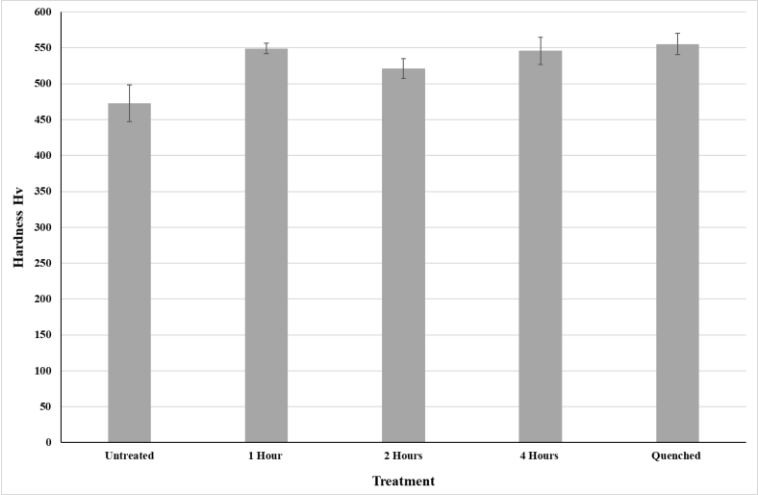

Figure 6.26: Changes in microhardness of the matrix phase of the WT-12 alloy after annealing at 1000ºC for various periods of time and after different cooling conditions.

Table 6.9: Changes in hardness of the WT-12 samples after each treatment with referecnce to an untreated sample.

	Bulk		Matrix	
Treatment	Hardness Hv	% Change	Hardness Hv	% Change
Untreated	510.56 (±11.41)	-	472.73 (±25.73)	-
1 Hour	552.62 (±6.3)	8.24	549.13 (±7.03)	16.16
2 Hour	549.43 (±14.8)	7.61	521.53 (±13.86)	10.32
4 Hour	559.41 (±6.7)	9.57	545.82 (±19)	15.46
Quenched	608.25 (±8.1)	19.13	555.23 (±14.84)	17.45

6.1.5.3.1 Phase Specific Nanoindentation Analysis of WT-12

Surface topography scans of an untreated WT-12 sample, and a sample treated for 4-hours (Figure 6.27a vs d) highlights the formation of the precipitated ternary phases within the matrix of the treated sample which were identified using SEM analysis. XPM analysis of these areas highlights changes in mechanical properties comparing the two samples following an annealing treatment. Comparing the hardness maps (Figure 6.27b vs e) indicates that the precipitate is harder than the surrounding matrix. The matrix region of the untreated sample remains at a consistent hardness whereas the map of the treated sample reveals areas of increased hardness which are a result of indents being performed on or in close proximity to the precipitates. A similar trend also occurred with the modulus where areas of the matrix of the treated sample displayed signs of increased modulus.

The average hardness and modulus after each treatment, calculated using XPM data, is presented in Table 6.10 and the distribution of the data is illustrated in Figure 6.28. The results indicate that the average hardness increased after each treatment, compared to an untreated

sample. The 1-hour treatment experienced the greatest increase in average hardness. Longer treatment times of 2 and 4-hours caused the average hardness to decrease, compared to the sample annealed for 1-hour, although the calculated values were still higher compared to the untreated sample.

The hardness data shown in Figure 6.28a displays a greater range of hardness readings with the sample treated for 1-hour compared to the untreated sample and the samples annealed for longer times. The upper quartile value for the sample annealed for 1-hour is greater than the maximum value obtained with the untreated sample. This shows that more than 25% of hardness readings were higher than the maximum value recorded with the untreated sample. The samples treated for 2 and 4-hours had a similar average hardness in addition to a similar data range. Although the maximum values and the majority of hardness readings recorded with these samples were higher compared to the data for the untreated sample, lower minimum values were recorded with the treated samples. This demonstrates that although the annealing process generally increased the hardness of the matrix, some areas experienced a decrease in hardness.

SEM analysis of the alloys microstructure after the annealing process identified phase precipitation throughout the matrix. Increased annealing time resulted in coarsening and increased quantity of the precipitates. This is reflected in the hardness results where increased number of outliers, which corresponded with measurements of these phases, were recorded after longer treatment times.

The modulus graphs (Figure 6.28c-d) demonstrate that the 1-hour treatment was the only sample that experienced improvements in modulus. The data shows that the upper quartile for this sample is a similar value to the maximum value recorded with the untreated sample which indicates that 25% of the readings where higher than the maximum modulus recording with the untreated sample. The median line is also greater than the upper quartile of the untreated sample, indicating that 50% of the readings were greater than 75% of the highest readings with the untreated sample. The data for the sample treated for 2-hours displays a significant increase in range of modulus data. Although the greatest maximum modulus readings were recorded with this sample, the majority of readings were lower compared to the sample treated for 1-hour and the untreated sample. The median line for this sample is less than the lowest values recorded with untreated sample and sample treated for 1-hour which demonstrates that more than 50% of readings were lower than the lowest readings of the untreated sample and samples annealed for 1-hour. Further decreases in modulus occurred with the sample treated for 4-hours where the highest reading for this sample was lower than the lowest value recorded with the untreated sample. These results indicate that whilst the shorter treatment time has a positive effect on the modulus, longer treatment times have detrimental effects.

Figure 6.29 illustrates that the annealing treatment had significant effects on the H/E ratio of the alloy's matrix. The results indicate the ratio increased after the 1-hour treatment which increased slightly after a 2-hour treatment. However, the ratio significantly increased after a longer 4-hour treatment. The results indicate the wear resistance of the matrix can be improved after an annealing treatment, particularly after longer annealing times.

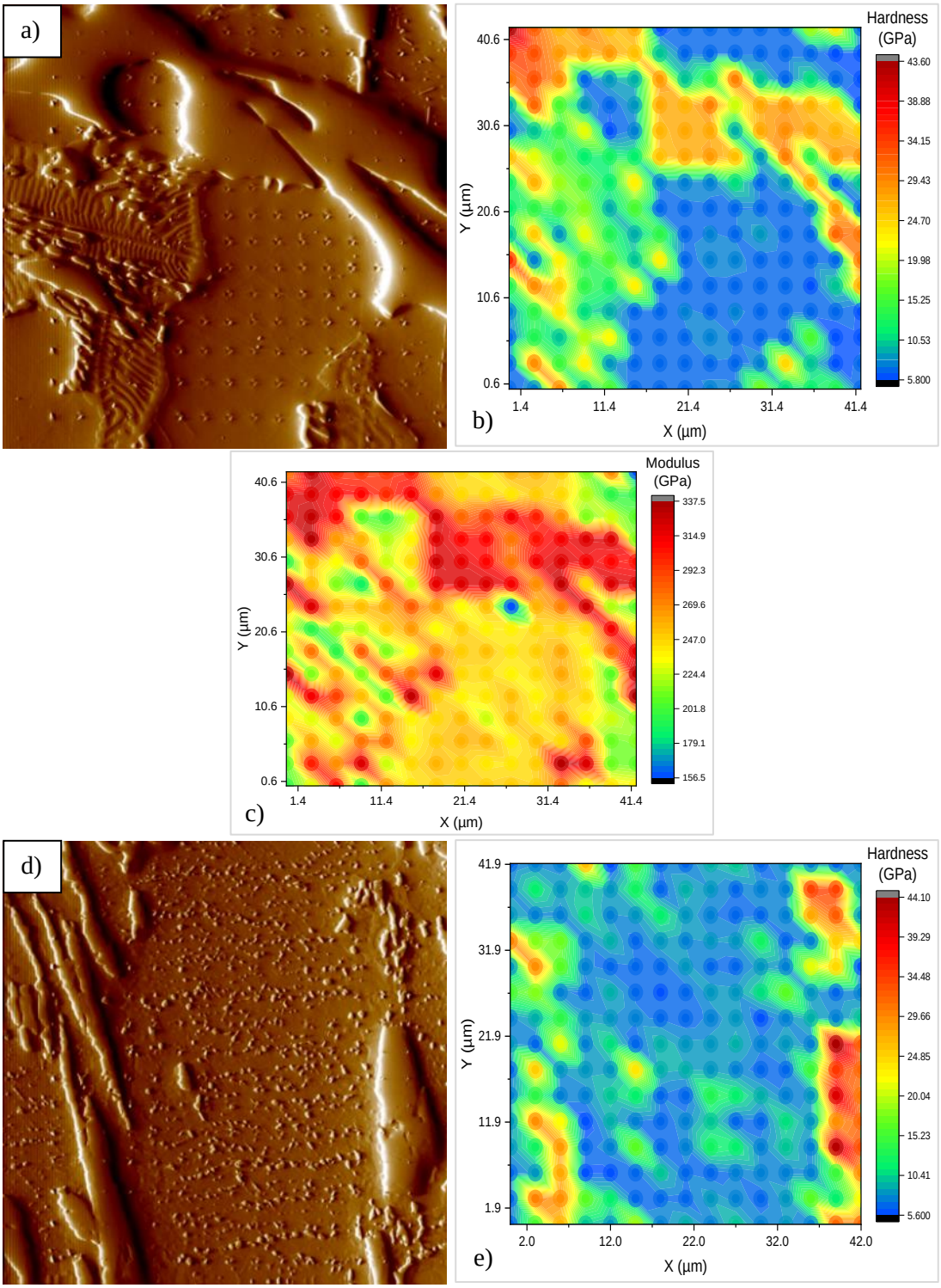

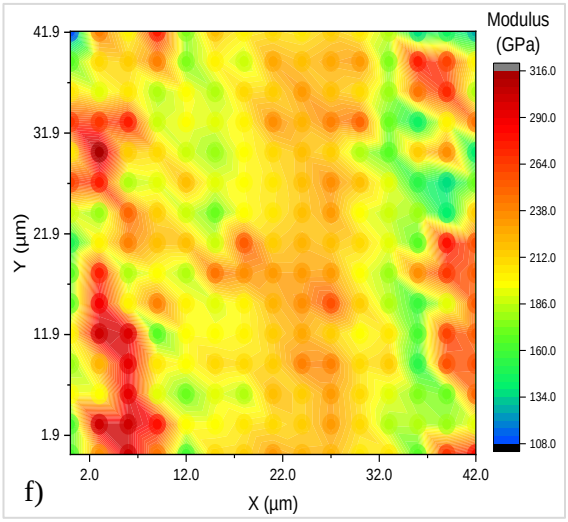

Figure 6.27: Nanoindentation analysis of matrix of the untreated and annealed WT-12 samples: a) SPM grid analysis of untreated sample, b and c) Corresponding XPM hardness and modulus maps, d) SPM grid analysis of sample annealed at 1000℃ for 4-hours and e and f) Corresponding XPM hardness and modulus map.

Table 6.10: Changes in matrix hardness and modulus after each treatment using XPM data.

Phase/Treatment	Hardness (GPa)	Modulus (GPa)
Co Solid Solution - Untreated	7.58 (±0.4)	235.58 (±7.42)
Co Solid Solution - 1 Hour	9.26 (±3.19)	248.56 (±16.2)
Co Solid Solution - 2 Hours	8.45 (±2.8)	215.33 (±22.95)
Co Solid Solution - 4 Hours	8.44 (±2.46)	179.31 (±13.74)

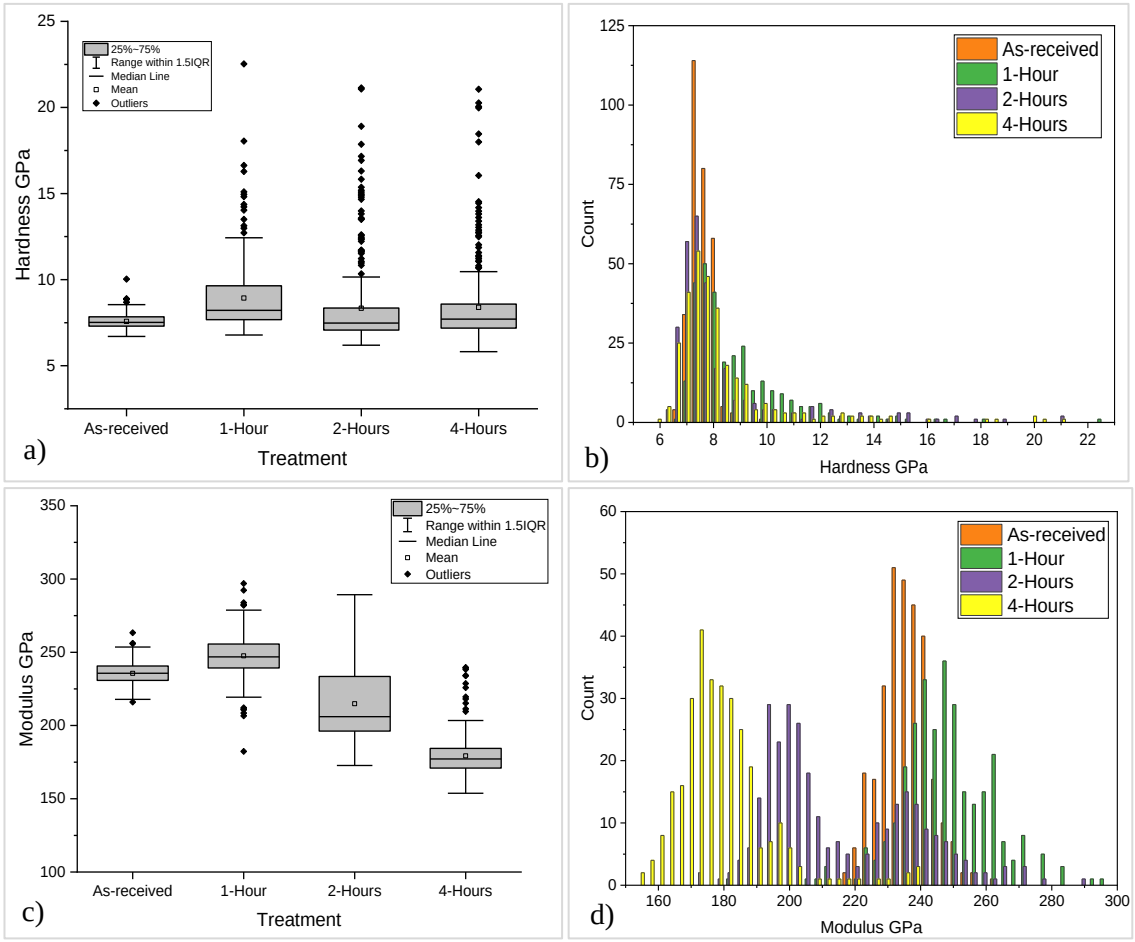

Figure 6.28: Distribution of hardness and modulus data after each treatment calculated from the XMP analysis: a and b) distribution of hardness data and c and d) distribution of modulus data.

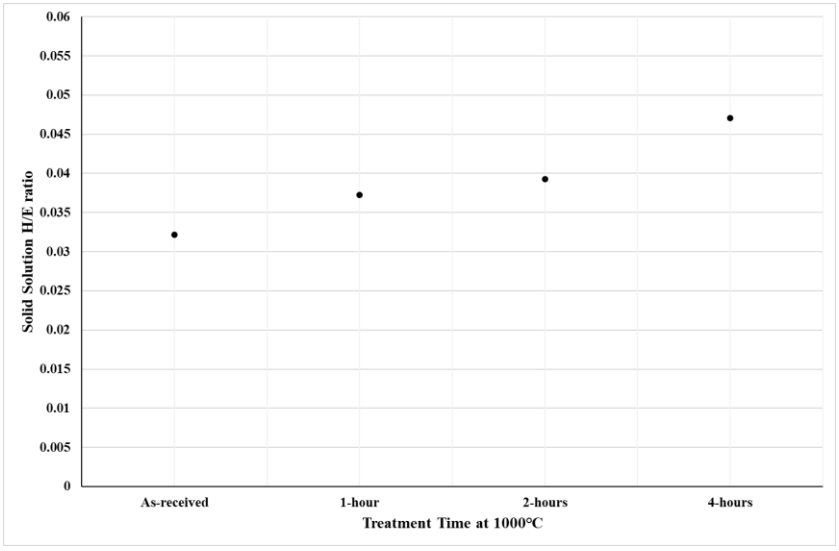

Figure 6.29: Matrix H/E ratios after various annealing times at 1000°C.

6.1.5.4 Macrohardness and Microhardness Analysis of Annealed T-800

Changes in material bulk hardness and microhardness of the matrix and Laves phase after various annealing heat treatments are presented in Figure 6.30 and Figure 6.31, respectively. The hardness results are summarised in Table 6.11 which calculates any changes in hardness as a percentage. The results demonstrate that the annealing treatment had detrimental effects on the overall hardness of the alloy. Compared to an untreated sample, the 1-hour treatment caused a slight drop in bulk hardness where the hardness dropped from 748Hv to 725Hv, on average. This trend continued with longer treatment times where the hardness gradually decreased. After a 4-hour treatment the overall hardness of the sample decreased from 748Hv to 698Hv, an overall decrease in material hardness of 7%. The sample that was quenched also experienced a minor drop in material hardness following a 1-hour annealing treatment, although it has been established that the T-800 Tribaloy is not suitable for quenching due to extreme material failure.

A similar trend was observed with the microhardness analysis of the matrix and Laves phase (Figure 6.31a and b) where the annealing process had negative effects on the hardness of the phases. The 1-hour treatment resulted in minor changes in the microhardness of the matrix. However, a 9% decrease in hardness occurred after a 2-hour treatment. A longer annealing time of 4-hours resulted in a 19% decrease in hardness where the hardness of the matrix decreased from 721Hv, with the untreated sample, to 585Hv. The Laves phase was less sensitive to the thermal treatment. Although gradual decreases in hardness were recorded after longer annealing times, the changes in hardness were relatively small where a 3% decrease in hardness was recorded after a 4-hour treatment.

The results indicate that annealing the T-800 Tribaloy at 1000°C has detrimental effects on the hardness of the alloy where increased annealing times resulted in a gradual reduction in material hardness. It was found that a combination of a decrease in hardness of the cobalt matrix and the primary Laves phase, which was more significant after longer treatments, resulted in greater reduction of the overall hardness of the alloy.

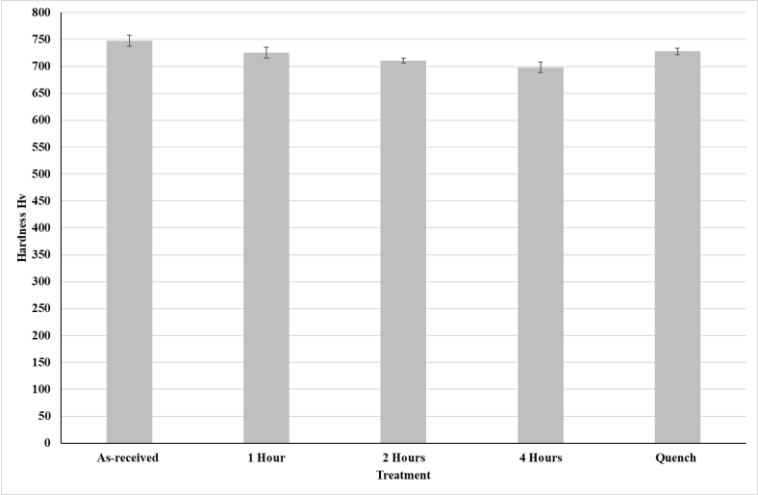

Figure 6.30 Changes in material bulk hardness of the WT-12 alloy after annealing at 1000ºC for various periods of time and after different cooling condition.

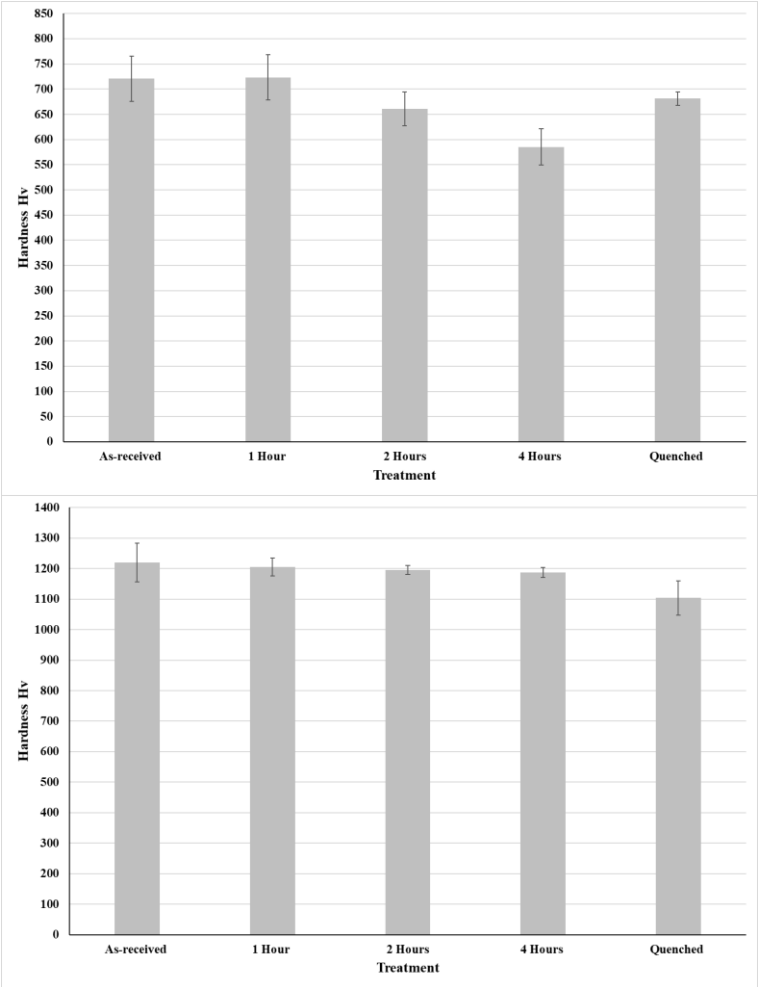

Figure 6.31: Changes in microhardness of the matrix phase and Laves phase of the T-800 Tribaloy after annealing at 1000ºC for various periods of time and after different cooling conditions: a) Matrix and b) Laves phase.

Table 6.11: Changes in hardness of the T-800 samples after each treatment with referecnce to an untreated sample.

	Bulk		Laves		Matrix	
Treatment	Hardness Hv	% Change	Hardness Hv	% Change	Hardness Hv	% Change
Untreated	747.64 (±10)	-	1219.8 (±63.7)	-	720.7 (±45.1)	-
1 Hour	725.698 (±10.1)	-2.9	1205.2 (±29.3)	-1.2	723.4 (±45.1)	0.4
2 Hour	710.9 (±4.62)	-4.9	1195.8 (±14.9)	-2	661.1 (±33.4)	-8.7
4 Hour	698.17 (±10)	-6.6	1187 (±15.8)	-2.7	585.1 (±36)	-18.8
Quenched	728.06 (±5.87)	-2.6	1103.6 (±56.7)	-9.5	681.4 (±13.1)	-5.5

6.1.5.4.1 Phase Specific Nanoindentation Analysis of T-800

The matrix of the untreated T-800 sample contained precipitates that were finely dispersed throughout the phase. It was found that the quantity of the precipitates increased after annealing the samples at 1000°C for various periods of time. Surface topography scans comparing the solid solution of an untreated and annealed sample are displayed in Figure 6.32a and d and the corresponding mechanical property maps are also presented. It was identified that the precipitates contained high levels of molybdenum so would therefore be harder than the surrounding softer matrix. Comparing the mechanical property maps does not give a clear indication of how the annealing process effected the hardness and modulus of the matrix as the precipitates existed in an untreated sample. Ensuring the analysis did not include any secondary Laves phases, XPM analysis provided an indication of the of how the alloys mechanical properties were influenced by the annealing process. Table 6.12 summarises the calculated average changes in hardness and modulus of the matrix after each treatment with reference to an untreated sample. The results indicate a minor increase in hardness and modulus occurred after a 1 and 2-hour treatment. After a 4-hour treatment the hardness and modulus decreased to values which were slightly lower compared to an untreated sample.

The distribution of hardness and modulus data is plotted in Figure 6.33 and gives a clearer representation of the changes in mechanical properties experienced after each treatment. The hardness graphs (Figure 6.33a and b) indicate only small differences in the range of data were recorded with the samples treated for 1 and 2-hour treatments. After a 1-hour treatment the hardness and modulus data range are smaller compared to the untreated sample. Although higher readings were recorded with the untreated sample, the lower values were higher with the treated sample where the minimum value was similar to the lower quartile recorded with the untreated sample. This shows that nearly all the hardness readings were higher than 25% of the lowest readings recorded with the untreated sample. After a 2-hour treatment a higher maximum value and lower minimum values were recorded compared to the untreated. The results indicate a significant drop in hardness data after a 4-hour treatment. The upper quartile range of the annealed

sample is similar to the lower quartile of the untreated sample. This indicates that 75% of the hardness readings with the treated sample were lower than 75% of the highest readings with the untreated sample. The drop in hardness with the sample is represented by a shift in hardness data to the left of the histogram, as shown in Figure 6.33b.

Similar trends were experienced with the modulus data. After a 1-hour treatment the maximum modulus reading was slightly lower with the treated sample, but the minimum value was higher where almost all the readings were higher than 25% of the lowest modulus readings of the untreated sample. A significant increase in modulus was recorded after a 2-hour treatment where 50% of readings were higher than all the modulus readings with the untreated sample and sample treated for 1-hour. A longer 4-hour treatment resulted in a decrease in modulus readings. However, improvements in modulus were experienced compared to the untreated sample.

These results suggest that shorter treatments times can benefit the nano-hardness and modulus of the matrix whereas longer treatment times begin to have detrimental effects on the mechanical properties of the phase. This is likely due increased precipitation that was observed after longer annealing times.

The H/E ratio of the matrix was calculated after each heat treatment using the XPM data, as shown in Figure 6.34. The results indicate no significant change after a 1 and 2-hour treatment. However, a longer 4-hour treatment had detrimental effects where a lower H/E ratio was recorded when compared to an untreated sample. This suggest that annealing this alloy reduces the wear resistance of the matrix.

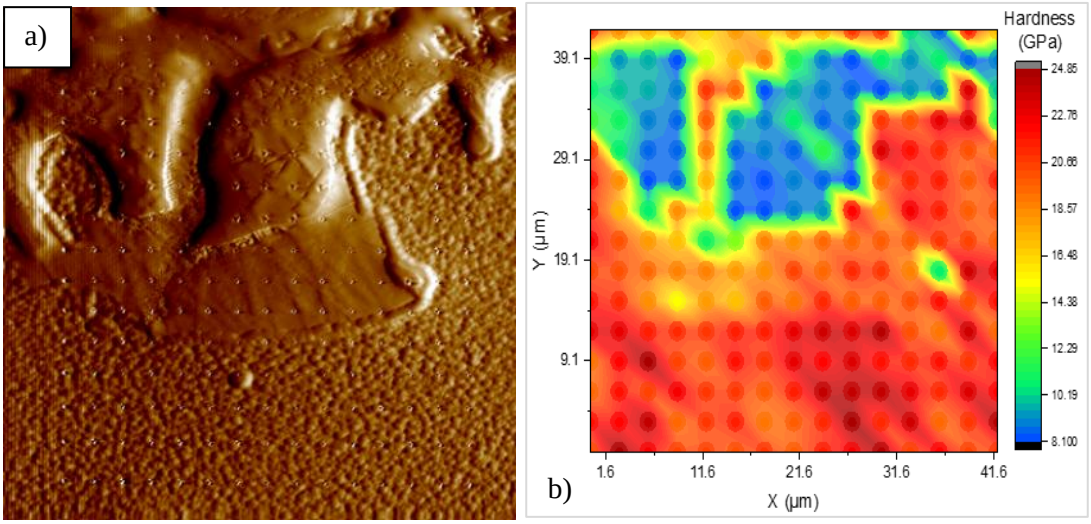

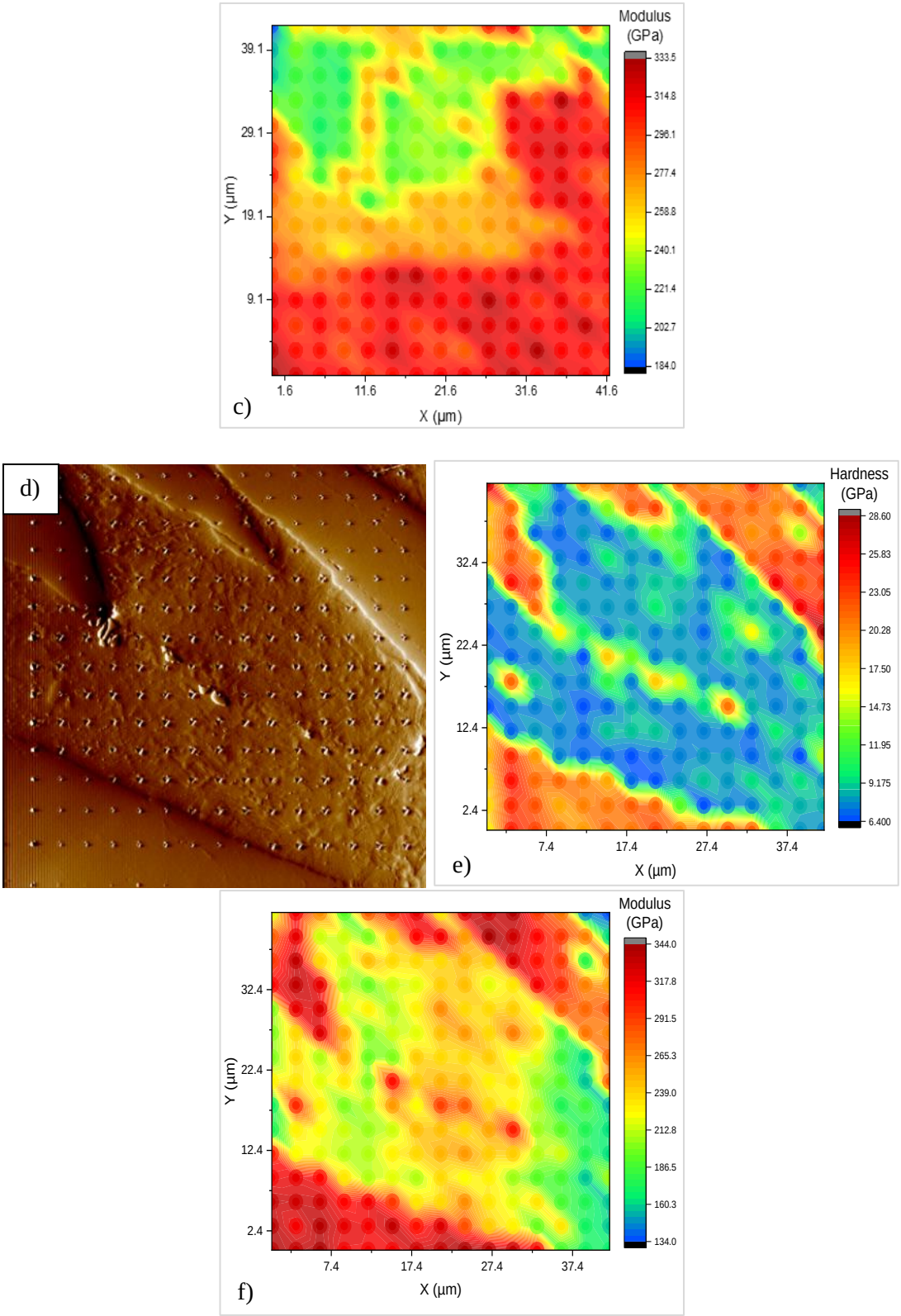

Figure 6.32: Nanoindentation analysis of matrix of the untreated and annealed T-800 samples: a) SPM grid analysis of untreated sample, b and c) Corresponding XPM hardness and modulus maps, d) SPM grid analysis of sample annealed at 1000℃ for 4-hours and e and f) Corresponding XPM hardness and modulus map.

Table 6.12: Changes in matrix hardness and modulus after each treatment using XPM data.

Phase/Treatment	Hardness (GPa)	Modulus (GPa)
Co Solid Solution - Untreated	10.8 (±1.2)	239.8 (±8.7)
Co Solid Solution - 1 Hour	11.3 (±1.1)	245.4 (±6.4)
Co Solid Solution - 2 Hours	11.9 (±1.5)	265.4 (±15.8)
Co Solid Solution - 4 Hours	9.7 (±2.3)	246.4 (±13.7)

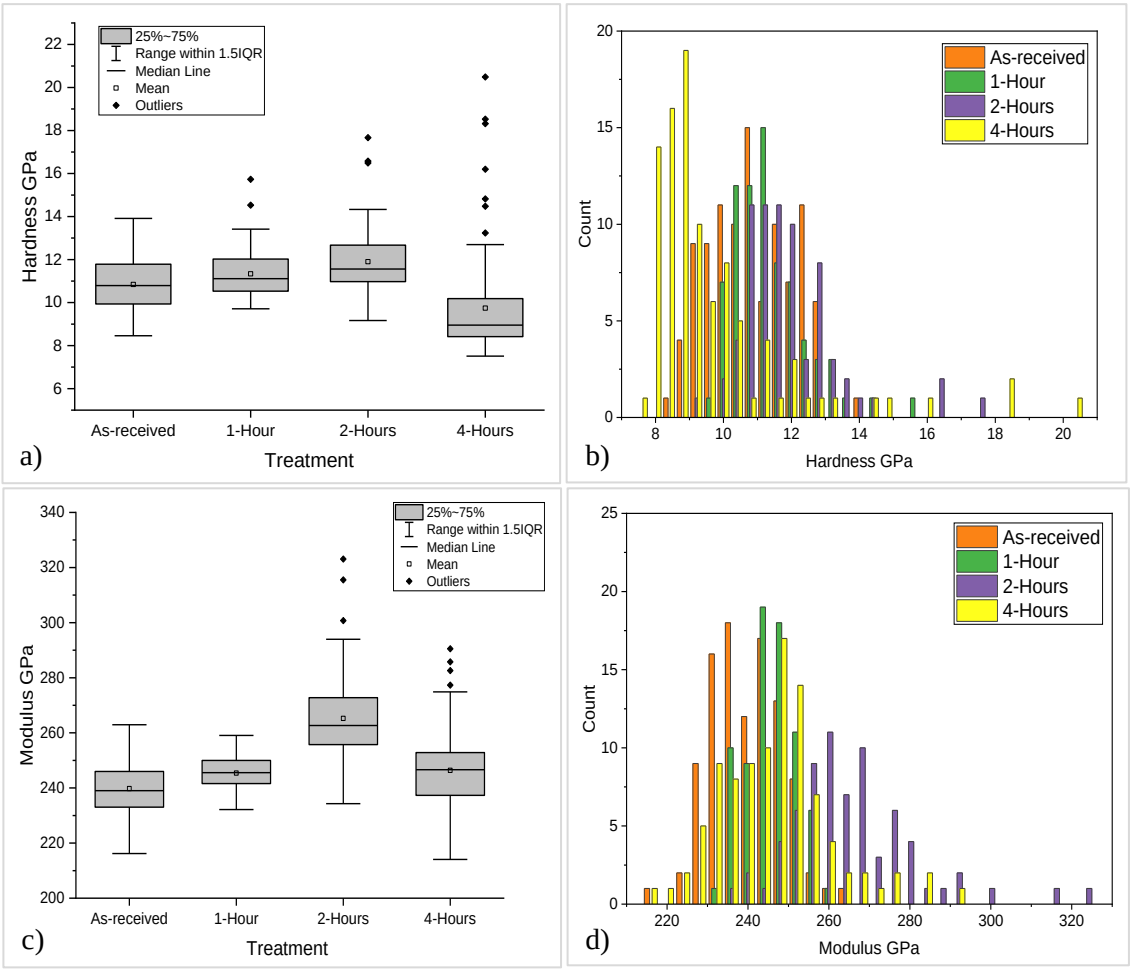

Figure 6.33: Distribution of hardness and modulus data after each treatment calculated from XMP analysis: a and b) distribution of hardness data and c and d) distribution of modulus data.

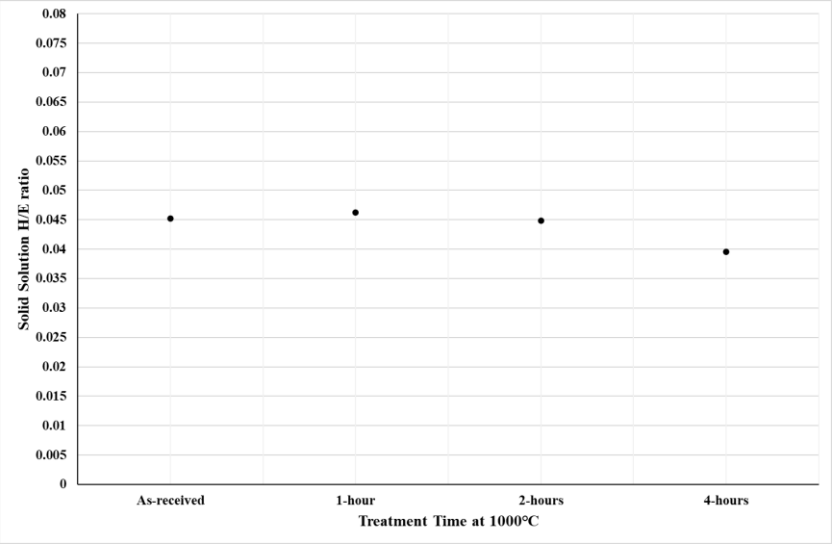

Figure 6.34: Matrix H/E ratios after various annealing times at 1000°C.

6.1.6 Comparisons of Changes in Microstructure Morphology and Hardness Trends Observed After a High Temperature Annealing Treatment

Microstructural analysis of the alloys after annealing at 1000°C for various periods of time revealed small changes in each of the alloy's microstructure. Similar trends were observed with each alloy where the heat treatment resulted in precipitation occurring throughout the matrix. With the CoCrW alloys the precipitated phase contained high levels of tungsten and chromium whereas the precipitates that formed with the CoCrMo Tribaloy consisted of high levels of molybdenum and silicon. Longer annealing times did not result in any significant additional microstructural changes with the WT-4 and WT-6 alloys where there was little evidence of dissolution of existing carbide phases into solid solution. However, more significant changes were observed with the WT-12 and T-800 alloys. Longer annealing times, with the WT-12 alloy, resulted in increased dissolution of the chromium-rich phases where a 7% decrease in the area fraction of the phase, in comparison to an untreated sample, was calculated. The secondary Laves phase, found in the eutectic matrix of the T-800's microstructure, became more spherical in appearance. This process was also reported by *Halstead* after investigating the effects of heat various treatments on T-400 and T-800 Tribaloys [108]. The eutectic CoMo solid solution phase experienced increased levels of dissolution and resulted in the formation of molybdenum-rich phases within the matrix. EDS analysis of each of the alloys identified that areas of the matrix became depleted in alloying elements due to the formation of the precipitated phases. Although, some areas of the matrix within the WT-12 alloy were found to become enriched with alloying elements due to carbide dissolution. It was recorded that with all the alloys, longer annealing times increased the quantity of precipitation where coarsening of precipitates also occurred.

Comparing the furnace cooled samples and the samples that were water quenched revealed similar diffusion trends with precipitation occurring within the matrix. However, the WT-6 alloy was the only alloy that did not show signs of material failure after the quenching process. The WT-4, WT-12 and T-800 alloys all demonstrated signs of considerable material failure in the form of large crack formation which would have been caused due to thermal shock from the quenching process.

The annealing process resulted in small changes to the overall hardness of each alloy whereas greater changes in the microhardness and nano-mechanical properties of the matrix occurred. The CoCrW alloys experienced slight improvements in bulk hardness after the annealing and furnace cooling process. The WT-4 alloy experienced the lowest increase in material hardness whereas the WT-12 alloy experienced the greatest increase in bulk hardness. The increase in material bulk hardness was attributed to precipitation occurring within the matrix. With the WT-4 and WT-6 alloys, maximum increases in matrix hardness occurred after a 1-hour and 2-hour treatment, respectively. A longer 4-hour treatment had detrimental effects on the matrix hardness which is likely due to over coarsening of the precipitates. The microhardness of the eutectic region of the WT-4 was also observed to increase after the annealing treatment. The initial 1-hour treatment resulted in the biggest increase in hardness which is believed to be due to the coarsening of phases within the eutectic region. Longer treatments experienced a decrease in hardness, although results were still higher compared to an untreated sample. The changes in bulk hardness experienced with the WT-12 alloy remained similar after each test. However, there was a noticeable drop in matrix microhardness after a 2-hour treatment. A larger increase in hardness was recorded after a 4-hour treatment which may correlate to dissolution of carbide phases which increased the concentration of alloying elements retained in the matrix which would have had a greater strengthening effect.

Microhardness analysis of the primary Laves phase and matrix also gradually decreased with increased annealing time. The combination resulted in an overall decrease in material hardness. The decrease in hardness of the primary Laves phase may be caused due to the homogenisation of the phase resulting in strain and dislocation removal at grain boundaries, as reported by *Wei Xu* [154]. The matrix of a cast T-800 Tribaloy comprises of a mixture FCC and HCP structures in metastable form. It has been found that heat treating the alloy at a high temperature results in a total transformation to FCC phases which reduced the hardness of the phase [108]. However, this transformation occurred after heating at 1250°C for 2-hours whereas the T-800 Tribaloy was annealed at 1000°C for a maximum time of 4-hours in this study. Therefore, a more likely explanation for the decrease in matrix hardness is due to the over coarsening of phases within the matrix.

EDS analysis discovered that areas of the matrix for each alloy became depleted in alloying elements due to precipitation throughout the matrix, although increased alloying concentrations were recorded in certain areas with the WT-12 alloy after longer annealing times due to carbide dissolution. This process was found to influence the mechanical properties of the each of the alloy's matrix. The formation of the tungsten-rich phase with the WT-6 alloy, and subsequent depletion of tungsten and chromium in the matrix, had negative effects on the nano-hardness of the phase. However, the modulus increased after an a 1-hour treatment, but longer treatments resulted in a gradual decrease in modulus readings much lower compared to the untreated sample. The matrix of WT-4, WT-12 and T-800 alloys experienced improvements in hardness and modulus after shorter treatments whereas longer treatments resulted in a gradual decrease in mechanical properties which we lower than the untreated samples. The results indicate that longer treatment times, with the CoCrW alloys, results in over coarsening of the precipitates and excess depletion of alloying elements in solid solution which reduces the nano-properties of the matrix.

The *H/E* ratio measures the level of elastic strain an alloy is subjected to prior to the onset of yielding. Materials with higher elastic strains prior to failure generally possess better wear resistant properties [143,145]. The annealing process altered the mechanical properties of the matrix of the alloys and therefore the *H/E* ratio was also modified. Minor improvements in the mean *H/E* ratio were calculated with the WT-6 and T-800 alloys suggesting the annealing process had little influence on the wear resistance of the matrix phase. However, significant improvements were calculated with the WT-4 and WT-12 alloys which suggests an improve in wear resistance of the phase.

The results indicate that the mechanical properties of the alloys can be influenced by annealing the alloys at 1000℃. Although improvements in bulk hardness, microhardness, nano-properties and *H/E* ratio of the WT-4 and WT-6 alloys can be achieved after annealing for certain times, the WT-12 alloy experienced the greatest improvements. The thermal process improved the microhardness and *H/E* ratio of the matrix where significant improvements in nano-hardness and modulus were recorded. This contributed to an overall increase in bulk hardness.

The annealing treatment had negative effects on the T-800 Tribaloy, particularly after longer treatments. The nano-properties and microhardness of the matrix and Laves phase decreased after the treatment which contributed to an overall drop in material hardness. The T-800 Tribaloy is very brittle in nature and very susceptible to impact failure and thermal shock. Although the annealing treatment reduced the hardness of the alloy, the treatment has the potential to improve the alloys ductility.

6.2 Solid Solution and Age Hardening Heat Treatment

The initial stage of the thermal process involved solution treating the alloys at 1275℃ for 6-hours before rapid cooling the samples via a quenching process. Heating the alloys at this temperature promotes dissolution of carbide phases to form a supersaturated solid solution phase and the quenching process prevent carbides reforming on cooling. Additional aging treatments were carried out at 850℃ for times ranging between 2-8-hours. The samples were then furnace cooled to room temperature. Further aging at this temperature allows for precipitation of fine carbide phases. The combined effect can significantly improve the hardness of cobalt-based superalloys.

6.2.1 Microstructure Analysis of Age Hardened WT-4

SEM analysis of the heat-treated WT-4 samples are displayed in Figure 6.35. The images indicate that prior to the aging treatments, the samples did not reach the same levels of diffusion in the initial solution treatment. Figure 6.35c+d show the samples microstructure after a solution treatment and subsequent aging treatments of 2 and 4-hours, respectively. The microstructure demonstrates signs of diffusion where the carbide phases are blockier in appearance as opposed to the fine lamella structure observed in the eutectic region of an untreated sample (Figure 6.35a). However, compared to the solution treated sample shown in Figure 6.35b, the samples appear to have experienced less diffusion. The carbide phases are less blocky and smaller in appearance and the microstructure is generally more comparable to an untreated sample in terms of dendrite size. The areas of carbide phases also resemble the eutectic regions in an untreated sample. The lower levels of diffusion experienced with these samples is most likely caused due to inefficient heating during the solution treatment where the treatment temperature either did not reach the desired temperature of 1275℃ or that the sample was not held at 1275℃ for a sufficient period. The sample displayed in Figure 6.35e appears to be in a more advanced stage of diffusion where the formation and dispersion of significantly larger phases are observed throughout the matrix. This is likely due to the treatment temperature exceeding the desired temperature or that the sample was held at a higher temperature for a longer period intended.

Analysis of the microstructures indicates the samples did not experience comparable thermal treatments so comparisons in microstructure morphology and mechanical properties could not be made. Therefore, these samples will not be investigated further.

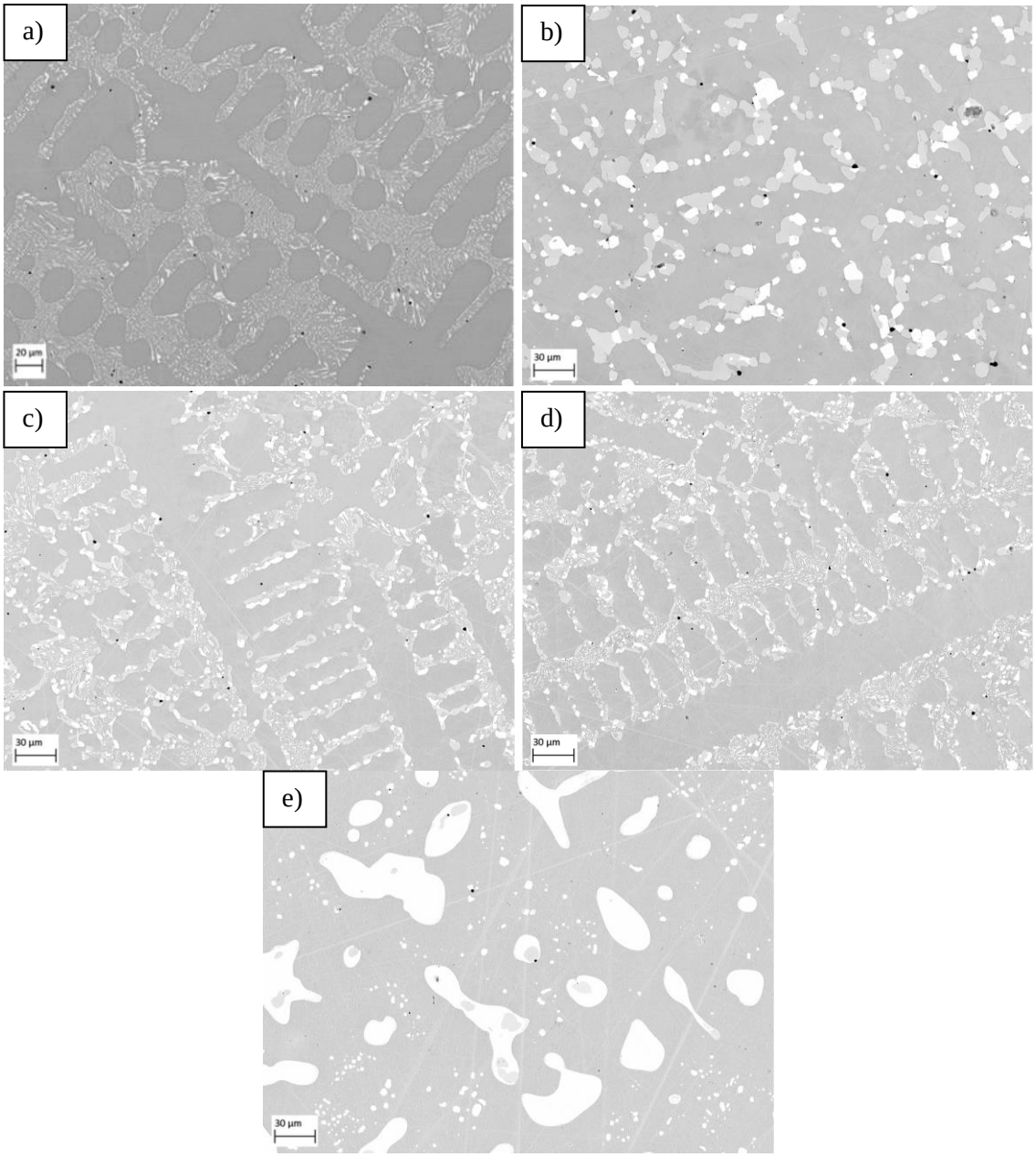

Figure 6.35: SEM microstructural analysis of WT-4 samples after solution treating at 1275°C for 6-hours and aging at 850°C for different times with comparisons made to an untreated sample: a) Untreated sample, b) Solution treated, c) 2-hour aging, d) 4-hour aging and e) 8-hour aging.

6.2.2 Microstructure Analysis of Age Hardened WT-6

The microstructure of the WT-6 samples after a solution treatment and subsequent aging for various times are displayed in Figure 6.36 with comparisons made to an untreated sample. The microstructure after the initial solution treatment (Figure 6.36b) demonstrates that the treatment did not result in complete dissolution of the eutectic carbide phases into solid solution. However, the morphology of the microstructure was significantly altered by the heat treatment.

Analysis indicates that the morphology of the chromium carbides changes to a more blocky and rounded appearance in contrast to the finer distribution of chromium carbides observed with the untreated sample (Figure 6.36a). A small quantity of a tungsten phase was also observed after the solution treatment where small clusters of fine tungsten and chromium phases were often observed to group together, as highlighted in Figure 6.36b and Figure 6.36e.

Additional age hardening treatments carried out after the solution treatment did not appear to alter the microstructure further. Area fraction analysis of the individual phases are presented in Table 6.13. The results demonstrate that the area fraction of the matrix did not change but a small reduction in the level of chromium-rich phase was recorded after the solution treatment. This coincided with a small increase in the quantity of tungsten-rich phases. This suggests that the solution treatment results in a small amount of diffusion of the chromium-rich phases and promotes the formation of the tungsten-rich phase. There were no additional changes after the ageing treatments indicating the process does not significantly change the microstructure further.

The diffusion of the carbide phases is highlighted in Figure 6.37 which presents the diffusion of two chromium phases after a solution treatment and an additional 8-hour aging cycle. It was found that the general composition of the phase (Spectrum 1) contained slightly less tungsten compared to the chromium phases analysed in an untreated sample. However, analysis of the inside edges of the larger chromium phases (Spectrum 2) demonstrates clear signs of diffusion where a significant drop in chromium was measured. It was frequently observed with each sample that the cluster of smaller phases were linked to each other and to larger chromium phases, as shown in Figure 6.37. Analysis of these phases identified a chromium rich phase (Spectrum 3) that was similar in composition to Spectrum 2 and a tungsten-rich phase (Spectrum 4). Figure 6.37 also highlights the fine dispersion of precipitates in close proximity to these phases. The precipitates were too small to accurately measure their composition, but the area contained higher levels of tungsten compared to the surrounding matrix. These results suggest the heat treatment results in the diffusion and possible breakup of the carbide phases which promotes the precipitation of the smaller chromium and tungsten phases. It is can also be proposed that some level of diffusion of alloying elements into solid solution also occurs in these regions. The formation of the precipitates was only observed in areas that had experienced dissolution of the carbide phases. There was also no apparent change in the composition of the surrounding matrix which supports this theory as the precipitation of these phases would have coincided with a decrease in alloying elements retained in solid solution.

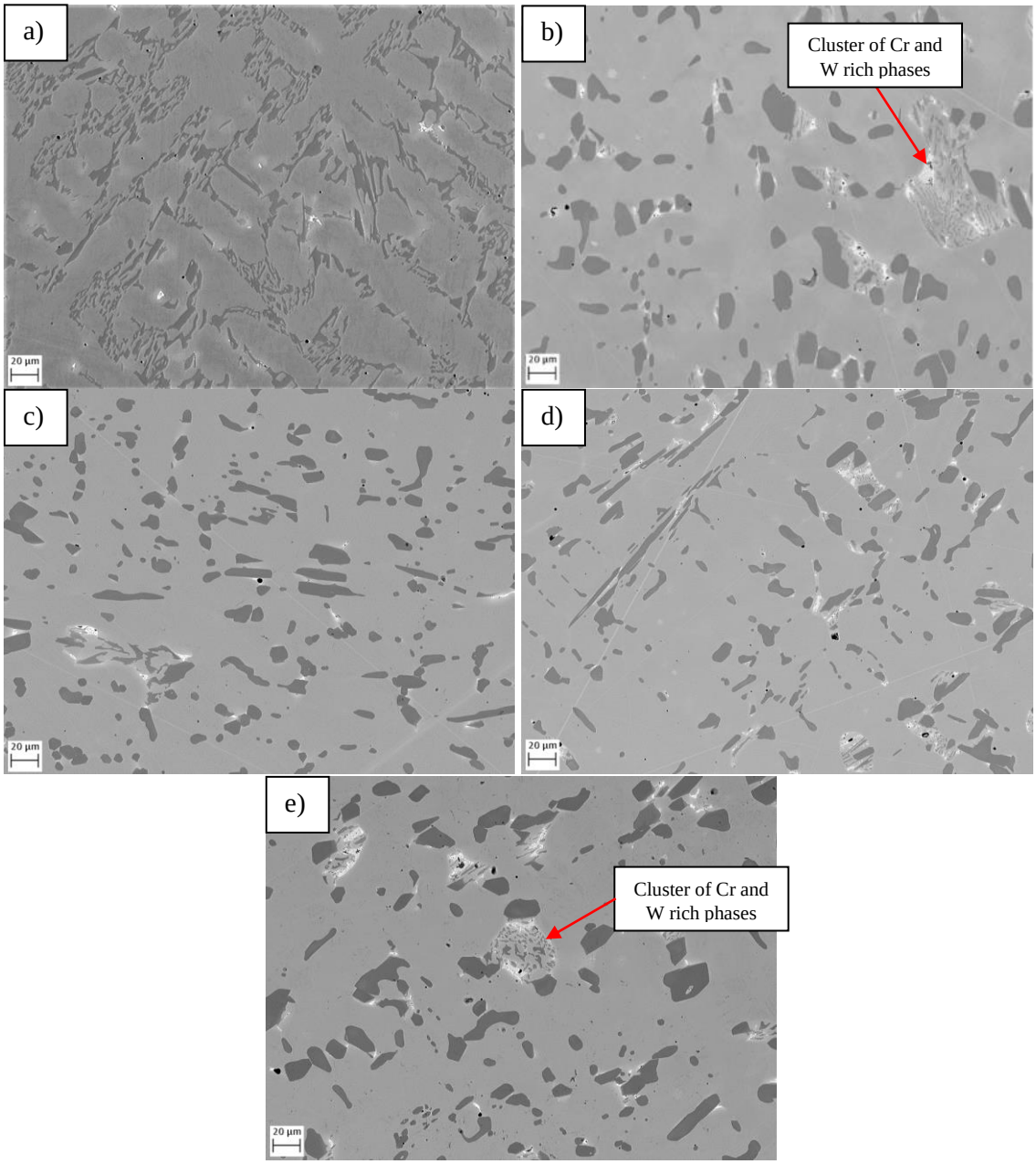

Figure 6.36: SEM microstructural analysis of WT-6 samples after solution treating at 1275°C for 6-hours and aging at 850°C for different times with comparisons made to an untreated sample: a) Untreated sample, b) Solution treated, c) 2-hour aging, d) 4-hour aging and e) 8-hour aging..

Table 6.13: Area fraction analysis of individual phases after each heat treatment with comparison to an untreated WT-6 sample.

Treatment / Phase	As received	Solid Solution	2 Hours	4 Hours	8 Hours
Co Solid Solution	83.8 (±0.9)	83.6 (±1.54)	84.87 (±0.81)	84.93 (±0.59)	84.88 (±1.18)
Eutectic Cr Carbide	17 (±0.2)	15.41 (±2.04)	14.59 (±1.13)	13.9 (±1.14)	14.22 (±1.24)
Eutectic W Carbide	0.2 (±0.1)	1.4 (±0.4)	0.92 (±0.46)	1.19 (±0.35)	1.6 (±0.56)

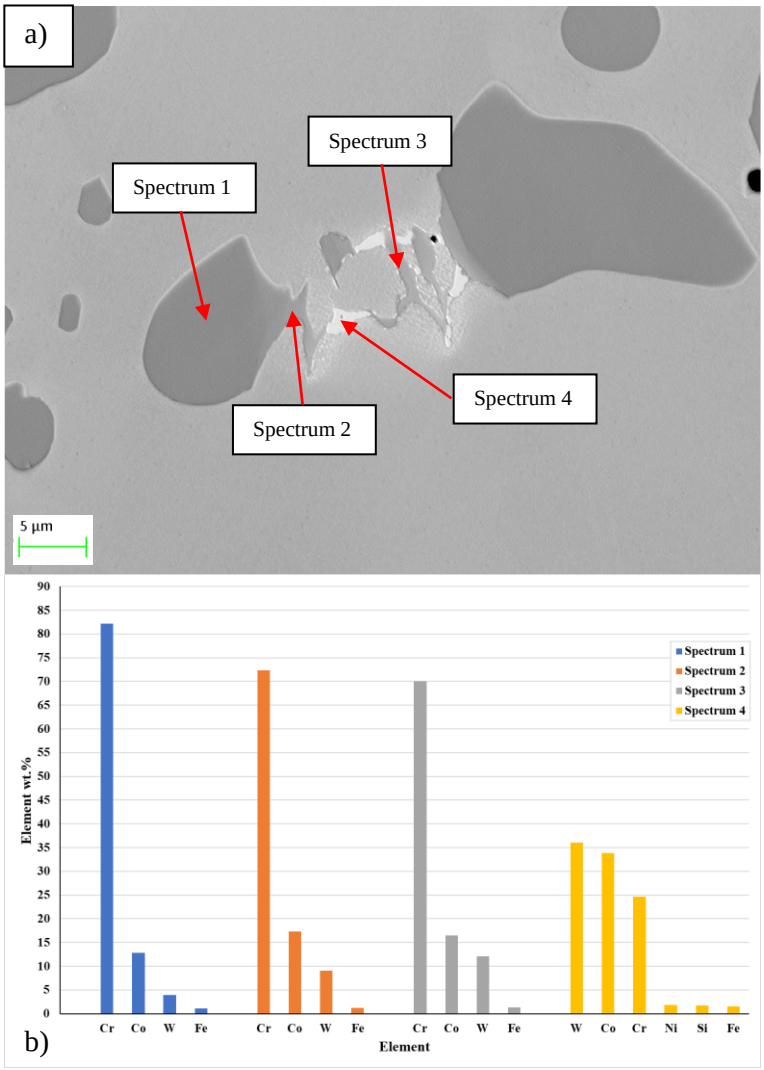

Figure 6.37: EDS point scan analysis of a WT-6 sample aged for 8-hours at 850ºC: a) Point scan locations and b) Corresponding point scan compositions.

6.2.3 Microstructure Analysis of Age Hardened WT-12

SEM analysis comparing the microstructures of an untreated WT-12 sample and samples that were exposed to a solution treatment and subsequent aging treatments for prolonged periods are presented in Figure 6.38. The images demonstrate that the solution treatment resulted in the coarsening of the chromium and tungsten phases, as shown in Figure 6.38b. The morphology of the phases was observed to become blockier and more rounded in appearance in contrast to the microstructure of an untreated sample (Figure 6.38a) which exhibits a fine dispersion of chromium carbides and a complex tungsten carbide network. The images indicate that no further significant changes in microstructure were experienced after additional aging treatments.

Area fraction analysis of the individual phases (Table 6.14) revealed a small decrease in the quantity of the chromium phases after the initial solution treatment. Consequently, the quantity

of the solid solution phase increased by a similar amount. This suggests that the heat treatment resulted in small levels of eutectic chromium carbide dissolution into solid solution. The area fraction of the tungsten phases remained consistent after the solution treatment indicating that although coarsening of the phases occurred, they did not experience any significant levels of dissolution. The area fraction of each phase remained at a similar level after the samples were subjected to further aging treatments. This implies that the aging process did not cause any further noticeable dissolution of the carbide phases or significant changes in microstructure. EDS point scan analysis confirmed the phases to be chromium carbides (dark grey) and tungsten carbides (white). Chemical analysis of the matrix of each of the treated samples revealed that certain areas contained significantly less cobalt and higher levels of chromium and tungsten. An example of the variation in composition is summarised in

Table 6.15. These results further validate the dissolution of the carbide phases into solid solution after the solution treatment.

Inspection of matrix revealed the fine dispersion of precipitated phases throughout the matrix of the samples that were exposed to additional aging treatments, as shown in Figure 6.39a. Precipitation was not observed with the sample that was solution treated and quenched to room temperature which suggests that aging the samples at 850°C allowed for precipitation to occur. It was also observed that in isolated areas of the microstructure increased precipitation occurred at grain boundaries. This is particularly noticeable in Figure 6.39b.

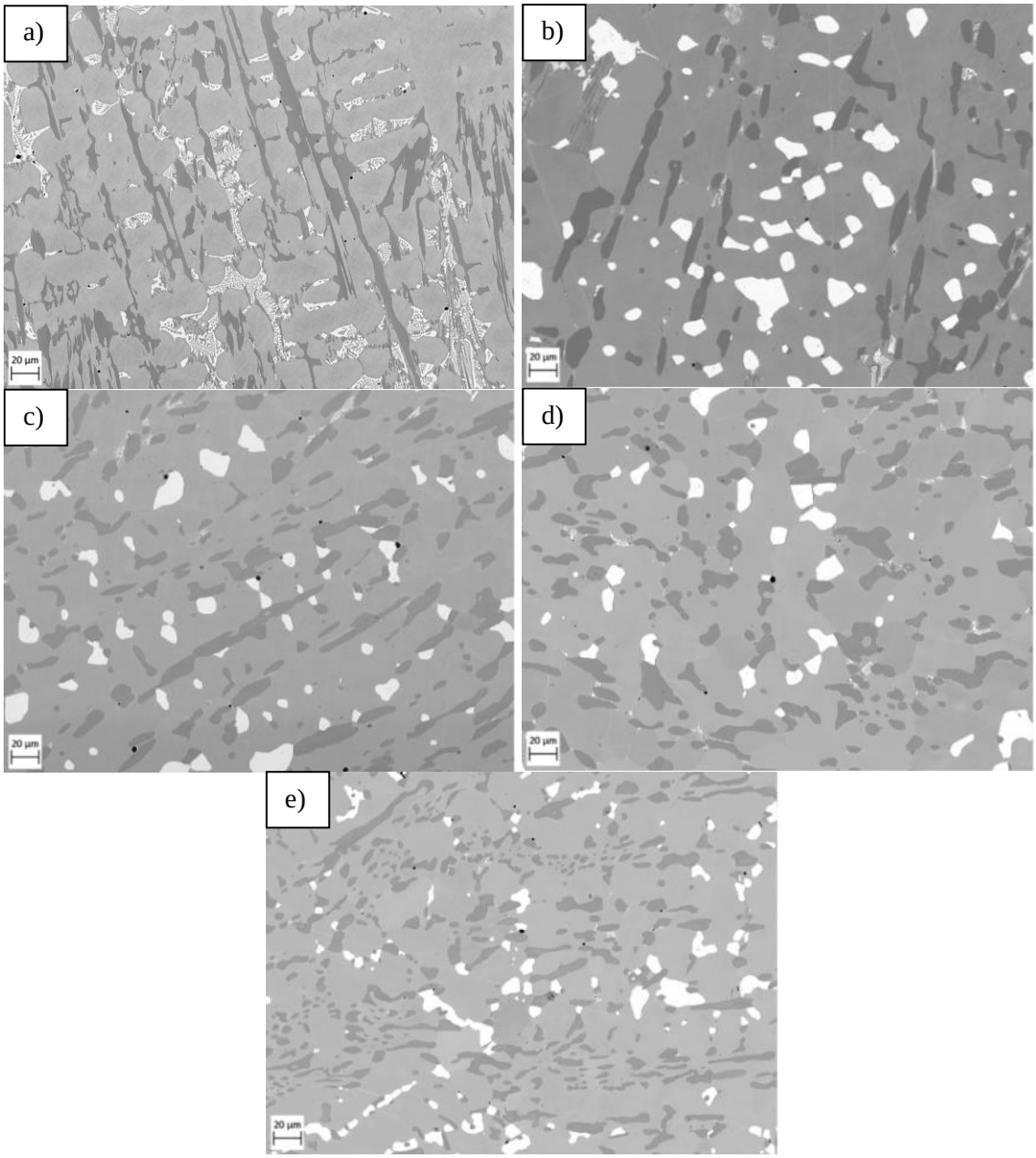

Figure 6.38: SEM microstructural analysis of WT-12 samples after solution treating at 1275°C for 6-hours and aging at 850°C for different times with comparisons made to an untreated sample: a) Untreated sample, b) Solution treated, c) 2-hour aging, d) 4-hour aging and e) 8-hour aging.

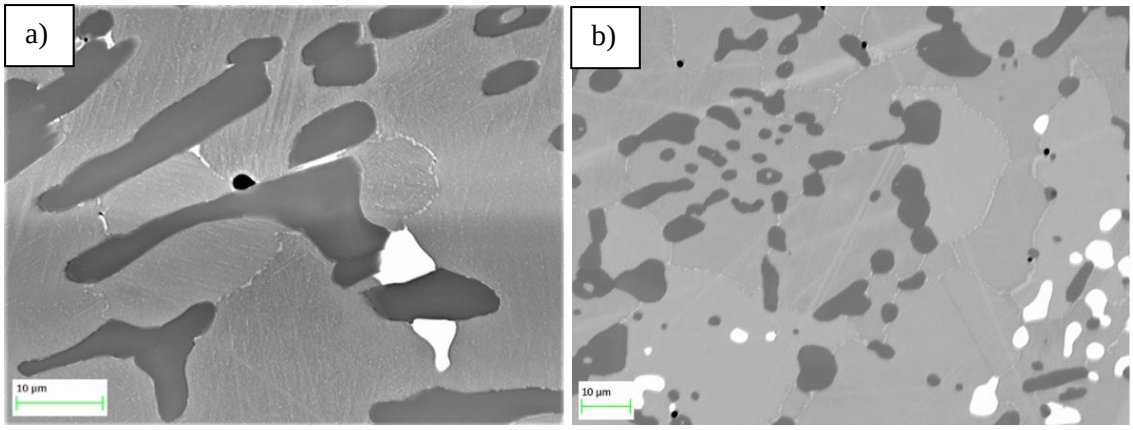

Figure 6.39: a and b) High magnification of WT-12 sample after an 8-hour aging treatment at 850°C illustrating precipitation throughout matrix and at grain boundaries.

Table 6.14: Area fraction analysis of individual phases after each heat treatment with comparison to an untreated WT-12 sample.

Treatment / Phase	As received	Solid Solution	2 Hours	4 Hours	8 Hours
Co Matrix	74.4 (±3.5)	77.1 (±0.3)	77.4 (±0.2)	77.4 (±0.2)	76.6 (±0.9)
Eutectic Cr Carbide	19.3 (±3.8)	15.7 (±2.04)	15.1 (±1.2)	16.2 (±1.6)	16.3 (±0.5)
Eutectic W Carbide	7.6 (±0.6)	7.3 (±2.6)	7.1 (±0.9)	6.9 (±1.4)	6.4 (±0.9)

Table 6.15 Variation in matrix composition between an untreated sample and a sample solution treated and aged for 4-hours aging.

	Element wt.%						
Treatment	Co	Cr	W	Ni	Fe	Si	Mn
Untreated	59.3	25.83	6.97	2.87	2.77	1.8	0.47
4-Hour Ageing	40.2	37.2	17.1	2	1.8	1.2	0.4

6.2.4 Hardness Variation of Age Hardened Samples

6.2.4.1 Macrohardness and Microhardness Analysis Age Hardened WT-6

Changes in material bulk hardness and the microhardness of the matrix after a solution treatment and additional age hardening treatments are displayed in Figure 6.40. The results are summarised in Table 6.16 where the changes in hardness as a percentage are also calculated. The results indicate that a solution treatment at 1250°C resulted in a small decrease in the overall hardness of the sample where the hardness dropped from 429Hv to 418Hv, a 3% reduction. Ageing the alloy at 850°C for 2-hours resulted in a significant increase in the alloys bulk hardness. An increase of 27% was calculated where hardness was recorded to increase from 429Hv, with the untreated sample, to 546Hv with the sample aged for 2-hours. Increasing the aging time to 4-

hours resulted in a further 5% increase in hardness where an average hardness of 574Hv was calculated. Although the hardness after a longer 8-hour aging treatment was higher compared to an untreated sample and the sample aged for 2-hours, the hardness was lower compared to the sample aged for 4-hours akin to a typical overaging behaviour.

A similar trend was observed with the microhardness analysis of the matrix. Figure 6.40b illustrates a 3% drop in hardness of the matrix after the initial solution treatment where the hardness dropped from 399Hv with the untreated sample to 388Hv after the solution treatment. Ageing the sample significantly increased the matrix hardness after each treatment. Aging for 2-hours increased the hardness to 535Hv which increased further to 554Hv after a 4-hour aging treatment, a 39% increase compared to an untreated sample. A longer treatment (8-hours) resulted in a decrease in hardness compared to the sample aged for 2 and 4-hour treatments where an average hardness of 523Hv was recorded. Although the hardness was observed to drop, compared to the samples aged for shorter times, the hardness is still significantly higher (30%) than an untreated sample.

These results show that significant improvements in the overall material hardness and microhardness of the matrix can be achieved through a solution treatment and additional aging treatments, but prolonged aging of the alloy begins to have detrimental effects in material hardness.

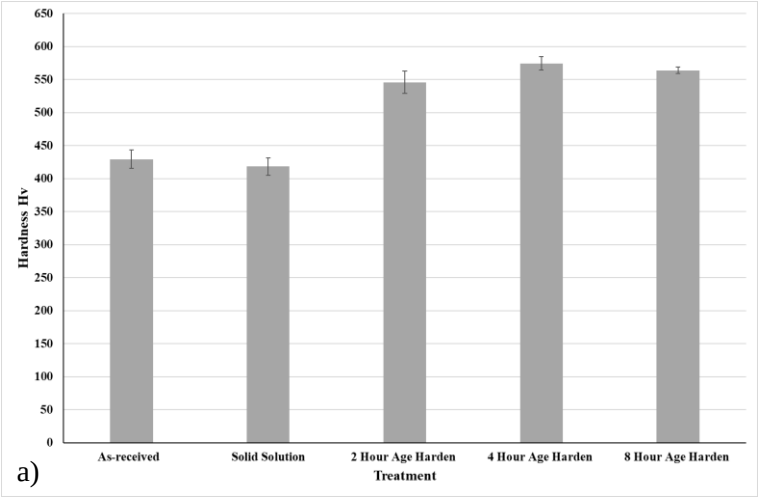

a)

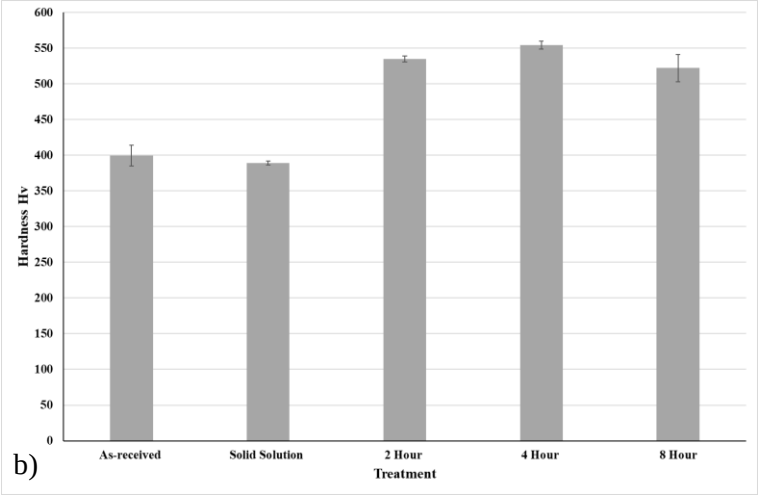

Figure 6.40: Changes in material bulk hardness and matrix microhardness of the WT-6 alloy after solution treating at 1275ºC for 6-hours and additional aging treatments at 850ºC for various periods of time: a) Bulk hardness and b) matrix microhardness

Table 6.16: Changes in bulk hardness and matrix microhardness calculated as a percentage after solution treating at 1275ºC for 8-hours and additional aging treatments at 850ºC various periods of time with comparisons to an untreated sample.

	Bulk		Matrix	
Treatment	Hardness Hv	% Change	Hardness Hv	% Change
Untreated	429.33 (±13.8)	-	399.67 (±14.5)	-
Solid Solution	418.2 (±13.4)	-2.6	388.5 (±2.8)	-2.7
2 Hour Age Harden	545.96 (±16.9)	27.2	535.1 (±4)	33.9
4 Hour Age Harden	574.52 (±10)	33.8	554.4 (±5.9)	38.7
8 Hour Age Harden	563.9 (±4.9)	31.3	522.8 (±19.1)	30.7

6.2.4.1.1 Phase Specific Nanoindentation Analysis of WT-6

The changes in matrix hardness and modulus after a solution treatment and various aging treatments are summarised in Table 6.17. The solution treatment had little effect on the average hardness but a small increase in average modulus was calculated. The 2-hour aging treatment resulted in a small increase in hardness compared to the solution treated sample, but the modulus did not change. A drop in hardness and modulus was observed with additional aging treatments whereby after an 8-hour treatment, the recorded average hardness and modulus was lower compared to an untreated sample.

The distribution of hardness data for the solution treated sample (Figure 6.41a+b) shows that the medium value was similar to the untreated sample, but the data range was smaller with the solution treated sample where the maximum value decreased, and the minimum value increased. The smaller data range indicates the hardness of the matrix was more uniform. The slight increase in the lowest readings may be due increased alloying elements identified in solid solution and the decrease in the higher range of readings may be due to the solution treatment

allowing fine carbides and precipitates within the matrix to diffuse. Improvements in modulus were recorded after the solution treatment where more than 75% of modulus readings were higher than all readings recorded with the untreated sample, as shown in Figure 6.41c.

Compared to the untreated sample, aging the alloy for 2-hours produced a smaller range of hardness data where the maximum hardness values recorded were similar for both samples. However, the minimum hardness value recorded with the aged sample was considerably greater. Therefore, 50% of hardness readings were higher than more than 75% of the readings with the untreated sample. The range of modulus data between the solution treated sample and 2-hour aged sample were very similar but nearly all the modulus readings for the aged sample were higher than the maximum value recorded with the untreated sample. Increasing the aging time to 4-hours resulted in a drop in hardness compared to the sample aged for 2-hours. The lower quartile value with the 2-hour sample was comparable to the upper quartile value of sample aged for 4-hours. This indicates that 75% of readings with the 2-hour sample were higher than more than 75% of the highest readings with the 4-hour sample. Although there was a decrease in hardness after the longer 4-hour treatment, compared to the sample aged for 2-hours, the hardness data was similar to an untreated sample. Increasing the aging time to 4-hours resulted in a decrease in modulus compared to the sample aged for 2-hours. 75% of readings with the 4-hour sample were lower than 75% of the highest values recorded with the solution treated and sample aged for 2-hours. However, almost 50% of the highest modulus readings with the 4-hour aged sample were higher than the maximum value recorded with the untreated sample. Increasing the aging time to 8-hours resulted in further decreases in matrix hardness and modulus where readings were lower than the untreated sample. Compared to the untreated sample, more than 75% of hardness readings were lower than 75% of the highest readings and 75% of modulus readings were lower than the minimum value. The drop in mechanical properties experienced in the matrix of the samples after longer aging times would have been caused due to overaging of precipitation throughout the matrix and a reduce in the quantity alloying elements in the solid solution. This appears to coincide with an increase in outliers that were recorded after longer aging treatments. The results indicate that shorter aging times can improve the hardness and modulus of the matrix whereas longer treatment times have detrimental effects on the mechanical properties.

Changes in the H/E ratio of the matrix after each treatment are shown in Figure 6.42. The results demonstrate a significant decrease after the solution treatment. Although subsequent aging for 2 and 4-hours did increase the calculated H/E ratio, the values were lower compared to an untreated sample. A longer 8-hour aging treatment increased the H/E ratio to a similar value recorded with the untreated sample. These results suggest that solution and aging treatment does not significantly improve the wear resistance of the matrix.

Table 6.17: Changes in matrix hardness and modulus after each treatment using XPM data.

Phase/Treatment	Hardness (GPa)	Modulus (GPa)
Co Solid Solution - Untreated	7.5 (±0.5)	220.4 (±6.3)
Co Solid Solution - Solution	7.4 (±0.2)	248.9 (±8.3)
Co Solid Solution - 2-Hour Aging	8 (±0.3)	249 (±6)
Co Solid Solution - 4-Hour Aging	7.5 (±0.6)	234.5 (±11.4)
Co Solid Solution - 8-Hour Aging	7 (±0.3)	204.6 (±18)

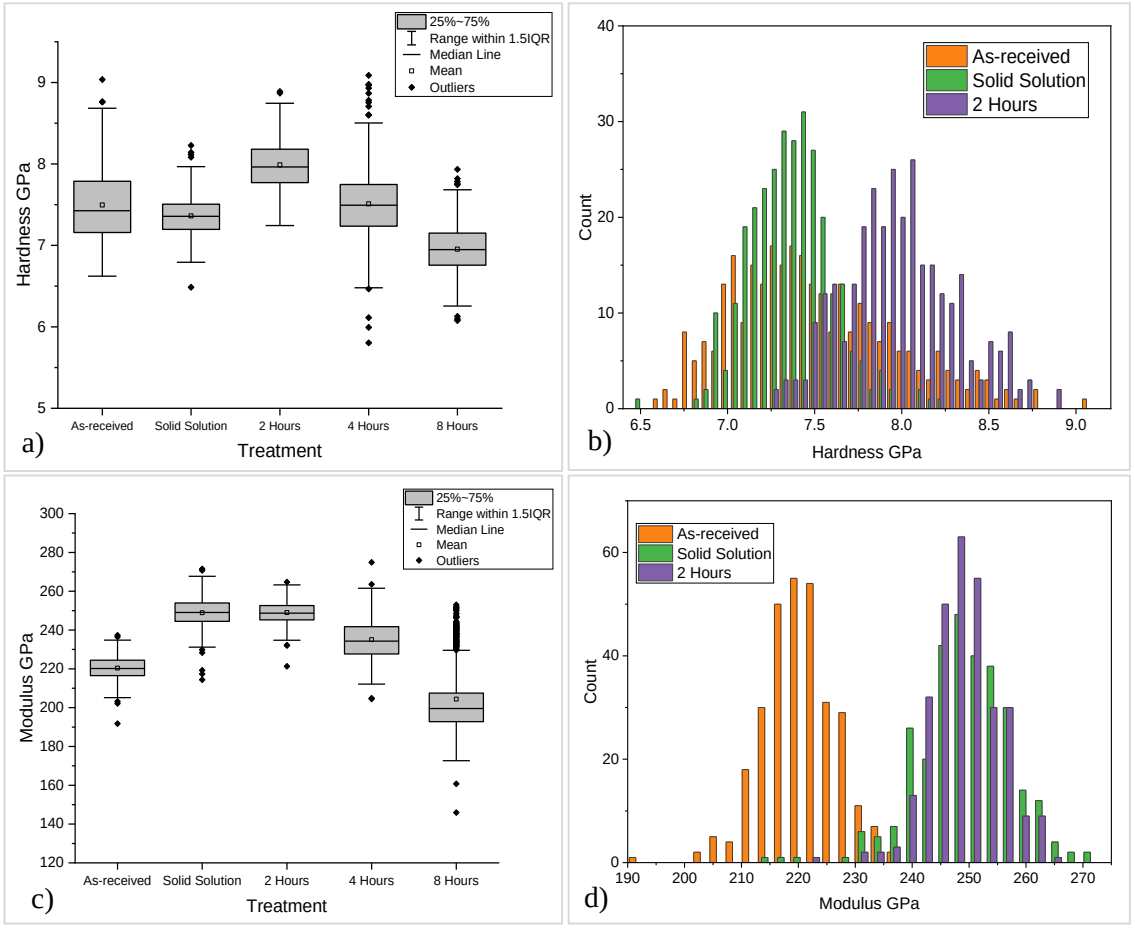

Figure 6.41: Distribution of hardness and modulus data after each treatment calculated from the XMP analysis: a and b) distribution of hardness data and c and d) distribution of modulus data.

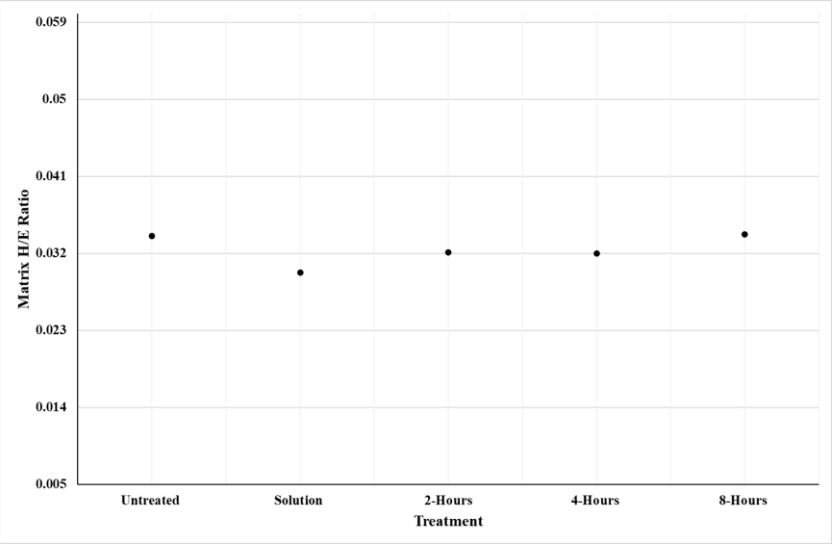

Figure 6.42: Matrix H/E ratios after a solution treatment at 1275℃ and additional aging treatments at 850℃.

6.2.4.2 Macrohardness and Microhardness Analysis of Age Hardened WT-12

Figure 6.43 displays the changes in alloy bulk hardness and the microhardness of the matrix after a solution treatment and additional age hardening treatments. The changes calculated as a percentage are presented in Table 6.18. The data indicates that the solution treatment resulted in a decrease in the bulk hardness of the alloy and the microhardness of the matrix. Compared to an untreated sample, bulk hardness was recorded to drop from 510Hv to 491Hv (-4%) and the hardness of the matrix decreased from 462Hv to 388Hv (-16%) after the solution treatment. Ageing the alloy for 2-hours resulted in a substantial increase in the hardness. The matrix increased to 527Hv from 462Hv (+14%) which contributed to an increase in the overall hardness of the alloy which increased to 571Hv, an increase in hardness of 12%. There were no clear signs of changes in hardness after a 4-hour treatment but increasing the aging time to 8-hours resulted in further improvements in material hardness. Compared to an untreated sample, the bulk hardness and matrix hardness increased to a maximum of 588Hv and 540Hv, respectively, after aging at 850℃ for 8-hours. This correlates to a 15% increase in bulk hardness and a 17% increase in matrix hardness.

These results indicate that significant improvements in alloy bulk hardness and matrix hardness can be achieved after a solution treatment and additional aging processes. Large increases occurred after a 2-hour aging treatment, but the hardness continued to gradually increase after 4 and 8-hour treatments.

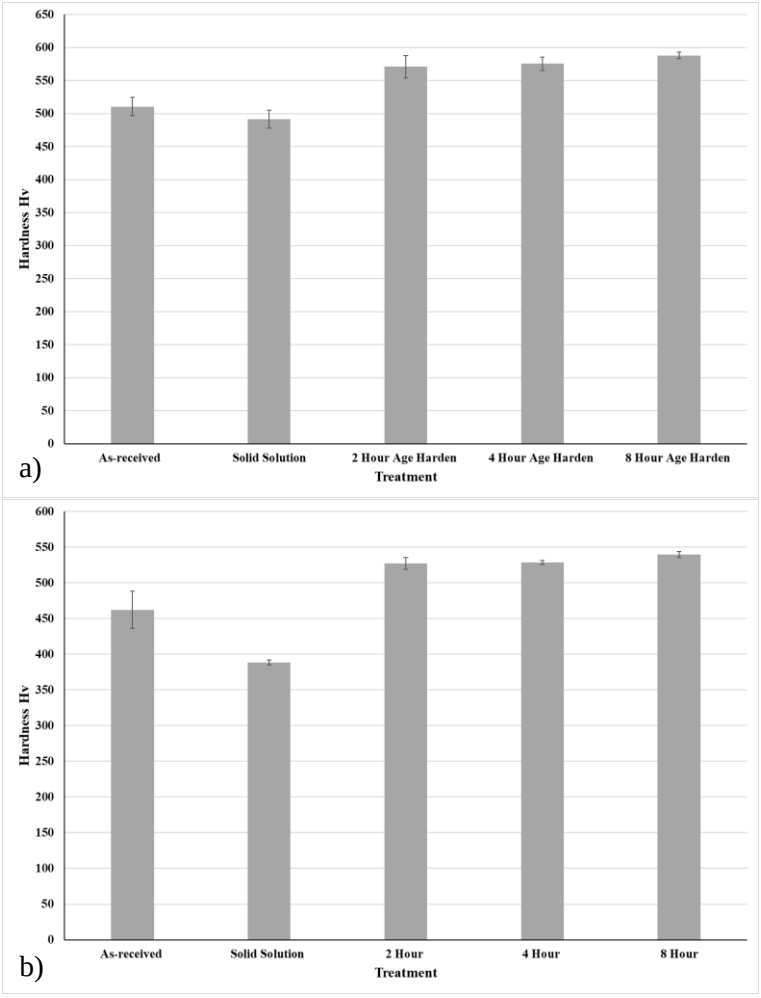

Figure 6.43: Changes in material bulk hardness and matrix microhardness of the WT-6 alloy after solution treating at 1275ºC for 8-hours and additional aging treatments at 850ºC various periods of time: a) Bulk hardness and b) matrix microhardness.

Table 6.18: Changes in bulk hardness and matrix microhardness calculated as a percentage after solution treating at 1275ºC for 8-hours and additional aging treatments at 850ºC various periods of time with comparisons to an untreated sample.

	Bulk		Matrix	
Treatment	Hardness Hv	% Change	Hardness Hv	% Change
Untreated	510 (±11.4)	-	462.4 (±25.7)	-
Solid Solution	491.3 (13.6)	-3.8	388.4 (±3.5)	-16
2 Hour Aging	571 (±11.2)	11.8	527.3 (±8.1)	14.1
4 Hour Aging	575.4 (±9.8)	12.7	528.7 (±5.9)	14.3
8 Hour Aging	587.9 (±10.5)	15.1	539.7 (±16.7)	16.7

6.2.4.2.1 Phase Specific Nanoindentation Analysis of WT-12

Solution treating the samples at 1275°C resulted in extreme coarsening of the chromium and tungsten carbide phases in addition to levels of carbide dissolution which increased chromium and tungsten content detected in solid solution. Additional aging of the alloy led to precipitates

forming throughout the matrix. The changes in hardness and modulus of the matrix after solution treating and aging the WT-12 samples are presented in Table 6.19. The results indicate that there is very little change in the average hardness or modulus after the initial solution treatment. However, aging the alloy for 2-hours increased the average hardness and modulus of the matrix. After the initial improvements in mechanical properties experienced after a 2-hour treatment, ageing the alloy for longer times resulted in a decrease in hardness and modulus.

The distribution of hardness and modulus data from XPM analysis is shown in Figure 6.44. Although the average hardness between the untreated sample and solution treated sample were similar, comparing the hardness XPM data (Figure 6.44a and b) illustrates a clear difference in the range of hardness data. The lower quartile with the untreated sample is similar to the median value recorded with the solution treated sample. This indicates that 75% of the highest hardness readings with the untreated sample were higher than 50% of the highest readings recorded with the solution treated sample. The smaller data range indicates a more uniform hardness of the matrix phase. This is also represented as a narrower peak with a higher peak intensity in the hardness histogram. This is due to the solution treatment promoting the dissolution of fine precipitates into solid solution. The range of modulus data for the untreated and solution treated sample remained similar. A significant increase hardness and modulus was experienced after a 2-hour aging treatment, compared to an untreated sample, where greater maximum and minimum values were recorded with both mechanical properties. The results indicate that 50% of hardness readings and over 25% of modulus readings were higher than the maximum values recorded with the untreated sample. The large increase in mechanical properties is likely due to the diffusion of tungsten and chromium into solid solution in addition to the aging treatment promoting the formation of precipitates throughout the matrix that was identified using SEM analysis. A 4-hour aging treatment reversed the improvements in mechanical properties experienced after a 2-hour treatment where hardness and modulus readings decreased to values that were comparable to an untreated sample. A longer 8-hour treatment resulted in increased hardness and modulus readings compared to the sample treated for 4-hours but lower values recorded compared to a 2-hour aging treatment. Compared to an untreated sample, 50% of the hardness and modulus readings were higher than 75% of reading with the untreated sample. The drop in mechanical properties compared to the 2-hour aged sample is most likely due to increased phases precipitation throughout the matrix that would have reduced chromium and tungsten concentrations in the surrounding matrix. However, due to diffusion of tungsten and chromium into solid solution after the solution treatment, improvements in mechanical properties were still observed when compared to an untreated sample. The results indicate that significant improvements in the hardness and modulus of the matrix can be achieved via a solution treatment

and additional aging. The greatest improvement was recorded after a shorter treatment time of 2-hours. Further aging of the alloy reversed the improvements experienced after a 2-hour treatment, although higher values were recorded after an 8-hour treatment compared to an untreated sample.

Figure 6.45 displays changes in H/E ratio experienced after each heat treatment. The results indicate that H/E dropped after the solution treatment. An additional aging treatment of 2-hours increased the H/E value where the value was higher compared to an untreated sample. Longer aging treatments of 4 and 8-hours resulted in a drop in H/E to a value comparable to an untreated sample. The results indicate that a shorter treatment can improve the wear resistance of the alloys matrix, but longer treatments reverse the gains experienced after a 2-hour treatment.

Table 6.19: Changes in matrix hardness and modulus after each treatment using XPM data.

Phase/Treatment	Hardness (GPa)	Modulus (GPa)
Co Solid Solution - Untreated	7.6 (±0.4)	235.6 (±7.4)
Co Solid Solution - Solution	7.3 (±0.2)	233.9 (±6.7)
Co Solid Solution - 2-Hour Aging	8.7 (±0.5)	248.8 (±9.3)
Co Solid Solution - 4-Hour Aging	7.5 (±0.3)	239.3 (±7.5)
Co Solid Solution - 8-Hour Aging	8.1 (±0.4)	246.6 (±7.5)

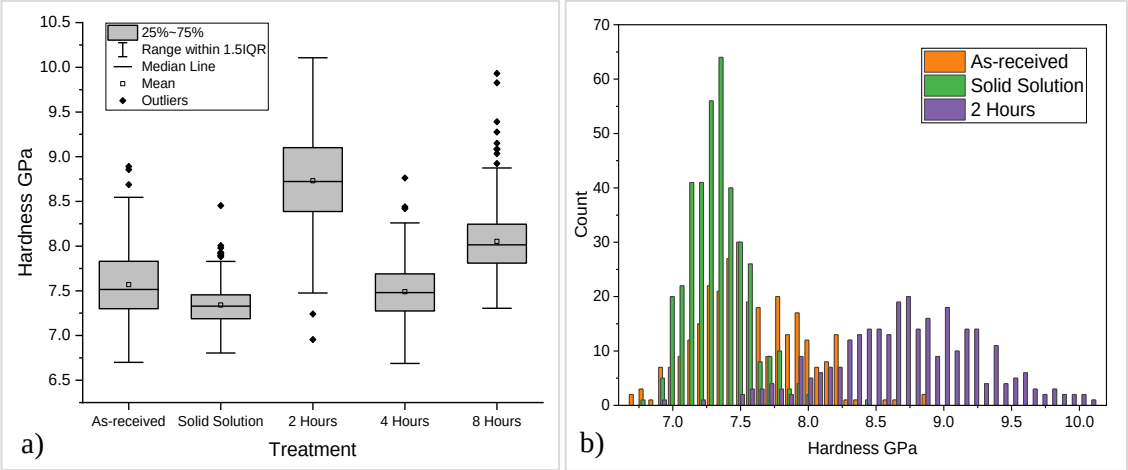

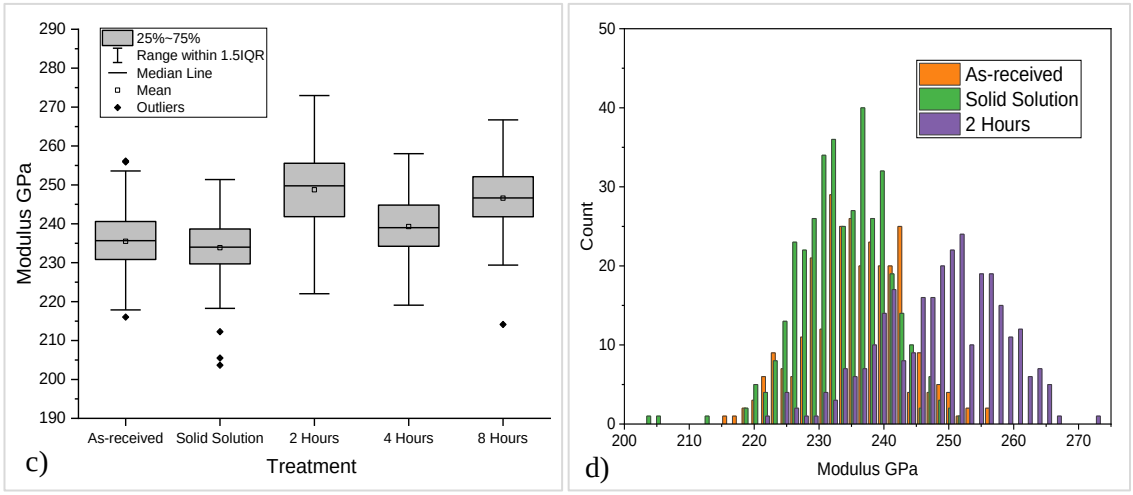

Figure 6.44: Distribution of hardness and modulus data after each treatment calculated from the XMP analysis: a and b) distribution of hardness data and c and d) distribution of modulus data.

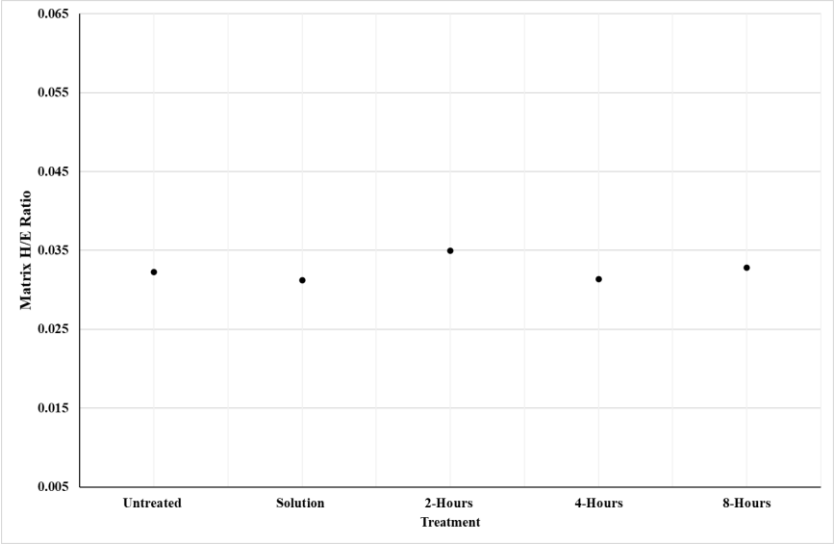

Figure 6.45: Matrix H/E ratios after a solution treatment at 1275℃ and additional aging treatments at 850℃.

6.2.5 Comparisons of Changes in Microstructure and Hardness Trends Observed After Solid Solution and Aging Heat Treatment

A solution treatment carried out at 1275°C for 6-hours did not result in complete dissolution of the eutectic carbide phases into solid solution but the treatment was observed to modify the microstructure of the alloys. The T-800 Tribaloy was not tested due to the extreme failure of the material during the quenching process after the solution treatment. No further investigation of the WT-4 was performed after microstructural analysis revealed the samples experienced different thermal treatments.

The WT-6 and WT-12 alloys displayed similar behaviour where the solution treatment resulted in extreme coarsening of the carbide phases and a change in morphology to a more rounded appearance compared to the finer distribution of carbides observed in the untreated samples. This process has also been reported by *Bedolla-Gil et al* [155]. It was identified that both alloys experienced levels of carbide dissolution after the solution treatment, but the quantity varied between the alloys. The dissolution of carbide phases into solid solution is supported by research carried out by *Lee et al* [156] where it was identified that increased levels of carbide dissolution, experienced with a CoCrMo alloy, occurred at higher treatment temperatures where the dissolution of the carbide phases increased the concentration of alloying elements retained in solid solution. After the solution treatment, a small decrease in the area fraction of the chromium carbides occurred with the WT-6 alloy which coincided with an increase in tungsten-rich phases. The composition of the matrix generally did not change after the solution treatment. However, areas of the matrix surrounding carbide phases that displayed signs of dissolution did contain higher levels of tungsten and what appeared to be tungsten rich precipitates. A reduction in the quantity of the chromium and tungsten phases recorded with the WT-12 alloy in addition to increased detection of chromium and tungsten content in the matrix confirms dissolution of the carbide phases into solid solution occurred after the solution treatment.

Additional aging of the WT-6 and WT-12 samples at 850℃ for various times did not significantly alter the microstructure further. Calculated area fraction indicated that there was no significant change in the quantity of individual phases, even after a prolonged aging time of 8-hours. However, more evident changes to the matrix of the WT-12 sample were recorded. In addition to areas of the matrix becoming enriched in alloying elements after the solution treatment, fine dispersion of precipitates was observed throughout the matrix where increased precipitation was often observed at grain boundaries. This was not observed with the sample that only received the solution treatment which indicates the aging treatment allowed for intragranular precipitation to occur. The increased amount of precipitation with the WT-12 alloy, compared to WT-6, is most likely due to the increased levels of carbon, chromium, and tungsten in the WT-12 alloys chemistry.

The change in microstructure morphology altered the alloys hardness properties. The initial solution treatment resulted in a decrease in material bulk hardness. Aging the alloys resulted in a significant increase in overall material hardness with both alloys. However, the length of the aging treatment influenced the alloys differently. The WT-6 alloy experienced the greatest improvements in bulk hardness and matrix hardness after a 4-hour treatment where a longer 8-hour treatment experienced lower increases in hardness. The hardness properties of the WT-12 remained similar after each aging treatment. Longer aging times had detrimental effects on the

nano-properties of the matrix with both alloys. The greatest improvements in hardness and modulus were recorded after a 2-hour treatment which gradually decreased with increasing aging. This is likely due to over coarsening of the precipitates observed within the matrix of samples which would have depleted the matrix of strengthening elements.

The mean *H/E* ratio gives an indication of a materials wear resistance [143,145]. The solution treatment reduced the alloys mean *H/E* ratio indicating in drop in wear resistance. Additional aging of the WT-6 alloy increased the *H/E* value which was comparable to an untreated sample. This indicates that the thermal process did not improve the wear resistance of the matrix. A slight improvement was experienced with the WT-12 alloy after a 2-hour aging treatment compared to an untreated sample. However longer aging times resulted in the mean *H/E* value decreasing. This suggests that a shorter aging time can improve the wear resistance of the matrix.

The results indicate that the mechanical properties of the alloys can be significantly improved with a solution and aging process where maximum improvements in the alloys mechanical properties were achieved after a certain aging time. The WT-6 experienced the greatest improvements in bulk hardness and microhardness after a 4-hour treatment. The matrix did not experience any detrimental effects in nano-hardness, but the modulus improved after a 2-hour treatment. The bulk hardness and matrix hardness of the WT-12 increased to similar levels with longer aging times. Compared to an untreated sample, improvements in nano-hardness and modulus were recorded where higher readings were documented after a 2-hour treatment. A 2-hour aging time also improved the wear resistance of the matrix.

7 Discussion

7.1 Untreated Alloys

The variation in alloy composition with the untreated alloys significantly changed the microstructure and mechanical properties of each alloy. Increased levels of carbon and tungsten with the CoCrW alloys or molybdenum with the CoCrMo alloy resulted in a higher area fraction of carbide or Laves phases within the microstructure in addition to higher concentrations of alloying elements being retained in solid solution. The composition of the WT-6 alloy contained the lowest level of carbon and tungsten and therefore consisted of the smallest area fraction of carbide phases in addition to having the lowest levels of tungsten retained in solid solution. Consequently, out of the four alloys studied, the lowest bulk hardness, matrix microhardness and lower matrix nano-hardness and modulus were recorded with WT-6. In contrast, the T-800 Tribaloy contained significantly higher levels of molybdenum which resulted in the microstructure being dominated by a primary Laves phase in addition to high levels of molybdenum being retained in the eutectic matrix. Therefore, the T-800 alloy, exhibited the highest bulk hardness, matrix microhardness and matrix nano-hardness and modulus. The hardness properties of the WT-4 and WT-12 alloys fell between the WT-6 and T-800 alloys. Comparing the WT-4 and WT-12 alloys demonstrated that the WT-4 alloy contained a higher are fraction of carbide phases as well as higher levels of tungsten in solid solution which provide the alloy with slightly higher hardness properties. There was little variation between the predicted wear performance of the matrix phase of the CoCrW alloys whereas a higher mean *H/E* ratio was calculated with the CoCrMo alloy. Therefore, a higher level of wear resistance is expected with cobalt rich phase of the CoCrMo alloy.

Progressive dip testing of the alloys in a molten zinc bath containing 0.35wt.% Al revealed that each alloy reacted with the bath after the first week of testing and that the depth of diffusion gradually increased after each stage of testing. Analysis of the microstructures after testing indicated that the carbide or Laves phases were more resistant to the diffusion process whereas the cobalt matrix was susceptible to diffusion and acted as the preferential route for molten metal ingress. With each alloy the diffusion of the cobalt rich matrix was characterised by the initial diffusion of aluminium into the alloy's matrix and the loss of cobalt from the alloy to form CoAl particles at the surface. The diffusion of aluminium was followed by the diffusion of zinc and the transformation of the cobalt matrix to form zinc rich intermetallic phases. This process resulted in the material loss at the alloys surface, particularly after longer dip times.

After each stage of testing the T-800 Tribaloy experienced the lowest diffusion depths in comparison to the CoCrW alloys. The T-800 also exhibited the lowest quantity of CoAl formation

at the surface. Comparison of the CoCrW alloys indicated that the WT-12 alloys experienced reduced diffusion depths after the first 2-weeks of testing whereas the WT-4 and WT-6 alloys experienced greater diffusion depths. Greater diffusion depths were recorded with the WT-4 and WT-12 alloys with longer immersion times whereas the WT-6 alloy experienced lower diffusion depths and displayed the lowest diffusion gradient indicating the slowest diffusion kinetics of the alloys. However, despite the WT-6 alloy experiencing reduced diffusion depths, detailed analysis of the matrix indicated increased levels of diffusion which severely depleted the matrix of alloying elements whereas the WT-4 and WT-12 alloys retained higher quantities of alloying elements in the diffusion layer. The increased saturations of aluminium and zinc at the surface of the WT-6 alloy may have slowed down the rate of diffusion and short circuit diffusion may have occurred to greater depths with the WT-4 and WT-12 alloys due to the reduced area fraction of the matrix phase exposed to the bath.

The results indicate that the T-800 Tribaloy possesses enhanced hardness properties and chemical resistance, compared to the CoCrW alloys, making it a promising material for journal bearing applications. The increased hardness of the Tribaloy would, in theory, provide increased wear resistance during operation and increased chemical resistance would restrict molten metal ingress as well as reducing the quantity of CoAl formation at the alloys surface. Reducing the rate of diffusion would allow the alloy to maintain its original mechanical properties and reducing the quantity of CoAl formation, which has largely been attributed to the degradation experienced by bearings, would reduce the quantity of abrasive wear debris. Both factors would contribute to the alloy maintaining high levels of wear resistance and prolong the stability and service life of the bearings.

7.2 Plasma Nitride Heat Treatment

A series of plasma nitriding treatments were carried out where one set of tests varied the treatment temperature between 400-550°C for a 15-hour treatment and the other set of tests varied the treatment time between 10-20-hours at a temperature of 475°C. The nitriding process resulted in the diffusion of nitrogen into the surface of each of the alloys to form a nitrogen rich diffusion layer. The carbides and Laves phases resisted the diffusion of nitrogen whereas nitrogen was able to diffuse into the cobalt rich matrix of each alloy. Increasing the treatment temperature or treatment time increased the level of nitrogen diffusion which resulted in thicker diffusion layers and increased concentrations of nitrogen in the diffusion layer. Analysis of the diffusion layer revealed a nitrogen concentration gradient where nitrogen content was greatest at the surface of the alloys and gradually decreased moving into the bulk of the alloy. The T-800 alloy experienced

the greatest depths of diffusion but also experienced the lowest concentrations of nitrogen. This is likely due to the reduced area of eutectic solid solution creating a short circuit diffusion path to greater depths and high levels of molybdenum retained in this phase may have reduced nitrogen concentrations. Comparison of the CoCrW alloys indicated that the WT-4 alloy experienced slightly thicker diffusion layers and higher levels of nitrogen concentrations. Again, this is likely due to short circuit diffusion as a result of the reduced size of the matrix phase with this alloy.

The nitriding process significantly improved the surface hardness of the alloys where the increase in hardness correlated to the treatment parameters and subsequent thickness of the diffusion layer. Increasing the treatment temperature or time, thus producing a thicker diffusion layer, resulted in increased hardness. Comparing the hardness data demonstrates that a thicker diffusion layer and larger increases in surface hardness can be achieved at higher treatment temperatures compared to longer treatment times at lower temperatures. Comparison of the CoCrW alloys indicated that the greatest increases in material hardness were achieved with the WT-12 alloy, despite the untreated WT-4 alloy having higher hardness properties prior to testing. This suggests that the strengthening mechanisms experienced with the WT-12 have a greater influence on the material hardness.

The formation of a nitrogen diffusion layer was not sufficient in preventing the diffusion of bath species into the alloy's matrix or the loss of alloying elements into the bath. As experienced with the untreated alloys, the diffusion process was characterised by the initial diffusion of aluminium into the alloy's matrix and the subsequent diffusion of zinc to form zinc rich intermetallic phases. Although diffusion was not prevented, the plasma treatment did benefit the performance of the alloys in molten zinc, particularly after longer treatment times. Similar diffusion depths were experienced with the alloys in the early stages of testing. However, with the CoCrW alloys, a reduced reaction layer thickness was measured by the fourth week of testing. Analysis of the plasma treated samples demonstrated that the diffusion layer contained higher levels of alloying elements after testing. Therefore, it is believed that the formation of nitride layer hinders the loss of alloying elements into the bath which reduces the rate of diffusion. The plasma treatment generally improved the integrity of the alloys surface as each alloy experienced less material loss. This was demonstrated by a relatively smooth surface and the persistence of the nitride layer after the fourth week of testing in contrast to a rough surface with the untreated alloys. This is likely due to increased retention of alloying elements within the diffusion layer. There was a clear reduction in the quantity of CoAl particles at the alloys surface with the plasma treated alloys. Initially it was thought that this may have been due to the nitride layer reducing cobalt loss into the bath which would reduce CoAl formation. However, compositional examination of the diffusion layer identified high levels of cobalt loss. Therefore, it is believed

that the nitride layer reduces the bonding strength of the CoAl phase with the alloys surface, and therefore they detach into the bath.

The results indicate that the plasma treatment could potentially improve the performance of the journal bearings in a number of ways; the significant increase in material hardness has the potential to improve the tribological properties of the alloys surface, higher quantities of the alloying elements reduce the rate of diffusion and maintain better mechanical properties and reducing the attachment of CoAl particles would reduce the likelihood of two-body abrasive wear if wear debris becomes entrapped between the bearings contact surfaces.

7.3 Annealing Heat Treatment

The annealing process was carried out 1000°C where samples were heated for times ranging between 1-4-hours. The treatment had little effect on the microstructure morphology with each alloy. The carbide and Laves phases were largely unaffected by the heat treatment but more significant changes were observed within the matrix of the alloys where phase precipitation throughout the matrix phase occurred with each alloy. The precipitates were chromium and tungsten rich with the CoCrW alloys and molybdenum and silicon rich with the CoCrMo alloy. Increasing the annealing time resulted in an increased area fraction and coarsening of the precipitates. This resulted in areas of the matrix being depleted in alloying elements such as chromium, tungsten and molybdenum.

The WT-6 and WT-4 alloys demonstrated little evidence of carbide dissolution, but increased precipitation of tungsten rich phases was observed with the WT-6 alloy and coarsening of the eutectic carbide phases occurred within the eutectic regions of the WT-4 alloys microstructure. A 4-hour annealing treatment of the WT-12 alloy resulted in a small amount of carbide dissolution into solid solution. This was demonstrated by a decline in the area fraction of chromium carbide phases which resulted in increased concentrations of chromium and tungsten in areas of the matrix. The primary Laves phase of the T-800 Tribaloy demonstrated minor signs of dissolution whereas the secondary Laves phases became more spherical in appearance. The CoMo eutectic solid solution phase experienced levels of dissolution which resulted in the formation of smaller phases and increased levels of alloying elements in the eutectic solid solution.

After the annealing stage of the thermal process, the alloys were subjected to different cooling cycles; furnace cooling which allowed the alloys too slowly cool to room temperature, and a water quenching process where the annealed alloys were rapidly cooled. Analysis of the microstructures revealed a similar diffusion process experienced with the furnace cooled and

water quenched samples characterised by precipitation within the matrix. However, the WT-4, WT-12 and T-800 alloys experienced significant crack propagation throughout the alloy's microstructure. The WT-6 alloy was the only alloy suitable for quenching as no material failure was observed after the cooling process.

The small changes in microstructure morphology observed with the alloys after the annealing treatment altered the mechanical properties of the alloys. The CoCrW alloys experienced small improvements in bulk hardness whereas larger changes in matrix microhardness were recorded. The changes in mechanical properties were attributed to the formation of precipitates throughout the matrix. It was identified that the alloys experienced greater improvements in hardness after certain treatment times where shorter times often resulted in greater increases in material hardness and longer treatments generally resulted in reduced improvements in material hardness. It was identified that longer treatments resulted in coarsening of the precipitates. The over coarsening of the precipitates resulted in a decrease in matrix microhardness which contributed to a decrease in material bulk hardness. The annealing heat treatment had detrimental effects on the hardness of the T-800 Tribaloy where longer treatment times resulted in a gradual decrease in the overall hardness of the alloy.

Although the WT-4, WT-12 and T-800 alloys were unsuitable for quenching due to the effects of thermal shock, the WT-6 alloy experienced significant improvements in matrix microhardness and the overall bulk hardness after quenching.

The depletion of alloying elements retained in solid solution, due to precipitation, influenced the nano-properties of each of the alloy's matrix. A similar behaviour trend experienced with the bulk hardness and microhardness was observed with the nano-properties where improvements in the matrix nano-hardness and modulus were observed with shorter annealing times. Longer annealing times had detrimental effects on the matrix properties which were often inferior to the properties recorded with the untreated alloys.

The results demonstrate that the annealing treatment can be used to slightly improve the hardness of the alloys investigated. This could potentially improve the performance of these alloys if used as journal bearing components. The annealing treatment improved the hardness of the CoCrW alloys which may improve their wear resistant properties. An improvement in wear resistance of the softer matrix phase, which is more vulnerable to wear compared to the significantly harder carbide phases, was demonstrated using a mean *H/E* ratio of the matrix. Although negligible improvements were observed with the WT-6 alloy, more significant improvements were calculated with the WT-4 and WT-12 alloys. The annealing process had detrimental effects on the hardness of the T-800 Tribaloy however, the decrease in hardness may improve the alloys ductility which is brittle by nature.

It is not known how the annealing process and changes in morphology of the alloy's matrix may affect the alloys chemical resistance when exposed to molten zinc. The formation of the precipitates could potentially offer increased diffusion resistance which may hinder molten metal ingress or the depletion of the alloying elements in the matrix, as a result of precipitation, may reduce resistance to diffusion. Therefore, further investigation is needed to confirm how the chemical performance of the alloy is influenced by an annealing treatment.

7.4 Solution and Aging Treatment

The alloys were initially solution treated at 1275℃ for 6-hours to promote dissolution of the carbide phases into solid solution. Samples were rapidly cooled by water quenching to produce a supersaturated solid solution phase by preventing precipitation. The sample were furnace cooled following additional aging treatments at 850℃ for times ranging between 2-8-hours. The T-800 Tribaloy experienced significant material failure after the solution treatment and the WT-4 samples received the incorrect thermal treatment, so they were not investigated further.

The solution treatment of the WT-6 and WT-12 alloys did not result in complete dissolution of the carbide phases, but their microstructures were significantly altered. This was characterised by extreme coarsening of the carbide phases to form large spherical phases in contrast to the fine dispersion of carbide phases observed with the untreated alloys. Area fraction analysis of the individual phases identified that small levels of chromium carbide dissolution with both alloys. This coincided with the formation of tungsten rich phases with the WT-6 alloy and an increased area fraction of the cobalt rich matrix with the WT-12 alloy. Additional aging of the alloys did not result in further changes in microstructure morphology. However, precipitation was observed throughout the matrix of the WT-12 where increased precipitation often occurred at grain boundaries. Precipitation was only observed in localised areas of the matrix with the WT-6 alloy.

The solution and aging treatments significantly changed the hardness of the WT-6 and WT-12 alloys. The solution treatment reduced the microhardness of the matrix which contributed to an overall decrease in material hardness with both alloys. This is likely due to the dissolution of fine carbide networks and precipitates within the matrix. Additional aging treatments significantly improved the hardness of the alloys. There was a clear correlation between the bulk hardness and microhardness measurements with the WT-6 alloys where greater improvements were achieved after a 4-hour aging treatment and a decrease in hardness was recorded after a longer 8-hour treatment. Little variation in material hardness was observed between the aging times with the WT-12 alloy.

Improvements in matrix nano-hardness and modulus were recorded after shorter aging times whereas longer treatments had detrimental effects, although these values were still higher compared to an untreated sample. This is likely due increased precipitation after longer treatment times which would have depleted the matrix of alloying elements. The nano-testing indicated that no significant improvement in the mean *H/E* ratio was experienced with the WT-6 alloy whereas an improvement with WT-12 was experienced after a 2-hour aging treatment.

8 Conclusions and Future Work

8.1 Conclusions

The results from the research can be summarised by the following conclusions:

Of the four alloys studied, the WT-6 alloy exhibited the lowest bulk hardness, matrix microhardness and lower matrix nano-hardness and modulus. In contrast, the T-800 Tribaloy exhibited the highest bulk hardness, matrix microhardness and matrix nano-hardness and modulus. The mechanical properties of the WT-4 and WT-12 alloys ranged between the WT-6 and T-800 alloys where the WT-4 possessed slightly higher hardness properties than the WT-12 alloy. There was little variation between the predicted wear performance of the matrix of the CoCrW alloys whereas a higher mean *H/E* ratio was calculated with the CoCrMo alloy.

When immersed in molten zinc containing 0.35wt.% Al, the untreated cast alloys demonstrated similar diffusion processes. The carbides and Laves phases were more resistant to the diffusion process whereas the cobalt matrix was vulnerable to diffusion and was the preferential route for molten metal ingress. For each alloy, the diffusion process was characterised by the initial diffusion of aluminium and iron and the subsequent diffusion of zinc and the transformation of the matrix into zinc-based intermetallic phases that formed behind the diffusion front. However, the rate of diffusion varied with each alloy. The CoCrMo alloy offered superior chemical resistance in comparison to the CoCrW alloys. Prolonged dip testing demonstrated that the CoCrMo alloy experienced the smallest diffusion layer thickness after each stage of testing in addition to exhibiting the least amount of cobalt-aluminide attachment at the alloys surface.

The plasma nitriding treatment resulted in the formation of a nitrogen rich diffusion layer at the alloys surface. Increasing the treatment temperature and treatment time produced thicker diffusion layers that contained higher nitrogen concentrations. The CoCrMo alloy experienced the greatest depths of nitrogen diffusion although lower nitrogen concentrations were achieved. The CoCrW alloys experienced similar levels of nitrogen diffusion where the WT-4 alloy experienced slightly higher diffusion depths and nitrogen concentrations.

Increasing the temperature or time of the plasma treatment increased the bulk hardness and microhardness of each of the alloys where there was a clear correlation between diffusion layer thickness and hardness i.e., increased hardness occurred with thicker diffusion layers.

The formation of a nitrogen diffusion layer did not prevent the diffusion of bath species into the alloys surface or the leaching of cobalt from the alloy into the bath. Similar diffusion depths were recorded after each stage of testing comparing untreated and plasma treated WT-6

and T-800 alloys. The plasma treated WT-4 and WT-12 alloys experienced long term improvements in bath resistance where a reduced diffusion depth was measured after 4-weeks of testing. The formation of a nitrogen layer did have the benefit of maintaining the integrity of the alloys surfaces as well as reducing the quantity of CoAl phases at the surface.

Annealing the alloys resulted in phase precipitation throughout the matrix of the samples which coarsened with increased annealing times. The precipitates were chromium and tungsten rich with the CoCrW alloys and molybdenum and silicon rich with the CoCrMo alloy where the precipitation of these phases left areas of the matrix depleted in alloying elements. There was little evidence of carbide dissolution with the WT-4 and WT-6 alloys but coarsening of carbide phases occurred with the WT-4 alloy and increased precipitation of a tungsten rich phase occurred with the WT-6 alloy. A longer heat treatment with the WT-12 alloy resulted in dissolution of chromium carbide phases into solid solution which increased the concentration of alloying elements in the matrix. Secondary Laves phases embedded in the eutectic solid solution of the T-800 Tribaloy became more spherical in appearance and the eutectic CoMo solid solution phase experienced levels of dissolution into solid solution after annealing.

The WT-6 alloy was the only alloy that did not fail after being quenched following annealing. The WT-4, WT-12 and T-800 alloys all experienced significant material failure and crack propagation due to thermal shock. Comparing the furnace cooled and quenched samples demonstrated there was no variations in microstructure morphology.

The changes in microstructure morphology that occurred after annealing altered the mechanical properties of each alloy. The annealing process slightly increased the bulk hardness of the CoCrW alloys where the WT-12 alloy experienced the greatest improvements in material hardness. The increase in hardness experienced with the CoCrW alloys was attributed to precipitation occurring within the matrix. Over coarsening of the precipitates was experienced after longer treatment times which had detrimental effects on material hardness, particularly the hardness of the matrix. The annealing process had detrimental effects on the T-800 Tribaloy where the bulk hardness of the alloy and the matrix hardness gradually decreased with longer treatments.

Similar trends were observed with the nano-hardness and modulus of the matrix. Improvement in nano properties were recorded with each alloy. However, longer treatments and the over coarsening of precipitates and increased depletion of alloying elements retained in solid solution had negative effectives on the alloy's nano-mechanical properties. Significant improvements in *H/E* ratios were achieved with the WT-4 and WT-12 alloys whereas only minor improvements occurred with the WT-6 and T-800 alloys.

A solution treatment with the WT-6 and WT-12 alloys did not result in significant dissolution of the carbide phases, but the treatment did result in significant changes in microstructure morphology. This was characterised by extreme coarsening of the carbide phases where the carbide phases were blockier and rounded in appearance. The WT-12 alloy experienced higher levels of carbide dissolution in contrast to the WT-6 alloy which experienced very little carbide diffusion. Additional aging of the WT-12 alloy resulted in precipitation throughout the matrix whereas only small amounts of precipitation occurred with the WT-6 in isolated areas of the matrix.

The mechanical properties of the WT-6 and WT-12 alloys can be significantly improved by a solution treatment and additional aging treatments. The initial solution treatment decreased the overall material hardness in both alloys in addition to the decreasing the microhardness and nano-properties of the matrix. Aging the alloys significantly increased the bulk hardness of each alloy and significantly improved the microhardness and nano-properties of the matrix compared to untreated alloys. Longer aging treatments had detrimental effects on the alloys mechanical properties compared to shorter treatment times, although improvements were still achieved compared to untreated alloys.

8.2 Future Work

The aim of this research was to identify better performing materials for journal bearing applications. This would be achieved by improving the wear and/or chemical resistance of the alloys which would have the benefits of prolonging the service life of the bearings and reducing vibration caused by degraded bearings. This would contribute to improving line productivity and coating quality. To reach this goal further research is needed to build upon the knowledge gained from this work and additional testing is required to identify if the heat treatment used in this study would improve the performance of the alloys in service. Future work would include:

1. Identifying any changes in chemical reactivity with the annealed and age hardened samples. This would involve progressive dip testing of the heat-treated alloys in molten zinc to investigate how the changes in microstructure morphology influences their chemical resistance.

2. Pursuing the development of the T-800 Tribaloy. It was identified that this alloy possessed superior mechanical and corrosion resistant properties which could potentially improve the performance of the journal bearings. However, the brittle nature of the alloy

limits its potential use. It was found that the annealing process reduced the hardness of the alloy which, in theory, would improve the materials ductility. Additional testing, such as impact testing, would be needed to analyse any changes in the materials ductility and impact toughness. Exploring the alloys chemistry offers another potential route for alloy development. Altering the alloys chemistry to improve its impact resistance or resistance to thermal shock, whilst retaining its wear and corrosion resistance would be extremely beneficial for the use as a journal bearing components.

3. General wear testing of heat-treated alloys. The mean *H/E* ratio indicates a materials wear resistance. The improvements in wear resistance calculated in this research should be confirmed using practical tribological testing. This type of testing should also be used to investigate the tribological behaviour of the plasma treated samples.

4. Carry out wear tests on a bespoke bearing wear testing rig capable of replicating galvanising line conditions. Testing of heat-treated alloys with comparisons made to untreated alloys would determine any changes in alloy performance. The bearing rig, described in the following section, offers the potential to trial novel bearing materials and bearings designs without the risk of interrupting galvanising line operations.

5. It would be beneficial to use thermodynamic software, such as Thermo-calc, to predict phase formation within the alloys that are related to treatment parameters such as treatment temperature and time.

8.2.1 Bearing Wear Testing Rig

During the course of this project, a bespoke bearing wear testing rig was designed and constructed with the purpose of researching and developing the performance of journal bearing components for molten zinc applications. An image of the bearing rig is displayed in Figure 8.1a. The complex nature of the journal bearing components makes it difficult to confidently justify the performance of novel bearing materials using other forms of wear testing equipment, such as pin-on-disk type tests, for trial on an operational industrial galvanising line. Although these simplified tests can provide useful information, such as wear rates or friction coefficients, they do not replicate the bearing contact mechanics or line conditions experienced by journal bearings during operation. They also do not account for the interaction with molten zinc during the wear process. Trialling novel bearing materials during the standard operation of a galvanising line runs the risk of unplanned line downtime if the bearings fail prematurely which can have significant negative

financial impacts. Therefore, the rig was designed to fully replicate the conditions experienced on a galvanising line whilst eliminating the potential risks of trialling novel bearing materials and bearing designs on an industrial galvanising line. Control of test parameters includes bath chemistry, bath temperature, line speeds, load, and testing time. The rig was also designed to run different types of tests that includes bar on plate tests for rapid material prototyping or full-scale corrector, stabilising or sink roll journal bearings. An example of a wear test is presented in Figure 8.1b and c which displays a stabilising roll sleeve that has been run against a half moon bushing.

Figure 8.1: Bearing wear testing rig and tested journal bearing components: a) Bearing rig, b) stabilising roll sleeve and c) half-moon bushing.

References

1. Azimi A, Ashrafizadeh F, Toroghinejad MR, Shahriari F. Metallurgical assessment of critical defects in continuous hot dip galvanized steel sheets. Surf Coatings Technol. 2012;206(21):4376–83.
2. Shibli SMA, Meena BN, Remya R. A review on recent approaches in the field of hot dip zinc galvanizing process. Surf Coatings Technol. 2015;262:210–5.
3. Rachamalla V V. A model of stabilizer roll bearing for a continuous hot-dip galvanizing line A Model of Stabilizer Roll Bearing for a Continuous Hot-dip Galvanizing Line Department of Mechanical and Aerospace Engineering. West Virgina University; 2006.
4. Bian J, Zhu Y, Liu XH, Wang GD. Development of Hot Dip Galvanized Steel Strip and Its Application in Automobile Industry. J Iron Steel Res Int. 2006;13(3):47–50.
5. Neghab AK, Hrymak AN, Goodwin FE. Near-roll dross particle interactions in a galvanizing bath. Iron Steel Technol. 2015;12(2):41–5.
6. Rajeev GP, Rahul MR, Kamaraj M, Bakshi SR. Microstructure and high temperature mechanical properties of wire arc additively deposited Stellite 6 alloy. Materialia. 2020;12(January):100724.
7. Scotti L, Mottura A. Interstitial diffusion of O, N, and C in α-Ti from first-principles: Analytical model and kinetic Monte Carlo simulations. J Chem Phys. 2016;144(8).
8. Koch G. Cost of corrosion. In: Trends in Oil and Gas Corrosion Research and Technologies: Production and Transmission. Elsevier Inc.; 2017. p. 3–30.
9. Penney DJ, Sullivan JH, Worsley DA. Investigation into the effects of metallic coating thickness on the corrosion properties of Zn-Al alloy galvanising coatings. Corros Sci. 2007;49:1321–39.
10. Marder AR. Metallurgy of zinc-coated steel. Prog Mater Sci. 2000;45:191–271.
11. Elsner CI, Seré PR, Di Sarli AR. Atmospheric corrosion of painted galvanized and 55 % Al-Zn steel sheets: Results of 12 years of exposure. Int J Corros. 2012;2012.
12. Yabuki A. Self-Healing Coatings for Corrosion Inhibition of Metals. Mod Appl Sci. 2015;9(7):214.
13. Neghab AK. Improving Galvanizing Bath Hardware. 2015;(May):1–28.
14. Berry L. Optimisation of the zinc coating surface for GI Full Finish for the automotive sector at high line speeds. Swansea University; 2018.
15. Snider JM. Zinc Pot Bearing Material Wear and Corrosion Characterization By. West Virginia University; 2004.
16. Escott L. Reducing the even wear damage of cobalt bearings that are submerged in molten zinc through material selection. Swansea University; 2015.
17. Hyun GY, Gi JA, Myung KC, Jong KK. Aerodynamic investigation of air knife system to find out the mechanism of the check mark in a continuous hot-dip galvanizing process. ASME Int Mech Eng Congr Expo Proc. 2009;10(PART A):233–9.
18. N. Parvini Ahmadi ER. Effect of Al on microstructure and Thickness of Galvanized Layers on Low Carbon Silicon-free Steel.pdf. Int J ISSI. 2009;Vol.6:25–9.

19. Culcasi JD, Seré PR, Elsner CI, Di Sarli AR. Control of the growth of zinc-iron phases in the hot-dip galvanizing process. Surf Coatings Technol. 1999;122:21–3.

20. Jordan CE, Marder AR. {Fe-Zn} phase formation in interstitial-free steels hot-dip galvanized at 450°C. J Mater Sci. 1997;32:5593–602.

21. Pokorny P, Kolisko J, Balik L, Novak P. Reaction kinetics of the formation of intermetallic Fe – Zn during hot - Dip galvanizing of steel. Metalurgija. 2016;55(1):111–4.

22. Nemai Chandra Gorain, T Venugopalan, K.K ray GM. Effect of Coating on Formability of Steel Sheets. In 2012.

23. Mandal GK, Mandal D, Das SK, Balasubramaniam R, Mehrotra SP. Microstructural study of galvanized coatings formed in pure as well as commercial grade zinc baths. Trans Indian Inst Met. 2009;62(1):35–40.

24. Hsu CW, Wang KK, Chang L, Gan D, Chang YL, Liang HY, et al. Formation of Fe2Al5-xZnx intermetallic crystals at the Fe-Zn interface in hot-dip galvanizing. Mater Charact. 2018;137(October 2017):189–200.

25. De Abreu Y, Da Silva A, Ruiz A, Réquiz R, Angulo N, Alanis R. Study of zinc coatings on steel substrate attained by two different techniques. Surf Coatings Technol. 1999;120–121:682–6.

26. Min T, Gao Y, Huang X, Gong Z, Li K, Ma S. Effects of aluminum concentration on the formation of inhibition layer during hot-dip galvanizing. Int J Heat Mass Transf. 2018;127:394–402.

27. Takata N, Nishimoto M, Kobayashi S, Takeyama M. Morphology and formation of Fe-Al intermetallic layers on iron hot-dipped in Al-Mg-Si alloy melt. Intermetallics. 2014;54:136–42.

28. Xie Y, Du A, Zhao X, Ma R, Fan Y, Cao X. Effect of Mg on Fe–Al interface structure of hot–dip galvanized Zn–Al–Mg alloy coatings. Surf Coatings Technol. 2018;337(29):313–20.

29. Katiforis N, Papadimitriou G. Influence of copper, cadmium and tin additions in the galvanizing bath on the structure, thickness and cracking behaviour of the galvanized coatings. Surf Coatings Technol. 1996;78(1–3):185–95.

30. Edavan RP, Kopinski R. Corrosion resistance of painted zinc alloy coated steels. Corros Sci. 2009;51(10):2429–42.

31. Schürz S, Luckeneder GH, Fleischanderl M, Mack P, Gsaller H, Kneissl AC, et al. Chemistry of corrosion products on Zn-Al-Mg alloy coated steel. Corros Sci. 2010;52(10):3271–9.

32. Prosek T, Larché N, Vlot M, Goodwin F, Thierry D. Corrosion performance of Zn-Al-Mg coatings in open and confined zones in conditions simulating automotive applications. Mater Corros. 2010;61(5):412–20.

33. Liu DYH, Filc AB, Tang N, Goodwin FE. Dross Buildup on Various Alloys in a Galvalume Bath. In: Galvanisers Association 99th Annual Meeting. 2007. p. 1–16.

34. McDermid JR, Kaye MH, Thompson WT. Fe solubility in the Zn-rich corner of the Zn-Al-Fe system for use in continuous galvanizing and galvannealing. Metall Mater Trans B Process Metall Mater Process Sci. 2007;38(2):215–30.

35. P. Sawaitul, S.A. Chowriwar IPL. Minimization of Dross Formation During the Continuous Galvanizing Process in the Steel Industry. Int J Emerg Technol Adv Eng. 2012;2(1).

36. Liu YH, Tang N, Zhang L, Denner SG, Goodwin FE. Dross Formation and Control During Transitions from Galvannealing to Galvanizing. 44 th MWSP Conf Proc. 2002;XL(September):781–90.

37. Bélisle S, Lezon V, Gagné M. The Solubility of Iron in Continuous Hot-Dip Galvanizing Baths. J Phase Equilibria. 1991;12(3):259–65.

38. Lin K-Y. The Dissolution of Iron from Automotive Steel Sheets in a Molten Zinc Bath and the Kinetics of the Nucleation and Growth of Dross Particles. Case Western Reserve University; 2011.

39. N.-Y. Tang, M. Dubois F. G. Progress in Development of Galvanising Bath Management Tools. In: 4th International Conference on Zinc and Zinc Alloy Coated Steel Sheet (Galvatech 1998)At: Tokyo, Japan. 1998.

40. Bright M, Ensminger A. Identification of Failure Mechanisms in Correcting Roll Bearings of a Continuous Galvanizing Line. 2004;1–19.

41. Yang KJ, Hong KS. Robust boundary control of an axially moving steel strip. Vol. 15, IFAC Proceedings Volumes (IFAC-PapersOnline). IFAC; 2002. 7–12 p.

42. Bhadra S. Energy Efficiency In Continuous Galvanizing Lines. West Virginia University; 2002.

43. Zhang K, Tang NY, Goodwin FE, Sexton S. Reaction of 316L stainless steel with a galvanizing bath. J Mater Sci. 2007;42(23):9736–45.

44. Ke Zhang, Nai-Yong Tang, Frank E Goodwin SS. ON-LINE TESTING OF 316L STAINLESS STEEL. In: Galvanizers Association 98th Meeting: Columbus, OH. 2006.

45. Loto RT, Özcan E. Corrosion Resistance Studies of Austenitic Stainless Steel Grades in Molten Zinc-Aluminum Alloy Galvanizing Bath. J Fail Anal Prev. 2016;16(3):427–37.

46. Seong BG, Hwang SY, Kim MC, Kim KY. Reaction of WC-Co coating with molten zinc in a zinc pot of a continuous galvanizing line. Surf Coatings Technol. 2001;138(1):101–10.

47. REN X jing, MEI X zhen, SHE J, MA J hong. Materials Resistance to Liquid Zinc Corrosion on Surface of Sink Roll. J Iron Steel Res Int. 2007;14(5 SUPPL. 1):130–6.

48. Huang T. Investigation and Improvement of Molten Zinc Corrosion of a Sink Roll with Thermal Sprayed WC-Co Coating. 2020.

49. Zhang J, Deng C, Song J, Deng C, Liu M, Zhou K. MoB-CoCr as alternatives to WC-12Co for stainless steel protective coating and its corrosion behavior in molten zinc. Surf Coatings Technol. 2013;235:811–8.

50. F.Goodwin. Development of Improved Materials for Continuous Steel Hot-Dipping Processes. 2005.

51. Rosalbino F, Scavino G. Corrosion behaviour assessment of cast and HIPed Stellite 6 alloy in a chloride-containing environment. Electrochim Acta. 2013;111:656–62.

52. Jiang WH, Guan HR, Hu ZQ. Effects of heat treatment on microstructures and mechanical properties of a directionally solidified cobalt-base superalloy. Mater Sci Eng

A. 1999;271(1–2):101–8.

53. Zhang K, Tang NY. On the wear of a cobalt-based superalloy in zinc baths. Metall Mater Trans A Phys Metall Mater Sci. 2003;34 A(10):2387–96.

54. Brunnock MS. Development of materials with improved resistance to molten metal attack in hot dip zinc coating lines for strip steel product. Swansea University; 1997.

55. Zhang K. Effects of test conditions on the tribological behaviour of a journal bearing in molten zinc. Wear. 2005;259(7–12):1248–53.

56. Ning Y, Zhang B. Hot Forming of Superalloy Parts and Structures. Ref Modul Mater Sci Mater Eng. 2020;1–13.

57. Liu L, Zhang J, Ai C. Nickel-Based Superalloys. Ref Modul Mater Sci Mater Eng. 2020;1–11.

58. Chang SH, Ko CC. Effects of MC carbide precipitates on the microstructure and mechanical properties of cobalt-based alloys adding TiC powder via vacuum sintering process. Mater Trans. 2013;54(3):399–404.

59. Zhu Z, Ouyang C, Qiao Y, Zhou X. Wear Characteristic of Stellite 6 Alloy Hardfacing Layer by Plasma Arc Surfacing Processes. Scanning. 2017;2017:1–7.

60. Halling J and RAB. Principles of Triboogy. Vol. 1. Macmillan; 1977.

61. Gahr KHZ. Wear by hard particles. Tribol Int. 1998;31(10):587–96.

62. Gok MS, Ozliman H. Investigation of abrasive wear behavior of industrial wastes on AL 6061 material using rubber wheel abrasion test (RWAT) method. Medziagotyra. 2019;25(1):47–53.

63. Stachowiak GW. Particle angularity and its relationship to abrasive and erosive wear. Wear. 2000;241(2):214–9.

64. Çimenoğlu H. Subsurface characteristics of an abraded low carbon steel. Wear. 1997;210(1–2):204–10.

65. Thakare MR, Wharton JA, Wood RJK, Menger C. Effect of abrasive particle size and the influence of microstructure on the wear mechanisms in wear-resistant materials. Wear. 2012;276–277:16–28.

66. Sadeghi F, Jalalahmadi B, Slack TS, Raje N, Arakere NK. A review of rolling contact fatigue. J Tribol. 2009;131(4):1–15.

67. Murakami Y. Contact fatigue. Met Fatigue. 2019;19(Ref 2):529–65.

68. Hua N, Hong X, Liao Z, Zhang L, Ye X, Wang Q, et al. Corrosive wear behaviors and mechanisms of a biocompatible Fe-based bulk metallic glass. J Non Cryst Solids. 2020;542(March):120088.

69. Alojali HM, Benyounis KY. Advances in Tool wear in Turning Process. Reference Module in Materials Science and Materials Engineering. Elsevier Ltd.; 2016. 1–15 p.

70. Bright M a, Road A, Ohio US a. Investigating Galvanneal Reactions on Pot Hardware Materials.

71. Bello JO, Wood RJK, Wharton JA. Synergistic effects of micro-abrasion-corrosion of UNS S30403, S31603 and S32760 stainless steels. Wear. 2007;263(1-6 SPEC. ISS.):149–59.

72. Yu Z, Chen M, Li F, Zhu S, Wang F. Synergistic effect of corrosion and wear of the 316 stainless steel in molten zinc alloy at 460 °C. Corros Sci. 2020;165(December 2019):108411.

73. De Carvalho Michalski MA, Zindeluk M, De Oliveira Rocha R. Influence of journal bearing axial grooves on the dynamic behavior of horizontal rotors. Shock Vib. 2006;13(4–5):285–300.

74. N.FM. Yusof ZMR. The Effect of Lubrication on the Vibration of Roller Bearings. In: MATEC Web of Conferences. EDP Sciences; 2018. p. 7.

75. Dubois A, Karim ANM. Metal Forming and Lubrication. Ref Modul Mater Sci Mater Eng. 2019;(May 2015):1–9.

76. Tamatam LR. Tribological performance of different crankshaft bearings in conjunction with textured shaft surfaces. Luleå University of Technology; 2017.

77. Pourret O, Faucon M. Cobalt. 2017;(August):1–4.

78. Erwin PF. Stellite: A History of the Haynes Stellite Company. Vol. 62, Journal of American History. 1976. 1034–1035 p.

79. Neville A, Malayoglu U. Aqueous corrosion of cobalt and its alloys. Shreir's Corros. 2010;1916–36.

80. Liu R, Yao JH, Zhang QL, Yao MX, Collier R. Sliding wear and solid-particle erosion resistance of a novel high-tungsten Stellite alloy. Wear. 2015;322–323:41–50.

81. Liu R, Wu XJ, Kapoor S, Yao MX, Collier R. Effects of Temperature on the Hardness and Wear Resistance of High-Tungsten Stellite Alloys. Metall Mater Trans A Phys Metall Mater Sci. 2015;46(2):587–99.

82. Kapoor S. High-Temperature Hardness and Wear Resistance of Stellite Alloys. Vol. 6, World Academy of Science, Engineering and Technology. 2012. 1–197 p.

83. Davis JR. ASM specialty handbook: Nickel, Cobalt, and Their Alloys. ASM International; 2000. 442 p.

84. Ratia VL, Zhang D, Carrington MJ, Daure JL, McCartney DG, Shipway PH, et al. Comparison of the sliding wear behaviour of self-mated HIPed Stellite 3 and Stellite 6 in a simulated PWR water environment. Wear. 2019;426–427(August 2018):1222–32.

85. Liu R, Xi SQ, Kapoor S, Wu XJ. EFFECTS OF CHEMICAL COMPOSITION ON SOLIDIFICATION , MICROSTRUCTURE AND HARDNESS OF Co-Cr-W-Ni and Co-Cr-Mo-Ni ALLOY SYSTEMS. Int J Res Rev Appl Sci. 2010;5(2):110–22.

86. Nsoesie S, Liu R, Jiang K, Liang M. High - temperature Hardness and Wear Resistance of Cobalt - based Tribaloy Alloys. 2013;2(3):48–56.

87. Liu R, Xu W, Yao MX, Patnaik PC, Wu XJ. A newly developed Tribaloy alloy with increased ductility. Scr Mater. 2005;53(12):1351–5.

88. Renz A, Prakash B, Hardell J, Lehmann O. High-temperature sliding wear behaviour of Stellite®12 and Tribaloy®T400. Wear. 2018;402–403(January):148–59.

89. Jiang K. Effects of Heat Treatment on Microstructure and Wear Resistance of Stainless Steels and Superalloys.

90. Scheid A, D'Oliveira ASCM. Effect of temperature and reactivity of molten 55Al-Zn

alloy on Co based alloy coatings. Mater Sci Technol. 2010;26(12):1487–93.

91. Tang N, Li YP, Kurosu S, Koizumi Y, Matsumoto H, Chiba A. Interfacial reactions of solid Co and solid Fe with liquid Al. Corros Sci. 2012;60:32–7.

92. Zhang K, Tang N. Reactions of Various Materials With a Galvanising Bath.

93. Yao MX, Wu JBC, Liu R. Microstructural characteristics and corrosion resistance in molten Zn-Al bath of Co-Mo-Cr-Si alloys. Mater Sci Eng A. 2005;407(1–2):299–305.

94. Zhang K. Wear of cobalt-based alloys sliding in molten zinc. Wear. 2003;255:545–55.

95. Zhang K, Tang N, Filc AB. A Practical Approach to Enhance Wear Resistance of Bearings in Molten Zinc. 94th Galvaniz Assoc Meet Detroit, MI, USA. 2002;1–11.

96. Zhang XM, Chen WP. Review on corrosion-wear resistance performance of materials in molten aluminum and its alloys. Trans Nonferrous Met Soc China (English Ed. 2015;25(6):1715–31.

97. Zhang K. Wear of cobalt-based alloys sliding in molten zinc. Wear. 2003;255(1–6):545–55.

98. Zhang K, Tang N-Y. Research and Development of Pot Bearings in Continuous Galvanizing. Galvatech'04 Conf Proc. 2004;605–15.

99. Shin JC, Doh JM, Yoon JK, Lee DY, Kim JS. Effect of molybdenum on the microstructure and wear resistance of cobalt-base Stellite hardfacing alloys. Surf Coatings Technol. 2003;166(2–3):117–26.

100. Radu I, Li DY, Llewellyn R. Tribological behavior of Stellite 21 modified with yttrium. Wear. 2004;257(11):1154–66.

101. Çelik H, Kaplan M. Effects of silicon on the wear behaviour of cobalt-based alloys at elevated temperature. Wear. 2004;257(5–6):606–11.

102. Xu W, Liu R, Patnaik PC, Yao MX, Wu XJ. Mechanical and tribological properties of newly developed Tribaloy alloys. Mater Sci Eng A. 2007;452–453:427–36.

103. Rehman A, Liang Y, Hassan Shirani Bidabadi M, Yu Z, Zhang C, Chen H, et al. Enhancement of cyclic oxidation resistance and effect of transition oxides on wear mechanism of yttrium plus aluminium modified tribaloy T-900 alloy. Corros Sci. 2020;163(April 2019):108283.

104. Yuduo Z, Zhigang Y, Chi Z, Hao L. Effect of Rhenium Addition on Isothermal Oxidation Behavior of Tribaloy T-800 Alloy. Chinese J Aeronaut. 2010;23(3):370–6.

105. Osma A, Kayali ES, Öveçoğlu ML. The effect of elevated temperature and silicon addition on a cobalt-based wear resistant superalloy. J Mater Sci. 1996;31(17):4603–8.

106. Kuzucu V, Ceylan M, Çelik H, Aksoy İ. An investigation of stellite-6 alloy containing 5.0 wt% silicon. J Mater Process Technol. 1998;79(1–3):47–51.

107. Kuzucu V, Ceylan M, Çelik H, Aksoy İ. Microstructure and phase analyses of Stellite 6 plus 6 wt.% Mo alloy. Vol. 69, Journal of Materials Processing Technology. 1997. p. 257–63.

108. Halstead A. Microstructure and Fracture of Two Cobalt Hardfacing Alloys. 1980.

109. Ren B, Zhang M, Chen C, Wang X, Zou T, Hu Z. Effect of Heat Treatment on Microstructure and Mechanical Properties of Stellite 12 Fabricated by Laser Additive

Manufacturing. J Mater Eng Perform. 2017;26(11):5404–13.

110. Yao MX, Wu JBC, Xu W, Liu R. Metallographic study and wear resistance of a high-C wrought Co-based alloy Stellite 706K. Mater Sci Eng A. 2005;407(1–2):291–8.

111. Yeh S-H, Chiu L-H, Chang H. Effects of Gas Nitriding on the Mechanical and Corrosion Properties of SACM 645 Steel. Engineering. 2011;03(09):942–8.

112. Vikas RC. Mechanical and Wear Properties of Carburized Mechanical and Wear Properties of Carburized. Int J Mod Trends Eng Sci. 2017;04(06):5.

113. Xiang S, Jonsson S, Hedström P, Zhu B, Odqvist J. Influence of ferritic nitrocarburizing on the high-temperature corrosion-fatigue properties of the Si-Mo-Al cast iron SiMo1000. Int J Fatigue. 2021;143(July 2020).

114. Suhadi A, Li CX, Bell T. Austenitic plasma nitrocarburising of carbon steel in N2 - H2 atmosphere with organic vapour additions. Surf Coatings Technol. 2006;200(14–15):4397–405.

115. Zhang ZL, Bell T. Structure and corrosion resistance of plasma nitrided stainless steel. Surf Eng. 1985;1(2):131–6.

116. De Souza SD, Olzon-Dionysio M, Basso RLO, De Souza S. Mössbauer spectroscopy study on the corrosion resistance of plasma nitrided ASTM F138 stainless steel in chloride solution. Mater Charact. 2010;61(10):992–9.

117. Li W, Li X, Dong H. Effect of tensile stress on the formation of S-phase during low-temperature plasma carburizing of 316L foil. Acta Mater. 2011;59(14):5765–74.

118. Lee I, Barua A. Behavior of the S-phase of plasma nitrocarburized 316L austenitic stainless steel on changing pulse frequency and discharge voltage at fixed pulse-off time. Surf Coatings Technol. 2016;307:1045–52.

119. Buhagiar J, Dong H. Low temperature plasma carbonitriding of ASTM F138 and ASTM F1586 biomedical stainless steels. Surf Eng. 2010;26(4):256–64.

120. Dong H. S-phase surface engineering of Fe-Cr, Co-Cr and Ni-Cr alloys. Vol. 55, International Materials Reviews. 2010.

121. Liu R. Surface Modification of ASTM F-1537 Co-Cr Alloy by Low Temperature Plasma Surface Alloying. The University of Birmingham; 2013.

122. Niinomi M, Boehlert CJ. Advances in Metallic Biomaterials. In 2015. p. 157–78. Available from: http://link.springer.com/10.1007/978-3-662-46836-4

123. Aherwar A, Singh AK, Patnaik A. Cobalt based alloy: A better choice biomaterial for hip implants. Trends Biomater Artif Organs. 2016;30(1):50–5.

124. Paul K. Chu, Shu Qin, Chung Chan, Nathan W. Cheung LAL. Plasma immersion ion implantation semiconductor processing - a fledgling technique for Paul. Vol. 17, Materials Science and Engineering. 1996.

125. Lutz J, Díaz C, García JA, Blawert C, Mändl S. Corrosion behaviour of medical CoCr alloy after nitrogen plasma immersion ion implantation. Surf Coatings Technol. 2011;205(8–9):3043–9.

126. Oliveira DB, Franco AR, Bozzi AC. Influence of low temperature plasma carbonitriding on cavitation erosion resistance of the Stellite 250 alloy – A preliminary evaluation. Wear. 2021;(September 2020):203653.

127. Chen J, Li XY, Bell T, Dong H. Improving the wear properties of Stellite 21 alloy by plasma surface alloying with carbon and nitrogen. 2008;264:157–65.

128. Korea S, Korea S, Braunschweig TU. Plasma diffusion treatment of stellite. 1995;75:425–30.

129. Brownlie F, Hodgkiess T, Pearson A, Galloway AM. Effect of nitriding on the corrosive wear performance of a single and double layer Stellite 6 weld cladding. Wear. 2017;376–377:1279–85.

130. Yao J, Ding Y, Liu R, Zhang Q, Wang L. Wear and corrosion performance of laser-clad low-carbon high-molybdenum Stellite alloys. Opt Laser Technol. 2018;107:32–45.

131. Singh R, Kumar D, Mishra SK, Tiwari SK. Laser cladding of Stellite 6 on stainless steel to enhance solid particle erosion and cavitation resistance. Surf Coatings Technol. 2014;251:87–97.

132. Przybylowicz J, Kusinski J. Laser cladding and erosive wear of Co-Mo-Cr-Si coatings. Surf Coatings Technol. 2000;125(1–3):13–8.

133. Sun S, Durandet Y, Brandt M. Parametric investigation of pulsed Nd: YAG laser cladding of stellite 6 on stainless steel. Surf Coatings Technol. 2005;194(2–3):225–31.

134. Huang Y. Characterization of dilution action in laser-induction hybrid cladding. Opt Laser Technol. 2011;43(5):965–73.

135. Ocelík V, de Oliveira U, de Boer M, de Hosson JTM. Thick Co-based coating on cast iron by side laser cladding: Analysis of processing conditions and coating properties. Surf Coatings Technol. 2007;201(12):5875–83.

136. Xie X, Yin F, Wang X, Ouyang X, Li M, Hu J. Corrosion Resistance to Molten Zinc of a Novel Cermet Coating Deposited by Activated Combustion High-Velocity Air Fuel (AC-HVAF). J Therm Spray Technol. 2019;28(6):1252–62.

137. Vuoristo P, Tuominen J, Nurminen J. Laser coating and thermal spraying - process basics and coating properties. Therm Spray 2005 Therm Spray Connect Explor its Surf potential! 2005;1270–7.

138. Jayakumar K, Senthil Kumar T, Shanmugarajan B. Review study of laser cladding processes on Ferrous substrates. Int J Adv Multidiscip Res. 2015;2(26):72–87.

139. Kusmoko, Ȧ A, Dunne, Ȧ D, Li, Ȧ H. A Comparative Study for Wear Resistant of Stellite 6 Coatings on Nickel Alloy Substrate Produced by Laser Cladding , HVOF and Plasma Spraying Techniques. Int J Curr Eng Technol. 2014;4(1):32–6.

140. Corvi F, Sadda SVR, Staurenghi G, Pellegrini M. Thresholding strategies to measure vessel density by optical coherence tomography angiography. Can J Ophthalmol. 2020;55(4):317–22.

141. Oliver WC, Pharr GM. An improved technique for determining hardness and elastic modulus using load and displacement sensing indentation experiments. 1992.

142. Milman Y V., Golubenko AA, Dub SN. Indentation size effect in nanohardness. Acta Mater. 2011;59(20):7480–7.

143. Leyland A, Matthews A. On the significance of the H/E ratio in wear control: A nanocomposite coating approach to optimised tribological behaviour. Wear. 2000;246(1–2):1–11.

144. Rebholz C, Leyland A, Larour P, Charitidis C, Logothetidis S, Matthews A. The effect of boron additions on the tribological behaviour of TiN coatings produced by electron-beam evaporative PVD. Surf Coatings Technol. 1999;116–119:648–53.

145. Doran M. Nanoindentation as Characterisation Tool for Wear Resistance in Stainless Steels. The Ohio State University; 2016.

146. Yu H, Ahmed R, Lovelock HDV, Davies S. Tribo-Mechanical Evaluations of Cobalt-Based (Stellite 4) Alloys Manufactured via HIPing and Casting. World Congr Eng. 2007;II(Stellite 4):2–7.

147. Yu H, Ahmed R, Lovelock HDV, Davies S. Influence of Manufacturing Process and Alloying Element Content on the Tribomechanical Properties of Cobalt-Based Alloys. J Tribol. 2009;131(1).

148. Liu R, Zhang JHYQL, Collier MXYR. Relations of Chemical Composition to Solidification Behavior and Associated Microstructure of Stellite Alloys. Metallogr Microstruct Anal. 2015;146–57.

149. Zafar S, Sharma AK. Materials Characterization Development and characterisations of WC – 12Co microwave clad. Mater Charact. 2014;96:241–8.

150. Gupta D, Sharma AK, Gupta D, Sharma AK. Microstructural Characterization of Cermet Cladding Developed Through Microwave Irradiation. 2012;21(October):2165–72.

151. Xu W. The Influence of Chemical Composition and Heat Treatment on Microstructure and Mechanical/Tribological Properties of Cobalt-based Tribaloy Alloys. Carleton University; 2005.

152. Yu H, Ahmed R, Villiers Lovelock de H, Davies H. Influence of Manufacturing Process and Alloying Element Content on the Tribomechanical Properties of Cobalt-Bases Alloys. J Tribol (Transactions ASME - F -). 2009;131(January):11601–6.

153. Snider JM. Zinc Pot Bearing Material Wear and Corrosion Characterization By. West Virgina University; 2004.

154. Xu W. The Influence of Chemical Composition and Heat Treatment on Microstructure and Mechanical/Tribological Properties of Cobalt-based Tribaloy Alloys. Dissertation. Carleton University; 2005.

155. Y.Bedolla-Gil, A. juarez-Hernandez, A. Perez-Unzueta, E. Garcia-Sanchez, R. Mercado-Solis, M.A.L H-R. Influence of heat treatments on mechanical properties of a biocompatility alloy ASTM F75. Rev Mex Física. 2009;55(1):1–5.

156. Lee SH, Takahashi E, Nomura N, Chiba A. Effect of heat treatment on microstructure and mechanical properties of Ni- and C-free Co-Cr-Mo alloys for medical applications. Nippon Kinzoku Gakkaishi/Journal Japan Inst Met. 2006;70(4):260–4.